

# Integration and Application of Passive Cooling Within a Wind Tower

Submitted in accordance with the requirements for the degree of Doctor  
of Philosophy

by

**John Kaiser Santos Calautit**

The University of Leeds  
School of Civil Engineering

August, 2013

The candidate confirms that the work submitted is his/her own, except where work which has formed part of jointly-authored publications has been included. The contribution of the candidate and the other authors to this work has been explicitly indicated below (**page iii**). The candidate confirms that appropriate credit has been given within the thesis where reference has been made to the work of others.

This copy has been supplied on the understanding that it is copyright material and that no quotation from the thesis may be published without proper acknowledgement

## Jointly-authored Publications Outline

**Title of publication no.1:** The Development of Commercial Wind Towers for Natural Ventilation: *A Review*

**Authors:** Ben Richard Hughes, John Kaiser Calautit, and Saud Ghani

**Journal:** Applied Energy

**Year:** 2012

**Volume:** 92, 606-627

I wrote sections 3 - 7 and this reviewed the different designs of wind tower systems and integrated cooling techniques which is now in chapter 2 (Literature Review) of the thesis, co-authors wrote sections 1, 2, and 8 which highlighted the recent advancements in the development of wind tower systems.

**Title of publication no.2:** A Numerical Investigation into the Feasibility of Integrating Green Building Technologies into Row Houses in the Middle East

**Authors:** John Kaiser Calautit, Ben Hughes, and Saud Ghani

**Journal:** Architectural Science Review Special Issue

**Year:** 2012

**Volume:** 1, 1-18

I wrote sections 4, 5, 6 and this summarised the CFD codes and methods for simulating air flows in a naturally ventilated building which is now in chapter 2 (Literature Review) of the thesis, co-authors wrote sections 1, 2, and 3 which highlighted the different design of row house building and discussed the feasibility of retrofitting traditional architecture with green technologies.

**Title of publication no.3:** Comparison between evaporative cooling and a heat pipe assisted thermal loop for a commercial wind tower in hot and dry climatic conditions

**Authors:** John Kaiser Calautit, Hassam Chaudhry, Ben Hughes, and Saud Ghani

**Journal:** Applied Energy

**Year:** 2013

**Volume:** 101, 740-755

I wrote sections 4, 5, 6, 7 and this summarised the current CFD work which compared the thermal performance of a evaporative cooling tower with a wind tower system incorporating heat transfer devices. The CFD methods are now in chapter 3 (CFD Theory and Modelling) of the thesis. The co-authors wrote sections 2, 3 and 4 which focused on simulating the multiphase flow of the heat transfer devices.

**Title of publication no.4:** CFD Analysis of a heat transfer device integrated wind tower system for hot and dry climate

**Authors:** John Kaiser Calautit, Ben Hughes, Hassam Chaudhry, and Saud Ghani

**Journal:** Applied Energy

**Year:** 2013

**Volume:** *In press*

I wrote sections 2, 4, 5, 6 and this summarised the current CFD work on the ventilation performance analysis of the wind tower integrated with horizontal and vertical heat transfer device, which is now in Chapter 3 (CFD Theory and Modelling) of the thesis, the co-authors wrote sections 1 and 7.

## **Acknowledgements**

This thesis was completed with the support of a number of important individuals and organisations to whom I am very thankful. First of all, I would like to thank my supervisor, Dr. Ben Richard Hughes for his constant support, guidance and encouragement throughout these years of study, not to mention his advice and unsurpassed scientific insights for which I am extremely grateful. Thank you for giving me the opportunity to work with you on this research project.

I would like to thank my parents and sister. They were always supporting me and encouraging me with their best wishes.

I would like to acknowledge all the support and encouragement I have received from my friends. Special thanks must go to my friend and research colleague, Hassam Chaudhry, for his advice and friendship, it has been greatly appreciated.

I would also like to acknowledge the academic and technical support of the University of Leeds and its staff for providing the facilities and academic support I required.

Finally, this project was made possible by a NPRP 09-138-2-059 grant from the Qatar National Research Fund (a member of the Qatar Foundation).

## **Abstract**

The aim of this work was to combine low energy heat transfer devices with a passive ventilation terminal to meet the internal comfort criteria in extreme external conditions using non-mechanical means. Heat transfer devices were installed inside the passive terminal of a wind tower unit, highlighting the potential to achieve minimal restriction in the external air flow stream while ensuring maximum contact time, thus optimising the cooling duty of the device. A numerical analysis was conducted using Computational Fluid Dynamics (CFD) software to simulate and analyse the air flow pattern, pressure and temperature distribution around and through the wind tower to a test room. Experimental investigations were carried out using a closed-loop subsonic wind tunnel at 1:10 scale to assess the accuracy of the simulation results. Pressure coefficients distribution, internal air speed and volumetric airflow were measured for a range of external conditions. Smoke visualisation testing enabled the detailed study and analysis of the air flow patterns in and around the wind tower models for different air incident angles.

The proposed cooling system was capable of reducing the air temperatures up to 15 K, depending on the configuration and operating conditions. Initial findings revealed that height was not a factor for the proposed heat transfer device arrangement, making it highly viable for commercial roof-mounted wind tower systems. Another advantage of the proposed system over the traditional evaporative cooling systems was the non-reliance on the constant supply of water to continue the cooling cycle.

In addition, four-sided and one-sided wind towers were utilised as benchmarks for the CFD investigations. Two heat transfer device (HTD) configurations were incorporated in the wind tower models namely vertical and horizontal HTD arrangements. Furthermore, the CFD model was also used to investigate the effect of the addition of extended surfaces and porous media on the thermal performance of the cooling wind tower.

The thermal environment of the test room equipped with a heat transfer device cooling wind tower was simulated and evaluated using Fluent Airpak. The thermal comfort was studied using the PMV index scale. The elements necessary to calculate the PMV and PPD were taken from the initial CFD and experimental results.

## Table of Contents

<b>Jointly-authored Publications Outline .....</b>	<b>iii</b>
<b>Acknowledgements.....</b>	<b>iv</b>
<b>Abstract.....</b>	<b>v</b>
<b>Table of Contents .....</b>	<b>vi</b>
<b>List of Tables .....</b>	<b>xi</b>
<b>List of Figures.....</b>	<b>xiii</b>
<b>Preface.....</b>	<b>xxvi</b>
<b>Nomenclature.....</b>	<b>xxviii</b>
<b>List of Abbreviation .....</b>	<b>xxx</b>
<b>Chapter 1 Introduction.....</b>	<b>1</b>
1.1 Wind towers .....	3
1.2 Aims and objectives .....	6
1.3 Project methodology .....	7
1.4 Thesis layout .....	8
1.5 Summary .....	9
<b>Chapter 2 Literature Review .....</b>	<b>10</b>
2.1 Introduction .....	10
2.2 Thermal comfort.....	10
2.2.1 Thermal comfort approaches.....	12
2.2.2 Thermal comfort in naturally ventilated buildings .....	14
2.3 Natural ventilation strategies.....	15
2.3.1 Solar chimneys .....	18
2.3.2 Structural night ventilation.....	21
2.3.3 Courtyards .....	22
2.3.4 Wind escapes and air vents .....	24
2.3.5 Wind scoops and suction cowls .....	25
2.3.6 Traditional wind towers .....	26
2.3.6.1 One-sided wind tower.....	28
2.3.6.2 Two-sided wind tower .....	32
2.3.6.3 Multi-directional wind tower.....	34
2.3.6.4 Limitations to traditional wind tower systems .....	38
2.3.7 Commercial wind towers .....	38
2.3.7.1 Numerical investigations using CFD.....	42

2.3.7.2 Experimental investigations and validation techniques.....	49
2.4 Wind tower cooling techniques.....	53
2.4.1 Evaporative cooling .....	54
2.4.1.1 Wind tower with wetted column and wetted surface .....	54
2.4.1.2 Wind towers integrated with ground cooling .....	59
2.5 Research gap .....	60
2.6 Summary .....	62
<b>Chapter 3 CFD Theory and Modelling .....</b>	<b>63</b>
3.1 Introduction .....	63
3.2 Physical domain .....	63
3.3 Computational domain .....	65
3.3.1 Mesh generation .....	66
3.3.2 Examining the mesh .....	68
3.3.3 Implementation of boundary conditions.....	71
3.3.4 Grid adaptation .....	75
3.4 Solving the model .....	76
3.4.1 Continuity equation .....	77
3.4.2 Momentum conservation equation .....	77
3.4.3 Energy equation.....	79
3.4.4 Navier-Stokes equations .....	79
3.4.5 Standard k- $\epsilon$ model transport equation.....	80
3.4.6 Species transport equation .....	80
3.5 Solution algorithm.....	81
3.6 Solution convergence .....	83
3.7 Post processing.....	84
3.8 Quantification of CFD uncertainties .....	85
3.9 Computational Fluid Dynamics (CFD) Modelling .....	86
3.9.1 Wind tower benchmark model .....	86
3.9.2 Wind tower device integrated with vertical and horizontal HTD arrangement .....	88
3.9.3 Wind tower device integrated with HTD arrangement and extended surfaces.....	91
3.9.4 Wind tower device integrated with HTD arrangement and porous medium .....	94
3.9.5 Thermal comfort model .....	98
3.10 Summary .....	102

<b>Chapter 4 Experimental techniques</b> .....	<b>103</b>
4.1 Introduction .....	103
4.2 Subsonic closed-loop wind tunnel .....	103
4.2.1 Operation of wind tunnel .....	105
4.2.2 Wind tunnel CFD and experimental modelling .....	106
4.2.3 Flow characterisation of wind tunnel.....	109
4.2.3.1 Test section wind profile .....	110
4.2.3.2 Flow uniformity and angularity.....	111
4.2.3.3 Wind tunnel test section with block model .....	113
4.3 Model scaling requirements and simulation of wind .....	115
4.3.1 Consistent modelling of all lengths.....	115
4.3.2 Blockage consideration .....	116
4.3.3 Selection of velocity scale.....	116
4.4 Experimental scale model .....	117
4.4.1 Benchmark wind tower model .....	119
4.4.2 Wind tower with heat transfer devices.....	121
4.4.3 Wind tower with finned heat transfer devices.....	123
4.4.4 Wind tower with heat transfer devices and porous mesh.....	124
4.4.5 Test room model .....	125
4.5 Experimental set-up and measurement procedures.....	126
4.5.1 Indoor airflow distribution .....	126
4.5.2 Volumetric flow supply rate .....	127
4.5.3 External airflow measurement .....	129
4.5.4 Pressure coefficients.....	129
4.5.5 Smoke visualisation .....	132
4.6 Experimental test equipment.....	134
4.6.1 Hot-wire anemometer and pitot-static tube .....	134
4.6.2 Pressure sensor .....	139
4.6.3 Data acquisition system .....	140
4.6.4 Smoke generator .....	141
4.6.5 High speed camera.....	141
4.7 Summary .....	142
<b>Chapter 5 CFD Results</b> .....	<b>143</b>
5.1 Introduction .....	143
5.2 Benchmark models.....	144

5.2.1	Four-sided wind tower .....	144
5.2.2	One-sided wind tower .....	149
5.3	Heat transfer device (HTD) integrated wind tower.....	155
5.3.1	Vertical HTD arrangement.....	156
5.3.2	Horizontal HTD arrangement .....	165
5.4	Heat transfer device (HTD) integrated wind tower with extended surfaces .....	175
5.4.1	Vertical HTD arrangement with extended surfaces .....	175
5.4.2	Horizontal HTD arrangement with extended surfaces.....	179
5.5	Heat transfer device (HTD) integrated wind tower with porous medium.....	182
5.5.1	Vertical HTD arrangement with porous medium.....	182
5.5.2	Horizontal HTD arrangement with porous medium .....	186
5.6	Thermal comfort modelling .....	189
5.6.1	Benchmark wind tower model .....	190
5.6.2	Wind tower with heat transfer device .....	193
5.6.3	Wind tower with heat transfer device and extended surfaces .....	195
5.7	Summary .....	197
<b>Chapter 6</b>	<b>Experimental Results.....</b>	<b>198</b>
6.1	Introduction .....	198
6.2	Benchmark wind tower testing .....	198
6.2.1	Indoor airflow distribution .....	199
6.2.2	Volumetric flow supply rate .....	200
6.2.3	Flow visualisation .....	204
6.3	Wind tower with heat transfer device .....	209
6.4	Wind tower with heat transfer device and extended surface.....	213
6.5	Wind tower with heat transfer device and porous medium.....	216
6.6	Summary .....	220
<b>Chapter 7</b>	<b>Validation of CFD model .....</b>	<b>221</b>
7.1	Introduction .....	221
7.2	Benchmark model validation .....	221
7.2.1	Four-sided wind tower .....	224
7.2.2	One-sided wind tower .....	227
7.3	Validation of wind tower model with heat transfer devices .....	231
7.4	Validation of wind tower model with heat transfer devices and extended surfaces.....	234

7.5 Validation of wind tower model with heat transfer devices and porous medium .....	236
7.6 Quantification of CFD uncertainties .....	238
7.7 Summary .....	238
<b>Chapter 8 Conclusions and Future Work.....</b>	<b>239</b>
8.1 Conclusions .....	239
8.2 Contribution to knowledge.....	241
8.3 Recommendations for further work .....	242
<b>List of References .....</b>	<b>244</b>
<b>Appendix A Wind Tunnel Design and Calculations .....</b>	<b>251</b>
A.1 Introduction .....	251
A.2 Test section.....	251
A.3 Contraction section.....	252
A.4 Diffuser section .....	253
A.5 Guide vanes .....	254
A.6 Total pressure loss .....	255
<b>Appendix B Wind Tunnel CFD Modelling .....</b>	<b>256</b>
B.1 Introduction .....	256
B.2 Computational domain .....	256
B.3 Solution methods .....	258
B.4 Grid adaptation .....	259
<b>Appendix Wind Tunnel Experimental Techniques .....</b>	<b>260</b>
C.1 Introduction .....	260
C.2 Empty wind tunnel test section.....	260
C.2.1 Flow turbulence measurements .....	261
C.2.2 Uniformity of the flow field .....	261
C.3 Wind tunnel test section with test block.....	262
C.3.1 Pressure coefficients .....	262
<b>Appendix D Wind Tunnel CFD and Experimental Results .....</b>	<b>264</b>
D.1 Introduction .....	264
D.2 Empty wind tunnel test section .....	264
D.2.1 Benchmark case: no guide vanes .....	264
D.2.2 Configuration 2: Upstream guide vanes.....	266
D.2.3 Configuration 3: Downstream guide vanes.....	267
D.2.4 Configuration 4: Upstream and Downstream guide vanes.....	269
D.3 Wind tunnel test section with test block.....	273

## List of Tables

<b>Table 3.1</b>	Range of skewness values and cell quality [FLUENT guide, 2006].....	69
<b>Table 3.2</b>	Summary of the CFD model boundary conditions.....	73
<b>Table 3.3</b>	Summary of the CFD model boundary conditions [Calautit <i>et al.</i> , 2012]..	74
<b>Table 3.4</b>	Summary of benchmark wind tower configurations. ....	87
<b>Table 3.5</b>	Summary of HTD integrated wind tower configurations.....	91
<b>Table 3.6</b>	Summary of HTD integrated wind tower with extended surfaces. ....	94
<b>Table 3.7</b>	Summary of HTD integrated wind tower with porous media. ....	97
<b>Table 3.8</b>	Summary of the CFD analysis. ....	97
<b>Table 3.9</b>	The 7-point thermal sensation scale. ....	99
<b>Table 4.1</b>	Summary of the design specification and dimensions of the wind tunnel components... ..	106
<b>Table 4.2</b>	Technical specifications of Testo 425 hot-wire anemometer.....	136
<b>Table 4.3</b>	Technical specifications of DPM ST650 Micro manometer.....	138
<b>Table 5.1</b>	Summary of the design of CFD modelling and analysis.....	143
<b>Table 5.2</b>	Summary of the benchmark geometry specifications .....	144
<b>Table 5.3</b>	Simulation results with the benchmark four-sided wind tower.....	149
<b>Table 5.4</b>	Summary of the benchmark geometry specifications. ....	150
<b>Table 5.5</b>	Simulation results with the benchmark four-sided wind tower.....	155
<b>Table 5.6</b>	Summary of the four-sided wind tower with HTD specifications .....	156
<b>Table 5.7</b>	Simulation results with the four-sided wind tower with HTD (Config 1). ....	165
<b>Table 5.8</b>	Simulation results with the four-sided wind tower with HTD (Config 2). ....	165
<b>Table 5.9</b>	Summary of the benchmark geometry specifications (one-sided wind tower with heat transfer devices). ....	166
<b>Table 5.10</b>	Simulation results with the one-sided wind tower with the horizontal HTD (Config 1).....	174
<b>Table 5.11</b>	Simulation results with the one-sided wind tower with the horizontal HTD (Config 2).....	175
<b>Table 5.12</b>	Simulation results with the four-sided wind tower with extended surfaces.....	179
<b>Table 5.13</b>	Simulation results with the one-sided wind tower with extended surfaces.....	182

<b>Table 5.14</b> Simulation results with the four-sided wind tower with porous medium.....	185
<b>Table 5.15</b> Simulation results with the one-sided wind tower with porous medium.....	189
<b>Table 5.16</b> Summary of the thermal comfort model analysis case 1..	190
<b>Table 5.17</b> Summary of the thermal comfort model analysis case 2..	193
<b>Table 5.18</b> Summary of the thermal comfort model analysis case 3. ....	195
<b>Table 6.1</b> Test room with four-sided wind tower sample points values [m/s]..	200
<b>Table 6.2</b> Test room with one-sided wind tower sample points values [m/s]..	200
<b>Table 6.3</b> Measured values of air flow velocity through the four-sided wind tower [m/s]. ....	201
<b>Table 6.4</b> Measured values of air flow velocity through the one-sided wind tower [m/s]. ....	203
<b>Table 6.5</b> Measured values of air flow velocity through the four-sided wind tower with heat transfer devices config. 1 [m/s]. ....	209
<b>Table 6.6</b> Measured values of air flow velocity through the one-sided wind tower with heat transfer devices config. 1.[m/s] .....	210
<b>Table 6.7</b> Measured values of air flow velocity through the four-sided wind tower incorporating heat transfer devices and extended surfaces [m/s]. ....	213
<b>Table 6.8</b> Measured values of air flow velocity through the one-sided wind tower with heat transfer devices and extended surfaces [m/s]. ....	214
<b>Table 6.9</b> Measured values of air flow velocity through the four-sided wind tower with heat transfer devices and porous medium [m/s]. ....	217
<b>Table 6.10</b> Measured values of air flow velocity through the one-sided wind tower with heat transfer devices and porous medium [m/s]. ....	218
<b>Table 7.1</b> Comparison between measured and CFD results for mean velocity at points A - G (X, Y, Z) around the four-sided wind tower model .....	224
<b>Table 7.2</b> Comparison between measured and CFD results for mean velocity at points A - G (X, Y, Z) around the one-sided wind tower model .....	232
<b>Table A.1</b> Summary of sectional pressure head losses.....	255
<b>Table B.1</b> Type and distribution of grid in the wind tunnel .....	257
<b>Table B.2</b> Summary of the CFD model boundary conditions. ....	259
<b>Table D.1</b> Percentage uniformity of flow in test section for the different guide vane configurations .....	272

## List of Figures

<b>Figure 1.1</b> Global energy consumption pie-chart. Potential building energy savings could be as much as total transport energy use today [WBCSD, 2011].	1
<b>Figure 1.2</b> Schematic view of an air handling unit (AHU) [Lazzarin and Castellotti, 2007]	2
<b>Figure 1.3</b> A flow diagram representing ventilation through a multi-direction wind tower device [Hughes <i>et al.</i> , 2012].	4
<b>Figure 1.4</b> A flow diagram representing ventilation through an evaporative cooling and a compact roof-mounted wind tower system .	5
<b>Figure 1.5</b> Project methodology flow chart.	8
<b>Figure 2.1</b> Heat from the human body is loss through sensible heat transfer [DPS, 2008].	11
<b>Figure 2.2</b> Relationship between Predicted Mean Vote and Predicted of percentage dissatisfied [Djongyang <i>et al.</i> , 2010].	12
<b>Figure 2.3</b> Comparison of the overall thermal comfort sensation for old buildings and new buildings [Ealiwaa <i>et al.</i> , 2001].	13
<b>Figure 2.4</b> Wind creates a positive pressure on the windward side of a structure and a negative pressure on the leeward side .	16
<b>Figure 2.5</b> Function of a wind tower in hot and dry region during summer day-time and night-time [Hughes <i>et al.</i> , 2012].	17
<b>Figure 2.6</b> Solar-wind tower system integrated to a naturally ventilated building [Hughes <i>et al.</i> , 2012].	19
<b>Figure 2.7</b> Cross-sectional diagram showing how a courtyard is used to regulate thermal environment of a typical Mzab dwelling [Bouchair, 2004].	23
<b>Figure 2.8</b> A funnel shaped roof ventilator illustrating Venturi effect [Lechner, 2001].	24
<b>Figure 2.9</b> Flow diagram representing ventilation through a structure with a wind escape and air vent [Hughes <i>et al.</i> , 2012].	25
<b>Figure 2.10</b> Stationary and omnidirectional wind scoop with single guide vane. [Hughes <i>et al.</i> , 2012]	26
<b>Figure 2.11</b> CFD analysis showing the positive pressure on wind ward façade and negative pressure on leeward [Hughes <i>et al.</i> , 2012].	27
<b>Figure 2.12</b> CFD analysis showing (a) negative pressure over the roof (b) positive pressure on the wind ward side of the wind tower and negative on the leeward [Hughes <i>et al.</i> , 2012].	28
<b>Figure 2.13</b> Traditional wind towers with different number of openings (a) one-sided, (b) two-sided, (c) four- sided, (d) octahedral [Hughes <i>et al.</i> , 2012].	28

<b>Figure 2.14</b> A flow diagram representing ventilation through a room with a one-sided wind tower [Hughes <i>et al.</i> , 2012]. .....	29
<b>Figure 2.15</b> Vernacular architecture integrated with Malkaf wind catchers and a domed roof. [Hughes <i>et al.</i> , 2012] .....	30
<b>Figure 2.16</b> Smoke visualisation testing, for (a) isolated wind catcher model and (b) placing under the short upstream object [Montazeri and Azizian, 2008].....	31
<b>Figure 2.17</b> Smoke visualisation testing shows the effect of placing: (a) one malkaf in front in combination with outlet openings in the back (b) two malkafs (windward and leeward) on the air flow pattern in the model [Attia and Herde, 2009].....	32
<b>Figure 2.18</b> A flow diagram representing ventilation through a room with a two-sided wind tower [Hughes <i>et al.</i> , 2012]. .....	33
<b>Figure 2.19</b> Velocity streamline inside the building with a two-sided wind tower for various approaching air incident angles [Montazeri <i>et al.</i> , 2010].....	34
<b>Figure 2.20</b> Flow diagram representing ventilation through a traditional structure incorporating Badgir towers [Hughes <i>et al.</i> , 2012] .....	35
<b>Figure 2.21</b> Four-sided wind tower (a) with the incident angle at 0° (b) with the incident angle at 45° [Hughes <i>et al.</i> , 2012].....	35
<b>Figure 2.22</b> Variation of net ventilated air flow rate into the building for the wind catcher models [Montazeri and Azizian, 2011].. .....	37
<b>Figure 2.23</b> Commercial wind tower device integrated with PV-panels [Hughes and Ghani, 2008].....	40
<b>Figure 2.24</b> Modern wind tower devices with damper control system [Hughes <i>et al.</i> , 2012] .....	41
<b>Figure 2.25</b> Schematic of a wind tower system integrated with a solar powered fan [Hughes <i>et al.</i> , 2012].....	42
<b>Figure 2.26</b> Effects on air velocity and pressure by damper angle variations [Hughes and Ghani, 2009].. .....	43
<b>Figure 2.27</b> The effect on wind vent fresh air delivery rates by an increase in external wind velocity [Hughes and Ghani, 2008].....	44
<b>Figure 2.28</b> Effect of external louver angles on the wind tower performance [Hughes and Ghani, 2009] .....	45
<b>Figure 2.29</b> Reference length of the wind catcher louver, $L_{reference} = L_{gap} \frac{A-B}{\sin \alpha}$ [Liu <i>et al.</i> , 2010].....	46
<b>Figure 2.30</b> (a) Schematic diagram of the wind tower showing the position of the fans (b) Analysis of fresh air supply rates per occupant at three different fan positions for 20 occupants [Hughes and Ghani, 2010].. .....	47
<b>Figure 2.31</b> CFD analysis showing the velocity streamlines of the air flow in and around the row house model integrated with wind towers [Calautit <i>et al.</i> , 2012]. .....	48
<b>Figure 2.32</b> CFD analysis showing the pressure difference across a (a) circular wind tower and (b) square wind tower.....	49

<b>Figure 2.33</b> Open-circuit wind tunnel for testing a fan-assisted wind tower [Priyadarsini <i>et al.</i> , 2003].....	51
<b>Figure 2.34</b> Experimental setup in the wind tunnel [Elmualim, 2006].....	51
<b>Figure 2.35</b> Schematic of the ventilation measurement setup [Su <i>et al.</i> , 2007].....	52
<b>Figure 2.36</b> Far-field experimental setup [Hughes and Cheuk-Ming 2011].....	52
<b>Figure 2.37</b> Concept design of a passive wind tower integrated with different cooling devices [Hughes <i>et al.</i> , 2011].....	53
<b>Figure 2.38</b> Wind tower integrated with wetted columns or clay conduits [Badran, 2003].....	55
<b>Figure 2.39</b> Thermal performance of a wind tower incorporating evaporative cooling devices [Hughes <i>et al.</i> , 2012].....	57
<b>Figure 2.40</b> Variation of temperature of airflow from the wind tower (height=10 m) inlet to outlet [Kalantar, 2009].....	58
<b>Figure 2.41</b> Wind tower integrated with wetted columns or clay conduits [Hughes <i>et al.</i> , 2012].....	59
<b>Figure 2.42</b> Wind tower systems integrated with underground cooling. [Hughes <i>et al.</i> , 2012] .....	60
<b>Figure 3.1</b> Extraction of fluid domain from a solid CAD model representing a room.. .....	64
<b>Figure 3.2</b> Physical representation of the geometry under investigation.. .....	65
<b>Figure 3.3</b> 2D hybrid grid generation around an aerofoil [Dussin <i>et al.</i> , 2009].....	66
<b>Figure 3.4</b> Meshing process in ANSYS Meshing software. ....	67
<b>Figure 3.5</b> (a) actual wind tower model inside the test section (b) view of the computational mesh of the wind tower model and test room .....	67
<b>Figure 3.6</b> Schematic diagram representing the complex face geometry face elements of the louver section.....	68
<b>Figure 3.7</b> Ideal and skewed triangle and quadrilaterals [FLUENT Guide, 2006].. .....	69
<b>Figure 3.8</b> Wall surface contours showing the equiangle skew.. .....	70
<b>Figure 3.9</b> Wall surface contours showing the $y^+$ value.....	71
<b>Figure 3.10</b> CFD flow domain representation of the micro and macro climate environment for the analysis of a four-sided wind tower.. .....	72
<b>Figure 3.11</b> CFD flow domain representation of the micro and macro climate environment for the analysis of a one-sided wind tower with HTD.....	73
<b>Figure 3.12</b> Actual Meteorological Year (AMY) data file for Doha, Qatar [Weather Analytics Station™, 2012].....	74
<b>Figure 3.13</b> Posterior error on the average velocity in the test-section using h-p grid adaptation method.....	76
<b>Figure 3.14</b> Viscous stress components applied to the faces of the control volume by the surrounding fluid.....	78

<b>Figure 3.15</b> Simple algorithm flowchart [Ahmed, 1998].....	82
<b>Figure 3.16</b> Converged solution residuals.....	83
<b>Figure 3.17</b> Solution residuals with higher convergence criteria.....	84
<b>Figure 3.18</b> ANSYS post processing tools.....	84
<b>Figure 3.19</b> CAD model of the four-sided wind tower mounted on the test room .....	86
<b>Figure 3.20</b> CAD model of the one-sided wind tower mounted on the test room.....	87
<b>Figure 3.21</b> Flow diagram representing ventilation and cooling through a heat transfer device integrated wind tower system.....	88
<b>Figure 3.22</b> Heat transfer device configurations [Calautit <i>et al.</i> , 2012].....	89
<b>Figure 3.23</b> CAD model schematic of the wind tower incorporating vertical HTD arrangement.....	90
<b>Figure 3.24</b> CAD model schematic of the wind tower incorporating horizontal HTD arrangement.....	90
<b>Figure 3.25</b> Schematic of the proposed wind tower systems incorporating vertical heat transfer devices with extended surfaces. ....	92
<b>Figure 3.26</b> Schematic of the extended surface plate for the vertical arrangement.....	93
<b>Figure 3.27</b> Schematic of the proposed wind tower systems incorporating horizontal heat transfer devices with extended surfaces. ....	93
<b>Figure 3.28</b> Schematic of the extended surface plate for the horizontal arrangement.....	93
<b>Figure 3.29</b> (a) Flow through a pipe with and without a porous mesh [Autodesk, 2008] (b) Uneven flow distribution inside a wind tower. ....	95
<b>Figure 3.30</b> Schematic of the proposed wind tower systems incorporating vertical heat transfer devices with porous medium.....	95
<b>Figure 3.31</b> Schematic of the proposed wind tower systems incorporating horizontal heat transfer devices with porous medium.....	96
<b>Figure 3.32</b> Thermal comfort analysis .....	98
<b>Figure 3.33</b> Computational domain of the test room model. ....	101
<b>Figure 3.34</b> Top view of the computational model of the test room showing occupants details and position.....	102
<b>Figure 4.1</b> Side view of the closed-loop subsonic wind tunnel facility for investigating the ventilation performance of the wind tower device: (a) final wind tunnel design (b) CAD model assembly for fabrication.....	104
<b>Figure 4.2</b> CFD model of the entire closed-circuit wind tunnel showing the boundary condition and flow direction. ....	107
<b>Figure 4.3</b> Wind tunnel guide vane and splitting plate design.....	108
<b>Figure 4.4</b> Top view of the test section showing the measurement positions (P01 - P09) and coordinates for the case of an empty test section. Dimensions in meters. ....	108

<b>Figure 4.5</b> Velocity streamline for configuration 4: upstream and downstream guide vanes.....	109
<b>Figure 4.6</b> Contours of velocity magnitude in a (a) vertical plane and (b) horizontal plane at 0.250 m height of the test section for the wind tunnel with upstream and downstream guide vanes.....	110
<b>Figure 4.7</b> Comparison between the (a) dimensionless mean velocity and (b) turbulence intensity of the flow at the test section for the different wind tunnel configurations (X = 0.25 m, P06). Highlighted (red) data points show measured wind tunnel values.....	111
<b>Figure 4.8</b> Comparison of the CFD and experimental results (P01 – P09) for the percentage uniformity of flow at: (a) Y = 0.25 m and (b) Y = 0.125 m (Configuration 4).....	112
<b>Figure 4.9</b> Flow angularity variation across the test section for different guide vane configurations: (a) X = 0.125 m, (b) Y = 0.250 m and (c) Y = 0.375 m. Red dotted line at $\pm 0.5^\circ$ .....	113
<b>Figure 4.10</b> Contours of velocity magnitude inside the wind tunnel with block test model.....	114
<b>Figure 4.11</b> Comparison between CFD and experimental values for surface pressure coefficients around the block model. Dotted lines represent 10 % error percentage.....	115
<b>Figure 4.12</b> Test section blockage ratio .....	116
<b>Figure 4.13</b> 3D prototyping system.....	118
<b>Figure 4.14</b> 3D prototyping software automatically creates tool paths for the RP machine .....	118
<b>Figure 4.15</b> (a) ABS material (b) rapid prototyping machine axis.....	119
<b>Figure 4.16</b> A 1:10 three-dimensional CAD model of the four-sided wind tower design (a) and the resulting 3D prototype model (b, c and d) built using the 3D printer.....	120
<b>Figure 4.17</b> Wind tower louver design and configuration. Dimensions in millimetres.....	120
<b>Figure 4.18</b> A 1:10 three-dimensional CAD model of the one-sided wind tower design (a) and the resulting 3D prototype model (b, c and d) built using the 3D printer.....	121
<b>Figure 4.19</b> A 1:10 three-dimensional CAD model of the four-sided wind tower design incorporating vertical HTD (a) and the resulting 3D prototype model (b, c and d) built using the 3D printer.....	122
<b>Figure 4.20</b> A 1:10 three-dimensional CAD model of the one-sided wind tower design incorporating horizontal HTD (a) and the resulting 3D prototype model (b, c and d) built using the 3D printer. Dimensions in meters. ....	123
<b>Figure 4.21</b> 1:10 prototype model of the four-sided wind tower design incorporating vertical HTD with extended surfaces. ....	124
<b>Figure 4.22</b> 1:10 prototype model of the one-sided wind tower design incorporating horizontal HTD with extended surfaces. ....	124

<b>Figure 4.23</b> 1:10 prototype model of the four-sided wind tower design incorporating horizontal HTD with porous mesh .....	125
<b>Figure 4.24</b> 1:10 prototype model of the one-sided wind tower design incorporating horizontal HTD with porous mesh .....	125
<b>Figure 4.25</b> 1:10 scale model of the test chamber mounted below the rotating wind tower system .....	126
<b>Figure 4.26</b> Measurement points inside the test section.....	127
<b>Figure 4.27</b> Section view of the four sided wind tower supply and exhausts channels showing the location of the measurement points (dimensions in mm).. .....	128
<b>Figure 4.28</b> Section view of the one sided wind tower supply and exhausts channels showing the location of the measurement points (dimensions in mm).. .....	128
<b>Figure 4.29</b> Top view of the test section showing the hot-wire anemometer measurement positions and coordinates with the wind tower test model. Dimensions in meters.....	129
<b>Figure 4.30</b> Surface pressure measurement setup .....	130
<b>Figure 4.31</b> Pressure tap locations and dimensions (four-sided wind tower). .....	131
<b>Figure 4.32</b> Pressure tap locations and dimensions (one-sided wind tower).. .....	131
<b>Figure 4.33</b> Test setup: block model inside the test section.....	132
<b>Figure 4.34</b> Wind tunnel smoke visualisation set-up.....	133
<b>Figure 4.35</b> Wind tower models flow visualisation setup.....	133
<b>Figure 4.36</b> Schematic of the test section with the instruments and data acquisition.....	134
<b>Figure 4.37</b> Testo 425 hot-wire anemometer.....	135
<b>Figure 4.38</b> Schematic of the Pitot-static tube .....	136
<b>Figure 4.39</b> 166T Telescoping Pitot-static tube.....	137
<b>Figure 4.40</b> DPM ST650 Micromanometer pressure connection.....	138
<b>Figure 4.41</b> (a) Testo 425 hot wire anemometer probe response to angle (b) Yaw angle error for 166T ellipsoidal Pitot-static tube.....	139
<b>Figure 4.42</b> DSA3217 pressure scanner.....	140
<b>Figure 4.43</b> DSALink3 Interface.....	140
<b>Figure 4.44</b> AFA 10 Smoke generator unit.....	141
<b>Figure 4.45</b> Motionblitz EoSens Cube7 high speed camera.....	142
<b>Figure 5.1</b> Benchmark four-sided wind tower. ....	144
<b>Figure 5.2</b> Velocity streamlines showing the flow distribution inside the test room. ....	145
<b>Figure 5.3</b> Velocity contour plot of a cross sectional plane in the test room with an inlet velocity of 3 m/s.....	146

<b>Figure 5.4</b> Ventilation performance at various external wind speeds.....	147
<b>Figure 5.5</b> Velocity contour plot of a horizontal plane (diffuser) inside the wind tower channel at different wind angles. ....	147
<b>Figure 5.6</b> Volumetric airflow through the wind tower quadrants for different wind directions.....	148
<b>Figure 5.7</b> Static pressure contour plot of a cross sectional plane in the test room with an inlet velocity of 3 m/s.....	149
<b>Figure 5.8</b> Benchmark one-sided wind tower. ....	150
<b>Figure 5.9</b> Velocity streamlines showing the flow distribution inside the test room with a one-sided wind tower.....	151
<b>Figure 5.10</b> Velocity contour plot of a cross sectional plane in the test room with an inlet velocity of 3 m/s.....	152
<b>Figure 5.11</b> Ventilation performance at various external wind speeds. ....	152
<b>Figure 5.12</b> Velocity contour plot of a horizontal plane (diffuser) inside the wind tower channel at different wind angles.. ....	153
<b>Figure 5.13</b> Volumetric airflow through the wind tower inlet and window opening.....	154
<b>Figure 5.14</b> Static pressure contour of a cross-sectional plane inside the micro-macro climate domain.. ....	155
<b>Figure 5.15</b> Four-sided wind tower with heat transfer devices.....	156
<b>Figure 5.16</b> Streamline representing the temperature distribution inside the test room with a four-sided wind tower incorporating heat transfer devices (Config 2).....	157
<b>Figure 5.17</b> Velocity contour of a mid-plane inside the test room with a wind tower incorporating vertical HTD arrangement (Configuration 1).....	158
<b>Figure 5.18</b> Velocity contour of a mid-plane inside the test room with a wind tower incorporating vertical HTD arrangement (Configuration 2).....	158
<b>Figure 5.19</b> Comparison between the average indoor air flow speed at various external wind speeds (Vertical HTD Config 1 and 2).....	159
<b>Figure 5.20</b> Static pressure contour of a cross-sectional plane inside the micro-macro climate domain (Configuration 1).....	159
<b>Figure 5.21</b> Static pressure contour of a cross-sectional plane inside the micro-macro climate domain (Configuration 2).....	160
<b>Figure 5.22</b> Temperature contour plot of a cross sectional plane in the test room with an inlet temperature of 318 K (vertical HTD Configuration 1). ....	161
<b>Figure 5.23</b> Temperature contour plot of a cross sectional plane in the test room with an inlet temperature of 318 K (vertical HTD Configuration 2).. ....	161
<b>Figure 5.24</b> Effect of varying external wind speed on the supply and indoor temperature.....	162
<b>Figure 5.25</b> Effect of various heat transfer device surface temperature on the supply and indoor temperature.....	163

<b>Figure 5.26</b> Effect of varying external wind angle on the supply and indoor temperature.....	163
<b>Figure 5.27</b> Summary of the results for indoor temperature, velocity and humidity..	164
<b>Figure 5.28</b> One-sided wind tower with horizontal HTD arrangement..	166
<b>Figure 5.29</b> Streamline representing the temperature distribution inside the test room with a heat transfer device integrated wind tower (configuration 2).....	167
<b>Figure 5.30</b> Velocity contour plot of a cross sectional plane in the test room with an inlet velocity of 3 m/s (horizontal HTD Configuration 1)..	168
<b>Figure 5.31</b> Velocity contour plot of a cross sectional plane in the test room with an inlet velocity of 3 m/s (horizontal HTD Configuration 2)..	168
<b>Figure 5.32</b> Comparison between the average indoor air flow speed at various external wind speeds (Horizontal HTD Config 1 and 2)..	169
<b>Figure 5.33</b> Static pressure contour plot of a cross sectional plane in the test room with an inlet velocity of 3 m/s (HTD Configuration 1).....	170
<b>Figure 5.34</b> Pressure contour plot of a cross sectional plane in the test room with an inlet velocity of 3 m/s (HTD Configuration 2)..	170
<b>Figure 5.35</b> Temperature contour plot of a cross sectional plane in the test room with an inlet velocity of 3 m/s (horizontal HTD Configuration 1). .....	171
<b>Figure 5.36</b> Temperature contour plot of a cross sectional plane in the test room with an inlet velocity of 3 m/s (horizontal HTD Configuration 2)..	171
<b>Figure 5.37</b> Effect of varying external wind speed on the supply and indoor temperature.....	172
<b>Figure 5.38</b> Effect of varying external wind direction on the temperature reduction.....	173
<b>Figure 5.39</b> Summary of the results for indoor temperature, velocity and humidity. ....	174
<b>Figure 5.40</b> Four-sided wind tower with vertical HTD arrangement and extended surfaces..	176
<b>Figure 5.41</b> Velocity contour plot of a cross sectional plane in the test room with a four-sided wind tower with finned heat transfer devices..	176
<b>Figure 5.42</b> A close-up view of the velocity streamlines inside the wind tower channel. ....	177
<b>Figure 5.43</b> Effect of varying external wind speed on the indoor air flow velocity.....	177
<b>Figure 5.44</b> Temperature contour plot of a cross sectional plane in the test room with a four-sided wind tower with finned heat transfer devices. ....	178
<b>Figure 5.45</b> Effect of varying external wind speed on the supply and indoor temperature .....	178
<b>Figure 5.46</b> One-sided wind tower with horizontal HTD arrangement and extended surfaces. ....	179

<b>Figure 5.47</b> Velocity contour plot of a cross sectional plane in the test room with an inlet velocity of 3 m/s.....	180
<b>Figure 5.48</b> Effect of varying external wind speed on the indoor air flow velocity.....	180
<b>Figure 5.49</b> Temperature contour plot of a cross sectional plane in the test room with an inlet velocity of 3 m/s.....	181
<b>Figure 5.50</b> Effect of varying external wind speed on the supply and indoor temperature.....	181
<b>Figure 5.51</b> Four-sided wind tower with the vertical HTD arrangement and porous medium.....	182
<b>Figure 5.52</b> Velocity contour plot of a cross sectional plane in the test room with an inlet velocity of 3 m/s.....	183
<b>Figure 5.53</b> A close-up view of the velocity streamlines inside the wind tower channel.....	183
<b>Figure 5.54</b> Effect of varying external wind speed on the indoor air flow velocity.....	184
<b>Figure 5.55</b> Temperature contour plot of a cross sectional plane in the test room with an inlet temperature of 318 K .....	184
<b>Figure 5.56</b> Effect of varying external wind speed on the supply and indoor temperature.....	185
<b>Figure 5.57</b> One-sided wind tower with the horizontal HTD arrangement and porous medium.....	186
<b>Figure 5.58</b> Velocity contour plot of a cross sectional plane in the test room with an inlet velocity of 3 m/s.....	187
<b>Figure 5.59</b> A close-up view of the velocity streamlines inside the wind tower channel.....	187
<b>Figure 5.60</b> Effect of varying external wind speed on the indoor velocity.....	188
<b>Figure 5.61</b> Temperature contour plot of a cross sectional plane in the test room with an inlet temperature of 318 K.....	188
<b>Figure 5.62</b> Effect of varying external wind speed on the indoor temperature.....	189
<b>Figure 5.63</b> PMV distribution inside the test room with the benchmark model (Winter).....	191
<b>Figure 5.64</b> Skin surface temperature of human models.....	191
<b>Figure 5.65</b> PMV distribution inside the test room with the benchmark model (Summer) .....	192
<b>Figure 5.66</b> Predicted Percentage Dissatisfied (Summer).....	193
<b>Figure 5.67</b> PMV distribution inside the test room with the heat transfer device integrated wind tower (Winter).....	194
<b>Figure 5.68</b> PMV distribution inside the test room with the heat transfer device integrated wind tower (Summer).....	194

<b>Figure 5.69</b> PMV distribution inside the test room with the finned heat transfer device integrated wind tower (Winter). .....	195
<b>Figure 5.70</b> PMV distribution inside the test room with the finned heat transfer device integrated wind tower (Summer).. .....	196
<b>Figure 5.71</b> PMV distribution inside the test room with the finned heat transfer device integrated wind tower (Summer, 40% humidity). .....	197
<b>Figure 6.1</b> 1:10 scale benchmark wind tower models (a) four-sided (b) one-sided.. .....	198
<b>Figure 6.2</b> Experimental and CFD flow domain of the macro-micro climate. ....	199
<b>Figure 6.3</b> Measurement points inside the test room model.. .....	199
<b>Figure 6.4</b> Section view of the four sided wind tower supply and exhausts channels showing the location of the measurement points (dimensions in mm).. .....	201
<b>Figure 6.5</b> Volumetric airflow rate through the wind tower supply and exhaust quadrants at various wind direction.. .....	202
<b>Figure 6.6</b> Section view of the one sided wind tower supply channel showing the location of the measurement points (dimensions in mm).. .....	202
<b>Figure 6.7</b> Volumetric airflow rate through the wind tower supply channel at various wind direction.....	203
<b>Figure 6.8</b> Experimental flow visualisation inside the test room with the benchmark four-sided wind tower. ....	204
<b>Figure 6.9</b> Visualised flow pattern inside the test room with a four-sided wind tower.....	205
<b>Figure 6.10</b> Visualised flow pattern inside the test room at various wind angles.....	206
<b>Figure 6.11</b> Experimental flow visualisation inside the test room with the benchmark one-sided wind tower.. .....	207
<b>Figure 6.12</b> Visualised flow pattern inside the test room at external wind speed of 3 m/s.....	207
<b>Figure 6.13</b> Experimental flow visualisation inside the test room with the one-sided wind tower at various wind angles.. .....	208
<b>Figure 6.14</b> 1:10 prototype model of the four and one-sided wind tower design incorporating horizontal heat transfer devices config 1.....	209
<b>Figure 6.15</b> Volumetric airflow rate through the wind tower supply and exhaust quadrants at various wind direction (four-sided wind tower with heat transfer devices config. 1).....	210
<b>Figure 6.16</b> Volumetric airflow through the wind tower supply channel at various wind direction (one-sided wind tower with heat transfer devices config. 1).....	211
<b>Figure 6.17</b> Detailed view of the flow inside the four-sided and one-sided wind tower with heat transfer devices.....	211
<b>Figure 6.18</b> Experimental flow visualisation inside the test room with the four-sided wind tower with heat transfer devices.. .....	212

<b>Figure 6.19</b> Experimental flow visualisation inside the test room with the one-sided wind tower with heat transfer devices. ....	212
<b>Figure 6.20</b> 1:10 prototype model of the four and one-sided wind tower design incorporating heat transfer devices and extended surfaces. ....	213
<b>Figure 6.21</b> Volumetric airflow through the wind tower supply and exhaust quadrants at various wind direction (four-sided wind tower with heat transfer devices and extended surfaces). ....	214
<b>Figure 6.22</b> Volumetric airflow through the wind tower supply channel at various wind direction (one-sided wind tower with heat transfer devices and extended surfaces). ....	215
<b>Figure 6.23</b> Experimental flow visualisation inside the test room with the four-sided wind tower with heat transfer devices and extended surfaces. ....	215
<b>Figure 6.24</b> Experimental flow visualisation inside the test room with the one-sided wind tower with heat transfer devices and extended surfaces. ....	216
<b>Figure 6.25</b> 1:10 prototype model of the four and one-sided wind tower design incorporating heat transfer devices and porous mesh. ....	216
<b>Figure 6.26</b> Volumetric airflow rate through the wind tower supply and exhaust quadrants at various wind direction (four-sided wind tower with heat transfer devices and porous medium). ....	217
<b>Figure 6.27</b> Volumetric airflow through the wind tower supply channel at various wind direction (four-sided wind tower with heat transfer devices and porous medium). ....	218
<b>Figure 6.28</b> Experimental flow visualisation inside the test room with the four-sided wind tower with heat transfer devices and porous medium. ....	219
<b>Figure 6.29</b> Experimental flow visualisation inside the test room with the one-sided wind tower with heat transfer devices and porous medium. ....	220
<b>Figure 7.1</b> Comparison between CFD and experimental indoor velocity (Four-sided wind tower benchmark model) with external wind speed at 3 m/s. ....	222
<b>Figure 7.2</b> Comparison between CFD and experimental results for the velocity in the supply and exhaust channels with external wind speed at 3 m/s (Four-sided wind tower benchmark model). ....	223
<b>Figure 7.3</b> Comparison between CFD and experimental values for surface pressure coefficients around the four-sided wind tower model. Dotted lines represent 10 % error percentage. ....	225
<b>Figure 7.4</b> Comparison between the indoor airflow distribution inside the test room with a standard four-sided wind tower model. ....	226
<b>Figure 7.5</b> Flow visualisation inside the supply and exhaust quadrant with external wind speed set at 3 m/s. ....	226
<b>Figure 7.6</b> Comparison between CFD and experimental indoor velocity with external wind speed at 3 m/s (One-sided wind tower benchmark model). ....	227
<b>Figure 7.7</b> Comparison between CFD and experimental results for the velocity in the supply channel (One-sided wind tower benchmark model). ....	228

<b>Figure 7.8</b> Comparison between CFD and experimental values for surface pressure coefficients around the wind tower model. Dotted lines represent 10 % error percentage..	230
<b>Figure 7.9</b> Comparison between the indoor airflow distribution inside the test room with a one-sided wind tower.....	231
<b>Figure 7.10</b> Comparison between CFD and experimental results for the velocity in the supply and exhaust channels with external wind at 3 m/s (Four-sided wind tower with HTD).....	231
<b>Figure 7.11</b> Comparison between CFD and experimental results for the velocity in the supply and exhaust channels with external wind speed at 3 m/s (One-sided wind tower with HTD).....	232
<b>Figure 7.12</b> Comparison between the indoor airflow distribution inside the test room (Four-sided wind tower with HTD).....	232
<b>Figure 7.13</b> Comparison between the indoor airflow distribution inside the test room with external wind speed at 3 m/s.....	233
<b>Figure 7.14</b> Comparison between the indoor airflow distribution inside the test room (One-sided wind tower with HTD).....	233
<b>Figure 7.15</b> Comparison between CFD and experimental results for the velocity in the supply and exhaust channels with external wind speed at 3 m/s (Four-sided wind tower with HTD and extended surface).....	234
<b>Figure 7.16</b> Comparison between CFD and experimental results for the velocity in the supply and exhaust channels with external wind speed at 3 m/s (One-sided wind tower with HTD and extended surfaces).....	234
<b>Figure 7.17</b> Comparison between the indoor airflow distribution inside the test room (Four-sided wind with HTD and extended surface).....	235
<b>Figure 7.18</b> Comparison between the indoor airflow distribution inside the test room (One-sided wind tower with HTD and extended surfaces).....	235
<b>Figure 7.19</b> Comparison between CFD and experimental results for the velocity in the supply and exhaust channels with external wind speed at 3 m/s (Four-sided wind tower with HTD and porous medium).....	236
<b>Figure 7.20</b> Comparison between CFD and experimental results for the velocity in the supply and exhaust channels with external wind speed at 3 m/s (One-sided wind with HTD and porous medium).....	237
<b>Figure 7.21</b> Comparison between the indoor airflow distribution inside the test room (Four-sided wind tower with HTD and porous medium).....	237
<b>Figure 7.22</b> Comparison between the indoor airflow distribution inside the test room (One-sided wind tower with HTD and porous medium).....	238
<b>Figure A.1</b> Comparison of flow in the wide angle diffuser: (a) without (b) with splitting plates.....	254
<b>Figure B.1</b> Actual photo of: (a) second corner guide vanes (b) diffuser exit. View of the computational mesh at the surface of: (c) the 90 corner guide vanes; (d) the diffuser splitting plates.....	257

<b>Figure B.2</b> (a) block model inside the test section (b) view of the computational mesh of the block model and test section floor.....	258
<b>Figure B.3</b> Posterior error on the average velocity in the test-section using h-p grid adaptation method.....	259
<b>Figure C.1</b> Top view of the test section showing the measurement positions (P01 - P09) and coordinates for the case of an empty test section. Dimensions in metres.....	260
<b>Figure C.2</b> Top view of the test section showing the hot-wire anemometer measurement positions and coordinates with the block test model. Dimensions in metres.....	262
<b>Figure C.3</b> (a) Pressure tap locations on the square block model. (b) Internal view of the block model showing the 15 pressure taps connections. (c) Test setup: block model inside the test section. Dimensions in metres.....	263
<b>Figure D.1</b> Velocity streamline for configuration 1: no guide vanes.....	265
<b>Figure D.2</b> Contours of velocity magnitude in a (a) vertical plane and (b) horizontal plane at 0.250 m height of the test section for the wind tunnel without guide vanes.....	265
<b>Figure D.3</b> Velocity streamline for configuration 2: upstream guide vanes.....	266
<b>Figure D.4</b> Contours of velocity magnitude in a (a) vertical plane and (b) horizontal plane at 0.250 m height of the test section for the wind tunnel with upstream guide vanes.....	267
<b>Figure D.5</b> Velocity streamline for configuration 3: downstream guide vanes.....	268
<b>Figure D.6</b> Contours of velocity magnitude in a (a) vertical plane and (b) horizontal plane at 0.250 m height of the test section for the wind tunnel with downstream guide vanes.....	269
<b>Figure D.7</b> Velocity streamline for configuration 4: upstream and downstream guide vanes.....	270
<b>Figure D.8</b> Contours of velocity magnitude in a (a) vertical plane and (b) horizontal plane at 0.250 m height of the test section for the wind tunnel with upstream and downstream guide vanes.....	270
<b>Figure D.9</b> Comparison between the dimensionless velocity and turbulence intensity profiles of the flow at the test section for different inlet conditions (Configuration 4).....	271
<b>Figure D.10</b> Comparison between the measured and CFD values for the dimensionless velocity components X (a), Y (b) and Z (c) for points A – G around the block type model. Data were made dimensionless with respect to the measured value at point A. Dotted lines indicate $\pm 10 - 20\%$ error.....	273
<b>Figure D.11</b> Comparison between the measured and CFD values for the turbulence intensity for points A – G around the block model. Dotted lines indicate the error percentage.....	274

## Preface

The work presented in this thesis was carried out between February 2011 and August 2013 in the School of Engineering of Physical Science, Heriot Watt University and the School of Civil Engineering, University of Leeds. As an outcome of this study, the following peer reviewed journal and conference papers have been published:

### Peer-reviewed journals:

- 1. J.K. Calautit, B.R. Hughes, and S.A. Ghani.** Numerical Investigation of the Integration of Heat Transfer Devices into Wind Towers. *Chemical Engineering Transactions Special Issue: SDEWES 2012*, 34, 43-48, 2013 DOI:10.3303/CET1334008
- 2. B.R. Hughes, H.N. Chaudhry, and J.K. Calautit.** Passive energy recovery from natural ventilation air streams. *Applied Energy*, 113, 127-140, 2013 DOI: 10.1016/j.apenergy.2013.07.019
- 3. J.K. Calautit, B.R. Hughes, H.N. Chaudhry, and S.A. Ghani.** CFD analysis of a heat transfer device integrated wind tower system for hot and dry climate. *Applied Energy*, 2013, Corrected Proof (In Press) DOI:10.1016/j.apenergy.2013.01.021
- 4. J.K. Calautit, H.N. Chaudhry, B.R. Hughes, and S.A. Ghani.** Comparison between evaporative cooling and a heat pipe assisted thermal loop for a commercial wind tower in hot and dry climatic conditions. *Applied Energy*, 101, 740-755, 2013 DOI:10.1016/j.apenergy.2012.07.034
- 5. J.K. Calautit, B.R. Hughes, and S.A. Ghani.** A Numerical Investigation into the Feasibility of Integrating Green Building Technologies into Row Houses in the Middle East. *Architectural Science Review Special Issue*, 1, 1-18, 2012 DOI: 10.1080/00038628.2012.686433
- 6. B.R. Hughes, J.K. Calautit, and S.A. Ghani.** The Development of Commercial Wind Towers for Natural Ventilation: A Review. *Applied Energy*, 92, 606-627, 2012 DOI: 10.1016/j.apenergy.2011.11.066

**Conference papers:**

**1. J.K. Calautit, B.R. Hughes, and S.A. Ghani.** Numerical Investigation of the Integration of Heat Transfer Device into Wind Tower, The 4<sup>th</sup> International Conference on Applied Energy, Suzhou (ICAE 2012), China, 5-8 July, 2012 SDEWES12-0037

**2. J.K. Calautit, B.R. Hughes, and S.A. Ghani.** Computational analysis of a heat transfer device integrated wind tower system for hot and humid climate. The 7<sup>th</sup> Sustainable Development of Energy, Water and Environment Systems (SDEWES 2012), Ohrid, Macedonia, 1-7 July 2012 ICAE2012-3-D1-5 (A10326)

## Nomenclature

$\vec{u}$	Fluid flow velocity, (m/s)
$\rho$	Local density, (kg/m <sup>3</sup> )
t	Time, (s)
$S_M$	Mass added to the continuous phase from the dispersed second phase, (kg)
u	x - momentum, (kg·m/s)
v	y - momentum, (kg·m/s)
w	z - momentum, (kg·m/s)
$\tau$	Time in the past contributing in the integral response, (s)
$k_{eff}$	Effective conductivity, (W/m·K)
$\vec{J}_j$	Diffusion flux, (mol/m <sup>2</sup> s)
$S_h$	Heat of chemical reaction and other volumetric heat source defined by user, (W)
p	Static pressure, (Pa)
$\mu$	Molecular viscosity, (Pa s)
k	Turbulence kinetic energy, (m <sup>2</sup> /s <sup>2</sup> )
$\epsilon$	Turbulence dissipation rate, (m <sup>2</sup> /s <sup>3</sup> )
$G_k$	Generation of turbulent kinetic energy due to the mean velocity gradients
$G_b$	Generation of turbulence kinetic energy due to buoyancy
$Y_M$	Fluctuating dilatation in compressible turbulence to the overall dissipation rate
$\sigma_k$	Turbulent Prandtl numbers for turbulence kinetic energy
$\sigma_\epsilon$	Turbulent Prandtl numbers for energy dissipation rate
$S_k$	User defined source term for turbulence kinetic energy, (m <sup>2</sup> /s <sup>2</sup> )
$S_\epsilon$	User defined source term for energy dissipation rate, (m <sup>2</sup> /s <sup>3</sup> )

$S_{H_2O}$	water vapour added to or removed from the air, (kg/s m <sup>2</sup> )
$D_{H_2O}$	diffusion coefficient of water vapour into air, (m <sup>2</sup> /s)
$Sc_t$	turbulent Schmidt number, (kg/s m <sup>2</sup> )
$Y$	mass fraction of species, (m)
$\mu_t$	turbulent viscosity, (Pa s)
$x, y, z$	Cartesian coordinate, (m)
$RH$	relative humidity, (%)
$U$	Velocity magnitude, (m/s)
$\alpha$	wind angle, (°)
$T$	static temperature, (K)
$T_w$	temperature of the base of the fin, (K)
$T_a$	temperature of the ambient, (K)
$Q$	heat transfer rate, (W)
$h$	heat transfer coefficient, (W/m <sup>2</sup> K)
$A$	Cross-sectional area, (m <sup>2</sup> )
$\vec{r}$	position vector
$\vec{s}$	direction vector
$\vec{s}'$	scattering direction vector
$s$	path length
$\alpha_c$	absorption coefficient
$n$	refractive index
$\sigma_s$	scattering coefficient
$\sigma$	Stefan-Boltzmann constant (5.669 x 10 <sup>-8</sup> W/m <sup>2</sup> K <sup>4</sup> )
$I$	radiation intensity
$\Phi$	phase function
$\Omega'$	solid angle

## List of Abbreviations

Air Handling Unit	AHU
Computational Fluid Dynamics	CFD
Greenhouse Gas	GHG
Indoor Air Quality	IAQ
International Energy Agency	IEA
International Organization for Standardization	ISO
Predicted Mean Vote	PMV
Predicted of Percentage Dissatisfied	PPD
Sick Building Syndrome	SBS
Heat Transfer Device	HTD
Heating, Ventilation and Air-conditioning	HVAC
World Business Council for Sustainable Development	WBCSD

## Chapter 1

### Introduction

There is increasing concern over end-user energy consumption and its adverse effects on the environment. This has raised the public awareness of the climate change implications and generated interest in understanding the energy influences and the barriers to low energy use. The increasing consumer demand exceeds the available clean energy supply and so Greenhouse Gas (GHG) emissions continue to rise. Buildings are at the centre of this problem. Commercial and residential buildings account for almost 30 - 40% of the world energy usage and are responsible for almost 40-50% of the global carbon emissions [Hughes *et al.*, 2011]. Recent reports by the World Business Council for Sustainable Development (WBCSD) projected that without fast and effective action, the energy used in buildings will be as much as transport and industry combined by 2050 (Figure 1.1).

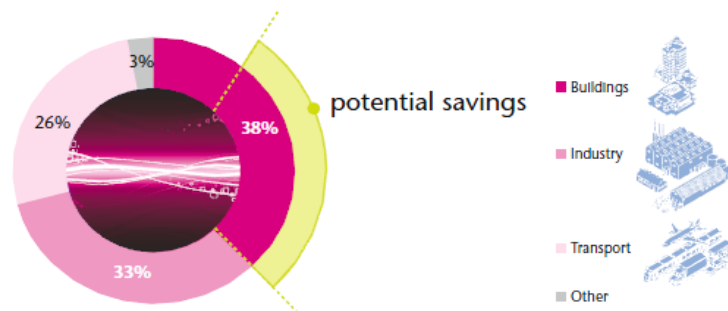


**Figure 1.1** Global energy consumption pie-chart. Potential building energy savings could be as much as total transport energy use today [WBCSD, 2011]

The need for transformation is essential for the whole building sector in order to achieve the International Energy Agency's (IEA) target of a 77% reduction in the planet's carbon footprint. Extensive efforts have been focused on an environmentally friendly approach to building design revealing the on-going interest of the scientific community on the topic [Duić *et al.*, 2013]. The advancement of energy efficient technologies in the building sector could play an active role among the efforts in the formation of a sustainable strategic framework towards a carbon neutral economy [Marinakis *et al.*, 2013].

With today's advanced knowledge and cutting edge technologies achieving zero carbon buildings is a possible and practical target [Webb, 2001]. However, a sustainable design must also aim to meet the standards for health and comfort with minimum use of resources. Thermal comfort cannot be compromised to reduce environmental impact. Comfortable and healthy microclimate conditions are necessary for any type of environment [Li *et al.*, 2013]. It is for these reasons that accurate and robust design procedures are so important.

Heating, Ventilating and Air-conditioning (HVAC) systems play a vital part in ensuring the required comfort levels of residents inside buildings. Most modern cooling equipment consumes high levels of electrical power, thus creating high energy consumption rates in buildings. HVAC systems account for approximately 50% of the energy use in buildings [Lombard *et al.*, 2008]. Conventional heating and cooling systems have an impact on carbon dioxide emissions, as well as on the security of energy supply [Chen *et al.*, 2010]. The most significant impact on energy use in the built environment would occur in the hot climates where building energy use is dominated by cooling requirements.

Building cooling technologies comprise consist of two strategies, namely active and passive. Typical examples of active or mechanical ventilation are fans and air conditioning units. Mechanical ventilation uses equipment to generate or move airflow.

The most common and widely used technologies in modern commercial residences are mechanical air handling units (AHU's); a schematic view of an AHU is shown in Figure 1.2. These systems are effective and reliable and offer reassurance to the designer that the fresh air requirements will be served adequately. The major mechanical components consist of a fan compartment, a supply duct and a heating or cooling coil.

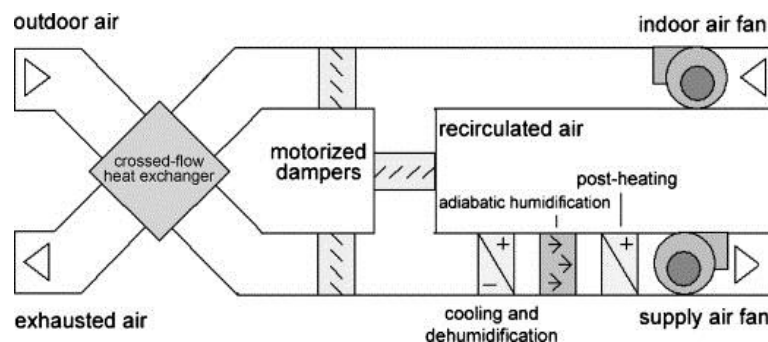


**Figure 1.2** Schematic view of an air handling unit (AHU) [Lazzarin and Castellotti, 2007]

Passive cooling, also called natural ventilation uses natural outside air movement to both passively cool and ventilate a building by displacing dissipated internal heat gains. For warm and hot climates, it can help meet a building's cooling loads without using mechanical air conditioning systems (night ventilation). During night time, the lower external air temperature cools the building mass, which provides additional cooling the following day [Asfour and Gadi, 2006]. This can be a large fraction of a building's total energy use. Passive cooling methods are increasingly being employed in new buildings to reduce the energy consumption and carbon foot print.

Furthermore, ventilation of the indoor environment plays a vital role in the health and well-being of the occupants [Hughes and Ghani, 2008]. The effectiveness of indoor flows in eliminating contaminants and supplying fresh air depends not only on their magnitude, but also on the locations where air enters and exits the ventilated space. With active systems, these factors are a primary part of the design and essentially remain constant. While with passive systems, there is less control over the magnitude and direction of indoor flows. However, mechanical systems do not always contribute to an acceptable indoor environment. In fact, occupants in naturally ventilated buildings often perceive the indoor environment to be better and report fewer Sick Building Syndrome (SBS) symptoms [Jones *et al.*, 2008].

Clearly, natural ventilation itself is not new. It is only in the past 150 years or so that mechanical ventilation has been used. Prior to this, all enclosures occupied by humans were naturally ventilated [Etheridge, 2011]. Much of the knowledge gained over the centuries can be seen in modern naturally ventilated buildings. A good example of this is the use of wind assisted devices such as wind towers.

## **1.1 Wind towers**

Wind towers have been in existence in various forms for centuries as a non-mechanical means of providing indoor ventilation. Increasing energy prices and climate change agendas have refocused engineers and researchers on the low carbon credentials of modern equivalents. The architecture of conventional and modern wind towers can be integrated into the design of new buildings to provide thermal comfort without the use of electrical energy.

Figure 1.3 illustrates passive ventilation through a four-sided wind tower device. The wind tower is divided by partitions to create different shafts. One of the shaft's functions as an inlet to supply the wind. The other shafts work as an outlet to extract the warm and stale air from the occupied space. The temperature difference between the micro and macro climates creates different pressures and resulting in air currents needed for the wind towers to be effective [Hughes and Mak, 2011].

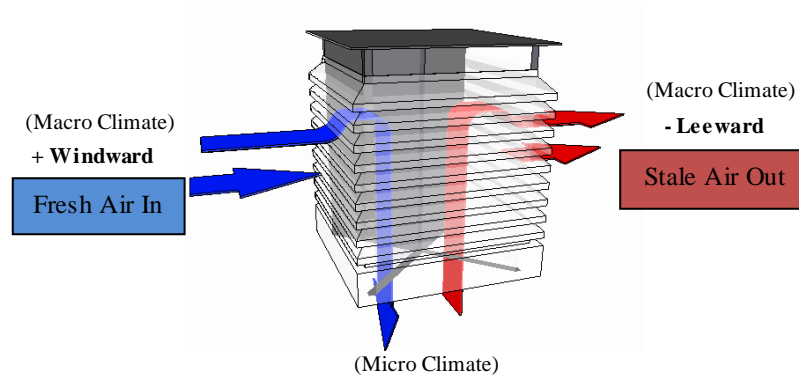


**Figure 1.3** A flow diagram representing ventilation through a four-sided wind tower device [Hughes *et al.*, 2012]

There are two driving forces for the wind tower. The primary force provides fresh air driven by the positive air pressure on windward side, exhausting stale air with the assistance of the suction pressure on the leeward side. The secondary force is temperature driven and termed "the stack effect". The density of air reduces as its temperature increases causing layers of air to be stacked [Hughes and Ghani, 2009]. The internal and external temperature difference (micro to macro climate) drives the airflow through the ventilator. The horizontal openings on top of the tower allow the device to capture wind at high elevations and direct the air flow into the interior living spaces of the building.

In hot and arid regions, such as those found in the Middle East, there is a huge dependency on electricity to run mechanical ventilation systems to provide thermal comfort. In these areas, using wind towers to achieve comfort is a well-known traditional technique. However, the cooling capabilities of wind towers which depend on the structure design itself are limited. Therefore it is essential to cool the air in order to reduce the building heat load and improve the thermal comfort of its occupants during the summer months. Traditionally, evaporative cooling wind towers were used extensively in parts of the Middle East, particularly Iran, Egypt, Dubai and Jordan [Kalantar, 2009].

A cooling wind tower is generally a tall structure with a height of between 1 and 33 m mounted on top of a building. At the top of the tower, openings allow air to enter. The induced warm air is passed through a column of wetted cloth or cooling pad, which holds water and allows air to flow through, evaporating the water in the process. The air passes through the cooling media, causing it to lower in temperature thereby becoming heavier and sinking to the bottom of the channel, while the warm air rises to the top. Other methods of evaporative cooling, such as the placement of water fountains, ground cooling or mist sprayers can also be integrated within wind towers [Hughes *et al.*, 2012].

Cooling wind towers are very large in scale and typically require integration into the architectural scheme of a building for aesthetic purposes. Also, high construction costs are associated with this system. Evaporative coolers use a substantial amount of water to run. Hence, this should be taken into consideration in areas where water is expensive or in short supply. In some areas, discarded water from the cooling tower can be an environmental concern. Another disadvantage of evaporative cooling towers is the dependence on dry outside air to operate effectively. Evaporative cooling is best used in hot and dry conditions due to the external low wet bulb air temperature. While in hot climates with high humidity levels, evaporative cooling can actually cause more discomfort than it does comfort. As the humidity increases, the ability to cool the air effectively decreases. Other drawback of the evaporative cooling system is the reliance on having additional outlet openings to enable air movement through the occupied space (cross-flow ventilation). Figure 1.4 shows the airflow through an evaporative cooling tower.

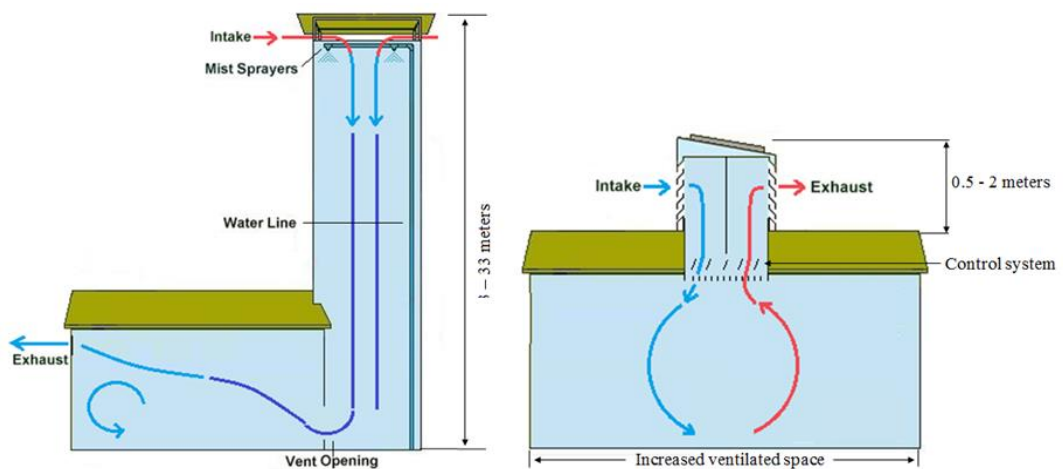


**Figure 1.4** A flow diagram representing ventilation through an evaporative cooling and a compact roof-mounted wind tower system.

Modern wind towers are usually compact and smaller in size compared to the traditional wind towers. The device extends out from the top of a structure to catch the wind at roof level and channels fresh air through a series of louvres into the enclosed space under the action of air pressure. The negative pressure simultaneously extracts stale air out of the room (Figure 1.4). Unlike the traditional wind towers with displacement outlets located near the floor, air is supplied to the enclosed space through the diffusers located at ceiling level. Hence, more free space is available for ventilation on the ceiling than on the corresponding floor of equal area [Hughes *et al.*, 2012].

Modern wind towers are equipped with volume control dampers and ceiling diffusers which allows the occupants to regulate the supply depending on air flow requirement. A recent improvement in the design of wind towers is the use of solar powered fan in the windvent [Hughes and Ghani, 2009], a wind tower for colder climates. The hybrid system incorporates a low-pressure solar powered fan installed inside the wind tower with the fan functioning, when required, to assist the flow of air during hot summer temperatures, thus improving the thermal conditions for the room occupants. The solar driven fan can also function as an exhaust device for extracting spent air out of the building. It provides a constant supply of ventilation air, even when there is little or no wind.

## **1.2 Aims and Objectives**

A wind tower system incorporating heat transfer devices was proposed to meet the internal comfort criteria in very hot and humid regions. Heat transfer devices were integrated into the passive terminal (no mechanical components for moving air) of a wind tower unit. The main area of challenge was to achieve minimal restriction to the air flow stream while ensuring maximum contact time for heat transfer, thus establishing a viable passive cooling ventilation device for extreme conditions. This will contribute to the knowledge and understanding in the application of low energy technologies within the built environment. The cooling technique will incorporate the operating capability of a low energy heat source to be integrated into the passive terminals, thus maximising the cooling capabilities of the device and maintaining the active power consumption rate as low as possible.

The following research objectives were identified:

1. Compare the ventilation and thermal performance of the vertical and horizontal device configurations.
2. Investigate the effect of varying the total number and spacing of the heat transfer devices within the passive terminal of a one and four-sided wind tower on the room supply temperature.
3. Investigate the effect of varying external conditions such as wind speed, external temperature and relative humidity on the ventilation and thermal performance of the proposed system.
4. Maximise the contact time between the wind-induced airflow and the heat transfer device by employing extended surfaces and porous media.
5. Determining the thermal comfort level in a standard classroom employing the cooling system in terms of air temperature, velocity, and relative humidity.
6. Compare the ventilation performance of the heat transfer device integrated wind tower measured in the wind tunnel against those predicted by the numerical model. The data collected will feedback into the predictive model (objective 1) and increase the understanding of its functionality and performance.

### **1.3 Project Methodology**

The study will conduct a thorough review of related literature from published research work on current low carbon devices for use in extreme temperature differential applications. The work will use CFD modelling to inform the design of a full scale thermal and aerodynamic simulation model, capable of producing internal comfort data in response to the supplied climatic data. The ANSYS Fluent CFD model will be used in the research. Numerical simulation of various design parameters will be carried out to optimise the geometry and components performance. A thorough analysis of the impact of outdoor conditions will be conducted, in particular the influence of varying the wind speed and directions on the internal air flow rate, humidity and temperature difference. The simulation work will be validated against 1:10 scaled experimental work using a subsonic closed loop wind tunnel.

The principal investigation parameters in determining the viability of the design and the comfort conditions are the wind characteristics (velocity and direction); indoor air flow

rate; indoor and outdoor temperature difference and the relative humidity of the air. Figure 1.6 shows the PhD project methodology flow chart.

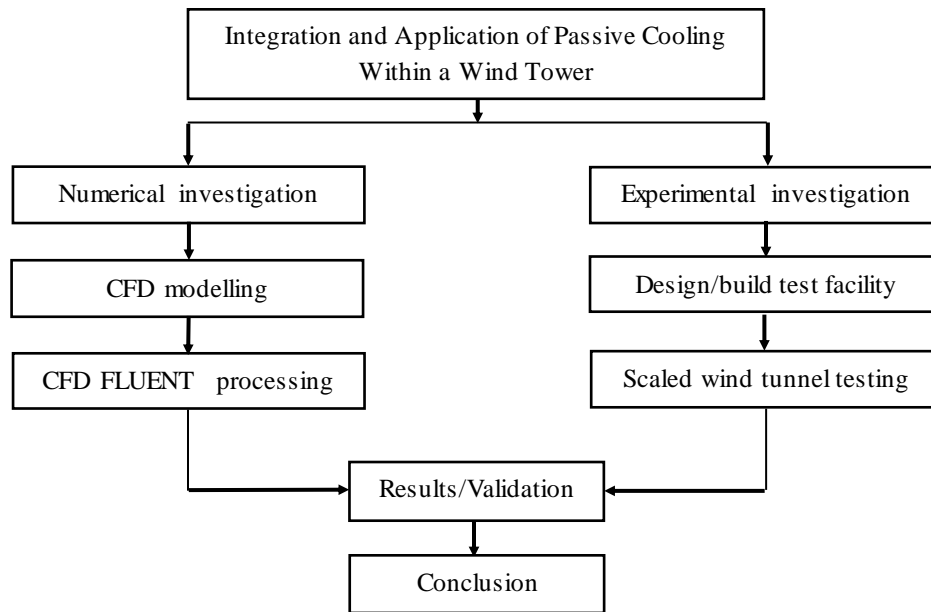


**Figure 1.5** Project methodology flow chart.

## 1.4 Thesis layout

The aim of the research described in this thesis is to develop a low energy technology for providing natural ventilation and thermal comfort in residential buildings situated in hot climates. The study will present a systematic methodology for predicting the performance of a novel form of wind tower system integrated with heat transfer devices. The numerical and experimental techniques used in the research will be useful as design tools for the development of new designs of wind tower systems.

The thesis is divided into 8 chapters. The collection of chapters will guide the reader through the research work that leads to the conclusions in Chapter 8. The summary of each chapter is listed below.

Chapter 1 provides an introduction to the existing design of wind tower systems and cooling strategies. This chapter also presents the key objectives and research methodologies.

Chapter 2 provides a comprehensive review of traditional and modern wind tower developments. The study covers various methodical and experimental aspects to assess

the overall effectiveness of current ventilation systems and gives an insight into the application of passive cooling systems as an alternative to mechanical ventilation systems. The review highlights the different cooling techniques which can be integrated with wind tower systems to improve its ventilation and thermal performance. This chapter identifies the research gap and appropriate methods of investigation to achieve the research objectives.

Chapter 3 details the numerical methods employed in the research covering the theory of the CFD, mesh generation, boundary conditions and post processing.

Chapter 4 details the experimental design and methodology covering the experimental set-up, rapid prototyping of the 3D CAD models and measurement procedures. The design specification of the closed-loop wind tunnel facility and the instrumentation are also presented in this chapter.

Chapter 5 presents the results from the CFD investigations. The results and findings of each geometrical configuration are also discussed.

Chapter 6 presents the experimental data obtained from the wind tunnel testing. The chapter details the numerical results in terms of the measured pressure coefficient distribution, internal air speed and volumetric airflow for various external conditions.

Chapter 7 compares the CFD results with the experimental findings to validate the numerical model used in the study. The accuracy of the CFD simulations is established with the quantification of computational uncertainties and sources of error.

Chapter 8 draws conclusions based upon the analysis of the results presented in the preceding chapters and identifies the future work that could be carried out to further knowledge in this field.

## **1.5 Summary**

This chapter has presented the background to the research. The research objectives and methodologies were clearly identified. The thesis has been introduced with a brief summary of each chapter provided.

## Chapter 2

### Literature Review

#### 2.1 Introduction

The aim of this chapter is provide a comprehensive review of current and potential wind tower development. This chapter outlines the key areas relevant to the study of a wind tower such as the principles of natural ventilation, thermal comfort and wind tower cooling techniques. Numerous studies have investigated the effects of different configurations and components on the performance of wind towers. Such studies include the use of evaporative cooling to improve thermal performance, the use of solar chimneys, courtyards and curved roofs to enhance the air movement inside the structure, and the use of volume control dampers and ceiling diffusers to optimise the fresh air flow rate and indoor conditions. The review has established the proven numerical and experimental methods and has identified the research gap to be filled through this research.

#### 2.2 Thermal comfort

Thermal comfort defines the well-being, physical and intellectual performance of a person, and houses should be able to have an internal climatic environment that can produce it [De Dear and Brager, 2002]. The ventilation of a building is directly related to thermal comfort. This means that occupants of the building will feel more comfortable, even though the building may not actually be being cooled. The acceptable air temperature will increase the as air speed increases. Modern buildings are equipped with HVAC (Heating Ventilation Air Conditioning) systems to control their indoor thermal environment.

With the current energy and economic situation, new methods for indoor temperature control are being used such as the utilisation of natural wind power to conserve conventional energy for achieving thermal comfort [Yao *et al.*, 2009]. Thermal comfort standards play a role in facilitating the suitable use of energy efficient, climate responsive building design strategies such as the integration of wind tower systems. The slight change in air pressure produced by the device can create sufficient airflow to improve the thermal comfort of the inhabitants. Thermal comfort is also a key parameter for a healthy and productive environment or workplace [Taylor *et al.*, 2008].

Thermal sensation is different among people even in the same environment [Kuchen and Fisch, 2009]. Due to the combination of a large number of factors that affect the thermal comfort perception, individuals staying in very similar places, exposed to the same climatic conditions, wearing the same clothing, engaged in the same activities, belonging to a common culture, may have dissimilar views on thermal comfort.

Cheng *et al.* [2007] stated that thermal comfort is influenced by many physical variables. Hence, it has always been difficult to evaluate and even harder to achieve which is the main reason why it has been attractive to researchers. De Dear and Brager [2002] stated that thermally comfortable environments depend on four local environmental parameters and two external parameters. The four environmental parameters are the rate of air movement, radiant exchange between the occupant and the surrounding surfaces, temperature of the surrounding air and the relative humidity of the air. Thermal comfort can be assessed in terms of many combinations of these physical or personal parameters such as the metabolic rate and the occupant's clothing. Thus, one determinant of whether a building occupant will feel thermally comfortable is how rapidly or slowly air moves in the vicinity of the individual. Heat from the human body needs to be lost through sensible heat transfer i.e. conduction, convection, radiation and, to a greater extent, evaporative latent heat loss as shown in Figure 2.1.

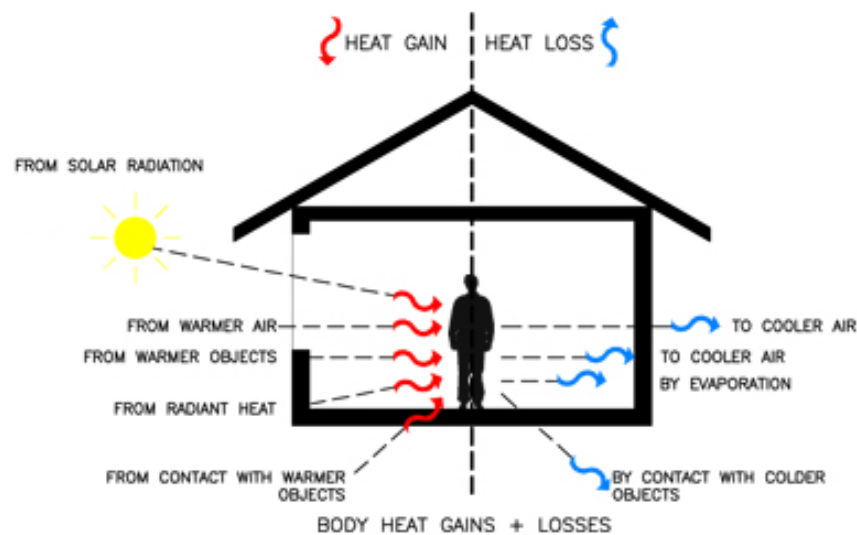


**Figure 2.1** Heat from the human body is lost through sensible heat transfer [Gruncodesign, 2011].

### 2.2.1 Thermal comfort approaches

When discussing thermal comfort, there are two main different models that can be used: the heat balance model and the conceptual thermal adaptation model. The first model uses data from controlled climate chamber studies to support its theory, best characterised by the works of Fanger [1970]. The approach combines the theory of heat transfer with the physiology of thermoregulation to determine a range of comfort temperatures which occupants of buildings will find comfortable. The range of comfort is determined by a Predicted Mean Vote (PMV), derived from studies of individuals in controlled conditions. Figure 2.2 shows the relationship between the Predicted Mean Vote (PMV) and the Predicted Percentage Dissatisfied (PPD).

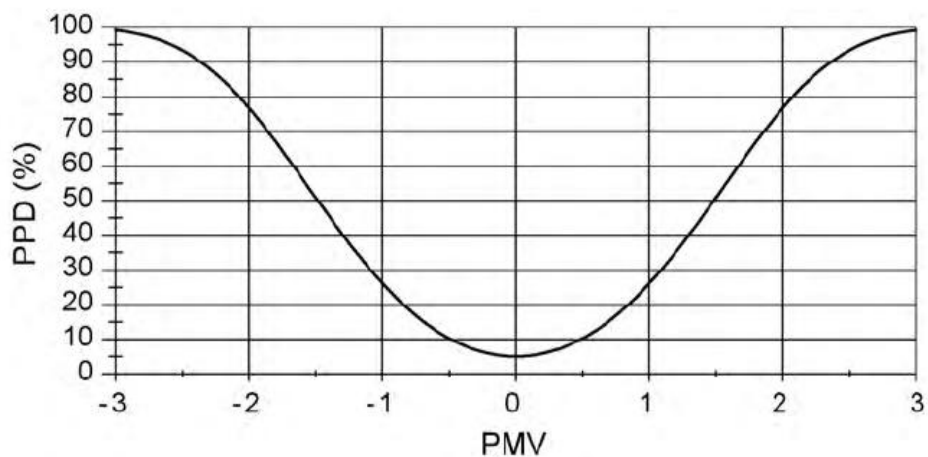


**Figure 2.2** Relationship between Predicted Mean Vote and Predicted Percentage Dissatisfied [Djongyang *et al.*, 2010].

The adaptive approach is based on the findings of surveys of thermal comfort conducted in the field. Field surveys concentrate on gathering data about the thermal environment and the simultaneous thermal response of subjects in real situations, with interventions by the researcher being kept to a minimum [Peeters *et al.*, 2009].

Djongyang *et al.* [2010] carried out a detailed review of the two thermal comfort approaches referred to above. The study showed that each approach has its potential benefits and limits. The heat balance approach produced reasonably precise predictions of thermal perception when the occupants are involved in sedentary or minimal activities and in steady-state conditions. While the adaptive approach allows for analysis of other aspects than those that can be simulated in spaces, as the subjects provide responses in

their everyday environments, wearing their everyday clothing and behaving without any additional restrictions. Furthermore, the study concluded that the actual standards should not be considered as absolute reference.

Ealiwa *et al.* [2001] used analytical and experimental methods to investigate the thermal comfort levels within two types of buildings; traditional and contemporary, situated in a hot and dry climate. A survey was collected from the occupants of 51 residential buildings; 24 traditional buildings that utilise natural ventilation systems such as wind towers and courtyards and 27 new buildings incorporating mechanical ventilation systems. The results showed that the measurements of the predicted mean vote in new mechanically ventilated buildings provided acceptable comfort conditions according to the international thermal comfort standards and the occupants agreed by indicating a satisfactory actual mean vote. The equivalent measurements and survey results in old traditional buildings indicated that although the PMV, based on measurements and international standards, implied discomfort, the occupants expressed their thermal satisfaction with the indoor comfort conditions. The field study also investigated occupant's overall impression of the indoor thermal conditions; the results indicated that people have an overall impression of a higher standard of thermal comfort in old buildings than in new buildings as shown in Figure 2.3.

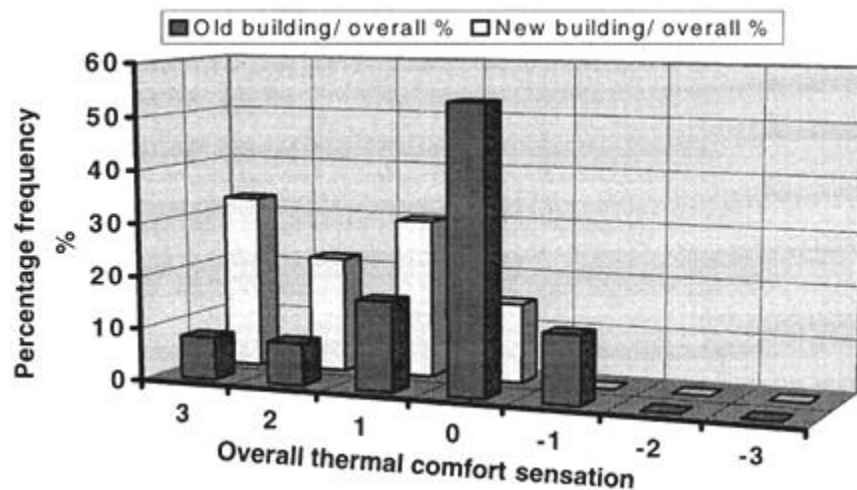


**Figure 2.3** Comparison of the overall thermal comfort sensation for old buildings and new buildings [Ealiwa *et al.*, 2001].

### 2.2.2 Thermal comfort in naturally ventilated buildings

The architectural design of buildings has highlighted the potential advantage of natural ventilation systems for occupancy comfort [Prianto and Depecker, 2003]. Architects have been keen on using natural forces to drive ventilation air through the interior spaces of a building. Natural ventilation has become an attractive solution for not only reducing the energy usage and cost but also for providing a good quality indoor air environment while sustaining a comfortable, healthy and productive internal climate. Natural ventilation systems use the natural pressure differences surrounding a structure, caused by wind and temperature driven forces, to direct the air flow through buildings. An example of one such low carbon ventilation system is the wind tower. Elmualim [2006a] stated that naturally ventilating buildings by means of wind towers provided increased control and reliability compared to cross-flow ventilation.

Candido *et al.* [2010] investigated the relationship between air movement acceptability and thermal comfort in naturally ventilated buildings situated in warm climates. The internal air velocity, air temperature, radiant air temperature and humidity were measured for different values of external wind speeds. The technique adopted for the study combined the indoor climatic data with questionnaires filled in by occupants of the naturally ventilated spaces. The results have indicated that the air movement level was found to be acceptable at speeds well in excess of the values suggested in the literature (0.2 to 1.5 m/s). It was found that the occupants demanded “more air movement” even in air speeds above 0.5 m/s. It was concluded that naturally ventilated buildings in hot and arid climates require higher air speeds in order to improve the occupant’s thermal comfort than in other climates. The work also highlighted the importance of the ability of the occupants to control the airflow inside the room according to their preference.

Daghigh *et al.* [2009] studied the effect of window-door arrangements on ventilation characteristics for thermal comfort in naturally ventilated buildings. The work evaluated the performance of the ventilation system using 14 different window-door opening configurations. A survey including questions on thermal environmental perception and indoor air quality was used to assess the thermal comfort levels of the occupants. The subjective results revealed that the temperature range was found to be beyond the acceptable comfort zone, the occupants have higher thermal comfort levels when

compared with the published international comfort standards and related prediction models.

Wang *et al.* [2010] investigated the human responses to the thermal conditions in naturally ventilated residential buildings. 423 sets of physical data and subjective questionnaires were collected from 257 families in six residential communities. The neutral temperature was 23.7 °C, with the clothing insulation of 0.54 Clo (1 Clo = 0.155 m<sup>2</sup>K/W, the unit Clo is used to measure the thermal insulation of clothing). The neutral temperature in Harbin is lower than neutral temperatures in countries with warmer climates, which are in accordance with the thermal adaptive model. 80% of the occupants can accept the air temperature range of 21.5-31.0 °C, which is wider than the summer comfort temperature limits set by the adaptive model. The preferred temperature range fell between 24.0 °C and 28.0 °C. 57.9% of the subjects voted 'no change' with the humidity ranging between 40% and 70%. 61.5% of the occupants voted 'no change' with the air velocity within the range of 0.05-0.30 m/s. In summer, the occupants preferred an air velocity of lower than 0.25 m/s even at a higher indoor temperature, which is different from the results obtained from other field studies. The work concluded that Harbin occupants in naturally ventilated dwellings can achieve thermal comfort by operable windows instead of running air-conditioners.

### **2.3 Natural ventilation strategies**

Natural ventilation plays a significant role in providing optimum indoor air quality and maintaining acceptable thermal comfort without the aid of mechanical systems, thus enabling fresh air delivery to occupants using sustainable and energy efficient methods. Allard [1998] defined optimum air quality as air free of contaminants or harmful materials that can present a health risk to the occupants, potentially causing irritation and discomfort. It is known that the indoor pollution level decreases exponentially with the airflow rate. Hence, optimising the supply of air is essential to ensure adequate indoor air quality while maintaining the ventilation rates within a certain range.

Natural ventilation is dependent on three climatic factors: wind velocity, wind direction and temperature difference. The speed and direction of the wind over a structure generates a pressure field around the building as shown in Figure 2.4.

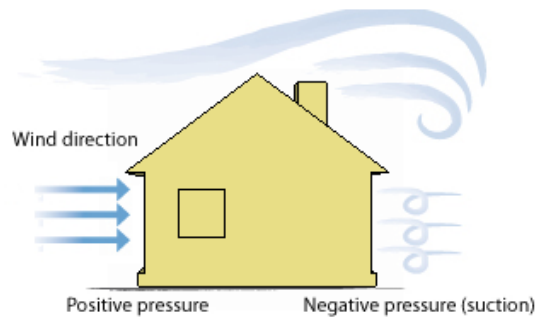


**Figure 2.4** Wind creates a positive pressure on the windward side of a structure and a negative pressure on the leeward side [Hughes *et al.*, 2012].

Passive ventilation devices such as the wind tower provide natural ventilation by taking advantage of the pressure differences surrounding the building. Therefore, it is essential that the device is positioned to maximise the pressure differential between the inlet and outlet. The primary driving force for the wind tower is the external driving wind, positive pressure on the windward side drives the fresh air into the room and the negative pressure on the leeward side extracts the stale and warm air. A slight change in air pressure can create sufficient airflow to improve the thermal comfort of the inhabitants. The wind changes direction over a certain range on an hourly, daily and seasonal basis, thus the pressure field surrounding a building will also change accordingly. A wind tower inlet opening can change from positive pressure to a negative pressure from one day to the next. In this case the opening will function as an exhaust vent.

Wind induced forces will always be the main factor influencing natural ventilation. However, in the absence of wind the driving force for the wind tower is buoyancy or the stack effect which is a result of the air temperature difference between the micro and macro climate. The subsequent variation of air density and pressure gradient of the indoor and outdoor air masses causes the warm air (less dense) to rise up and escape through the exhaust. Consequently, new air is drawn in to replace the air that has escaped.

Hughes and Mak [2011] used CFD modelling to investigate the wind pressure and buoyancy driven flows through a natural ventilation system. The experimental and numerical results showed that wind driven force is the primary driving force for the wind tower device, providing 76% more indoor ventilation than buoyancy driven forces. The study also confirmed that the effect of the buoyancy force is insignificant in wind

tower systems without additional airflow openings. However, the effective addition of windows and vents in combination with buoyancy driven flows has the potential of increasing the internal ventilation and overcoming the unavailability of wind driven forces in dense and urban areas. Jones and Kirby [2009] used a semi-empirical approach to predict the performance of a similar wind tower device. They concluded that the buoyancy effect is significant only at relatively low wind velocities.

Kleiven [2003] has highlighted the importance of minimising the resistance in the airflow path through the structure. Thus, the building itself, with its interior and exterior interfaces, rooms, hallways and staircase are used as air paths rather than the ducts used by mechanical ventilation systems. Naturally induced airflow is an important parameter among all the other parameters influencing the design and architecture of a building.

Figure 2.5 shows the operation and function of a wind tower in hot and dry regions during the summer. During the day, the warm ambient air is partially cooled by the tower structure before entering the building. During night time, the lower external air temperature cools the building mass, which provides additional cooling the next day [Bahadori, 1994].

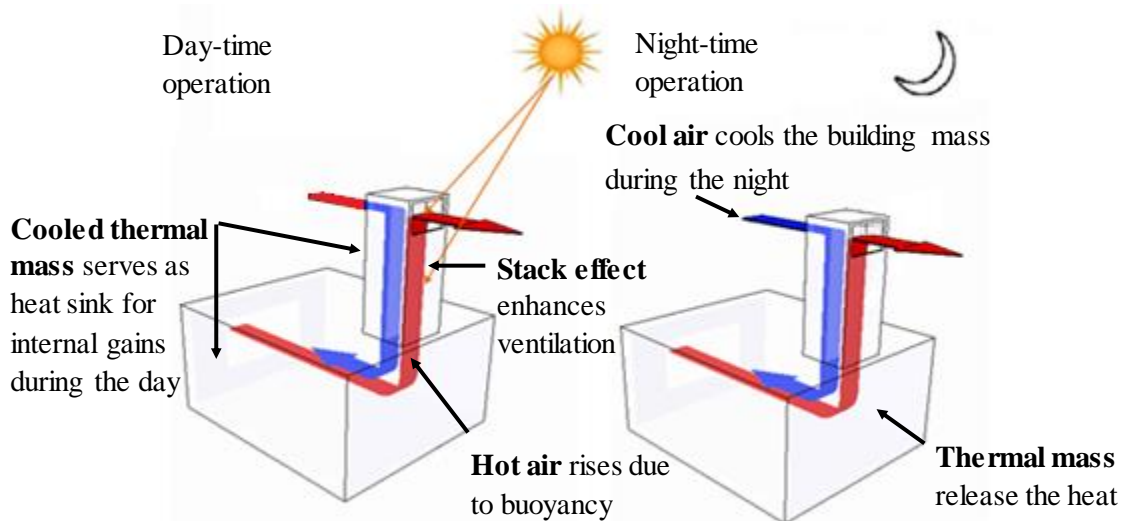


**Figure 2.5** Function of a wind tower in hot and dry region during summer day-time and night-time [Hughes *et al.*, 2012].

Furthermore, the wind condition in an urban environment determines the potential for natural ventilation for buildings. Therefore, defining and controlling the wind flow in built-up areas are critical factors for the design of a climatically responsive structure. Elizalde and Mumovic [2008] highlighted the effect of urban structures on the macro-

micro climatic conditions. Generally, wind speed is reduced by 10-20% in urban regions, although high wind speeds can occur due to urban canyons which channels and accelerates the wind flow. The main urban design elements which can modify the wind conditions are: the city form, size and height of the individual buildings; the existence of high-rise buildings; orientation of the streets, and the availability, size distribution and design details of open spaces.

### **2.3.1 Solar chimneys**

Solar or thermal chimneys are used to enhance natural ventilation through stack effects for exhausts at purposefully designed exits with the effect of thermally induced ventilation in buildings [Bansal *et al.*, 1993]. The air flow rate through the solar chimney is influenced mainly by a pressure differential between the inlet and outlet, caused by thermal gradients (naturally-driven convection) and the incident wind (forced convection). Forced convection takes place when the flow is induced by an external force such as the negative pressure generated by the wind current at the outlet of the tower (venture effect). Natural or buoyancy flow convection occurs when the air is driven by the presence of a temperature gradient. Solar energy heats the wall of the solar chimney and warms the air within it. Consequently, warm air rises and exits at the top of the tower (air updraft) and draws cool air in through the openings or vents [Arce *et al.* 2009].

The basic design of a solar chimney encompasses three main components, namely the solar collector area, the ventilation shaft and the inlet and outlet openings. The solar collector is located in the top part of the solar chimney or can include the entire shaft as shown in Figure 2.6. The orientation, type of glazing, insulation and thermal properties of the collector are essential for harnessing, storing and utilising the solar gains. The vertical shaft connects the interior and exterior of the building. The height, cross-sectional area and thermal properties of the ventilation shaft can also affect the performance of the passive device.

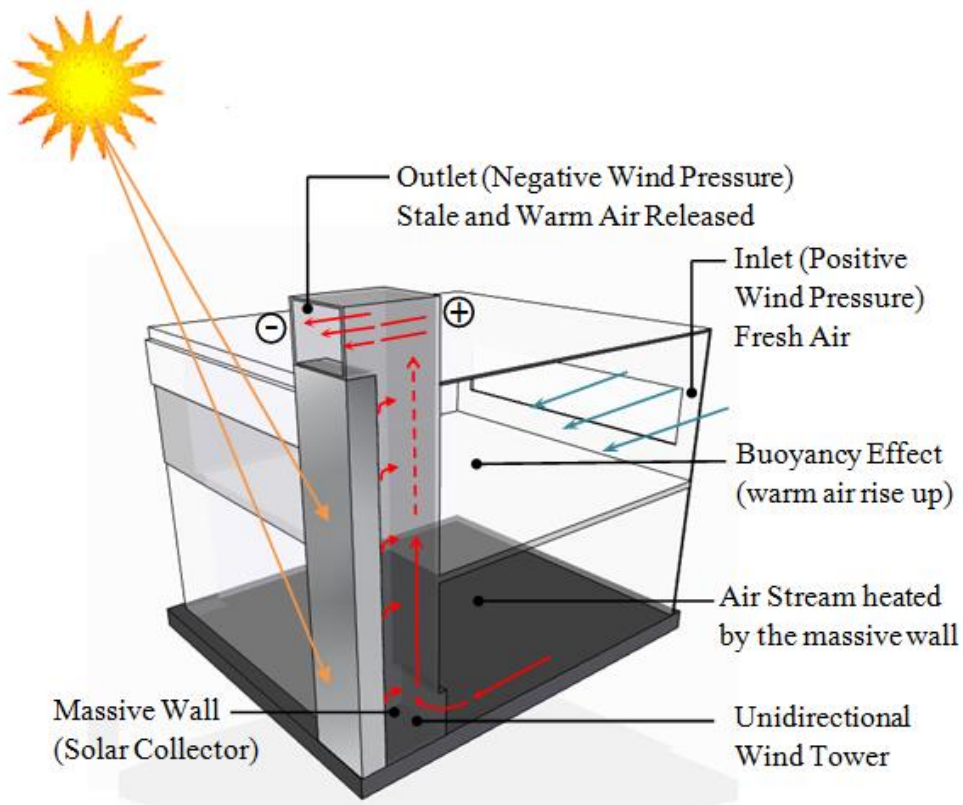


**Figure 2.6** Solar-wind tower system integrated to a naturally ventilated building [Hughes *et al.*, 2012].

The use of a solar chimney and its potential benefits regarding natural ventilation has been widely investigated over recent years. However, the majority of the studies have dealt with situations based on the buoyancy induced flow of air. The concept of a solar chimney coupled with a wind tower to induce natural ventilation has been studied analytically and numerically. These studies have reported on the feasibility of solar chimneys integrated with wind towers for enhancing the ventilation rates. Wind tower systems integrated with solar chimneys are capable of enhancing the cross flow ventilation and providing natural ventilation on hot windless days.

Bansal *et al.* [1993] used a mathematical model to predict the performance of a wind tower system integrated with a solar chimney. The work aimed to predict the results based on the proposed energy balance equation of the solar chimney and air flow rate equations. The study also confirmed that the thermal performance of the solar chimney was comparatively higher for lower incident winds. The result showed that the solar chimney can increase the mass flow rate of induced air by up to 50% for the case of high incident solar radiation and low wind speeds. The solar chimney integrated with a wind tower was able to generate airflow up to 1.4 kg/s which doubles that of a single wind

tower producing only up to 0.75 kg/s. The authors concluded that the effect of the solar system is more significant than that of the wind tower and combining both systems will enhance the ventilation rates by increasing the mass flow rate of induced air.

Nouanégué *et al.* [2008] carried out a numerical investigation of solar-wind tower systems integrated to a passive house. The work focused on establishing the governing parameters (constant Prandtl, Reynolds and Rayleigh numbers) and geometrical parameters (dimensional shape, outlet size and wall thickness) influencing the ventilation and thermal performance of the solar chimney. Simplified algorithm and control volume methods were applied to solve the equations for the conservation of mass, momentum and energy. The effect of wall thickness and outlet size was found to have a significant impact on the system's ventilation performance for high Reynolds and Rayleigh numbers. The numerical study indicated that the solar-wind tower system achieved maximum performance for forced convection heat transfers, which is a result of negative air pressure generated at the outlet. Strong convection with some reverse flow at the outlet was observed and the cooling of the heated surface is effective with high temperature gradients on the surface. It was found that increasing the height of the tower will increase the updraft. However, this would reduce the heat transfer at the outlet. The work concluded that Reynolds and Rayleigh numbers are major parameters influencing the performance of the solar-wind tower system. The authors also suggested that geometrical parameters can be optimised to obtain the highest ventilation performance.

Zamora and Kaiser [2010] studied the effect of wind and buoyancy induced air flows on the ventilation performance of a building incorporating a solar chimney. The work developed a mathematical and CFD model to analyse the induced mass flow rate, pressure coefficients and average Nusselt number of the air flow within the updraft tower for varying wind velocities (0-10 m/s). Different values of Rayleigh number were applied to simulate the heating conditions of the channel wall (isothermal and uniform heat flux). The Reynolds k-w turbulence model proved to be the most effective model for this type of analysis.

The numerical results showed that for a positive wind velocity (windward side exposed to the prevailing wind) of 2-3 m/s, the wind driven force was the primary driving force for the device, obtaining significantly higher values of induced mass flow rate compared

to buoyancy induced flow. However, for lower values of wind velocity, a combined buoyancy-wind induced flow was observed inside the thermal chimney. For a negative wind velocity (leeward side facing the prevailing wind), the mass flow rate becomes negative through the solar chimney. As a result, external air comes in through the upper opening of the chimney and generates pockets of reverse air flow at the top. The pressure analysis showed that for positive values of wind velocity, outlet suction of the chimney generates substantial suction relative to the velocity pressure of wind and overpressure was observed for negative values of wind velocity. The results obtained for the average Nusselt number also confirmed that the wind driving force was dominant for wind velocities of 2-3 m/s and wind suction effects were significant even at low values of wind velocity.

### **2.3.2 Structural night ventilation**

Hughes *et al.* [2011] defined structural night ventilation as a passive cooling strategy that relies solely on wind-driven or buoyancy forces. Thermal comfort during the day is provided by cooling the internal surface of the wind tower channel during the night time, which results in heat absorption during the day time. Night time coolness stored in walls and partitions of the wind tower cools the air induced during the day, making it denser so it sinks down through the base of the tower and into the occupied space. Naturally, the tower heats up itself as the tower cools the air passing through it. The cooling effect of the tower is lost when the temperature of the thermal mass reaches the same temperature as the ambient air. Bahadori [1985] suggested that wind tower systems may use shaft dividers which are arranged to provide more surfaces in contact with the flowing air, so that the air can interact thermally with the heat stored in the mass of the shaft dividers. Ghaemmaghani and Mahmoudi [2005] described the shaft dividers used in the traditional wind towers as thermal sinks made of mud bricks which functioned like radiator fins, absorbing the heat during the day and releasing the stored heat during the night.

In most conditions, the ambient air is only adequately cold during night-time. Therefore, a storage media is required to allow the ventilation system to be used during the day and the coolness created during the previous night. The coolness which is stored for use to equalise heat loads is relative to the storage capacity of the structure. The amount of thermal mass a tower has controls how much coolness it can store and how

rapidly it heats up the next day. Towers with low thermal mass cannot store much coolness and heat up very quickly. The major disadvantage of structural night ventilation is the limited controllability and slowness of the charge/discharge process as surface heat transfer relies on natural convection.

Wang *et al.* [2010] investigated the feasibility of night ventilation control strategies in office buildings. Energy Plus software was used to simulate the internal thermal conditions and energy consumption in office buildings integrated with night ventilation. The study also analysed the factors influencing the performance of night ventilation such as ventilation rates, thermal mass and weather conditions. The study concluded that the efficiency of a night ventilation strategy is higher when the active cooling time is nearly equivalent to the night ventilation operation time. It was found that the mean radiant temperature of the interiors was reduced by up to 3.9 °C with the night ventilation rate of 10 air change per hour.

### **2.3.3 Courtyards**

The traditional vernacular style of architecture in the Middle East is influenced mainly by the local climate, culture and the availability of the building materials. Houses are constructed close to each other, with high walls, creating narrow alleys in between the structures which provided shading for the inhabitants throughout the day. The rooms with large windows are built around an open courtyard, allowing the wind to circulate freely throughout the room and provide daylight [Roaf, 2008].

The courtyard is exposed to solar radiation for long hours. Hence, the air in the courtyard becomes warmer and rises up due to buoyancy forces. To replace it, cool make up air from the ground level flows through the openings of the living spaces, thus creating the indoor air flow as shown in Figure 2.7.

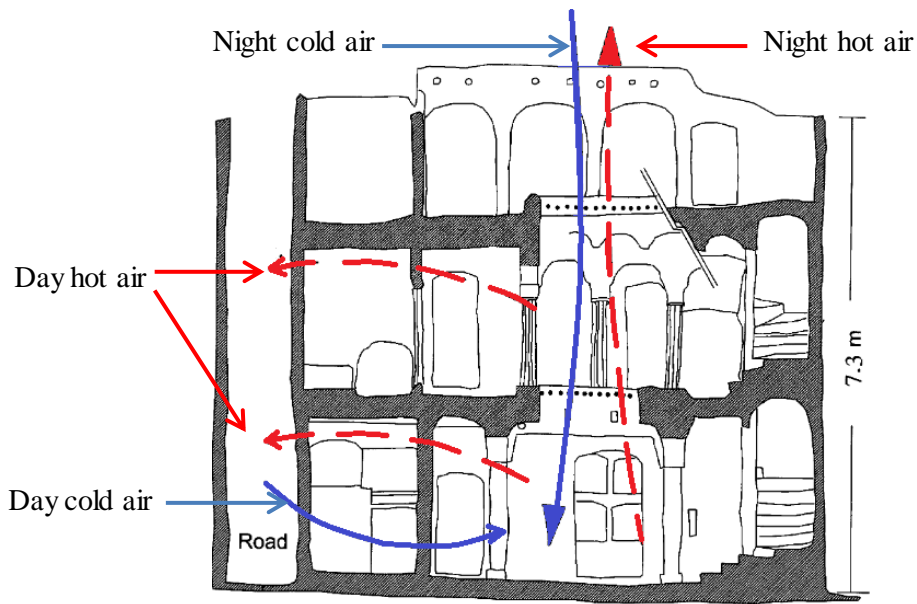


**Figure 2.7** Cross-sectional diagram showing how a courtyard is used to regulate thermal environment of a typical Mزاب dwelling [Bouchair, 2004].

During the night, the cooling process is reversed. The cooled surface air of the roof sinks down to the court and this cooled air enter the rooms through the low level openings and leaves through higher level openings. This system can work effectively in hot climates where day time ventilation is undesirable. However, when the courtyard receives extreme solar radiation, much heat will be conducted and radiated into the living spaces as against the induced draft of air which will significantly reduce the efficiency of the design configuration [Safarzadeh and Bahadori, 2005].

Traditional courtyards are also integrated with evaporative cooling towers which contributed significantly to enhancing the thermal conditions within the courtyard and enclosed spaces. This proved to be an effective method in creating an enclosed space that has unique environmental qualities within an extreme climatic environment. The courtyard is turned into a thermal sink that provides coolness to the rooms around it with less humidity and a suitable place for creating a comfortable environment [Edwards *et al.*, 2005].

Sharples and Bensalem [2001] investigated the air flow pattern through a courtyard and atrium buildings located within an urban setting. The study used experimental wind tunnel testing to analyse different ventilation strategies resulting from the use of different courtyard and atrium pressure systems (positive pressure and suction). The model structures were observed both in isolation and in simulated urban settings of

different group layout densities. The effect of wind direction on the ventilation performance was also observed. The research found that at  $0^\circ$  wind angle the open courtyard in an urban environment had a poor ventilation performance while an atrium roof with openings operating under a negative pressure was more effective. However, changing the wind direction to  $45^\circ$  incidence angle had the effect of making the difference in the observed flows between the models significantly smaller.

### 2.3.4 Wind escapes and air vents

The technique of using the suction caused by low air-pressure zones to generate steady air movement indoors is used in the design of the wind escape. Figure 2.8 shows a venturi tube used as a roof ventilator. The venturi effect causes air to be exhausted through the roof openings, and at or near the ridge. The wind escape system is based on the Venturi effect, which increases the air velocity as it is forced through a reduced area.

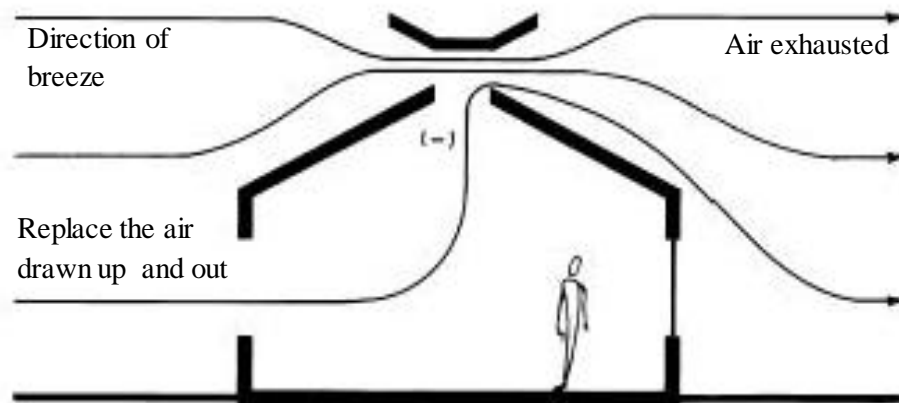


**Figure 2.8** A funnel shaped roof ventilator illustrating the Venturi effect [Lechner, 2001]

This concept can be applied more advantageously in designs for use above ground as shown in Figure 2.9. The wind escape can accelerate effective natural ventilation and air circulation when integrated with other devices for air movement such as windows and doors.

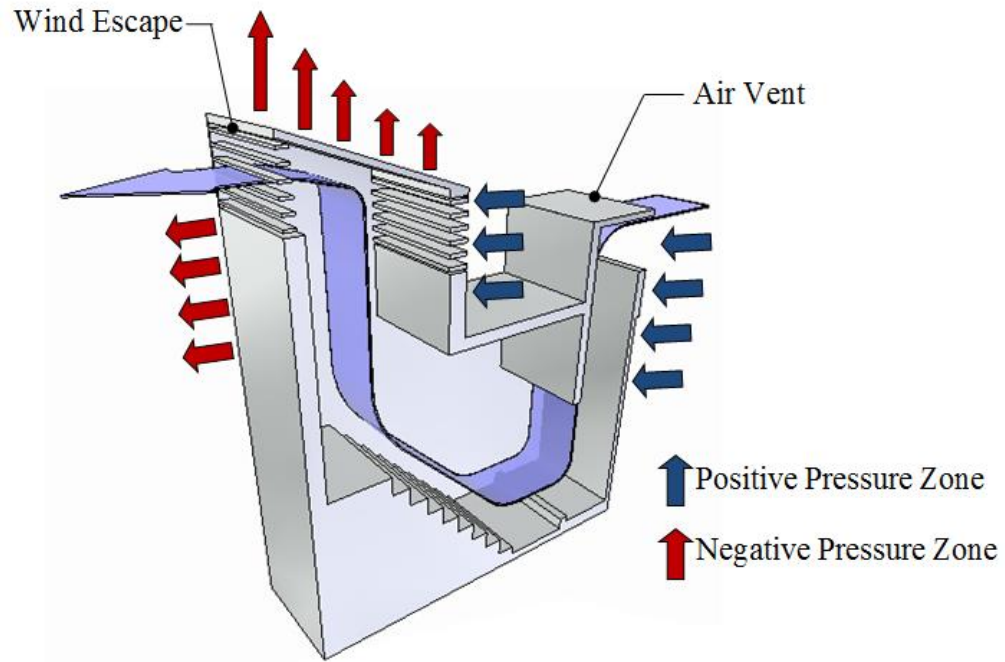


**Figure 2.9** Flow diagram representing ventilation through a structure with a wind escape and air vent [Hughes *et al.*, 2012].

### 2.3.5 Wind scoops and suction cowls

Wind scoops are designed to catch the prevailing wind and direct the fresh air into the building. To operate efficiently they must be omnidirectional, rotating about an axis so as to always have the opening facing the incident wind. Stationary or fixed wind scoops become ineffective when the wind changes its direction other than its design range and will even work in reverse functioning as a suction cowl. The omnidirectional wind scoop catches the wind at the area of greatest positive pressure. The opening of the wind scoop is arc-shaped to help catch wind that deviates away from head-on wind. The device must be very responsive to varying wind direction and capable of moving easily into the wind. A balanced structure with a good centre of gravity is essential to allow the wind scoop to rotate easily. A single or double vane can be used to direct the scoop into the wind (Figure 2.10).

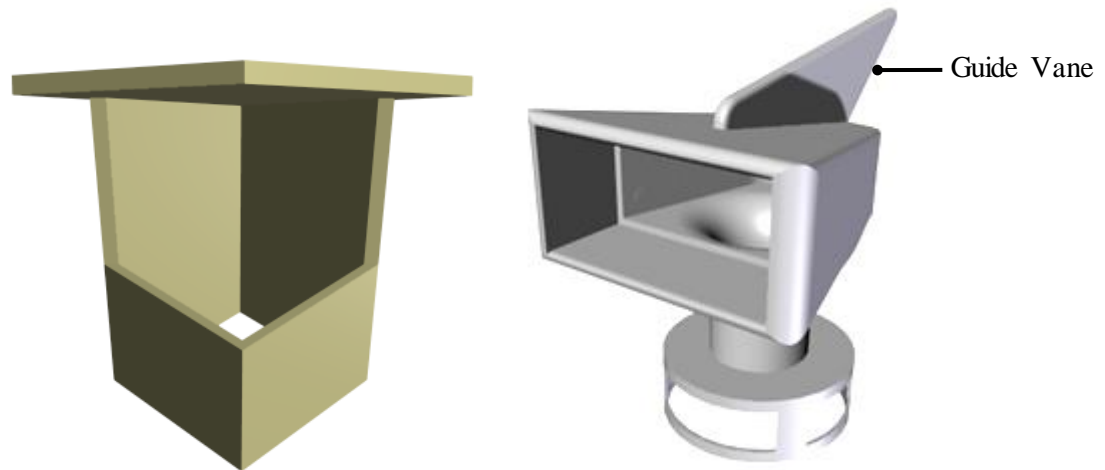


**Figure 2.10** Stationary and omnidirectional wind scoop with single guide vane [Hughes *et al.*, 2012].

Wind scoops are traditionally common in areas where the wind blows from a predominant direction. They can be used in conjunction with wind towers to create a system by which cool and fresh air is supplied by wind scoops and warm air is removed through the wind towers. Suction cowls use wind induction and the stack effect to dissipate exhaust air into the atmosphere. Similarly, cowls could be stationary or rotating about an axis so to always have the opening facing the leeward side (negative pressure) [La Fianza *et al.*, 2010].

### 2.3.6 Traditional wind towers

The wind tower design is based on the natural cooling systems in Iranian traditional architecture [El-Shorbaghy, 2010]. It has been used in the Middle East for many years to provide natural ventilation and passive cooling to buildings. Almost all historic buildings were naturally ventilated. Domed roof and air vent systems were incorporated in building systems as early as 3000BC in Iran. Some of the most significant, examples of traditional wind tower systems utilising both wind and the stack effect for natural ventilation can be found in the Middle East regions.

Montazeri *et al.* [2010] stated that the ventilation efficiency of wind towers is reliant upon creating the maximum pressure difference between the air inlet openings and exhaust of the passive device. The air movement around the structure will determine the size, location and form of the wind tower and its openings, so as to maximise the pressure differential. The accurate sizing and positioning of the openings of the wind

tower contributes to its cooling operation. Wind tower inlet openings are provided in the direction of the prevailing wind and the outlet on the opposite side, to take advantage of the pressure difference created by the wind speed and direction. The wind tower is most effective when located at the windward edge of the roof where the positive pressure is greatest and less effective at the leeward side as shown in Figure 2.11. The opening size depends on factors such as the location, topography and required air flow rate.

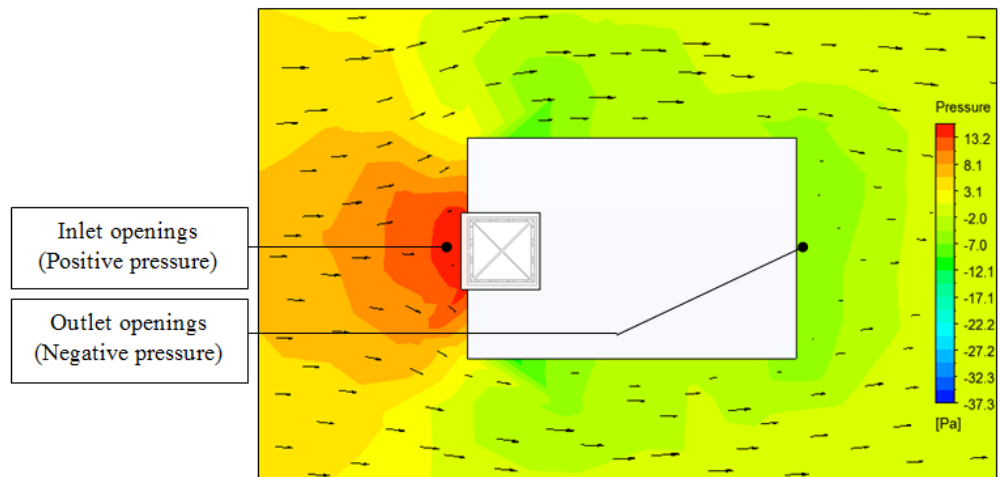


**Figure 2.11** CFD analysis showing the positive pressure on wind ward façade and negative pressure on leeward [Hughes *et al.*, 2012].

Gage and Graham [2000] described traditional wind towers as tall structures which generally rise up to between 5 and 33 metres. The extrusion of the wind tower creates the same effect as the structure formed by obstructing the wind current and generating a lower pressure over the opening (Figure 2.12). It has vertical openings on top which captures wind at high elevations and directs the air flow into the interior living spaces of the building. This structure extracts and supplies air into the buildings using ventilation principles of the wind tower and the stack effect. It directly cools the occupant by increasing the convective and evaporative heat transfer from the interior surfaces and indirectly by eliminating the heat stored within the structure.

Wind towers can be divided into one-sided, two-sided, four sided, hexahedral and octahedral (Figure 2.13). It is essential that a natural ventilation system will perform well for all wind conditions. A'zami [2005] suggested that structures with multi-directional wind towers are often built in conditions where there is no predictable prevailing wind direction.

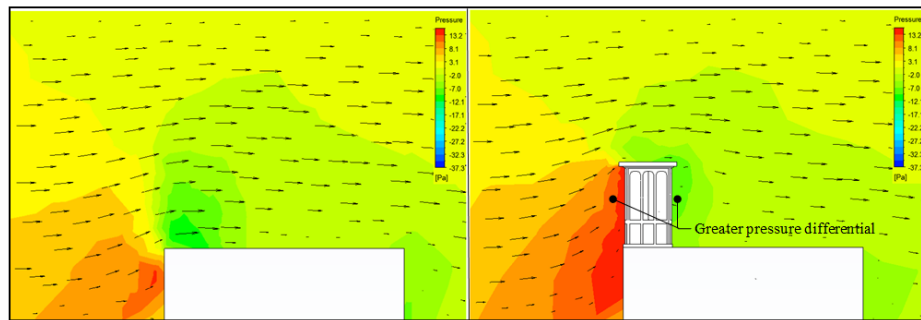


**Figure 2.12** CFD analysis showing (a) negative pressure over the roof (b) positive pressure on the wind ward side of the wind tower and negative on the leeward [Hughes *et al.*, 2012].

In general, the induced air flow rate decreases by increasing the number of openings. A one or two-sided wind catcher will induce more air into the room at zero wind angles. On the other hand, the sensitivity of wind towers against the incident wind angle decreases by increasing the number of openings. The optimum angle in which every wind tower model induces the highest volume of air is the angle in which there is the most effective area exposed to the wind current.

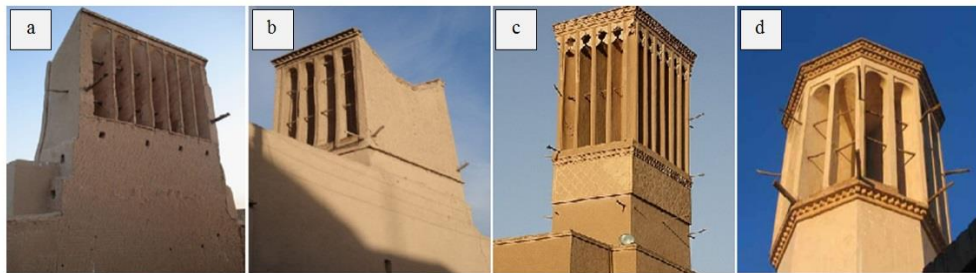


**Figure 2.13** Traditional wind towers with different number of openings (a) one-sided, (b) two-sided, (c) four- sided, (d) octahedral [Hughes *et al.*, 2012].

### 2.3.6.1 One-sided wind tower

The traditional one-side wind tower is a shaft mounted on top of the building with an opening facing the prevailing wind (Figure 2.14). The one-sided wind tower is more effective when employed in dense cities with moderately hot climates, where thermal comfort relies mostly on the movement of air. Dense development in urban areas reduces the wind speed at street-level, making windows insufficient for ventilation.

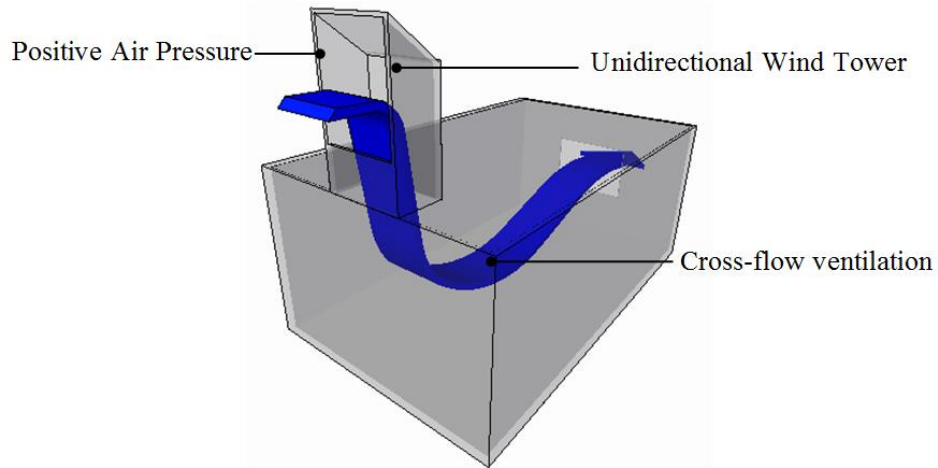


**Figure 2.14** A flow diagram representing ventilation through a room with a one-sided wind tower [Hughes *et al.*, 2012].

A one-sided wind tower will not function when the incident wind blows from a direction other than its design range unless the air inlet is at a sufficiently high level for the buoyancy forces to overcome the unfavourable wind conditions. In this case, the tower will function as a solar chimney and the airflow will be reversed. Detailed metrological data is available for most areas and this will give wind speed and direction. However, the wind blows from directions other than the prevailing directions for a significant amount of time. In urban areas, local airflows can be significantly different from prevailing directions because it is dependent on the surrounding buildings which may be erected or demolished in the future.

The traditional one-sided wind tower can be combined with an air escape to increase the cross-flow ventilation. The warm air stored inside the building is drawn out through the wind escape by suction and the indoor airflow movement is accelerated. The system is driven mainly by air movement which is created by the pressure differential surrounding the devices. The wind tower is positioned at the wind ward side of the building which is facing the prevailing wind and the air escape is located on the other end which has negative pressure. The temperature difference between the exterior and interior air can also enhance the air movement, creating a natural draft and forcing the air to flow through the structure. The airflow rate is directly proportional to the size and elevation of the inlet and outlet openings. The external conditions determine the size of the tower. Larger wind towers were used in areas with a low ambient air temperature while smaller towers were employed in areas with high external temperatures. Incorporating wetted

surfaces inside the device can increase the ventilation rates and provide effective cooling during extreme conditions [Attia and Herde, 2009].

Figure 2.15 illustrates a traditional one-sided wind tower or Malkaf placed directly over a roof opening of a vernacular architectural design. The Malkaf traps the cool breeze and channels it down into the lower floor which is a result of the increased air pressure at the entrance of the tower. Within the structure, the air slows down and flows through the central area, with some of the air escaping through the domed roof and some flowing directly to the outflow vents of the air escape which has a lower air pressure. The temperature difference between the lower and upper floors and strategic arrangement of the openings ensures air circulation even when the external air is at very low speeds.

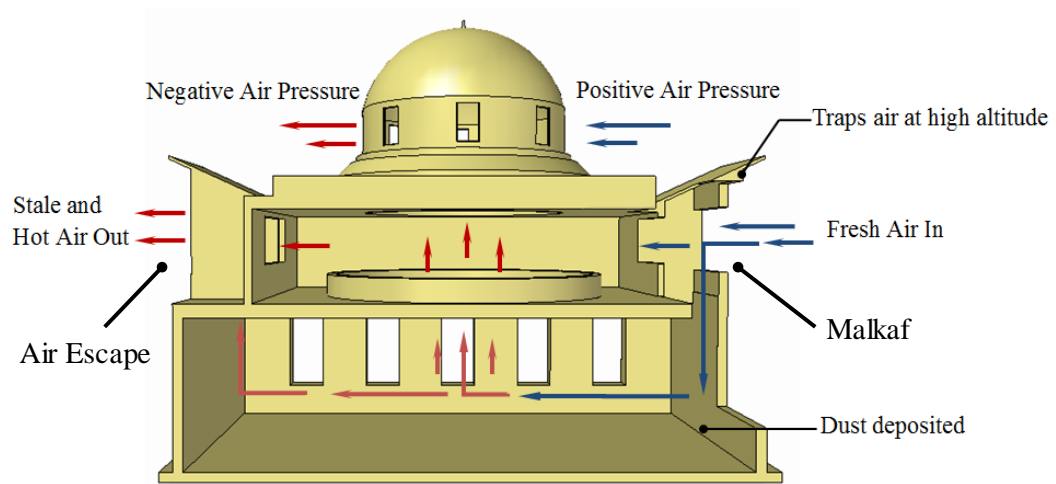


**Figure 2.15** Vernacular architecture integrated with Malkaf wind catchers and a domed roof [Hughes *et al.*, 2012].

Montazeri and Azizian [2008] evaluated the performance of a one-sided wind tower using experimental wind tunnel and smoke visualisation testing. A 0.7x 0.4 x1.45 m scale model of an ancient wind tower was setup in a test room which was installed below the base of the wind tunnel device. The induced airflow rate into the test room and the pressure coefficients around all surfaces of its channel were measured for different values of approaching air incident angles. Neglecting the dependence of the discharge coefficient on the flow direction, the natural ventilation performance of the one-sided wind catcher was estimated using a non-dimensional analytical model. The results showed that the existence of separation zones and wake regions near the lower edge of the opening causes a variation in the pressure coefficient at the tower's entrance. As a result, the wind tower could not achieve its maximum efficiency.

The work also investigated the effect of locating the wind tower in the wake of an upstream object which simulates the condition in urban areas where the air flow is obstructed by neighbouring buildings as shown in Figure 2.16. It was found that for an isolated wind tower model, the highest efficiency was attained at zero air incident angles. Placing a shorter upstream object before the wind tower reduced the circulation region at the entrance opening and the area of the lower edges. This increases the effective inlet area of the wind tower and significantly increased its ventilation capacity. For a taller upstream object, the opening of the tower lay in the wake region of the upwind model and the one-sided wind tower thereby acted as a suction device. The work concluded that the one-sided wind catcher has the potential to be an effective ventilation design for an urban setting.

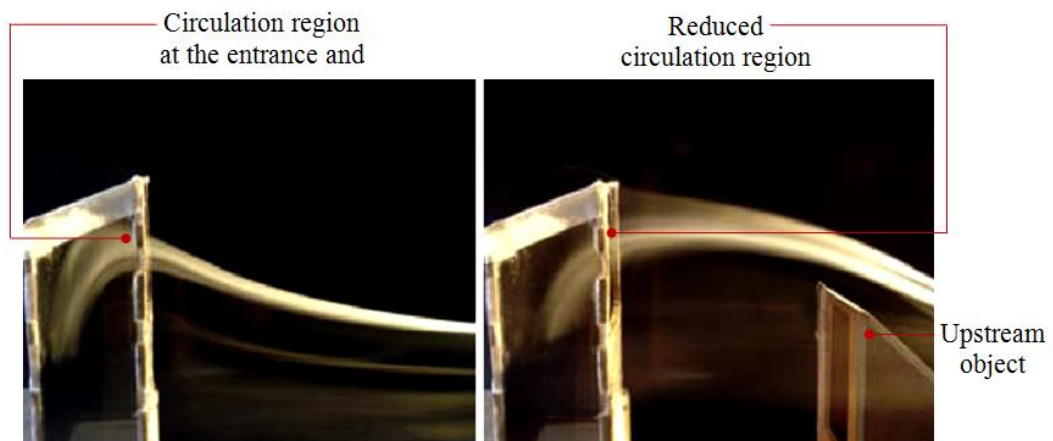


**Figure 2.16** Smoke visualisation testing, for (a) isolated wind catcher model and (b) placing under the short upstream object [Montazeri and Azizian, 2008]

Attia and Herde [2009] investigated the ventilation performance of Egyptian Malkaf wind towers used in low rise buildings. Experimental wind tunnel and smoke visualisation testing were carried out to evaluate the air flow rate and distribution in a scale model test room integrated with a Malkaf wind tower (Figure 2.17). Two different design configurations was used for the experimental analysis, one with a single one-sided Malkaf tower facing the prevailing wind and the other with two Malkaf towers placed at both end of the structure (inlet and outlet). Both device configurations proved to be effective in improving the air flow distribution inside the building. It was found that the first configuration with a single one-sided tower obtained up to 4 ACH with an outlet wall to opening ratio of 0.6 and external wind speed of 2 m/s. While the combined system obtained up to 5.6 ACH with the same opening ratio and external conditions. The

results established that the maximum indoor air flow pattern can be achieved by sizing and positioning the inlet and outlet of the Malkaf as large and high as possible.

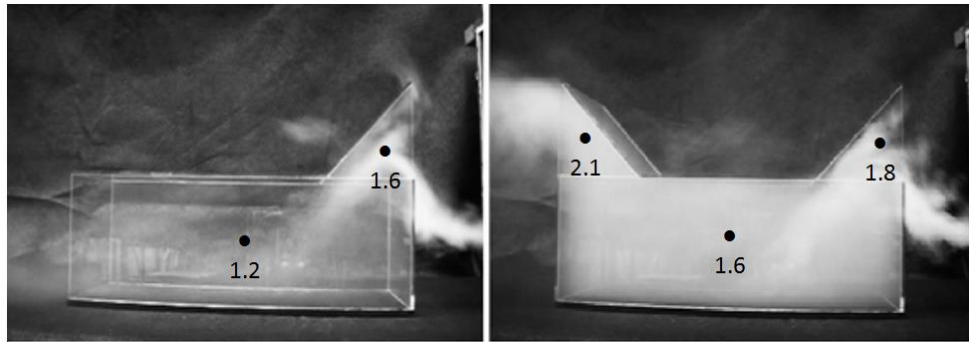


**Figure 2.17** Smoke visualisation testing shows the effect of placing; (a) one Malkaf in front in combination with outlet openings in the back (b) two Malkafs (windward and leeward) on the air flow pattern in the model [Attia and Herde, 2009]

### 2.3.6.2 Two-sided wind tower

A two-sided wind tower has two openings and two separate lower channels. It is often used in areas where there is a strong prevailing wind (Figure 2.18). The wind tower is divided into two halves for the purpose of air supply and extraction. The main advantage of a two-sided wind tower over the one-sided version is related to the angle in which the one-sided tower opening is exposed under the transition angle and the airflow rate through it tends to zero. For the same wind incident angles, the maximum air flow rate occurs at the transition angle of the leeward side of a two-sided wind tower. A disadvantage of multi-directional wind towers is air short circuiting. Short circuiting is a harmful phenomenon in wind tower systems which causes the air to enter through the supply opening and leaves through another without flowing inside the enclosed space. For a two-sided wind tower, there is no air short-circuiting for lower air incident angles. However for higher incident angles, short-circuiting occurs and reaches its maximum at  $60^\circ$  incident angle.

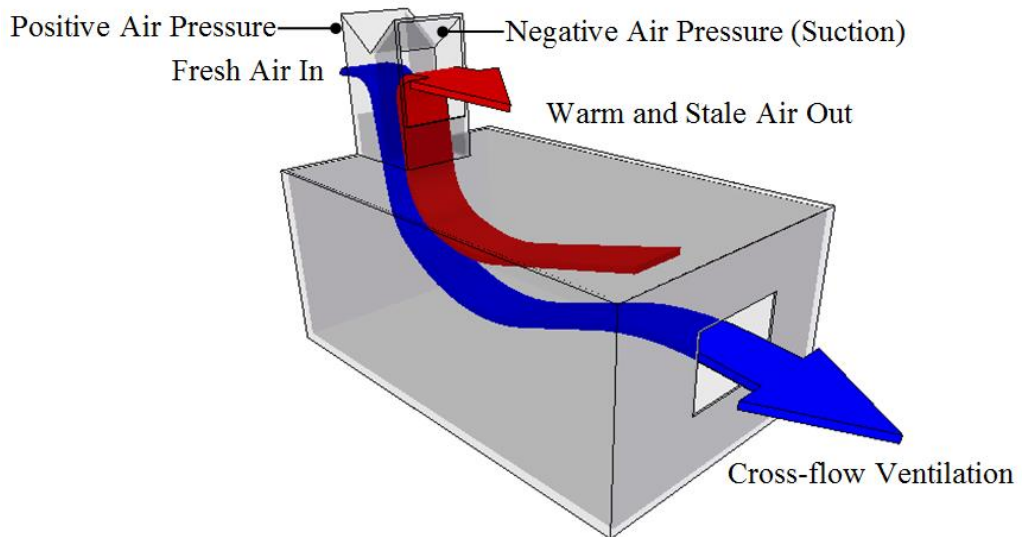


**Figure 2.18** A flow diagram representing ventilation through a room with a two-sided wind tower [Hughes *et al.*, 2012].

Montazeri *et al.* [2010] evaluated the natural ventilation performance of a two-sided wind tower device. Experimental and numerical techniques were used to analyse the effect of the pressure coefficient distributions at the wind catcher openings on the level of performance. The work also developed numerical CFD and analytical models to validate the accuracy of the experimental results. Good correlation between the different methods of analysis was observed. The results showed that the pressure coefficient varies sharply with the wind incidence angle. For the leeward side of the wind tower a uniform pressure distribution was observed. Increasing the incidence angle results in the average pressure coefficient reducing rapidly to reach its minimum value of  $90^\circ$ . The experimental investigations demonstrated the potential of a two-sided wind catcher for enhancing the natural ventilation inside residential buildings. The authors also concluded that the one-sided wind tower is more effective for areas with a prevailing wind from an economic point of view. Figure 2.19 shows the airflow through a two-sided wind tower at various wind angles.

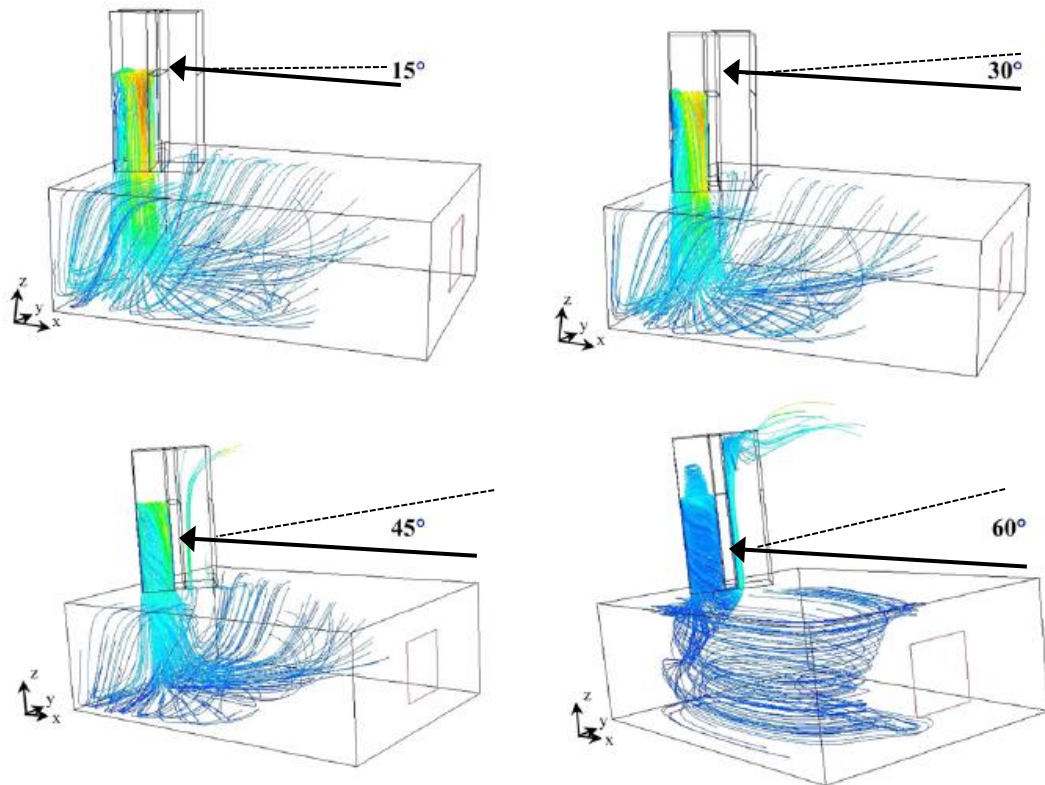


**Figure 2.19** Velocity streamline inside the building with a two-sided wind tower for various approaching air incident angles [Montazeri *et al.*, 2010].

### 2.3.6.3 Multi-directional wind tower

A multi-directional wind tower has a shaft with the top opening on two or four sides and has dividers placed diagonally across each other down its length to catch the wind coming from any direction. The shaft extends down to a level that allows the air flow to reach the lower floors of the structure as shown in Figure 2.20. This would allow the stale and warm air to exit through window openings and doors with negative or lower values of pressure coefficients. Multi-directional wind towers can also lower the indoor temperature by removing the hot air stored inside the structure through its exhaust openings [Zarandi, 2009].

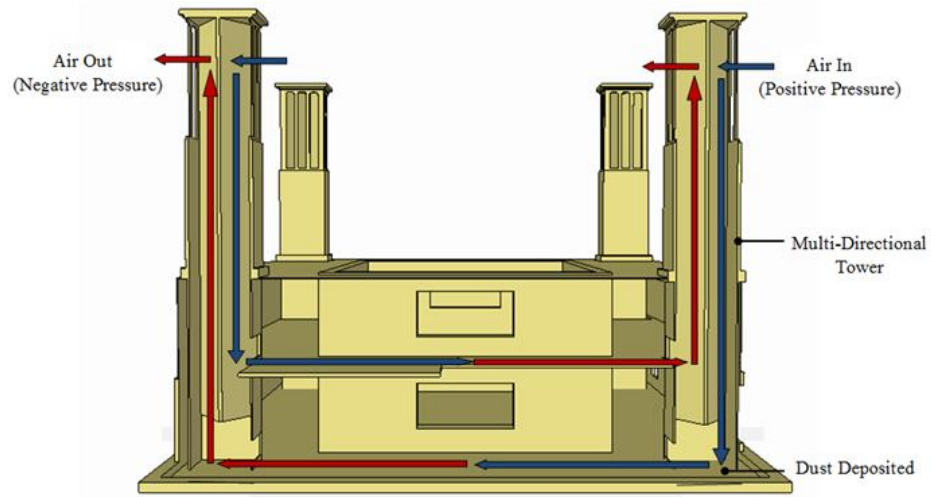


**Figure 2.20** Flow diagram representing ventilation through a traditional structure incorporating multi-directional towers or Badgir [Hughes *et al.*, 2012].

Figure 2.21 shows the operation of a four-sided wind tower oriented at  $0^\circ$  and  $45^\circ$  into the prevailing wind. A smaller area is available to the incoming wind when the tower is oriented at  $0^\circ$ . Turbulence is created by the air flow moving down and striking the dividers at  $45^\circ$ . This slows down the speed of the air moving down to the enclosed space below it. Three of the four quadrants are available to the stale air moving out of the building due to negative pressure and stack effect. While the tower oriented at  $45^\circ$  into the prevailing wind has a larger area available to capture the wind. The air moves more directly down the tower with less turbulence at its opening. In this case, two windward quadrants are available for air flowing into the tower and two leeward quadrants for the air flowing out of the tower.

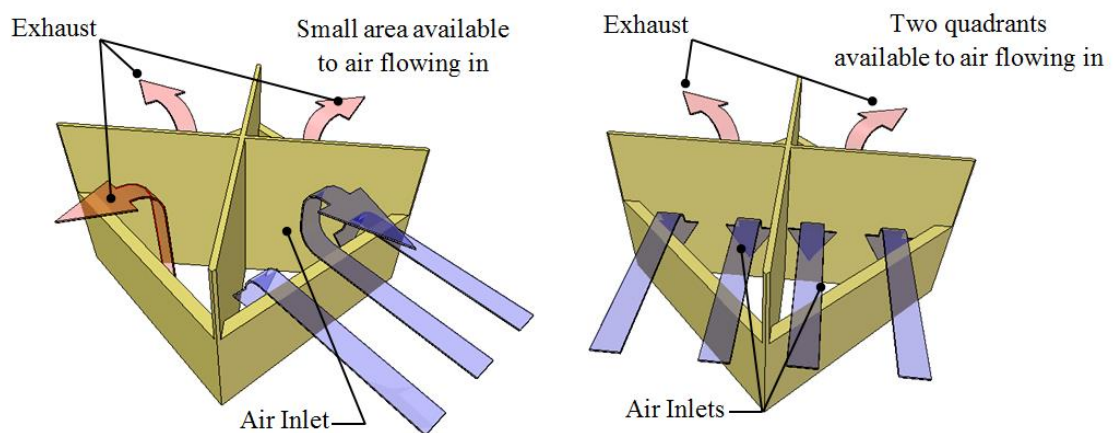


**Figure 2.21** Four-sided wind tower (a) with the incident angle at  $0^\circ$  (b) with the incident angle at  $45^\circ$  [Hughes *et al.*, 2012].

The wind tower functions according to the condition of the wind and solar radiation in the region. In different regions with varying wind speed and direction, traditional wind towers were built with different height and level, cross-sectional area of air passage, orientation, and positioning of inlet and outlet openings [Roaf, 2008].

Gage and Graham [2000] carried out experimental wind tunnel testing to compare the performance of a four and six-sided wind tower and analysing the effect of wind speed and direction. The wind tower scale models were connected to a test room which was located below the wind tunnel. Three different configurations were used to study the air flow rate and pressure differences inside the device. The first two experiments were a set of artificially controlled tests; pump and blower devices were placed underneath the floors to allow the flow rate to be set independently of the external wind. The final experiment was carried out with a direct flow through the device to simulate the conditions during normal operation. The results confirmed that driving pressure for the wind tower is reduced as the flow rate flowing through the device is increased.

The work concluded that in variable wind conditions, multi-directional wind towers with more than four openings have a more consistent, predictable and reliable performance. However, in areas with a predominant prevailing wind, the four sided wind tower will generate the highest pressure difference between the inlet and outlet openings when oriented at 45° to the wind direction. It was also established that the airflow speed is reduced approximately 80 to 88% than the external wind speed as it enters the towers channel.

A'zami [2005] investigated the designs of Badgir wind towers in traditional Iranian structures. The work examined and classified different types of wind tower based on its climatic function, location, size and the construction materials used. It was found that each region had a unique type of its own wind tower with a unique range of tower height, dimension and orientation resulting from local geomorphology, macro and micro climatic conditions and the social and traditions of a particular settlement. This study further highlighted the capability of the wind tower to create a temperature balance in the building during night and daytime. The walls exposed to sun heat up the indoor air which rises up during the day. The air released from the exhaust side of the wind tower is compensated by replacing it with cool air. The cool night air sinks down to the structure and cools the internal walls which provides additional cooling the next day.

The author concluded that strategic arrangement of the wind tower allows it to provide thermal comfort in hot regions by relying only on natural wind energy and temperature differences.

Montazeri [2011] investigated the natural ventilation performance of various multi-opening wind towers using wind tunnel and smoke visualisation testing as well as computational fluid dynamics (CFD) modelling. The study demonstrated the effect of the number of openings on the hydrodynamic performance of wind tower systems. Five cylindrical scale models with similar cross-sectional areas and vertical height were divided internally into several sections; two-sided, three-sided, four-sided and twelve sided configurations. The achieved experimental and numerical results showed that increasing the number of the wind tower openings reduces the induced internal air flow rate. However, increasing the number of openings can reduce the sensitivity of the natural ventilation device against the wind angle. It was found that the two-sided wind catcher delivers the most amount of air supply into the room at zero air incidence angle as shown in Figure 2.22.

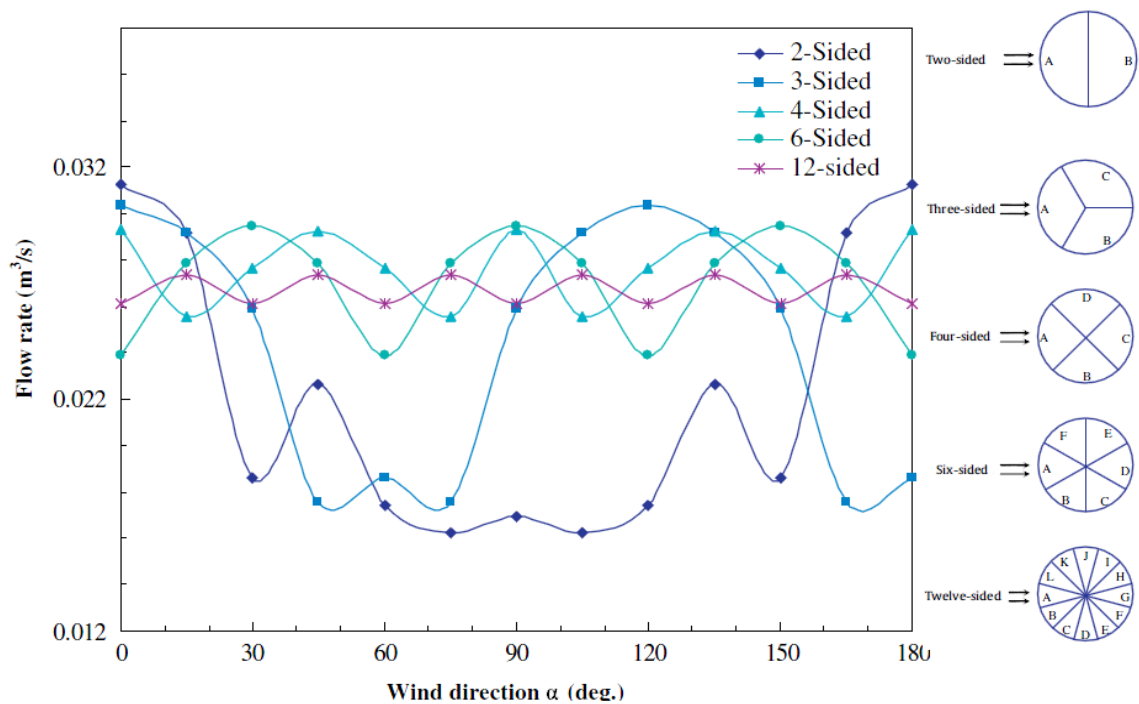


**Figure 2.22** Variation of net ventilated air flow rate into the building for the wind catcher models [Montazeri, 2011].

#### **2.3.6.4 Limitations of traditional wind tower systems**

Wind towers in general are limited by the restrictions on where they can be located. In dense urban areas, local airflows can be significantly different from the prevailing wind. Buildings are often located quite close to each other and the natural ventilation device will be strongly influenced by the surrounding structures. Wind tower systems do not perform well in dense urban environments because of the serious reduction of the wind speed due to urban canyons. Therefore, the wind tower has to be very high to be able to catch enough air. However, this may not be feasible in some areas where the elevation of the tower must be weighted up against aesthetic concerns and planning restrictions. Also, taller towers are more expensive to build and maintain. Efficient integration of natural ventilation systems in dense urban areas requires full understanding of the urban wind environments characteristics, as well as adaptation of the ventilation components to local conditions. Other limitations to the wind tower systems situated in an urban environment are outdoor pollution and noise pollution

Another limitation of the wind tower system is the unpredictability of the driving forces. Detailed metrological data is available for most areas and this will give the speed and direction of the wind. However, the wind blows from directions other than the prevailing directions for a significant amount of time. This hampers the ventilation requirements during periods of relatively extreme conditions and could have a significant impact such as flow reversal [Khan *et al.*, 2008]. Multi-directional wind tower systems can be used in such conditions where there is no predictable prevailing wind direction although air short-circuiting can occur in multi-directional wind tower. Short circuiting is a harmful phenomenon in wind tower systems which causes the air to enter through the supply opening and leaves through another without flowing inside the space to be ventilated.

Traditional wind towers have been designed and built using old technologies therefore they have design limitations which can be eliminated with modern technology. Traditional architecture can give ideas to enrich modern architecture by using renewable energy systems.

#### **2.3.7 Commercial wind towers**

Modern architects and engineers have integrated the principles of traditional wind towers with modern technology as helpful devices to increase the quality and efficiency

of the supplied air. Modern wind towers provide natural ventilation and light to any space in a building. Hughes and Ghani [2008] described a commercial wind tower as a top-down roof mounted, four-sided device used for naturally ventilating buildings. Modern wind towers are usually compact and smaller in size compared with the traditional wind towers. The device extends out from the top of a structure to catch the wind at roof level and channels fresh air through a series of louvres into the enclosed space under the action of air pressure, and, simultaneously, the negative pressure extracts stale air out of the space. Unlike the traditional wind tower systems, air is supplied to the enclosed space through the diffusers located at ceiling level. Hence, more free space is available for ventilation on the ceiling than on the corresponding floor of equal area.

The windvent is a commercially available natural ventilation device. The device is constructed from sheet metal and works on the principle of creating a pressure differential. Warm air rises, creating a low pressure in the receiving room, which then draws in the fresh air. The windvent is divided into four quadrants which allow fresh air to enter as well as stale air to escape, irrespective of the direction of the wind. The device is equipped with volume control dampers and ceiling diffusers which allow the occupants to regulate the air flow depending on the temperature requirement, CO<sub>2</sub> level and air distribution inside the building. The windvent louvre protects the interior from rainwater, snow, direct sunlight or noise while allowing the external air into the living space. Figure 2.23 shows a windvent device incorporating solar panels. The solar panel can be used to power a small fan to overcome excessive heat gains and boost the air movement through the wind tower when extra ventilation is required.



**Figure 2.23** Commercial wind tower device integrated with PV-panels [Hughes and Ghani, 2008].

Jones *et al.* [2008] compared the performance of two natural ventilation devices employed in classrooms in the UK, namely wind towers and conventional windows. The study focused on assessing the potential of the commercial wind tower to replace the ventilation provided by windows. The performance of the wind tower was measured in terms of the air quality supplied to the occupied space. The work further highlighted the capability of the wind tower to provide night cooling without affecting the occupant's security. The results showed that the classroom equipped with wind towers was able to meet the UK Government requirements for carbon dioxide levels and thermal comfort, while the classroom relying only on windows failed to provide the fresh air delivery rates. Also, it was found that night-time ventilation could reduce indoor temperatures by up to 2.8K.

The air circulation and air change rate are determined by controlling the amount of air that passes through the wind tower channel. A damper control system allows the occupants to reduce and regulate the air flow depending on the indoor and outdoor temperature, CO<sub>2</sub> level and air distribution inside the building. The volume control dampers are either manually or automatically operated through actuators, and provide the basis of the control mechanisms for the natural ventilation device [Hughes and Ghani, 2009].

Figure 2.24 shows a series of adjustable dampers installed inside the wind tower at room ceiling level. Modern wind catchers with automated volume control damper systems constantly control the airflow into and out of the occupied space. This would allow the ventilation device to serve different conditions such as summer or winter and day-time or night-time cooling. In the hot summer months the control dampers are programmed to fully open at night to maximise night-time cooling, allowing the fresh and cool air to enter the building and extract the stale air out. Occupants may override the control settings at any time using a wall-mounted override switch that will fully open or close the dampers.

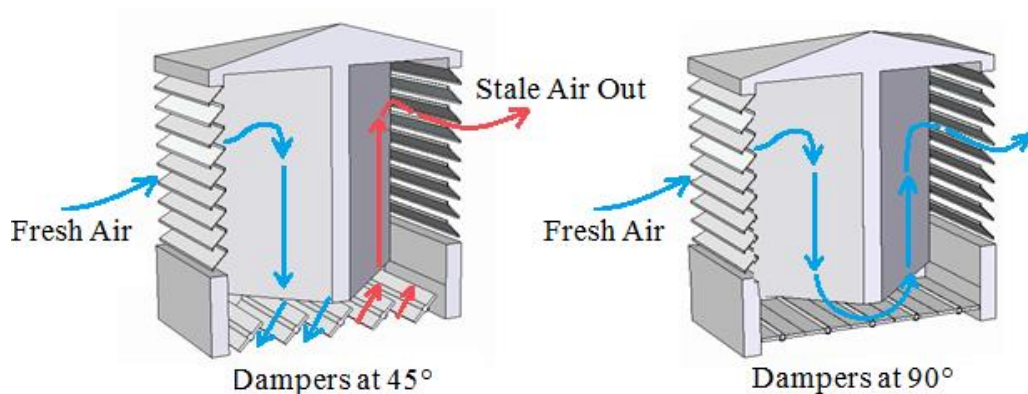


**Figure 2.24** Modern wind tower devices with a damper control system [Hughes *et al.*, 2012].

Wind tower louvres are horizontal blades mounted in the air inlets and exhausts of the ventilation device. The louvre blades are angled against the prevailing wind to allow the external air to enter the enclosed space and prevent rainwater, snow, direct sunlight and noise from entering the device. The louvre blade angle has an important role in the movement of air at the inlet and outlet. A properly designed louvre will minimise the wind resistance and maximise the internal airflow rate. The number of layers and length of louvres are other design aspects that affect the performance of the wind tower. Proper louvre length should both improve performance and reduce the manufacturing costs. Modern wind towers incorporate an adjustable louvre system which allows the louvre blades to be raised and lowered to alter the size of the opening according to the control strategy. The maximum air flow rate is achieved when the louvres are fully open. The system is able to modulate their position to increase the resistance of the louvre, or they can be fully shut to prevent the ingress of rain and snow, which any open louvre system is susceptible to [Liu and Mak, 2007].

Passive natural ventilation devices supply fresh air into the interior of a building and exhaust stale air out without requiring mechanical or electrically driven components. However, airflow rates achieved through standard wind towers often cannot meet the required indoor ventilation rates due to their sole dependence on the speed and direction of the wind. Hughes and Ghani [2010b] suggested that a passive-assisted natural ventilation system may be employed to provide continuous supply of fresh air without affecting the energy requirements of the wind tower. The hybrid system incorporates a low-powered fan installed inside the wind tower with the fan functioning, when required, to assist the flow of air between the building exterior and interior via the ventilator (Figure 2.25). The solar driven fan can also function as an exhaust device for extracting stale air out of the building. It provides a constant supply of ventilation air, even when there is no wind.

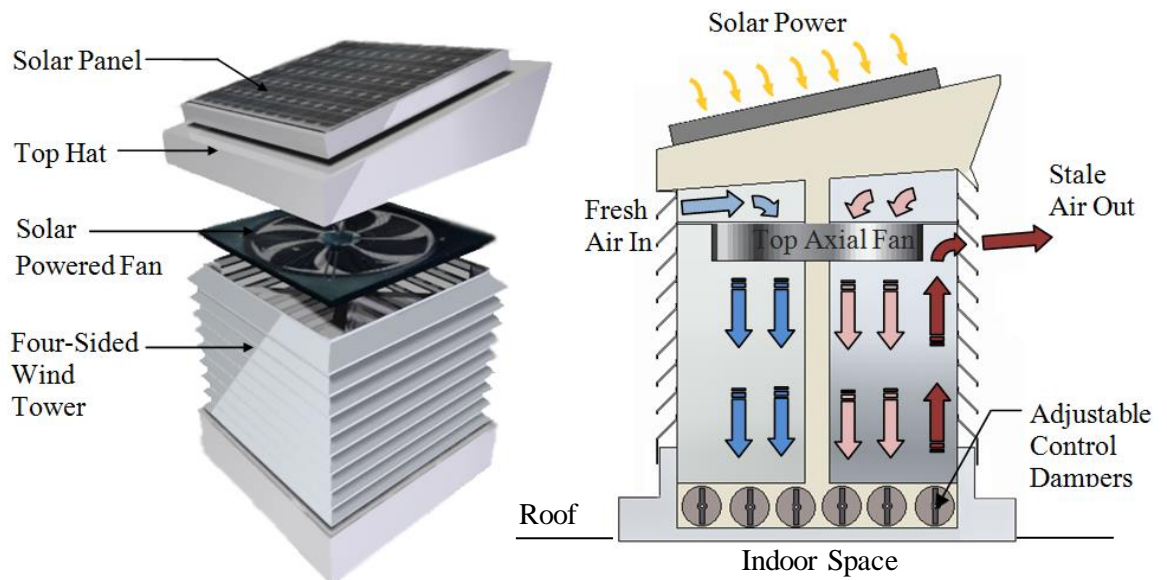


**Figure 2.25** Schematic of a wind tower system integrated with a solar powered fan [Hughes *et al.*, 2012].

### 2.3.7.1 Numerical investigations using CFD

Hughes and Ghani [2009] investigated the performance of a wind catcher device integrated with a controlled damper system using computational fluid dynamics (CFD). The CFD code used the finite volume method and employed the semi-implicit method for pressure-linked equations consistent (SIMPLEC) velocity-pressure coupling algorithm. The turbulent nature of the flow was modelled by the standard  $k-\epsilon$  model. In

order to accurately resolve the solution fields, the grid was refined and enriched using the hp grid adaptation method.

The work demonstrated the effect of different damper angles on the achieved velocity and pressure distributions inside the test model. The work simulated 19 different numerical models with the dampers rotated  $5^\circ$  for each test, for a range of 0 to  $90^\circ$ .

Results showed that optimum operating range for the windvent dampers is of the range  $45$  to  $55^\circ$ . It was observed that increasing the angle of the dampers decreases the air flow velocity and increases the pressure drop as shown in Figure 2.26. This is a result of the flow path restriction caused by the dampers oriented at a certain angle. The intersection of the two lines represents the optimum angle for the dampers. The authors concluded that the integrated damper control system was able to control the air movement effectively, thus sustaining a constant fresh air delivery rate. The computational results showed a good correlation with the experiments conducted by Elmualim [2006b].

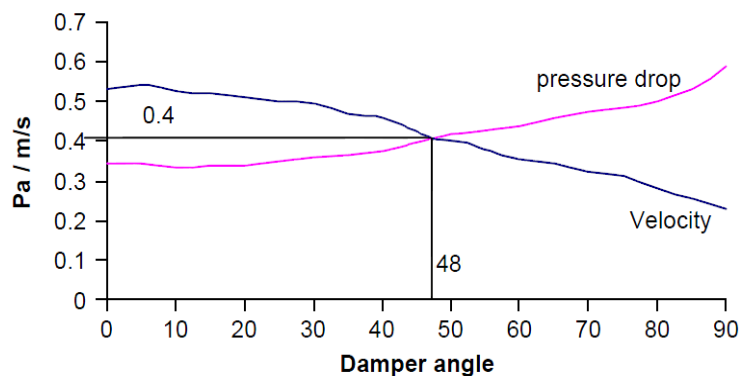


**Figure 2.26** Effects on air velocity and pressure by damper angle variations [Hughes and Ghani, 2009].

Hughes and Ghani [2008] investigated the CFD modelling of a commercial wind tower device. The turbulent nature of the flow was modelled by the standard k-epsilon model. The work focused on the effects of varying the external wind speed and direction on the capability of the passive ventilation device in providing fresh air at the recommended air delivery rates. The 1x1 m square wind tower was connected to a small room with a recommended 20 occupants. The study further highlighted the effect of the dampers on the airflow and its potential to limit the short-circuiting of the air movement which decreases the efficiency of the device. This was achieved by running the numerical model with varying wind velocity and two wind directions, concurrent and counter-

current. Figure 2.27 shows that at 1 m/s the wind tower barely supplied the minimum, however this was easily exceeded as the velocity was increased.

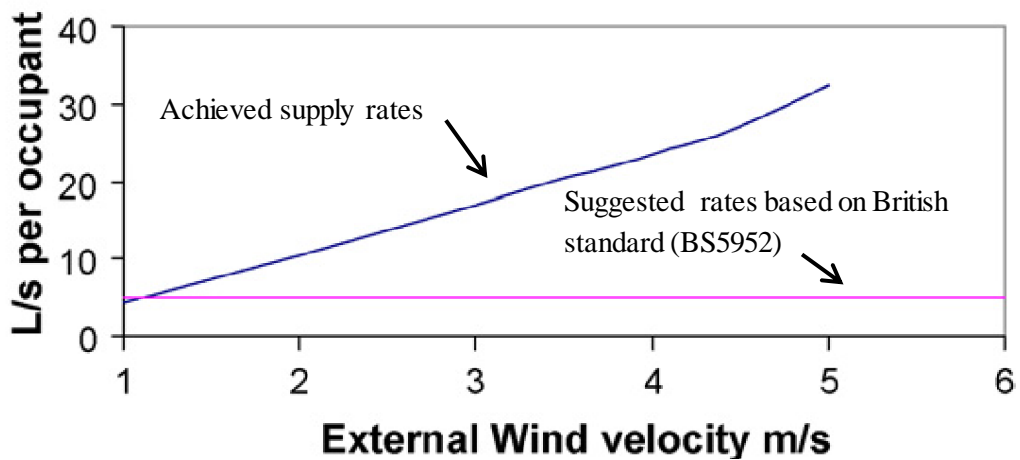


**Figure 2.27** The effect on windvent fresh air delivery rates by an increase in external wind velocity [Hughes and Ghani, 2008]

The results demonstrated the potential of the modern wind tower in delivering the required fresh air supply and providing a sustainable alternative ventilation system. However, at a low external wind velocity of 1 m/s the device barely supplies the minimum ventilation rate, providing only 4 L/s per occupant which is lower than the recommended minimum of 5 L/s per occupant. However as the external velocity was increased the recommended rates were exceeded, reaching up to 23 L/s for an external wind velocity of 4 m/s.

Hughes and Ghani [2009] also used CFD to analyse the effect of varying the angle of the louvres on the velocity and pressure distributions inside the wind tower's channel and the space below it. Eight numerical models were developed with the louvre angles rotated in 5° increments for a range of 10 to 45°. The study also highlighted the effect of the louvre stall angle on the performance of the wind tower. The louvre was compared to a thin aerofoil which was subjected to similar aerodynamic forces. The results demonstrated that for an external velocity of 4.5 m/s, the blade angle of 35° provided the maximum air velocity inside the microclimate, as shown in Figure 2.28. The research also established the stall angle of the wind tower as 35-40°, at which the angle of attack goes beyond the critical value and the separation of flow occurs above the surface of the blades. Comparing the performance of a 35° louvre with the standard 45° louvre

demonstrated a 45% increase in internal comfort level and 42% reduction in trailing edge stall.

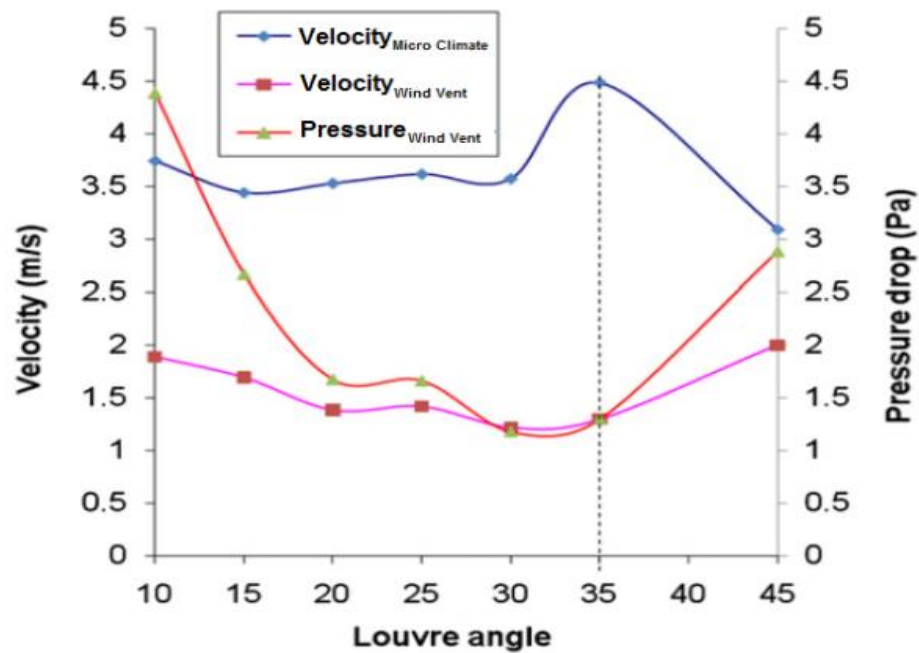


**Figure 2.28** Effect of external louvre angles on the wind tower performance [Hughes and Ghani, 2009].

Liu *et al.* [2011] also used CFD to investigate different louvre configurations for a similar wind tower system. The work focused on evaluating the ventilation performance of the device using a different number of layers and length of louvres. The study showed that increasing the number of louvre layers increased the air flow induced into the wind tower. The addition of 2 to 3 layers of louvres improved the airflow rate by 12.7%. However, less improvement in air flow was observed when using 6 or more layers, improving the airflow below 1.5%. This is a result of the flow short circuiting the top layers. It was also observed that the maximum indoor ventilation rate was achieved once the length of louvre equated with the reference length as shown in Figure 2.29. However, increasing it further than the reference length will reduce the airflow significantly and long louvres would increase the complexity of the design and manufacturing cost. The study concluded that the proposed louvre configuration is effectively stimulating airflow inside the structure.

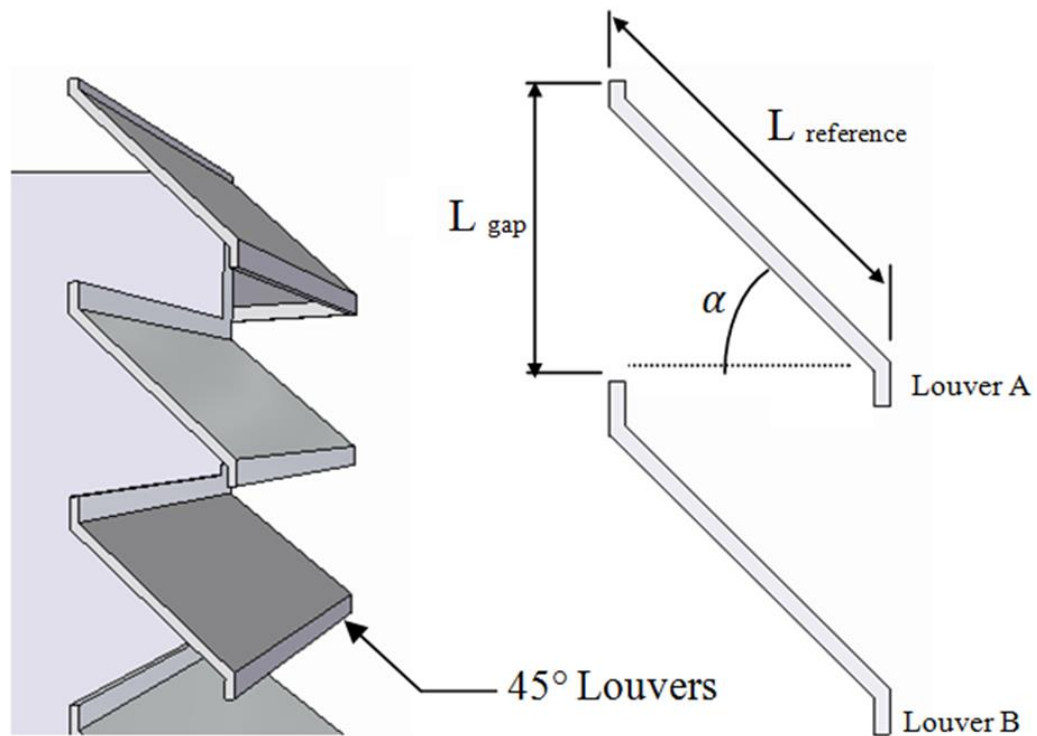


**Figure 2.29** Reference length of the wind catcher louvre,  $L_{\text{reference}} = L_{\text{gap}} / \sin \alpha$  [Liu *et al.*, 2011].

In Figure 2.29,  $L$  is the nominal length of louvre, while  $L_{\text{reference}}$  is the louvre length when the dimension of louvre projection on the corresponding quadrant equates with the gap between two adjacent louvres,  $L_{\text{gap}}$  [Liu *et al.*, 2011].

Moreover, Hughes and Ghani [2010b] studied the feasibility of a passive-assisted natural ventilation stack device using computational fluid dynamics (CFD). A standard wind tower model combined with a simulated low powered axial flow fan was used for the numerical analysis. The CFD results demonstrated the effect of the fan in top, middle and bottom positions (Figure 2.30). It was observed that the fan mounted on top, effectively draws fresh air flow and directs it down centrally through the wind tower channel and the space beneath while allowing the stale air to exit on the sides of the fan controlled air flow. In contrast, fans positioned in the middle and bottom positions did not provide a clear path for the exhaust air to exit the wind tower. Hence, fresh air supply rates were reduced. The numerical investigation confirmed that external wind speeds of 1 m/s combined with the induced fan pressure of 20 Pa satisfied the minimum recommended fresh air requirements for residential buildings in the UK.

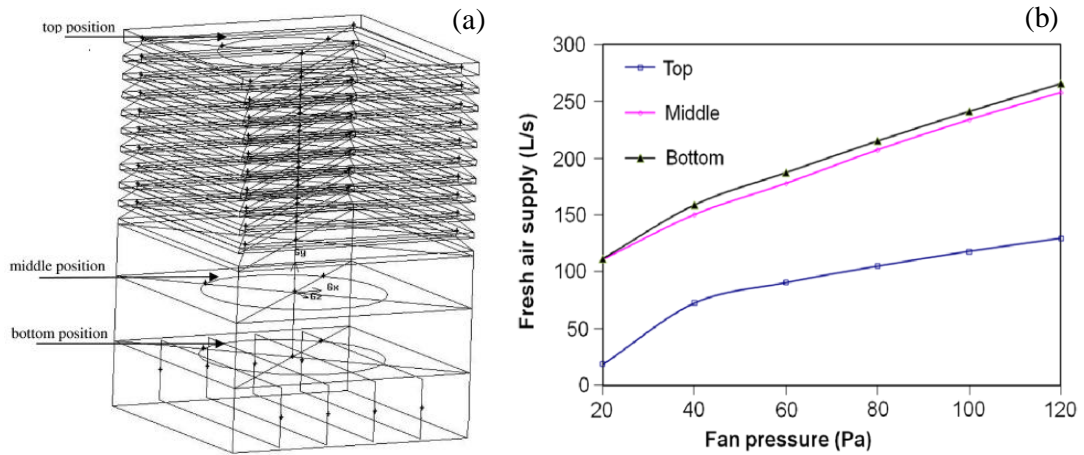


**Figure 2.30** (a) Schematic diagram of the wind tower showing the position of the fans  
 (b) Analysis of fresh air supply rates per occupant at three different fan positions for 20 occupants [Hughes and Ghani, 2010b].

Calautit *et al.* [2012a] used CFD to investigate the ventilation and thermal performance of a row house model integrated with a modern four-sided wind tower. The k-epsilon (2eqn) viscous model with standard wall functions was used for the numerical simulation. Grid adaptation was used to validate the programming and computational operation of the computational model. The numerical grid was refined and locally enriched using the hp-method grid adaptation technique. Results have shown that both systems were capable of supplying the required internal air supply rates however the reductions in internal temperature of (1-2 K) were insignificant. Therefore it is essential to cool the air in order to reduce the building heat load and improve the thermal comfort of its occupants during the summer months. Figure 2.31 displays the air flow pattern in and around the row house model integrated with wind towers.

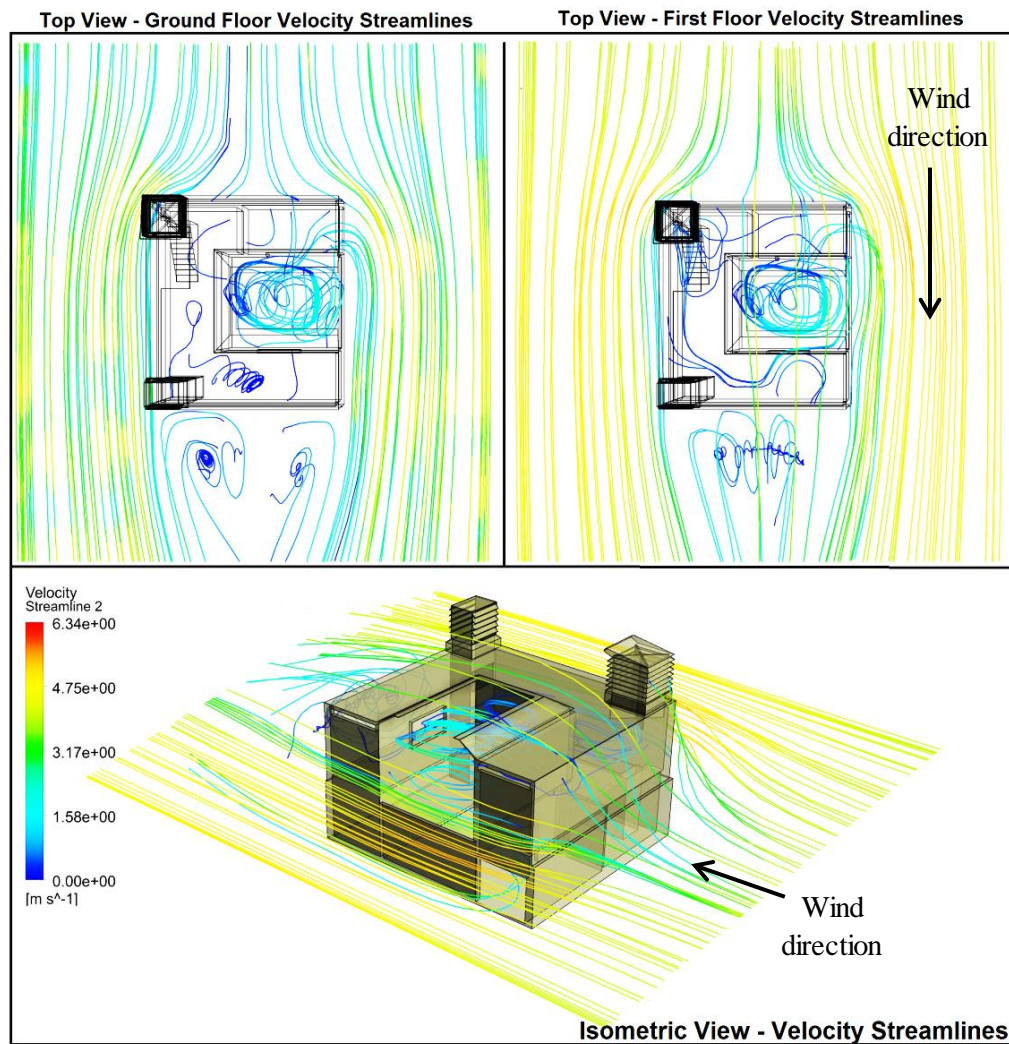


**Figure 2.31** CFD analysis showing the velocity streamlines of the air flow in and around the row house model integrated with wind towers [Calautit *et al.*, 2012a].

Calautit *et al.* [2013] carried out an investigation into a thermal comparison between evaporative cooling and heat transfer device integrated wind towers. Steady-state and three-dimensional CFD simulations, using standard  $k$ -epsilon equations models, were carried out to predict the air velocity flow and temperature distribution within the wind tower device. The work used a finite-volume discretisation method and second-order upwind differencing scheme to achieve a higher accuracy of the solutions. H-p grid adaption methods were used to verify the grid independence. The numerical results for velocity and temperature showed good agreement between the different sizes and types of grid distributions used.

### 2.3.7.2 Experimental investigations and validation techniques

Elmualim and Awbi [2002] compared the natural ventilation performance of wind towers with square and circular cross-sections using experimental and numerical analysis. Wind tunnel testing was carried out on a full scale model based on the design of a commercial wind tower. The study analysed the pressure distribution, internal wind velocity and volumetric air flow rate achieved by the device for varying wind speeds and directions. The wind tower device was also subject to numerical CFD analysis to validate the accuracy of the experimental results. Good correlation between both methods of analysis was observed.

The performance of both devices was found to be primarily dependent on the speed and direction of the prevailing wind. The ventilation rate decreased with the increase in the wind direction angles from  $0^\circ$  to  $45^\circ$ , measured from the normal to the face of the device. The achieved results showed that the square two-sided wind tower provided a higher efficiency (13%) compared with a tower with a circular cross-section for the same external wind speed. The authors concluded that this was a result of the aerodynamic shape of the square wind tower. The sharp edges of the square wind tower create a large region of flow separation and a higher pressure difference across the device as shown in Figure 2.32.

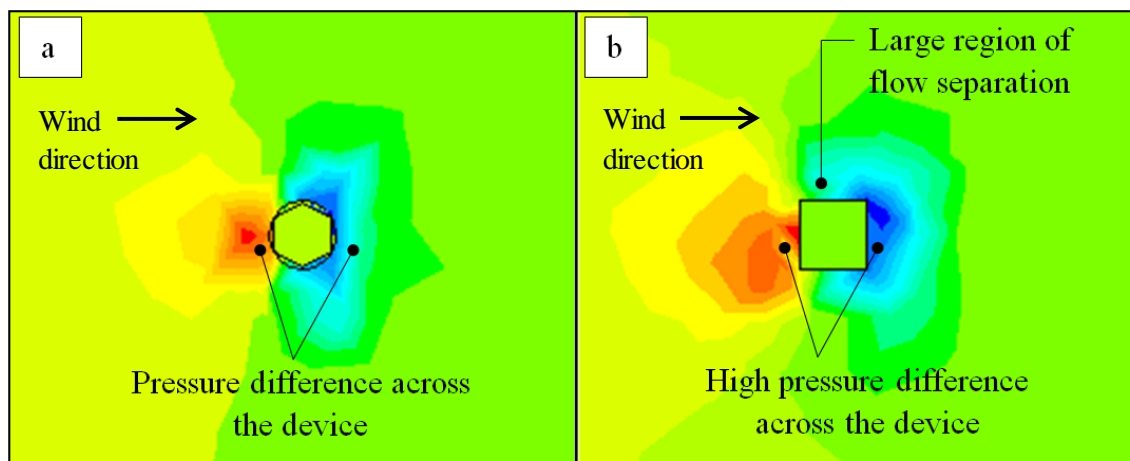


**Figure 2.32** CFD analysis showing the pressure difference across a (a) circular wind tower and (b) square wind tower [Hughes *et al.*, 2012].

Priyadarsini *et al.* [2004] used experimental and CFD techniques to investigate the feasibility of the application of an active (fan-assisted) and passive stack device to

improve the natural ventilation inside the enclosed space. The air movement along the passive stack ventilation system was achieved by just the temperature difference or moisture in the air. The results showed that the increase in the internal air velocity of the active stack is proportional to the increase of the speed of the extract fan and size of stack. The integration of the active stack in the ventilation system resulted in the internal air velocities ranging from 0.26 to 0.69 m/s. A similar device was used for the testing of the passive stack but with the extract fan removed. It was found that the temperature difference inside the passive stack device was only 10 °C and a low indoor air velocity was observed. Similarly, increasing the size of the passive stack enhances the air flow. However, larger stacks won't be economical because of the reduction in the internal space in the building. The study concluded that the active stack system was significantly more effective in providing indoor ventilation than the passive stack. The study further highlights the remarkable energy efficiency of an active stack system with solar powered internal fans. Figure 2.33 shows a schematic of the open-circuit wind tunnel used for the testing of the fan-assisted wind tower.

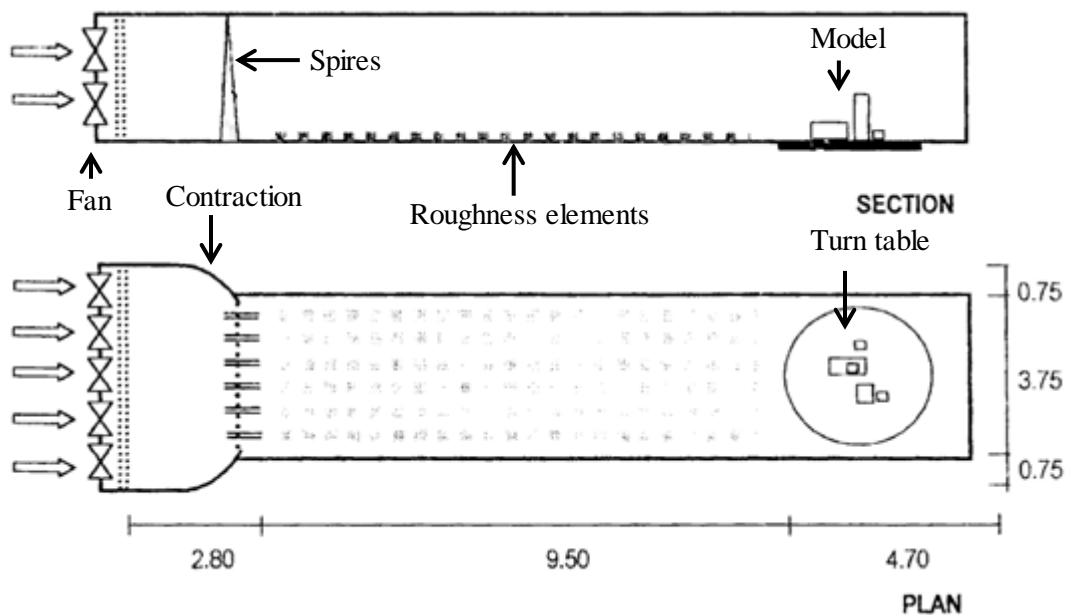


**Figure 2.33** Open-circuit wind tunnel for testing a fan-assisted wind tower [Priyadarsini *et al.*, 2004]

Elmualim [2006b] studied the effect of volume control dampers on the performance of wind towers using experimental wind tunnel testing and numerical CFD model. For the experimental analysis, a 0.5 m x 0.5 m x 1.5 m four-sided wind tower scale model was

connected to a test room mounted below the wind tunnel (Figure 2.34). The experimental results were then compared with that of a simulated wind tunnel configuration subject to CFD analysis. The approach showed a good correlation between the two methods of analysis. The indoor air speed, pressure difference and air flow distribution was investigated using a model simulated for varying wind speeds and a single direction.

The results showed that the integration of the dampers and diffusers was able to successfully reduce the air flow inside the enclosed space. The supply air flow rate was reduced by 20 % to 50 % and the exhaust air flow rate by 29 % to 33 % at an external wind speed of 1 to 3 m/s. The study further highlighted the effect of installing heat source inside the enclosed area, increasing the intake air flow rate by 7 % to 54 % and reducing the indoor temperature by 6 - 8 K. Therefore, it was concluded that the wind tower system would be suitable for installation in spaces with heat gains during the overheated period of the summer.

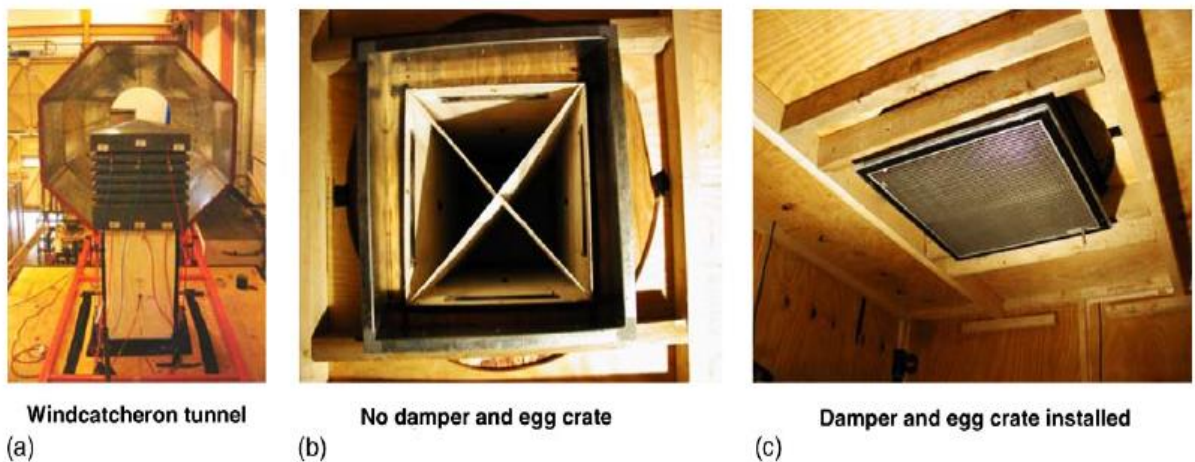


**Figure 2.34** Experimental setup in the wind tunnel [Elmualim, 2006b]

Su *et al.* [2008] used CFD modelling, experimental and far-field testing to evaluate the ventilation rate of a commercial wind tower device for different external wind speeds. A cone flow metre and a blower fan were used to simulate the outdoor conditions and measure the ventilation rates (Figure 2.35). CFD modelling of the wind catcher is carried out to create the conditions similar to the situation of outdoor far field wind. It was found that the calculated extract flow rate of the wind tower in a far field wind is approximately double that for the situation using a blower fan. The effect of the

direction of the wind on the extract flow rate was found to be insignificant. The results also confirmed that a buoyancy driven flows have a negligible effect on the flow rates of the wind tower at a higher wind speed.

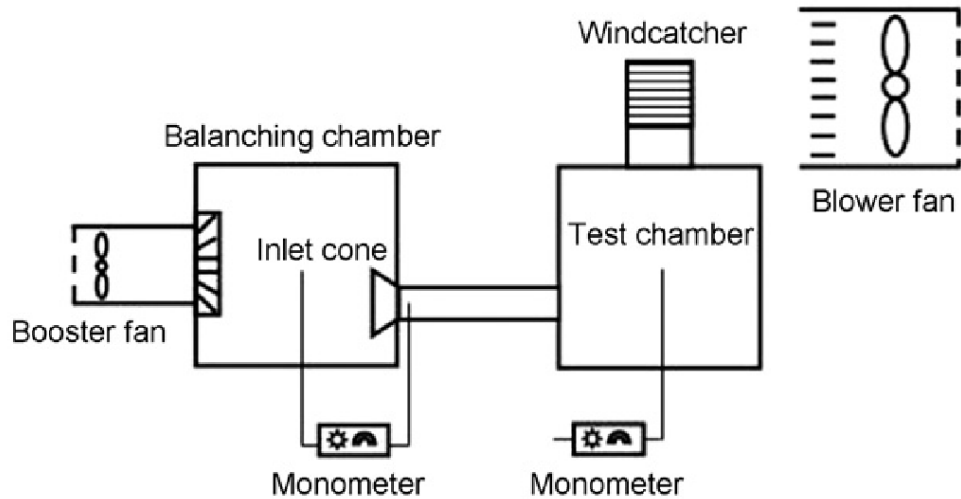


**Figure 2.35** Schematic of the ventilation measurement setup [Su *et al.*, 2008].

Hughes and Mak [2011] used far-field experimental testing and CFD modelling to study the wind pressure and buoyancy driven flows through a four-sided wind tower. The work examined the relationship between the two driving forces for the natural ventilation device. Steady-state and three-dimensional CFD simulations, using standard  $k$ -epsilon equations models, were carried out to predict the air flow velocity within the wind tower device. The Hp-grid adaptive method was used to verify the computational mesh. The numerical results were validated against full scale experimental testing and a good correlation between the different methods of analysis was observed. Figure 2.36 shows the commercial wind tower system mounted on top of a room in Sheffield Hallam University used for the full-scale experimental methods.



**Figure 2.36** Far-field experimental setup [Hughes and Mak, 2011].

## 2.4 Wind tower cooling techniques

Naturally ventilated buildings do not require additional energy to move the airflow within a structure. However, the cooling capabilities of conventional wind towers which depend on the structure design itself are limited. Therefore it is essential to cool the air in order to improve the thermal comfort of its occupants [Bahadori, 1994]. This section looks at cooling techniques which can be incorporated to a standard wind tower design to improve its ventilation and thermal performance.

Figure 2.37 shows the concept design of a wind tower system integrated with cooling devices. Evaporative cooling pads sit at the top of the wind tower with a pump recirculating water over them. Hot air is passed through these pads and cooled by water evaporation. Cool moist air is denser than ambient air and sinks down the tower and into the enclosed space. In order for the cool air to flow in, hot air must be released. A Solar chimney is located directly opposite the wind tower to establish effective cross-flow ventilation inside the structure and exhaust the stored hot air using buoyancy-driven forces.

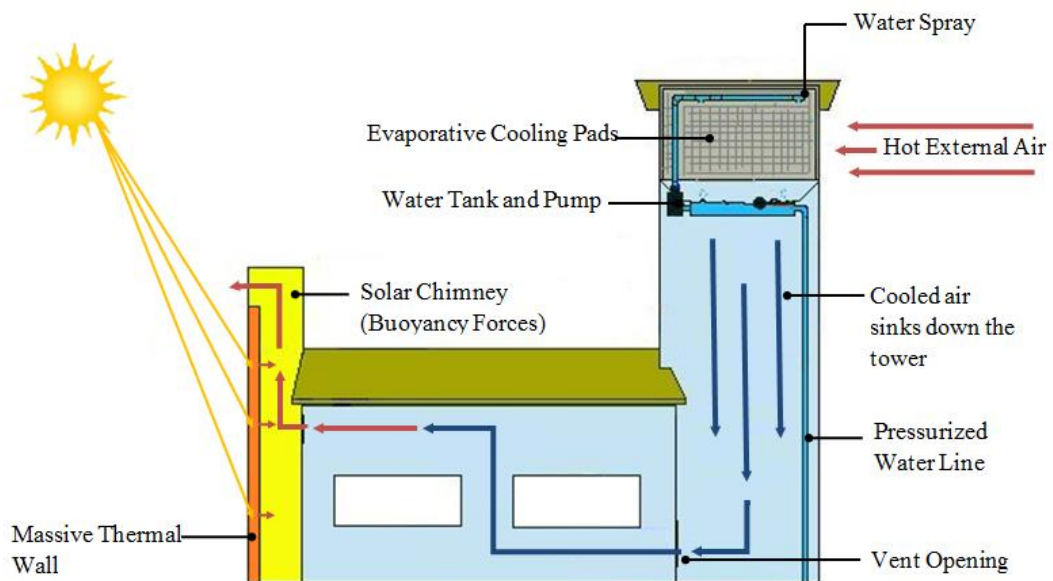


**Figure 2.37** Concept design of a passive wind tower integrated with different cooling devices [Hughes *et al.*, 2012].

Hughes *et al.* [2012] reviewed the different cooling techniques integrated with wind tower systems to improve thermal performance. Key parameters including the ventilation rates and temperature were evaluated in order to determine the viability of

implementing the devices for their respective use. The results showed that the highest temperature reductions were achieved by incorporating evaporative cooling techniques into the wind tower such as a wetted column (clay conduits) and wetted surfaces (cooling pads). The temperature reduction was found to be in the range of 12 –15 K. The study also highlighted the effect of the addition of the cooling devices inside the device which reduces the air flow rates and reduces the overall efficiency of the wind tower.

### **2.4.1 Evaporative cooling**

Passive evaporative cooling is a traditional method used in old Middle Eastern buildings to improve its natural ventilation and thermal performance. This type of cooling is particularly effective in relatively dry and humid climates [Bouchachm *et al.*, 2011]. External air is cooled down to its dew point temperature by saturating it with moisture. The ambient air is passed through wetted columns or over underground water streams before entering the structure (2.4.1.2). The evaporative cooling capability of a wind tower combined with the high airflow rates can be fully utilised in the summer to reduce the internal temperature load and provide greater thermal comfort for the inhabitants.

#### **2.4.1.1 Wind tower with wetted column and wetted surface**

Wind towers equipped with wetted columns or wetted surfaces improves the ventilation and thermal performance of the passive device and overcomes the limitations of the conventional design. These towers can be employed in the hot arid regions and provide great saving in the electrical energy consumed for the summer cooling of buildings [Bahadori *et al.*, 2008]. The evaporative cooling systems pre-cool the external air before admitting it into the structure. The cooled air becomes denser than the ambient air and sinks down the tower. Hence, air loss through other tower openings will be reduced. Wind towers incorporating wetted columns are equipped with cloth curtains or clay conduits, spaced 5-10 cm from each other and hanging vertically inside the column as shown in Figure 2.40. The curtains are wetted by spraying drops of water through a nozzle system at the top of the tower. Wind towers with wetted surfaces are equipped with evaporative cooling pads at the entrance of the wind tower. Similarly the cooling pads are wetted by spraying water on top of the device. The cooling system is particularly suitable in arid regions with good winds.

Badran [2003] also investigated the performance of an evaporative cooling wind tower system but chose to measure the air flow rates and internal temperature for a multi-directional tower. A mathematical model was developed to analyse the condition of air passing through the evaporative cooling column of the tower for different external conditions. Similarly, clay conduits were installed inside the tower's channel to cool the passing airflow before inducing it inside the structure as shown in Figure 2.38. During the night, the ambient air coolness is stored in the conduits mass to let it function during the day. The results showed that a 0.57 x 0.57m evaporative cooling tower with a vertical height of 4m can generate an airflow of 0.3m<sup>3</sup>/s and reduce the internal temperature by 11K which is equivalent to the capacity of a 1 ton refrigeration system. Therefore, the author suggested that reducing the height of the wind tower which generally reached up to 15m can decrease the construction cost without having a noticeable decrease in performance. It was evident that the four sided wind tower was capable of reducing the indoor temperature and supplying air into the building at much higher air flow rates than the one-sided wind tower proposed by Bouchahm.

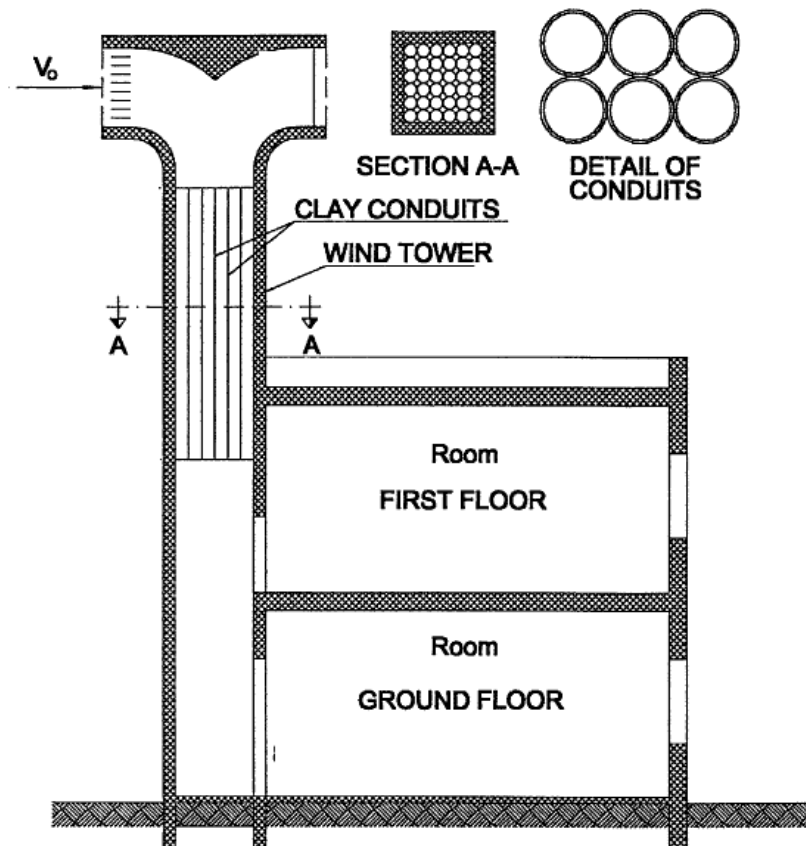


**Figure 2.38** Wind tower integrated with wetted columns or clay conduits [Badran, 2003].

Correia Da Silva [2005] evaluated the level of performance of passive evaporative cooling systems integrated in an auditorium building. A theoretical model was developed to predict the temperature and relative humidity of the air entering and leaving the structure through the cooling towers. The model was also used to demonstrate the influence of the physical parameters of the cooling device on the thermal environment within the building. The results showed that the performance of the passive cooling system was mainly dependent upon the evaporative cooling efficiency and number of cooling degree hours. The author concluded that the use of passive cooling methods in the summer is a suitable means of improving the internal thermal comfort and reducing the usage of conventional air-conditioning.

Bahadori *et al.* [2008] evaluated the thermal performance of two novel designs of cooling tower systems using experimental testing. The two designs consisted of one with wetted columns, equipped with cloth curtains suspended in the tower and one with wetted surfaces was equipped with evaporative cooling pads at the entrance (Figure 2.39). The results established that the tower with a wetted column was more effective during high wind conditions while the tower with wetted surfaces was more effective during low wind conditions. The work concluded that integrating a cooling device to the conventional wind tower system proved successful, with the air exiting the towers at a significantly lower temperature than the external air. However, a small reduction in the airflow movement was observed inside the cooling tower.

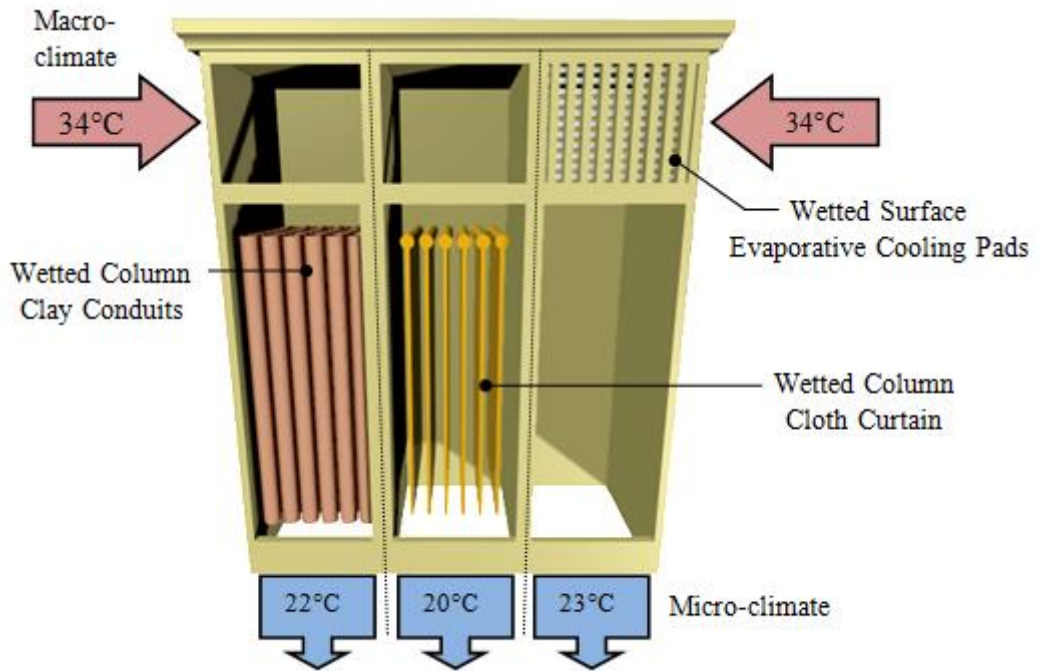


**Figure 2.39** Thermal performance of a wind tower incorporating evaporative cooling devices [Hughes *et al.*, 2012].

Kalantar [2009] attempted to evaluate the ventilation and thermal performance of a Badgir wind tower in the hot and arid region of Yazd. The work developed a numerical CFD model to simulate and analyse the airflow pattern inside the wind tower in three-dimensional and steady state conditions. The study also presented a numerical technique to simulate the effect of integrating evaporative cooling systems to the wind tower's performance. The effect of several design parameters such as wind speed, temperature, humidity and density was also considered. The result yielded a good correlation between the numerical simulations and experimental data obtained from literature. It was found that the Badgir wind tower was able to reduce the air temperatures by 10 to 15°C at its optimum performance (Figure 2.40).

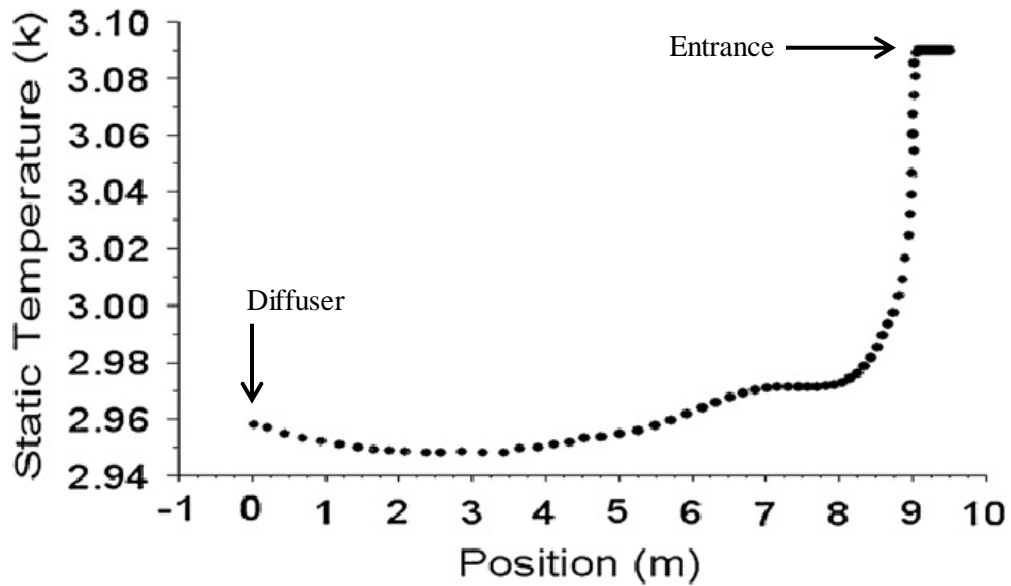


**Figure 2.40** Variation of temperature of airflow from a 10 m high wind tower [Kalantar, 2009].

Bouchahm *et al.* [2011] evaluated the ventilation and thermal performance of a one-sided wind tower system incorporated to a climatically adaptable house using experimental and theoretical methods of analysis. The purpose of this investigation was to assess the potential of the evaporative cooling devices integrated to the passive ventilation system. Clay conduits were mounted inside the shaft of the one-sided tower to improve the mass and heat transfer and a water pool was situated at the bottom of the device to increase the humidification process (Figure 2.41). The analytical model was validated against the experimental measurements and a good agreement between the results was observed. The results confirmed that the airflow induced by the 0.75 x 0.70 m tower had a direct effect on the reduction of internal temperature. It was found that by using small sized partitions (created by increasing the number of conduits) better efficiency was achieved than with a higher wetted column of the cooling tower. The cooling tower integrated with wetted interior surfaces was able to reduce the indoor air temperature by up to 17.6 K depending on the height, diameter of the conduit partitions and climatic conditions.

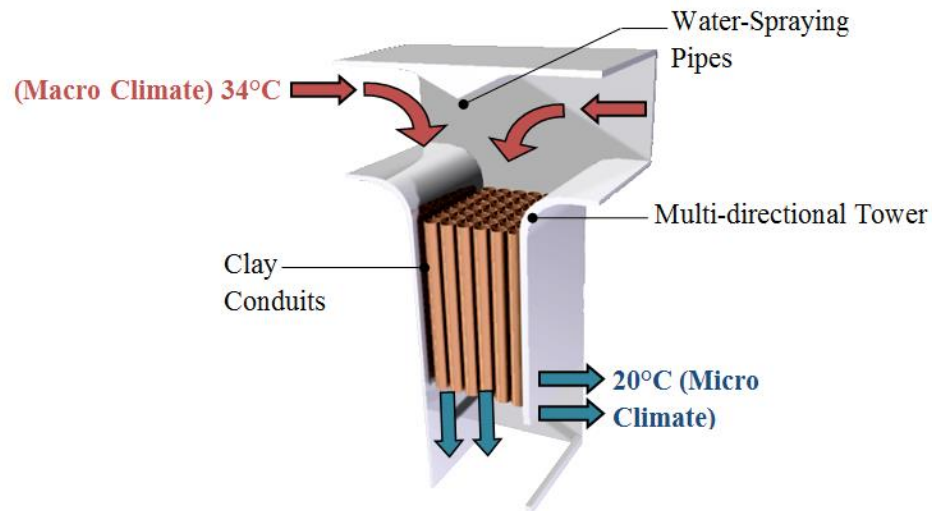


**Figure 2.41** Wind tower integrated with wetted columns or clay conduits [Hughes *et al.*, 2012].

Bouchahm's research concluded that wind towers can provide a fresh supply of air and improve the thermal comfort of the inhabitants regardless of the extreme external conditions. The work demonstrated the significance of passive cooling towers and its potential as an alternative to the more prevalent mechanical ventilation systems.

Furthermore, Safari and Hosseinnia [2009] used CFD modelling to investigate the thermal performance of new designs of wind towers under different structural parameters and external conditions. One novel wind tower design was equipped with wetted curtains suspended inside the column of the cooling device. These were formed as surfaces that injected droplets of water at extremely low speeds. A multi-phase CFD model, based on the Lagrangian–Eulerian approach, was used to study the effect of the diameter and temperature of the injected water droplets on the level of performance of the device. The numerical results showed that the 10 m high wetted columns were able to reduce the internal air temperature by 12° C and increase the relative humidity of the air by 22%. The study also revealed that the decrease in diameter of the injected water droplets resulted in a reduction of temperature of the air leaving the wetted columns. The small diameter droplets formed a larger evaporation surface area which led to better heat and mass transfer.

#### **2.4.1.2 Wind towers integrated with ground cooling**

Wind tower and underground cooling systems have been used in arid climates for many years [Boustani, 2009]. The wind tower is positioned above the house with its opening

facing away from the direction of the prevailing wind. The airflow across the vertical shaft generates a lower pressure at the leeward side of the structure. As a result, cool air is drawn from the qanat tunnel to replace the released warm and stale air. The cool air from the qanat is drawn into the tunnel at some distance away from the structure as shown in Figure 2.42. The hot air is passed through the cooled tunnel wall (several metres beneath the ground, the earth stays continuously cool) and a water stream running through the qanat, giving up its latent heat of evaporation as water evaporates into the air [Bahadori, 1978]. Hence, the air is relatively cooler when it reaches the rooms with the water vapour from the qanat having an added cooling effect.

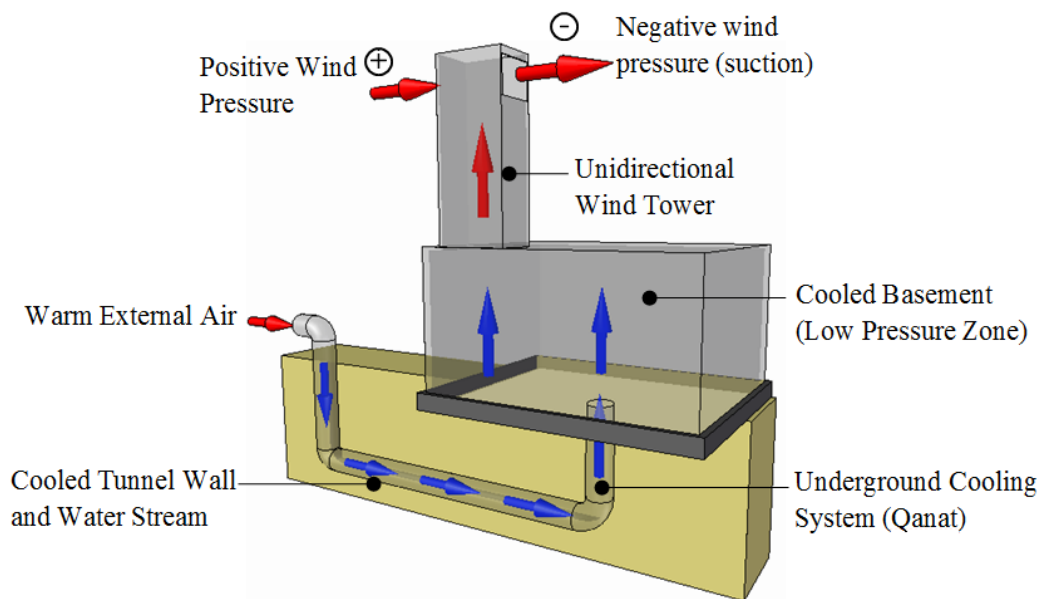


**Figure 2.42** Wind tower systems integrated with underground cooling [Hughes *et al.*, 2012].

Early studies on the integration of wind tower and underground ground cooling were carried out for a traditional house built in Iran. Wind tower and qanat cooling have been used in desert climates for over 1000 years. In dry desert climates this can result in a greater than 15°C reduction in the air temperature coming from the qanat; the mixed air still feels dry, so the basement is cool and only comfortably moist.

## 2.5 Research gap

This chapter presented a comprehensive review of traditional and modern wind tower developments. The review covered various methodical and experimental aspects to assess the overall effectiveness of current ventilation systems and gives insight into the

application of passive cooling systems as an alternative to mechanical ventilation systems. The literature review highlighted the different cooling techniques which can be integrated with wind tower systems to improve its ventilation and thermal performance. However, the following were not resolved in the literature review:

1. There was no data available on the application of modern wind tower systems in extreme temperature conditions.
2. There was no work that involves the simulation of modern wind tower systems incorporating heat transfer devices to improve their thermal performance
3. There was no attempt to determine the cooling load of a heat transfer device integrated wind tower under different climatic conditions.
4. There was no attempt to maximise the thermal performance of a heat transfer device integrated wind tower system using extended surfaces and porous media.
5. There was no data available on the thermal comfort delivered by modern wind tower systems.
6. There was no work that involves experimental testing of modern wind tower systems incorporating heat transfer devices.

This study will use the computational models and experimental techniques highlighted in the literature review to fill the identified research gap. A novel wind tower system integrating heat transfer devices will be designed to meet the internal comfort criteria in extreme conditions. Heat transfer devices will be installed inside the passive terminal of the wind tower unit, establishing the potential to achieve minimal restriction in the external air flow stream while ensuring maximum contact time, thus maximising the cooling duty of the device. This will contribute to the knowledge and understanding of the application of low energy technologies within the built environment.

To fill the identified research gap the study will use:

1. CFD simulation, specifically the standard k-e function [Calautit *et al.*, 2012a, Hughes and Ghani, 2010, Elmualim, 2006b].
2. Scaled experimental wind tunnel testing to measure the ventilation rates [Esfeh *et al.*, 2012, Montazeri *et al.*, 2010, Elmualim, 2006b].
3. Smoke testing to visualise the flow in and around the wind tower [Esfeh *et al.*, 2012, Hughes and Ghani, 2010, Montazeri *et al.*, 2010].

## 2.6 Summary

In reviewing the previous published work, the following points were concluded:

1. CFD techniques are well established in this field [Calautit *et al.*, 2012a, Hughes and Mak, 2011, Liu and Mak, 2007].
2. The k-epsilon turbulence model is the most suitable turbulence model for this application [Calautit *et al.*, 2012a, Montazeri and Azizian, 2008, Hughes and Ghani, 2010].
3. The hp grid adaptation technique is the most appropriate grid verification method for this type of numerical analysis [Hughes and Ghani, 2010, Kalantar, 2009, Elmualim, 2006b].
4. Scaled experimental wind tunnel methods are used extensively as a validation tool [Montazeri and Azizian, 2008, Bahadori *et al.*, 2008, Elmualim, 2006b].
5. Good correlation between the numerical and experimental analysis suggests that CFD techniques are suitable for this type of device and such have been used for the purpose of this research [Hughes and Ghani, 2010, Kalantar, 2009, Elmualim and Awbi, 2002].

## **Chapter 3**

### **CFD Theory and Modelling**

#### **3.1 Introduction**

CFD uses numerical methods and algorithms to solve and analyse large amounts of data involving fluid flows in a cost effective manner. With the rapid progress of CFD and computer technology, it has been used increasingly in aerodynamic design alongside traditional methods (wind tunnel). CFD gives an insight into flow patterns that are difficult, expensive or impossible to study using experimental techniques. CFD analysis is intended to be more advantageous than wind tunnel testing to explore some of the properties of wind tower systems such as flow short-circuiting and recirculation, vortex regions and supply and extract segments [Hughes and Ghani, 2009].

The three basic steps of a CFD computation are the same irrespective of the method. In all the approaches the same basic process is followed:

- Pre-processing – Discretisation of the body surface or the computational domain. This involves defining the physical domain, generation of mesh, and setting boundary conditions.
- Processing – Iterative solving of the equations at steady-state or transient
- Post-processing – Visualisation and analysis of computational results.

This chapter presents a brief introduction of the theories behind CFD and the process of translating the defined physical domain to a computational domain, which is solved and analysed using a commercial CFD package FLUENT in ANSYS Workbench.

#### **3.2 Physical domain**

There are two options for creating geometry for the fluid flow analysis; it can be modelled in ANSYS DesignModeler (FLUENT pre-processor) or imported from a Computer Aided Design (CAD) software package. DesignModeler does not have the same dedicated CAD tools as a geometric modelling programme, thus the creation of complex geometry is strictly limited. An additional advantage of CAD packages is the ability to dynamically modify a model. ANSYS DesignModeler allows the seamless

importing of the geometry data including the design parameters. The parameters can be adjusted and the design updated (and vice versa) for modification or simplification of the problem. This will be advantageous since the complete model is an assembly of many components. When any of the parts are modified, the software automatically updates the final assembly model. This study will analyse various models and arrangements. A modelling software with dynamical modelling capabilities was necessary. Hence, the secondary option of using a CAD modelling package was employed. A commercial 3D CAD parametric modelling software Solid Edge V3 with synchronous technology was used. The same software was also used for generating CAD files for rapid prototyping the wind tunnel simulation models (Chapter 5).

The solid parts of the wind tower and test room geometry were created using the 3D CAD software. Replicating the physical geometry of the wind tower does not represent a computational domain. To achieve this, the fluid volume must be defined before generating a computational mesh. The fluid volume, which is the area within the geometry which is under investigation, is extracted from the solid model as shown in Figure 3.1.

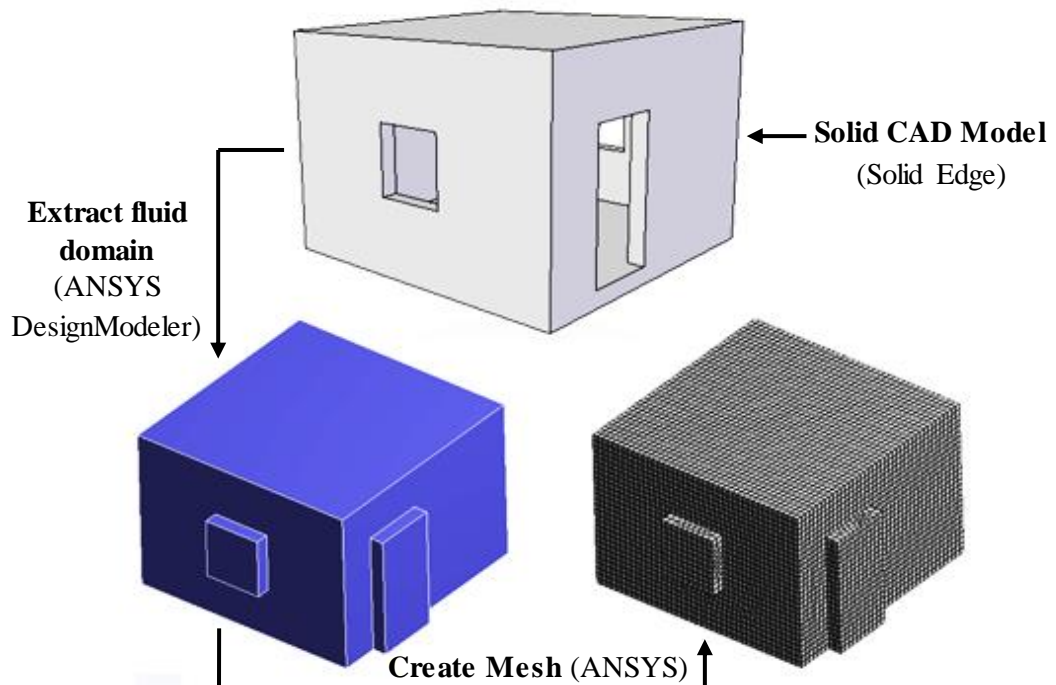


**Figure 3.1** Extraction of fluid domain from a solid CAD model representing a room.

A flow domain representation of the physical geometry of the wind tower design under investigation and the location of set boundary conditions are shown in Figure 3.2. The

enclosure (macro-climate) was created to simulate the external wind velocity. The enclosure consists of a velocity inlet (operating velocity) at the right hand side of the enclosure, and a pressure outlet (atmospheric pressure) on the opposing boundary wall of the macro climate.

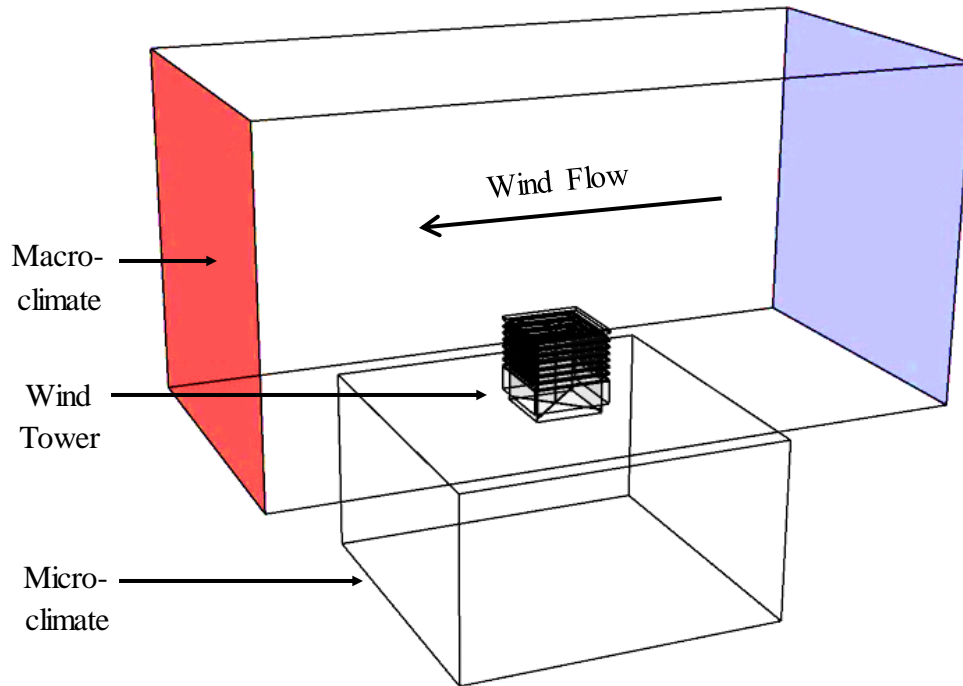


**Figure 3.2** Physical representation of the geometry under investigation.

The distance between the wall of the geometry under investigation and the wall of the enclosure was determined by calculating the blockage caused by the wind tower model. The blockage speeds-up and distorts the flow around the model. In order to eliminate or minimise this, the macro-climate must be sized correctly. The complete macro-climate dimensions were 5 x 5 x 10 m. According to the dimensions of the wind tower, the model produced a maximum blockage of 4.8%, hence no corrections were made to the measurements obtained with these configurations [Montazeri, 2011].

### 3.3 Computational domain

Defining the computational domain from the physical domain consists of four key stages:

3.1. Mesh generation

3.2. Examining the mesh

### 3.3. Implementation of boundary conditions

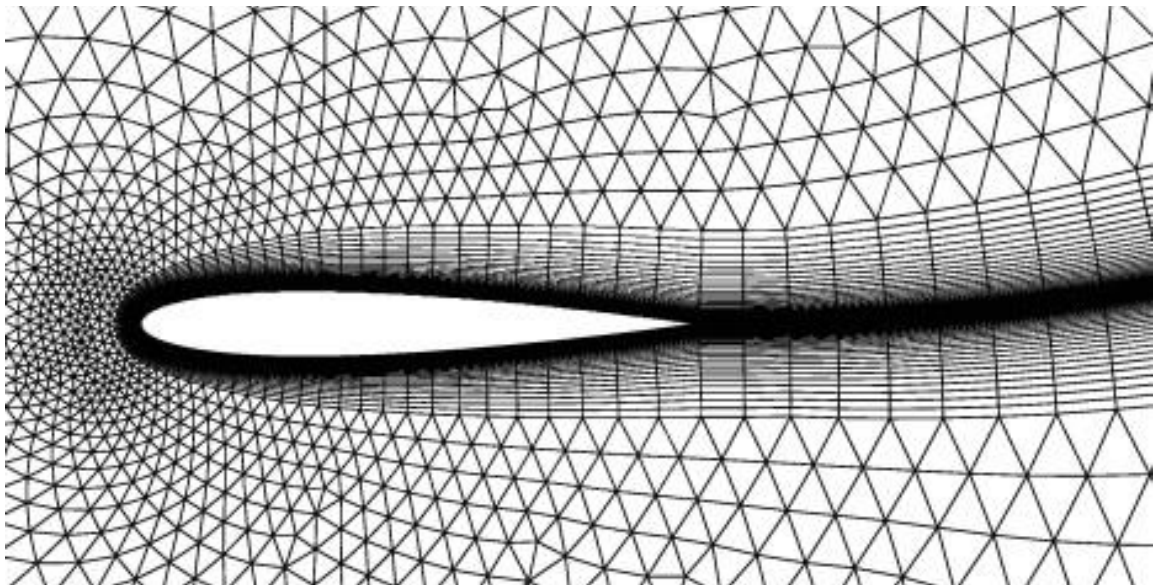
### 3.4. Grid adaptation

#### 3.3.1 Mesh generation

Prior to the numerical solution of the governing equations, the surfaces of the boundaries must be discretised and a volume mesh must be generated inside the flow domain. The mesh designates the cells or elements on which the flow is solved and groups the cells into boundary zones where boundary conditions are applied. The mesh influences the accuracy, convergence and speed of the solution. There are three main types of grid generation methods [Blazek, 2001]:

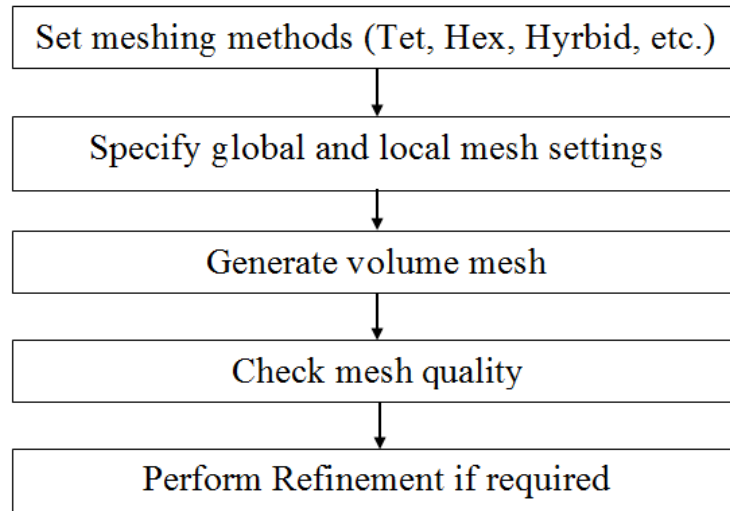
- Structured – mesh follows a structure, single or multi block, not applicable for complex geometries
- Unstructured – mesh does not follow a structure, cells are arranged arbitrarily, typically composed of tetrahedral cells.
- Hybrid – utilises the most suitable mesh type in any combination, non-conformal, suitable for very complex geometries, greatest flexibility

Figure 3.3 shows a hybrid mesh generation around an object. The boundary layer was generated using structured quadrilateral elements and the outer grid generated using unstructured triangle grids.



**Figure 3.3** 2D hybrid grid generation around an airfoil [Dussin *et al.*, 2009].

The appropriate choice of grid type depends on the complexity of the geometry, flow domain, computational time and the grid and element types supported by the solver. Figure 3.4 shows the meshing process in ANSYS Meshing software [FLUENT guide, 2006].



**Figure 3.4** Meshing process in the ANSYS Meshing software.

In this study, the fluid domain was subdivided into a smaller block to facilitate the grid refinement (Figure 3.5). Due to the complexity of the wind tower geometry, a combined tetrahedral/hybrid mesh generation method was used. This scheme specifies that the mesh is composed primarily of tetrahedral elements. The method also uses the hexahedral mesh where appropriate. Mesh node spacing and meshing options were varied to refine the grid and achieve grid adaption.

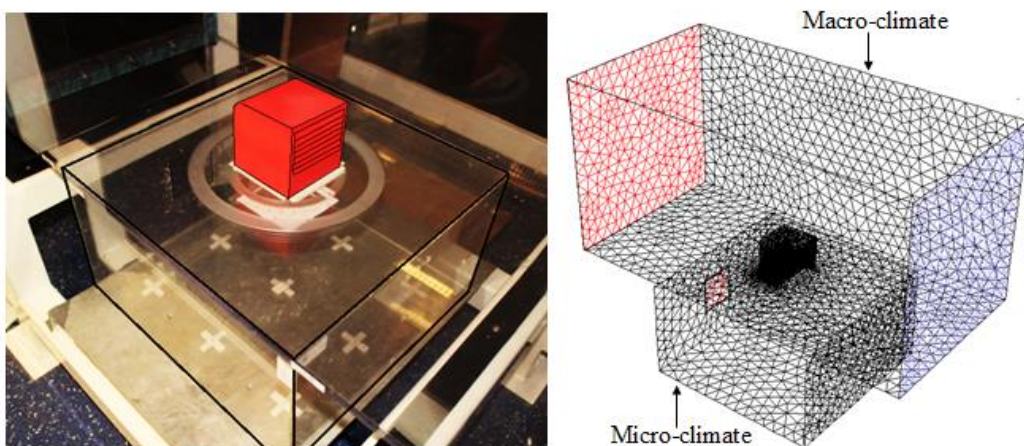


**Figure 3.5** (a) actual wind tower model inside the test section (b) view of the computational mesh of the wind tower model and test room.

The accuracy of the results achieved from the CFD modelling is highly dependent on the quality of the mesh, which equally has implications on the convergence of the model [Chung, 2002]. The grid is modified and refined around critical areas of interest or values in the simulation. The size of the mesh element was extended smoothly to resolve the sections with high gradient mesh and to improve the accuracy of the results of the velocity and temperature fields. Inflation parameters are set for the complex geometry face elements (louvres and heat transfer devices) to generate a finely resolved mesh normal to the wall and coarse parallel to it, as shown in Figure 3.6. The two-dimensional faces elements at the selected wall or boundaries are inflated into 3d prism elements which resolve boundary layer properly at relatively less computational cost.

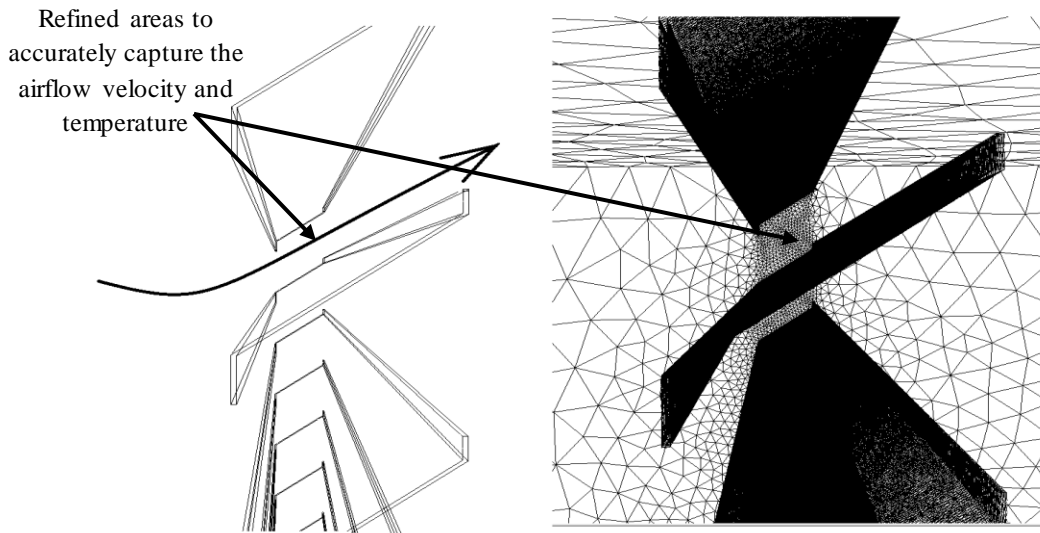


**Figure 3.6** Schematic diagram representing the complex face geometry face elements of the louvre section.

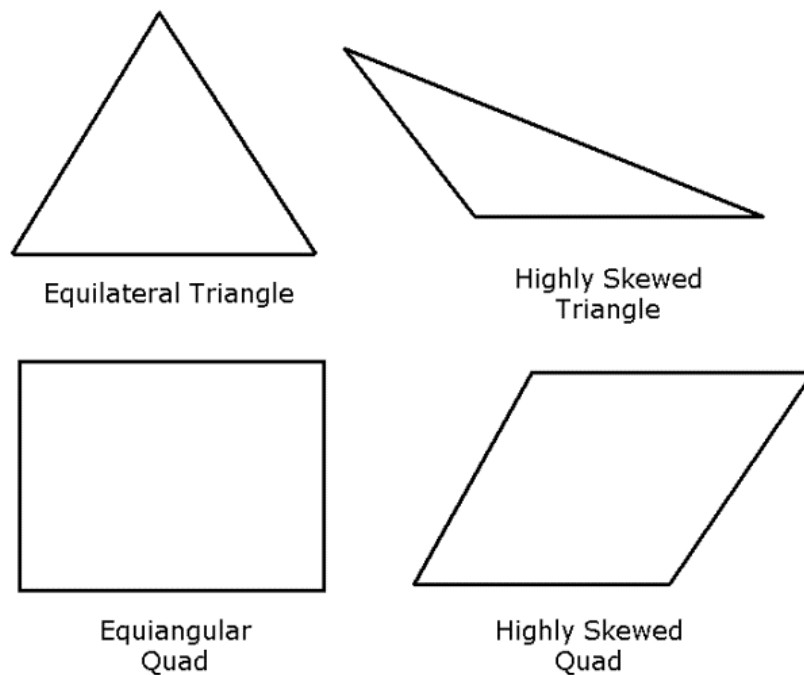
### 3.3.2 Examining the mesh

The mesh was examined computationally using the skewness tool provided by the FLUENT software. The skewness (range 0 - 1) is one of the primary quality measures for computational mesh. It is the distribution relationship between the mesh nodes; a skewness value of 0 indicates an equilateral cell (normal distribution). Hence, data points are symmetrical about a mean. A value of 1 indicates a completely degenerate cell (stretched distribution). Highly skewed cells can lead to under-estimation of the solution variables and an inaccurate solution. Table 3.1 lists the range of FLUENT skewness values and the corresponding cell quality.

**Table 3.1** Range of skewness values and cell quality [FLUENT guide, 2006].

Skewness value	Cell quality
1	highly skewed
0.9 — <1	bad
0.75 — 0.9	poor
0.5 — 0.75	fair
0.25 — 0.5	good
>0 — 0.25	excellent
0	equilateral

If the skewness factor is above 0.97 (default maximum), the accuracy of the solution is deemed unacceptable. Figure 3.7 shows an example of an ideal and highly skewed cell.

**Figure 3.7** Ideal and skewed triangle and quadrilaterals [FLUENT Guide, 2006].

The mesh was examined to eliminate any potential problems prior to exporting to the solver. Figure 3.8 shows an example of the cell skewness analysis for the wind tower model with heat transfer devices. Elements with a high skewness value were highlighted in red (colour map). Maximum skewness value obtained from the computational mesh was 0.5 (edges of the louvre surfaces) with the average skewness

value of 0.3. The FLUENT software also features a grid check case function which analyse and report the overall skewness of each mesh before running the solver.

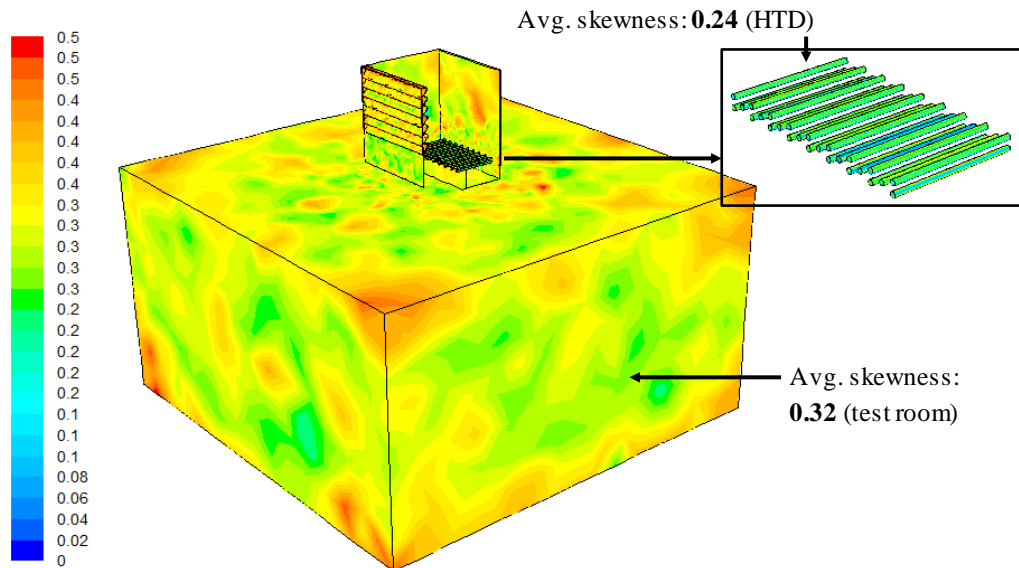


**Figure 3.8** Wall surface contours showing the equiangle skew.

Furthermore, the grid resolution was determined taking into account an acceptable value for the wall  $y^+$  (average value of 146.8). The log-law, which is valid for equilibrium boundary layers and fully developed flows, provides upper and lower limits of the acceptable distance between the near-wall cell centroid and the wall. The distance is usually measured in the dimensionless wall units,  $y^+$ . For standard wall functions, each wall-adjacent cell's centroid should be located within the log-law layer,  $30 < y^+ < 300$  [FLUENT guide, 2006]. Figure 3.9 shows an example of the wall  $y^+$  analysis for the wind tower model.

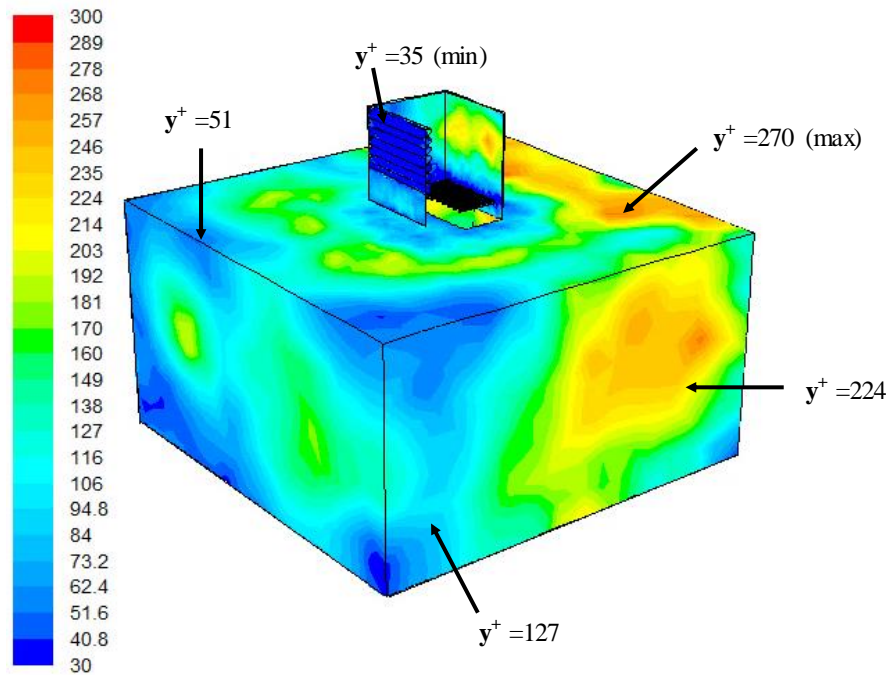


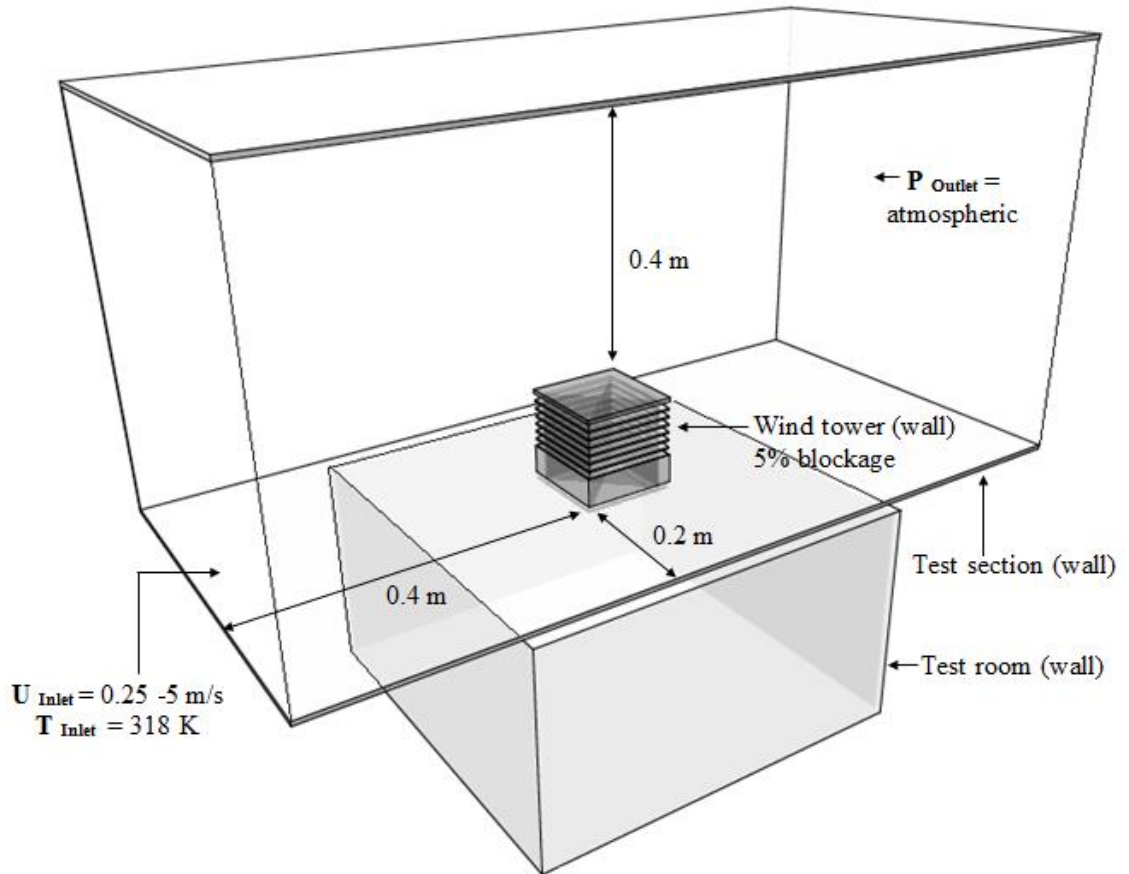
**Figure 3.9** Wall surface contours showing the  $y^+$  value.

### 3.3.3 Implementation of boundary conditions

The boundary conditions define the flow and thermal variables on the boundaries of a computational model. The types of boundary conditions available in FLUENT are classified as:

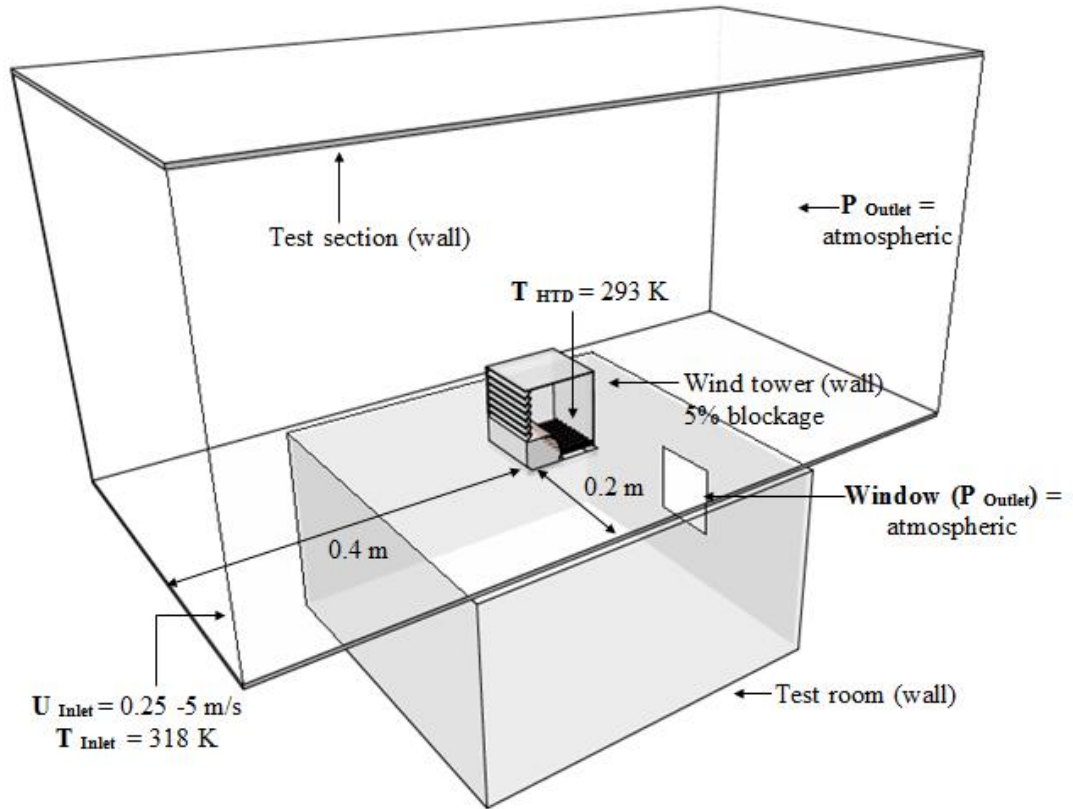
- Internal cell zones – a group of cells for which all active equations are solved (fluid) and a group of cells for which only heat conduction problem are solved (solid)
- Wall boundaries – bounds fluid and solid zones
- Flow inlet and exit – permits the flow to enter and exit a zone
- Internal face boundaries - fans, radiators, internal wall and porous jump

Figure 3.10 shows the physical domain containing the macro-climate and micro-climate fluid volumes. A wall boundary condition was used to create a boundary between each region. The macro-climate fluid volume, used to simulate the external velocity flow field, generates a velocity into the wind tower. To generate a velocity flow field one horizontal plane was named as a velocity inlet, with the opposite boundary wall set as pressure outlet.



**Figure 3.10** CFD flow domain representation of the micro and macro climate environment for the analysis of a four-sided wind tower.

Figure 3.11 shows the physical domain containing the macro-climate and micro-climate fluid volumes for the analysis of the wind tower incorporating the heat transfer devices. Similarly, one horizontal plane was set as a velocity inlet, with the opposite boundary wall set as pressure outlet to simulate the external conditions. The test room window opening was also set as a pressure outlet (atmospheric).



**Figure 3.11** CFD flow domain representation of the micro and macro climate environment for the analysis of a one-sided wind tower with HTD.

The boundary conditions for the CFD model are summarised in Table 3.2.

**Table 3.2** Summary of the CFD model boundary conditions.

Discretisation Scheme	Second order upwind
Algorithm	SIMPLE
Time	Steady State
Viscous model	k-epsilon two equation
Velocity inlet (m/s)	0.5 – 5 m/s
Pressure outlet	Atmospheric
Gravity	-9.81
External Temperature (K)	318
HTD Temperature (K)	293
Relative Humidity	50 %

Figure 3.12 shows the monthly average temperature, wind speed and relative humidity for January 2001 through December 2012 taken from OTBD Weather Station, Doha, Qatar (Lat/Long: 25.28°, 51.52°). The weather data file provided the inlet boundary conditions for the transient model.

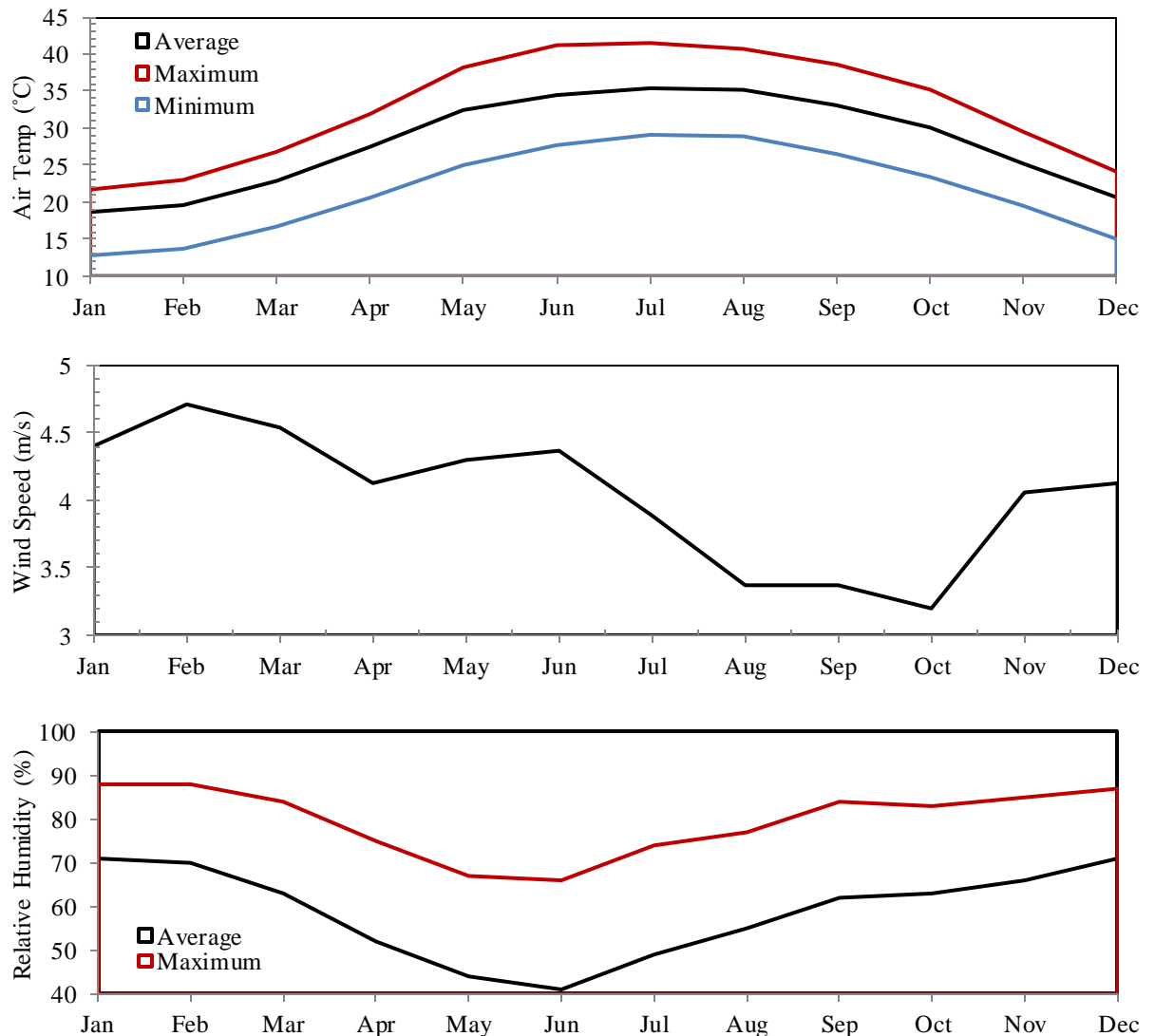


**Figure 3.12** Actual Meteorological Year (AMY) data file for Doha, Qatar [Weather Analytics Station™, 2012]

The CFD model material properties are summarised in Table 3.3.

**Table 3.3** Summary of the CFD model boundary conditions [Calautit *et al.*, 2012].

Parameter	Test room walls	Wind tower walls	Heat transfer device	Extended surface
BC Type	Wall	Wall	Wall	Wall

Thickness	0.1 m	0.01 m	-	-
Material	Concrete	Steel	Copper	Aluminium
Thermal conductivity	0.40 W/m.K	16.27 W/m.K	387.6 W/m.K	202.4 W/m.K
Specific heat capacity	960 J/kg.K	502 J/kg.K	381 J/kg.K	871 J/kg.K
Density	2400 kg/m <sup>3</sup>	8030 kg/m <sup>3</sup>	8978 kg/m <sup>3</sup>	2719 kg/m <sup>3</sup>
Roughness height	0.3x10 <sup>-3</sup> m	0.015x10 <sup>-3</sup> m	0.001x10 <sup>-3</sup> m	0.001x10 <sup>-3</sup> m

### 3.3.4 Grid adaptation

To investigate the solution independency from the grid several meshes were generated. The grid adaptation method was used to validate the programming and computational operation of the computational model. The numerical grid was refined and locally enriched using the hp-method grid adaptation technique. The hp-method is a combination of two methods; h-method (mesh refinement) and p-method (mesh enrichment). Mesh refinement refers to the targeting of areas of the mesh which have high levels of skewness and replacing them with an increased number of elements or cells, or a different element type. Mesh enrichment refers to an increase in the degree of the polynomials or higher order approximations [Chung, 2002].

This procedure of evaluation requires the use of different mesh by the use of a posterior error estimates. The grid was evaluated and refined until the posterior estimate error became insignificant between the number of nodes and elements, computational iterations and the posterior error indicator [Calautit *et al.*, 2012a]. The grid adaptation method starts with a coarse mesh and gradually refines it until the variation observed between the results are smaller than the predefined acceptable error. The accuracy of the results is improved by using successively smaller cell sizes for the computation. The applied boundary conditions remained fixed throughout the simulation process to ascertain precise comparison of the numerical results.

Figure 3.13 displays the posterior error percentage for average velocity in the test-section at increasing grid sizes. The maximum error for average velocity was recorded 0.34%. The discretisation error was found to be the lowest at over 7 million cells for both indicated variables. The applied boundary conditions were remained fixed

throughout the simulation process to ascertain precise comparison of the posterior error estimate.

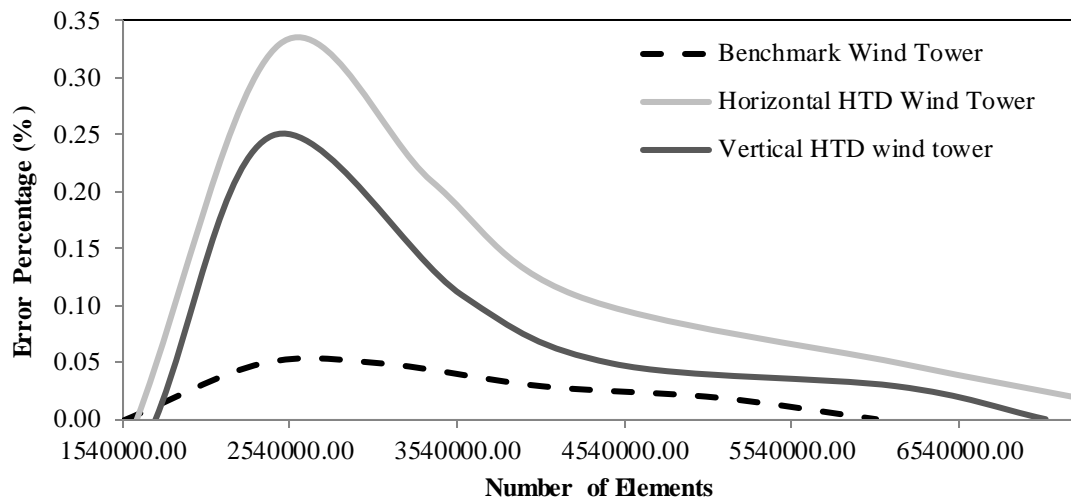


**Figure 3.13** Posterior error on the average velocity in the test-section using h-p grid adaptation method.

### 3.4 Solving the model

The basic assumptions for the CFD simulation include a three-dimensional, fully turbulent, and incompressible flow. The CFD code uses the Finite Volume Method (FVM) approach and employs the Semi-Implicit Method for Pressure-Linked Equations (SIMPLE) velocity-pressure coupling algorithm with the second order upwind discretisation. The turbulent nature of the flow was modeled by the standard k-epsilon viscous model with standard wall functions as it is the most widely used and validated turbulence model for investigating natural ventilation systems as detailed in the literature review (Chapter 2)

The standard k-epsilon model was used to carry out the computational work reported in this study with the following governing equations solved:

- Continuity equation
- Momentum conservation equation
- Energy equation
- Navier-Stokes equation
- Standard k-epsilon model transport equation
- Species transport equation

### 3.4.1 Continuity equation

In fluid dynamics, the continuity equation is an expression of conservation of mass. In (vector) differential form, it is written as:

$$\frac{\partial \rho}{\partial t} + \nabla \cdot (\rho \vec{u}) = S_m \quad \text{Equation 3.1}$$

Where,  $\rho$  is density,  $t$  is time, and  $\vec{u}$  is fluid velocity.

$$\nabla = \frac{\partial}{\partial x} + \frac{\partial}{\partial y} + \frac{\partial}{\partial z} \quad \text{Equation 3.2}$$

Equation 3.1 is the general form of the mass conservation equation and is valid for incompressible as well as compressible flows. The source  $S_m$  is the mass added to the continuous phase from dispersed second phase.

### 3.4.2 Momentum conservation equation

Newton's second law states that the rate of change of momentum of a fluid particle equals the sum of forces on the fluid particle by [Chung, 2002]. The rates of increase of x, y and z-momentum per unit volume of a fluid particle is given:

$$\rho \frac{Du}{Dt}, \quad \rho \frac{Dv}{Dt}, \quad \rho \frac{Dw}{Dt} \quad \text{Equation 3.3}$$

There are two types of forces acting on the control volume.

- Surface forces - acts directly on the surface of the control volume.
  - (a) Pressure force - imposed by the outside fluid surrounding the control volume
  - (b) Shear and normal stresses - resulting from friction between the fluid and the surface of the control volume.
- External volume or body forces – acts directly on the mass of the volume. These are the gravitational, buoyancy and centrifugal forces.

The body forces overall effect is by the sources:  $S_{Mx}$ ,  $S_{My}$ ,  $S_{Mz}$  of the x, y and z component. The x-component of the momentum equation is found by setting the rate of change of x-momentum of the fluid particle (Equation 3.3) equal to the total force in the x-direction on the element due to surface stresses plus the rate of increase of x-momentum due to sources [Chung, 2002]:

$$\rho \frac{Du}{Dt} = -\frac{\partial p}{\partial x} + \frac{\partial \tau_{xx}}{\partial x} + \frac{\partial \tau_{yx}}{\partial y} + \frac{\partial \tau_{zx}}{\partial z} + S_{Mx} \quad \text{Equation 3.4}$$

The y-component of the momentum equation is given by:

$$\rho \frac{Dv}{Dt} = -\frac{\partial p}{\partial y} + \frac{\partial \tau_{xx}}{\partial x} + \frac{\partial \tau_{yx}}{\partial y} + \frac{\partial \tau_{zx}}{\partial z} + S_{My} \quad \text{Equation 3.5}$$

The z-component of the momentum equation is given by:

$$\rho \frac{Dw}{Dt} = -\frac{\partial p}{\partial z} + \frac{\partial \tau_{xz}}{\partial x} + \frac{\partial \tau_{yz}}{\partial y} + \frac{\partial \tau_{zz}}{\partial z} + S_{Mz} \quad \text{Equation 3.6}$$

Equations 3.4, 3.5 and 3.6 make use of Newton's second law of motion with their left-hand sides representing mass acceleration per unit volume and their right-hand sides representing the sum of net forces per unit volume acting on the fluid which consists of surface and body forces. The first term on the right-hand side denotes the net pressure force per unit volume and the minus sign arises because, by definition, a positive pressure acts inward. The second, third and fourth terms denote the viscous forces per unit volume, and they arise as a result of the different components of normal and shear stresses shown in Figure 3.14 the first subscript to the symbol  $\tau$  represents the direction of the stress and the second the direction of the surface normal [Cebeci *et al.*, 2005]

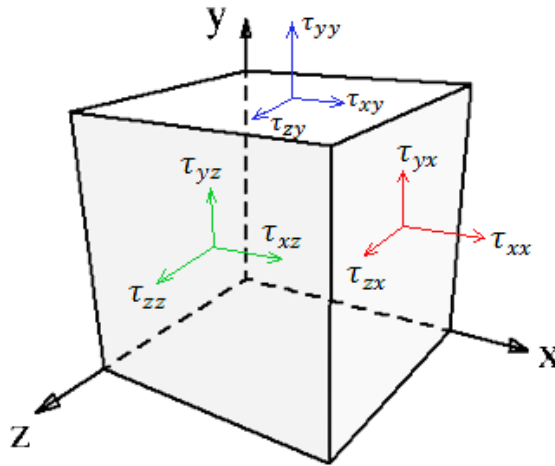


**Figure 3.14** Viscous stress components applied to the faces of the control volume by the surrounding fluid.

### 3.4.3 Energy equation

The energy equation is derived from the first law of thermodynamics, which states that the rate of change of energy of a fluid particle is equal to the rate of heat addition to the fluid particle plus the rate of work done on the particle [FLUENT guide, 2006].

The energy equation is derived from the rate of increase of energy of a fluid per unit volume which is given by:

$$\rho \frac{DE}{DT} \quad \text{Equation 3.7}$$

The general form of the governing equations can be generalised as:

$$\frac{\partial}{\partial t}(\rho E) + (\vec{u}(\rho E + p)) = \nabla \left( k_{eff} \nabla T - \sum_j h_j \vec{J}_j + (\overline{\tau_{eff} \times \vec{u}}) \right) + S_h \quad \text{Equation 3.8}$$

Where  $k_{eff}$  is the effective conductivity,  $\vec{J}_j$  is the diffusion flux  $j$  and  $S_h$  include the heat of chemical reaction and other volumetric heat source that the user defined.

### 3.4.4 Navier-Stokes equations

The Navier-Stokes equations are used to define the fluid flow viscous stress components  $\tau_{ij}$ . In three dimensional flows, the local rate of the deformation is composed of the linear deformation rate and the volumetric deformation rate. The three linear deformation components are [Versteeg and Malalasekera, 2007]:

$$s_{xx} = \frac{\partial u}{\partial x}, \quad s_{yy} = \frac{\partial v}{\partial y}, \quad s_{zz} = \frac{\partial w}{\partial z} \quad \text{Equation 3.9}$$

The six shearing linear deformation component are:

$$s_{xy} = s_{yx} = \frac{1}{2} \left( \frac{\partial u}{\partial y} + \frac{\partial v}{\partial x} \right), \quad s_{xz} = s_{yz} = \frac{1}{2} \left( \frac{\partial u}{\partial z} + \frac{\partial w}{\partial x} \right), \quad s_{yz} = s_{zy} = \frac{1}{2} \left( \frac{\partial v}{\partial z} + \frac{\partial w}{\partial y} \right) \quad \text{Equation 3.10}$$

The x-component of the Navier-Stokes equation is given by:

$$\rho \frac{Du}{Dt} = -\frac{\partial p}{\partial x} + \nabla(\mu \text{ grad } u) + S_{Mx} \quad \text{Equation 3.11}$$

The y-component of the Navier-Stokes equation is given by:

$$\rho \frac{Dv}{Dt} = -\frac{\partial p}{\partial y} + \nabla(\mu \text{ grad } v) + S_{My} \quad \text{Equation 3.12}$$

The z-component of the Navier-Stokes equation is given by:

$$\rho \frac{Dw}{Dt} = -\frac{\partial p}{\partial z} + \nabla(\mu \text{ grad } w) + S_{Mz} \quad \text{Equation 3.13}$$

### 3.4.5 Standard k- $\epsilon$ model transport equation

The standard  $k$ - $\epsilon$  model is a semi-empirical model based on model transport equations for the turbulence kinetic energy ( $k$ ) and its dissipation rate ( $\epsilon$ ) [Chung, 2002]. In the derivation of the  $k$ - $\epsilon$  model, the assumption is that the flow is fully turbulent, and the effects of molecular viscosity are negligible. The turbulence kinetic energy,  $k$ , and its rate of dissipation,  $\epsilon$  are obtained from the following transport equations:

$$\frac{\partial}{\partial t}(\rho k) + \frac{\partial}{\partial x_i}(\rho k u_i) = \frac{\partial}{\partial x_j} \left[ \left( \mu + \frac{\mu_t}{\sigma_k} \right) \frac{\partial k}{\partial x_j} \right] + G_k + G_{kb} - \rho \epsilon - Y_M + S_k \quad \text{Equation 3.14}$$

and

$$\frac{\partial}{\partial t}(\rho \epsilon) + \frac{\partial}{\partial x_i}(\rho \epsilon u_i) = \frac{\partial}{\partial x_i} \left[ \left( \mu + \frac{\mu_t}{\sigma_\epsilon} \right) \frac{\partial \epsilon}{\partial x_i} \right] + C_{1\epsilon} \frac{\epsilon}{k} (G_k + C_{3\epsilon} G_b) - C_{2\epsilon} \rho \frac{\epsilon^2}{k} + S_\epsilon \quad \text{Equation 3.15}$$

Where,  $G_k$  represents the generation of turbulent kinetic energy due to the mean velocity gradients and  $G_b$  is the generation of turbulence kinetic energy due to buoyancy.  $Y_M$  is the contribution of the fluctuating dilatation in compressible turbulence to the overall dissipation rate. While  $C_{1\epsilon}$ ,  $C_{2\epsilon}$ , and  $C_{3\epsilon}$  are constants.  $\sigma_k$  and  $\sigma_\epsilon$  are turbulent Prandtl numbers for  $k$  and  $\epsilon$  [FLUENT guide, 2006].

### 3.4.6 Species transport equation

- The species transport equation of water vapour into air is written in the form;

$$\frac{\partial}{\partial x_j}(\rho Y_{H_2O} u_j) = \frac{\partial}{\partial x_j} \left[ \left( \rho D_{H_2O} + \frac{\mu_t}{Sc_t} \right) \frac{\partial Y_{H_2O}}{\partial x_j} \right] + S_{H_2O} \quad \text{Equation 3.16}$$

Where,  $S_{H_2O}$  is the water vapour added to the air due to the evaporation. While,  $D_{H_2O}$  is the diffusion coefficient of water vapour into air and  $Sc_t$  is the turbulent Schmidt number [FLUENT guide, 2006].

These governing equations are established and widely used, full description and derivation are available in [FLUENT guide, 2006]. No attempt was made during this study to modify any of these standard equations.

### 3.5 Solution algorithm

Solution algorithms are tools used to dictate the method in which the progressive iterations are carried out. FLUENT provides the option to choose from four segregated methods for pressure-velocity coupling in the solver [FLUENT guide, 2006]:

- SIMPLE (Semi-Implicit Method for Pressure-Linked Equations) - default scheme, robust
- SIMPLER (SIMPLE-Consistent) – uncomplicated problems, quick convergence
- PISO (Pressure-Implicit with Splitting of Operators) – transient flow calculations, increased computational expense
- FSM (Fractional Step Method) – unsteady flows

The SIMPLE algorithm was used in this study to carry out the numerical work. The SIMPLE algorithm, illustrated in Figure 3.15 provides the basic steps for calculating pressures and velocity fields.

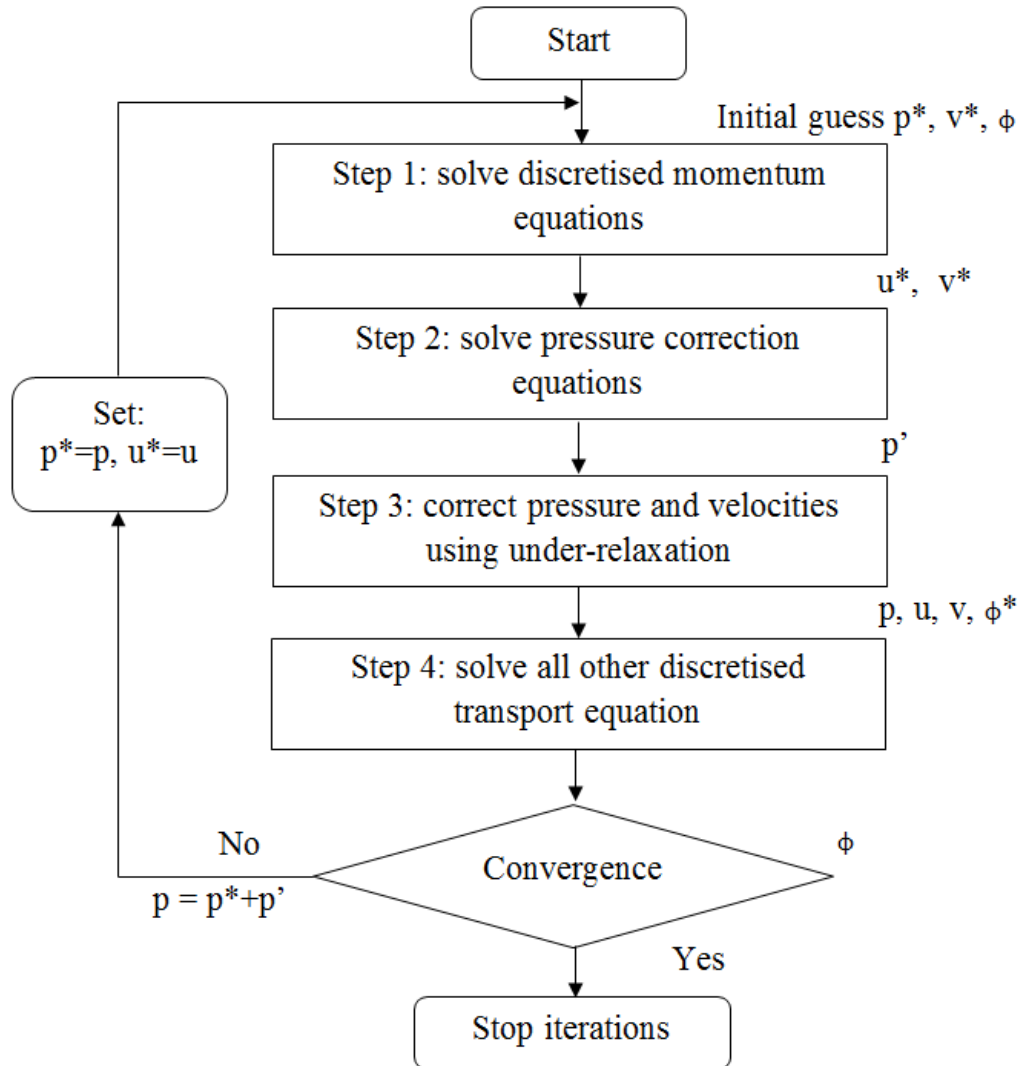


**Figure 3.15** Simple algorithm flowchart [Ahmed, 1998].

The pressure-based segregated algorithm uses a solution algorithm where the governing equations are solved sequentially. Because the governing equations are non-linear and coupled, the solution loop must be carried out iteratively in order to obtain a converged numerical solution. The intermediate velocity field is obtained by solving the discretised momentum equation and the pressure gradient term is calculated using the pressure distribution obtained from the previous iteration or initial guess. The pressure correction equation is solved in order to produce the new pressure distribution. Finally, the cell velocities are corrected and a new set of conservative fluxes is solved.

### 3.6 Solution convergence

Convergence is the term for a numerical method using iterations to produce a solution of the grid, whereby the error approaches zero. Solutions are based on iterations against pre-defined convergence criteria [FLUENT guide, 2006]. For most problems, the default convergence criterion in FLUENT is sufficient. This criterion requires that the scaled residuals defined by the equations selected decrease to  $10^{-3}$  and  $10^{-6}$  for the energy equation. The plot of the scaled residuals against the iterations indicates the status of the convergence (Figure 3.16). When the set convergence criterion is met the iteration process is complete.

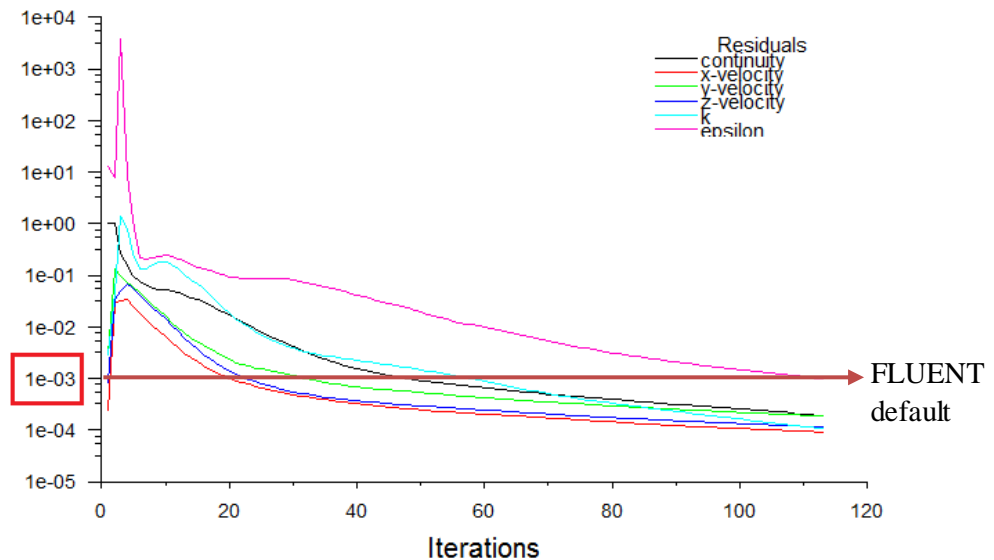


**Figure 3.16** Converged solution residuals.

There are no general metrics for judging solution convergence. Residual definitions that are useful for one class of problem are sometimes misleading for other classes of problem. Therefore it is useful to monitor convergence not only by examining residual levels, but also by monitoring relevant integrated quantities such as the volume averaged velocity. In order to ascertain the accuracy of the default convergence criteria, the set point was reduced from  $10^{-3}$  to  $10^{-9}$  and the values were monitored (Figure 3.17).

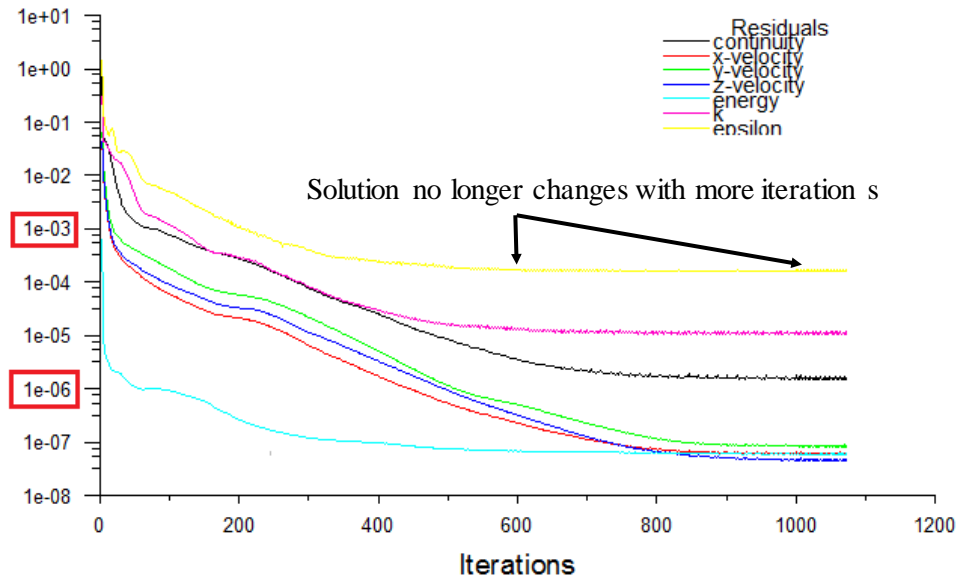


**Figure 3.17** Solution residuals with higher convergence criteria.

### 3.7 Post processing

The ANSYS Results post processing tool was used to visualise the contours, vectors and streamlines of the airflow through the wind tower and into the test room model. Furthermore, nine data points in an equally spaced 3 by 3 grid were created within the test room at a height of 1.5 m which allow for measurements to be made for velocity, pressure and temperature within the test room (Figure 3.18). Additionally, three data points were positioned at the bottom of the room (central), below the supply and exhaust channels of the wind towers.

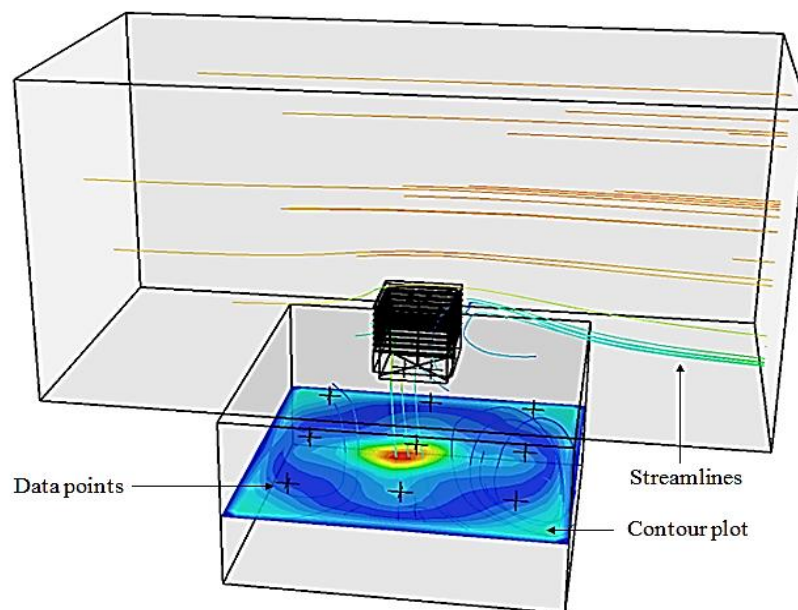


**Figure 3.18** ANSYS post processing tools.

### 3.8 Quantification of CFD uncertainties

The application of computational models involves significant unknowns and uncertainties that may have implications on the reliability of its predictions. Hence, it is important to identify uncertainties associated with the computational modelling and simulation process. Sources of computational uncertainties can be group in four general categories [Perez, 2008]:

- Physical modelling - arise from mathematical model form assumptions, boundary conditions, initial conditions, and data input to a code.
- Discretisation and solution errors – difference between the exact solution and the discrete equations and analytical solutions to the partial differential equations.
- Computer round-off error – difference between the exact solution to the discrete equations and the computer solution.
- Programming errors – arise from the mistakes made in programming or writing code

The quantification of uncertainty in CFD predictions is a substantial challenge and a significant goal. Quantification of uncertainty involves more than just obtaining a good error estimate. Several methods to quantification of uncertainty in CFD have their relative advantages, involving algebraic simplicity of local estimators vs. higher-order accurate solutions, single-grid vs. multiple-grid generations and post processing vs. CFD code modifications. Roache [1997] stated that systematic grid convergence studies are the most common, most straightforward and reliable method for the quantification of CFD uncertainty. This method requires no code modifications but does require multiple grid generations. This study used a posterior error estimate based on the hp grid-convergence procedure (Section 3.1.2.4).

Furthermore, independent model validation must be made through experimentation to minimise potential modelling errors and to ensure that the models accurately represent the reality. The simulation model used in this study has been validated against scaled experimental wind tunnel testing (Chapter 5).

### 3.9 Computational Fluid Dynamics (CFD) Modelling

A four-sided and one-sided wind tower were utilised as a benchmark for the CFD investigations. Two heat transfer device (HTD) configurations were incorporated to the wind tower models; vertical and horizontal HTD arrangements. Furthermore, the CFD model also investigated the effect of the addition of extended surfaces and porous media on the thermal performance of the cooling wind tower. The device was mounted centrally above a 5 x 5 x 3 m test room model representing a small standard classroom. The macro and micro climates geometry remained constant in each CFD model (described in Section 3.2). Tests were performed for external wind speeds of 0.5 - 5 m/s at various wind directions (0 to 180°).

#### 3.9.1 Wind tower benchmark model

Two types of wind towers were utilised as benchmark models; four-sided and one-sided.

A modern multi-directional or four-sided wind tower with a length of 1.1 m, width of 1.1 m and height of 1.2 m was used as a benchmark model. The square wind catcher was divided into four equal quadrants by a four way diagonal cross divider which allows for air flow supply, regardless of the direction of the wind. The quadrants ran the full length of the wind catcher. A total of seven louvres were designed at an angle of 45° with a length of 1.1 m. The wind tower was mounted centrally on top of a test room model representing a small classroom [Building Bulletin 98, 2004] with a length, width and height of 5, 5 and 3 m (Figure 3.19).

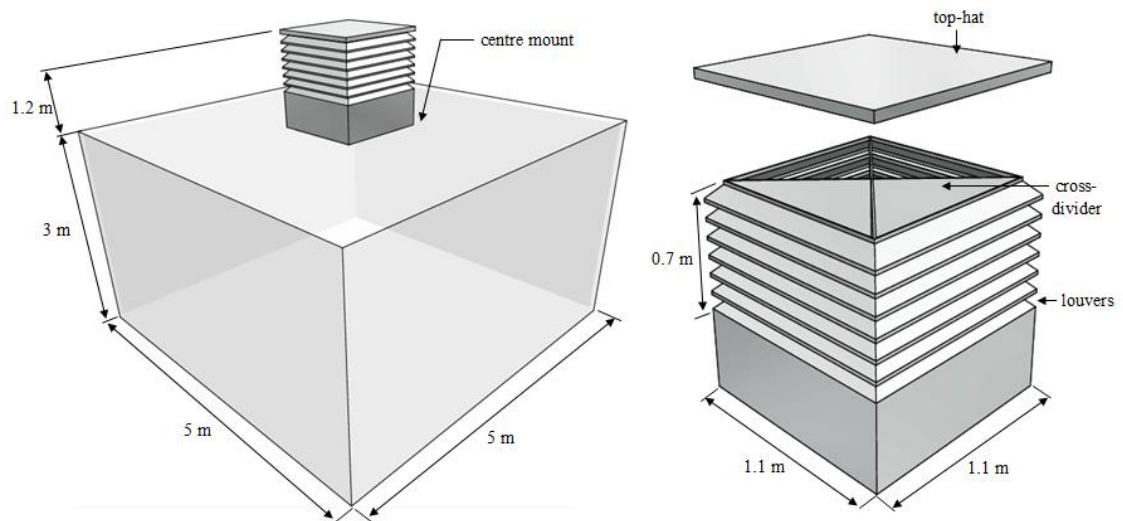


**Figure 3.19** CAD model of the four-sided wind tower mounted on the test room.

Figure 3.20 shows the second benchmark model, a uni-directional or one-sided wind tower system with a length of 1.1 m, width of 1.1 m and height of 1.2 m mounted centrally on top of the test room supplying the air flow at ceiling level. The 1 x 1 m<sup>2</sup> window opening located at the leeward side of the room will aid the cross-flow ventilation [Hughes *et al.*, 2011].

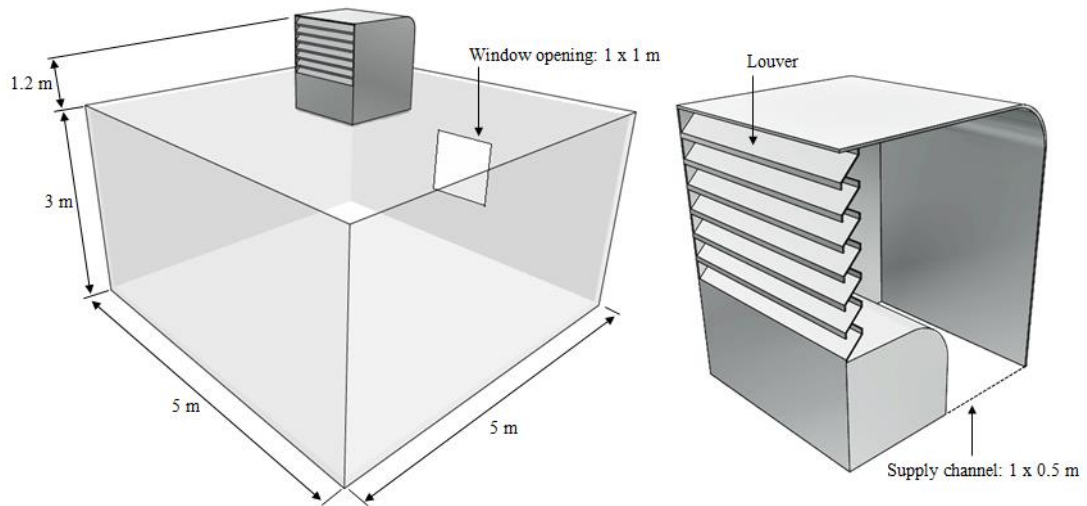


**Figure 3.20** CAD model of the one-sided wind tower mounted on the test room.

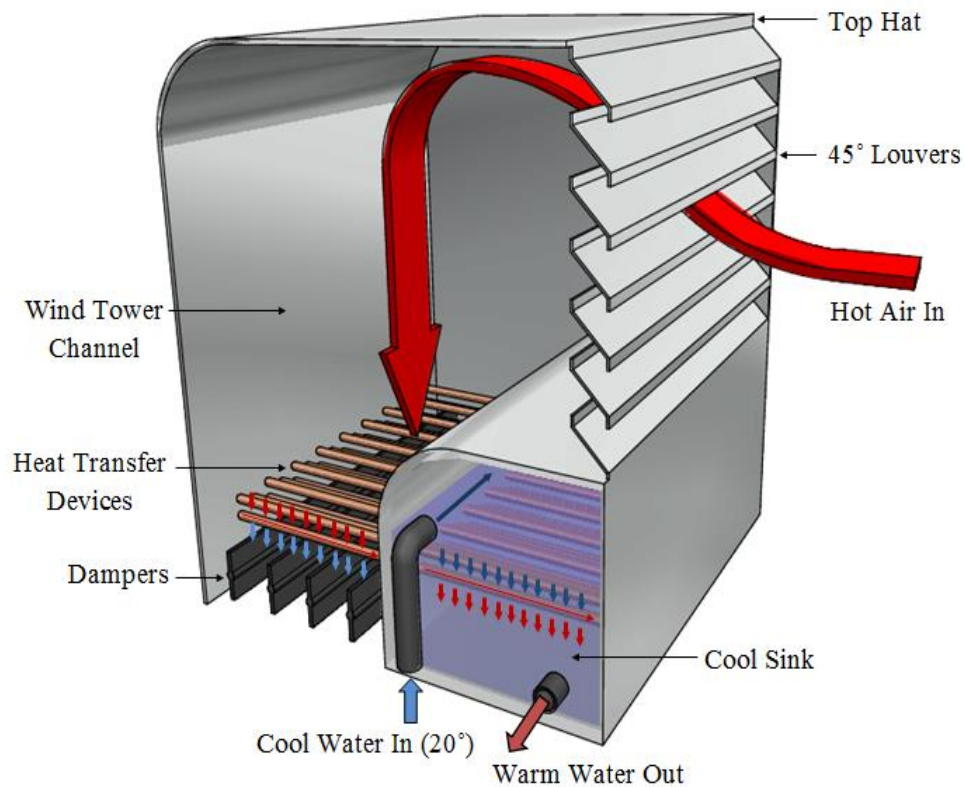
Tests were performed for external wind speeds of 0.5, 1, 2, 3, 4 and 5 m/s at various wind directions (0 to 180°). To simplify the benchmark wind tower CFD models, control dampers and ceiling diffusers were not assessed in the numerical simulation. Table 3.4 summarises the benchmark wind tower design specifications.

**Table 3.4** Summary of benchmark wind tower configurations.

Parameters	Four-sided	One-sided
Dimension	1 x 1 x 1.2 m	1 x 1 x 1.2 m
Louvre type	7 louvres at 45°	7 louvres at 45°
Louvre spacing	0.1 m	0.1 m
Supply area	0.25 m <sup>2</sup> (1 quadrant)	0.5 m <sup>2</sup> (1 channel)
Window opening	-	1 m <sup>2</sup>

### 3.9.2 Wind tower device integrated with vertical and horizontal HTD arrangement

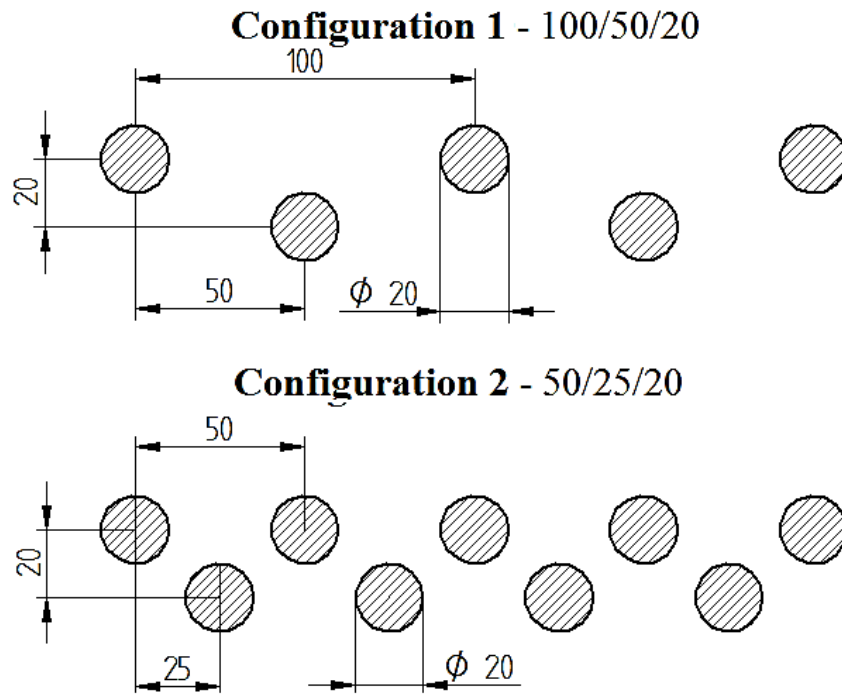
The ventilation and cooling principles of the proposed wind tower system are illustrated in Figure 3.21. The warm external air enters the wind tower through the louvres angled at 45°. The air flow is directed downwards and passed through a series of cylindrical heat transfer devices. The heat is removed and transferred to a parallel, water cooling system. This is similar to the evaporative cooling system but unlike the traditional method the water is recirculated back to the source (i.e. ground source). The cooled air is supplied to the room below the channel via the ceiling diffusers which incorporate adjustable dampers to control the supply flow rate.



**Figure 3.21** Flow diagram representing ventilation and cooling through a heat transfer device integrated wind tower system.

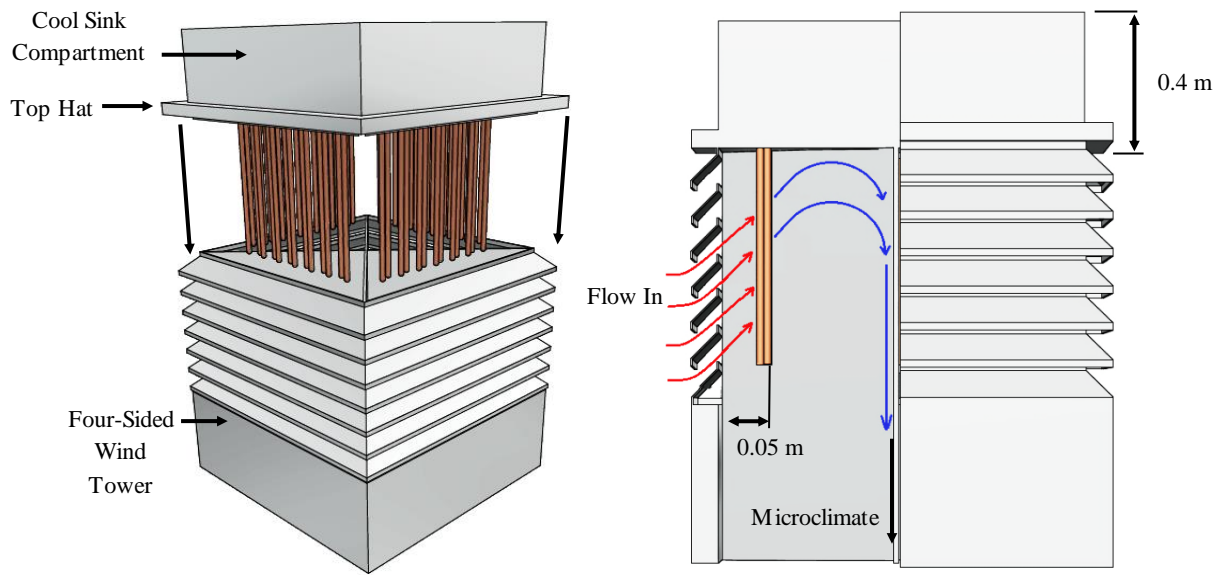
Figure 3.22 shows the schematic arrangements of the heat transfer devices that were incorporated to the wind tower benchmark models (Section 3.1.2.2). The CFD analysis investigated the cooling potential of the proposed system and the effect of the addition of the cylindrical tubes on the air flow stream. Tests were performed for various external

wind speeds (0.5 - 5 m/s) and wind directions (0 - 180°). Detailed investigation of the performance of the cool sink is outside the scope of the study. In order to reduce the computational meshing and time, the cool sink was modelled as a solid block in the CAD software and was subtracted from the fluid volume to be analysed. This method will retain the external walls of the cool sink geometry but excludes the internal volume of the cool sink from the simulations.



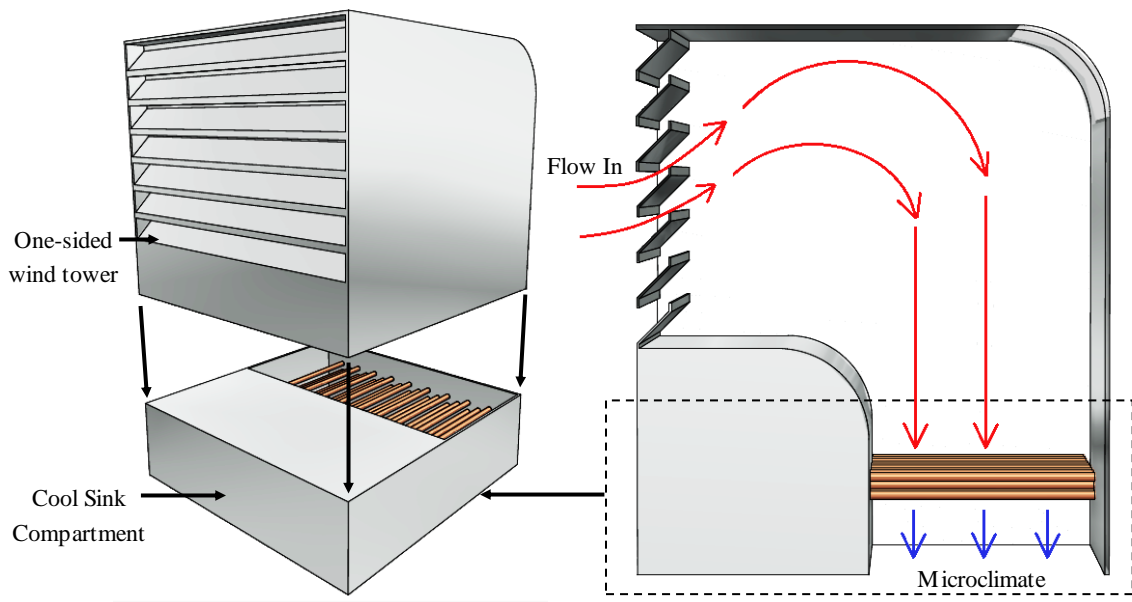
**Figure 3.22** Heat transfer device configurations [Calautit *et al.*, 2012].

Figure 3.23 shows the heat transfer devices incorporated in the benchmark four-sided wind tower model. In order to minimise the flow obstruction inside the wind tower channel, the cool sink was mounted above the wind tower adding an extra 0.4 m to the total height of the model.



**Figure 3.23** CAD model schematic of the wind tower incorporating vertical HTD arrangement.

Figure 3.24 displays the one-sided wind tower was used for the analysis of the horizontal heat transfer device configuration.



**Figure 3.24** CAD model schematic of the wind tower incorporating horizontal HTD arrangement.

Table 3.5 summarises the HTD integrated wind tower design specifications

**Table 3.5** Summary of HTD integrated wind tower configurations.

Parameter	Configuration 1	Configuration 2
HTD Orientation	Vertical	Horizontal
Wind tower model	Four-sided	One-sided
Dimension	1 x 1 x 1.5 m <sup>2</sup>	1 x 1 x 1.2 m <sup>2</sup>
No. of HTD	13 in 1 quadrant (0.24 m <sup>2</sup> )	26 in 1 channel (0.48m <sup>2</sup> )
HTD diameter	0.02 m	0.02 m
HTD length	1 m (0.6 m in quadrant)	1 m (0.5 m in channel)
HTD spacing	100/50/20	100/50/20
HTD surface material	Copper	Copper

### 3.9.3 Wind tower device integrated with HTD arrangement and extended surfaces

Extended surfaces, which are commonly known as fins, are used to augment heat transfer from electronic components, condenser and evaporators in cooling systems and automobile engines. Finned tubes are used extensively in heat recovery systems in which process liquids flows inside the tubes, and atmospheric air is circulated outside the extended surfaces. In various applications heat from the extended surfaces is dissipated by natural as well as forced convection [Rao *et al.*, 2006].The heat transfer rate from an extended surface is defined by the following equation:

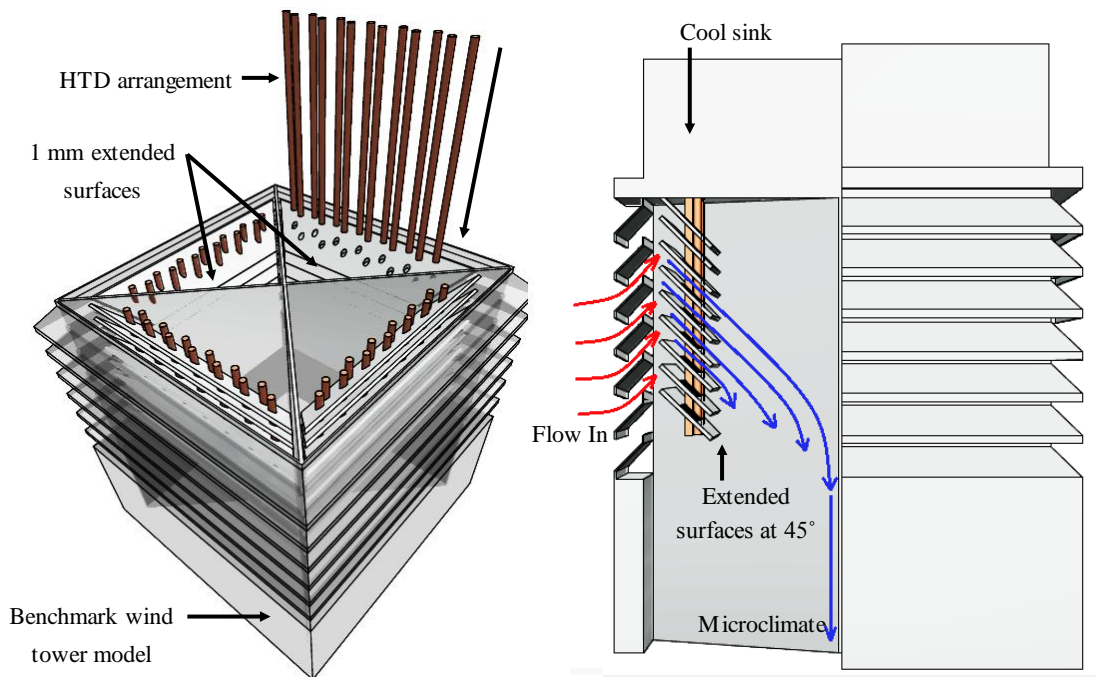
$$Q = h \times A_f(T_w - T_a) \quad \text{Equation 3.17}$$

where  $h$  is the heat transfer coefficient,  $A_f$  is the cross sectional area of the fin,  $T_w$  is the temperature of the base of the fin and  $T_a$  is the ambient temperature.

In this study, an array of extended surfaces was integrated into the cooling system to enhance the rate of heat transfer between the heat transfer device surfaces and air flow (fluid). A total of 36 extended surface plates (9 plates per quadrant) were used, increasing the total surface area of the heat transfer device (2.21 m<sup>2</sup>) by approximately 8.5 m<sup>2</sup> (0.238 m<sup>2</sup> per plate).

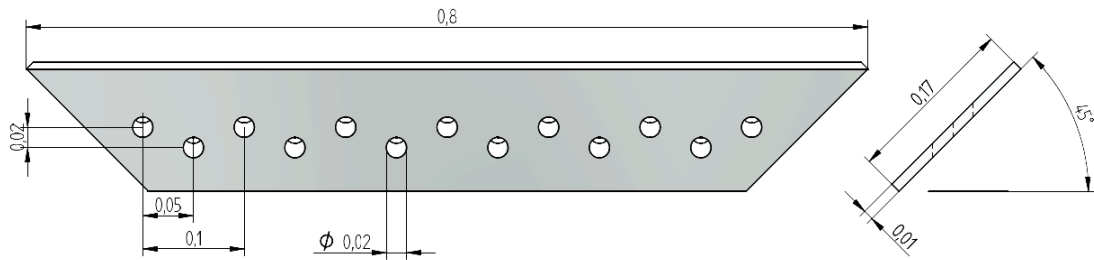
The CFD model analysed the effect of the addition of extended surfaces on the thermal performance of the heat transfer device integrated wind tower and the associated pressure drop. However, detailed investigations of the performance of the extended surfaces such as the shape, spacing, arrangement and material properties are outside the scope of the study.

Figure 3.25 shows the wind tower integrated with the vertical HTD arrangement and extended surfaces. The extended surfaces inclined at  $45^\circ$  will also function as a guide vane redirecting the flow towards the bottom of the channel and to the room. This will reduce the flow separations occurring at the bottom left corner of the wind tower channel [Hughes and Ghani, 2009].



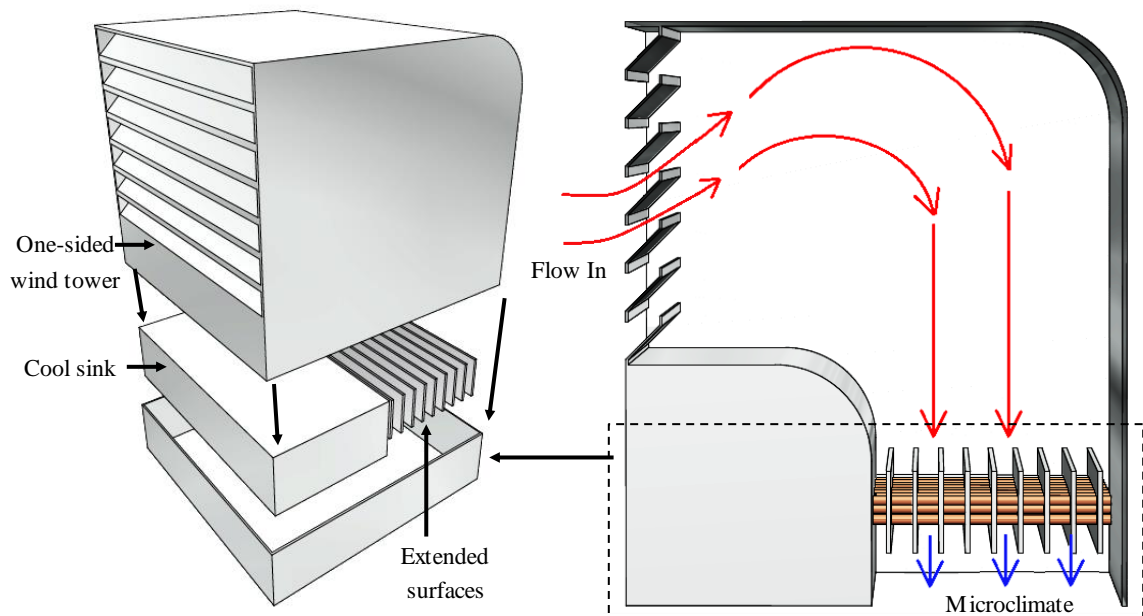
**Figure 3.25** Schematic of the proposed wind tower systems incorporating vertical heat transfer devices with extended surfaces.

Figure 3.26 displays a diagram of the inclined extended surface plate with the dimensions.



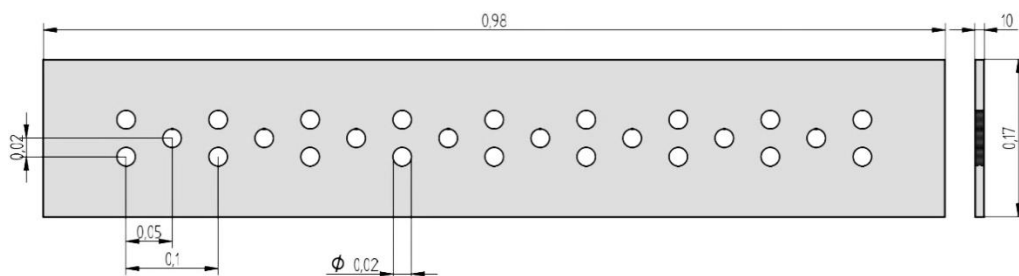
**Figure 3.26** Schematic of the extended surface plate for the vertical arrangement.

Figure 3.27 shows the wind tower integrated with horizontal HTD arrangement and extended surfaces. A total of 9 continuous extended surface plates were used, increasing the total surface area of the heat transfer device ( $0.55 \text{ m}^2$ ) by approximately  $2.142 \text{ m}^2$  ( $0.238 \text{ m}^2$  per plate).



**Figure 3.27** Schematic of the proposed wind tower systems incorporating horizontal heat transfer devices with extended surfaces.

Figure 3.28 displays a schematic of a continuous extended surface plate with the dimensions.



**Figure 3.28** Schematic of the extended surface plate for the horizontal arrangement.

Table 3.6 summarises the design specifications of the HTD integrated wind tower with extended surfaces

**Table 3.6** Summary of HTD integrated wind tower with extended surfaces.

<b>Parameter</b>	<b>Configuration 1</b>	<b>Configuration 2</b>
HTD Arrangement	Vertical	Horizontal
Wind tower model	Four-sided	One-sided
Outer dimensions	1 x 1 x 1.5 m <sup>2</sup>	1 x 1 x 1.2 m <sup>2</sup>
No. of extended surface	9 per supply quadrant	9 per supply channel
Ext. surf. dimensions	0.8 x 0.17 x 0.01 m	0.98 x 0.17 x 0.01 m
Ext. surf. spacing	0.05 m	0.05 m
Ext. surf. angle	45° (downward)	0° (parallel to flow)
Ext. surf. material	Aluminium	Aluminium

#### **3.9.4 Wind tower device integrated with HTD arrangement and porous media**

Flow control devices such as porous mesh screens placed across an airflow will have an evening effect, distributing both the velocity and pressure across the screen [Roberts, 2002]. Figure 3.29a shows the flow pattern inside a channel with and without a porous screen. It can be seen from the velocity contour that the airflow is faster at the upper section of the pipe without the porous screen. Similar flow patterns can be observed inside the wind tower channel in Figure 3.29b, separated flow and circulation zones exist at the entrance opening and near the lower edge of the channel. Adding the porous media will spread the flow widely over the cross-section of the lower channel and reduce the scale of any separated flow region.

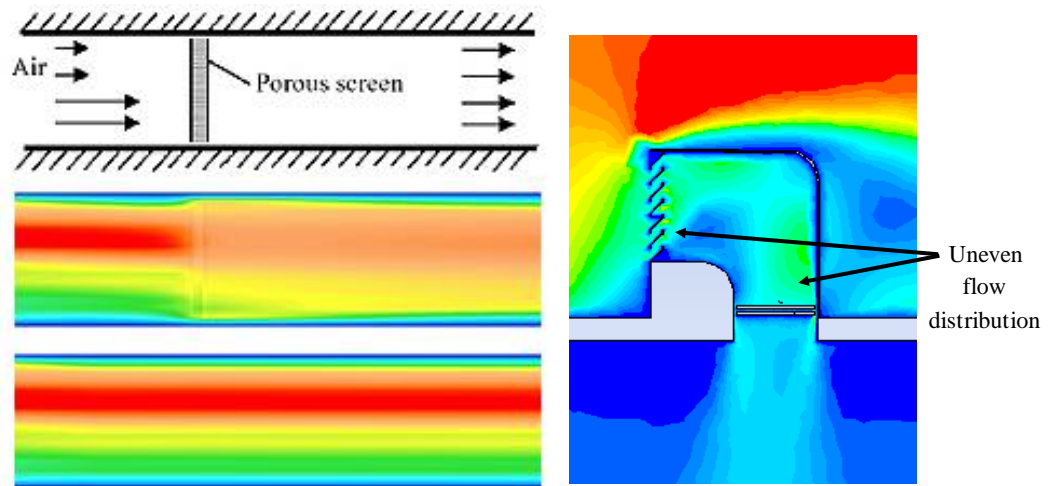


**Figure 3.29** (a) Flow through a pipe with and without a porous mesh [Autodesk, 2008]  
 (b) Uneven flow distribution inside a wind tower.

The CFD model analysed the effect of the addition of a porous media on the ventilation and thermal performance of the wind tower with heat transfer devices. Figure 3.30 illustrates the wind tower with the porous media located upstream of the vertical heat transfer device arrangement. Detailed investigations of the performance of the porous mesh such as the spacing of voids, the structure and material properties are outside the scope of the study.

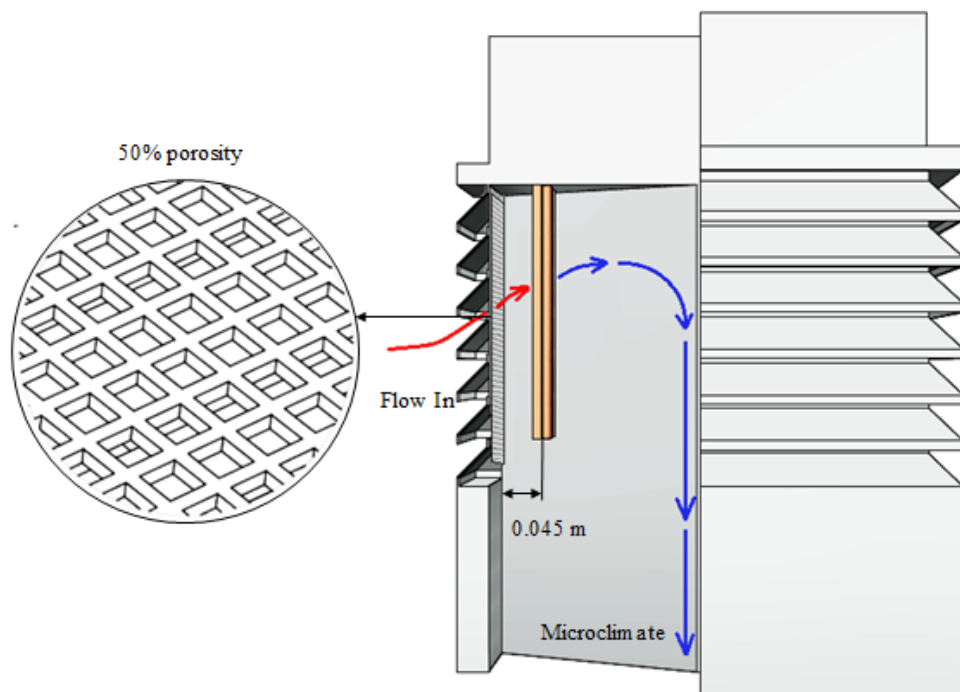


**Figure 3.30** Schematic of the proposed wind tower systems incorporating vertical heat transfer devices with a porous media.

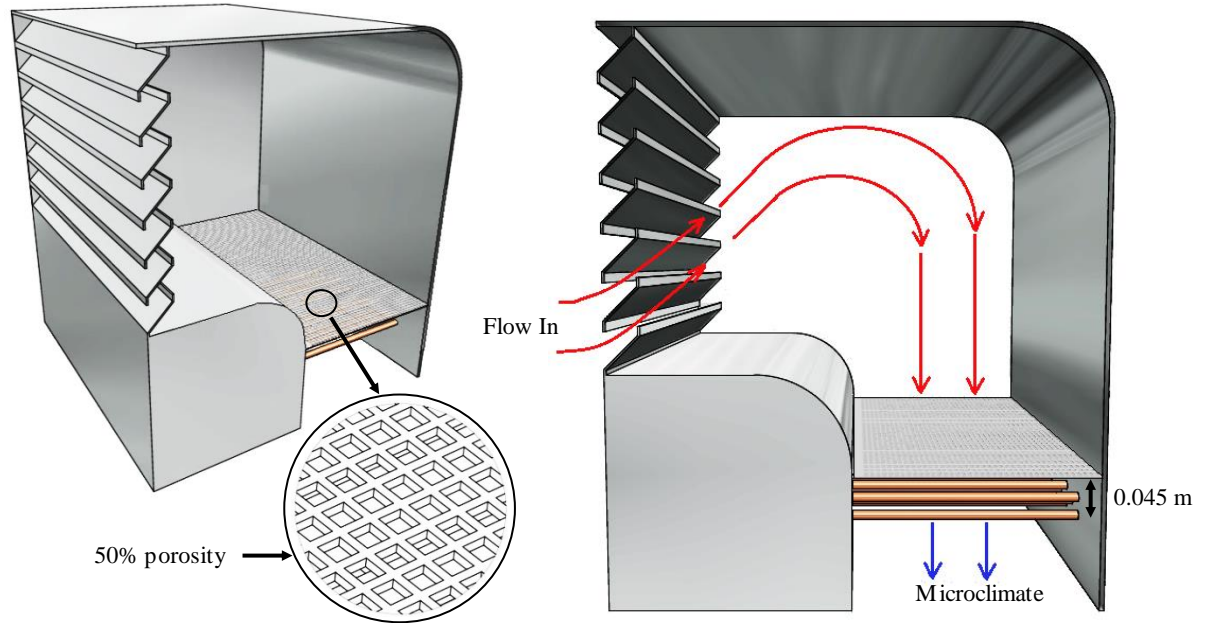


**Figure 3.31** Schematic of the proposed wind tower systems incorporating horizontal heat transfer devices with porous media.

The porous mesh was modelled as a fluid volume and was set as a porous zone in FLUENT. The CFD program is capable of simulating a fluid flow through a porous media with a specific porosity and inertial resistance. The fluid porosity relates to the volume of open spaces compared with the total volume. The inertial resistance is defined by the following equation [FLUENT guide, 2006]:

$$C_2 = \frac{1}{c^2} \frac{\left(\frac{A_p}{A_f}\right)^2}{t_p} \quad \text{Equation 3.18}$$

Where  $c$  is the coefficient based on the Reynolds number and  $t$ ,  $A_p$  is the total area,  $A_f$  is the free area and  $t_p$  is plate thickness.

A fluid porosity of 0.5 was used in order to spread out the flow evenly over the channel's cross-section and also to ensure that there won't be an excessive pressure drop [Swaminathan and Mahalakshmi, 2010]. Table 3.7 summarises the design specifications of the wind tower with a porous media.

**Table 3.7** Summary of HTD integrated wind tower with porous media.

<b>Parameter</b>	<b>Configuration 1</b>	<b>Configuration 2</b>
HTD Arrangement	Vertical	Horizontal
Wind tower model	Four-sided	One-sided
Outer dimensions	1 x 1 x 1.5 m <sup>2</sup>	1 x 1 x 1.2 m <sup>2</sup>
No. of porous mesh	1 per supply quadrant	1 per supply channel
Porous mesh dim.	0.1 x 0.6 m	0.1 x 0.5 m
Thickness	0.00035 m	0.00035 m
Porous mesh porosity	50 %	50 %

Table 3.8 summarises the CFD models and simulations. Test were performed for various external wind speeds (0.5 - 5 m/s) and wind directions (0 - 180°).

**Table 3.8** Summary of the CFD analysis.

<b>CFD Models</b>	<b>Wind speed (m/s)</b>	<b>Wind Angle (°)</b>	<b>Ext. Temp. (K)</b>	<b>CFD Test</b>
Benchmark Four-sided	0.5 – 5	0 - 90	318 K	Full, Scaled
Benchmark One-Sided	0.5 – 5	0 - 180	318 K	Full, Scaled
Vertical HTD (Config. 1 and 2)	0.5 – 5	0 - 90	318 K	Full, Scaled
Horizontal HTD (Config. 1 and 2)	0.5 – 5	0 - 180	318 K	Full, Scaled
Vertical HTD with extended surfaces	0.5 – 5	0 - 90	318 K	Full, Scaled
Horizontal HTD with extended surfaces	0.5 – 5	0 - 180	318 K	Full, Scaled
Vertical HTD with porous media	0.5 – 5	0 - 90	318 K	Full, Scaled
Horizontal HTD with porous media	0.5 – 5	0 - 180	318 K	Full, Scaled

### 3.9.5 Thermal comfort model

The use of standardised scales to gather the thermal response from groups of individuals has allowed the evaluation of the thermal comfort levels in a given environment [Catalina *et al.*, 2009]. The adaptive approach or thermal response of real subjects through field surveys are recommended, however these studies are costly and require a large number of participants in order to gather statistically significant data. In this study the Predicted Mean Vote (PMV) and the Predicted Percentage Dissatisfied (PPD) values were used to evaluate the steady-state thermal comfort performance of a test room model incorporated with the wind tower system. The following cases were selected for the thermal comfort simulation:

- Case 1: Benchmark wind tower model
- Case 2: Wind tower model with heat transfer devices
- Case 3: Wind tower model with heat transfer devices and extended surfaces

The platform for implementing and demonstrating CFD simulations in the thermal comfort study was the FLUENT Airpak package. FLUENT Airpak is a specialised design tool for ventilation systems that are required to provide a good indoor air quality and thermal comfort for the occupants. Airpak is coupled with the FLUENT CFD solver for the thermal and fluid flow calculations. Figure 3.32 shows how the data obtained from the initial CFD study were coupled with the thermal comfort analysis.

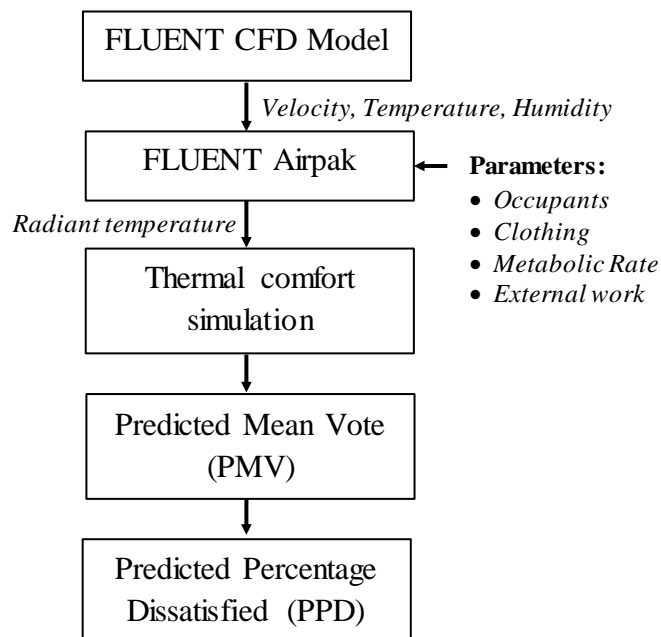


**Figure 3.32** Thermal comfort analysis

Thermal comfort was evaluated using the PMV and PPD index. Fanger [1970] calculated the thermal load at the actual activity level and developed a relationship between the thermal load and predicted mean vote, assessing them based on seven levels (Table 3.9):

**Table 3.9** The 7-point thermal sensation scale [Fanger, 1970].

PMV	Thermal sensation
+ 3	Cold
+ 2	Cool
+ 1	Slightly cool
0	Comfortable
- 1	Slightly warm
- 2	Warm
-3	Hot

The Fanger model is one of the earliest and most widely used prediction models for the thermal comfort of a given combination of personal factors and other thermal environmental parameters. The PMV equation is given by the following equation [ISO7730, 2005]:

$$PMV = [0.303 \cdot e^{-0.036 \cdot M} + 0.028] \cdot L \quad \text{Equation 3.19}$$

Where L is the thermal load defined as the difference between the internal heat production and the heat loss to the actual environment for an individual:

$$L = (M - W) - E_c - C_{res} - E_{res} - H \quad \text{Equation 3.20}$$

Where;

**M** is the occupant's metabolic rate in W/m<sup>2</sup>

**W** is the effective mechanical power (W/m<sup>2</sup>)

$$E_c = 3.05 \cdot 10^{-3} [5733 - 6.99 \cdot (M - W) - p_a]$$

$$+ 0.42 \cdot (M - W - 58.15);$$

$$\text{Equation 3.21}$$

**C<sub>res</sub>** = 0.0014 · M · (34 - t<sub>a</sub>) is the respiratory sensible heat loss;

$E_{res} = 1.72 \cdot 10^{-5} \cdot M \cdot (5867 - p_a)$  is the resp. evaporative heat loss; Equation 3.22

$p_a$  is the water vapour partial pressure in (Pa);

$t_a$  is the air temperature in (°C);

The dry heat loss  $H$  was calculated using the following:

$$H = 3.96 \cdot 10^{-8} \cdot f_{cl} \cdot [(t_{cl} + 273)^4 - (t_r + 273)^4] - f_{cl} \cdot h_c \cdot (t_{cl} - t_a) \quad \text{Equation 3.23}$$

Where;

$f_{cl}$  is the clothing surface factor;

$t_r$  is the radiant temperature in (°C);

$h_c$  is the convective heat transfer coefficient in (W/m<sup>2</sup>-k);

$t_{cl}$  is the clothing surface temperature in (°C);

Calculation of the  $t_{cl}$  is an iterative process and was calculated using the following equation:

$$t_{cl} = 35.7 - 0.028 \cdot (M - W) - I_{cl} \cdot H \quad \text{Equation 3.24}$$

The Predicted Percentage Dissatisfied (PPD) value is a quantitative measure of the thermal comfort of a group of people at a particular thermal environment. With the PMV value determined, PPD was calculated using the following equation [ISO7730, 2005]:

$$PPD = 100 - 95 \cdot \exp(-0.03353 \cdot PMV^4 - 0.2179 \cdot PMV^2) \quad \text{Equation 3.25}$$

From Equations 3.19 – 3.24 the main parameters required to calculate the PMV value were the air velocity ( $U_a$ ), air temperature ( $t_a$ ), relative humidity ( $t_r$ ), mean radiant temperature ( $t_r$ ) and the two personal parameters which are the metabolic rate ( $M$ ) and clothing insulation ( $I_{cl}$ ) of the person. In this study, the velocity, temperature and relative humidity parameters were obtained from the initial CFD models and used as inlet boundary conditions for the thermal environment. The values for the activities and clothing of the occupants were obtained from the standards [ISO7730, 2005] and set in the software.

The mean radiant temperature was modeled in FLUENT Airpak using the discrete ordinates (DO) model. The method is suitable for the analysis of models containing extremely large number of surfaces which is difficult to calculate using the form factor method [Airpak 2.0 User Guide, 2001]. The DO model considers the Radiative Transfer Equation (RTE) in the direction  $\vec{s}$  as a field equation [FLUENT12 Theory guide, 2012]:

$$\nabla \cdot (I(\vec{r}, \vec{s})\vec{s}) + (\alpha + \sigma_s)I(\vec{r}, \vec{s}) = \alpha n^2 \frac{\sigma T^4}{\pi} + \frac{\sigma_s}{4\pi} \int_0^{4\pi} I(\vec{r}, \vec{s}') \Phi(\vec{s} \cdot \vec{s}') d\Omega' \quad \text{Equation 3.26}$$

The micro-climate model representing a standard classroom was used as the thermal environment. The recommended occupancy figure for a 5 x 5 x 3 m small classroom are 12 occupants [Building Bulletin 98, 2004]. 12 human models were included in the model as shown in Figure 3.33 and 3.34. For each, a metabolic rate unit of 1 met (58.2 W/m<sup>2</sup>) was set which corresponds to sedentary activities. Equipment, appliances, and lighting in the room were not considered in the thermal comfort simulations.

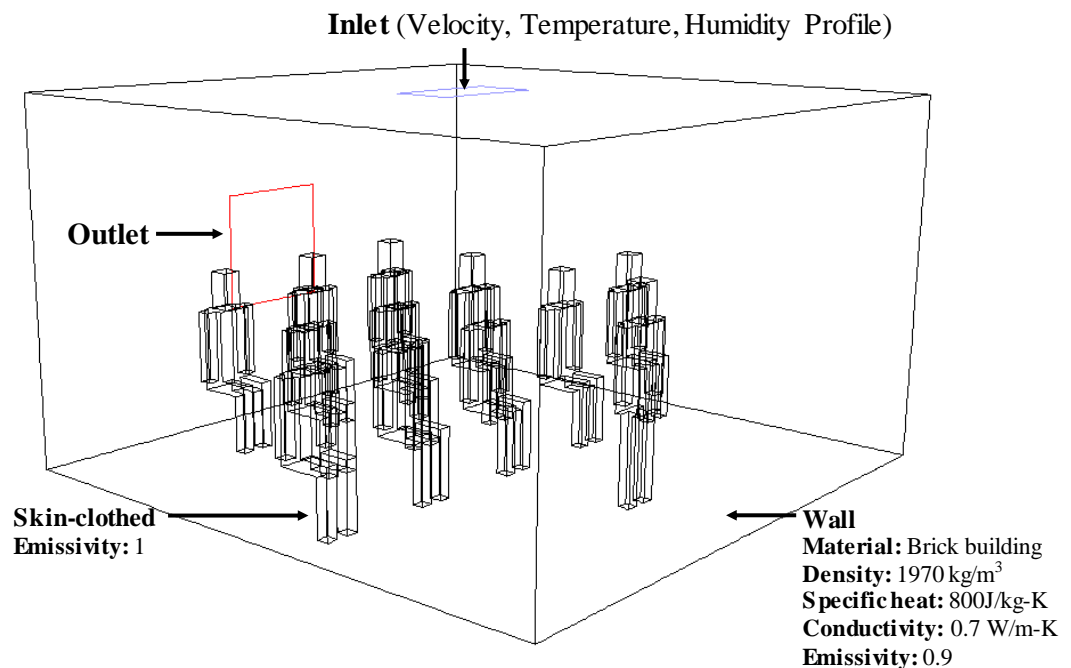


**Figure 3.33** Computational domain of the test room model.

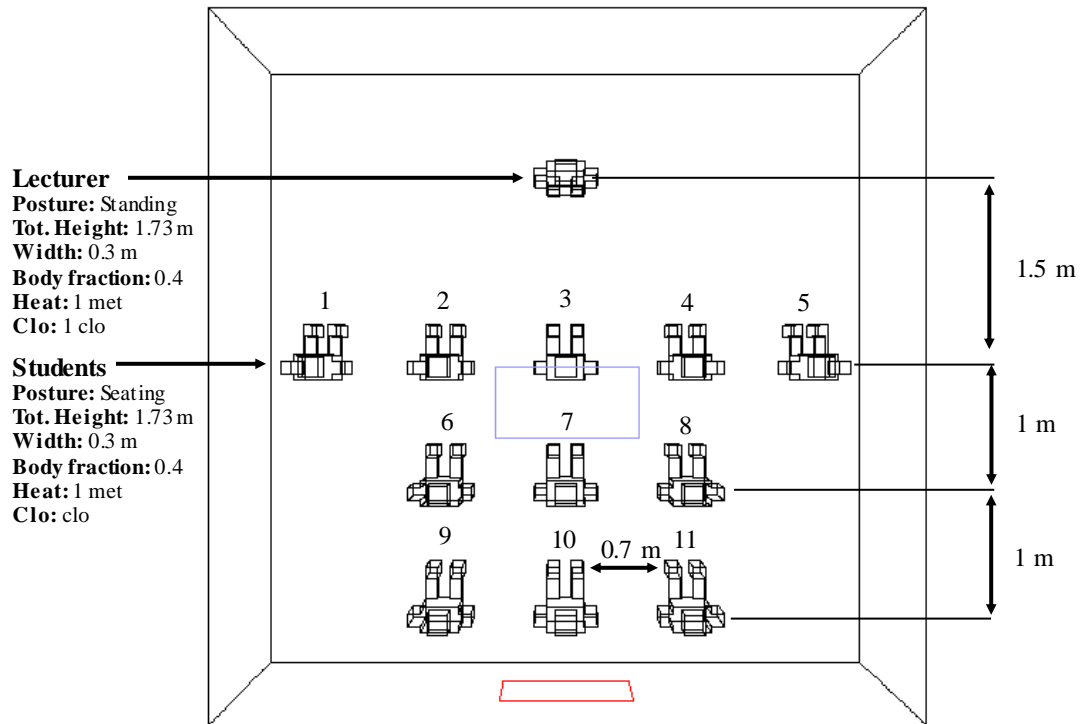


**Figure 3.34** Top view of the test room showing occupants details and position.

### 3.10 Summary

This chapter presented the specific CFD theory and modelling used for the purpose of this investigation. The three main areas of the CFD process were described namely pre-processing, solving, and post-processing. The pre-processing section highlighted the physical domain and the computational mesh generation. The solving area detailed the selection of solvers and equations; and solution convergence. Furthermore, the methods used to visualise and analyse the solution data are covered in the post-processing area.

In total, ten different wind tower designs were modelled and analysed using CFD. A modern four-sided and one-sided wind tower were utilised as benchmark CFD models. Different heat transfer device (HTD) arrangements were integrated to the wind tower models. Furthermore, extended surfaces and porous media were added to the cooling wind tower design.

Finally, the test room model representing a standard classroom was used for the assessment of the thermal comfort performance of the cooling wind towers. The platform for implementing and demonstrating CFD simulations in the thermal comfort study was the FLUENT Airpak package.

## **Chapter 4**

### **Experimental Techniques**

#### **4.1 Introduction**

As part of this study, scaled experimental wind tunnel testing was undertaken to validate the CFD simulation work carried out. This chapter presents the design parameters and requirements for the closed-loop wind tunnel.

The experimental design and methodology are presented in this chapter covering the experimental set-up, rapid prototyping of the 3D CAD models and measurement procedures. Finally, the chapter introduces the operating principle, specifications and accuracy of the equipment used in the experimental testing.

#### **4.2 Subsonic closed-loop wind tunnel**

This research engaged on designing and commissioning a purpose build wind tunnel to carry out experimental test on different types of wind tower models in a controlled environment and validate the data obtained by computational modelling.

Construction and testing of the full scale design is often costly and time consuming, especially when repeated several times - building the full scale model, testing, analysing the data, optimising the model, and then building another full design. Cost effective testing can be achieved through wind tunnels coupled with high speed data acquisition and rapid prototyping. Rapid prototyping techniques allow designers and engineers to rapidly and economically assess parts of the design, analyse the data and then build a full scale model. However, it is also important for engineers to realise that by their very definition, prototype models will present some compromise from the fully working model. Inaccurate construction of the scaled prototype will not yield full scale conditions. Hence, the scale must be selected carefully based on the test section size of to reduce the aerodynamic problems introduced by the test section walls [Irwin *et al.*, 2013].

A wind tunnel is a research apparatus used in aerodynamic investigations to study the effects of air moving past solid objects. There are many types of wind tunnels, each is designed and built to suit certain applications. They can be classified according to the

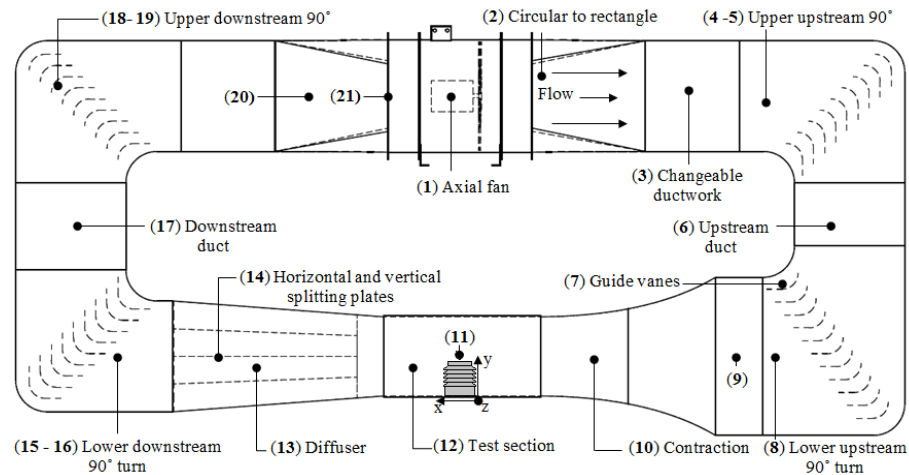
speed in test section relative the speed of sound: subsonic, transonic, supersonic and hypersonic [Cermak, 2003]. Wind tunnels are also categorised by the shape of the wind tunnel: open loop and closed-loop. Open loop wind tunnel draws air from the room into the contraction, test section and diffuser in a straight line. Generally, an open-loop wind tunnel is inexpensive to build. However, open wind tunnels suffer from entry conditions because of the way the air is being drawn and blown out of the tunnel. Other disadvantage includes high operation costs and noisy operation. While a closed-loop wind tunnel recirculates the air inside the tunnel therefore requiring more sections to form a loop. Advantages of the closed loop wind tunnel are controlled quality (turning vanes and flow straighteners), low operation costs and low noise operation.

Based on the previous related work [Montazeri *et al.*, 2010, Elmualim, 2006b] it was established that a low speed wind tunnel was suitable for this application and was constructed for the purpose of this research.

The wind tunnel consisted of an overall plan length of 5.6 m with a test section of the height, width, and length of 0.5, 0.5, and 1 m. The tunnel operates as closed circuit or return flow, air that passes through the test section is drawn back into the fan and recirculated into the test section repeatedly. Guide vanes are used to turn the air flow around the corners of the wind tunnel while minimising the turbulence and power loss. The contraction, diffuser, test section and two corners are located at floor level and the return legs set with the axial fan are positioned vertically above the test section. The air coming out of the tunnel exhaust is recirculated into the supply end of the tunnel to help boost the total airspeed and reduce the operational cost [Barlow *et al.*, 1999]. Figure 4.1 shows the details of the wind tunnel system.



(a) Actual subsonic closed loop wind tunnel system



(b) Wind tunnel details (Elevation)

**Figure 4.1** Side view of the closed-loop subsonic wind tunnel facility for investigating the ventilation performance of the wind tower device: (a) final wind tunnel design (b) CAD model assembly for fabrication.

#### 4.2.1 Operation of wind tunnel

A 2.1 kW axial variable-revolution fan (1) drives the wind tunnel system, it can create stationary wind flow within a range of 2 - 12 m/s. Behind the fan, is a smooth transition (2) of the cross-section from circular to a  $1 \times 0.7 \text{ m}^2$  rectangular duct (3). The neoprene circular to rectangle transition duct is used to reduce/absorb the vibration from the fan to the other wind tunnel components. In the  $90^\circ$  upstream section (4), 9 guide vanes (5) with 0.1 m trailing edges are located to reduce the flow separation occurring at the turn. The 0.4 m long upstream duct (6) connects the two upstream corners. Another set of guide vanes with trailing edges (7) are positioned in the lower upstream  $90^\circ$  turn (8) forcing the flow to be parallel to the test section centre line and improved the uniformity of the flow before the contraction. A contraction section (10) with a 4:1 ratio and total length of 1.1 m connects the outlet of the settling chamber (9) to test section upstream. The  $1(W) \times 1(H) \times 0.3(L)$  settling chamber will allow the integration of honeycomb and wire mesh for flow optimisation or adjustment of turbulence. The scale model (11) is positioned in the test section (12) which has a square cross-sectional area of  $0.5 \times 0.5 \text{ m}^2$  and a length of 1m. Downstream of the test section is the diffuser section (13) which decelerates the flow in order to minimise the loss of flow kinetic energy. Particular effort is made to avoid flow separation in the diffuser, which can significantly reduce its efficiency and the overall performance of the wind tunnel. In order to avoid this

occurrences, horizontal and vertical splitting plates (14) are installed inside the exit diffuser. The downstream turn (15, 16) has a  $1 \times 1 \text{ m}^2$  square cross-section at the outlet of the diffuser, which gradually narrows to  $1 \times 0.7 \text{ m}^2$  rectangular cross-section at the downstream straight duct (17). In the  $90^\circ$  upper downstream section (18), 9 guide vanes (19) with 0.1 m trailing edges are located to order to reduce the flow separation occurring it the turn. After the downstream, an abrupt transition of the cross-section from rectangular to circular cross-section (20) to take the flow into the fan. A highly porous safety mesh (21) is located at the end of the rectangle to round annular section to prevent model parts entering the axial fan section and damaging the fan blade in case of model failure.

Table 4.1 summarises the design specification and dimensions of wind tunnel components.

**Table 4.1** Summary of the design specification and dimensions of the wind tunnel components.

<b>Component</b>	<b>Basic Dimensions (m)</b>	<b>Specifications</b>
Test Section	0.5 (W) x 0.5 (H) x 1 (L)	Square cross-section
Contraction	1 x 1 (inlet) / 0.5 x 0.5 (exit), 1.3 (length)	4:1 ratio
Diffuser	0.5 x 0.5 (inlet) / 1 x 0.7 (exit), 1.1 (length)	$11^\circ$ and $4^\circ$ angles
Transition Duct	0.7 (Diameter) / 1 x 0.7	Anti-vibration
Settling Chamber	1 (W) x 1 (H) x 0.4 (L)	Honeycomb
Axial Fan	0.7 (Diameter) / 0.5 (L)	2.1 kW /1440 rpm

#### 4.2.2 Wind tunnel CFD and experimental modelling

The commercial ANSYS Fluent numerical code was used for predicting the flow characteristics inside the closed-loop wind tunnel. The analytical model for estimating the pressure losses were directed as input boundary conditions for the CFD model. Full details of the design and calculations of the wind tunnel components are summarised in Appendix A.

Two sets of simulations were conducted: numerical modelling of the wind tunnel with an empty test section and with a test block model located centrally in the test section. As suggested by [Moonen *et al.*, 2006], a full-scale CFD model of the entire wind tunnel was considered instead of the conventional approach, in which only the flow in the test section was modeled and applying similar inlet boundary conditions as measured in the actual system. Figure 4.2 shows the model of the entire closed-circuit wind tunnel.

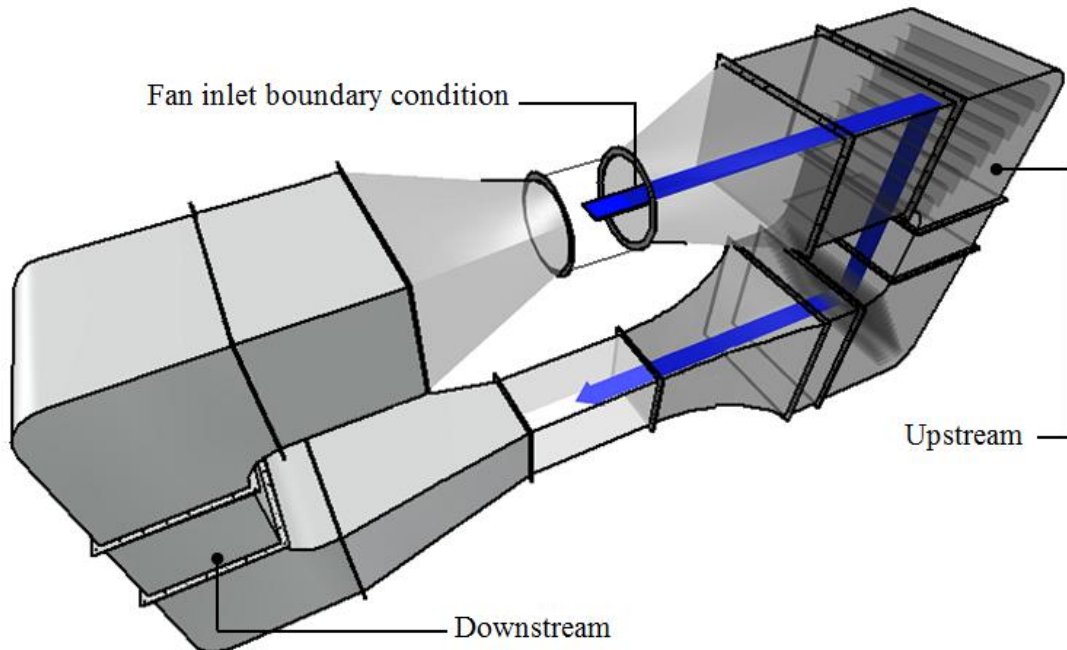


**Figure 4.2** CFD model of the entire closed-circuit wind tunnel showing the boundary condition and flow direction.

The established CFD method accounted for the influence of the specific features of the wind tunnels such as guide vanes and splitting plates. This allowed for the optimisation of the flow not only in the test section but also the flow in other wind tunnel sections. Moreover, the “conventional approach” was not suitable for designing new wind tunnels as it requires experimental data to simulate the inlet boundary conditions and was only useful for studying existing wind tunnel systems.

During the design stage, four different wind tunnel configurations were investigated using CFD. The first model was the reference configuration in which no guide vanes were present. This configuration was compared to three others: with only guide vanes at the upstream, only guide vanes at the downstream and combined upstream and downstream guide vanes, correspondingly. The numerical work evaluated the influence of the presence of guide vanes on the test section flow quality (uniformity of the velocity

flow field, flow angularity and turbulence intensity). Guide vanes with a chord length of 0.1 m and spacing of 0.1 m were positioned at all 4 corners to straighten the flow and avoid areas of re-circulation (Figure 4.3).

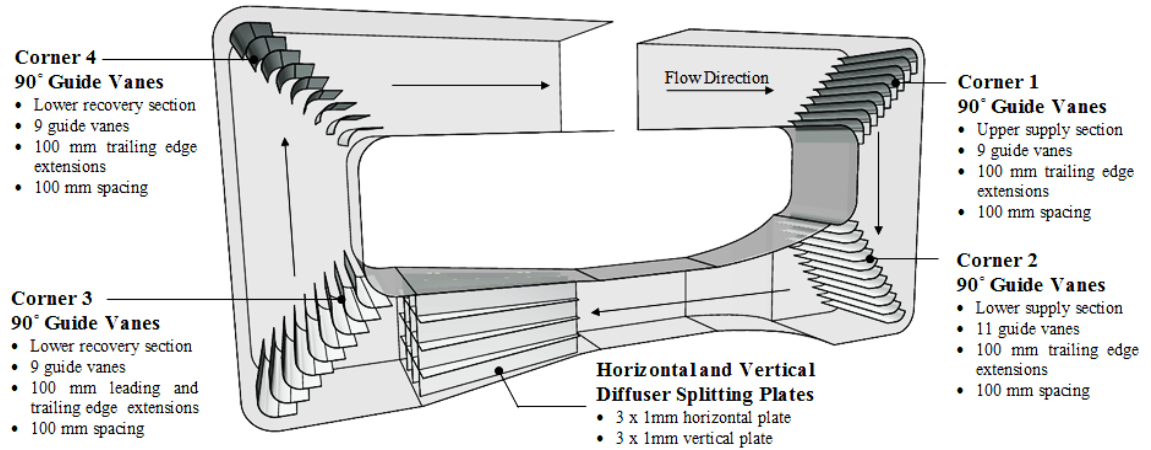


**Figure 4.3** Wind tunnel guide vane and splitting plate design.

Complete characterisation of wind tunnel test environment is a massive task due to the very extensive range of achievable configurations including scaled model testing [Balendra *et al.*, 2002]. Initial experimental testing was conducted in an empty test section. The experiment comprised of measuring air velocities, pressure, and turbulence intensity inside the empty test-section. Wind speed measurements were performed along 9 vertical lines located in the test-section (P01 – P09), at intervals of 0.25m (horizontal) and 0.125 m (vertical) as shown in Figure 4.4.

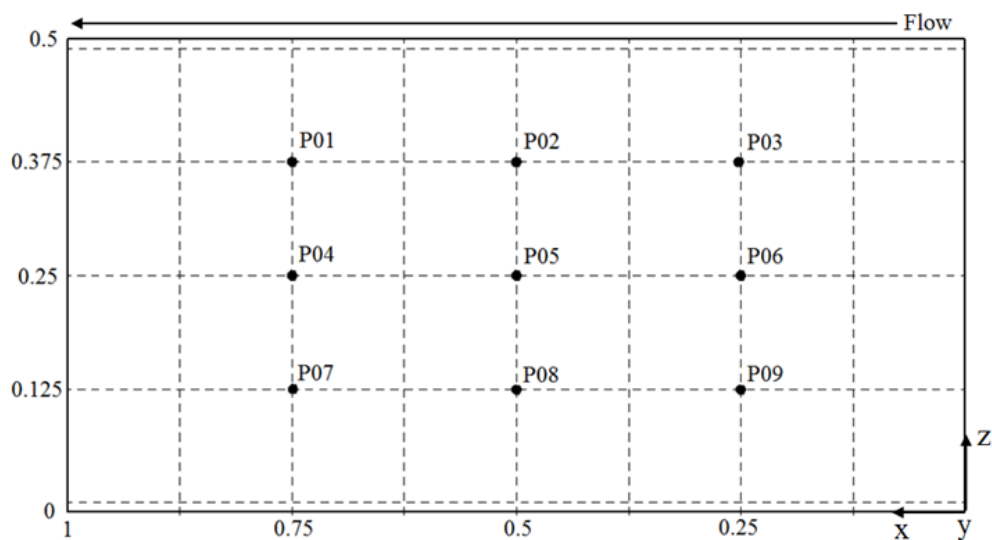
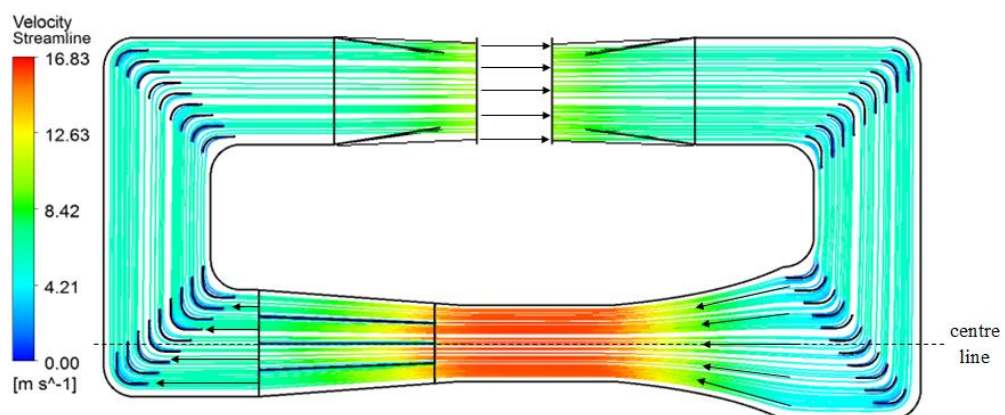


**Figure 4.4** Top view of the test section showing the measurement positions (P01 - P09) and coordinates for the case of an empty test section. Dimensions are in metres.

The second experiment included velocity, pressure and turbulence intensity measurements around a test block model of the length, width and height of 0.11 x 0.11 x 0.11 m located centrally in the test section. The purpose of this test was to evaluate the accuracy of simulating or achieving the flow characteristics for which the wind tunnel was designed. Full details of the CFD modelling and experimental validation of the wind tunnel system are summarised in Appendix B and C.

### 4.2.3 Flow characterisation of the wind tunnel

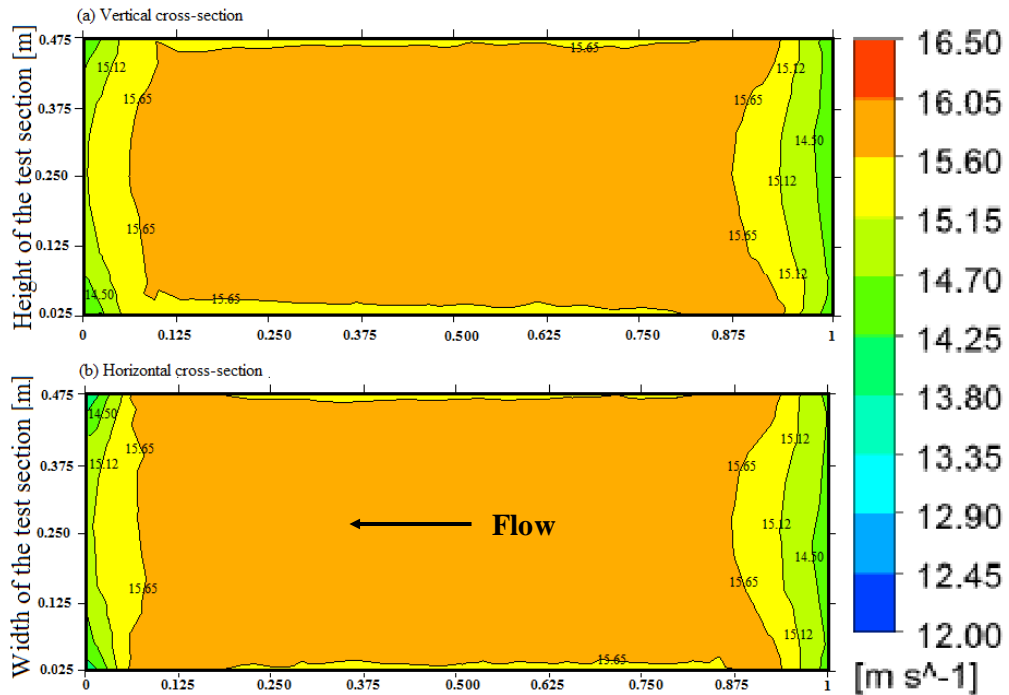
Figure 4.5 shows the velocity streamlines of a middle plane in the wind tunnel with upstream and downstream guide vanes. The formation of velocity rotations at the corners which were observed from configurations 1 - 3 were eliminated by adding guide vanes to the upstream and downstream 90° corners. The upstream corner guide vanes with 0.1m trailing edges effectively maintained a comparatively straight flow throughout the upstream circuit and no over or under turn were observed. It can be seen that the lower vanes effectively forcing the flow to be parallel to the test section centre line and improved the uniformity of the flow before the contraction section. Furthermore, the third corner guide vane with 0.1m leading and trailing edges effectively directed the flow to the upper downstream sections without over and under turn. The fourth corner guide vanes sufficiently reduced the velocity variation of the return flow before the fan section.



**Figure 4.5** Velocity streamline for configuration 4: upstream and downstream guide vanes.

Figure 4.6 shows a close up view of the vertical and horizontal wind speed profile in the test section of the fourth configuration. The effect of the addition of the guide vanes in

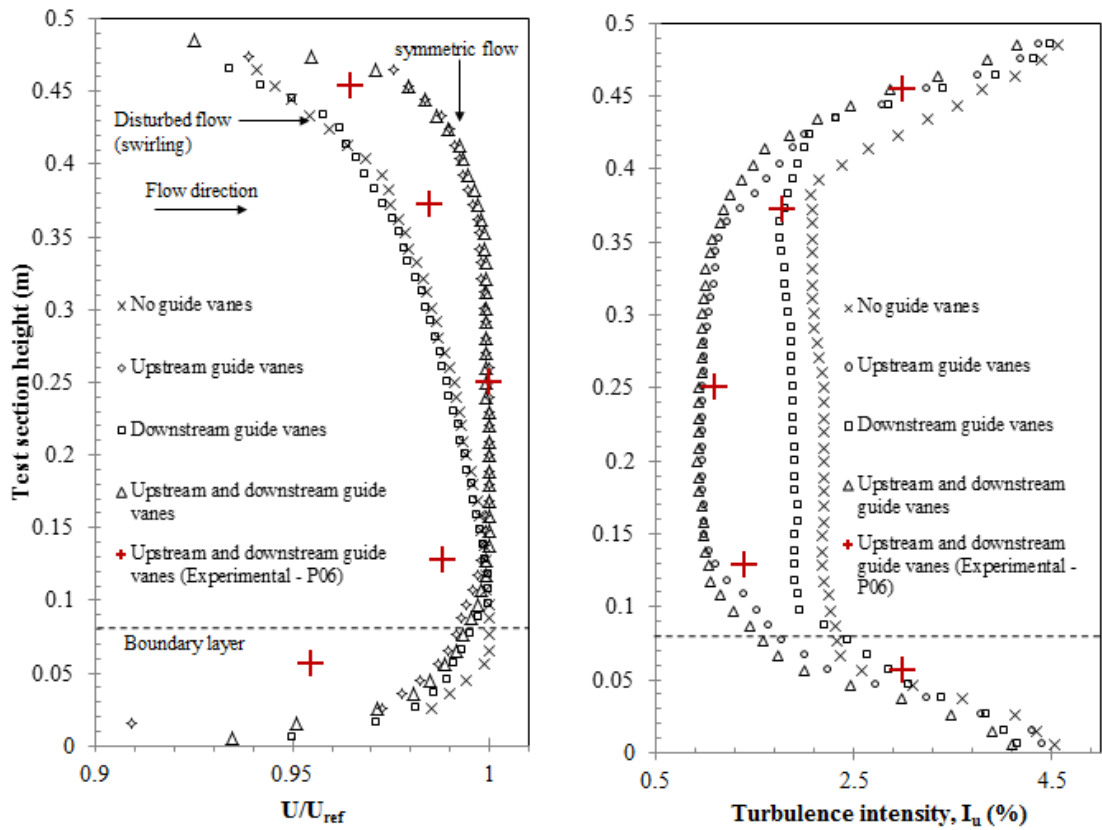
all corners was evident from the velocity contour; symmetric uniform flow was observed throughout the entire test section length.



**Figure 4.6** Contours of velocity magnitude in a (a) vertical plane and (b) horizontal plane at 0.250 m height of the test section for the wind tunnel with upstream and downstream guide vanes.

#### 4.2.3.1 Test section wind profile

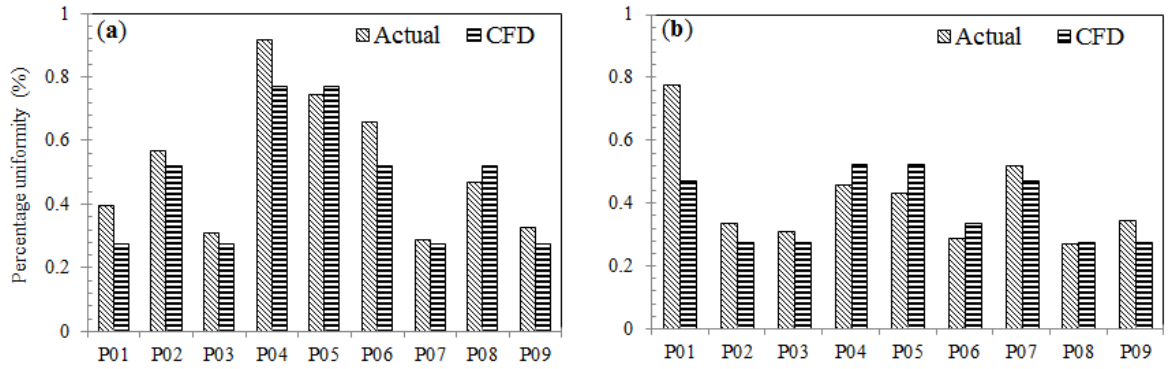
The results in Figure 4.7 shows the vertical wind speed profiles (Figure 4.14a) and turbulent intensity profiles (Figure 4.14b) at position P06 (0.25 m away from the inlet) of the test section for the different guide vane configurations. The wind speed values were made dimensionless by division by the reference velocity (maximum velocity across the vertical profile). Good correlation was observed between the measured and CFD velocity and turbulence intensity profiles.



**Figure 4.7** Comparison between the (a) dimensionless mean velocity and (b) turbulence intensity of the flow at the test section for the different wind tunnel configurations ( $X = 0.25$  m, P06). Highlighted (red) data points show measured wind tunnel values.

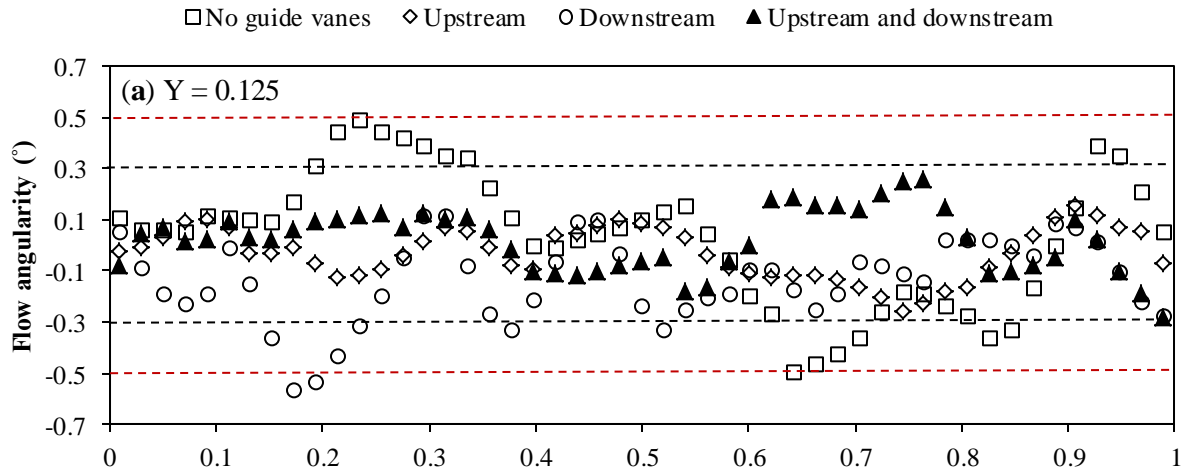
#### 4.2.3.2 Flow uniformity and angularity

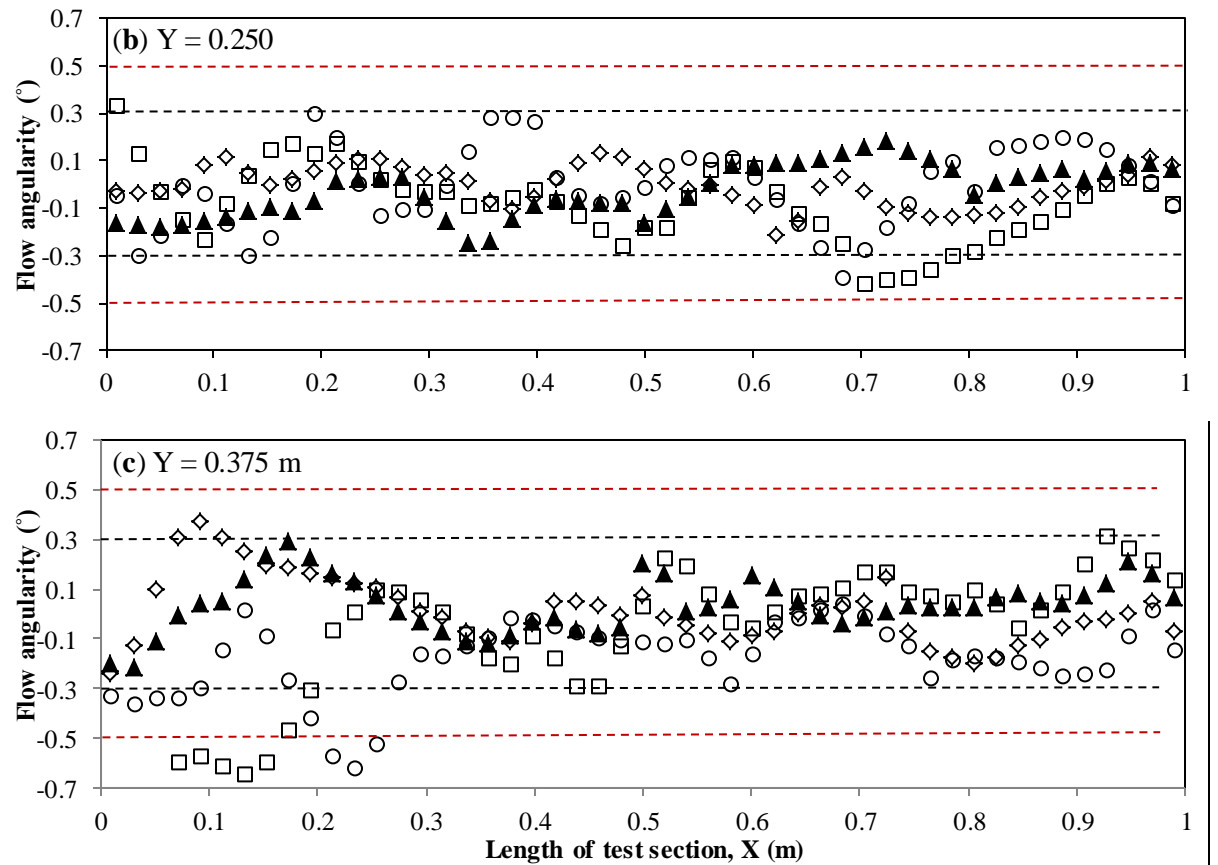
Figure 4.8 shows a comparison between the numerical and experimental results for the uniformity coefficient. While for the bottom plane ( $Y = 0.25$  m), the average error across the measurement points was 14% with point P01 getting the maximum error. While for the top plane ( $Y = 0.125$  m), the average error across the measurement points was 12%. Similarly, point P01 getting the maximum error. Average uniformity of 0.54% was obtained from the middle section points and 0.48% from the bottoms section points.



**Figure 4.8** Comparison of the CFD and experimental results (P01 – P09) for the percentage uniformity of flow at: (a)  $Y = 0.25$  m and (b)  $Y = 0.125$  m (Configuration 4)

Figure 4.9 shows the flow angularity variation across the test section height for different guide vane configurations. The flow angularity was measured at three different test section height; bottom, centre and top at test section mean wind speed of 15.65 m/s. The measurements revealed a slight increase in the angularity of the flow near the test section roof and floor. It can be observed that the flow angularity for the first (no guide vanes) and third configuration (downstream) went above  $0.5^\circ$  particularly near the entrance and exit of the test section, while the second configuration with the upstream guide vanes maintained the flow angularity below  $0.5^\circ$  and the combined upstream and downstream below  $0.3^\circ$ .

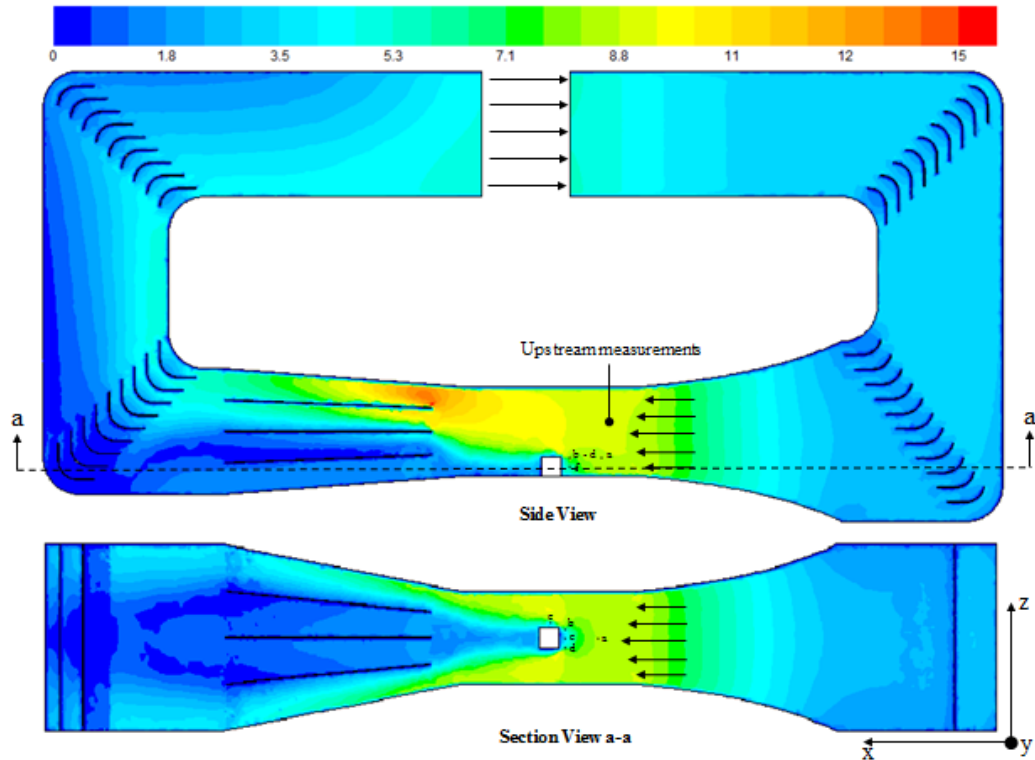




**Figure 4.9** Flow angularity variation across the test section for different guide vane configurations: (a)  $X = 0.125$  m, (b)  $Y = 0.250$  m and (c)  $Y = 0.375$  m. Red dotted line at  $\pm 0.5^\circ$ .

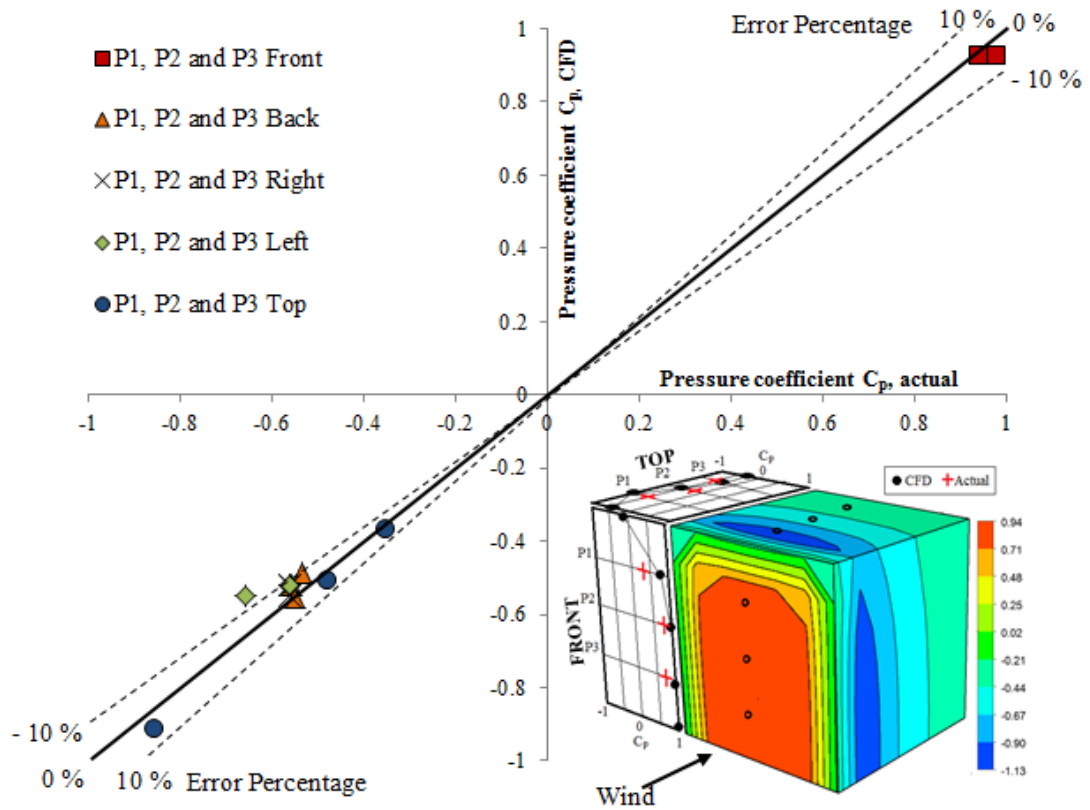
#### 4.2.3.3 Wind tunnel test section with block model

Figure 4.10 shows the velocity contour of a vertical and horizontal cross sectional plane in the wind tunnel with the block model. A symmetric wind profile was observed before the test section and non-uniform profile at the exit due to the blockage of the test block model. A uniform air flow enters the test section inlet with the flow splitting at the front side of the block shearing across the top and side surfaces and exiting to the diffuser section. Existence of flow separation and wake regions were seen at the leeward side of the block model.



**Figure 4.10** Contours of velocity magnitude inside the wind tunnel with block test model.

Figure 4.11 shows the measured and CFD values for the pressure coefficients at the front, back, left, right and top surfaces of the test block model. As expected the points located at the front surface experiences the maximum value, and with the moving air stream towards the top, right and left side, the pressure coefficient decreases, indicating the acceleration of the flow. The measured pressure coefficient along the right and left surface of the block were very close, indicating the flow symmetry for the zero incident angle wind. In point P1 – Top, the pressure coefficient drop sharply. This point was at the front edge of the top surface where flow separation occurs. While for the back side of the of the block model, a uniform pressure distribution was observed. This was because of the separation of the air stream from the sides; an almost uniform low pressure wake was formed around the back surface. CFD and experimental results showed good agreement, with the error below 10% except for point P1 - left which seem to be sensitive to the angle of attack. Measurements at the front surface of the block gave the highest accuracy with average error of only 2% between the points.



**Figure 4.11** Comparison between CFD and experimental values for surface pressure coefficients around the block model. Dotted lines represent 10 % error percentage.

### 4.3 Model scaling requirements and simulation of wind

#### 4.3.1 Consistent modelling of all lengths

The geometric scale of the model of a structure should be selected to maintain, as close as possible, equality of model and prototype ratios of overall building dimensions to the important meteorological lengths of the simulated wind. Depending on the structure studied, the length scale selection is based on an attempt to satisfy the Jensen number equality [Griffis *et al.*, 2009]:

$$\left(\frac{L_b}{z_0}\right)_{model} = \left(\frac{L_b}{z_0}\right)_{prototype} \quad \text{Equation 4.1}$$

where  $L_b$  is the characteristic dimension of the structure and  $z_0$  is the surface roughness. This was easily achieved, all the relevant dimensions of the prototype wind tower model and building were equally scaled down by the appropriate factor. The scale used in the work is 1:10 of the full-scale model.

### 4.3.2 Blockage consideration

It is important to minimise the effect of wind tunnel walls and excessive blockages of the test section when selecting the model. Models cause a blockage of the wind tunnel, as its size becomes significant comparative to the cross-section of the test section. The blockage speeds-up and distorts the flow around the model. Correcting the effect of the flow distortion is more difficult than correctly sizing the model. For a blockage ratio (ratio of the frontal area of the model structure relative to the cross-sectional area of the test section) of 5% and below, distortion effects are negligible [Cermak, 1981]. While for blockage ratios between 5 - 10%, distortion effects becomes significant and must be considered. Model blockage above 10% required validation through additional tests.

According to the dimensions of the 1:10 model and the wind tunnel cross-section, the wind tower scale model produced a maximum wind tunnel blockage of 4.8%, and no corrections were made to the measurements obtained with these configurations (Figure 4.12).

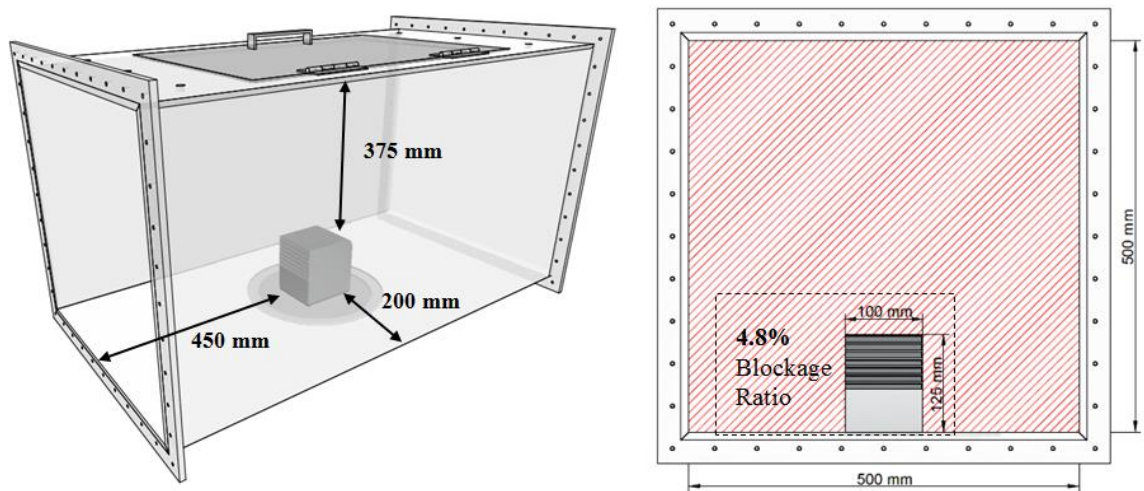


**Figure 4.12** Test section blockage ratio.

### 4.3.3 Selection of velocity scale

In aerodynamic studies, the air flow patterns around a structure or a building and thus wind loads on it are a function of the Reynolds number. Hence wind tunnel testing on scaled models should ideally be simulated at the same Reynolds number as would be experienced by the full scale model, thus satisfying Reynolds number similarity [Griffis *et al.*, 2009]. Strict scaling of wind and turbulence Reynolds number for the simulated flow is generally not possible for wind tunnel model testing of building and structures, even

in the largest, high speed and most expensive wind tunnels [Montazeri *et al.*, 2008]. For example, a 1:100 scale model of a structure exposed to external wind speed of 5 m/s should be tested at velocities about 100 times of the prevailing wind, 500 m/s. This is difficult to accomplish especially for subsonic wind tunnel systems.

However a recent study by [Irwin, *et al.*, 2013] showed that for sharp-edged structures or buildings, which constitute the majority, the air flow patterns are dictated by the flow separation off the sharp corners of the geometries and are independent of the Reynolds number. The flow separation points are fixed at these sharp corner location regardless of the Reynolds number, so that wind responses tends to be less sensitive to the Reynolds number. Therefore, for most buildings the necessary relaxation of Reynolds number similarity in wind tunnel test has little impact on the validity of results [Bahadori, 1981].

#### **4.4 Experimental scale model**

The creation of an accurate scaled wind tunnel prototype was essential for the experimental study. The wind tower geometry features a variety of unconventional and complex parts such as the external louvres, cross-dividers and slanting top hat. A model of this type made using conventional technology would have taken several months to construct and test. Therefore the wind tunnel models was constructed using rapid prototyping, a technique used to quickly manufacture a scale model of a part or assembly using three dimensional computer aided design (CAD) data. Furthermore, 3D prototyping makes it possible to easily embed equipment into the model such as pressure measurement devices and vents for smoke discharge.

Figure 4.13 shows the HP 3D rapid prototyping system used for building the wind tower scale models. The HP 3D printer uses the Fused Deposition Modelling (FDM) or additive manufacturing process. FDM builds the three dimensional parts by melting and advancing a fine ribbon of acrylonitrile butadiene styrene (ABS) plastic through a computer-controlled extrusion head.

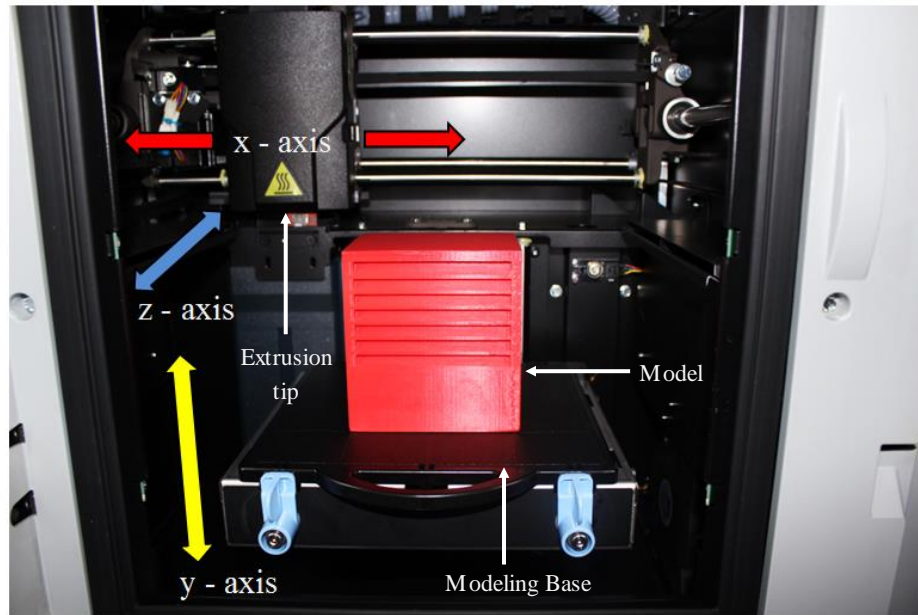


**Figure 4.13** 3D prototyping system,

The basic methodology for Fused Deposition Modelling (FDM) rapid prototyping techniques can be summarised as follows:

- From 3D CAD data, pre-processing software (HP Designjet 3D Software Solution) processes the STereoLithography (STL) file by creating sliced layers of the model, calculates support structures and creates tool paths that are optimised for the rapid prototyping machine (Figure 4.14).

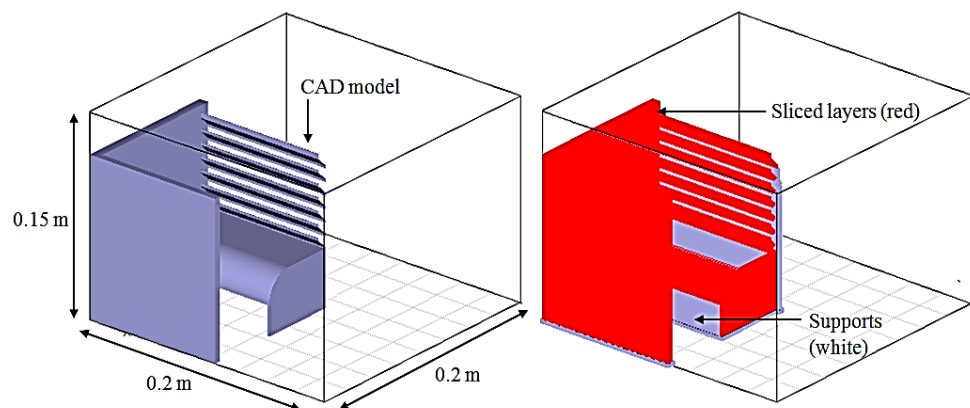


**Figure 4.14** 3D prototyping software automatically creates tool paths for the RP machine

- The rapid prototyping machine forms the item by depositing the material (ABS plastic) in layers through a computer controlled extrusion head, starting with the

bottom layer, onto a platform. Dual extrusion heads precisely lay down thermo-plastic model and support material to create each layer (Figure 4.15).

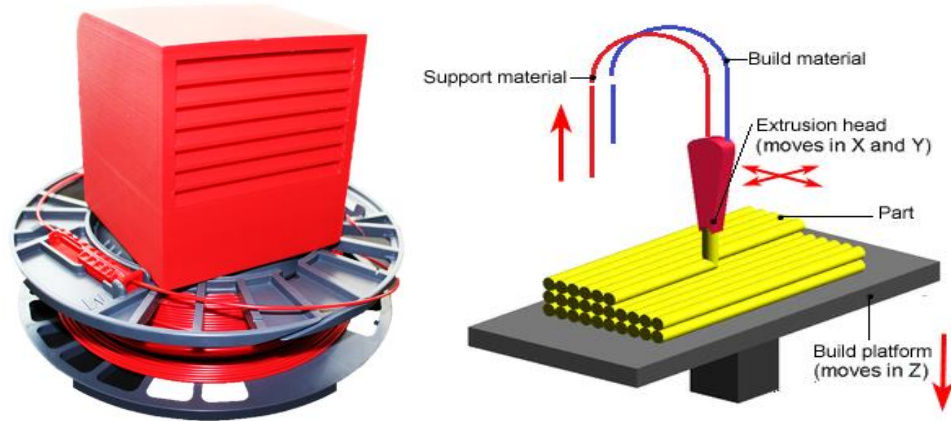
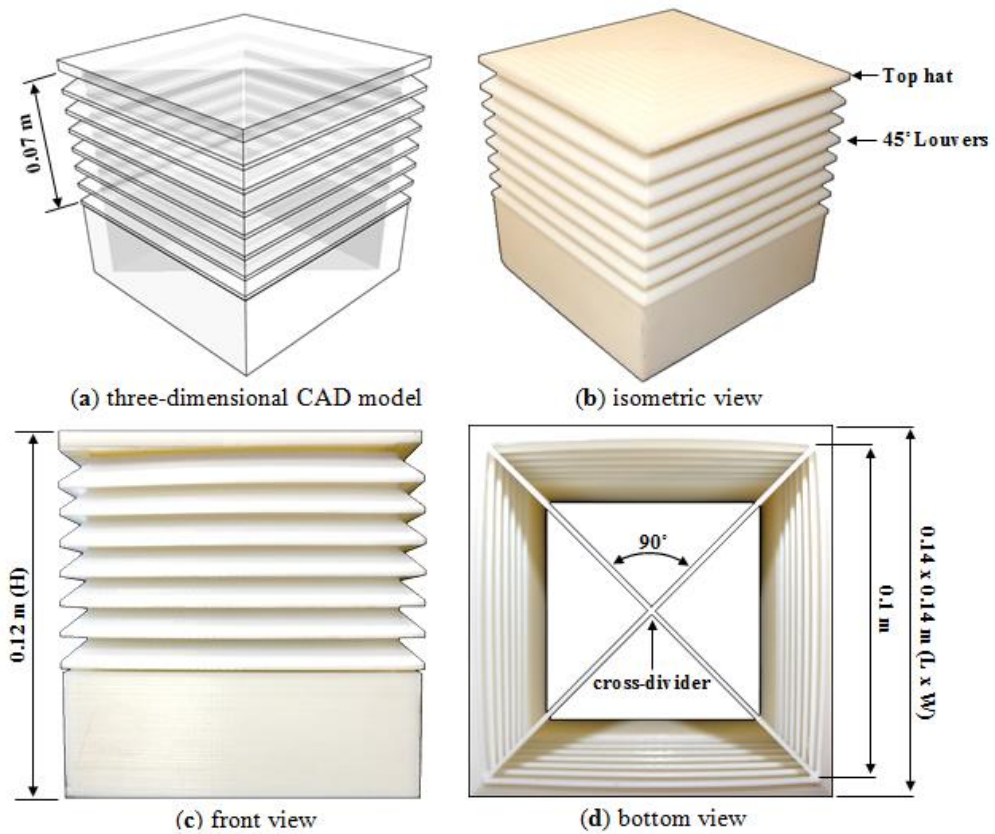


**Figure 4.15** (a) ABS material (b) rapid prototyping machine axis

- Temporary support structures are removed. Soluble support material automatically dissolves in a water-based solution.

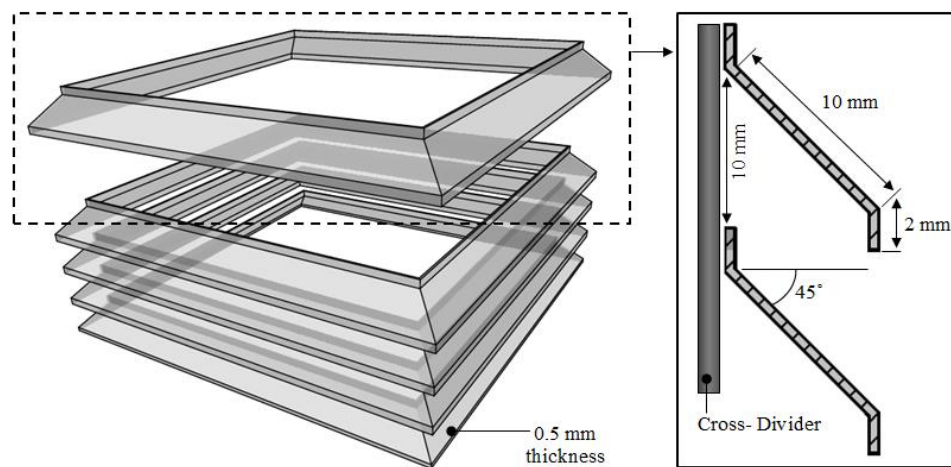
#### 4.4.1 Benchmark wind tower model

Figure 4.16 shows the 1:10 four-sided wind tower scale model design with internal dimensions of 0.1 x 0.1 x 0.1 m. The 3D CAD model of the benchmark wind tower (Figure 4.16a) was divided into two sections; wind tower base and top hat. This will allow the square wind tower prototype to be used interchangeably between the benchmark and the heat transfer device wind tower model. This will reduce the build time and the material cost. Different views of the resulting prototype assembly model are shown in Figure 4.16 b-d.



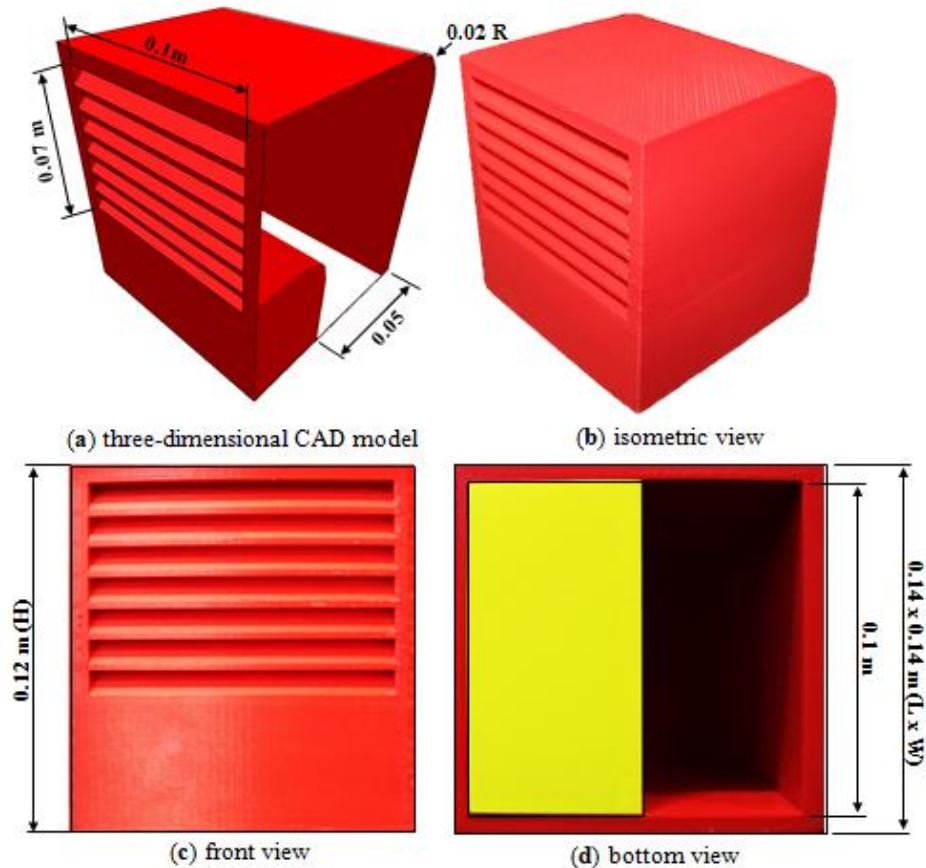
**Figure 4.16** A 1:10 three-dimensional CAD model of the four-sided wind tower design (a) and the resulting 3D prototype model (b, c and d) built using the 3D printer.

Figure 4.17 displays the wind tower louvre CAD model. In order to accurately replicate the CFD model, the louvres and cross-divider were printed as a single part. This will ensure that the positioning of the louvres is matching the numerical model.



**Figure 4.17** Wind tower louvre design and configuration. Dimensions in millimetres.

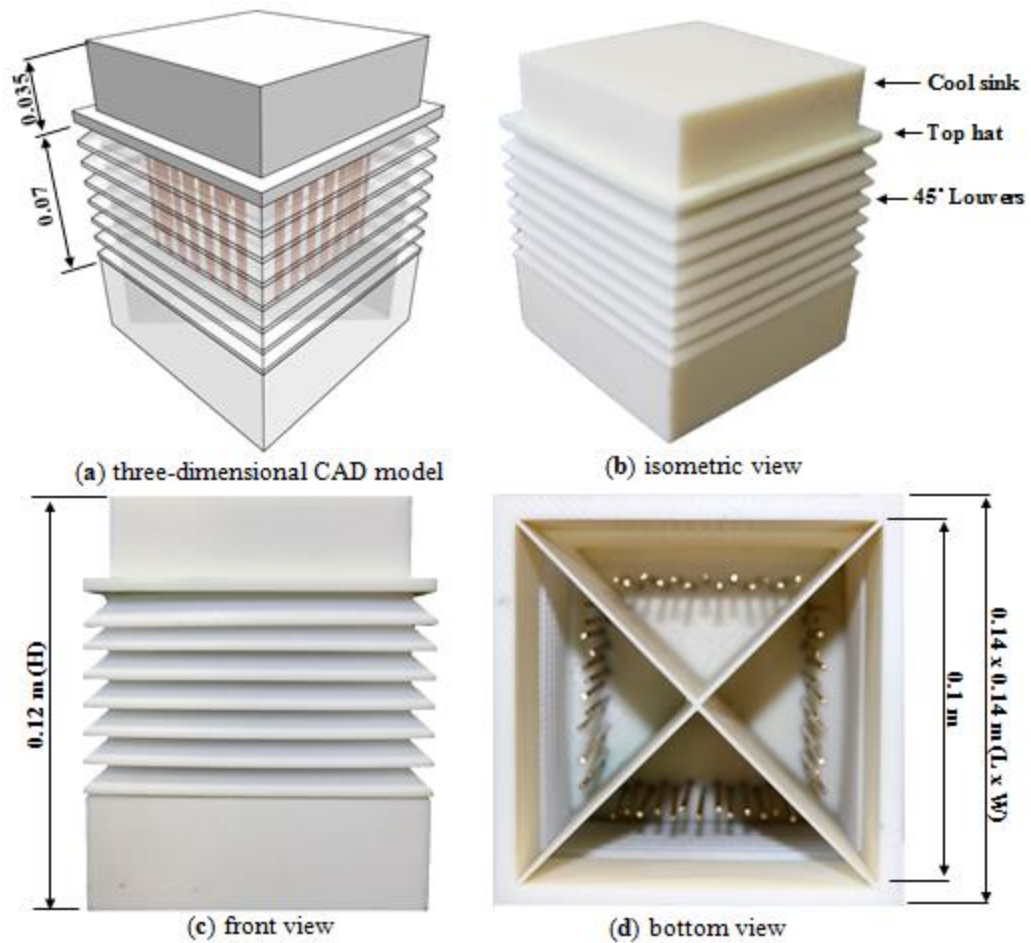
Figure 4.18a illustrates the one-sided wind tower with internal dimensions of 0.1 x 0.1 x 0.1. Similarly, the one-sided wind tower prototype was designed so it could be used interchangeably between the benchmark and heat transfer device configurations. The wind tower and the bottom compartment were separated into two parts which could then be assembled together to construct the final model (Figure 4.18 c-d).



**Figure 4.18** A 1:10 three-dimensional CAD model of the one-sided wind tower design (a) and the resulting 3D prototype model (b, c and d) built using the 3D printer.

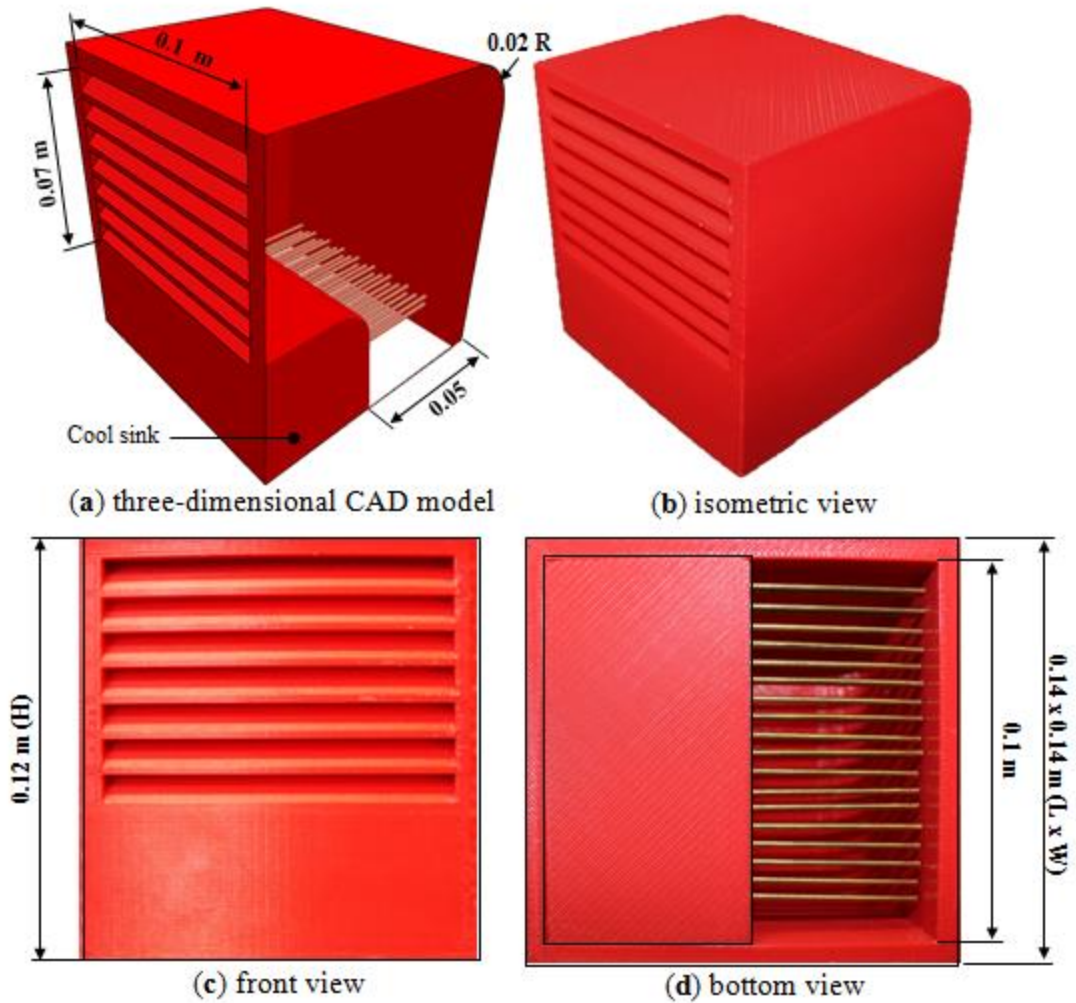
#### 4.4.2 Wind tower with heat transfer devices

Figure 4.19 displays the prototype model of the four-sided wind tower integrated with the heat transfer devices. Cylindrical rods with an outer diameter of 0.002 m were used to model the heat transfer devices. The cool sink was printed as a solid block with the heat transfer device hole patterns so that the cylindrical rods can be easily slotted in. This will ensure that the distance between the cylindrical heat transfer devices are identical to the numerical model. The cool sink mounts on the top of the four-sided wind tower benchmark model in (Section 4.4.1) as shown in Figure 4.19 b-d.



**Figure 4.19** A 1:10 three-dimensional CAD model of the four-sided wind tower design incorporating vertical HTD (a) and the resulting 3D prototype model (b, c and d) built using the 3D printer.

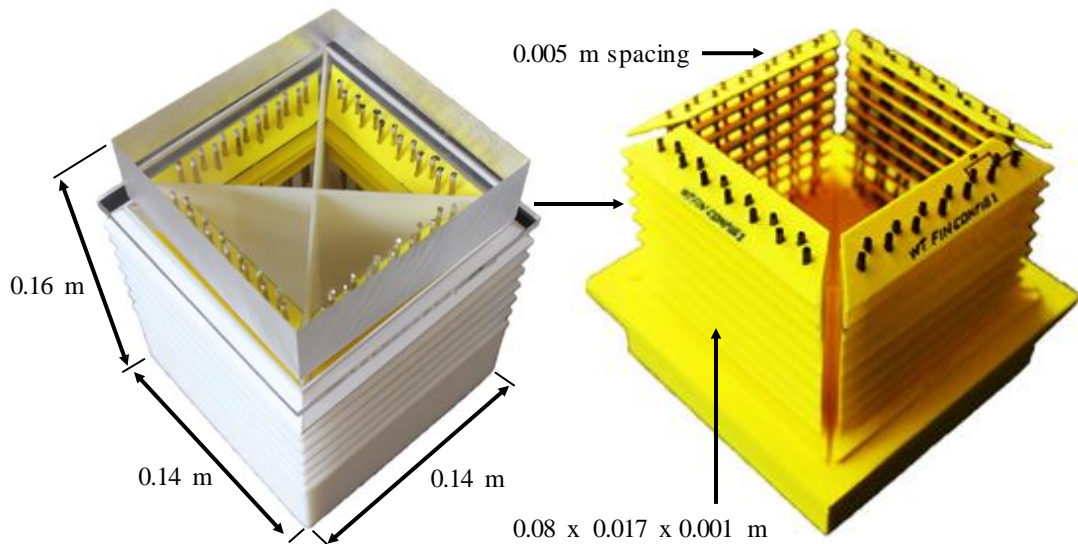
Figure 4.20 displays the prototype model of the one-sided wind tower integrated with the heat transfer devices. Due to the limitations of the rapid prototyping machine, cylindrical rods with an outer diameter of 0.002 m were used to model the heat transfer devices. Similarly, the bottom section of the wind tower was printed as a separate model with the heat transfer device hole patterns so that the cylindrical rods can be easily slotted in. This will ensure that the distance between the cylindrical heat transfer devices are matching simulation model.



**Figure 4.20** A 1:10 three-dimensional CAD model of the one-sided wind tower design incorporating horizontal HTD (a) and the resulting 3D prototype model (b, c and d) built using the 3D printer. Dimensions in metres.

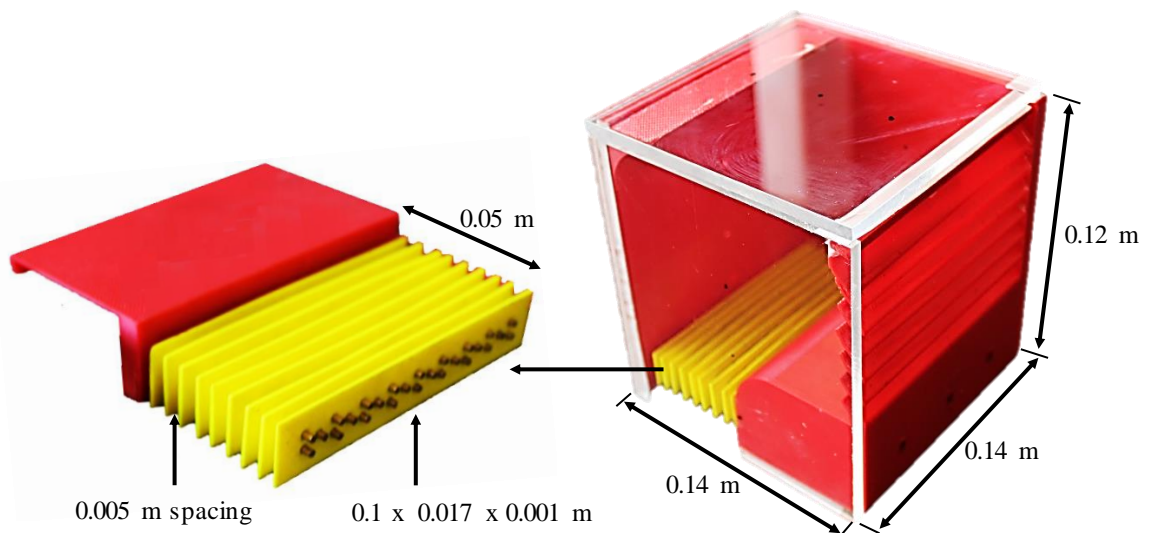
#### 4.4.3 Wind tower with finned heat transfer devices

Figure 4.21 displays the prototype model of the wind towers integrated with the heat transfer devices and extended surfaces. A total of 36 inclined extended surface plates were assembled to the cool sink assembly in Figure 4.19.



**Figure 4.21** 1:10 prototype model of the four-sided wind tower design incorporating vertical HTD with extended surfaces.

Figure 4.22 shows the wind tower integrated with horizontal HTD arrangement and extended surfaces. A total of 9 extended surface plates were modelled and assembled to the cool sink assembly in Figure 4.20.

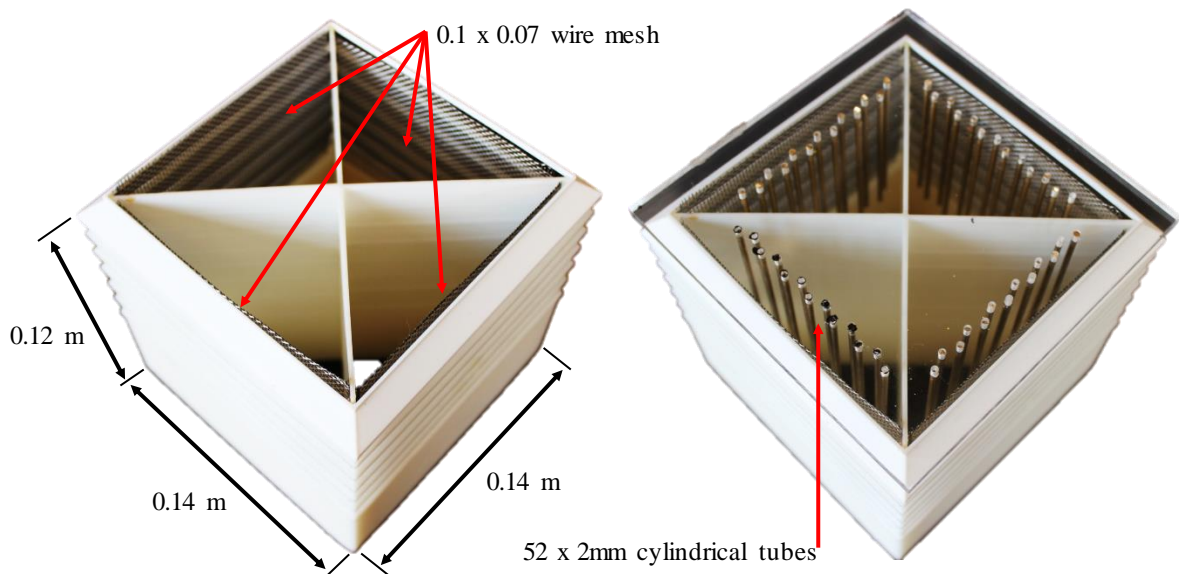


**Figure 4.22** 1:10 prototype model of the one-sided wind tower design incorporating horizontal HTD with extended surfaces.

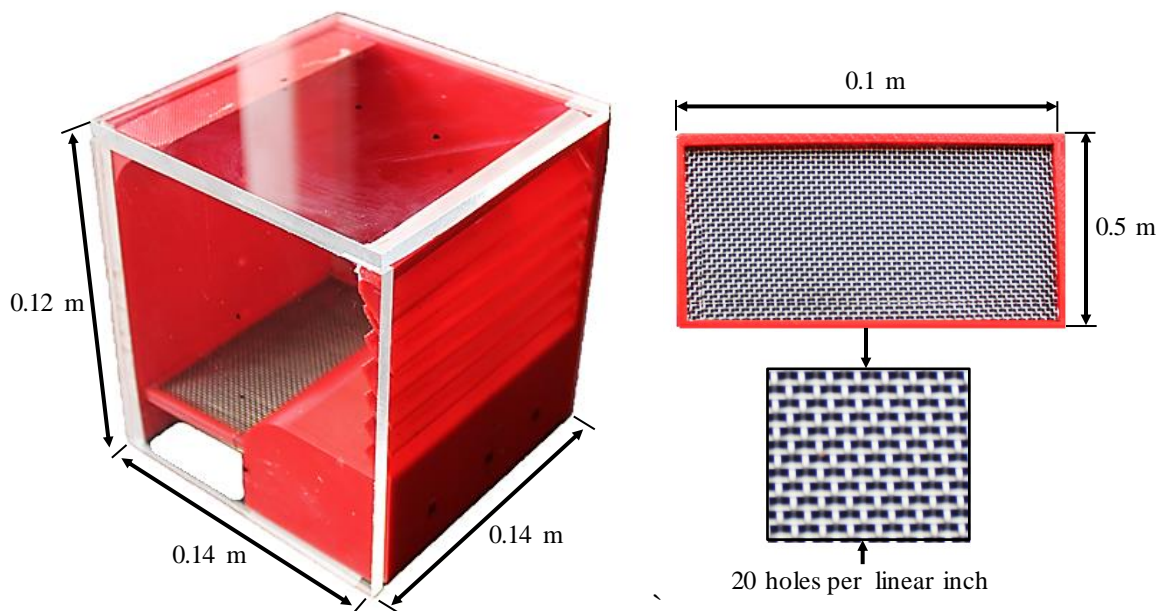
#### 4.4.4 Wind tower with heat transfer devices and porous mesh

Figure 4.23 and 4.34 displays the prototype model of the wind towers integrated with the heat transfer devices and porous mesh. The porous structure was made of wire mesh

with porosity of approximately 0.5 (20 holes per linear inch, the wires are 0.35 mm in diameter and the apertures are 0.92 mm).



**Figure 4.23** 1:10 prototype model of the four-sided wind tower design incorporating horizontal HTD with porous mesh.



**Figure 4.24** 1:10 prototype model of the one-sided wind tower design incorporating horizontal HTD with porous mesh.

#### 4.4.5 Test room model

The wind tower model was connected to a 0.5 x 0.5 x 0.3 m test room (representing the ventilated space), which was mounted underneath the wind tunnel test section. The test room model was made of acrylic perspex sheet to facilitate flow visualisation testing as

well as to be able to clearly see the measurement points markers. A single 0.1 x 0.1 m outlet window located at the leeward side of the room was used for testing the one-sided wind tower. The window was sealed off when testing the four-sided wind towers. The test room top plate was constructed that it could be rotated in the test section in order to test different approaching wind directions (0 to 180°). In order to measure the velocity inside the room at the points using the hot-wire anemometer, a total of 14 holes were drilled into the front and side wall of the room as shown in Figure 4.25.

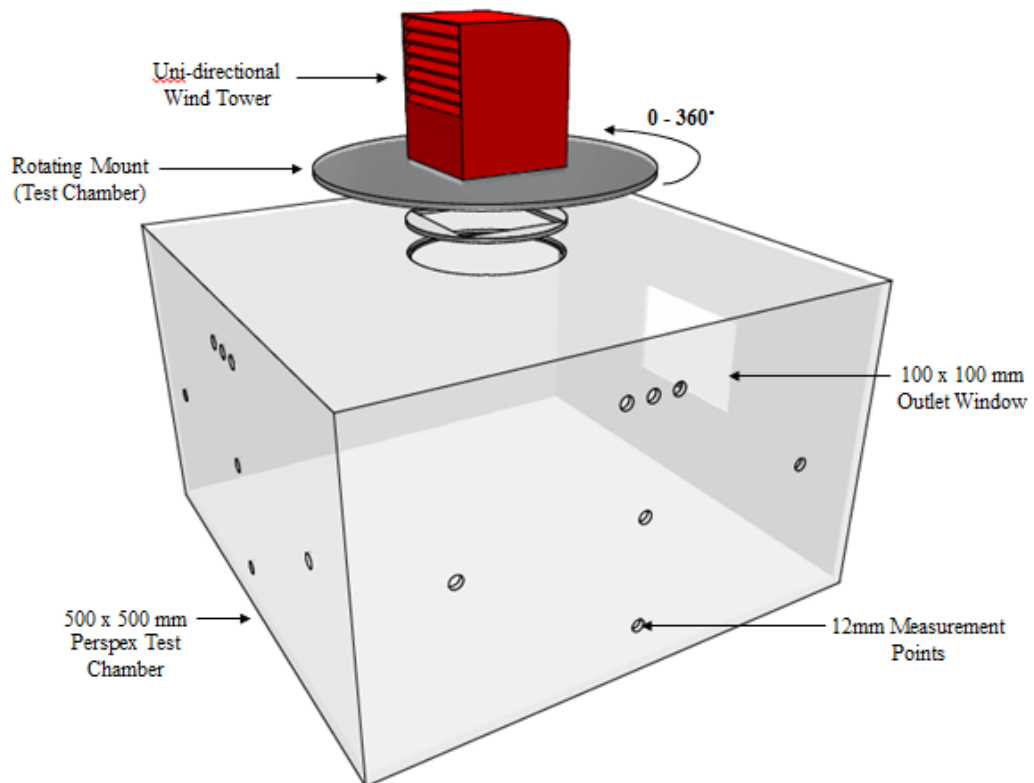


**Figure 4.25** 1:10 scale model of the test chamber mounted below the rotating wind tower system.

## 4.5 Experimental set-up and measurement procedures

### 4.5.1 Indoor airflow distribution

In this study the airflow inside the test room model was measured using a hot-wire anemometer. Nine data points in an equally spaced 3 by 3 grid were created within the test room at a height of 1.5 m which allow for measurements to be made for velocity within the test room (Figure 4.26). Additionally, three data points were positioned at the bottom of the room (central), below the supply and exhaust channels of the wind towers. The values of the velocity were obtained from the three components of the vector (X, Y,

and Z). The tests were carried out between 3 m/s and 5 m/s. These velocities were confirmed during the setup and configuration of the wind tunnel during commissioning. The flow in the wind tunnel was allowed to normalise and steady state flow occur before measurements were taken. The sample for each point was taken and averaged over a two minute period with the results and start/finish times recorded.

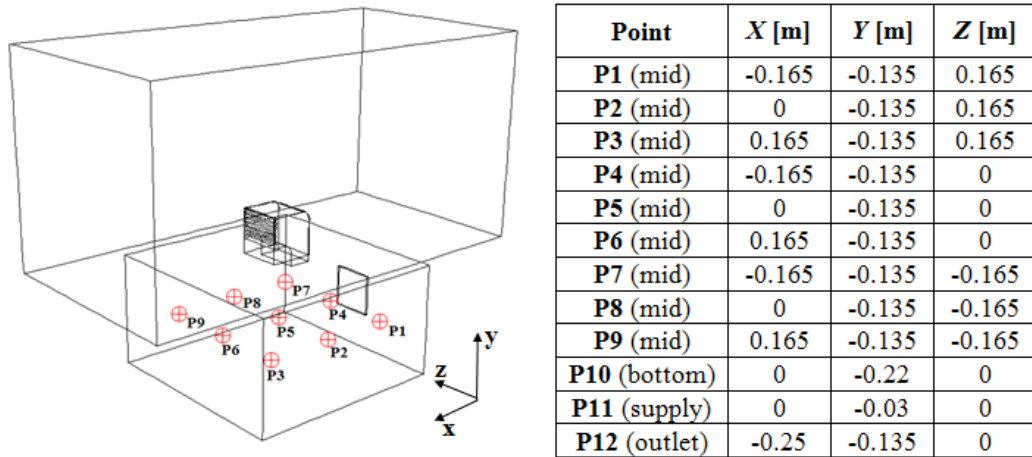


Figure 4.26 Measurement points inside the test section.

#### 4.5.2 Volumetric flow supply rate

In this study the induced airflow into the test room was measured using the hot wire anemometer position below the channels of the wind tower device. The cross-sectional area of the wind tower channel was divided into several portions and the airflow rate through it was calculated as follows:

$$Q = \sum_{i=1}^n A_i \times U_i \quad \text{Equation 4.2}$$

Where Q is the air flow rate through the wind tower channel,  $A_i$  is the area of point i and  $U_i$  is the velocity of point i. Figure 4.27 shows the location of the point inside the channel quadrants at a height of 270 mm from the test room floor. The tests were carried out in the uniform flow wind tunnel at various wind angles (0 - 90°). Similarly, sample for each point was taken and averaged over a two minute period with the results and start/finish times recorded.

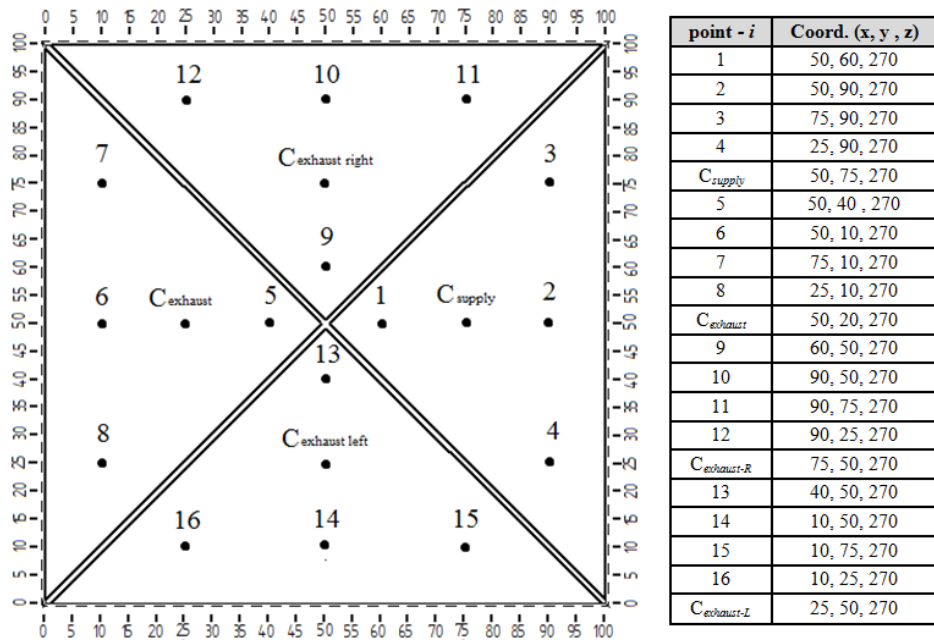


**Figure 4.27** Section view of the four sided wind tower supply and exhausts channels showing the location of the measurement points (dimensions in mm).

Figure 4.28 shows the location of the point inside the channel of the one-sided wind tower at a height of 270 mm from the test room floor.

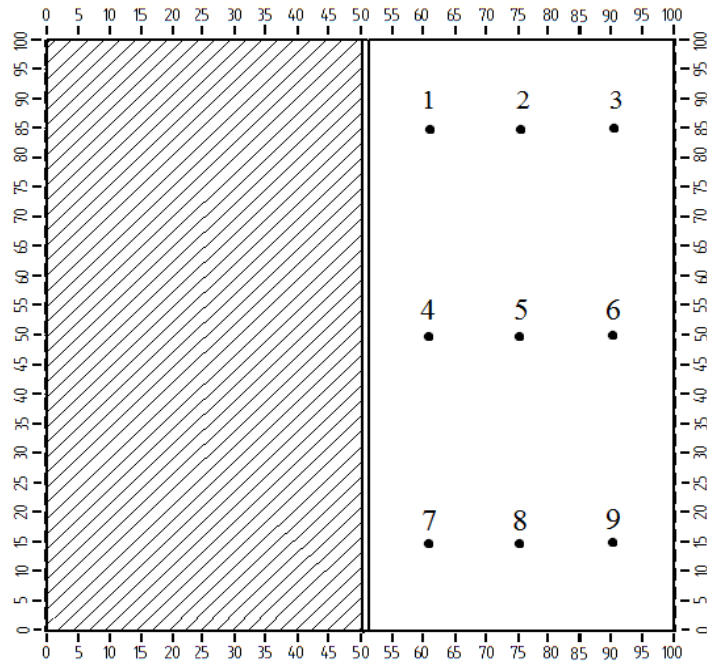


**Figure 4.28** Section view of the one sided wind tower supply and exhausts channels showing the location of the measurement points (dimensions in mm).

### 4.5.3 External airflow measurement

In this study the velocity of the airflow around the wind tower model were measured using the hot-wire anemometer. The purpose of this test was to evaluate the accuracy of simulating or achieving the flow characteristics around the wind tower model. According to the dimension of the model and wind tunnel cross-section, the model produces a maximum blockage of 5%, and no corrections were made to the pressure measurements obtained with this configuration [Xu, 2013]. Figure 4.29 shows the measurement locations around the model. The values of the velocity were obtained from the three components of the vector (X, Y, and Z).

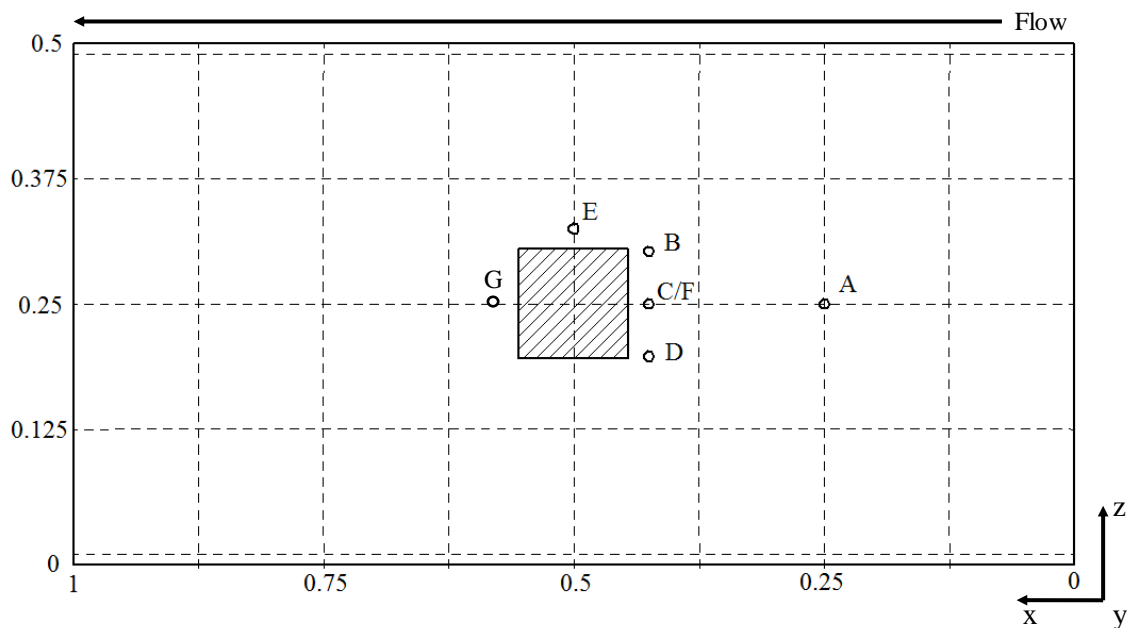


**Figure 4.29** Top view of the test section showing the hot-wire anemometer measurement positions and coordinates with the wind tower test model. Dimensions in metres.

### 4.5.4 Pressure coefficients

A geometrical model of the benchmark one and four-sided wind tower model were employed in the measurements of the surface pressures, see Figure 4.30. The pressure measurements were referred to the upstream dynamic pressure using the reference velocity in the test section in the case of a uniform wind flow. The air pressure coefficient  $C_p$  is calculated using the following equation [35]:

$$C_p = \frac{p - p_s}{\frac{1}{2}\rho U_{ref}^2} \quad \text{Equation 4.3}$$

Where  $p$  is the surface pressure obtained from the pressure tap measurement,  $p_s$  is the static pressure at the upstream and  $\frac{1}{2}\rho U_{ref}^2$  is the dynamic pressure of the uniform wind. The model was fitted with 15 pressure taps located inside the model (See Figure 4.36). The mean velocity and turbulence intensity profiles of the wind flow were measured using the hot-wire anemometer. The reference velocity, static and dynamic pressure were monitored using the pitot and static tubes mounted at the roof height of the wind tower model.

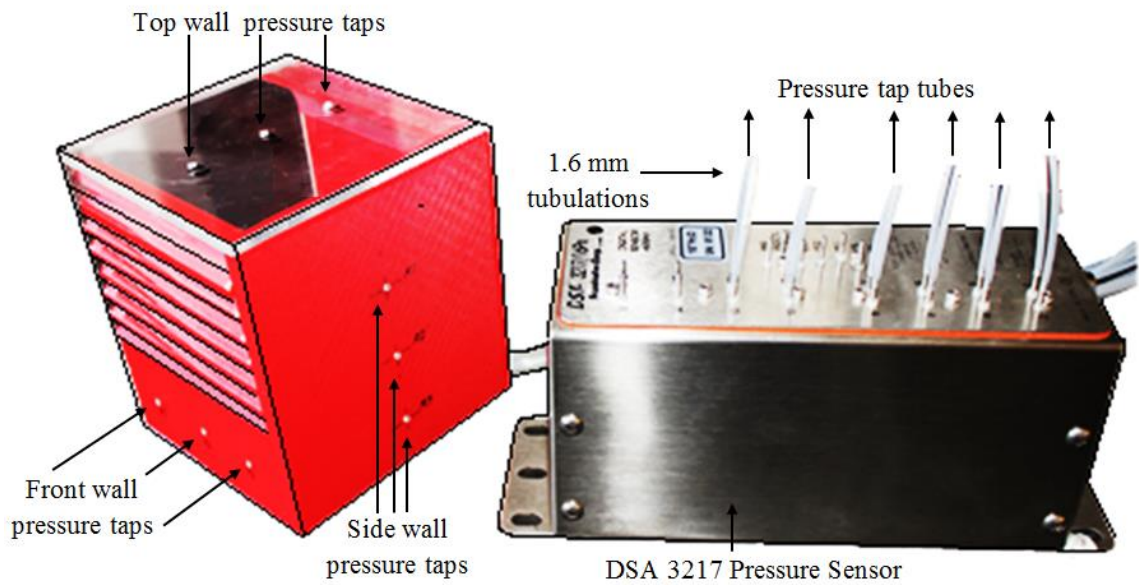


**Figure 4.31** Surface pressure measurement setup.

Figure 4.31 and Figure 4.32 shows the location and dimensions of the pressure tap holes around the wind tower models.

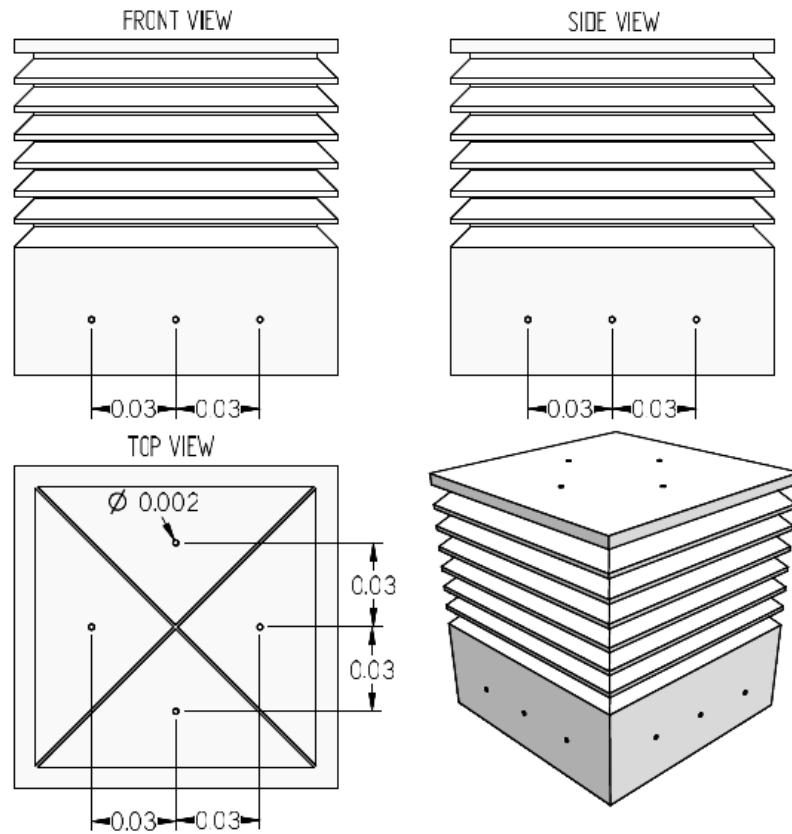


**Figure 4.31** Pressure tap locations and dimensions (four-sided wind tower).

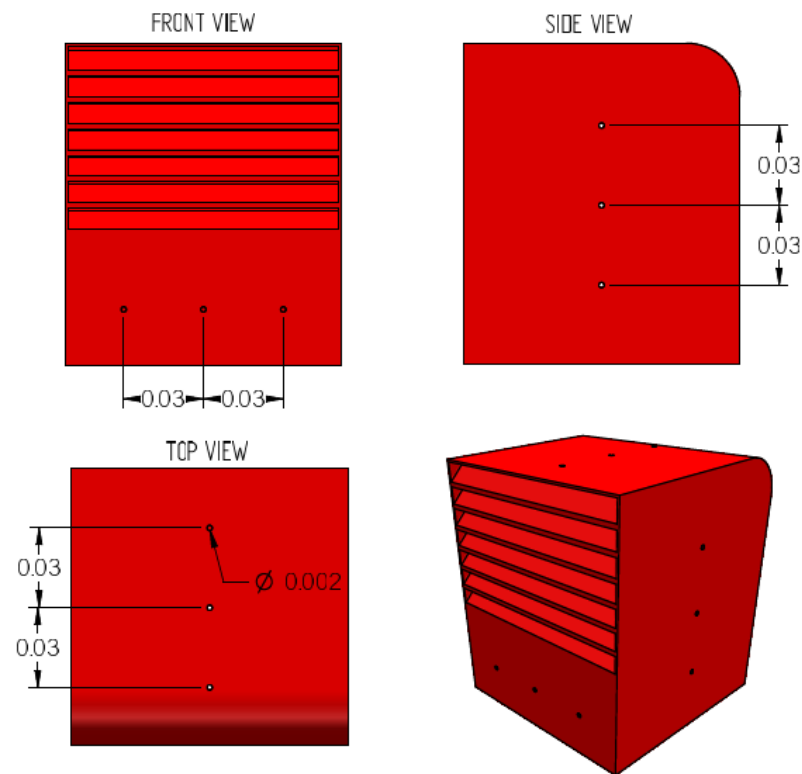


**Figure 4.32** Pressure tap locations and dimensions (one-sided wind tower).

Figure 4.33 displays the test setup inside the test section. The surface pressure was transmitted to a Scanivalve digital pressure transducer, a sixteen channel DSA3217 digital sensor array, through the 0.0016 m outside diameter tubulations. Each channel has its own temperature compensated piezoresistive pressure sensor. The unit contains a 16 bit A/D converter and it communicates data to DSALink3 via Ethernet connection. The data were acquired at a sampling rate of 1000 samples/sec. For each pressure tap, 5 records of the pressure data, each comprising of 1,000 data points, were acquired.

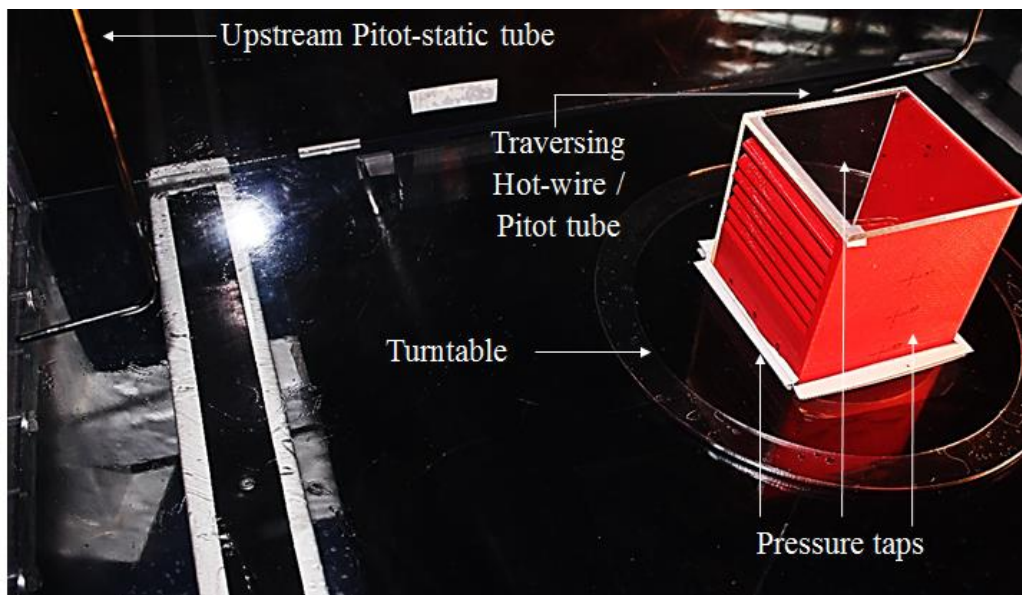


**Figure 4.33** Test setup: block model inside the test section.

#### 4.5.5 Smoke visualisation

In order to recognise the flow pattern in and around the wind catcher model, smoke visualisation tests were also carried out. The tests were carried out in the uniform flow wind tunnel for three different wind velocities of 3, 4 and 5 m/s at various wind angles ( $0 - 180^\circ$ ). Figure 4.34 shows the smoke visualisation testing setup in the test section.

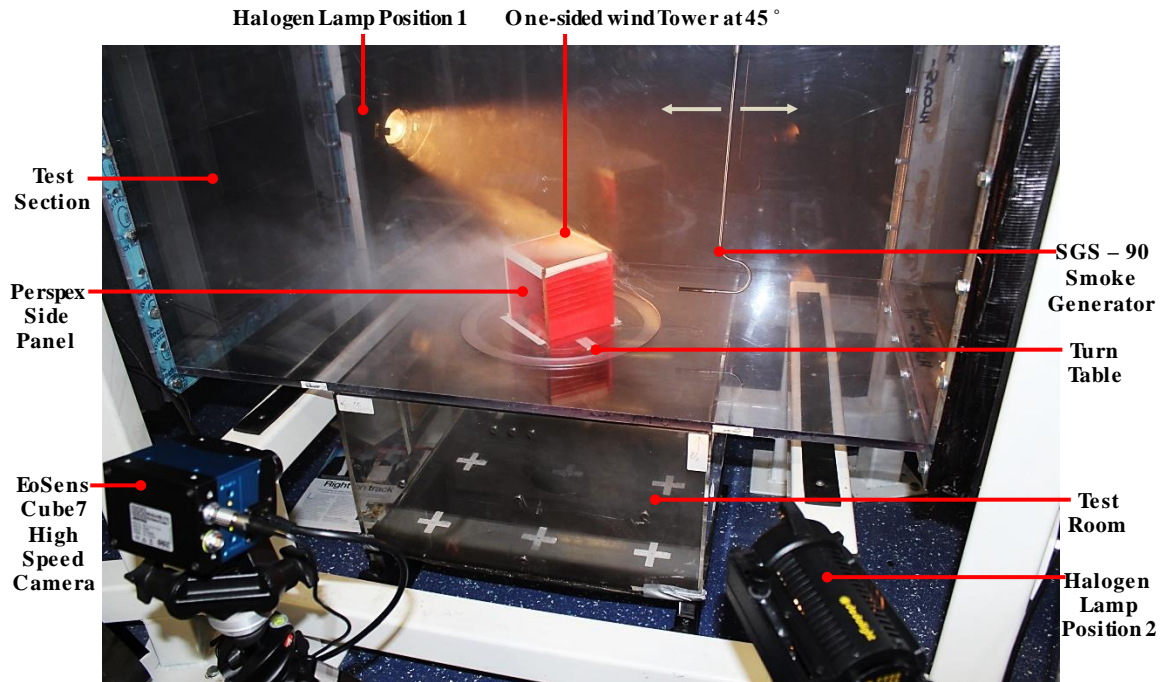


Figure 4.34 Wind tunnel smoke visualisation set-up.

The roof and one side of a one-sided wind catcher model and top hat of the four-sided wind tower were built of acrylic perspex (Figure 4.35). The model was exposed to a free stream air velocity of 3 m/s to obtain smoke of a sufficiently high concentration. These flow visualisation tests helped to identify the supply and extract segments during all tests.

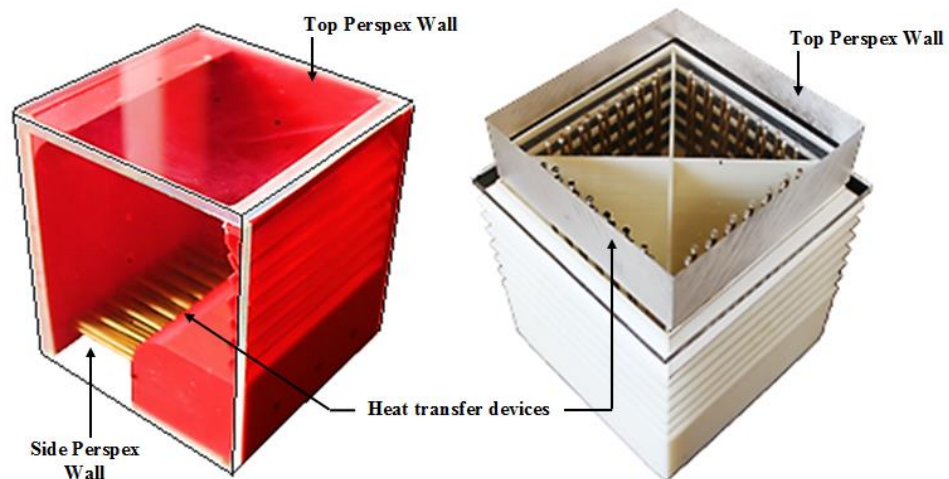


Figure 4.35 Wind tower models flow visualisation setup.

## 4.6 Experimental test equipment

The purpose of the experimental testing was to investigate the aerodynamic performance of the benchmark and heat transfer device integrated wind towers. To determine the velocity, pressure coefficient and air flow path in and around the wind tower model, the following test equipment were used:

- Testo 425 hot-wire anemometer
- Dwyer telescoping Pitot-static tube and DPM ST650 micro manometer
- DSA 3217 Scanivalve Digital Sensor Array
- DSALink3 data acquisition system
- AFA130 Smoke generator
- EoSens Cube7 High speed camera

Figure 4.36 shows a schematic of the full layout of the instruments and data acquisition used.

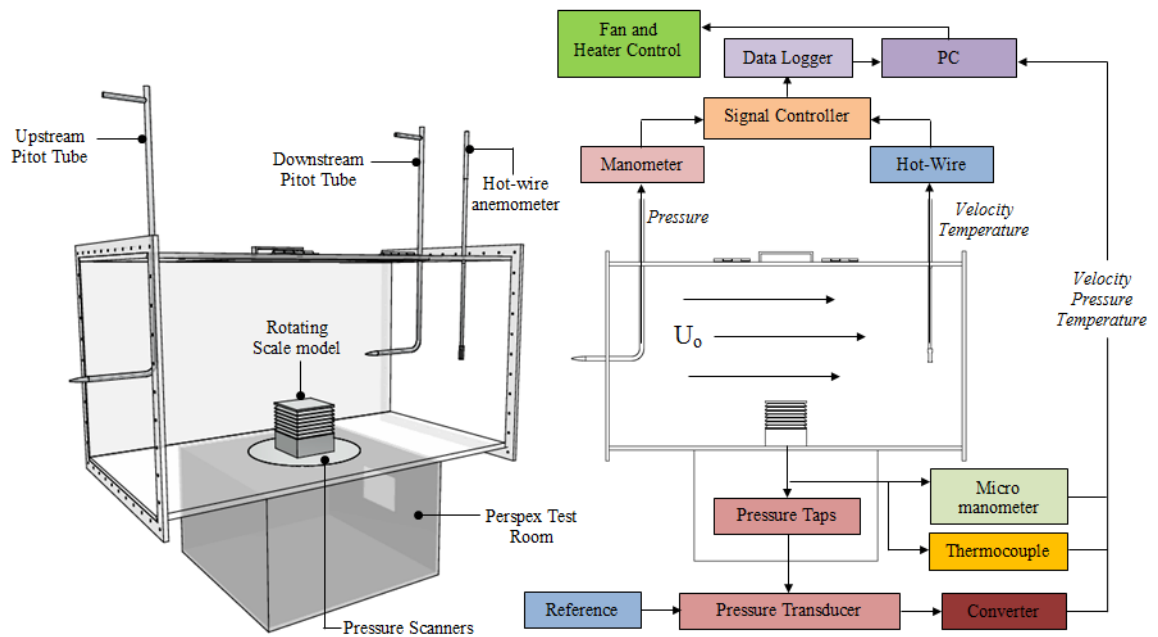


**Figure 4.36** Schematic of the test section with the instruments and data acquisition.

### 4.6.1 Hot-wire anemometer and Pitot - static tube

Hot-wire anemometers have been used extensively in wind tunnel experiments over several decades. They are typically accurate and sensitive in terrestrial conditions, they can also be multi-dimensional and have reasonably fast response times. The

measurement technique relies on electrically heating a thin wire or foil which is then cooled by the flow of air. The cooling rate is thus related to the wind speed. Challenges to this technique are conductive losses and temperature dependences in addition to the sensitivity to atmospheric properties.

Furthermore, hot-wire anemometers are sensitive to very small internal velocities, which were present during this investigation. Thermal velocity probes have a very small intrinsic error. This means that thermal probes are mainly suitable for the measurement of low air velocities, as the uncertainty of measurement increases linearly as the air velocity rises.

The hot-wire anemometer used for measuring the velocity in the test chamber was the Testo 425 (Figure 4.37). It is a compact anemometer with a fixed thermal flow velocity probe. The probe head has a diameter of 0.0075 m. With the telescope which can extend up to 0.820 m. The Testo 425 air velocity metre instrument covers the air velocity range from 0 to 20 m/s and the temperature range from  $-20$  to  $70^{\circ}\text{C}$ . The compact 425 uses a heated wire NTC sensor on a hand held telescopic probe to measure velocity and temperature at different points in the micro-climate. The device can also perform timed multi-point mean calculation of the mean volume flow, flow speed and temperature reading in the micro and macro-climate.



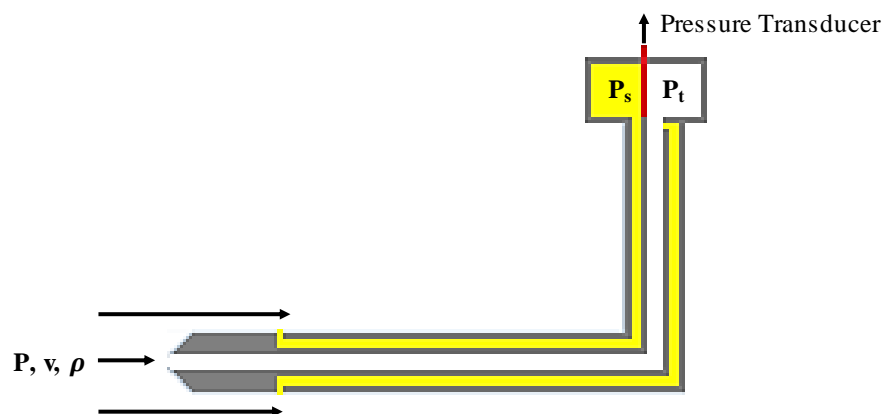
**Figure 4.37** Testo 425 hot-wire anemometer.

Table 4.2 summarise the technical specifications of the Testo 425 hot-wire anemometer.

**Table 4.2** Technical specifications of Testo 425 hot-wire anemometer.

Probe type	Thermal	NTC
Velocity	Measuring Range	0 to 20 m/s
	Accuracy	0.03 m/s +5% rdg.
	Resolution	0.01 m/s
Temperature	Measuring Range	- 20 to 70 °C
	Accuracy	± 0.9 °C
	Resolution	0.1 °C

The most common device for determining the total pressure or total head and the static pressure of a fluid in motion is the pitot-static tube, an instrument that yield both the total head and the static pressure. As seen in Figure 4.38, the outside holes that are perpendicular to the direction of the flow are pressurised by the local random component velocity. The pressure in these tubes is the static pressure  $P_s$ . While the centre opening is pointed in the direction of the flow and is pressurised by both the random and the ordered air velocity. The pressure in this tube is the total pressure  $P_t$ . The difference between these two pressures is the dynamic pressure. Connecting a differential pressure transducer across the two ports will directly measure the dynamic pressure.



**Figure 4.38** Schematic of the Pitot-static tube.

The Pitot - static tube used for measuring the static pressure and velocity in the test section was the 166T telescoping Pitot-static tube. The device can be adjusted for any

insertion length from 0.29 to 0.91 m allowing the measurement at different points. Hemispherical tip has 1.0 flow coefficient and 3.2 mm diameter (Figure 4.39).

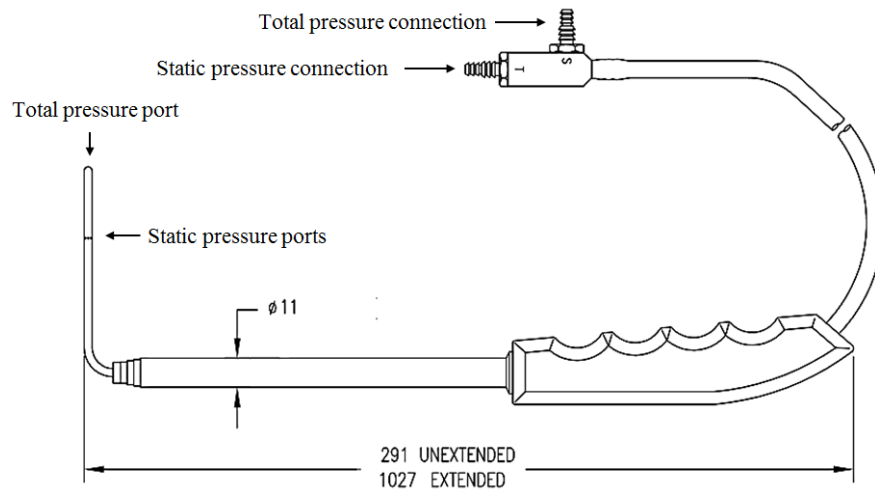


**Figure 4.39** 166T Telescoping Pitot-static tube.

The 166T Telescoping Pitot-static tube was connected to the DPM ST650 micro manometer (Figure 4.40). It uses a piezoelectric sensors to detect extremely small differences in pressure and responds with electrical signal that is proportionate to the pressure changes which is used to calculate the velocity and pressure values. The device can store up to 4000 readings that can be downloaded via the DPMUSB software which can also be used for continuous monitoring of the flow velocity and pressure in the test section.

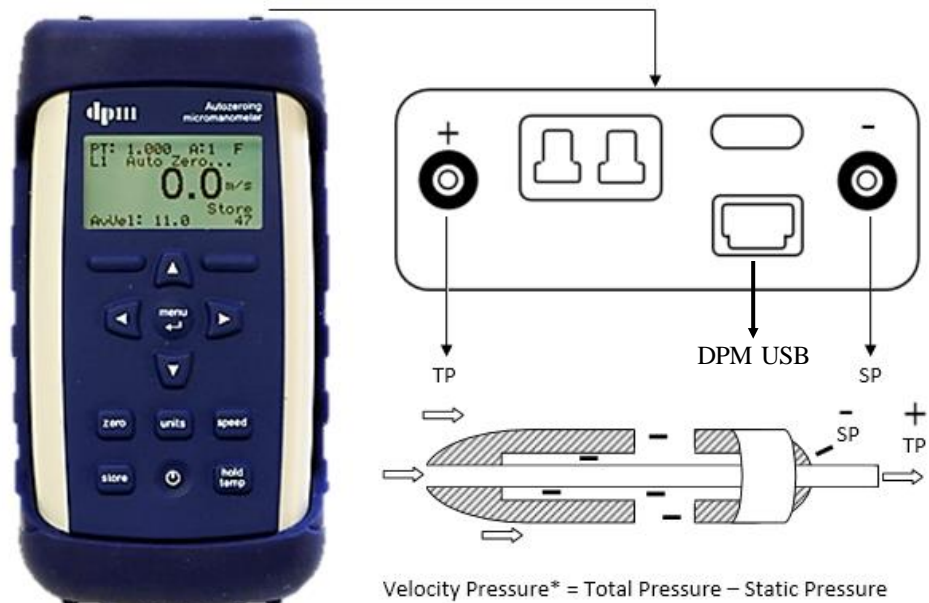


**Figure 4.40** DPM ST650 Micromanometer pressure connections.

Table 4.3 summarises the technical specifications of the DPM ST650 Micro manometer.

**Table 4.3** Technical specifications of DPM ST650 Micro manometer.

Probe type	Ellipsoidal	Thermal
Pressure	Measuring Range	$\pm 0.4$ to 1000 Pa
	Accuracy	$\pm 1\%$ of rdg
Velocity	Measuring Range	0.7 to 30 m/s
	Accuracy	$\pm 0.05$ m/s
Temperature	Measuring Range	$\pm 0$ to 500 °C
	Accuracy	$\pm 2$ °C

The uncertainties associated with the pressure readings (166T ellipsoidal Pitot-static tubes and micro manometer) are estimated to be  $\pm 1.0\%$  of reading at 22°C. As for the air velocity, the hot wire probe (Testo 425) gave velocity measurements with uncertainty of  $\pm 1.0\%$  rdg. at speeds lower than 8 m/s and uncertainty of  $\pm 0.5\%$  rdg. at higher speeds (8 – 20 m/s). The directional sensitivity of the hot wire probe and valid yaw

angle for the pitot-static tubes are show in in Figure 4.41. The valid angle range for the Pitot - static tube calibration is within the range of  $\pm 11^\circ$ .

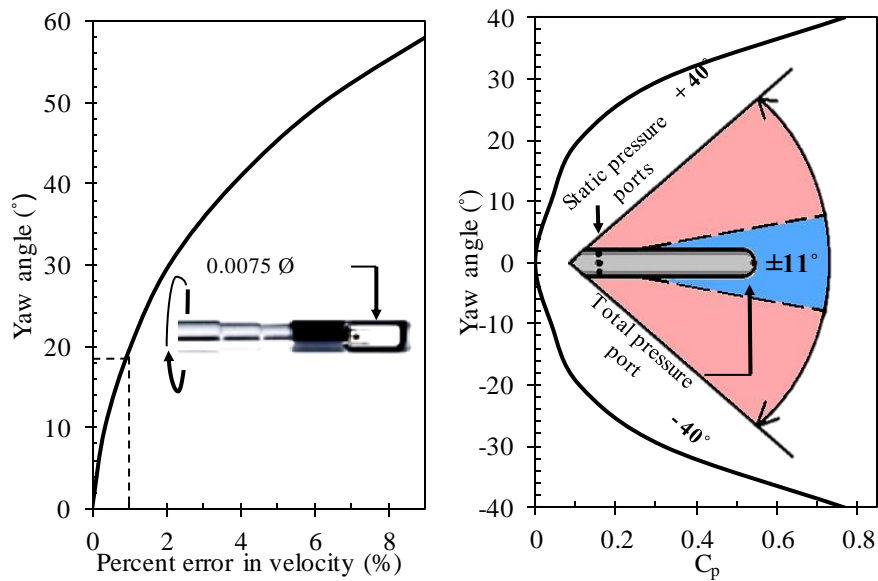


**Figure 4.41** (a) Testo 425 hot wire anemometer probe response to angle (b) Yaw angle error for 166T ellipsoidal Pitot-static tube.

#### 4.6.2 Pressure sensor

The Scanivalve DSA 3217 incorporates 16 temperature compensated piezoresistive pressure sensors with a pneumatic calibration valve, RAM, 16 bit A/D converter, and a microprocessor in one housing unit (Figure 4.42). The sensor has a range of  $\pm 1$  psid and an accuracy of 0.12 % of full scale and is set up to use Ethernet (10baseT) communication with the host computer via TCP/IP protocol interface with DSALink3 at a maximum scan rate of 500 Hz/channel. The pressures measured by the DSA 3217 are temperature compensated over a range of 0 °C to 60 °C with a maximum thermal error of  $\pm 0.001$  % of full scale/°C, eliminating the need for temperature compensation on recorded data.

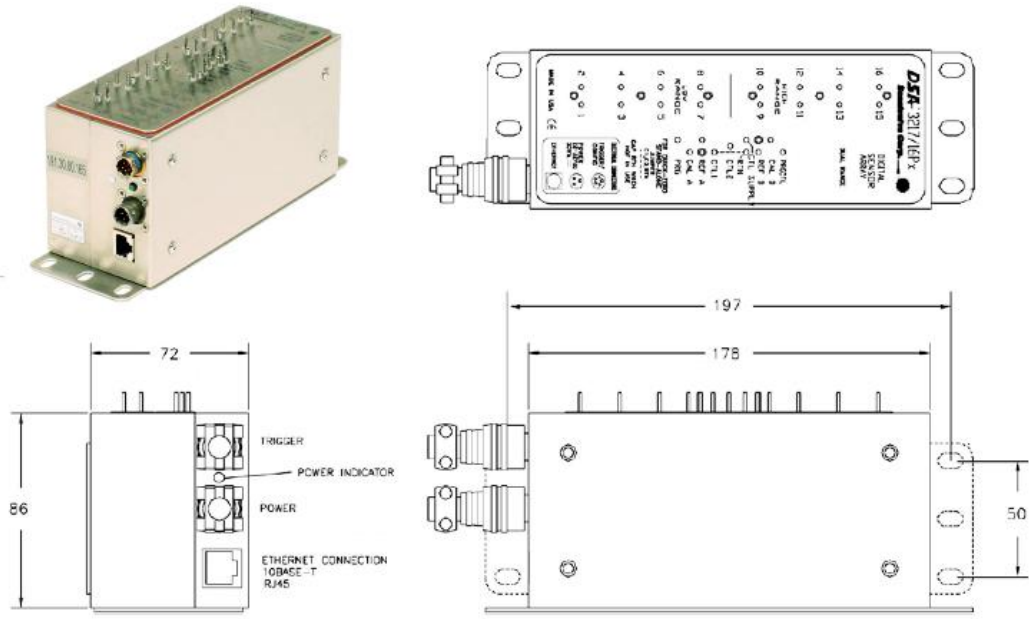


Figure 4.42 DSA3217 pressure scanner.

### 4.6.3 Data acquisition system

The DSALink3 Software provides a means of communication between DSA 3217 Modules and a PC. It features tools necessary to be able to interface to a pressure scanner. The interface display real-time reading of the pressure and temperature values as numbers and in bar graph format (Figure 4.43). The software allows storage of data in a format specified during setup.

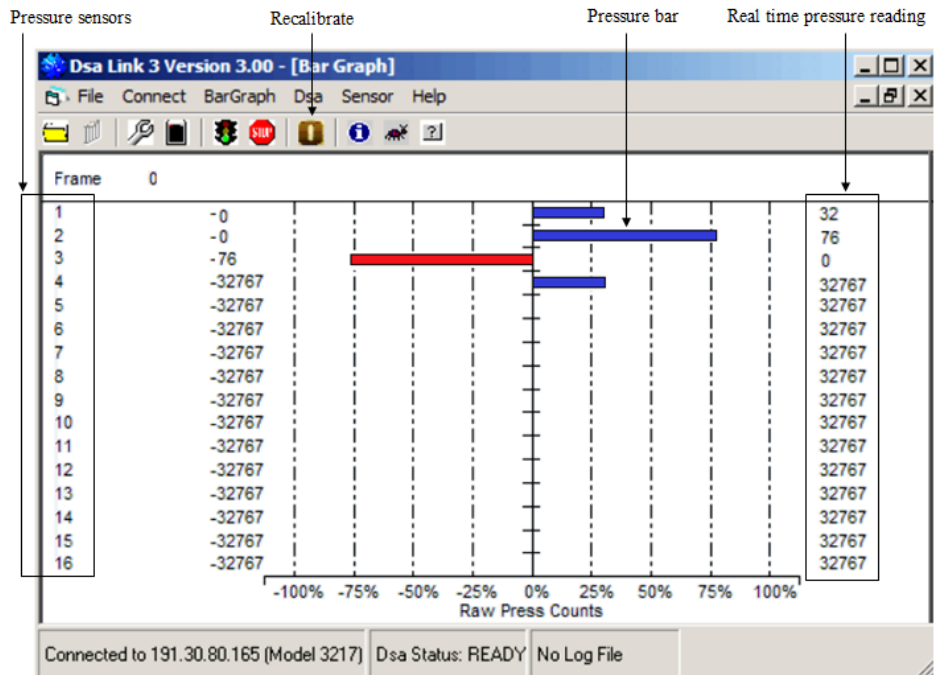


Figure 4.43 DSALink3 Interface.

#### 4.6.4 Smoke generator

The AFA10 smoke generator was used to visualise the flow in and around the wind tower models (Figure 4.44). The unit is mainly used in subsonic wind tunnel and other low flow rate air flow applications. It has control unit that pumps smoke oil to the tip of a probe. A low-voltage electrical coil at the probe tip heats the oil to produce a fine smoke trail. The smoke moves into the air stream smoothly and steadily. It has an adjustable control unit to change the smoke strength to suit the air flow conditions



**Figure 4.44** AFA 10 Smoke generator unit.

#### 4.6.5 High speed camera

For the purpose of flow visualisation a high speed camera was used to record and analyse the movement of smoke-visualised airflow paths inside and around the wind tower models. The high speed camera will provide the best combination of resolution, sensitivity and frame rate. The high quality video obtained by recoding the fast movement of the smoke through the wind tower was first separated into frames using the software, MotionBlitzDirector2. The RGB image files (frames) were extracted from the recorded videos in order to track the movement of the smoke in the images, frame by frame to determine lengths of the different flow paths. Figure 4.45 shows the

Motionblitz EoSens Cube7 high speed camera which can capture videos at frame rates up to 523 frames per second and resolutions up to 1696 x 1710.



**Figure 4.45** Motionblitz EoSens Cube7 high speed camera.

## **4.7 Summary**

This chapter described the experimental design and methodology covering the rapid prototyping of the 3D CAD models, experimental set-up and measurement procedures. The design specification and accuracy of the closed-loop wind tunnel facility and the instrumentation were also described in detail with further information provided in Appendix A, B, C and D.

## Chapter 5 CFD Results

### 5.1 Introduction

A four-sided and one-sided wind tower were utilised as benchmark models for the CFD investigations. Two heat transfer device (HTD) configurations were incorporated to the wind tower models; vertical and horizontal HTD arrangement. Furthermore, the effect of the addition of extended surfaces and porous media on the ventilation and thermal performance of the cooling wind tower were also investigated. The macro and micro climates geometry remained constant in each CFD model (described in Section 3.2). Test were performed for external wind speeds of 0.5 – 5 m/s at various wind directions (0 to 180°).

Table 5.1 summarises the CFD modelling and analysis of the different wind tower designs. The system's performance was assessed based on the following measured data responses.

**Table 5.1** Summary of the design of CFD modelling and analysis.

CFD experiment	Measured response				
	Velocity (m/s)	Pressure (Pa)	Internal air flow distribution (m/s)	Temperature (K)	Relative humidity (%)
Benchmark four-sided wind tower	✓	✓	✓		
Benchmark one-sided wind tower	✓	✓	✓		
Four-sided wind tower with HTD Config 1	✓	✓	✓	✓	✓
Four-sided wind tower with HTD Config 2	✓	✓	✓	✓	✓
One-sided wind tower with HTD Config 1	✓	✓	✓	✓	✓
One-sided wind tower with HTD Config 2	✓	✓	✓	✓	✓
Four-sided wind tower with finned HTD	✓	✓	✓	✓	✓
One-sided wind tower with finned HTD	✓	✓	✓	✓	✓
Four-sided wind tower with HTD and mesh	✓	✓	✓	✓	✓
One-sided wind tower with HTD and mesh	✓	✓	✓	✓	✓

## 5.2 Benchmark models

### 5.2.1 Four-sided wind tower

The four-sided wind tower geometry (detailed in Chapter 3) was used a simulation benchmark model for the analysis, shown in Figure 5.1, the design specifications are summarised in Table 5.2. Test were performed for external wind speeds of 0.5, 1, 2, 3, 4 and 5 m/s at various wind directions (0 or 180°).

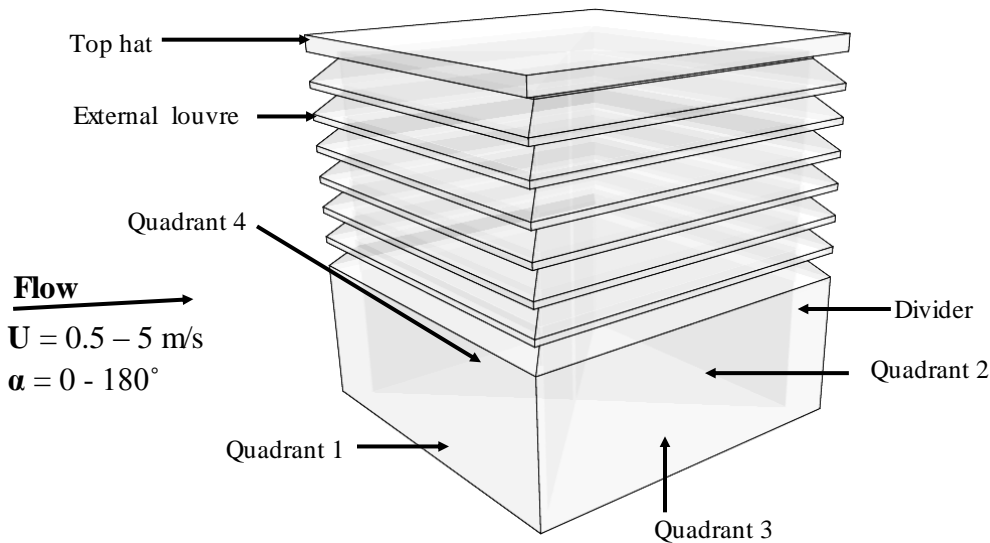


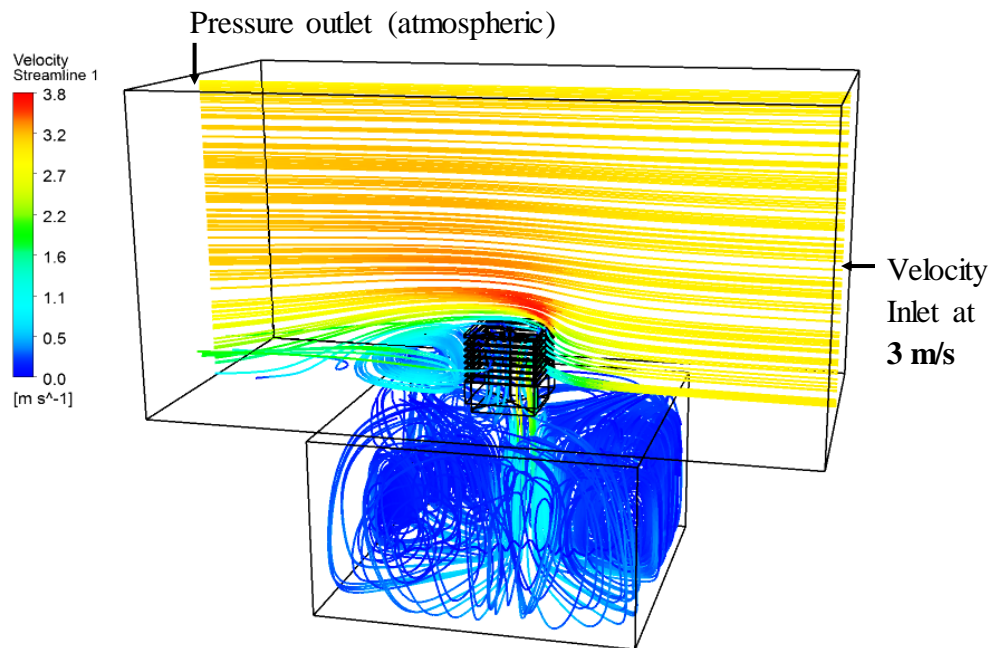
**Figure 5.1** Benchmark four-sided wind tower.

**Table 5.2** Summary of the benchmark geometry specifications.

Geometry	Specifications
Dimensions	1 x 1 x 1.2 m
External louvre angle	45°
Number of external louvre	7
Distance between external louvre	0.1 m
Divider / Cool sink	1
Damper/ supply	Fully open
Openings/windows	1
Heat transfer devices	-

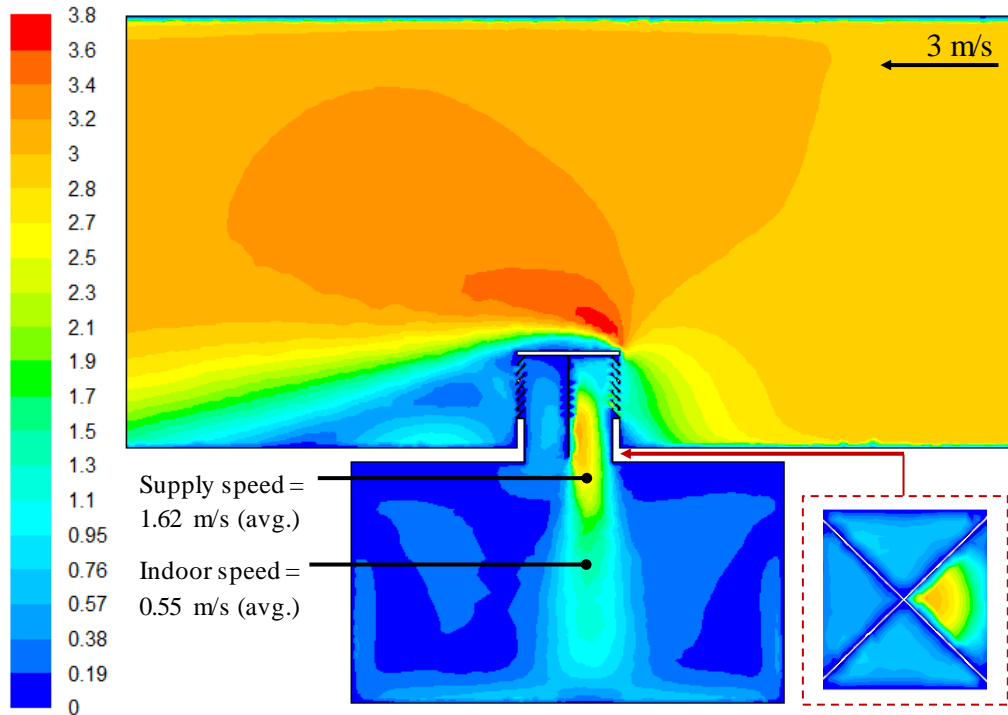
Figure 5.2 illustrates the flow path predicted in the CFD benchmark model. The left hand side of the streamline plot shows the scale of velocity (m/s). The streamlines in the fluid domain are colour coded and related to the CFD colour map. The velocity streamlines shows the macro-micro climate flow distribution. The flow enters from the velocity inlet boundary and splits at the wind tower front wall with some of the air

entering the test room and remaining flow passing over and exiting the pressure outlet boundary.



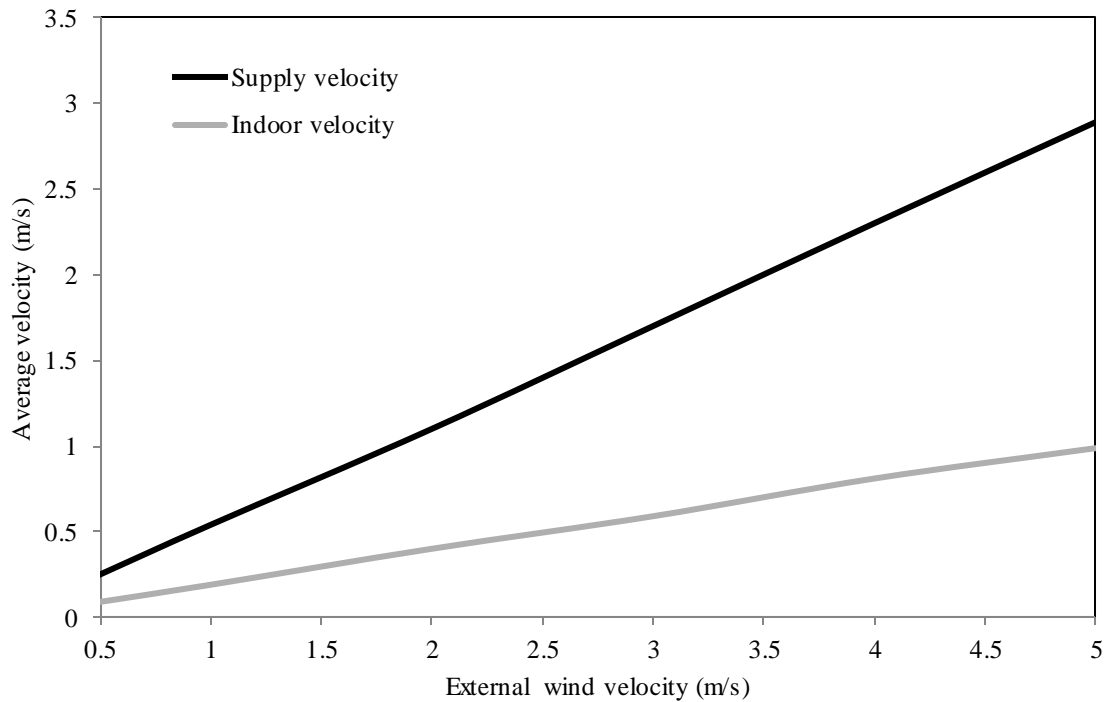
**Figure 5.2** Velocity streamlines showing the flow distribution inside the test room.

Figure 5.3 shows the velocity contour plot through the centre of the model showing an accurate cross-section of the model to assist the illustrative analysis. From the plot, the air flow enters the inlet boundary velocity on the right and the flow splits with some of the air entering the wind tower and some passing over or shearing and exiting to the pressure outlet on the left. The flow entering the wind tower accelerates as it enters the device reaching maximum velocity of 2.5 m/s as it hits the cross-dividers and forces the flow down into the diffuser. At an inlet velocity of 3 m/s, the average velocity exiting the wind tower diffuser was 1.62 m/s while the average velocity in the microclimate was obtained at 0.55 m/s. Minor air short-circuiting was observed below the wind tower channel.



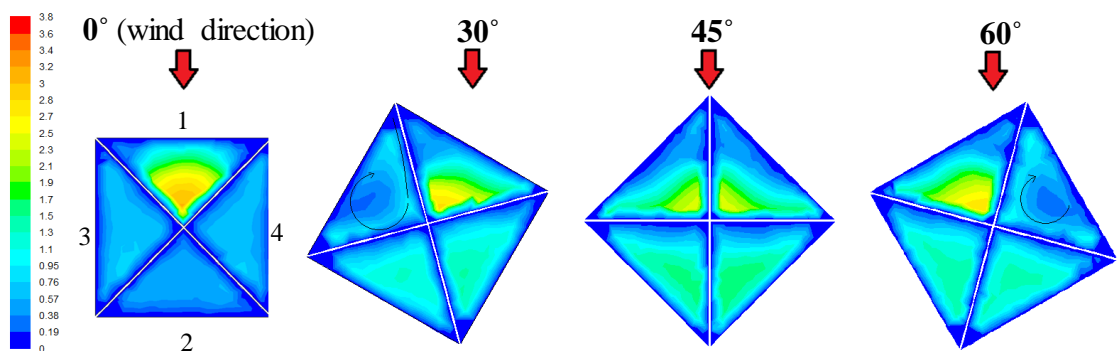
**Figure 5.3** Velocity contour plot of a cross sectional plane in the test room with an inlet velocity of 3 m/s.

The maximum velocity and pressure differential was around the inlet and outlet areas of the wind tower as this was the point of air exchange. Therefore, the connecting interface (diffuser) was used as a performance indicator. Figure 5.4 shows the increased air-exchange across the supply channel (diffuser) and within the test room as a direct result of an increased external wind velocity. At an inlet velocity of 3 m/s, the average velocity exiting the wind tower diffuser was 1.62 m/s while the average velocity in the microclimate was obtained at 0.55 m/s.



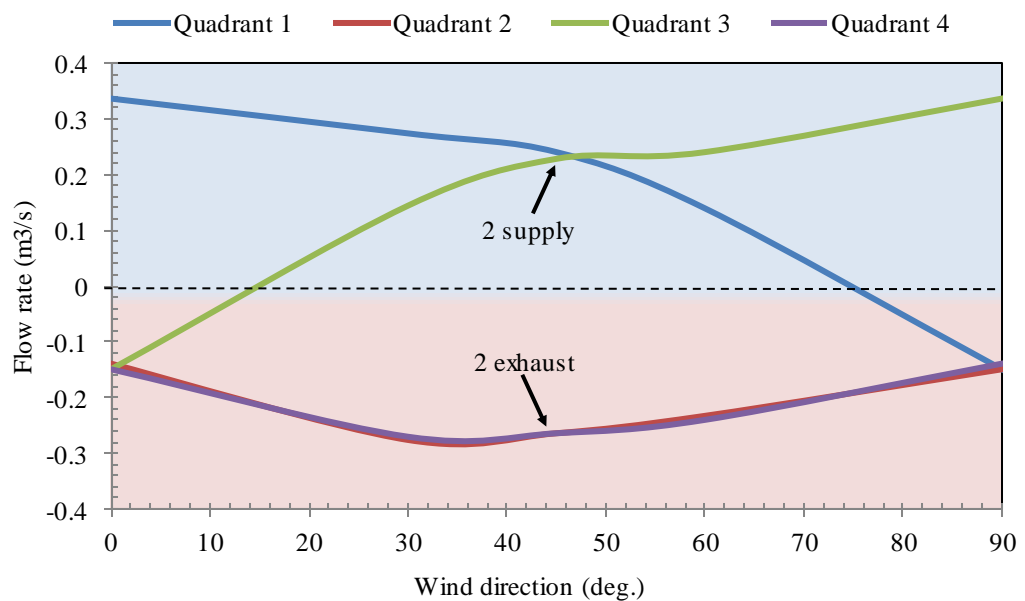
**Figure 5.4** Ventilation performance at various external wind speeds.

Different incident wind angles were investigated to examine the effect on the overall performance of the benchmark four-sided wind tower model. 5 different models (0, 30, 45, 60, 90°) were generated and solved at an external wind speed of 3 m/s. Figure 5.5 displays the horizontal contour plot inside the wind tower channel. It can be observed that at 0° angle, a large volume of the wind tower was used for extract purposes (three of the four quadrants). While the tower oriented at 45° into the prevailing wind has a larger area available to capture the wind. In this case, two windward quadrants are available for the air flowing into the tower and two leeward quadrants for the air flowing out of the tower.



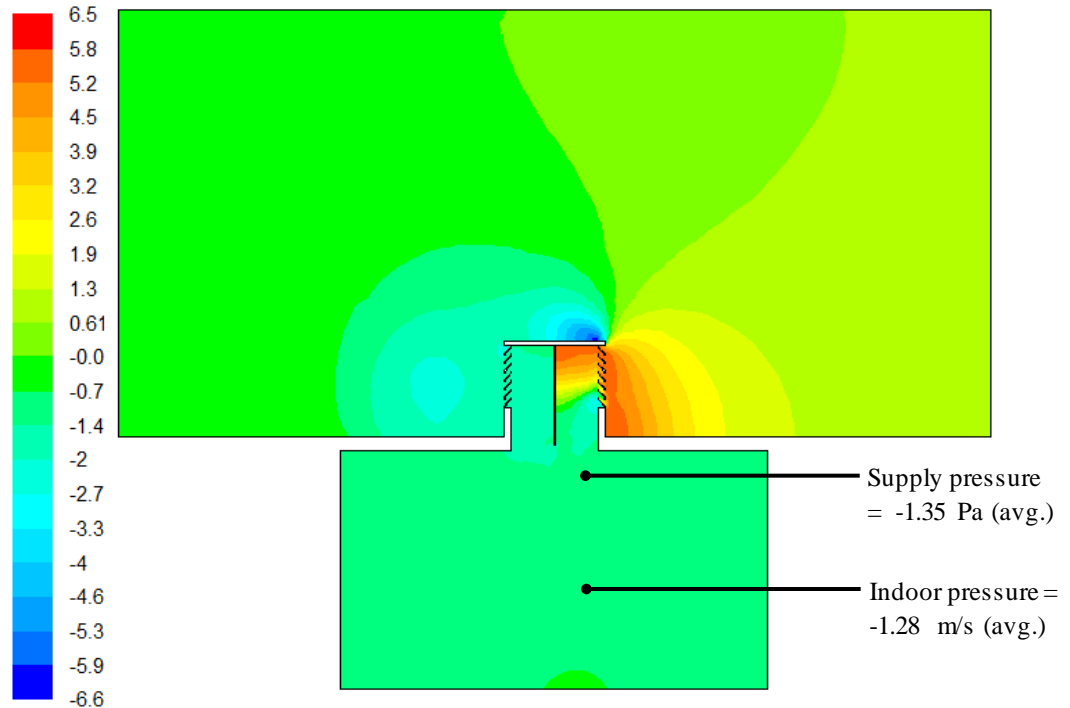
**Figure 5.5** Velocity contour plot of a horizontal plane (diffuser) inside the wind tower channel at different wind angles.

Figure 5.6 shows the volumetric airflow through the four-sided wind tower quadrant at different wind angles. In this figure, the supply and the extract segments are recognised by positive and negative values of airflow rate. A volumetric airflow rate of  $0.32 \text{ m}^3/\text{s}$  was achieved through the supply quadrant 1 at  $0^\circ$  for an average wind speed of  $3 \text{ m/s}$ . As the wind angle increases the supply airflow through quadrant 1 decreases. Exceeding the wind angle over the transition angle ( $> 70^\circ$ ), caused a change in airflow direction into quadrant 1. At  $45^\circ$  wind angle, a net volumetric flow rate of  $0.47 \text{ m}^3/\text{s}$  was achieved through combined supply quadrants 1 and 3 with the exhaust flow rate from the opposite quadrants at its maximum.



**Figure 5.6** Volumetric airflow through the wind tower quadrants for different wind directions.

Figure 5.7 displays the static pressure contour of the cross-sectional plane inside the test room with a standard four-sided wind tower model. The highest pressure (red area) was obtained upstream of the louvres with a maximum value of  $5.8 \text{ Pa}$ . Negative pressure (blue area) was observed at the exit and upper side of the wind tower with a minimum value of  $-6.6 \text{ Pa}$ . The average pressure inside the microclimate was  $-1.28 \text{ Pa}$ . Since, airflow always flows from higher relative pressure to lower relative pressure. A room under negative pressure indicates that less air is supplied to a room than exhausted which was the case for this configuration, there are three exhaust quadrants and only one supply quadrant.



**Figure 5.7** Static pressure contour plot of a cross sectional plane in the test room with an inlet velocity of 3 m/s.

The simulation model was solved for the full range of velocities. The velocity and static pressure readings were taken from the weighted-average of the indoor points and diffuser surface. The results for the simulations are summarised in Table 5.3.

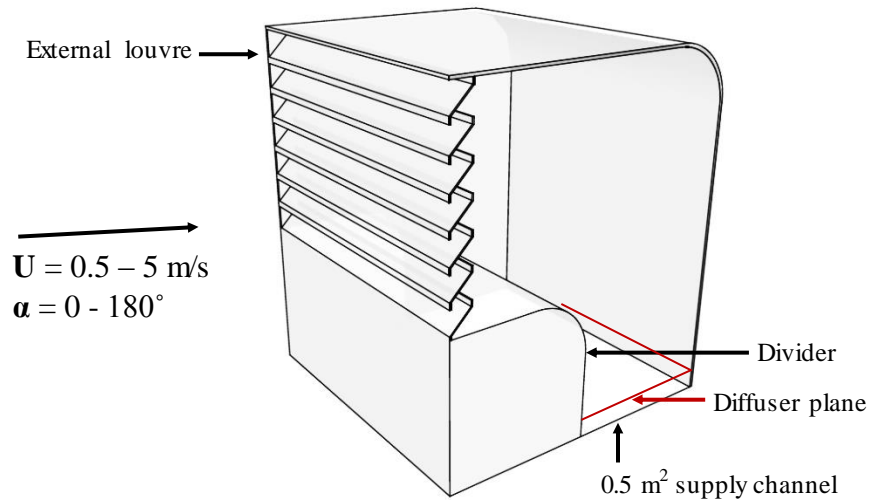
**Table 5.3** Simulation results with the benchmark four-sided wind tower.

Velocity inlet speed [m/s]	Diffuser supply velocity [m/s]	Average indoor velocity [m/s]	Diffuser supply pressure [Pa]	Average indoor pressure [Pa]
0.5	0.25	0.09	-0.05	-0.05
1	0.54	0.19	-0.13	-0.117
2	1.10	0.4	-0.65	-0.61
3	1.62	0.55	-1.35	-1.28
4	2.30	0.81	-2.48	-2.41
5	2.89	0.99	-3.72	-3.64

## 5.2.2 One-sided wind tower

The one-sided wind tower geometry (detailed in Chapter 3) was used as a simulation benchmark model for the analysis, as shown in Figure 5.8. Tests were performed for

external wind speeds of 0.5, 1, 2, 3, 4 and 5 m/s at various wind directions (0 to 180°). The connecting interface (wind tower diffuser) was used for measuring the supply rates.



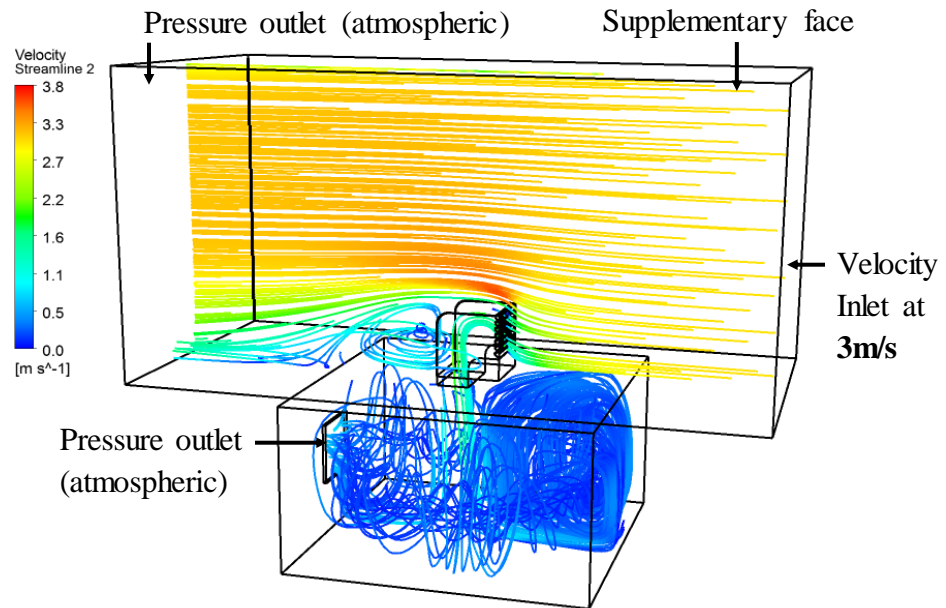
**Figure 5.8** Benchmark one-sided wind tower.

Table 5.4 summarises the design specifications of the benchmark one-sided wind tower.

**Table 5.4** Summary of the benchmark geometry specifications.

Geometry	Specifications
Dimensions	1 x 1 x 1.2 m
External louvre angle	45°
Number of external louvre	7
Distance between external louvre	0.1 m
Divider / Cool sink	1
Damper/ supply	Fully open
Openings/windows	1
Heat transfer devices	-

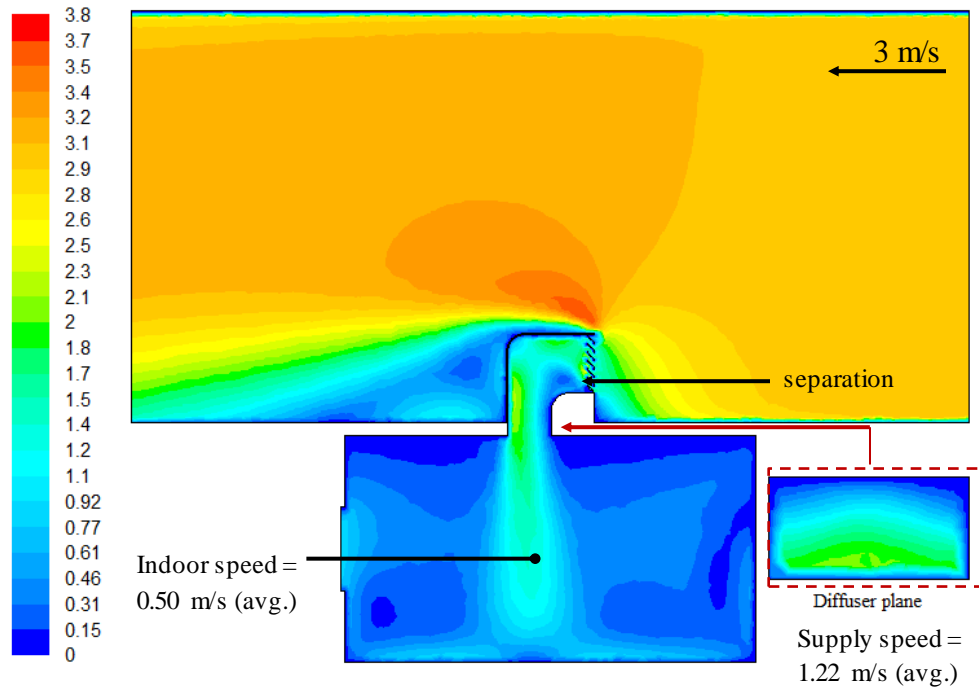
Figure 5.9 illustrates the micro-macro climate fluid domain and the boundary locations for the inlet and outlet. The figure also shows the flow path lines of the particles which are released from the velocity inlet plane parallel to the wind tower opening. From the streamline analysis, it was observed that the airflow induced inside the test room was distributed evenly, with some of the flow recirculated and some exiting the window opening.



**Figure 5.9** Velocity streamlines showing the flow distribution inside the test room with a one-sided wind tower.

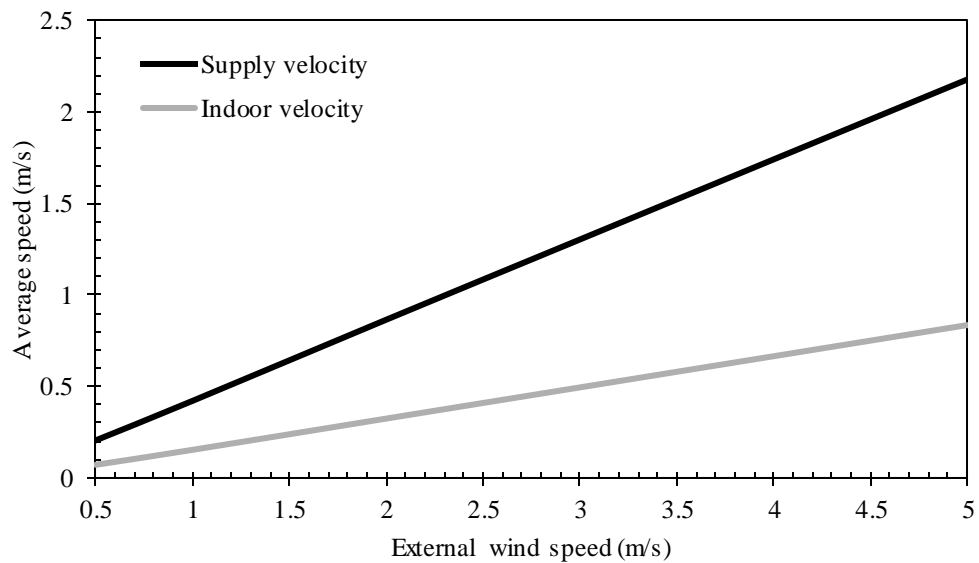
Figure 5.10 shows the velocity contours of the cross sectional plane in the test room model with the one-sided wind tower. As seen in the illustration, the air flow enters from the right side of the enclosure (velocity inlet) passing around the wind tower with some of the air induced inside the channel and exiting to the pressure outlet on the left. The flow entering the wind tower speeds up as it enters the device reaching maximum velocity of 2.3 m/s as it hits the rear wall of the channel and forces the flow down into the test room. Separated flow and wake region were observed near the lower edge of the opening which caused a sharp variation in velocity in this region, reducing the maximum efficiency of the wind tower. This is a common problem with one-sided wind tower systems [Montazeri and Azizian, 2008].

The air stream is circulated inside the structure and exits the opening located on the far side of the receiving room. An average air velocity of 0.50 m/s was obtained inside the test room model, 10% lower compared to the four-sided model. The velocity contours confirmed a reduced internal air movement.



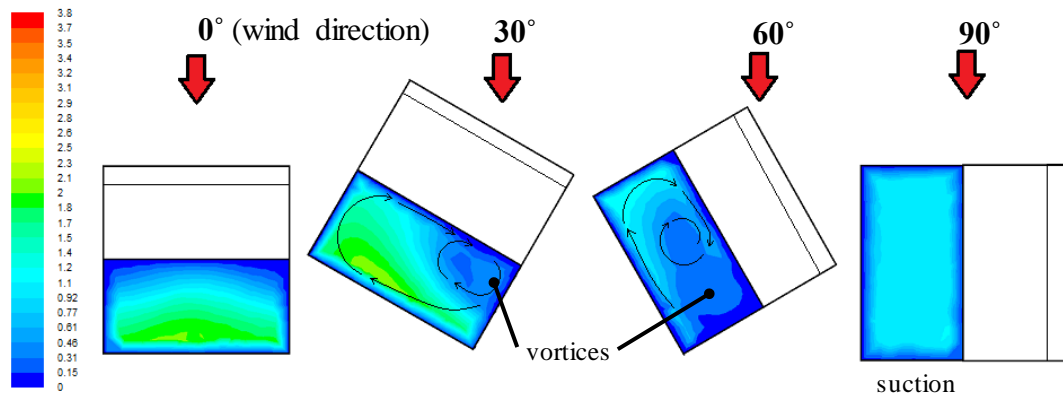
**Figure 5.10** Velocity contour plot of a cross sectional plane in the test room with an inlet velocity of 3 m/s.

Figure 5.11 shows the relation between the varying external wind speeds and performance of the wind tower in terms of the supply velocity and internal air distribution. At an inlet velocity of 3 m/s, the average velocity exiting the wind tower diffuser was 1.3 m/s which was 18.8 % lower compared to the four-sided wind tower supply speed (Figure 5.3).



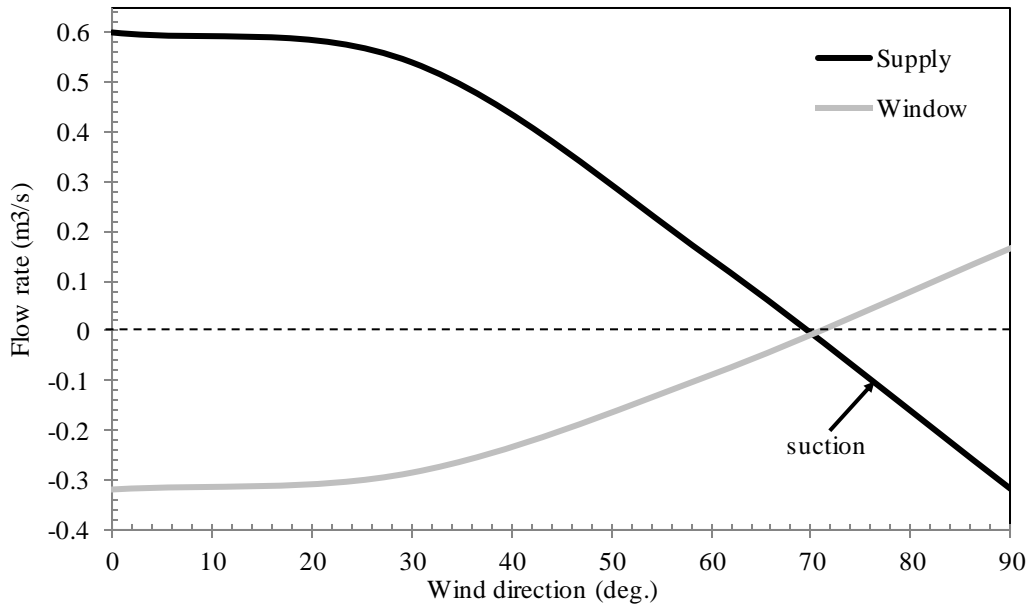
**Figure 5.11** Ventilation performance at various external wind speeds.

Figure 5.12 displays the horizontal velocity contour plot inside the wind tower angled at 0, 30, 60, and 90°. Locating the wind tower on the path of predominant wind streams (0° angle); will cause the maximum entrance flow rate into the windward opening. With increasing external wind angle and the developing region of vortices, the induced operation of wind tower reduced continuously to its minimum value at the transition angle. Exceeding the wind angle over the transition angle causes a change in the airflow direction into the windward channel. At 90° wind angle the wind tower acts as a suction device. This is due to the fact that exposing the body of the wind tower on the path of the air flow caused a low pressure region on its side and positioning its opening in this region with a lower pressure than the environment will result in an airflow from the window to the wind tower opening.



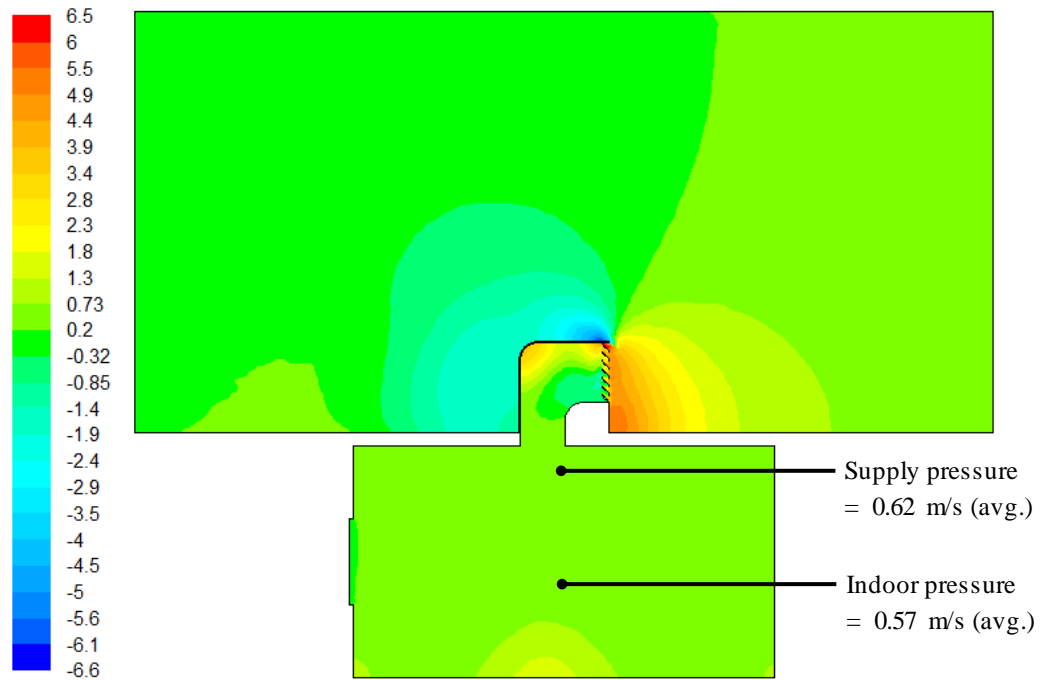
**Figure 5.12** Velocity contour plot of a horizontal plane (diffuser) inside the wind tower channel at different wind angles.

Figure 5.13 shows the CFD results of the volumetric airflow through the windward and leeward sides and through the window of the test room model. In this figure the supply and the extract sections are recognised by positive and negative values of airflow correspondingly. A volumetric airflow rate of 0.6 m<sup>3</sup>/s was achieved through the supply channel at 0° for an average wind speed of 3 m/s.



**Figure 5.13** Volumetric airflow through the wind tower inlet and window opening.

Figure 5.14 displays the static pressure contour of the cross-sectional plane inside the test room with a standard one-sided wind tower model. The highest pressure was obtained upstream of the louvres with a maximum value of 6 Pa. Negative pressure was observed at the leeward and upper side of the wind tower with a minimum value of -6.6 Pa. The average pressure inside the microclimate was 0.57 Pa. Since, airflow always flows from higher relative pressure to lower relative pressure. A room under positive pressure indicates that more air is supplied to a room than exhausted which was the case for this configuration. Unlike, the four-sided wind tower there was only one exhaust opening hence less air was exhausted from the room.



**Figure 5.14** Static pressure contour of a cross-sectional plane inside the micro-macro climate domain.

The simulation model was solved for the full range of velocities. The velocity and static pressure readings were taken from the weighted-average of the indoor points and diffuser surface. The results for the simulations are summarised in Table 5.5.

**Table 5.5** Simulation results with the benchmark four-sided wind tower

Velocity inlet speed [m/s]	Diffuser supply velocity [m/s]	Average indoor velocity [m/s]	Diffuser supply pressure [Pa]	Average indoor pressure [Pa]
0.5	0.20	0.07	0.02	0.02
1	0.40	0.15	0.06	0.06
2	0.86	0.32	0.3	0.28
3	1.22	0.50	0.62	0.57
4	1.74	0.66	1.22	1.10
5	2.18	0.83	1.09	1.77

### 5.3 Heat Transfer Device (HTD) integrated wind tower

The key objective of this work was to investigate the effect of the addition of heat transfer devices on the cooling potential of wind towers. Two different wind tower arrangements were investigated: a four-sided wind tower system integrated with vertical heat transfer device arrangement and a one-sided wind tower integrated with horizontal heat transfer device. The velocity and temperature contour plots were used to assess the

ventilation and thermal performance of each setup. In order to directly compare the results with simulation benchmarks, all the model's volumes (micro-macro climate) were remained constant.

### 5.3.1 Vertical HTD arrangement

Figure 5.15 illustrates the four sided wind tower with heat transfer device geometry (detailed in Chapter 3). Tests were performed for various external wind speeds (0.5 - 5 m/s) and wind directions (0 - 180°). A constant inlet temperature of 318 K was set to replicate a hot outdoor environment. In order to cool the induced air, wall temperature of 293 K (operating temperature) was applied to the heat transfer devices surface. Two HTD configurations (detailed in Chapter 3) were simulated and compared side by side; Configuration 1 (100-20-50) and Configuration 2 (50-20-25).

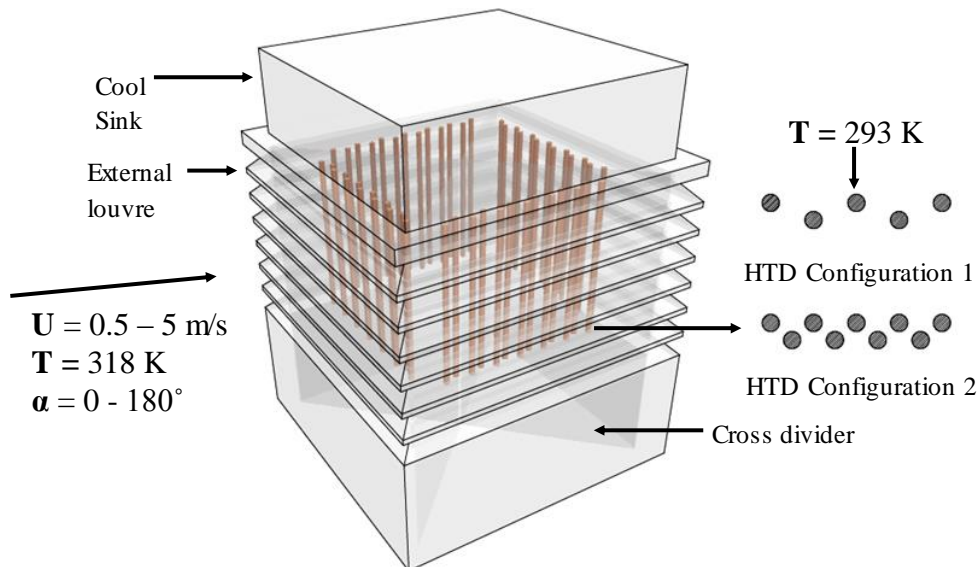


**Figure 5.15** Four-sided wind tower with heat transfer devices.

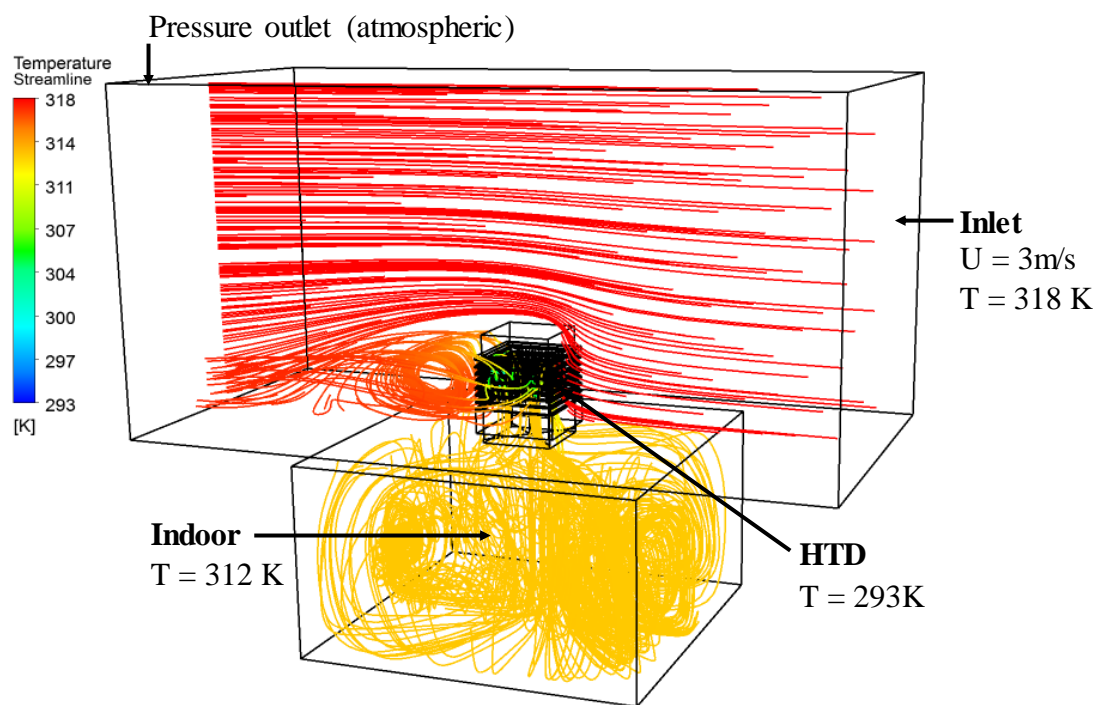
Table 5.6 summarise the specifications of the four-sided wind tower with heat transfer devices.

**Table 5.6** Summary of the four-sided wind tower with HTD specifications

Geometry	Specifications
Dimensions	1 x 1 x 1.5 m
External louvre angle	45°
Number of external louvre	7
Distance between external louvre	0.1 m

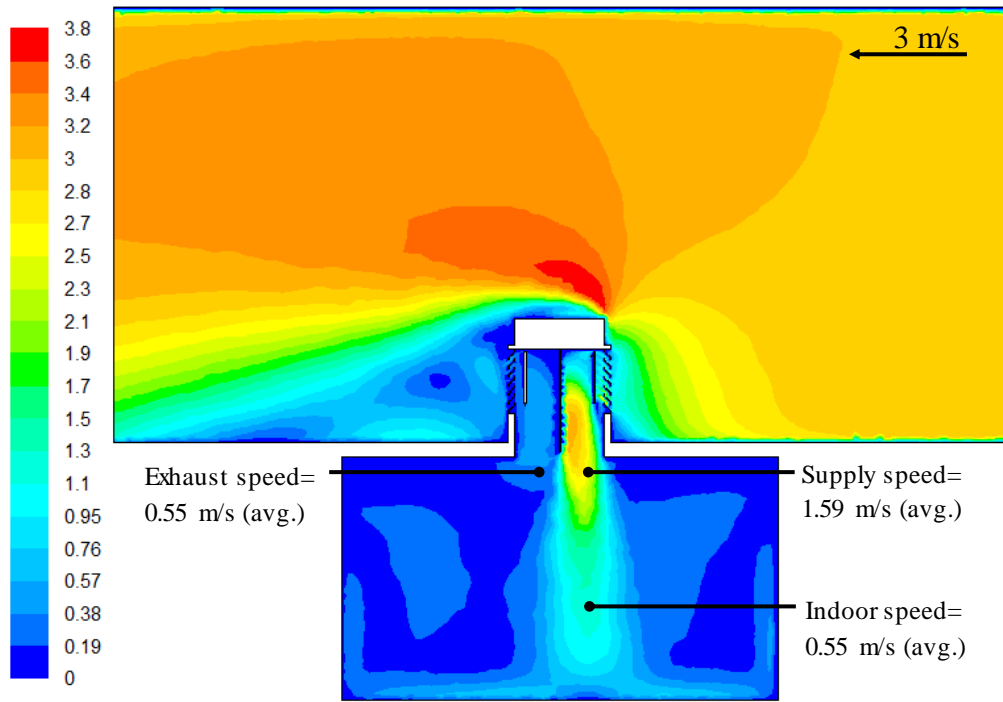
Divider / Cool sink	1
Damper/ supply	Fully open
Openings/windows	-
Heat transfer devices	Config 1 and 2

Figure 5.16 depicts the micro-macro climate fluid domain and the boundary locations for the inlet and outlet. The left hand side of the streamline plot shows the scale of static temperature (K). The streamlines in the fluid domain are colour coded and related to the CFD colour map. From the streamline analysis, it was observed that the airflow induced inside the test room was distributed evenly, with some of the flow recirculated and some exiting the exhaust quadrants. Furthermore, the heat transfer devices effectively reduced the induced airflow temperature by up to 6 K as seen in the streamlines flowing inside the test room.

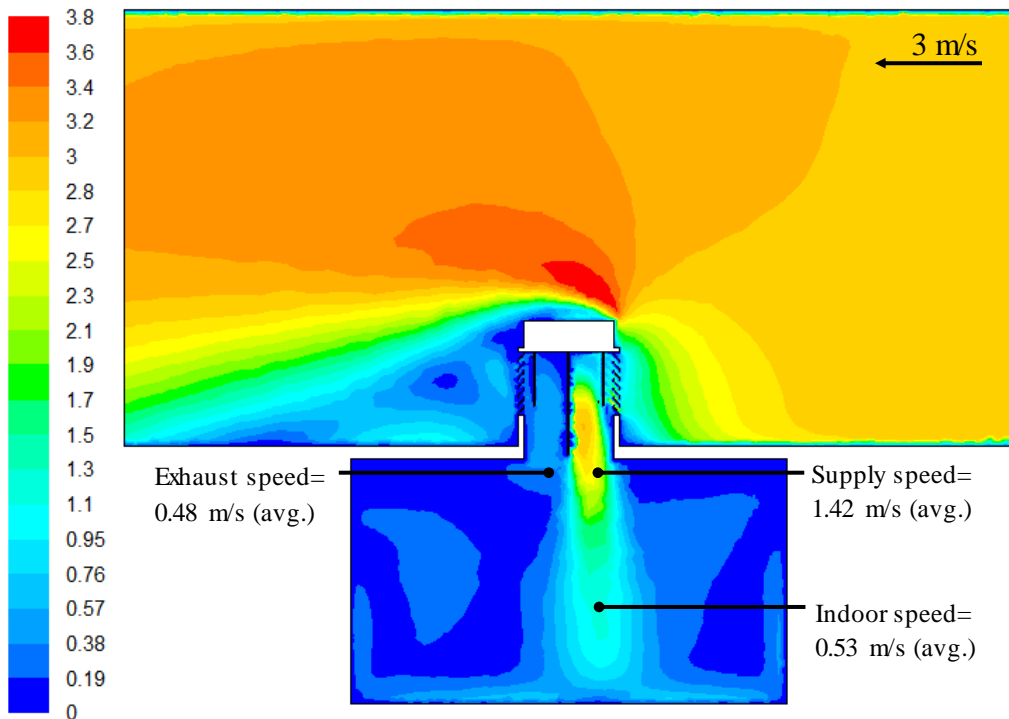


**Figure 5.16** Streamline representing the temperature distribution inside the test room with a four-sided wind tower incorporating heat transfer devices (Config 2).

Figure 5.17 and 5.18 compares the air flow distribution inside the test room with the vertical HTD wind tower configuration 1 and 2. At 3 m/s inlet speed, the average speed inside the test room (Figure 5.18) was 0.55 m/s which was 3.6 % higher compared to the second arrangement.



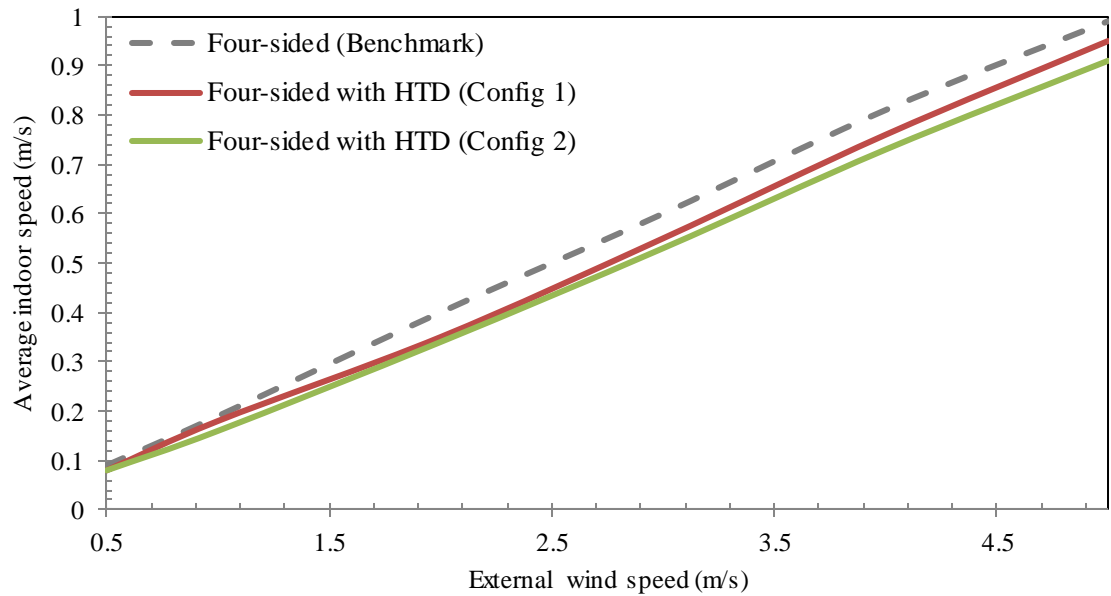
**Figure 5.17** Velocity contour of a mid-plane inside the test room with a wind tower incorporating vertical HTD arrangement (Configuration 1).



**Figure 5.18** Velocity contour of a mid-plane inside the test room with a wind tower incorporating vertical HTD arrangement (Configuration 2).

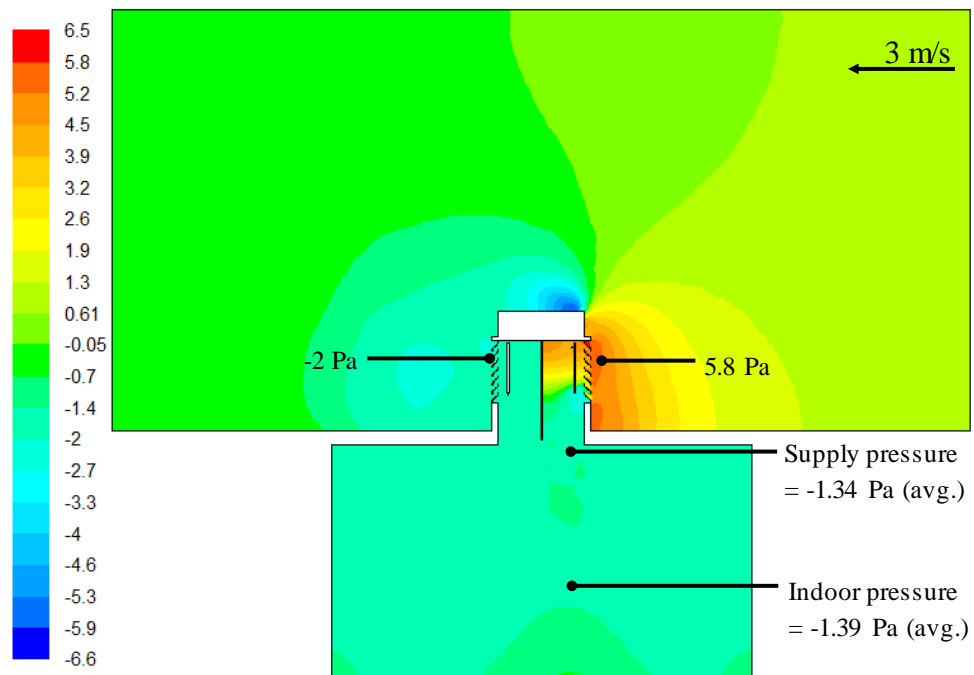
Figure 5.19 shows a comparison between the average indoor air flow speed at various external wind speeds. The average indoor air speed was reduced by 4.2 – 11 %

following the addition of the vertical HTD configuration 1 and by 4.2 - 15.8 % following the addition of the vertical HTD configuration 2.

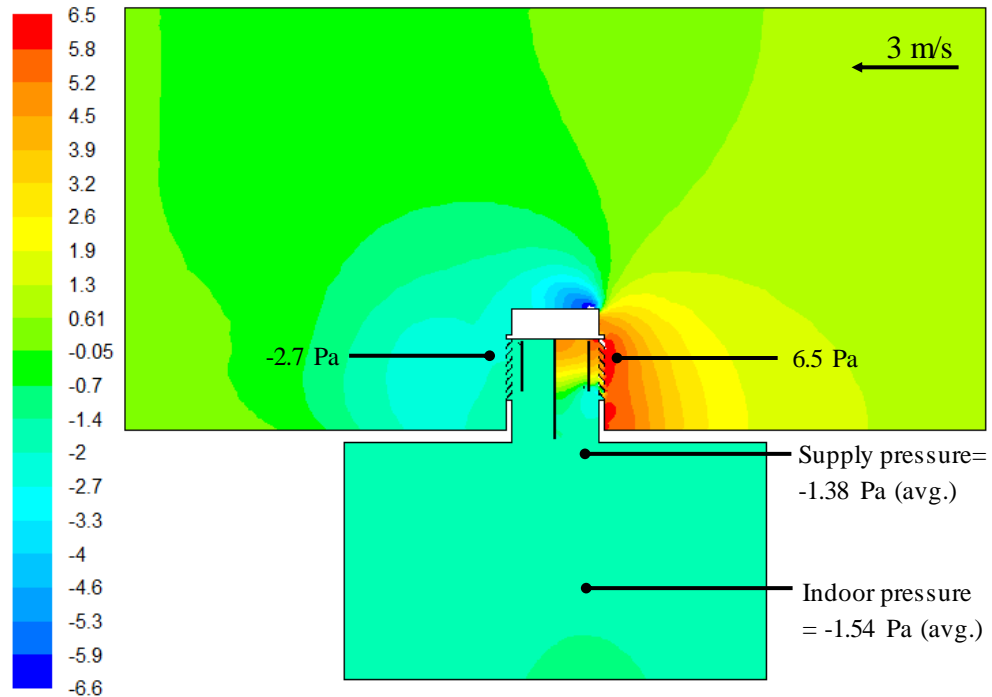


**Figure 5.19** Comparison between the average indoor air flow speed at various external wind speeds (Vertical HTD Config 1 and 2)

Figure 5.20 and Figure 5.21 compares the pressure distribution inside the test room with the four-sided wind tower with the heat transfer device configuration 1 and 2.



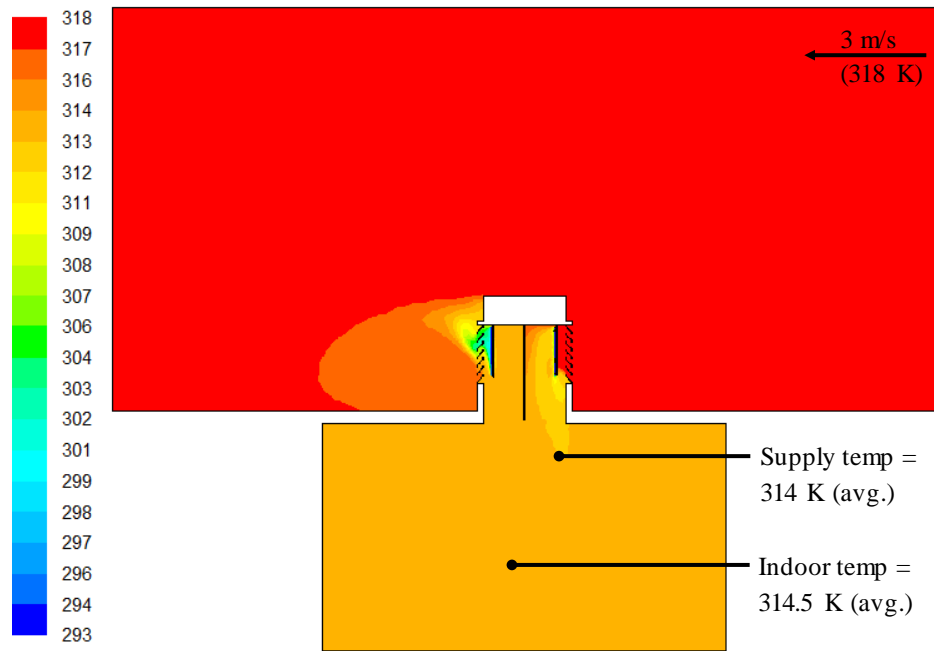
**Figure 5.20** Static pressure contour of a cross-sectional plane inside the micro-macro climate domain (Configuration 1).



**Figure 5.21** Static pressure contour of a cross-sectional plane inside the micro-macro climate domain (Configuration 2).

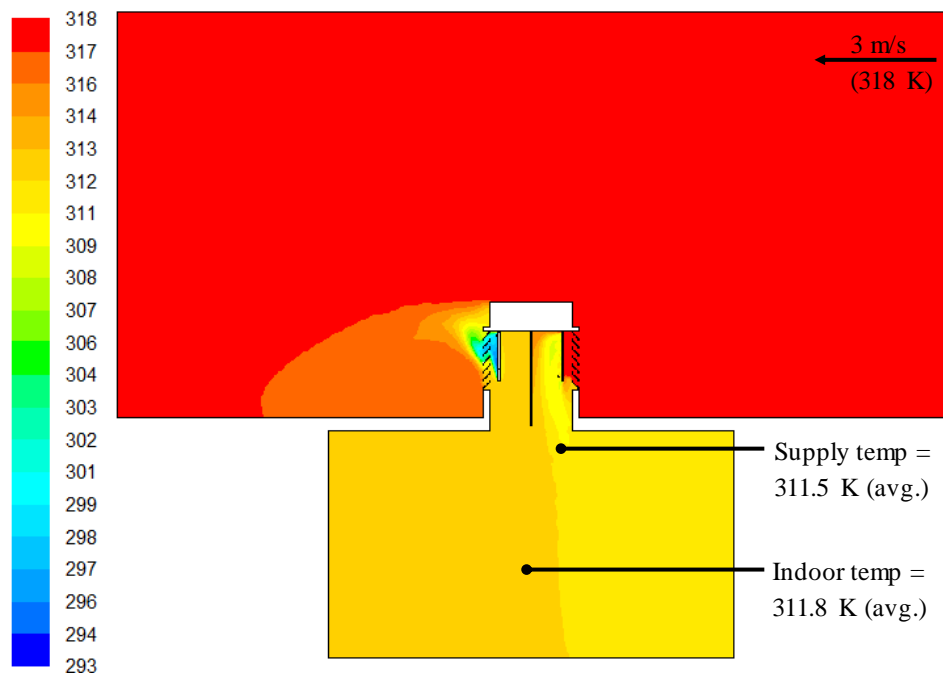
As observed from the two diagrams, increasing the number of cylindrical heat transfer devices inside the wind tower channel restricted the velocity and increased the pressure drop across the louvres. The pressure difference between windward and leeward side openings increased from 7.8 Pa to 9.2 Pa. A higher negative internal pressure was also observed inside the test room in (Figure 5.21) indicating that lesser airflow was supplied to the room than exhausted. This was due to the increased negative pressure at the exhaust side of the four-sided wind tower allowing a greater suction effect.

Figure 5.22 illustrates temperature distribution inside the test room with a heat transfer device integrated wind tower system. The average temperature inside the microclimate was 314.5 K with the macro climate temperature set at 318 K. A greater temperature reduction was obtained at the immediate downstream of the heat transfer devices with a supply temperature value of 314 K. The results displayed that the heat transfer devices was capable of reducing the induced air stream temperature.



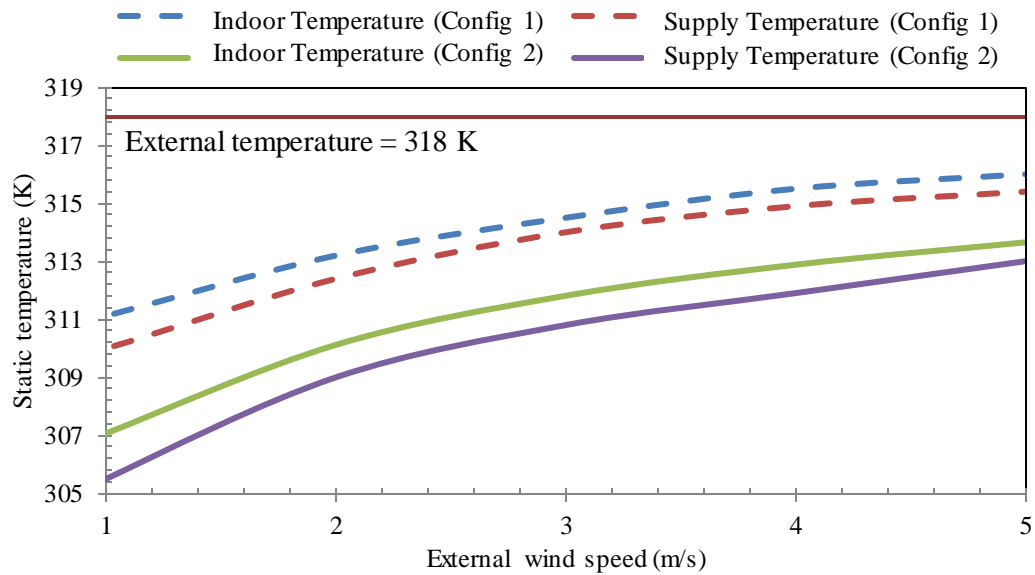
**Figure 5.22** Temperature contour plot of a cross sectional plane in the test room with an inlet temperature of 318 K (vertical HTD Configuration 1).

As expected, increasing the number of heat transfer devices (increased surface area) and reducing the spacing (Configuration 2), improved the cooling performance of the system as shown in Figure 5.23. Temperature reduction of up to 6.2 K was achieved following the reconfiguration of the heat transfer devices arrangement.



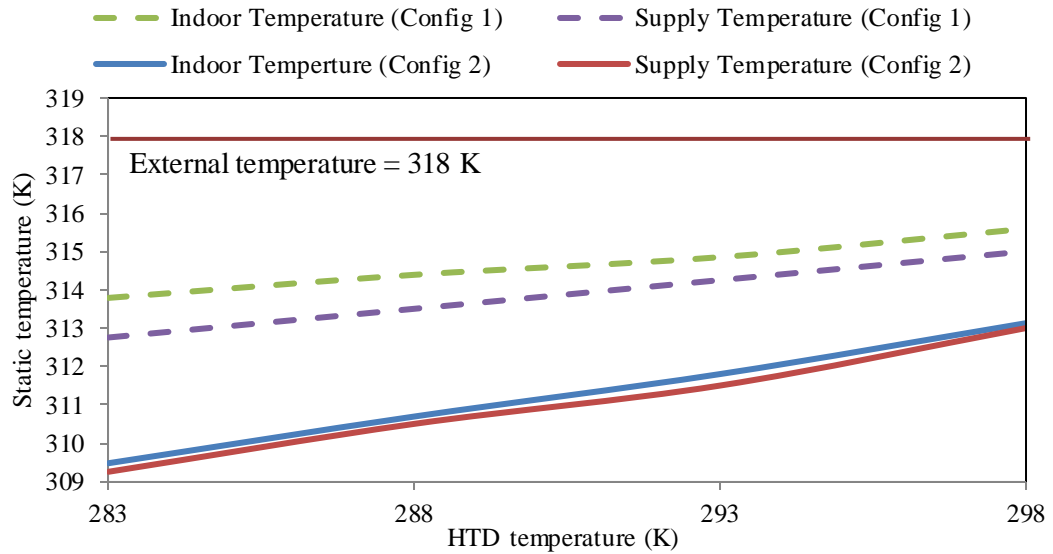
**Figure 5.23** Temperature contour plot of a cross sectional plane in the test room with an inlet temperature of 318 K (vertical HTD Configuration 2).

Figure 5.24 shows the effect of the increasing external wind speeds (1 to 5 m/s) on the thermal performance of the heat transfer devices integrated wind tower. As observed, the cooling performance of the heat transfer devices decreases as the air flow speed through it increases. At 5 m/s outdoor speed, the air temperature was reduced by 2 (config 1) – 4.8 K (config 2). Substantial reduction in temperature was observed at lower wind speeds (1 - 2 m/s), up to 4.8 - 6.9 K (config 1) and 7.8 – 10.9 K (config 2).



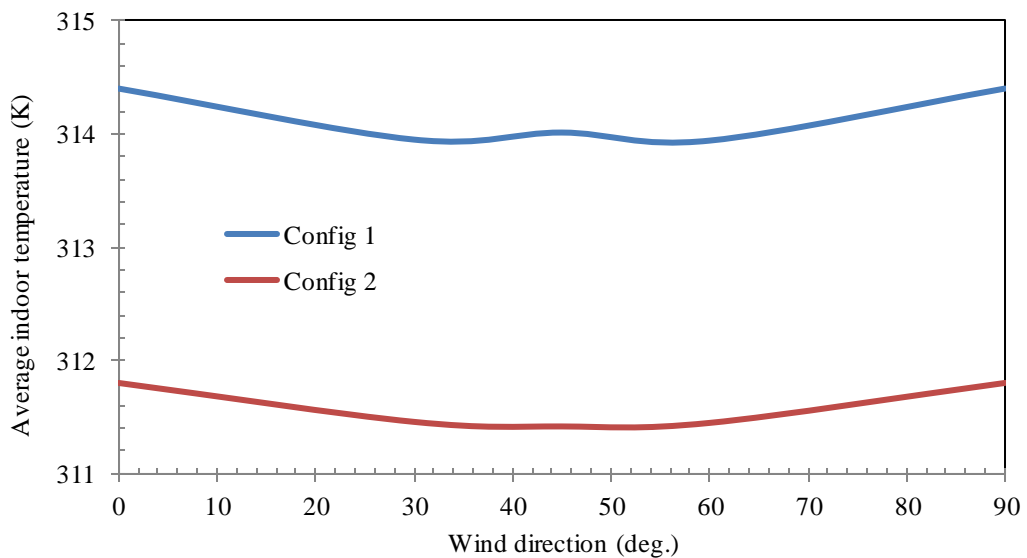
**Figure 5.24** Effect of varying external wind speed on the supply and indoor temperature.

Figure 5.25 shows the reduced air temperature within the test room as a direct result of reduced heat transfer device surface temperature. The heat transfer device surface temperature was varied between 298 and 283 K and the outdoor velocity was set and maintained at 3 m/s. It was observed that reducing the HTD surface temperature from 298 to 283 K (by 15 K) only improved the temperature reduction by 1.8 (config 1) - 3.6 K (config 2).



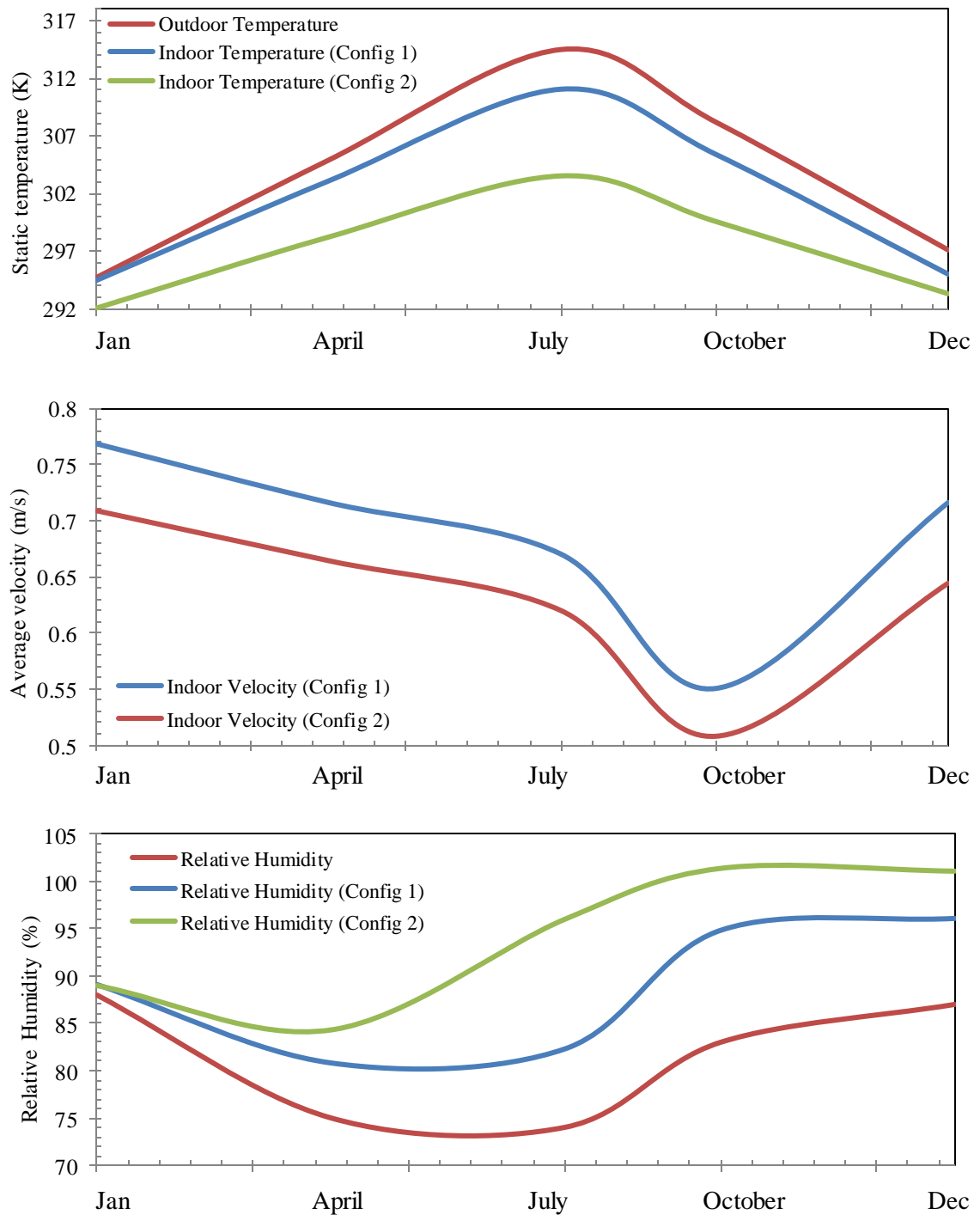
**Figure 5.25** Effect of various heat transfer device surface temperature on the supply and indoor temperature.

Figure 5.26 displays the effect of the wind direction on the thermal performance of the wind tower system with HTD. The wind direction was varied between 0 to 90° and the outdoor velocity was set at 3 m/s. As observed, the four-sided wind tower system was operational in all wind directions with a maximum temperature variation of  $\pm 0.4$  K, therefore the system can be used in such conditions where there is no predictable prevailing wind direction.



**Figure 5.26** Effect of varying external wind angle on the supply and indoor temperature.

A second objectives of this study was to investigate the effect of varying external conditions such as wind speed, wind direction, external temperature and relative humidity on the ventilation and thermal performance of the proposed system. The CFD model was coupled with the weather data (detailed in Chapter 3, Section 3.3.3) which provided the inlet boundary conditions for the wind speed, temperature and relative humidity. Figure 5.27 summarises the results for temperature, velocity and humidity.



**Figure 5.27** Summary of the results for indoor temperature, velocity and humidity.

Table 5.7 and 5.8 summarises the data obtained from the CFD analysis of the wind tower with the vertical HTD configuration 1 and 2.

**Table 5.7** Simulation results with the four-sided wind tower with HTD (Config 1).

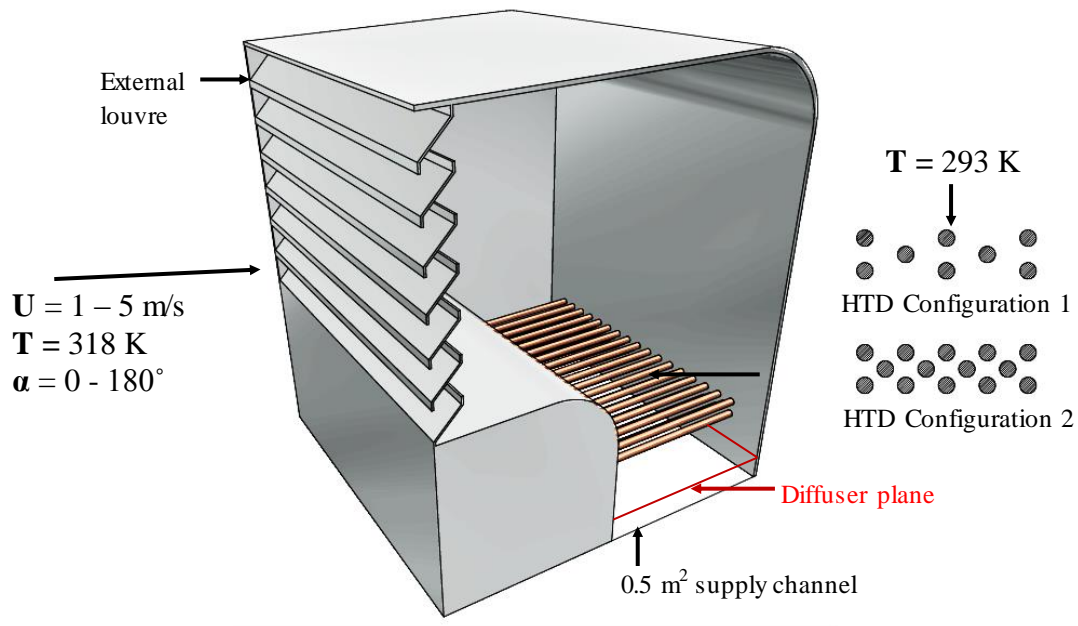
Velocity inlet speed [m/s]	Diffuser supply velocity [m/s]	Average indoor velocity [m/s]	Average indoor pressure [Pa]	Average indoor temperature [K]
0.5	0.21	0.08	-0.07	310.12
1	0.45	0.18	-0.16	311.12
2	1.01	0.35	-0.68	313.2
3	1.59	0.55	-1.39	314.5
4	2.2	0.76	-3.1	315.5
5	2.8	0.95	-4	316

**Table 5.8** Simulation results with the four-sided wind tower with HTD (Config 2).

Velocity inlet speed [m/s]	Diffuser supply velocity [m/s]	Average indoor velocity [m/s]	Average indoor pressure [Pa]	Average indoor temperature [K]
0.5	0.2	0.08	-0.08	305.5
1	0.42	0.16	-0.14	307.07
2	0.92	0.34	-0.66	310.12
3	1.42	0.53	-1.54	311.81
4	2.07	0.73	-2.81	312.88
5	2.4	0.91	-4.46	313.65

### 5.3.2 Horizontal HTD arrangement

Figure 5.28 shows the one-sided wind tower with heat transfer devices geometry (detailed in Chapter 3). Test was performed for various external wind speeds (0.5 - 5 m/s) and wind directions (0 - 90°). A constant inlet temperature of 318 K was set to simulate a hot outdoor environment. In order to cool the induced air, wall temperature of 293 K (operating temperature) was applied to the heat transfer devices surfaces. Two HTD configurations (detailed in Chapter 3) were simulated and compared side by side; Configuration 1 (100-20-50) and Configuration 2 (50-20-25).



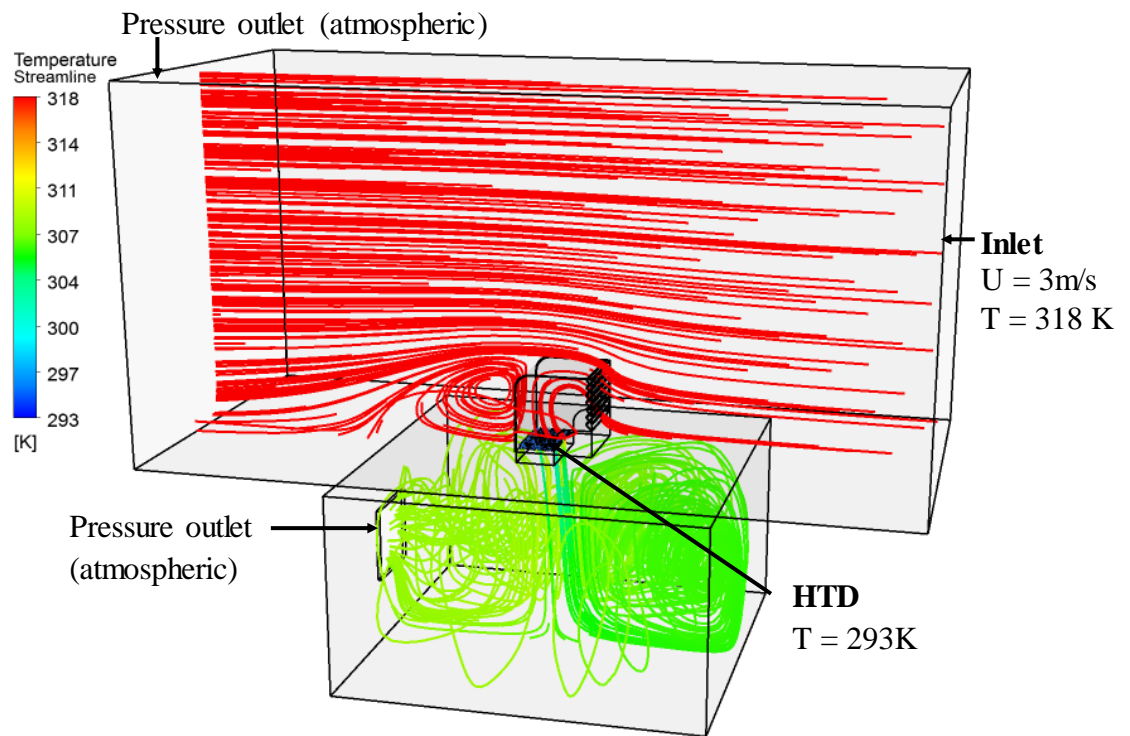
**Figure 5.28** One-sided wind tower with horizontal HTD arrangement.

Table 5.9 summarise the specifications of the one-sided wind tower with heat transfer devices.

**Table 5.9** Summary of the benchmark geometry specifications (one-sided wind tower with heat transfer devices).

Geometry	Specifications
Dimensions	1 x 1 x 1.2 m
External louvre angle	45°
Number of external louvre	7
Distance between external louvre	0.1 m
Divider / Cool sink	1
Damper/ supply	Fully open
Openings/windows	1
Heat transfer devices	Config 1 and 2

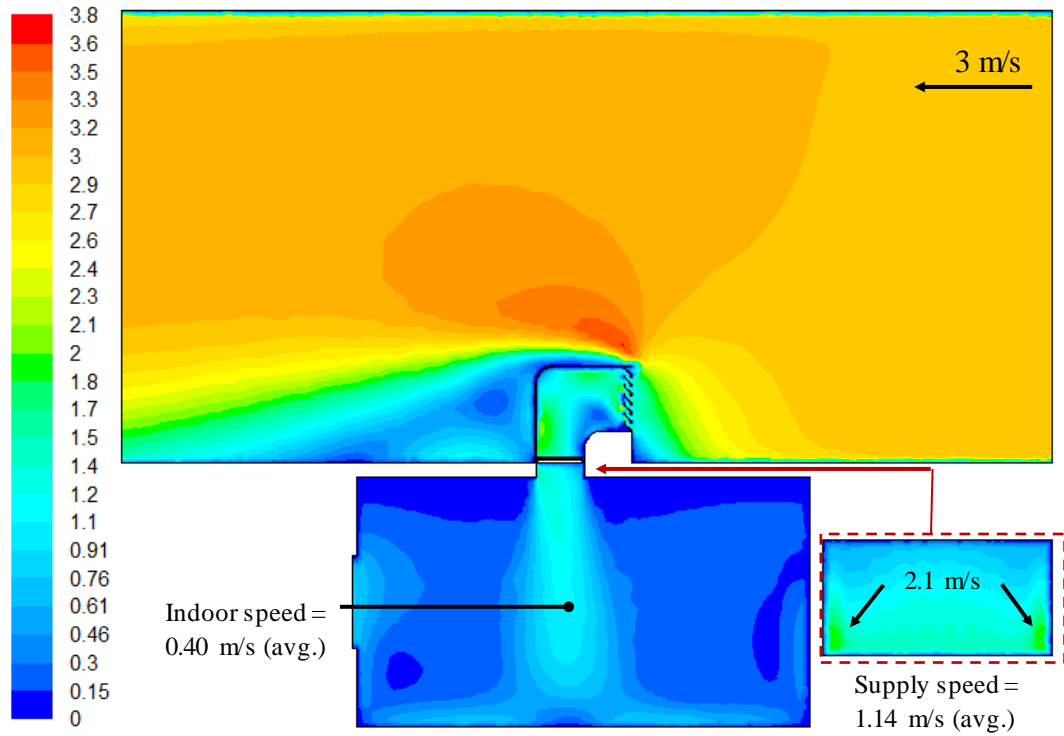
Figure 5.29 depicts the micro-macro climate fluid domain and the boundary locations for the inlet and outlet. The streamlines shows the temperature of the airflow flowing in and out of the wind tower systems.



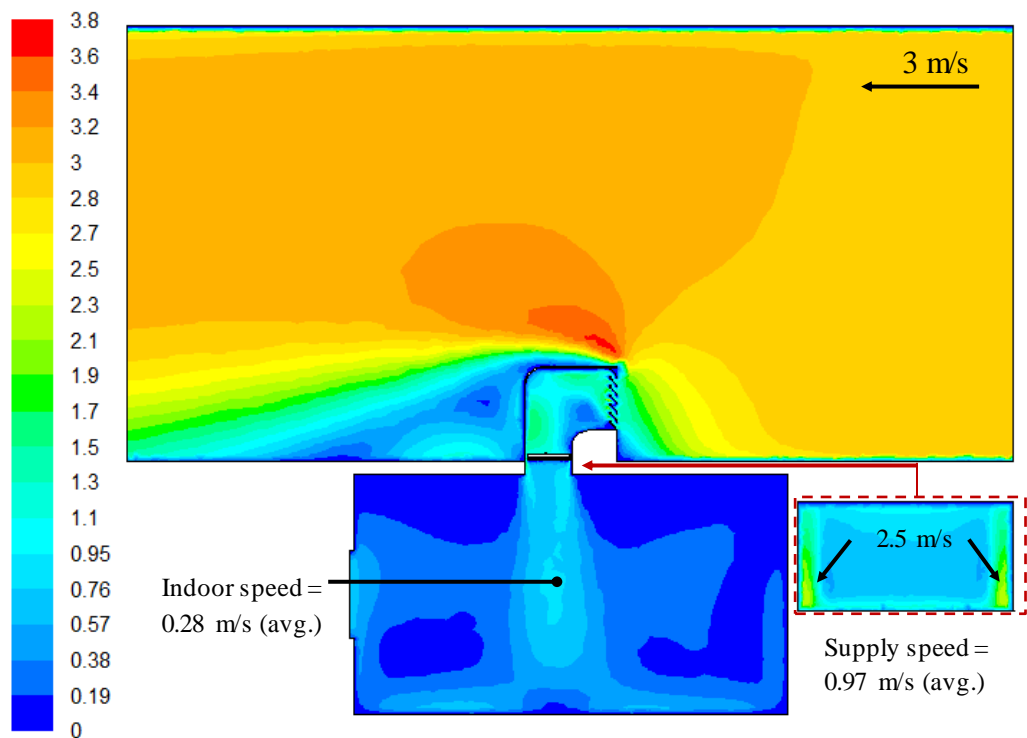
**Figure 5.29** Streamline representing the temperature distribution inside the test room with a heat transfer device integrated wind tower (configuration 2).

Figure 5.30 shows the air flow distribution inside the test rooms with the heat transfer device integrated one-sided wind tower. At an inlet velocity of 3 m/s, the average velocity at the wind tower diffuser was 1.14 m/s while the average velocity in the microclimate was obtained at 0.40 m/s. As observed from the supplementary contour plane inside the diffuser section, the heat transfer devices redirected some of the flow to the sides of the channel accelerating the flow up to 2.1 m/s.

The simulation results in Figure 5.31 confirmed that the indoor airflow speed was significantly reduced following the addition of heat transfer devices with smaller spacing inside the wind tower channel. The average indoor velocity was 30% lower compared to the first configuration.

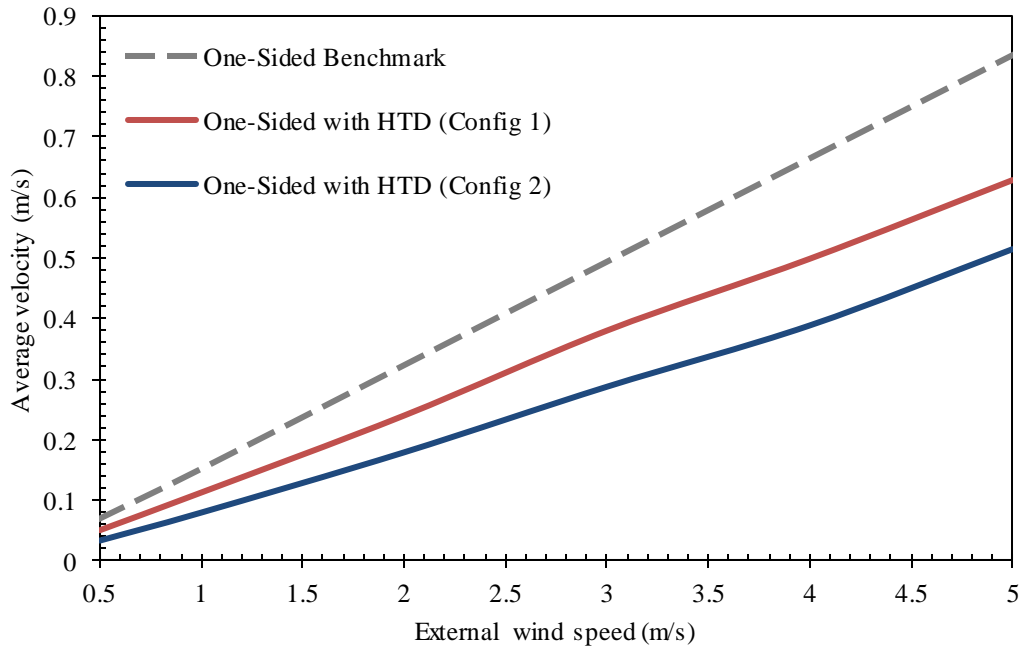


**Figure 5.30** Velocity contour plot of a cross sectional plane in the test room with an inlet velocity of 3 m/s (horizontal HTD Configuration 1).



**Figure 5.31** Velocity contour plot of a cross sectional plane in the test room with an inlet velocity of 3 m/s (horizontal HTD Configuration 2).

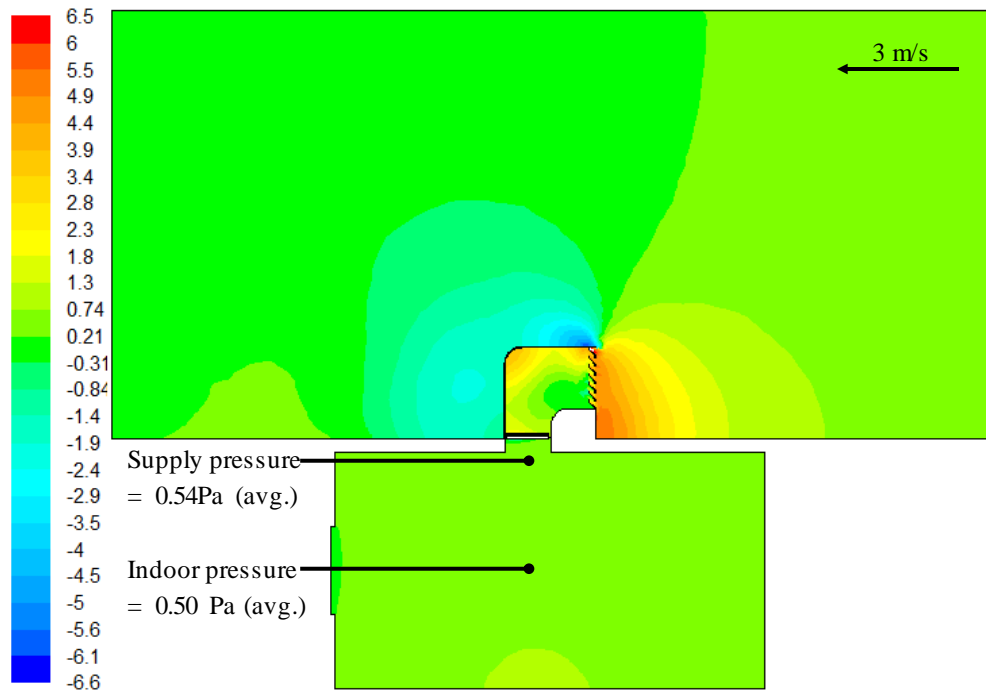
Figure 5.32 shows a comparison between the average indoor air flow speed at various external wind speeds. The average indoor air speed was reduced by up to 27.6 % following the addition of the vertical HTD configuration 1 and by up to 52 % following the addition of the vertical HTD configuration 2.



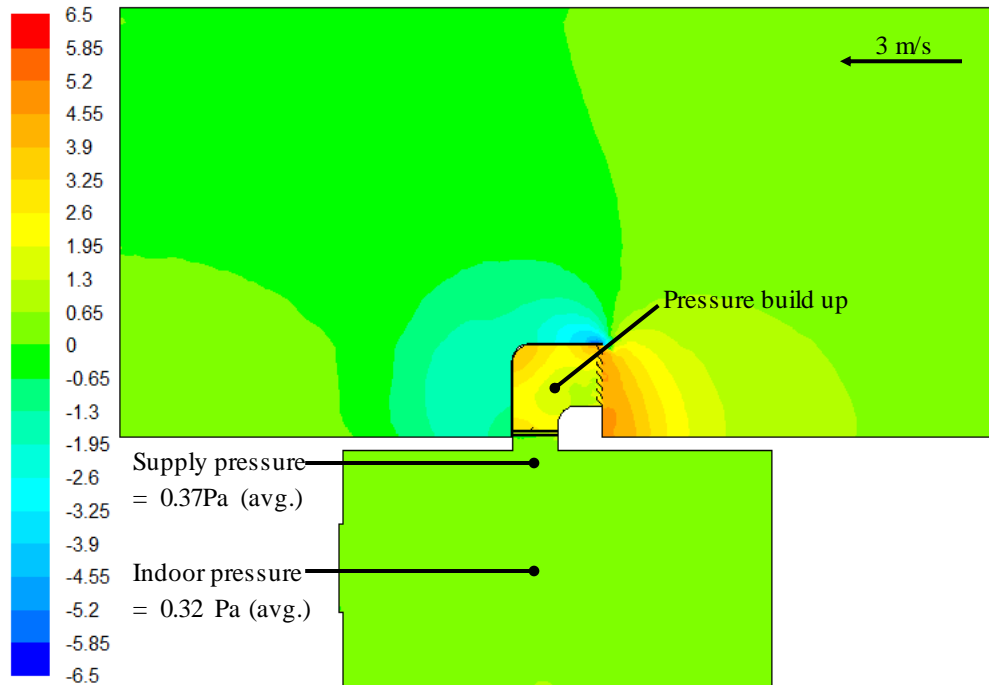
**Figure 5.32** Comparison between the average indoor air flow speed at various external wind speeds (Horizontal HTD Config 1 and 2).

Figure 5.33 displays the static pressure contour of the cross-sectional plane inside the test room with a one-sided wind tower integrated with the heat transfer device configuration 1. The highest pressure was obtained upstream of the louvres with a maximum value of 5.5 Pa. Negative pressure was observed at the leeward and upper side of the wind tower with a minimum value of -6.6 Pa. The average pressure inside the microclimate was 0.50 Pa.

As expected, the reduction of the supply airflow inside the test room (Figure 5.32) also reduced the indoor air pressure (Figure 5.34) by approximately 36 %. A higher pressure drop was observed between the upstream (2.6 Pa) and downstream (0.37 Pa) of the heat transfer device arrangement with reduced spacing.

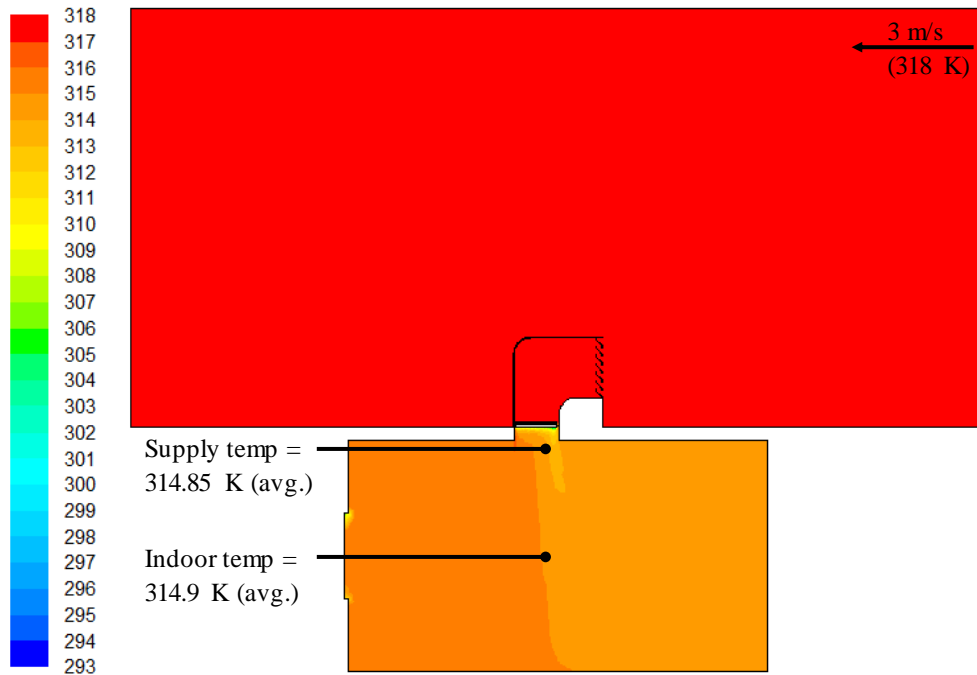


**Figure 5.33** Static pressure contour plot of a cross sectional plane in the test room with an inlet velocity of 3 m/s (HTD Configuration 1).

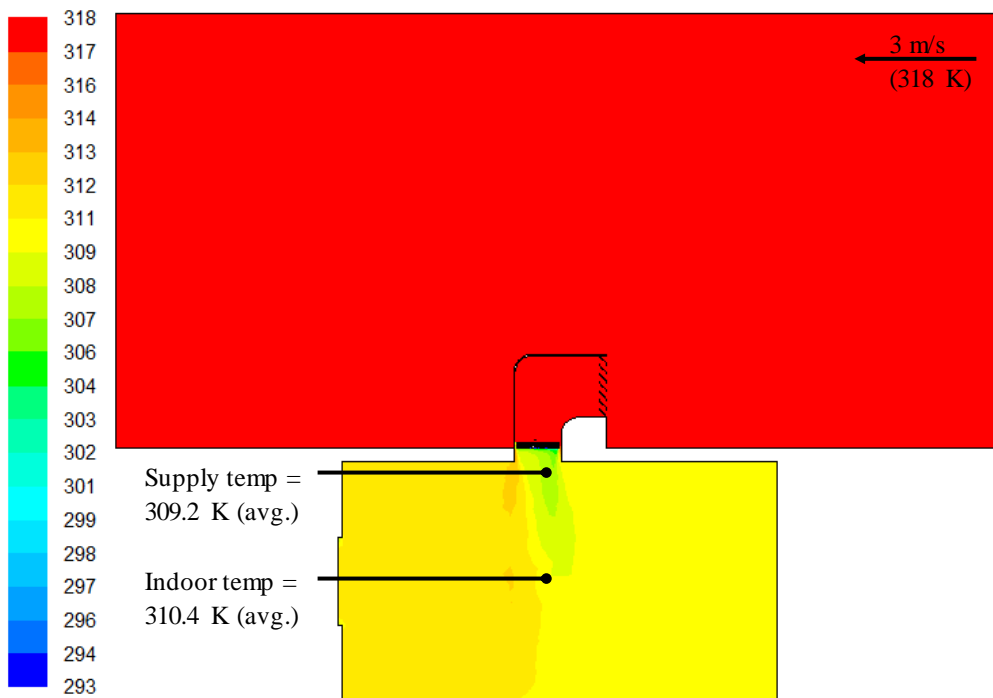


**Figure 5.34** Pressure contour plot of a cross sectional plane in the test room with an inlet velocity of 3 m/s (HTD Configuration 2).

Figure 5.35 and 5.36 compares the thermal performance of the wind tower with the horizontal heat transfer device configuration 1 and 2.

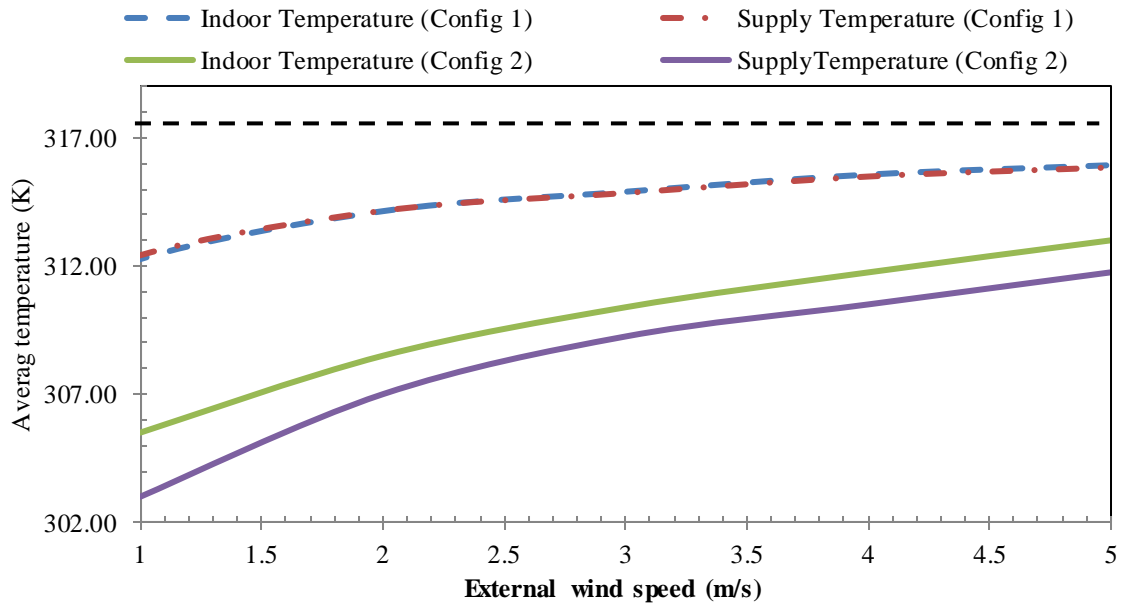


**Figure 5.35** Temperature contour plot of a cross sectional plane in the test room with an inlet velocity of 3 m/s (horizontal HTD Configuration 1).



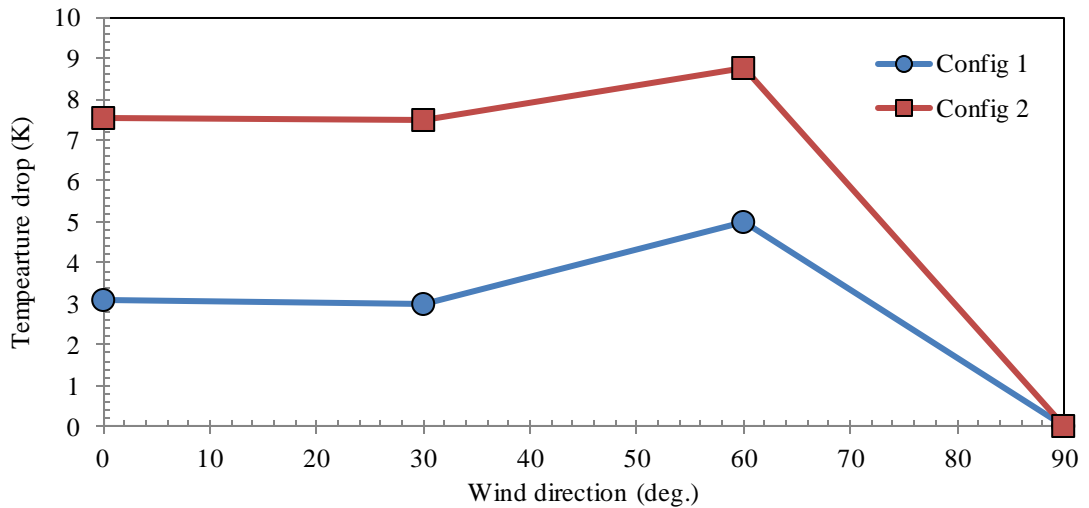
**Figure 5.36** Temperature contour plot of a cross sectional plane in the test room with an inlet velocity of 3 m/s (horizontal HTD Configuration 2).

Figure 5.37 shows the effect of the increasing external wind speeds (1 to 5 m/s) on the thermal performance of the heat transfer devices integrated wind tower. As observed, the cooling performance of the heat transfer devices decreases as the air flow speed through it increases. At 5 m/s outdoor speed, the air temperature was reduced by 2.1 (config 1) – 5 K (config 2). Significant reduction in temperature was observed at lower wind speeds (1 – 2 m/s), up to 4 – 6 K (config 1) and 9.5 – 12 K (config 2).



**Figure 5.37** Effect of varying external wind speed on the supply and indoor temperature.

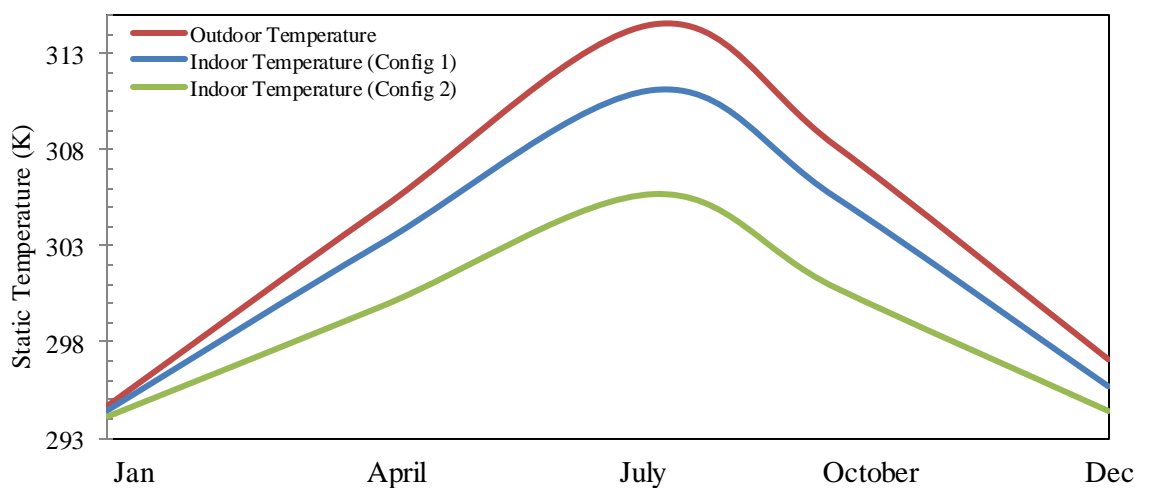
Figure 5.38 shows the effect of varying wind direction on the thermal performance of a one-sided wind tower with heat transfer devices. As observed, exceeding the wind angle over the transition angle ( $> 70^\circ$ ) causes the temperature drop to reduce continuously to its minimum value which is due to the changes in the flow direction. Maximum temperature reduction was achieved at  $60^\circ$  wind angle when regions of vortices or reticulations were present inside the channel which reduced the air supply speed and increases the rate of heat transfer.



**Figure 5.38** Effect of varying external wind direction on the temperature reduction.

In order to investigate the performance of the wind tower system under different conditions, the CFD model was coupled with the weather data (detailed in Chapter 3, Section 3.3.3). The weather data provided the inlet boundary conditions for the wind speed, temperature and relative humidity simulating a hot and humid climatic condition. Figure 5.38 summarises the results for temperature, velocity and humidity.

The maximum temperature reduction was achieved during the month of July when the outside temperature was at 314.5 K and wind speed at 3.8 m/s. The lowest internal airflow velocity measured inside the test room was during the least windy month of October, with an average speed 3.2 m/s.



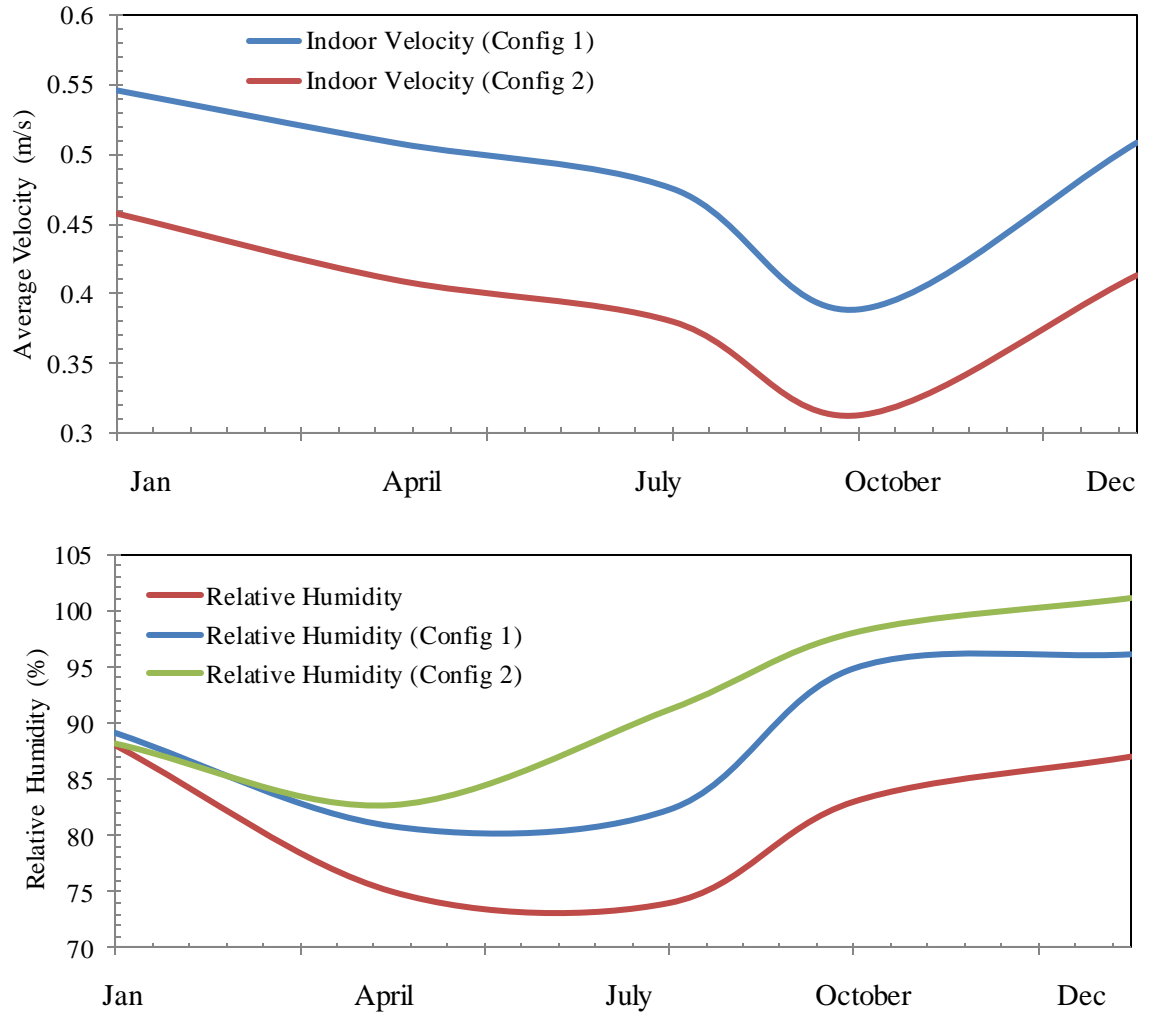


**Figure 5.39** Summary of the results for indoor temperature, velocity and humidity.

Table 5.10 and 5.11 summarises the data obtained from the CFD analysis of the wind tower with the horizontal HTD configuration 1 and 2.

**Table 5.10** Simulation results with the one-sided wind tower with the horizontal HTD (Config 1).

Velocity inlet speed [m/s]	Diffuser supply velocity [m/s]	Average indoor velocity [m/s]	Average indoor pressure [Pa]	Average indoor temperature [K]
0.5	0.17	0.05	0.01	309.78
1	0.38	0.11	0.05	312.27
2	0.78	0.24	0.20	314.14
3	1.14	0.40	0.50	314.90
4	1.61	0.50	0.85	315.57
5	2.02	0.63	1.34	315.93

**Table 5.11** Simulation results with the one-sided wind tower with the horizontal HTD (Config 2)

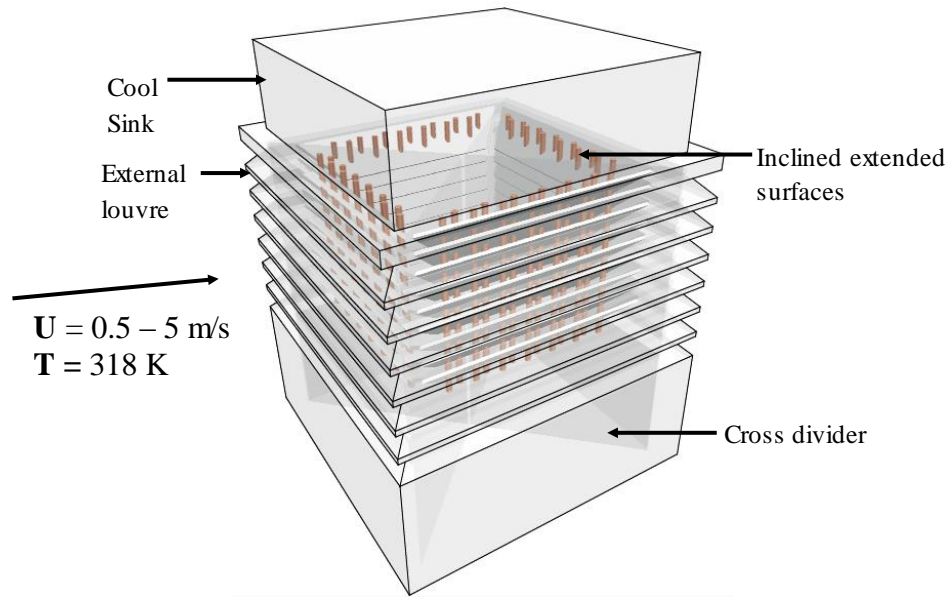
Velocity inlet speed [m/s]	Diffuser supply velocity [m/s]	Average indoor velocity [m/s]	Average indoor pressure [Pa]	Average indoor temperature [K]
0.5	0.13	0.03	0.01	301.83
1	0.29	0.08	0.03	302.56
2	0.65	0.18	0.13	305.10
3	0.97	0.29	0.32	306.76
4	1.39	0.39	0.59	308.74
5	1.68	0.51	0.98	309.44

## 5.4 Heat transfer device (HTD) integrated wind tower with extended surfaces

Following the successful investigation of the effect of the addition of heat transfer devices, different arrangements and various external conditions on the cooling potential of the wind tower the next step was to maximise the cooling performance of the system by employing extended surface. In order to directly compare the results with simulation benchmarks, all the model's volumes (micro-macro climate) were maintained.

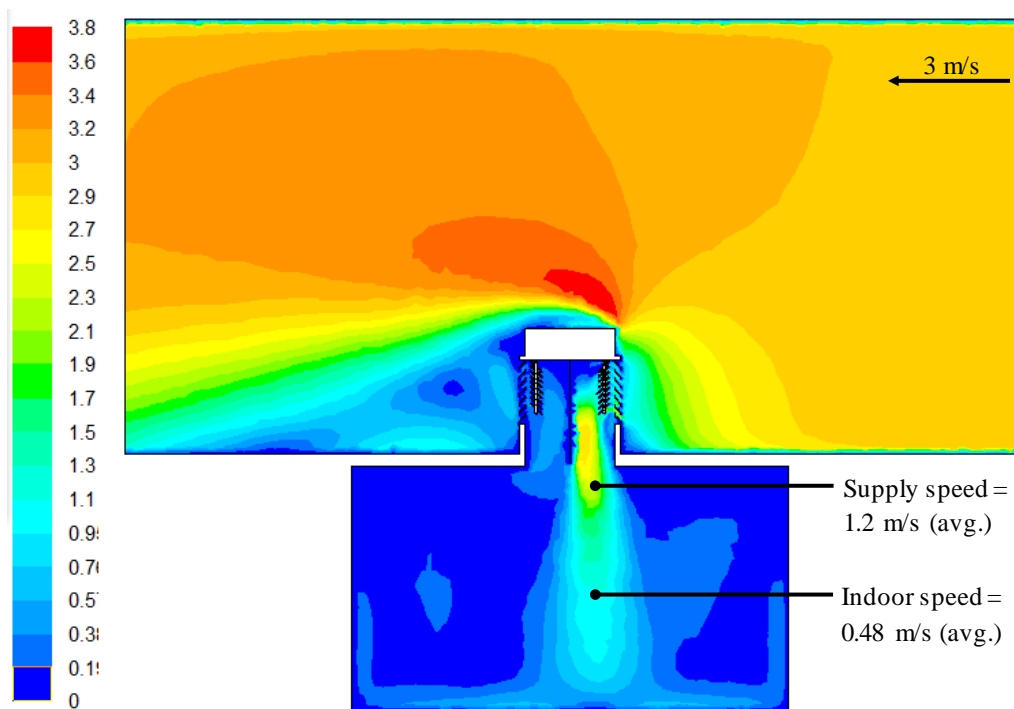
### 5.4.1 Vertical HTD arrangement with extended surfaces

Figure 5.40 illustrates the four sided wind tower with heat transfer devices geometry and extended surfaces (detailed in Chapter 3). Tests were performed for various external wind speeds (0.5 – 5 m/s). A constant inlet temperature of 318 K was set to replicate the outdoor environment. In order to cool the induced air, surface temperature of 293 K (operating temperature) was applied to the heat transfer devices walls.



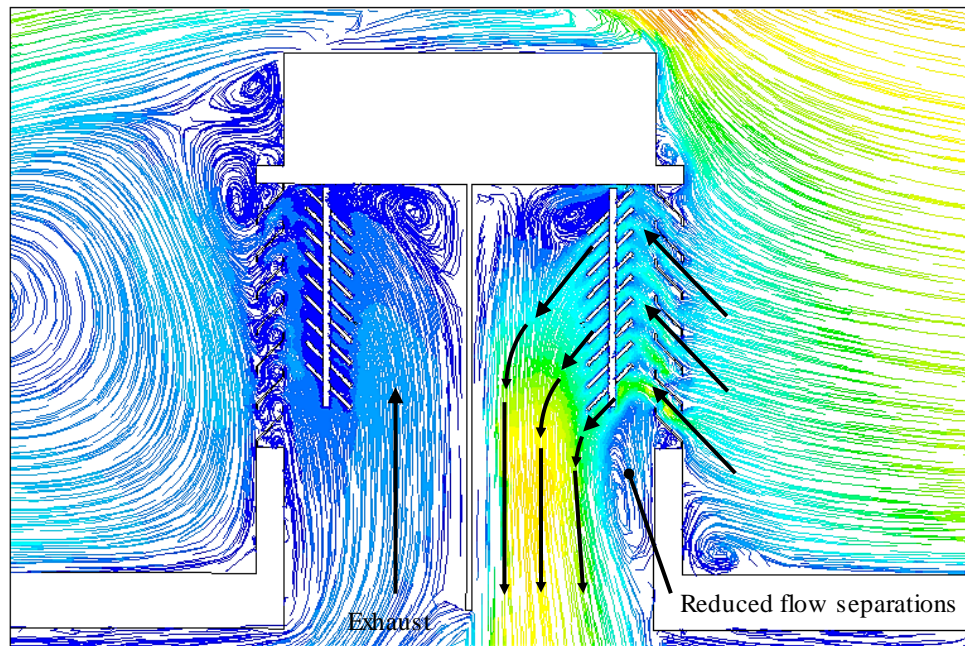
**Figure 5.40** Four-sided wind tower with vertical HTD arrangement and extended surfaces.

Figure 5.41 illustrates the velocity contour of the airflow distribution inside the test room. At an inlet velocity of 3 m/s, the average velocity at the wind tower diffuser was 1.2 m/s while the average velocity in the microclimate was obtained at 0.48 m/s.



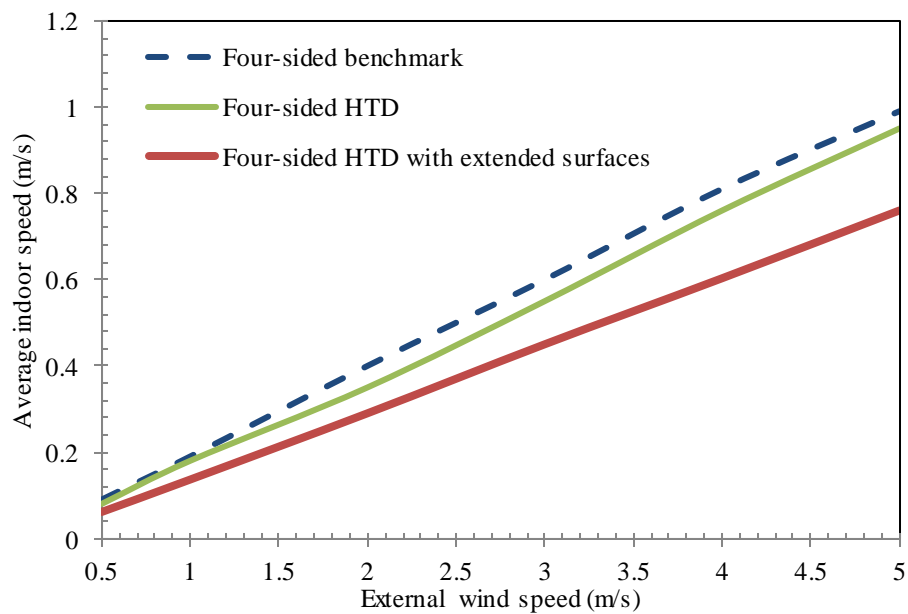
**Figure 5.41** Velocity contour plot of a cross sectional plane in the test room with a four-sided wind tower with finned heat transfer devices.

Figure 5.42 displays the flow inside the wind tower with the vertical heat transfer devices and extended surfaces inclined at 45°.



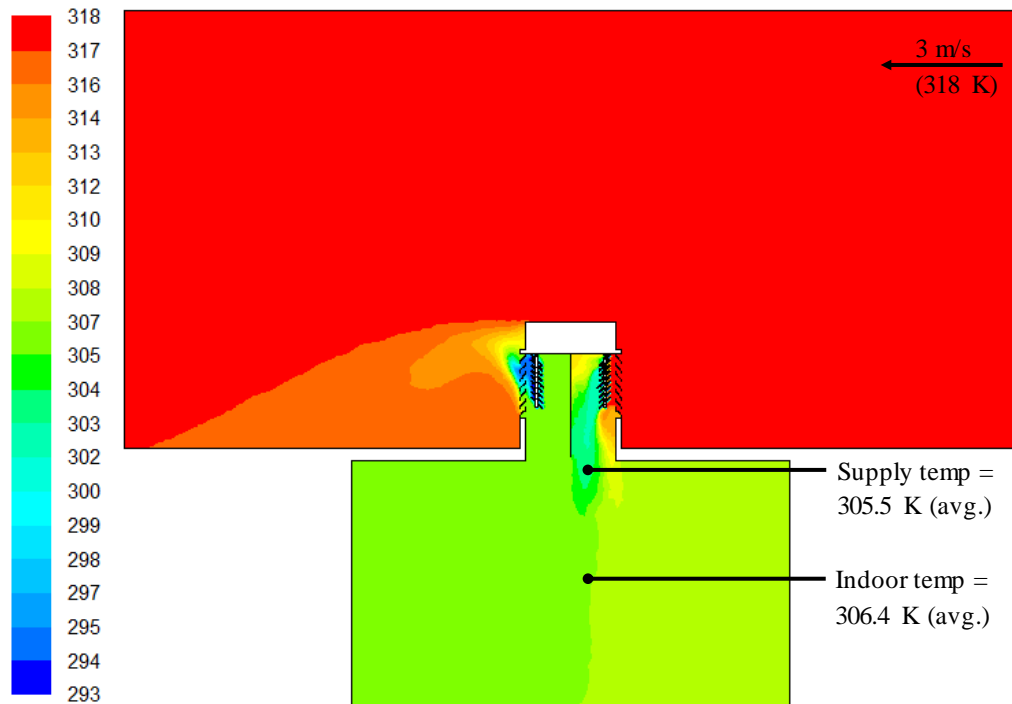
**Figure 5.42** A close-up view of the velocity streamlines inside the wind tower channel.

Figure 5.43 shows a comparison between the average indoor air flow speed at various external wind speeds. The average indoor air speed was reduced by up to 32 % following the addition of the vertical HTD configuration with extended surfaces.



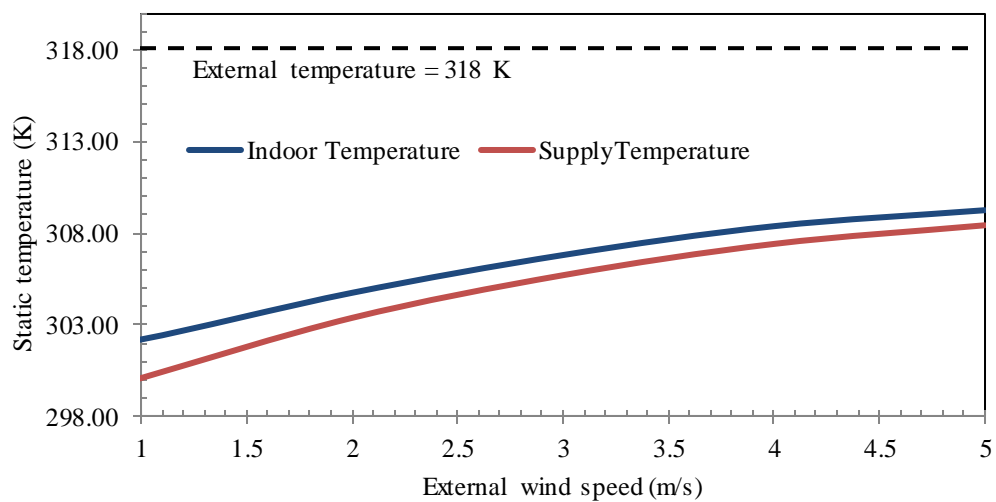
**Figure 5.43** Effect of varying external wind speed on the indoor air flow velocity.

Figure 5.44 illustrates temperature distribution inside the test room with a heat transfer device integrated wind tower system. The average temperature inside the microclimate was 306.4 K with the macro climate temperature set at 318 K.



**Figure 5.44** Temperature contour plot of a cross sectional plane in the test room with a four-sided wind tower with finned heat transfer devices.

Figure 5.45 shows the effect of the increasing external wind speeds (1 to 5 m/s) on the thermal performance of the heat transfer devices integrated wind tower with extended surfaces.



**Figure 5.45** Effect of varying external wind speed on the supply and indoor temperature.

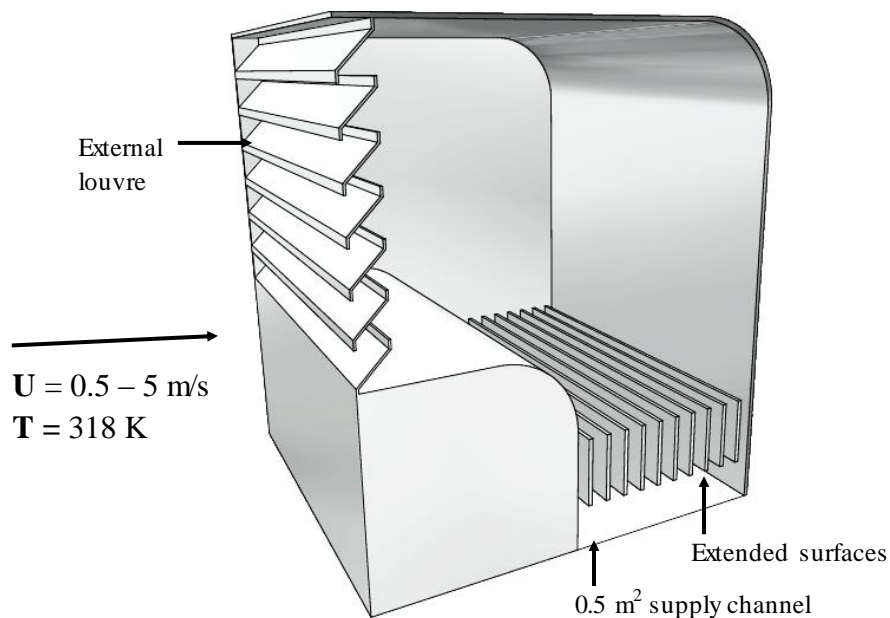
Table 5.12 summarises the data obtained from the CFD analysis of the wind tower with the vertical HTD configuration and extended surfaces

**Table 5.12** Simulation results with the four-sided wind tower with extended surfaces.

Velocity inlet speed [m/s]	Diffuser supply velocity [m/s]	Average indoor velocity [m/s]	Average indoor pressure [Pa]	Average indoor temperature [K]
1	0.40	0.14	0.05	303.20
2	0.83	0.29	0.20	304.74
3	1.20	0.48	0.50	306.40
4	1.69	0.60	0.85	308.37
5	2.12	0.76	1.34	309.08

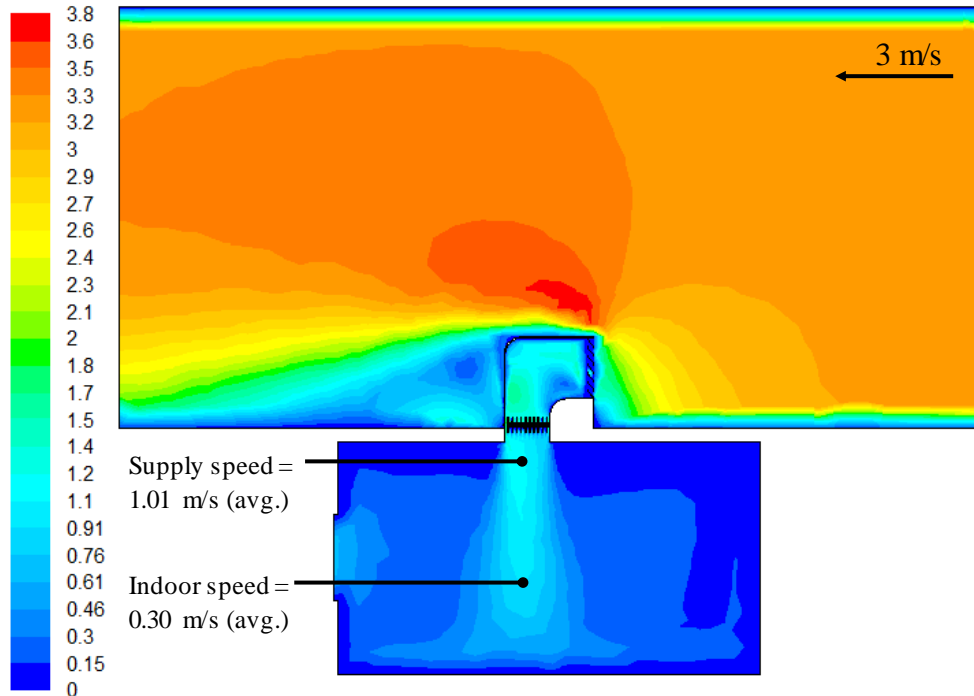
#### 5.4.2 Horizontal HTD arrangement with extended surfaces

Figure 5.46 shows the one-sided wind tower with heat transfer devices geometry and extended surfaces (detailed in Chapter 3). Tests were performed for various external wind speeds (0.5 – 5 m/s). A constant inlet temperature of 318 K was set to simulate the external environment. In order to cool the induced air, wall temperature of 293 K (operating temperature) was applied to the heat transfer devices surfaces.



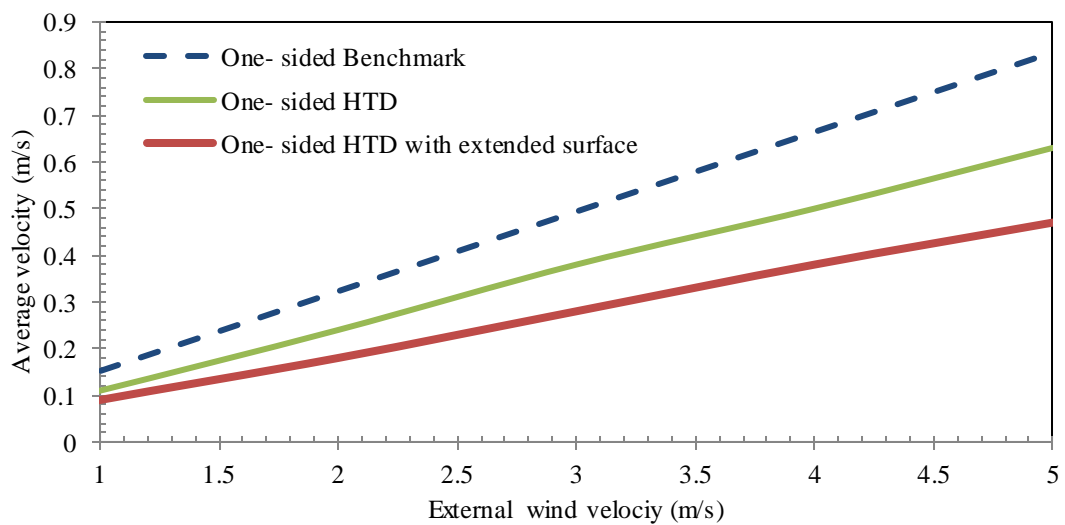
**Figure 5.46** One-sided wind tower with horizontal HTD arrangement and extended surfaces.

Figure 5.47 illustrates the velocity contour of the airflow distribution inside the test room. At an inlet velocity of 3 m/s, the average velocity at the wind tower diffuser was 1.01 m/s while the average velocity in the microclimate was obtained at 0.30 m/s.



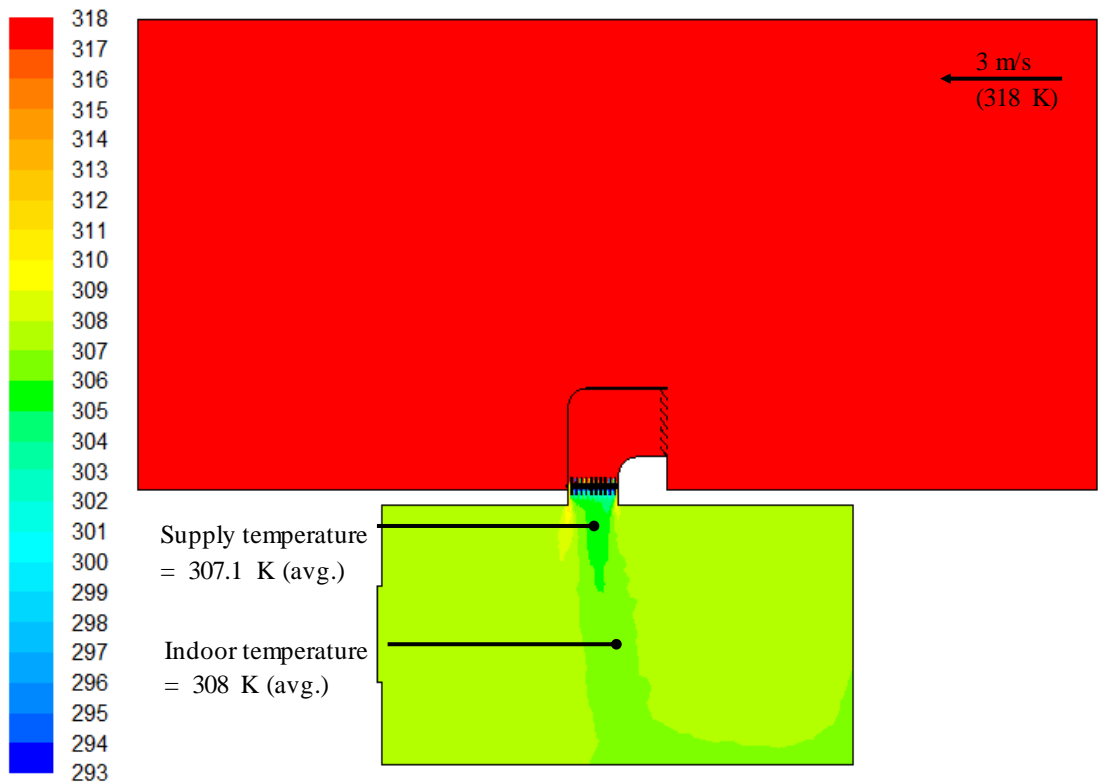
**Figure 5.47** Velocity contour plot of a cross sectional plane in the test room with an inlet velocity of 3 m/s.

The average indoor air speed was reduced by up to 44.2 % following the addition of the horizontal heat transfer devices with extended surfaces (Figure 5.48).



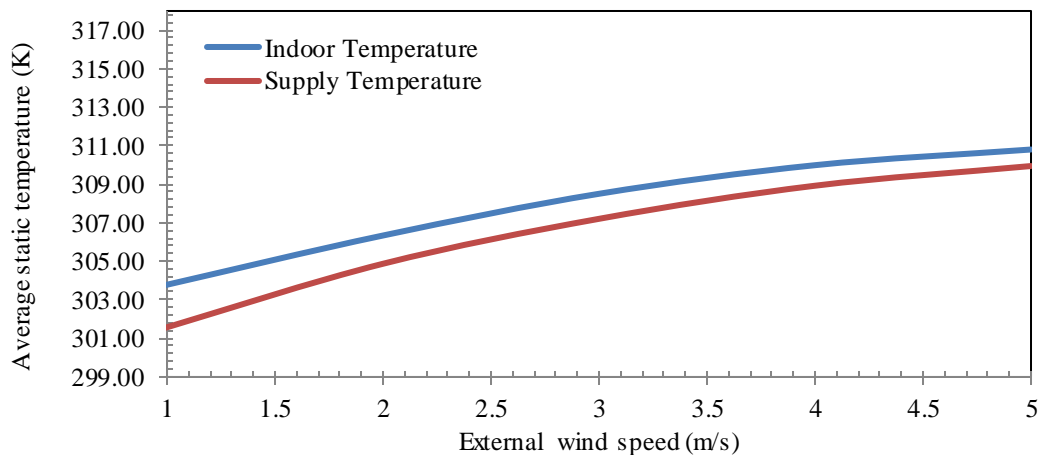
**Figure 5.48** Effect of varying external wind speed on the indoor air flow velocity

Figure 5.49 illustrates temperature distribution inside the test room with a horizontal heat transfer device integrated wind tower system. The average temperature inside the microclimate was 308 K with the macro climate temperature set at 318 K.



**Figure 5.49** Temperature contour plot of a cross sectional plane in the test room with an inlet velocity of 3 m/s.

Figure 5.50 shows the effect of the increasing external wind speeds (1 to 5 m/s) on the thermal performance of the heat transfer devices integrated wind tower with the extended surfaces.



**Figure 5.50** Effect of varying external wind speed on the supply and indoor temperature.

Table 5.13 summarises the data obtained from the CFD analysis of the wind tower with the horizontal HTD configuration and extended surfaces

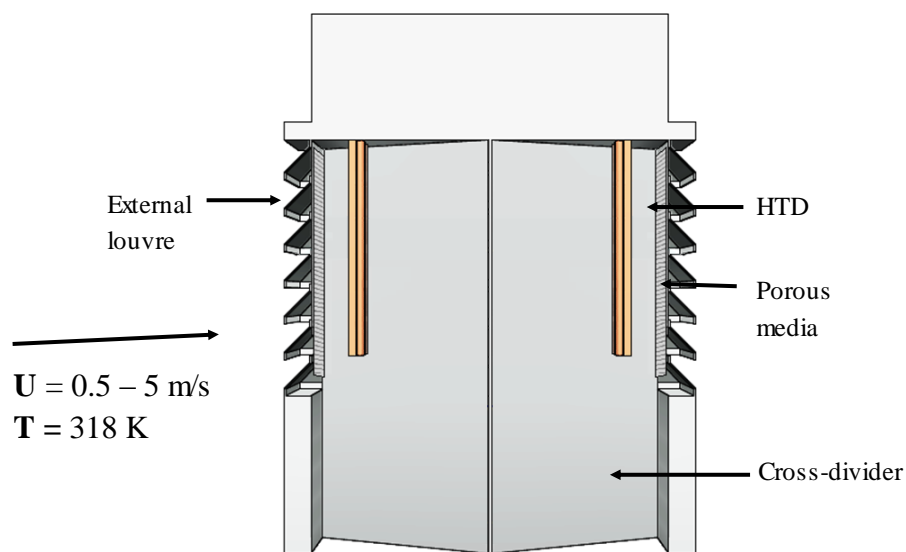
**Table 5.13** Simulation results with the one-sided wind tower with extended surfaces.

Velocity inlet speed [m/s]	Diffuser supply velocity [m/s]	Average indoor velocity [m/s]	Average indoor pressure [Pa]	Average indoor temperature [K]
0.5	0.15	0.04	0.01	303.05
1	0.33	0.09	0.05	303.78
2	0.70	0.18	0.20	306.33
3	1.01	0.30	0.50	308.00
4	1.42	0.38	0.85	309.98
5	1.79	0.47	1.34	310.70

## 5.5 Heat transfer device (HTD) integrated wind tower with porous media

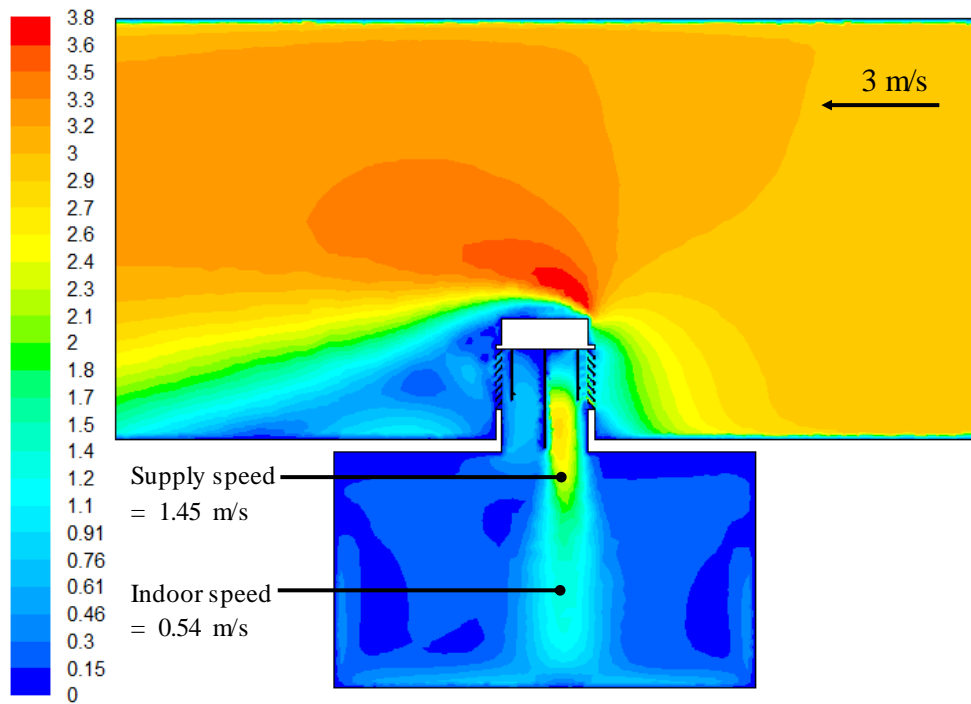
### 5.5.1 Vertical HTD arrangement with porous media

Figure 5.51 illustrates the four sided wind tower with heat transfer devices and porous media (detailed in Chapter 3). A constant inlet temperature of 318 K was set to replicate the outdoor environment. In order to cool the induced air, a surface temperature of 293 K (operating temperature) was applied to the heat transfer devices walls. The porous media was modelled as a fluid volume and was set as a porous zone in FLUENT with a porosity value of 0.5.



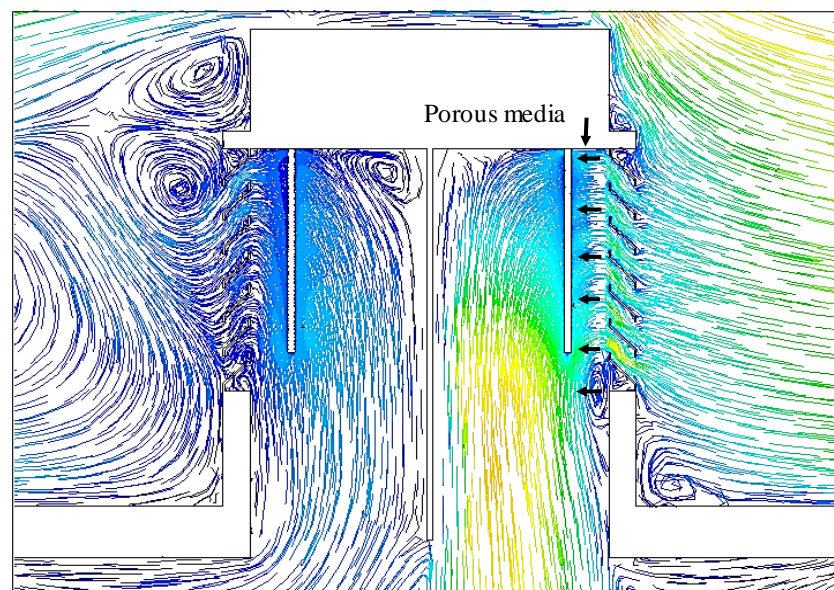
**Figure 5.51** Four-sided wind tower with the vertical HTD arrangement and porous media.

Figure 5.52 illustrates the velocity contour of the airflow distribution inside the test room with the vertical HTD wind tower and porous media.



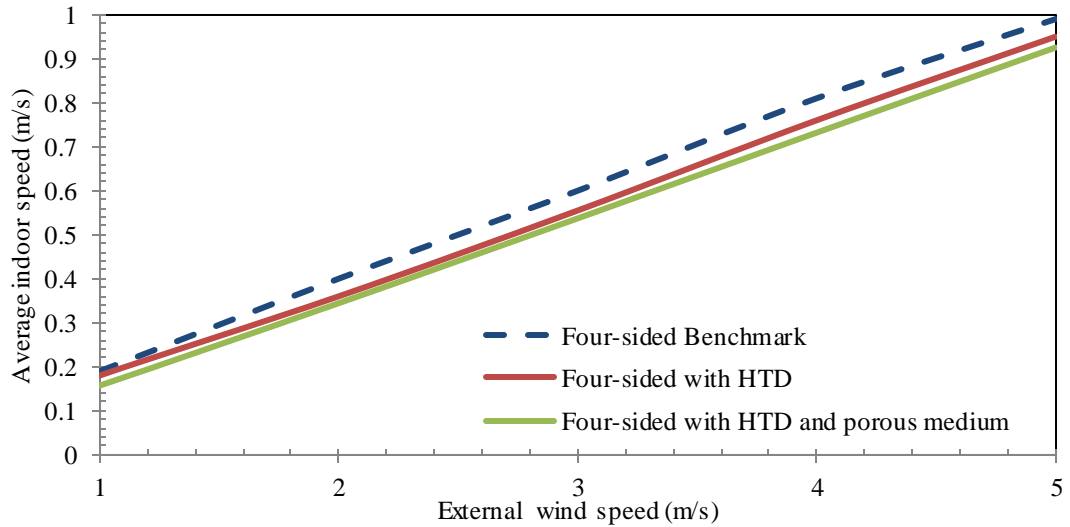
**Figure 5.52** Velocity contour plot of a cross sectional plane in the test room with an inlet velocity of 3 m/s

Figure 5.53 shows a close-up view of the flow inside the wind tower channel with the porous media located between the louvres and the heat transfer devices.



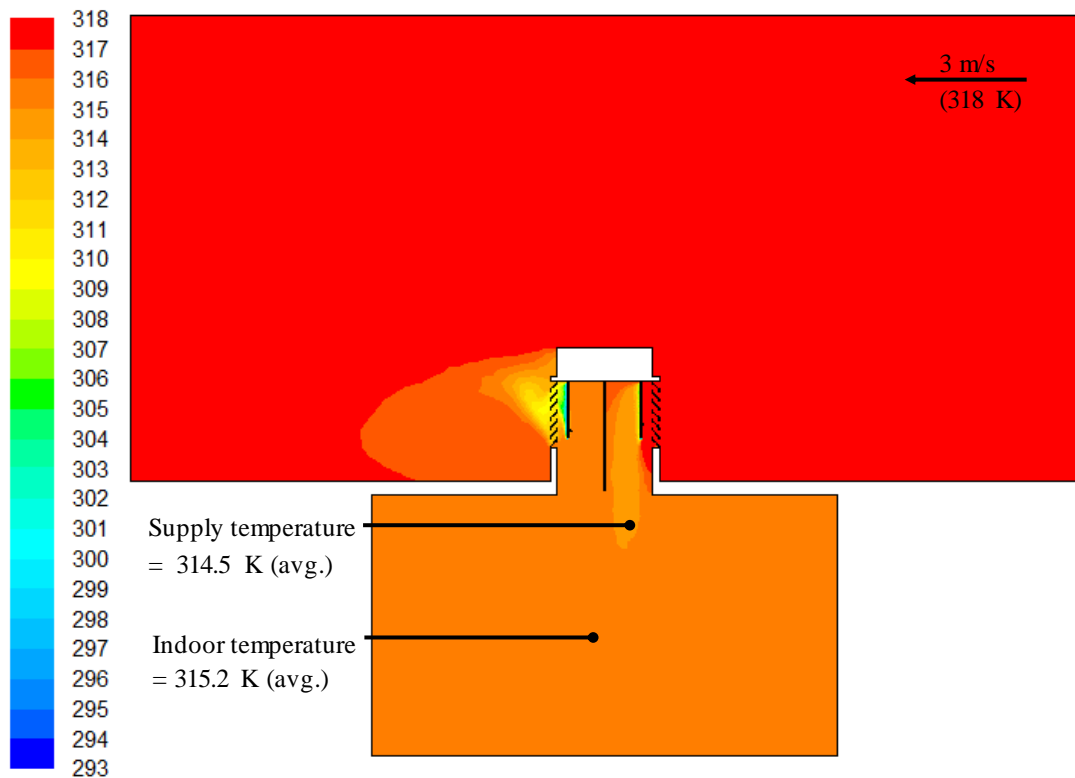
**Figure 5.53** A close-up view of the velocity streamlines inside the wind tower channel.

The average indoor air speed was reduced by 2.5 - 12.7 % following the addition of the porous media to the heat transfer device integrated wind tower (Figure 5.54).



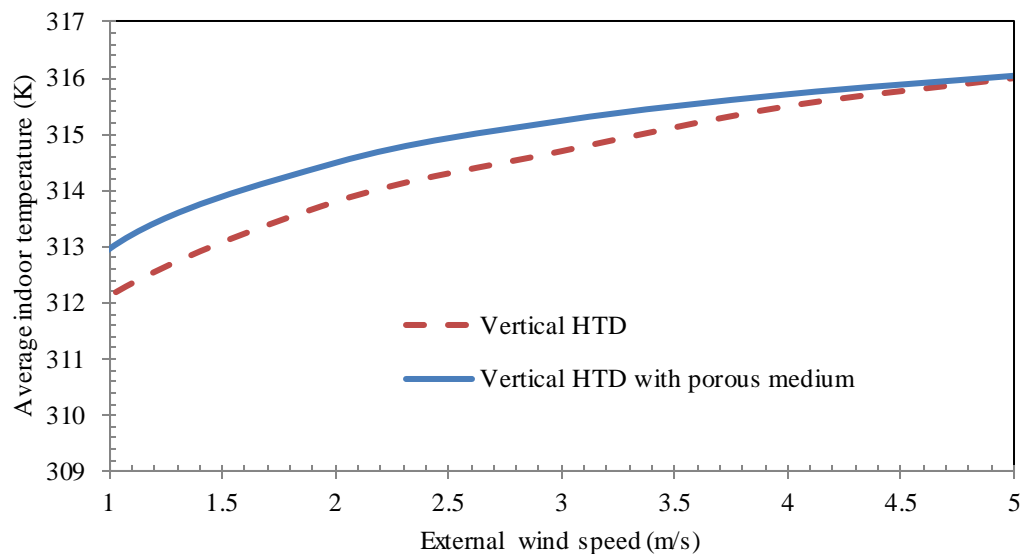
**Figure 5.54** Effect of varying external wind speed on the indoor air flow velocity.

Figure 5.55 illustrates temperature distribution inside the test room with the vertical heat transfer device integrated wind tower system. The average temperature inside the microclimate was 315.2 K with the macro climate temperature set at 318 K.



**Figure 5.55** Temperature contour plot of a cross sectional plane in the test room with an inlet temperature of 318 K.

As seen in the streamline analysis diagram in Figure 5.56, the porous section effectively straightened the flow and improved the velocity distribution across the heat transfer devices. However, the addition of the porous device also reduced the flow turbulence and thus reducing the heat transfer between the airflow and the cylindrical devices. Turbulent flows produce better heat transfer, because it mixes the fluid [Bartlett, 1996]. A slight decrease in cooling performance was observed in the comparison chart in Figure 5.57 essentially at low speeds.



**Figure 5.56** Effect of varying external wind speed on the supply and indoor temperature.

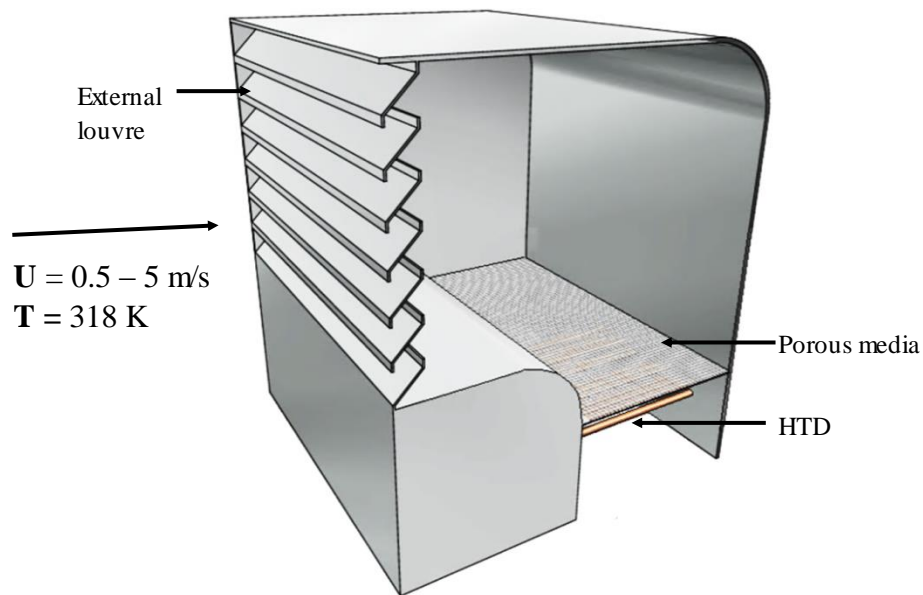
Table 5.14 summarises the data obtained from the CFD analysis of the wind tower with the vertical HTD configuration and porous media.

**Table 5.14** Simulation results with the four-sided wind tower with porous media.

Velocity inlet speed [m/s]	Diffuser supply velocity [m/s]	Average indoor velocity [m/s]	Average indoor pressure [Pa]	Average indoor temperature [K]
0.5	0.20	0.07	-0.07	310.12
1	0.44	0.16	-0.12	312.96
2	0.98	0.34	-0.54	314.49
3	1.45	0.54	-1.26	315.24
4	1.98	0.73	-2.28	315.71
5	2.54	0.93	-3.62	316.04

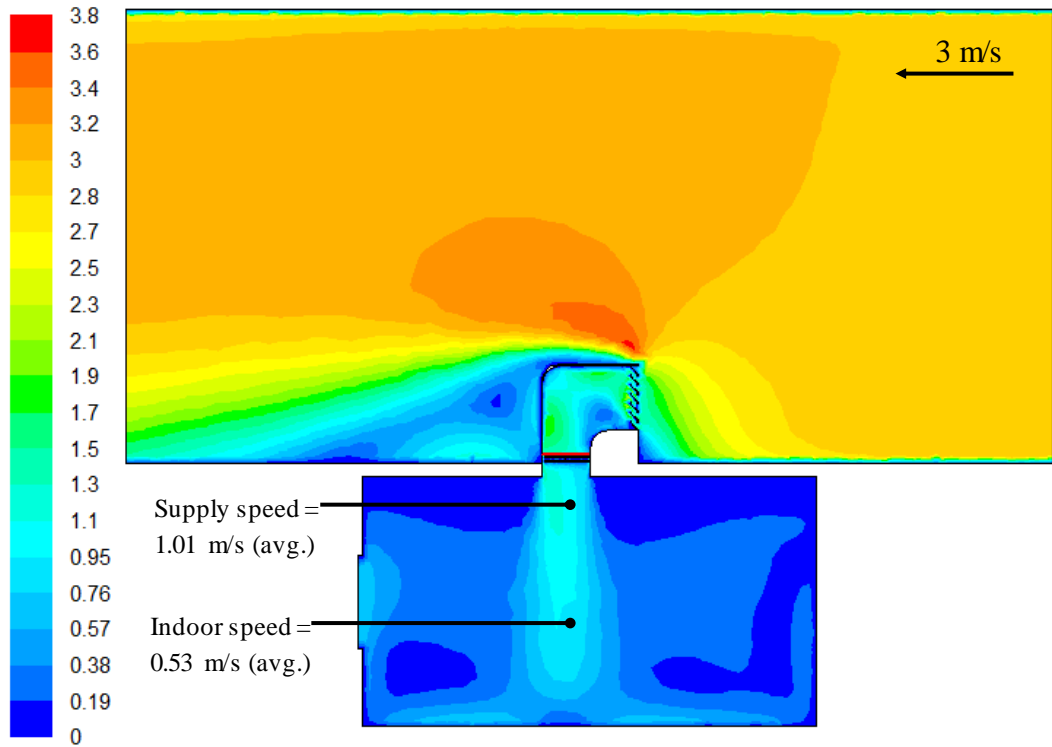
### 5.5.2 Horizontal HTD arrangement with porous media

Figure 5.57 illustrates the one-sided wind tower with heat transfer devices and porous media (detailed in Chapter 3). Tests were performed for various external wind speeds (0.5 – 5 m/s). A constant inlet temperature of 318 K was set to replicate the outdoor environment. In order to cool the induced air, surface temperature of 293 K (operating temperature) was applied to the heat transfer devices walls. The porous media was modelled as a fluid volume and was set as a porous zone in FLUENT with a porosity value of 0.5.



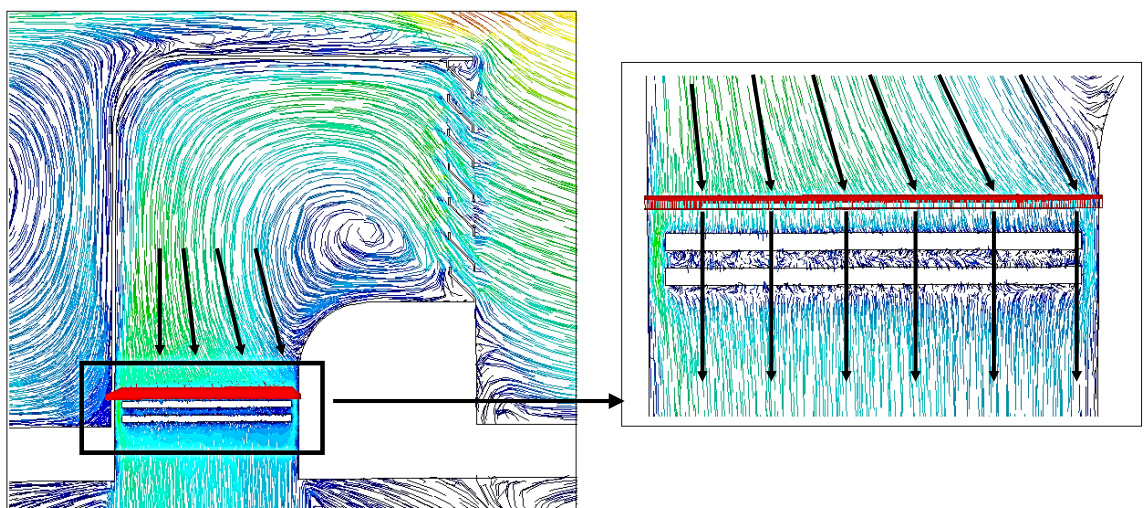
**Figure 5.57** One-sided wind tower with the horizontal HTD arrangement and porous media.

Figure 5.58 illustrates the velocity contour of the airflow distribution inside the test room with the vertical HTD wind tower and porous media.



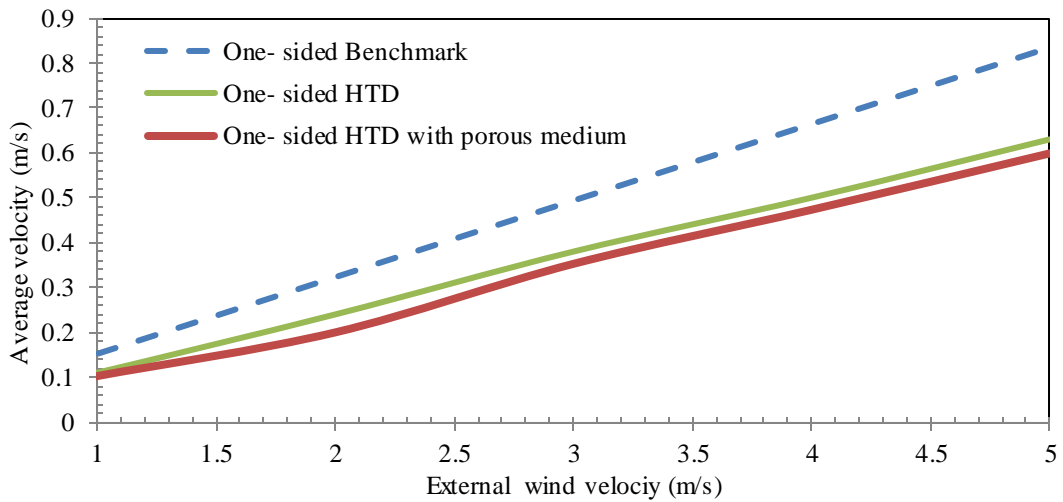
**Figure 5.58** Velocity contour plot of a cross sectional plane in the test room with an inlet velocity of 3 m/s

Figure 5.59 shows a detailed view of the internal of the wind tower channel with the porous media located at the upstream of the heat transfer devices. The porous media section effectively straightened the flow direction and produced an even velocity distribution across the diffuser channel.



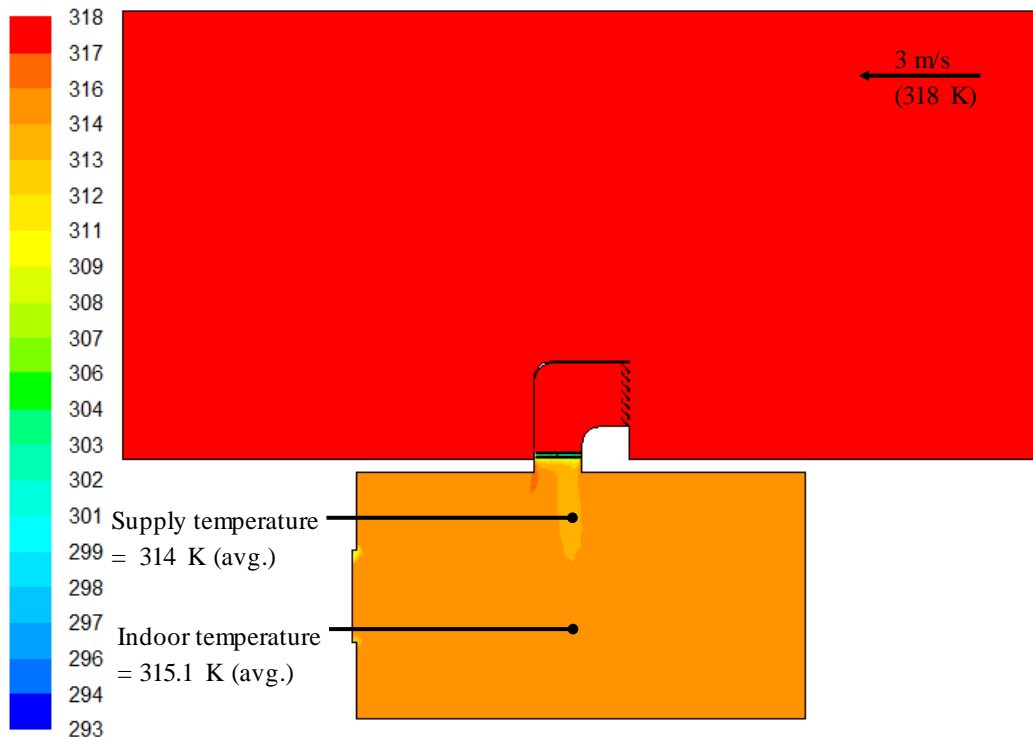
**Figure 5.59** A close-up view of the velocity streamlines inside the wind tower channel.

Figure 5.60 shows a comparison between the average indoor air flow speed at various external wind speeds. The average indoor air speed was reduced by up to 32 % following the addition of the vertical HTD configuration with extended surfaces.



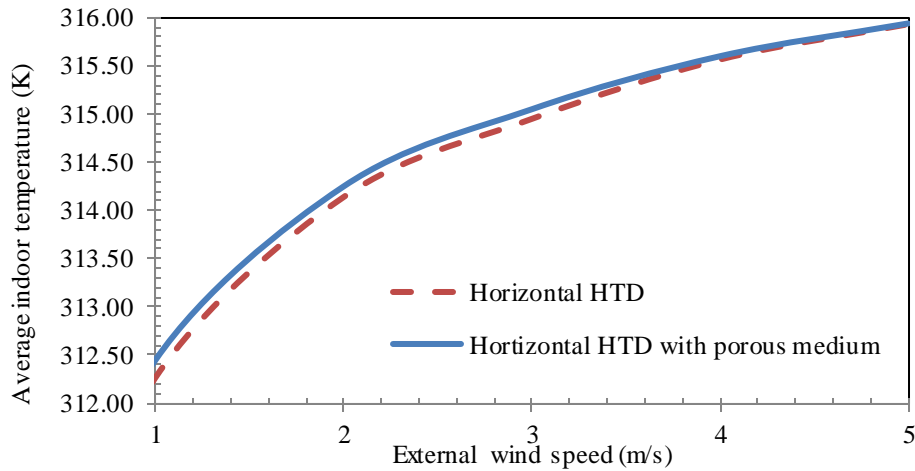
**Figure 5.60** Effect of varying external wind speed on the indoor velocity.

Figure 5.61 illustrates temperature distribution inside the test room with the horizontal heat transfer device integrated wind tower system. The average temperature inside the microclimate was 315.1 K with the macro climate temperature set at 318 K.



**Figure 5.61** Temperature contour plot of a cross sectional plane in the test room with an inlet temperature of 318 K.

Similarly, the cooling performance of the system was slightly reduced following the addition of the porous media. The temperature drop was reduced by up to 0.2 K (Figure 5.62).



**Figure 5.62** Effect of varying external wind speed on the indoor temperature.

Table 5.15 summarises the data obtained from the CFD analysis of the wind tower with the horizontal HTD configuration and porous media.

**Table 5.15** Simulation results with the one-sided wind tower with porous media.

Velocity inlet speed [m/s]	Diffuser supply velocity [m/s]	Average indoor velocity [m/s]	Average indoor pressure [Pa]	Average indoor temperature [K]
0.5	0.15	0.05	0.01	310.00
1	0.34	0.10	0.04	312.45
2	0.75	0.20	0.18	314.25
3	1.07	0.35	0.46	315.05
4	1.45	0.47	0.83	315.60
5	1.82	0.60	1.31	315.94

## 5.7 Thermal comfort modelling

In this study the Predicted Mean Vote (PMV) and the Predicted Percentage Dissatisfied (PPD) were used to evaluate the steady-state thermal comfort performance of a test room model incorporated with the wind tower system. The following cases were selected for the thermal comfort simulation:

- Case 1: Benchmark wind tower model
- Case 2: Wind tower model with heat transfer devices

- Case 3: Wind tower model with heat transfer devices and extended surfaces

The platform for implementing and demonstrating CFD simulations in the thermal comfort study was the FLUENT Airpak package.

### 5.6.1 Benchmark wind tower model

The one-sided wind tower was utilised as a benchmark model for the thermal comfort analysis. The test room geometry remained constant in each CFD model (described in Section 3.9.5). The velocity, temperature and relative humidity flow profiles were obtained from the initial CFD models and used as inlet boundary conditions for the thermal environment. Twelve human models were included in the model. For each, a metabolic rate unit of 1 met (sedentary activities) and clothing insulation level of 1 clo (light clothing) were defined in the program.

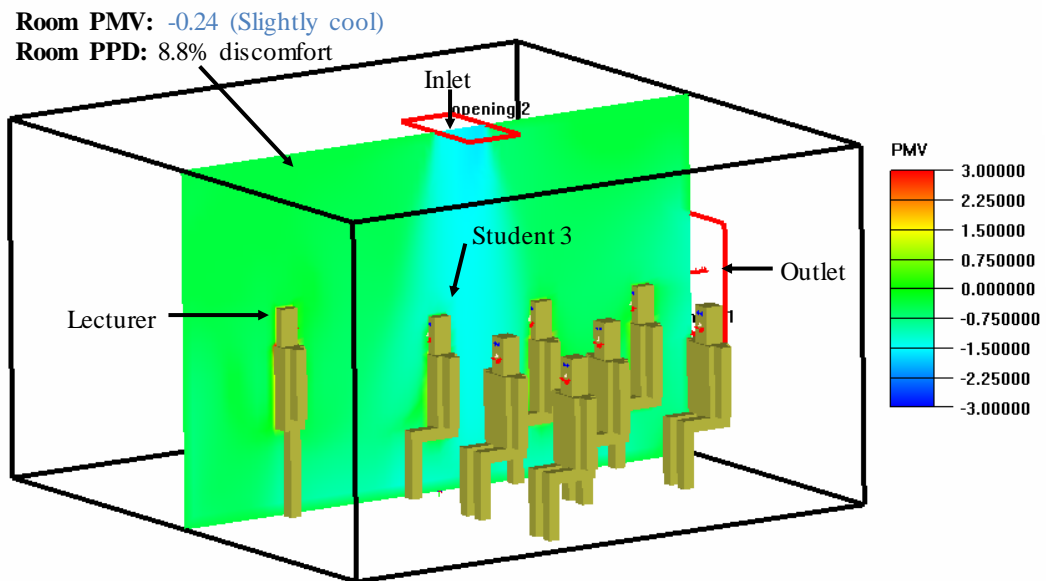
Table 5.16 summarises the thermal comfort analysis of the benchmark wind tower model. The thermal comfort values were measured under simulated summer (hottest month) and winter conditions (coldest month). The mean values of all the parameters were within the limits recommended in [ISO 7730, 2005] excluding the benchmark model (no cooling device) with air temperatures going up to 314.5 K during summer. This has exceeded the limit of the range recommended in the standard. The PMV index cannot accurately describe the comfort during summer but it can predict the increase or the fall of the comfort votes quite realistically [Bodart and Evrard, 2011].

Table 5.16 summarises the thermal comfort analysis of the benchmark wind tower model.

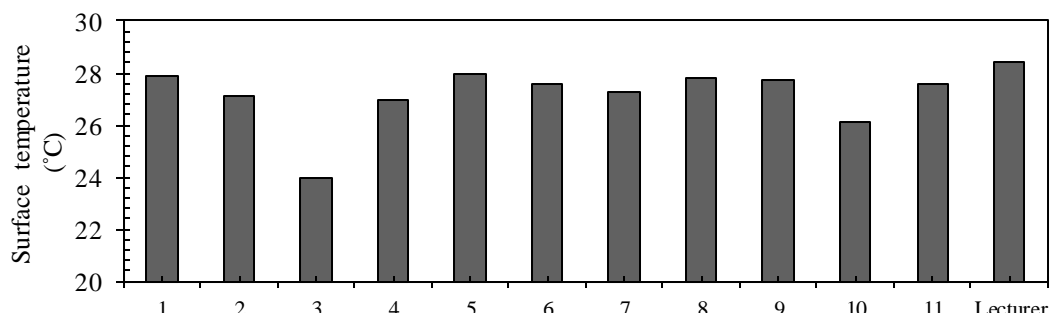
**Table 5.16** Summary of the thermal comfort model analysis case 1.

Parameters	Configuration	
Wind tower	Standard one-sided wind tower	
Test room size	5 x 5 x 3 m	
Number of occupants	12	
Location	Doha, Qatar	
Month	January	July
Outdoor speed	4.4 m/s	3.8 m/s
Outdoor temperature (max average)	294.7 K	314.5 K
Average indoor temperature	294.7 K	314.5 K
Outdoor humidity (max average)	88 %	74 %
Average indoor humidity	88 %	74 %

Figure 5.63 shows the Predicted Mean Vote (PMV) contours of a cross-sectional plane inside the test room with the benchmark wind tower model. The right hand side of the contour plot shows the scale of PMV index ranging between +3 to -3, where the positive value stands for hot feeling and negative for cold feeling, 0 being a neutral value. The contours in the fluid domain are colour coded and related to the CFD colour map. The calculated average PMV value inside the test room was -0.24, while the calculated PPD was 8.8 %. These indicated that the test room was observed to be slightly cool and that approximately 9 % of the occupants were expected to express dissatisfaction with the environment during the month of January. Furthermore, the plot demonstrated that the roof mounted system creates a non-uniform distribution of the thermal comfort in the test room (Figure 5.64). The students (student 3) seated directly below the diffuser of the wind tower and near window (student 10) will experience a different level of comfort than the rest of the occupants in the room.

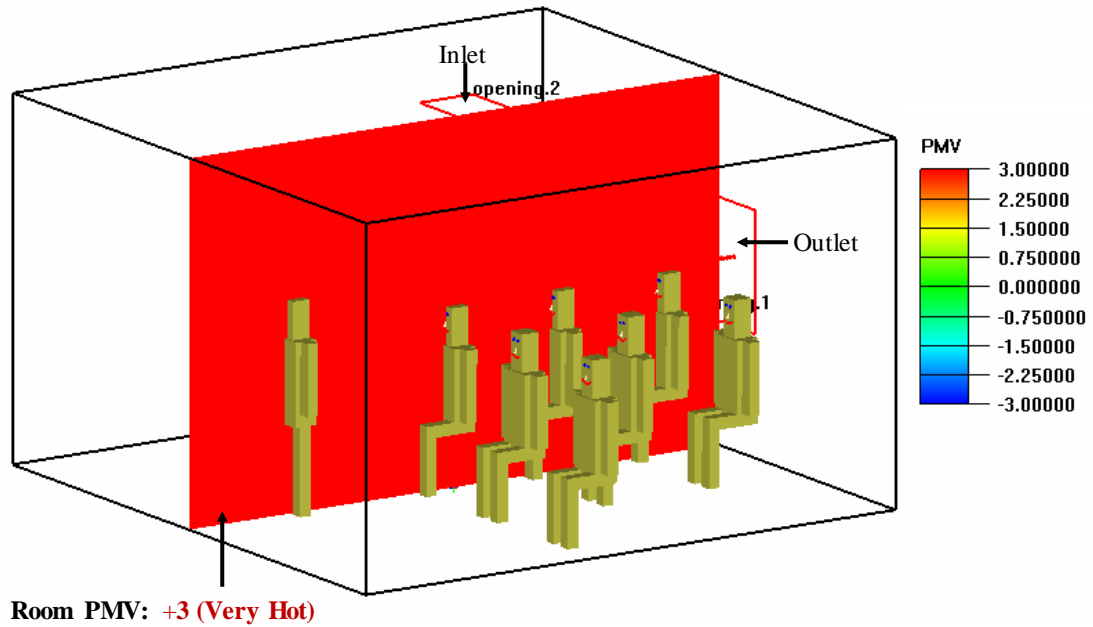


**Figure 5.63** PMV distribution inside the test room with the benchmark model (Winter).



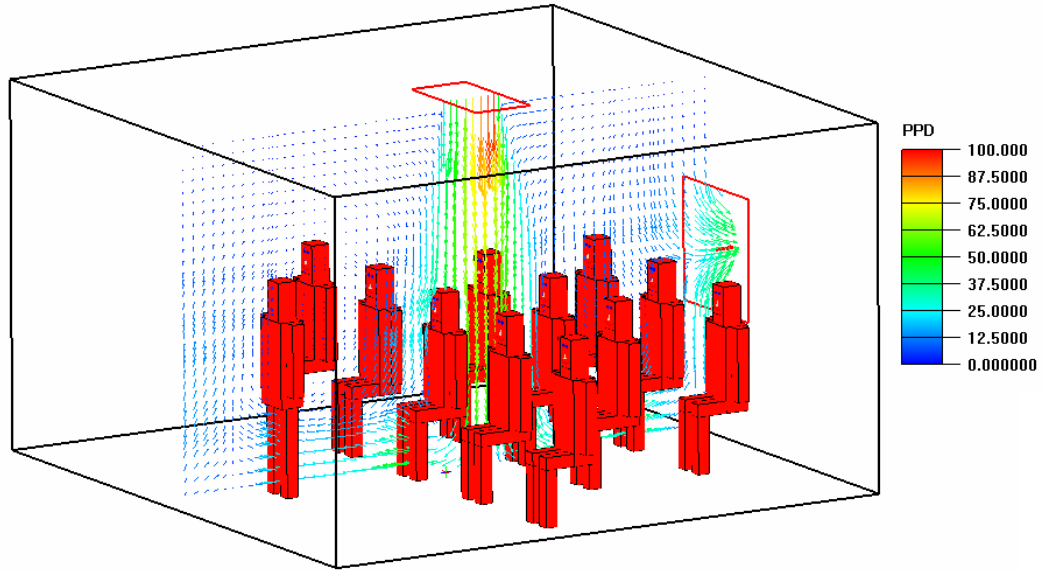
**Figure 5.64** Skin surface temperature of human models.

Figure 5.65 shows the PMV results for the simulation of the same benchmark model under typical extremely hot and humid summer conditions. Average PMV values calculated was +3 (very hot). As expected, a naturally ventilated room combined with very high outdoor temperatures and humidity levels resulted in a very uncomfortable indoor environment.



**Figure 5.65** PMV distribution inside the test room with the benchmark model (Summer).

Figure 5.66 shows the calculated values for the Predicted Percentage Dissatisfied (PPD) surface contours of the human models inside the test room with the standard wind tower model. Based on the PMV and PPD calculation, 100% of the occupants expressed dissatisfaction with the indoor environment. From the velocity vector plot, although good air movement was observed inside the room it didn't improve the occupant's comfort because of very high internal air temperatures.



**Figure 5.66** Predicted Percentage Dissatisfied (Summer).

## 5.6.2 Wind tower with heat transfer device

Table 5.17 summarises the thermal comfort analysis of the wind tower with heat transfer device model.

**Table 5.17** Summary of the thermal comfort model analysis case 2.

Geometry	Specifications	
Wind tower	Horizontal HTD (Config 2)	
Test room size	5 x 5 x 3 m	
Number of occupants	12	
Location	Doha, Qatar	
Month	January	July
Outdoor speed	4.4 m/s	3.8 m/s
Outdoor temperature (max average)	294.7 K	314.5 K
Average indoor temperature	294.2 K	306K
Outdoor humidity (max average)	88 %	71 %
Average indoor humidity	89 %	82 %

Figure 5.67 shows the Predicted Mean Vote (PMV) contours of a cross-sectional plane inside the flow domain simulating the conditions in a test room with a heat transfer device integrated wind tower. The calculated average PMV value inside the test room was -0.5 (slightly cool), while the calculated PPD was 14.8 % indicating that the thermal comfort decreased following the addition of heat transfer devices. The addition of the heat transfer device further lowered the indoor temperature by 0.5 K and increased the

relative humidity level by approximately 1%, all contributed to the reduced indoor comfort level.

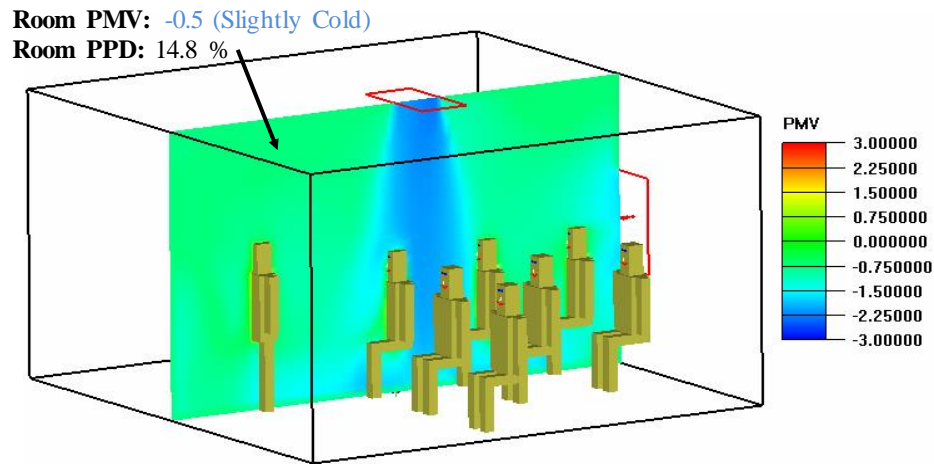


**Figure 5.67** PMV distribution inside the test room with the heat transfer device integrated wind tower (Winter).

Indoor air temperature with the heat transfer device integrated wind tower was 8 K lower than that with the standard wind tower model, leading to a slightly lower predicted mean vote (PMV) during summer conditions. Average PMV inside the room was + 2.8 (Hot) and PPD was 98 % (Figure 5.68). Although the temperature was significantly reduced, the thermal comfort level was still very high due to high indoor relative humidity.

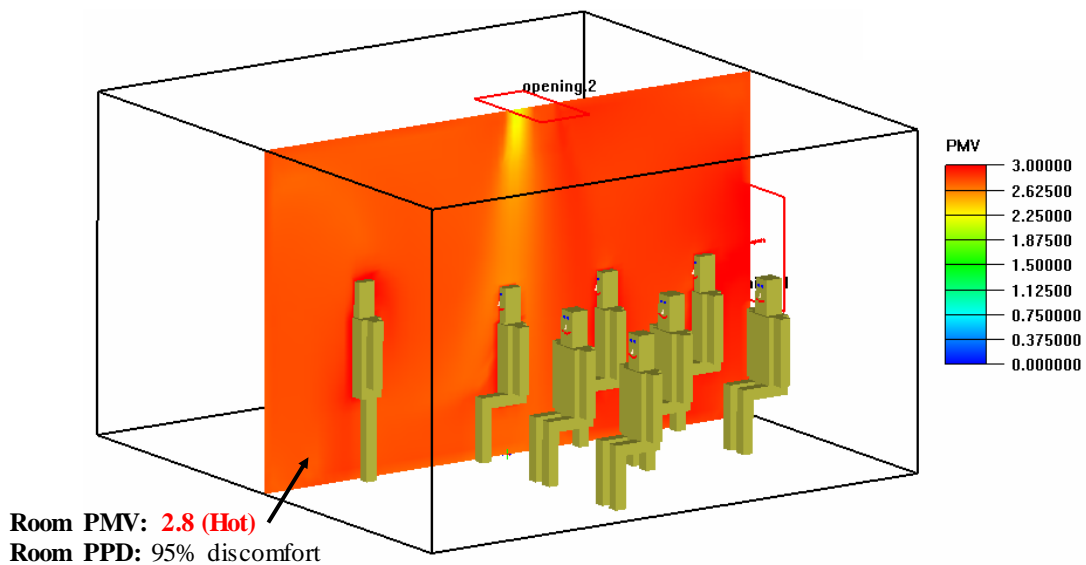


**Figure 5.68** PMV distribution inside the test room with the heat transfer device integrated wind tower (Summer).

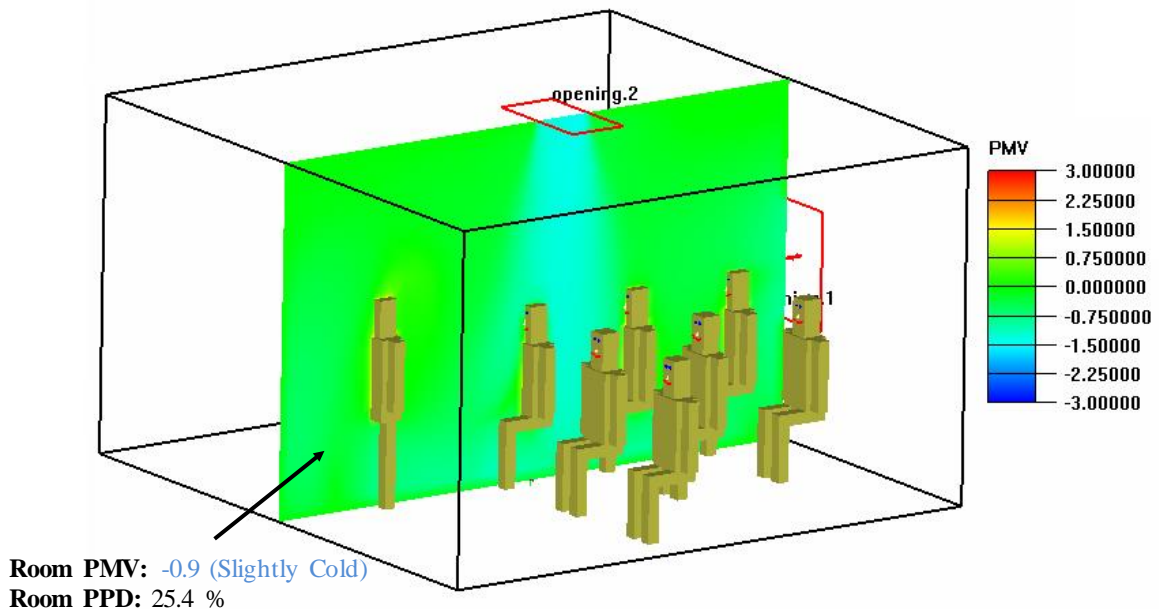
### 5.6.3 Wind tower with heat transfer device and extended surfaces

Table 5.18 summarises the thermal comfort analysis of the wind tower with heat transfer device model and extended surface.

**Table 5.18** Summary of the thermal comfort model analysis case 3.

Geometry	Specifications	
Wind tower	Horizontal HTD with extended surface	
Test room size	5 x 5 x 3 m	
Number of occupants	12	
Month	January	July
Outdoor speed	4.4 m/s	3.8 m/s
Outdoor temperature	294.7 K	314.5 K
Indoor temperature	293.9 K	303 K
Outdoor humidity	88 %	71 %
Indoor humidity	90 %	100 %

Figure 5.69 shows the Predicted Mean Vote (PMV) contours of a cross-sectional plane inside the flow domain simulating the conditions in a test room incorporating heat transfer device integrated wind tower with extended surfaces. The calculated average PMV value inside the test room was -0.9 (cool), while the calculated PPD was 25.4 %.



**Figure 5.69** PMV distribution inside the test room with the finned heat transfer device integrated wind tower (Winter).

Adding the extended surfaces to the heat transfer devices reduced the indoor temperature by up to 303 K, leading to a lower predicted mean vote (PMV) during summer conditions. The calculated average PMV value inside the test room was + 2.5, while the calculated PPD was 92 % (figure 5.70). These indicated that the test room was observed to be hot and that approximately 92 % of the occupants were expected to express dissatisfaction with the environment during the month of July.

As observed, the thermal comfort level was not improved solely by reducing the indoor temperatures. The high relative humidity levels (90 -100 %) had a great impact on the occupants comfort. Simulating the same model with a reduced humidity value (40 %) improved the comfort level (Figure 5.71).

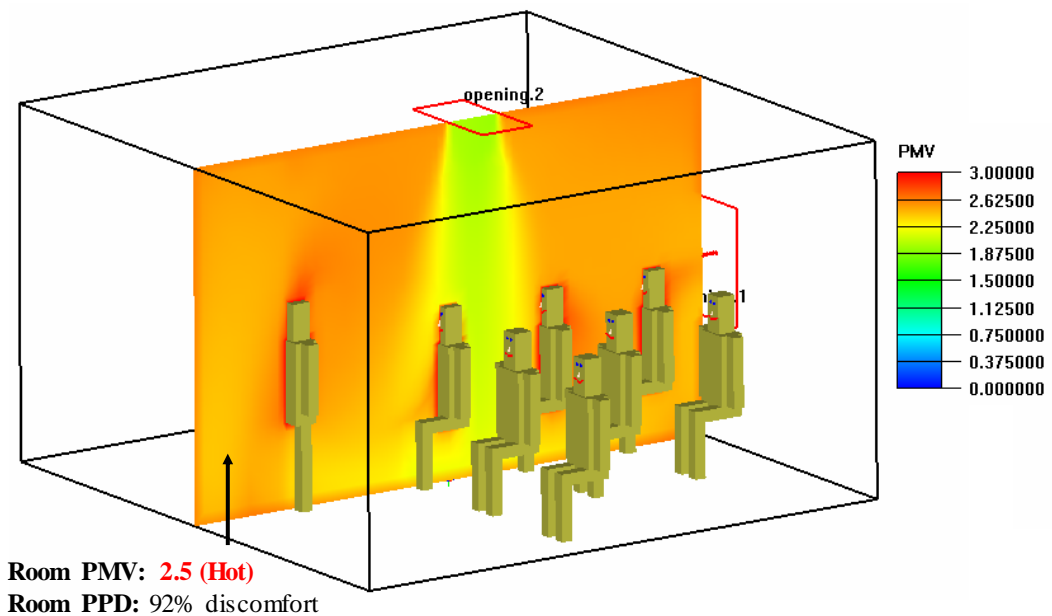


**Figure 5.70** PMV distribution inside the test room with the finned heat transfer device integrated wind tower (Summer, 90 -100% humidity).

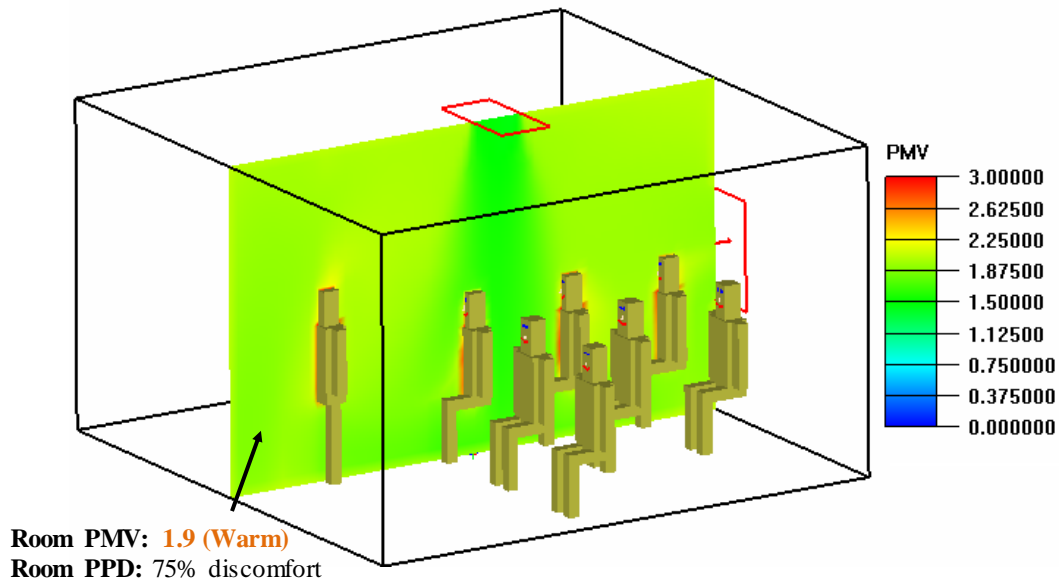


**Figure 5.71** PMV distribution inside the test room with the finned heat transfer device integrated wind tower (Summer, 40% humidity).

## 5.7 Summary

This chapter presented the results from the CFD investigations. The results and findings of each geometrical configuration have been discussed thoroughly. Four performance parameters have been stipulated and used to evaluate the wind tower performance. The results have been presented in graphical, contours, streamlines and tabular form. A four-sided and one-sided wind tower have been utilised as a benchmark model for the CFD investigations. Two heat transfer device (HTD) configurations have been incorporated to the wind tower models; vertical and horizontal HTD arrangement. The effect of the addition of extended surfaces and porous media on the ventilation and thermal performance of the cooling wind tower have been investigated.

The Predicted Mean Vote (PMV) and the Predicted Percentage Dissatisfied (PPD) have been used to evaluate the steady-state thermal comfort performance of a test room model incorporated with the cooling wind tower system.

## Chapter 6

### Experimental Results

#### 6.1 Introduction

Experimental wind tunnel and smoke visualisation testing were conducted to investigate the ventilation performance of the different wind tower designs (detailed in Chapter 4). Experimental investigations of the 1:10 scaled wind tower models were carried out using the closed-loop wind tunnel and the induced volumetric airflow and indoor airflow were measured at various wind speeds (3 – 5m/s) and wind angles (0 – 90°). In order to recognise the flow pattern in and around the wind tower models, smoke visualization tests were also carried out. Each variant of the wind tower was subjected to the test procedure (detailed in Section 4.5) with the results presented in this chapter. In order to compare the numerical results, all the models retained the same boundary conditions.

#### 6.2 Benchmark wind tower testing

The benchmark models consisted of a 0.1 x 0.1 m four-sided and one-sided wind tower with seven 45° louvres (as detailed in Chapter 4) shown in Figure 6.1 The wind tower model was connected to a 0.5 x 0.5 x 0.3 m test room (representing the ventilated space), which was mounted underneath the wind tunnel test section.



**Figure 6.1** 1:10 scale benchmark wind tower models (a) four-sided (b) one-sided.

The test room model was made of acrylic perspex sheet to facilitate flow visualisation testing as well as to be able to clearly see the measurement points markers. The test room top plate was constructed that it could be rotated in the test section in order to test

different approaching wind directions (0 to 180°). In order to validate the numerical results, all the models retained the same boundary conditions (Figure 6.2).

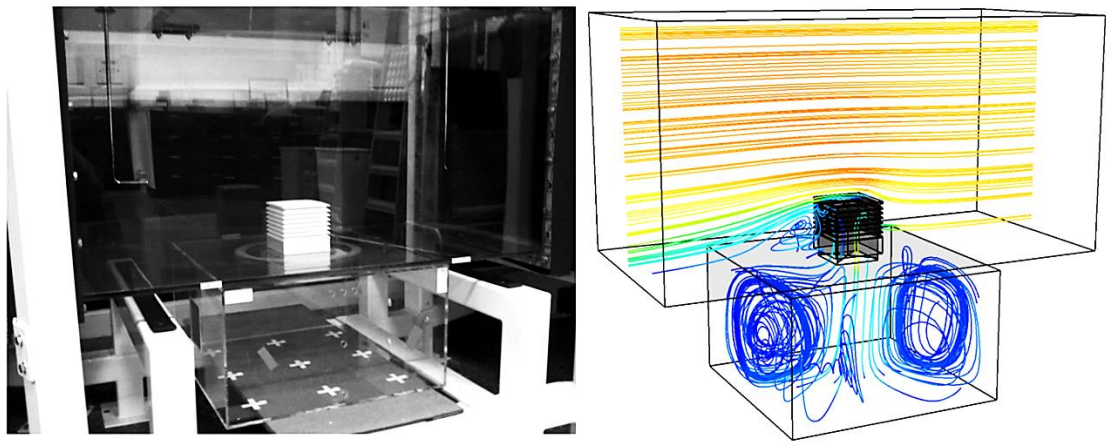
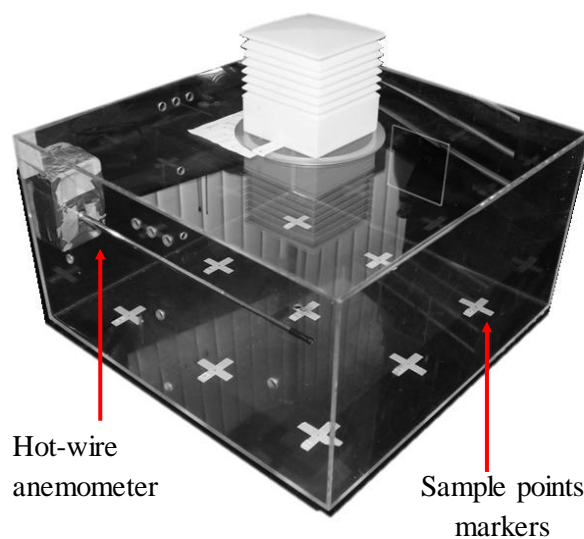


**Figure 6.2** Experimental and CFD flow domain of the macro-micro climate.

### 6.2.1 Indoor airflow distribution

In this study the airflow inside the test room model was measured using a hot-wire anemometer. Nine data points in an equally spaced 3 by 3 grid were created within the test room at a height of 1.5 m which allow for measurements to be made for velocity within the test room (Figure 6.3). Additionally, three data points were positioned at the bottom of the room (central), below the supply and exhaust channels of the wind towers. The values of the velocity were obtained from the three components of the vector (X, Y, and Z).



Point	X [m]	Y [m]	Z [m]
P1 (mid)	-0.165	-0.135	0.165
P2 (mid)	0	-0.135	0.165
P3 (mid)	0.165	-0.135	0.165
P4 (mid)	-0.165	-0.135	0
P5 (mid)	0	-0.135	0
P6 (mid)	0.165	-0.135	0
P7 (mid)	-0.165	-0.135	-0.165
P8 (mid)	0	-0.135	-0.165
P9 (mid)	0.165	-0.135	-0.165
P10 (bottom)	0	-0.22	0
P11 (supply)	0	-0.03	0
P12 (outlet)	-0.25	-0.135	0

**Figure 6.3** Measurement points inside the test room model.

The tests were carried out between 3 m/s and 5 m/s. A sample for each point was taken and averaged over a two minute period with the results and start/finish times recorded. Table 6.1 and 6.2 summarise the averaged results for the sample points inside the test room with the benchmark four-sided and one-sided wind tower. At inlet speed of 3 m/s the average air speed inside the test room with the four-sided wind tower was 0.56 m/s which was 17.8 % higher compared to the one-sided wind tower.

**Table 6.1** Test room with four-sided wind tower sample points values [m/s].

	P1	P2	P3	P4	P5	P6	P7	P8	P9	P10	P11	P12	Avg.
3 m/s	0.27	0.24	0.25	0.25	1.03	0.24	0.25	0.26	0.28	0.82	2.53	0.34	<b>0.56</b>
4 m/s	0.43	0.32	0.37	0.36	1.55	0.32	0.41	0.27	0.49	1.12	3.71	0.44	<b>0.81</b>
5 m/s	0.44	0.40	0.46	0.47	2.01	0.33	0.49	0.20	0.35	1.18	4.32	0.81	<b>0.97</b>

**Table 6.2** Test room with one-sided wind tower sample points values [m/s].

	P1	P2	P3	P4	P5	P6	P7	P8	P9	P10	P11	Avg.
3 m/s	0.33	0.31	0.20	0.27	1.09	0.22	0.33	0.17	0.26	0.53	1.32	<b>0.46</b>
4 m/s	0.39	0.47	0.30	0.41	1.45	0.32	0.36	0.25	0.30	0.68	1.81	<b>0.61</b>
5 m/s	0.45	0.61	0.29	0.50	1.73	0.36	0.42	0.43	0.43	0.91	2.37	<b>0.79</b>

### 6.2.2 Volumetric flow supply rate

In this study the induced airflow into the test room was measured using the hot wire anemometer position below the channels of the wind tower device. The cross-sectional area of the wind tower channel was divided into several portions and the airflow rate through it was calculated (Figure 6.4). The tests were carried conducted in the uniform flow wind tunnel at various wind angles (0 - 90°). Sample for each point was taken and averaged over a two minute period with the results and start/finish times recorded.

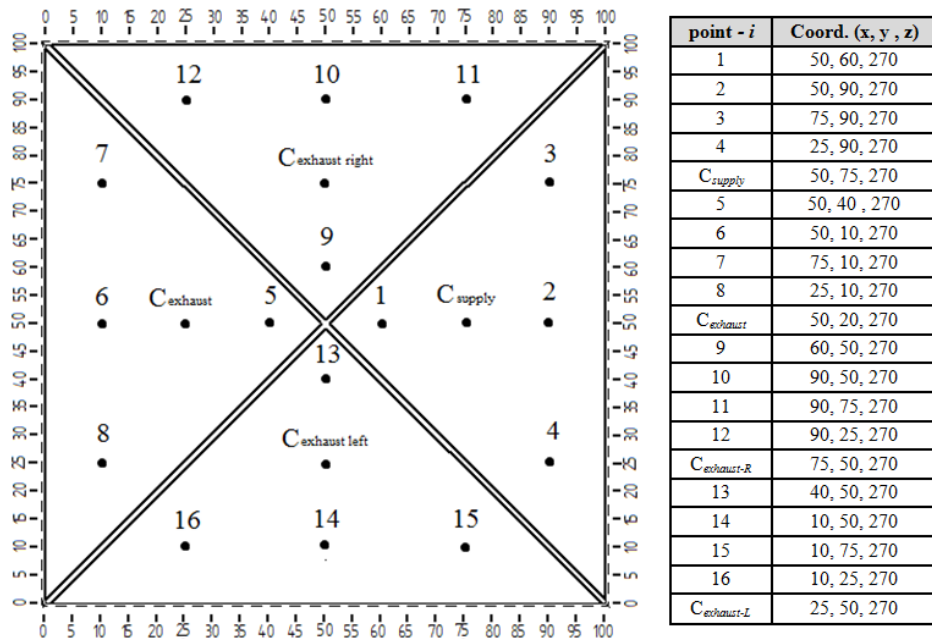


**Figure 6.4** Section view of the four sided wind tower supply and exhausts channels showing the location of the measurement points (dimensions in mm).

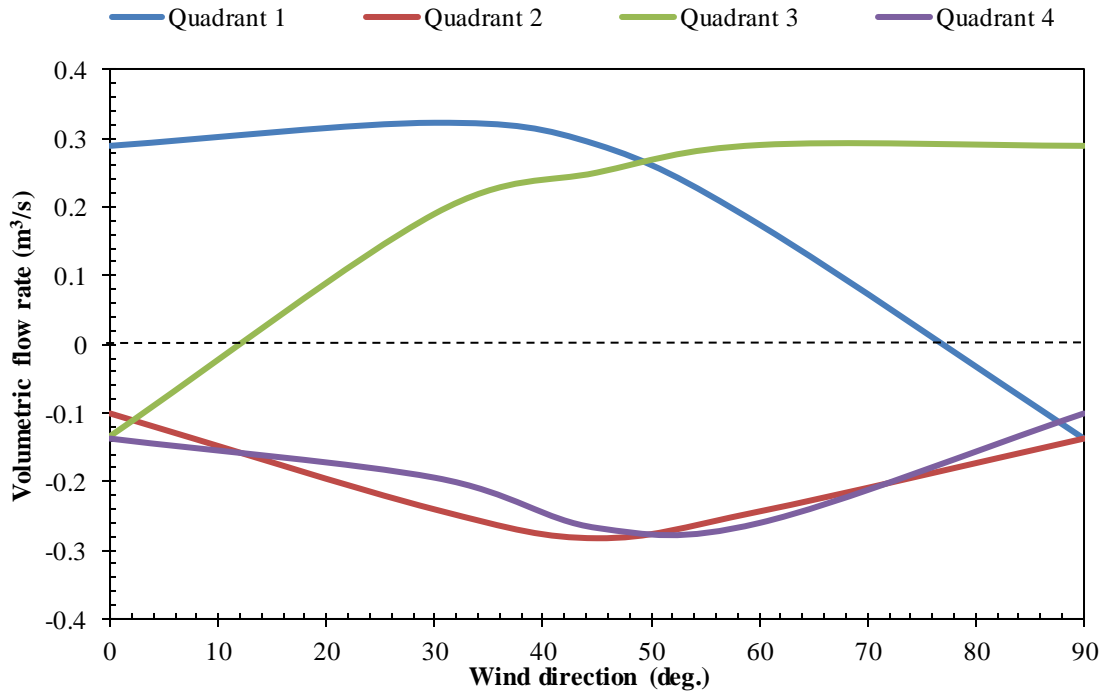
Table 6.4 summarises the experimental results of the airflow speed through the four-sided wind tower channel.

**Table 6.3** Measured values of air flow velocity through the four-sided wind tower [m/s].

(°)	Quadrant 1				Quadrant 2				Quadrant 3				Quadrant 4			
	1	2	3	4	5	6	7	8	9	10	11	12	13	14	15	16
<b>0°</b>	2.81	1.28	0.38	0.35	0.41	0.48	0.41	0.38	0.57	0.55	0.55	0.56	0.58	0.57	0.58	0.56
<b>30°</b>	2.59	1.07	0.43	1.29	0.86	1.2	0.65	1.3	1.07	0.43	1.07	0.60	0.43	1.3	0.21	1.3
<b>45°</b>	2.3	0.45	0.71	1.39	0.71	1.41	0.94	1.65	2.32	0.22	0.71	0.92	0.71	1.64	1.64	0.47
<b>60°</b>	0.89	0.24	0.89	0.89	0.83	1.2	0.62	1.41	2.62	0.67	0.40	1.15	1.23	1.24	0.61	1.26

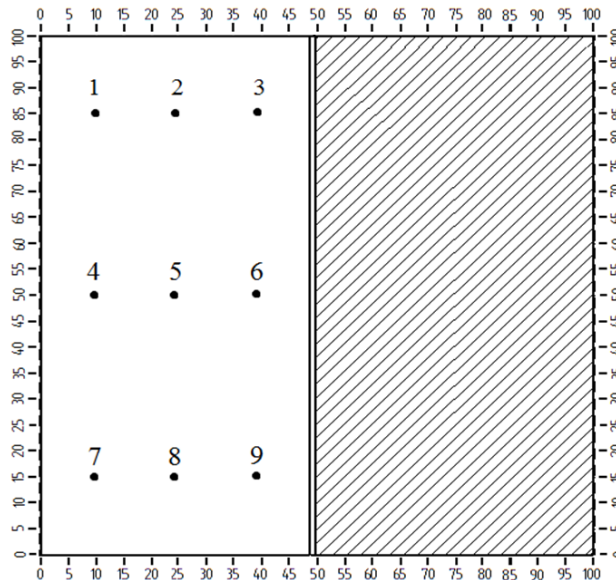
Figure 6.5 shows the experimental results of the volumetric airflow through the four-sided wind tower quadrant at different wind angles. In this figure the supply and the extract segments are recognised by positive and negative values of airflow rate. A volumetric airflow rate of  $0.29 \text{ m}^3/\text{s}$  was achieved through the supply quadrant 1 at  $0^\circ$  for an average wind speed of 3 m/s. As the wind angle increases the supply airflow through quadrant 1 decreases. Exceeding the wind angle over the transition angle ( $> 70^\circ$ ), caused a change in airflow direction into quadrant 1. At  $45^\circ$  wind angle, net

volumetric flow rate of 0.50 m<sup>3</sup>/s was achieved through combined supply quadrants 1 and 3 with the exhaust flow rate from the opposite quadrants at its maximum.



**Figure 6.5** Volumetric airflow rate through the wind tower supply and exhaust quadrants at various wind direction.

Figure 6.6 shows the location of the point inside the channel of the one-sided wind tower at a height of 270 mm from the test room floor.



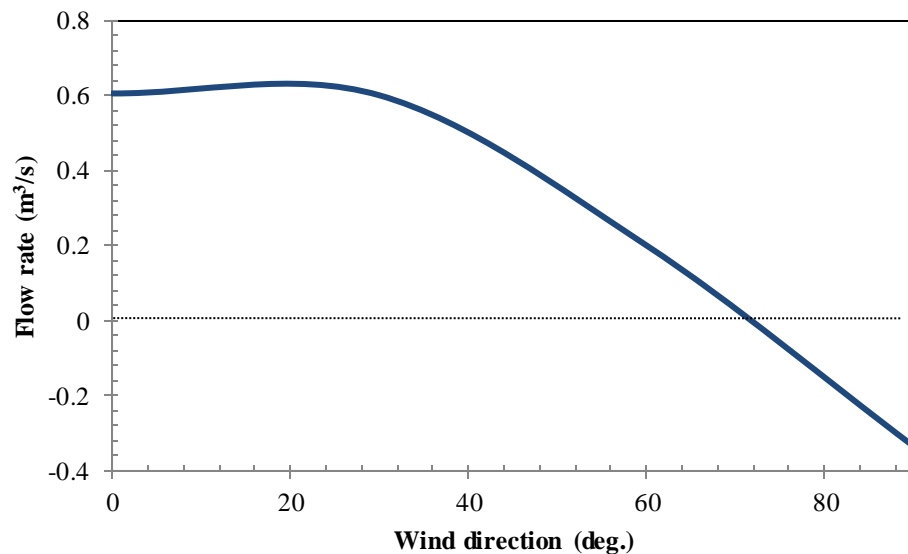
**Figure 6.6** Section view of the one sided wind tower supply channel showing the location of the measurement points (dimensions in mm).

Table 6.4 summarises the experimental results of the airflow speed through the one-sided wind tower channel.

**Table 6.4** Measured values of air flow velocity through the one-sided wind tower [m/s].

	1	2	3	4	5	6	7	8	9	Avg.
<b>0°</b>	2.07	1.25	0.48	2.00	1.48	0.54	1.84	0.83	0.41	<b>1.21</b>
<b>30°</b>	1.85	1.56	1.08	1.98	1.14	0.55	1.73	0.63	0.40	<b>1.20</b>
<b>60°</b>	0.64	0.38	0.38	0.33	0.29	0.29	0.71	0.27	0.25	<b>0.40</b>
<b>90°</b>	0.62	0.70	0.70	0.63	0.70	0.67	0.64	0.68	0.69	<b>0.67</b>

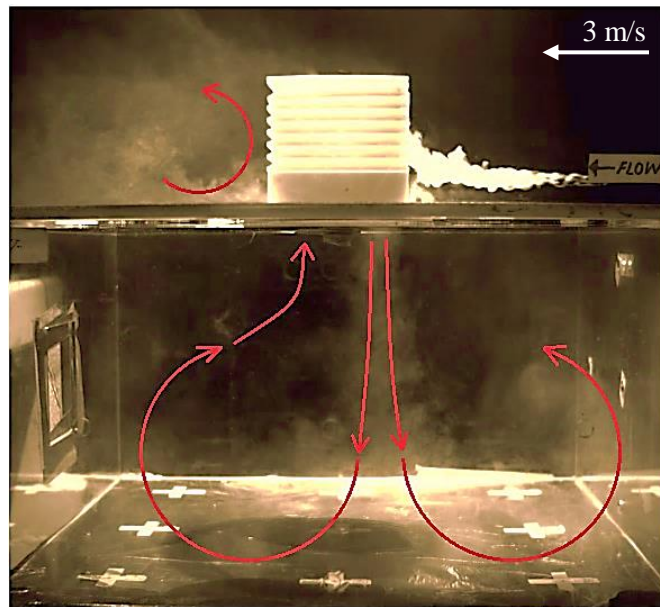
Figure 6.7 shows the experimental results of the volumetric airflow through the wind tower channel. In this figure the flow direction in the supply channel are recognised by positive and negative values of airflow correspondingly. A volumetric airflow rate of 0.6 m<sup>3</sup>/s was achieved through the supply channel at 0° for an external wind speed of 3 m/s.



**Figure 6.7** Volumetric airflow rate through the wind tower supply channel at various wind direction.

### 6.2.3 Flow visualisation

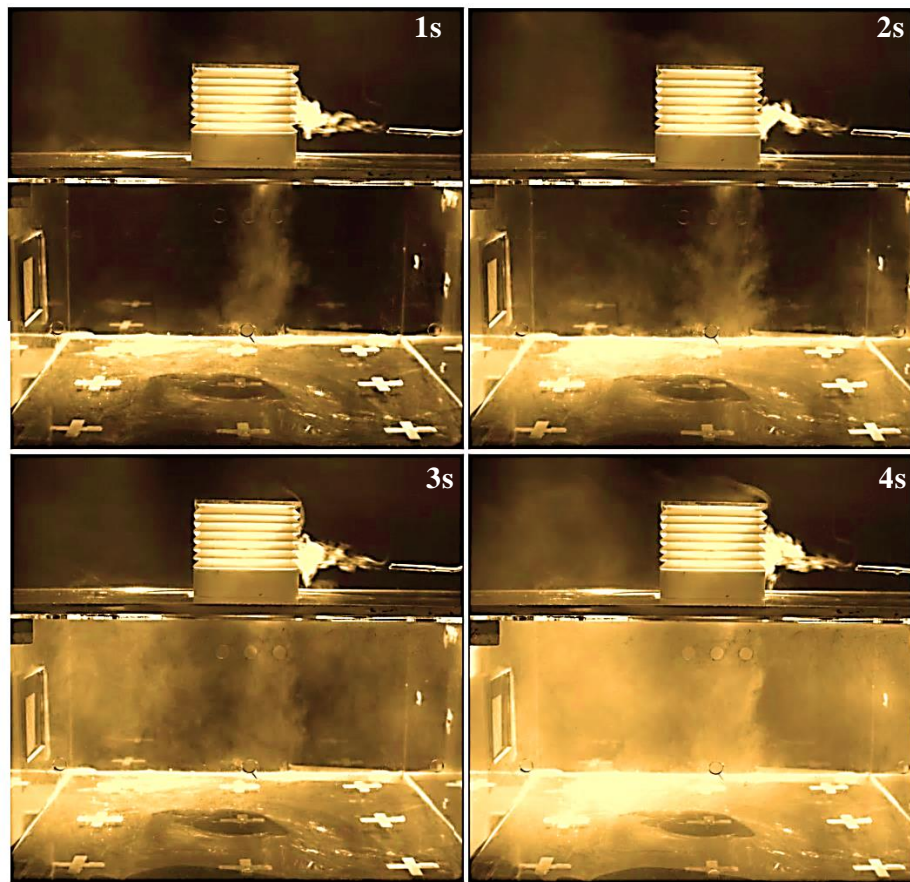
In order to recognise the flow pattern in and around the wind tower model, smoke visualisation tests were also carried out. The tests were carried out in the uniform flow wind tunnel at various wind angles (0 - 90°). Figure 6.8 shows the visualised flow pattern inside the test room model, the flow smoothly passes around and over the wind tower with some of the air entering the wind tower supply channel through the 45° louvres. The air entered at a higher velocity due to the external driving velocity. The higher velocity at the point of entry was more visible due to the amount of smoke being displaced at this side of the wind tower. The airflow was directed towards the floor of the test section and spread outwards in all directions. As the airflow hits the bottom surface the air slows down and flows through the side walls, with some of the air escaping through the exhaust quadrant of the wind tower which has a lower air pressure. A region of highly unsteady and recirculating flow was observed immediately at the downstream of the wind tower.



**Figure 6.8** Experimental flow visualisation inside the test room with the benchmark four-sided wind tower.

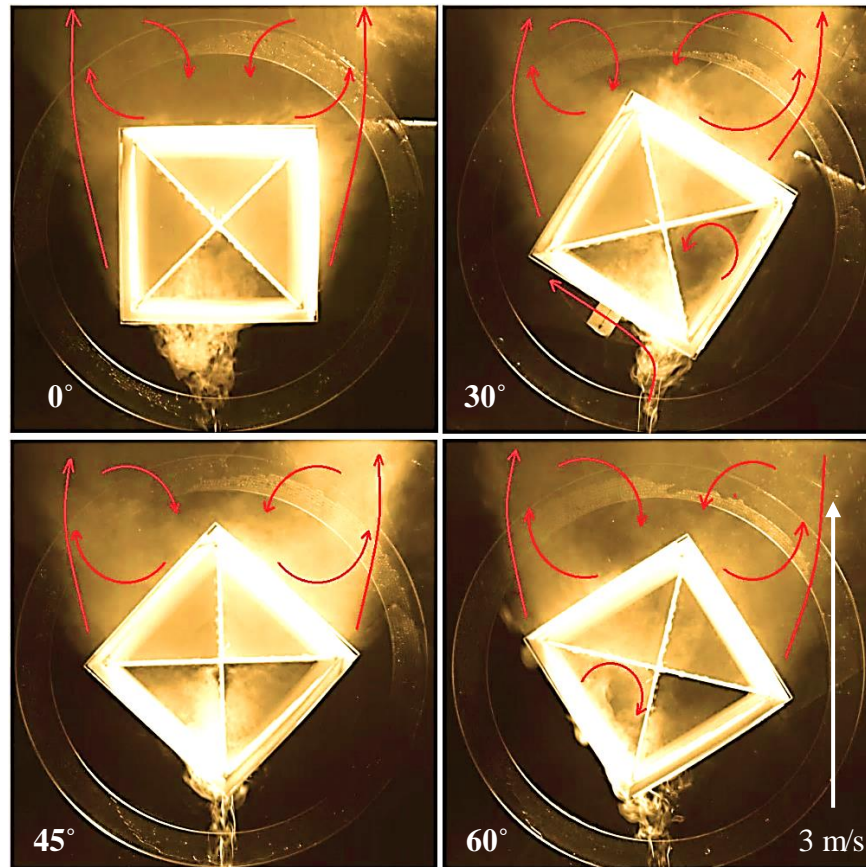
Realisation of flow imaging at high frame rates was essential to the visualisation of the flow through the wind tower. Four stages of the flow through the test room model are shown in Figure 6.9. From the smoke visualisation analysis, it was observed that the

airflow induced inside the test room was distributed evenly, with some of the flow recirculated and some exiting the exhaust quadrants.



**Figure 6.9** Visualised flow pattern inside the test room with a four-sided wind tower.

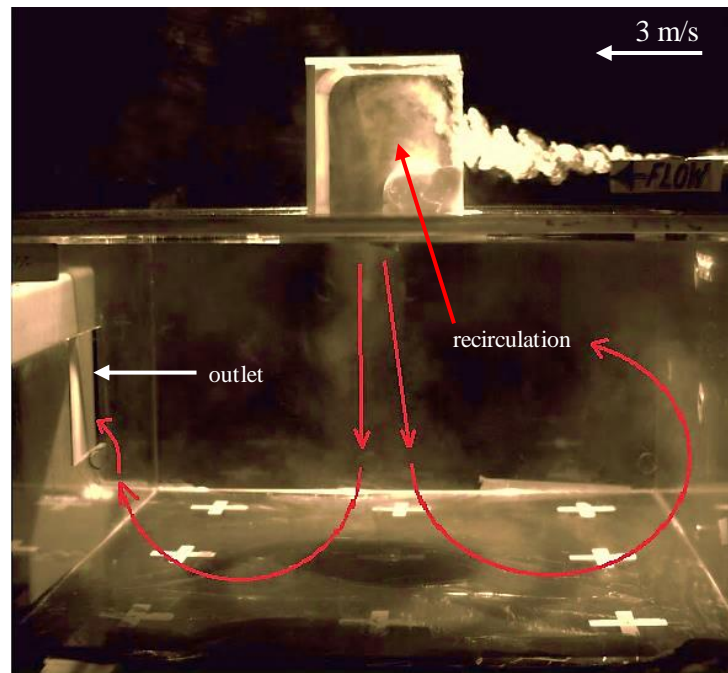
Visualisation tests were carried out to demonstrate the top view of the passing flow through the benchmark four-sided wind tower model for various wind angles (Figure 6.10). It was observed that at  $0^\circ$  angle, a large volume of the wind tower is used for extract purposes (three of the four quadrants). While the tower oriented at  $45^\circ$  into the prevailing wind has a larger area available to capture the wind. In this case, two windward quadrants were used for air flowing into the tower and two leeward quadrants for the air flowing out of the tower. A developing region of recirculation and vortices were observed inside the windward quadrants at wind angles of  $30^\circ$  and  $60^\circ$  which reduces the induce operation of the four-sided wind tower. Furthermore, areas of highly unsteady and recirculating flow at the downstream of the wind tower also increased with the wind angle.



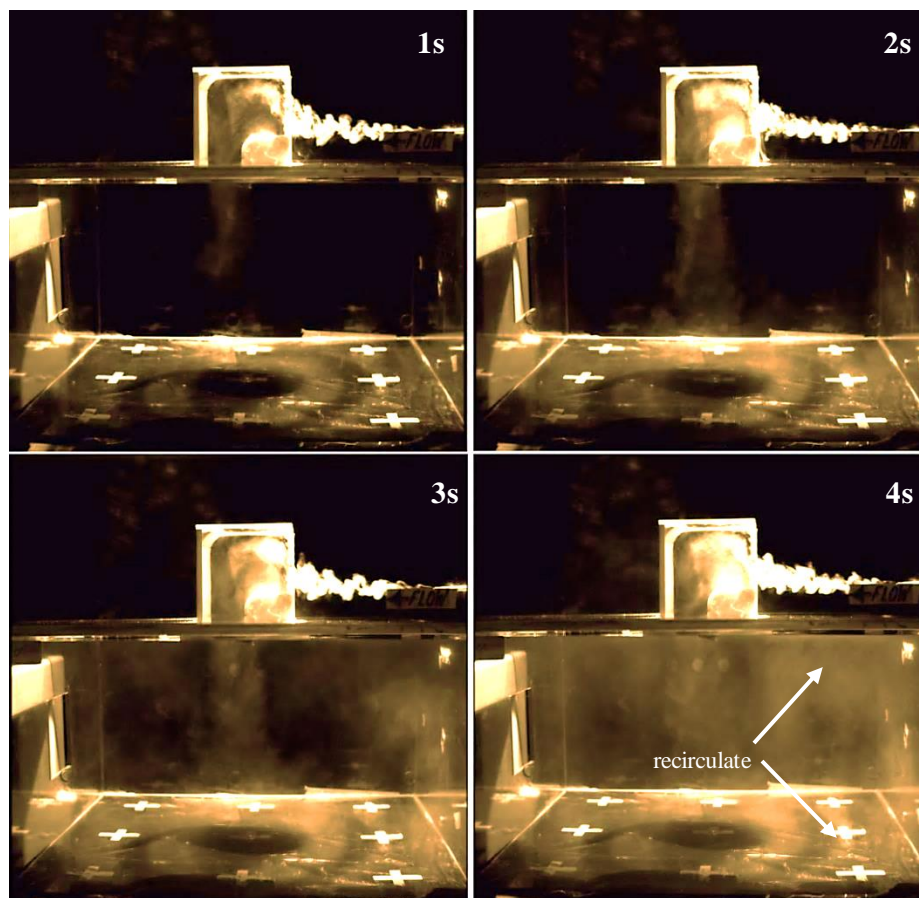
**Figure 6.10** Visualised flow pattern inside the test room at various wind angles.

Figure 6.11 shows the flow visualisation of air flow pattern inside the test room model with one-sided wind tower. The air flow enters the wind tower channel through the free area of  $45^\circ$  louvre section and accelerates as it hits the channel wall and forces the flow down into the diffuser section. Separated flow and wake region was observed near the lower edge of the opening which caused a sharp variation in velocity in this region, reducing the effective flow passage area. The airflow exiting the wind tower channel was directed towards the floor of the test section and spread outwards in all directions. As the airflow hits the bottom surface the air slows down and flows through the side walls, with some of the air escaping through the window opening.

Four stages of the flow through the test room model with the one-sided wind tower are shown in Figure 6.12. From the smoke visualisation test, it was observed that the airflow induced inside the test room was distributed evenly, with some of the flow recirculated and some exiting the window opening. Increased air recirculation was observed in the right corner of the test room with no outlet opening.

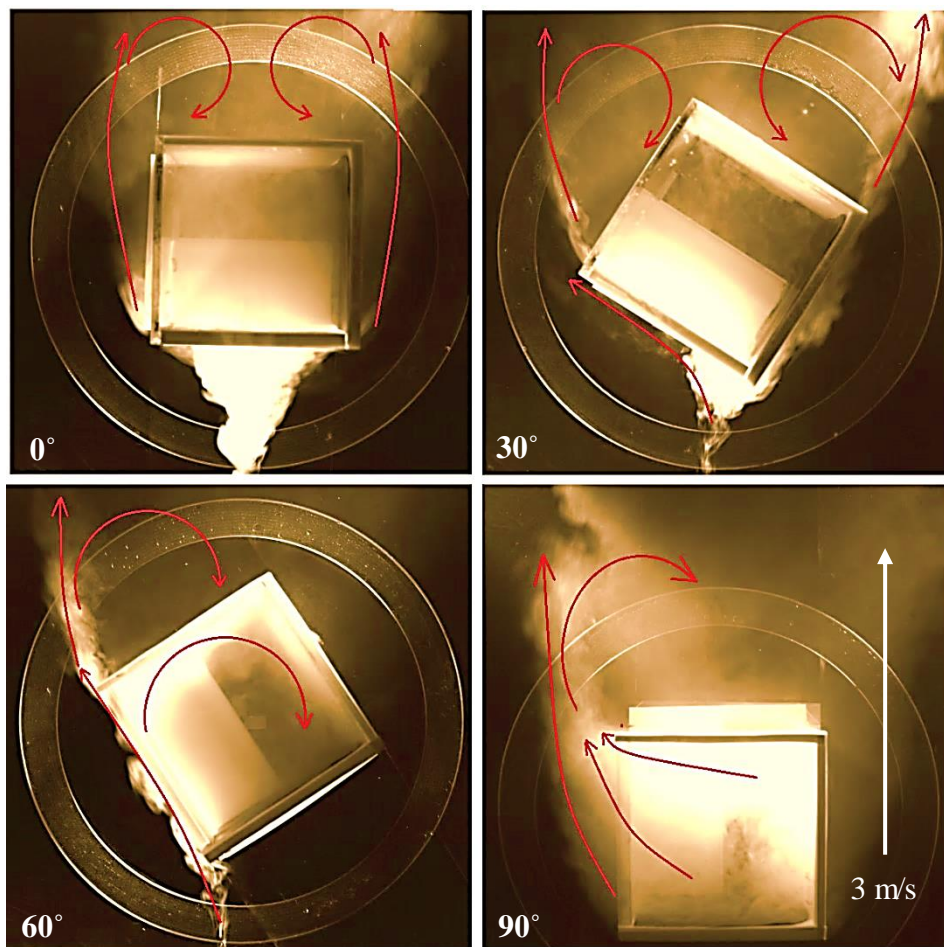


**Figure 6.11** Experimental flow visualisation inside the test room with the benchmark one-sided wind tower.



**Figure 6.12** Visualised flow pattern inside the test room at external wind speed of 3 m/s.

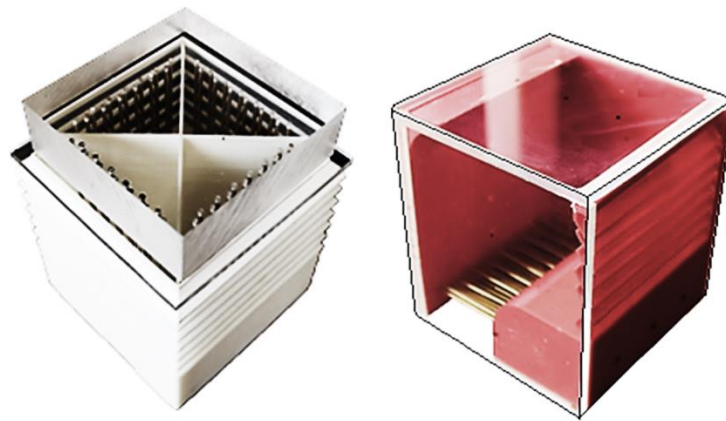
Figure 6.13 shows the visualisation tests from the top view of the passing flow through the benchmark one-sided wind tower model for various wind angles. Clearly, locating the wind tower on the path of predominant wind streams ( $0^\circ$  angle); will cause the maximum entrance flow rate into the windward opening. With increasing external wind angle and the developing region of vortices, the induced operation of wind tower was reduced continuously to its minimum value at the transition angle. Exceeding the wind angle over the transition angle, causes a change in the airflow direction into the windward channel. At  $90^\circ$  wind angle the wind tower acts as a suction device. This is due to the fact that exposing the body of the wind tower on the path of the air flow caused a low pressure region on its side and positioning its opening in this region with a lower pressure than the environment, will result in an airflow from the window to the wind tower opening. The smoke was released inside the test room when testing the wind tower at  $90^\circ$  wind angle.



**Figure 6.13** Experimental flow visualisation inside the test room with the one-sided wind tower at various wind angles.

### 6.3 Wind tower with heat transfer devices

In this study the induced airflow into the test room was measured below the channels of the wind tower device. The cross-sectional area of the wind tower channel was divided into several portions and the airflow rate through it was calculated. The tests were conducted in the uniform flow wind tunnel at various wind angles (0 - 90°). A sample for each point was taken and averaged over a two minute period with the results and start/finish times recorded. Figure 6.14 displays the prototype model of the four and one-sided wind tower integrated with the heat transfer devices (detailed in Chapter 4).



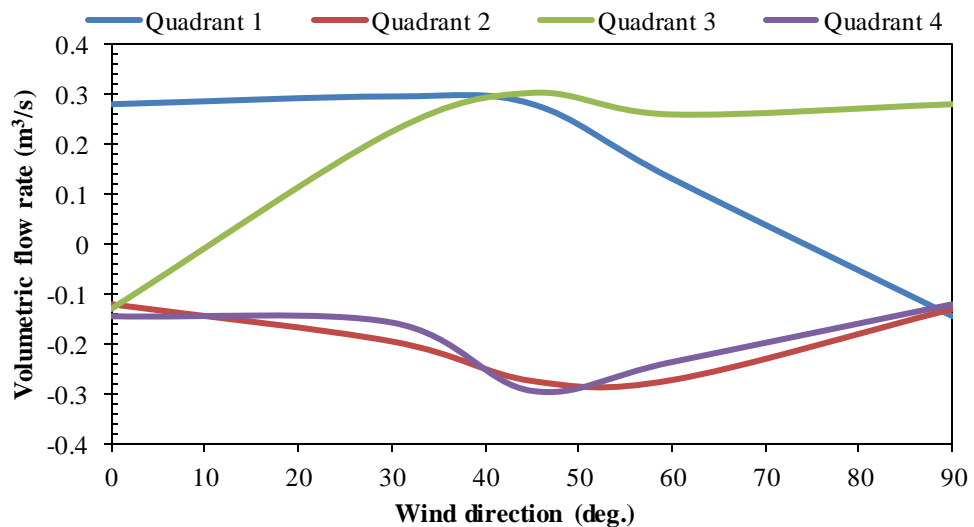
**Figure 6.14** 1:10 prototype model of the four and one-sided wind tower design incorporating horizontal heat transfer devices config 1.

Table 6.5 summarises the experimental results of the airflow speed through the four-sided wind tower with heat transfer devices.

**Table 6.5** Measured values of air flow velocity through the four-sided wind tower with heat transfer devices config. 1 [m/s].

(°)	Quadrant 1				Quadrant 2				Quadrant 3				Quadrant 4			
	1	2	3	4	5	6	7	8	9	10	11	12	13	14	15	16
<b>0°</b>	2.59	1.20	0.45	0.44	0.46	0.57	0.57	0.39	0.55	0.63	0.43	0.54	0.51	0.77	0.47	0.64
<b>30°</b>	2.14	1.13	0.72	0.95	0.81	1.12	0.5	0.8	0.94	1.01	0.80	1.01	0.72	0.52	0.77	0.59
<b>45°</b>	2.18	1.18	0.58	0.75	0.99	1.38	0.99	1.19	2.38	1.10	0.99	0.59	1.19	1.35	1.35	0.99
<b>60°</b>	0.62	0.35	0.89	0.34	0.98	1.25	1.18	1.11	2.21	1.34	0.44	0.35	0.98	1.25	0.71	0.98

Figure 6.15 shows the experimental results of the volumetric airflow through the four-sided wind tower quadrant at different wind angles. In this figure the supply and the extract segments are recognised by positive and negative values of airflow rate. A volumetric airflow rate of  $0.28 \text{ m}^3/\text{s}$  was achieved through the supply quadrant 1 at  $0^\circ$  for an average wind speed of  $3 \text{ m/s}$ . At  $45^\circ$  wind angle, net volumetric flow rate of  $0.50 \text{ m}^3/\text{s}$  was achieved through combined supply quadrants 1 and 3 with the exhaust flow rate from the opposite quadrants at its maximum.



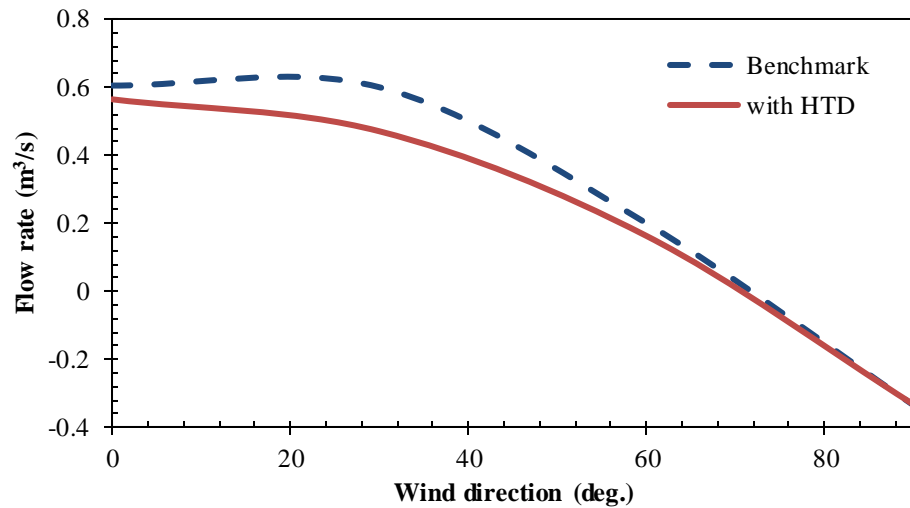
**Figure 6.15** Volumetric airflow rate through the wind tower supply and exhaust quadrants at various wind direction (four-sided wind tower with heat transfer devices config. 1).

Table 6.6 summarises the experimental results of the airflow speed through the one-sided wind tower model with heat transfer devices.

**Table 6.6** Measured values of air flow velocity through the one-sided wind tower with heat transfer devices config. 1. [m/s]

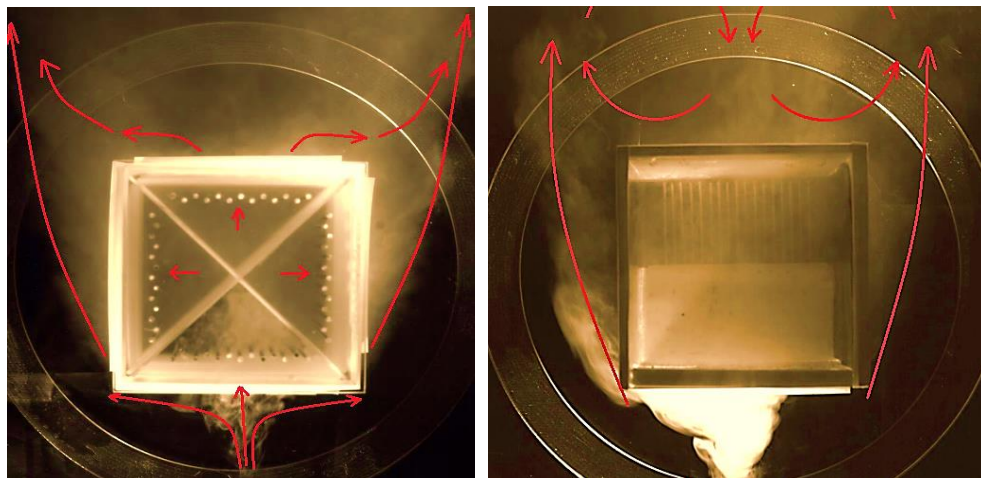
	1	2	3	4	5	6	7	8	9	Avg.
<b>0°</b>	1.51	1.25	0.61	1.32	1.27	1.01	1.45	1.18	0.56	<b>1.12</b>
<b>30°</b>	1.28	1.18	0.98	1.79	1.1	0.66	0.96	0.29	0.23	<b>0.94</b>
<b>60°</b>	0.64	0.43	0.41	0.23	0.15	0.19	0.5	0.15	0.23	<b>0.33</b>
<b>90°</b>	0.67	0.67	0.68	0.67	0.68	0.68	0.63	0.68	0.63	<b>0.67</b>

Figure 6.16 shows the experimental results of the volumetric airflow through the one-sided wind tower channel with heat transfer devices. In this figure the flow direction in the supply channel are recognised by positive and negative values of airflow correspondingly. A volumetric airflow rate of  $0.57 \text{ m}^3/\text{s}$  was achieved through the supply channel at  $0^\circ$  for an external wind speed of  $3 \text{ m/s}$ .



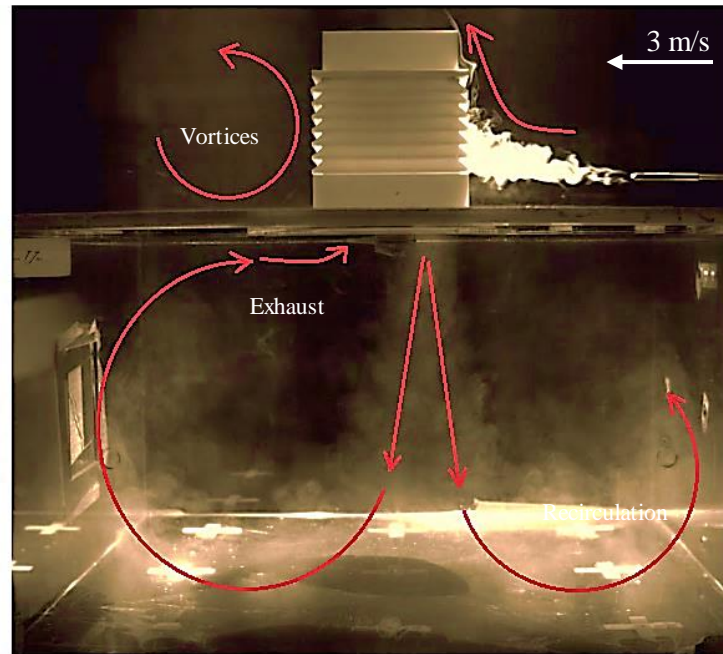
**Figure 6.16** Volumetric airflow through the wind tower supply channel at various wind direction (one-sided wind tower with heat transfer devices config. 1).

Figure 6.17 shows the visualised flow pattern inside the wind tower channels from top view. The flow visualisation method showed that the four quadrants were all working to both draw in the external air and exhaust the stale air out of the test room.



**Figure 6.17** Detailed view of the flow inside the four-sided and one-sided wind tower with heat transfer devices.

Figure 6.18 and Figure 6.19 shows the visualised flow pattern inside the test room model with the heat transfer device integrated wind tower model. The flow pattern was similar to the benchmark models (Figure 6.7 and Figure 6.10) hence, the effect of the addition of the heat transfer devices on the indoor air flow pattern were minimal.



**Figure 6.18** Experimental flow visualisation inside the test room with the four-sided wind tower with heat transfer devices.

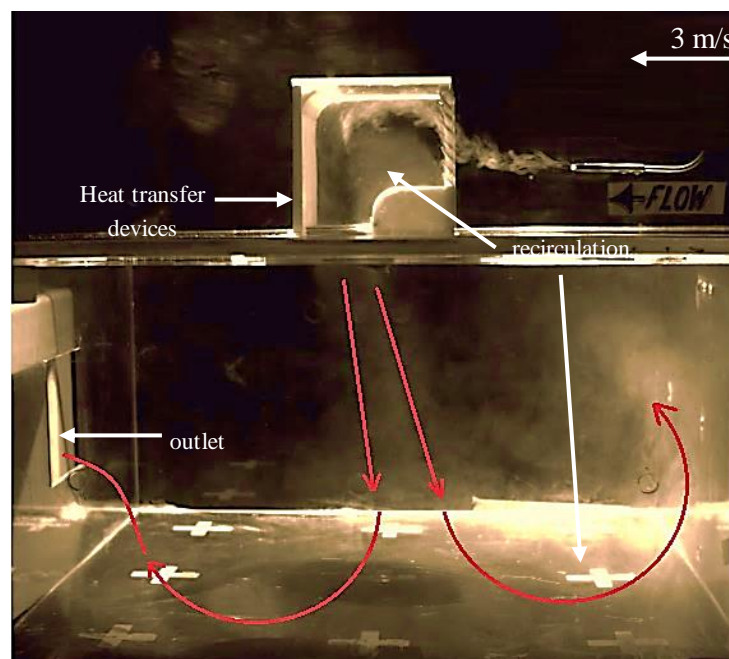


**Figure 6.19** Experimental flow visualisation inside the test room with the one-sided wind tower with heat transfer devices.

## 6.4 Wind tower with heat transfer devices and extended surfaces

Figure 6.20 displays the prototype models of the four-sided wind tower integrated with the heat transfer devices extended surfaces (detailed in Chapter 4). The tests were carried out in the uniform flow wind tunnel at various wind angles (0 - 90°). A sample for each point was taken and averaged over a two minute period with the results and start/finish times recorded.



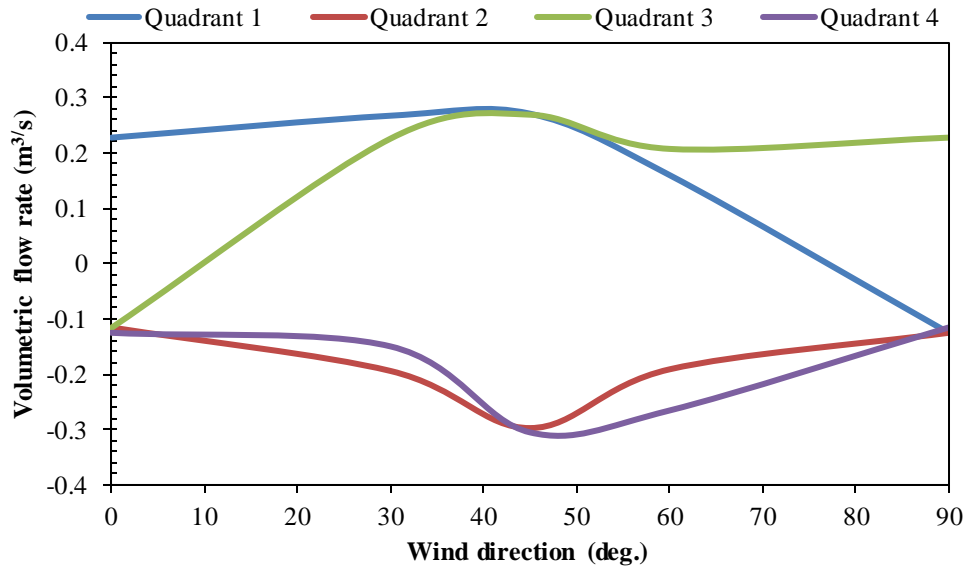
**Figure 6.20** 1:10 prototype model of the four and one-sided wind tower design incorporating heat transfer devices and extended surfaces.

Table 6.7 summarises the experimental results of the airflow speed through the four-sided wind tower with heat transfer devices and extended surfaces.

**Table 6.7** Measured values of air flow velocity through the four-sided wind tower incorporating heat transfer devices and extended surfaces.

	Quadrant 1				Quadrant 2				Quadrant 3				Quadrant 4			
	1	2	3	4	5	6	7	8	9	10	11	12	13	14	15	16
<b>0°</b>	2.53	0.44	0.42	0.40	0.43	0.51	0.54	0.45	0.57	0.62	0.37	0.38	0.48	0.65	0.45	0.51
<b>30°</b>	2.10	0.78	0.37	1.20	0.85	0.97	0.44	0.98	0.58	1.14	1.10	0.94	0.70	0.49	0.43	0.88
<b>45°</b>	2.04	0.72	0.59	1.16	1.03	1.47	1.43	1.03	2.11	0.71	0.54	1.12	1.14	1.05	1.49	1.41
<b>60°</b>	0.88	0.34	0.84	0.60	0.47	1.20	0.61	0.91	0.94	0.85	0.83	0.83	2.12	0.49	0.50	1.32

Figure 6.21 shows the experimental results of the volumetric airflow through the four-sided wind tower with HTD and extended surfaces at different wind angles.



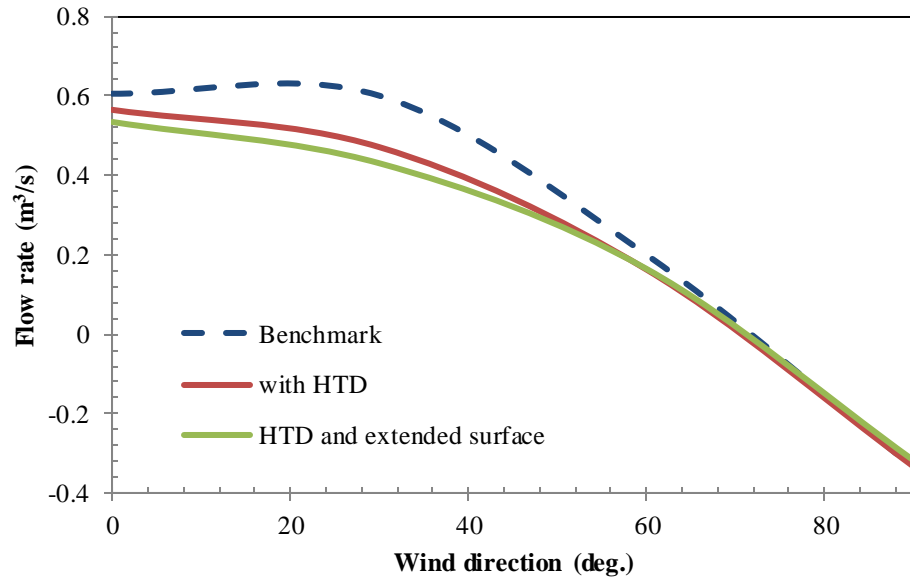
**Figure 6.21** Volumetric airflow through the wind tower supply and exhaust quadrants at various wind direction (four-sided wind tower with heat transfer devices and extended surfaces).

Table 6.8 summarises the experimental results of the airflow speed through the one-sided wind tower model with heat transfer devices and extended surfaces.

**Table 6.8** Measured values of air flow velocity through the one-sided wind tower with heat transfer devices and extended surfaces [m/s].

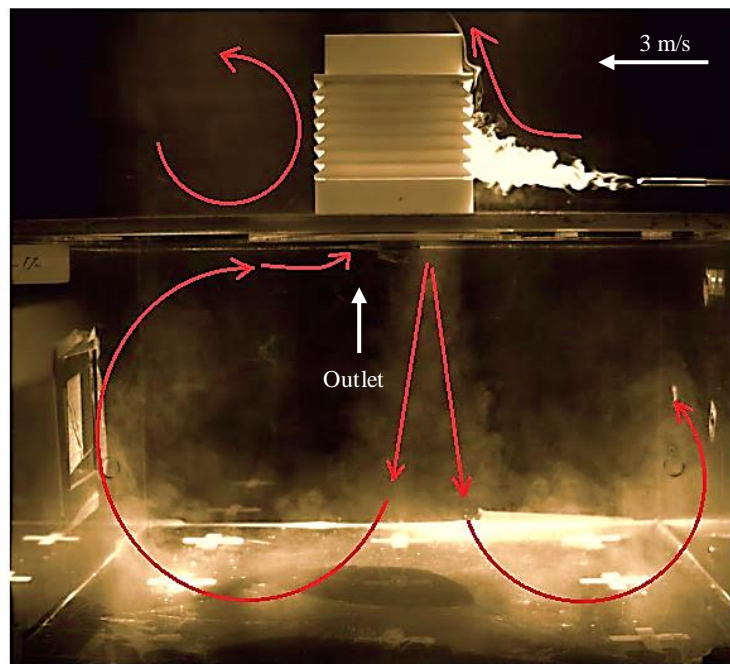
	1	2	3	4	5	6	7	8	9	Avg.
<b>0°</b>	1.63	0.87	1.01	1.21	1.01	0.64	1.41	1.09	0.74	<b>1.07</b>
<b>30°</b>	1.04	0.9	0.77	1.37	0.80	0.70	1.24	0.62	0.30	<b>0.86</b>
<b>60°</b>	0.56	0.42	0.40	0.37	0.12	0.10	0.57	0.24	0.18	<b>0.33</b>
<b>90°</b>	0.70	0.67	0.70	0.64	0.53	0.59	0.69	0.59	0.60	<b>0.63</b>

Figure 6.22 shows the experimental results of the volumetric airflow rate through the one-sided wind tower channel with heat transfer devices and extended surfaces. In this figure the flow direction in the supply channel are recognised by positive and negative values of airflow correspondingly. A volumetric airflow rate of 0.53 m<sup>3</sup>/s was achieved through the supply channel at 0° for an external wind speed of 3 m/s. At wind angle of 90°, the exhaust flow rate was not affected by the addition of the heat transfer device and extended surfaces.



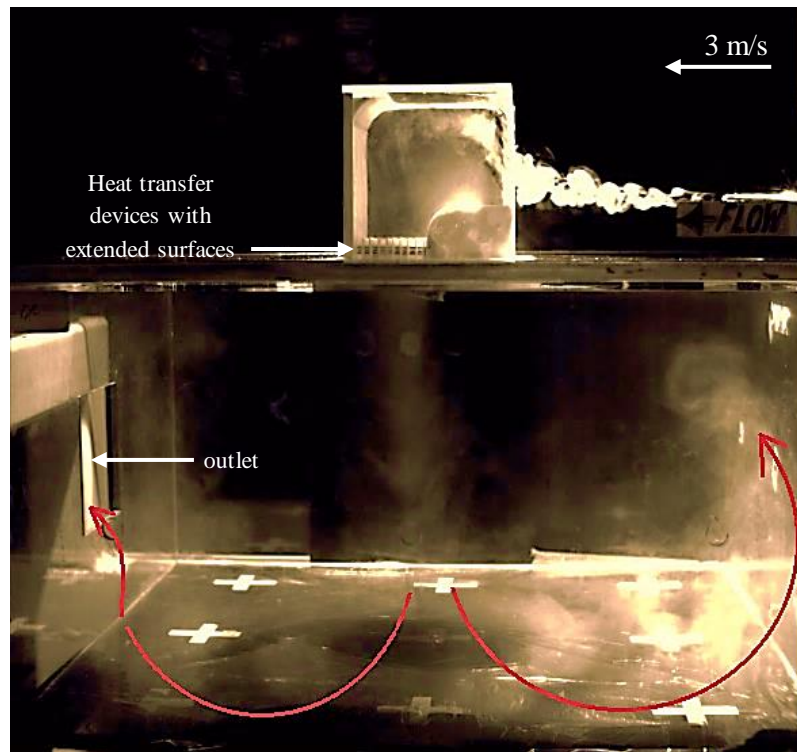
**Figure 6.22** Volumetric airflow through the wind tower supply channel at various wind direction (one-sided wind tower with heat transfer devices and extended surfaces).

Figure 6.23 displays the visualised flow pattern inside the test room model with the vertical heat transfer device integrated wind tower model and extended surfaces.



**Figure 6.23** Experimental flow visualisation inside the test room with the four-sided wind tower with heat transfer devices and extended surfaces.

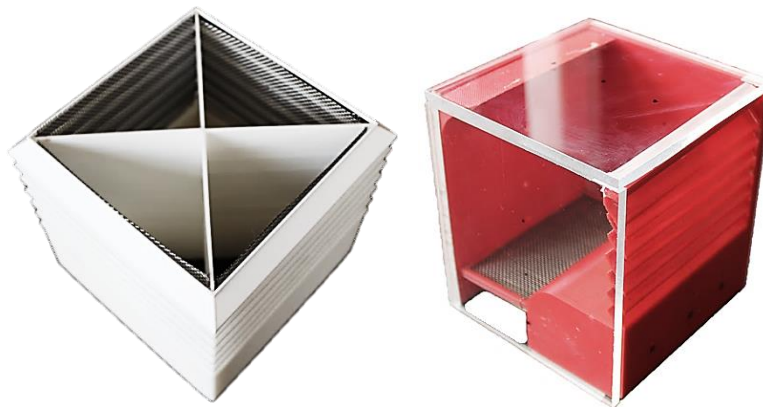
Figure 6.24 displays the visualised flow pattern inside the test room model with the horizontal heat transfer device integrated wind tower model and extended surfaces.



**Figure 6.24** Experimental flow visualisation inside the test room with the one-sided wind tower with heat transfer devices and extended surfaces.

## 6.5 Wind tower with heat transfer devices and porous media

Figure 6.25 displays the prototype model of the four-sided wind tower integrated with the heat transfer devices porous media (detailed in Chapter 4). The tests were carried conducted in the uniform flow wind tunnel at various wind angles ( $0 - 90^\circ$ ). Sample for each point was taken and averaged over a two minute period with the results and start/finish times recorded.



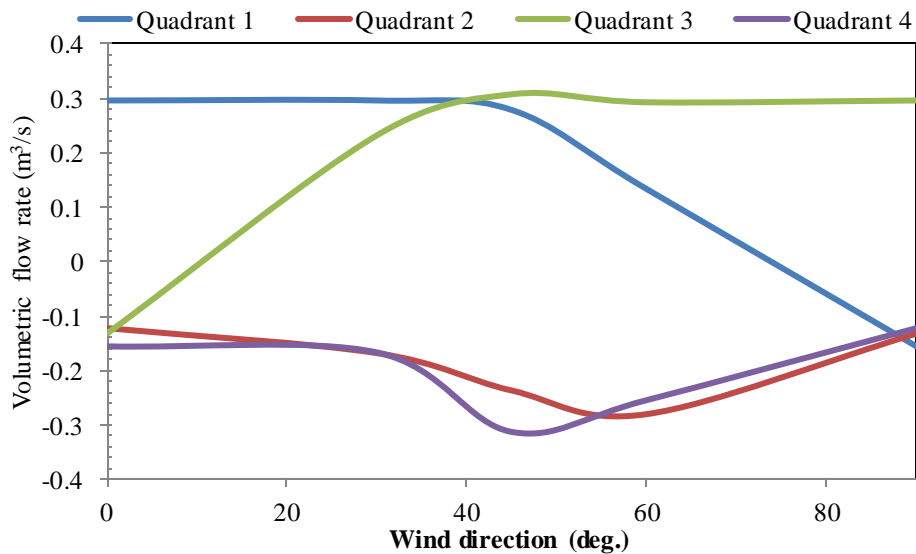
**Figure 6.25** 1:10 prototype model of the four and one-sided wind tower design incorporating heat transfer devices and porous mesh.

Table 6.9 summarises the experimental results of the airflow speed through the four-sided wind tower with heat transfer devices and extended surfaces.

**Table 6.9** Measured values of air flow velocity through the four-sided wind tower with heat transfer devices and porous media [m/s].

	Quadrant 1				Quadrant 2				Quadrant 3				Quadrant 4			
	1	2	3	4	5	6	7	8	9	10	11	12	13	14	15	16
<b>2.5</b>	2.59	1.20	0.41	0.43	0.46	0.63	0.57	0.38	0.55	0.63	0.43	0.59	0.51	0.85	0.47	0.77
<b>30°</b>	2.12	1.13	0.73	0.95	0.81	0.72	0.51	0.81	0.94	1.01	0.80	1.11	0.73	0.57	0.77	0.71
<b>45°</b>	2.15	1.17	0.57	0.75	0.98	0.79	0.99	1.19	2.38	1.10	0.99	0.65	1.19	1.49	1.35	1.19
<b>60°</b>	0.64	0.35	0.89	0.34	0.98	1.40	1.18	1.11	2.21	1.34	0.44	0.39	0.98	1.38	0.71	1.18

Figure 6.26 shows the experimental results of the volumetric airflow through the four-sided wind tower with HTD and porous media at different wind angles.



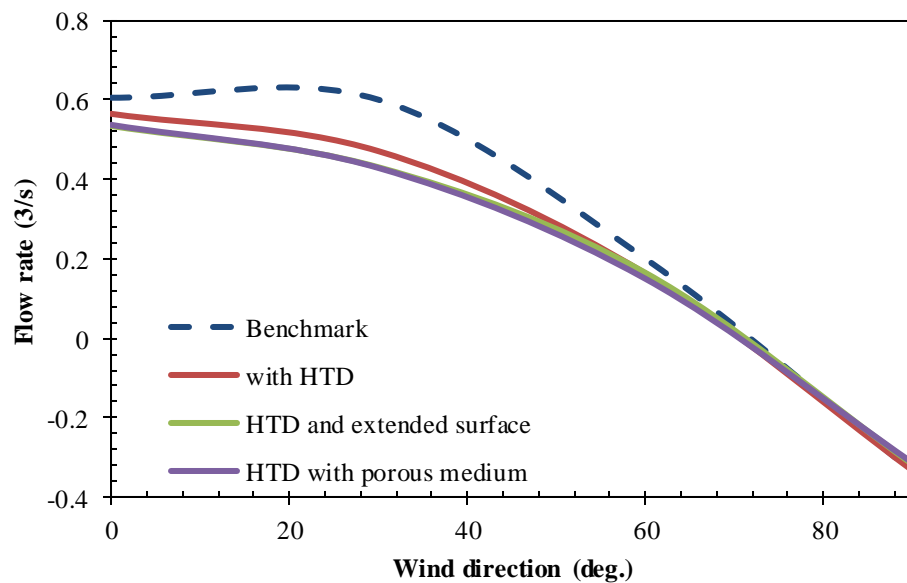
**Figure 6.26** Volumetric airflow rate through the wind tower supply and exhaust quadrants at various wind direction (four-sided wind tower with heat transfer devices and porous media).

Table 6.10 summarises the experimental results of the airflow speed through the one-sided wind tower model with heat transfer devices with extended surfaces.

**Table 6.10** Measured values of air flow velocity through the one-sided wind tower with heat transfer devices and porous media [m/s].

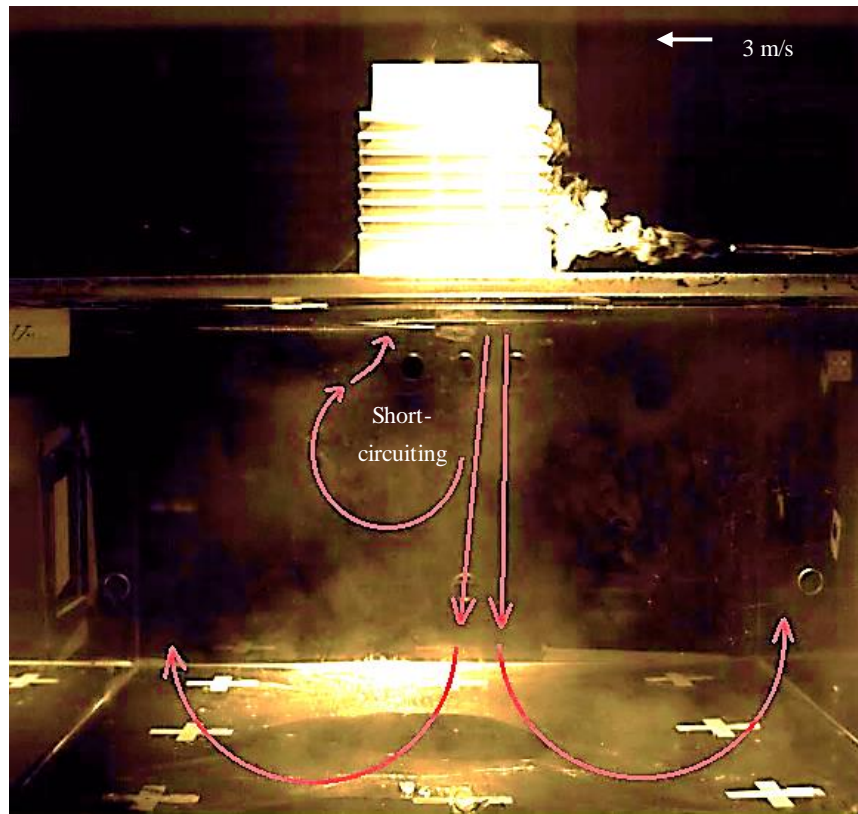
	1	2	3	4	5	6	7	8	9	Avg.
<b>0°</b>	1.19	0.99	1.00	1.30	1.05	0.98	1.10	0.90	1.15	<b>1.07</b>
<b>30°</b>	0.90	0.97	0.86	0.90	0.60	0.82	1.10	1.08	0.48	<b>0.86</b>
<b>60°</b>	0.48	0.29	0.60	0.20	0.15	0.14	0.46	0.20	0.17	<b>0.30</b>
<b>90°</b>	0.67	0.60	0.75	0.57	0.54	0.52	0.67	0.69	0.63	<b>0.63</b>

Figure 6.27 shows the experimental results of the volumetric airflow rate through the wind tower channel with heat transfer devices. In this figure the flow direction in the supply channel are recognised by positive and negative values of airflow correspondingly. A volumetric airflow rate of 0.55 m<sup>3</sup>/s was achieved through the supply channel at 0° for an external wind speed of 3 m/s.



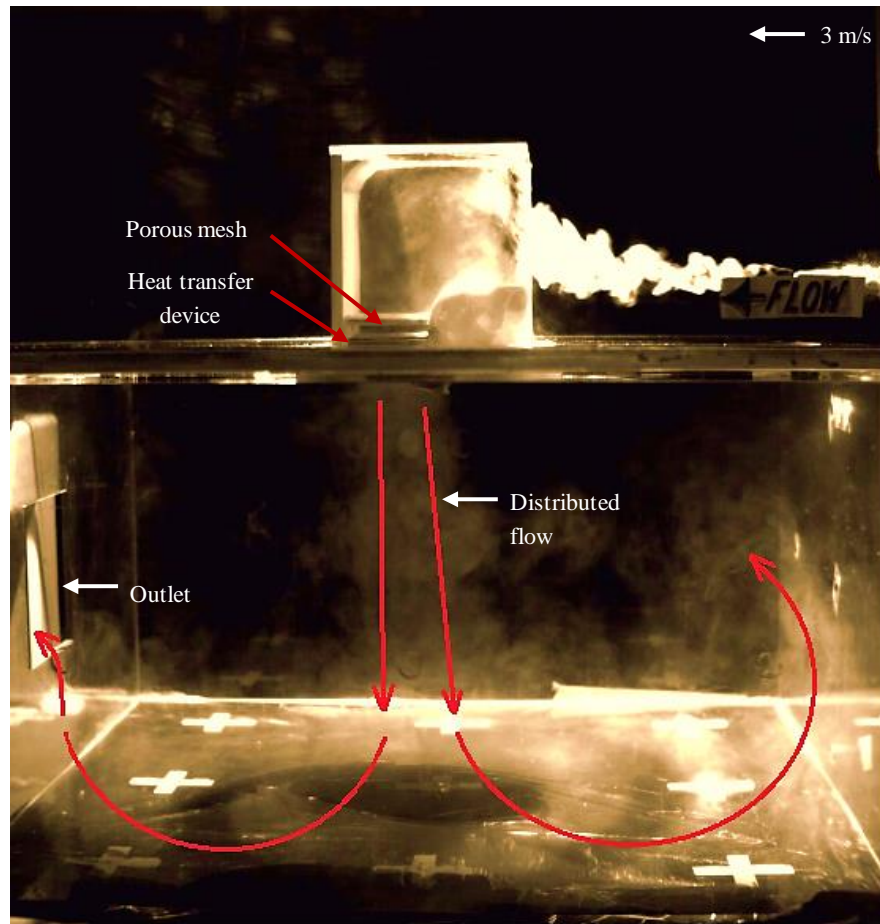
**Figure 6.27** Volumetric airflow through the wind tower supply channel at various wind direction (four-sided wind tower with heat transfer devices and porous media).

Figure 6.28 displays the visualised flow pattern inside the test room model with the vertical heat transfer device integrated wind tower model and porous media.



**Figure 6.28** Experimental flow visualisation inside the test room with the four-sided wind tower with heat transfer devices and porous media.

Figure 6.29 displays the visualised flow pattern inside the test room model with the horizontal heat transfer device integrated wind tower model and porous media.



**Figure 6.29** Experimental flow visualisation inside the test room with the one-sided wind tower with heat transfer devices and porous media.

## 6.6 Summary

This chapter presented the experimental investigations of the different wind tower designs (detailed in Chapter 4) using wind tunnel and smoke visualisation testing. Each variant of the wind tower was subjected to the test procedure (detailed in Section 4.5) with the results presented in this chapter. The experimental results were presented in both tabular and chart form. The flow visualisation results were accompanied with results from hot wire velocimetry measurements.

## **Chapter 7**

### **Validation of CFD Model**

#### **7.1 Introduction**

This chapter validated the CFD numerical results using the data acquired from the experimental test. Experimental results were used for all the eight wind tower configurations to validate the numerical methods and corresponding results. Comparisons were drawn between the CFD results and experiments and presented in chart form. To validate the simulated flow, the experimental flow visualisation was compared for all the wind tower models. In order to make an accurate comparison between the experimental models and the CFD models, pre-determined data collection points were directly compared with the experimental model (detailed in Chapter 4).

#### **7.2 Benchmark model validation**

A comparison between the experimental and the CFD model of the benchmark wind tower was carried out focusing this a set of parameters; air velocity within the test room, volumetric flow rates, air flow patterns in and around the wind tower model and surface pressure coefficients.

##### **7.2.1 Four-sided wind tower**

Figure 7.1 displays the velocity contours from top view of the microclimate with a standard four-sided wind tower model. As expected, the maximum velocity was achieved at the centre of the room with a maximum value of 1.4 m/s. A uniform trend was achieved across the other sides of the domain as the velocity decreased to an average value of 0.44 m/s across the remaining vertices. The graph shows a comparison between the experimental and CFD results for the velocity measurements. It was observed that the CFD slightly over or underestimated the airflow speeds at the measurement points. The trend (points 1 -12) shows that the CFD model was capable of predicting the airflow inside the test room. Average error across the points was 7 %.

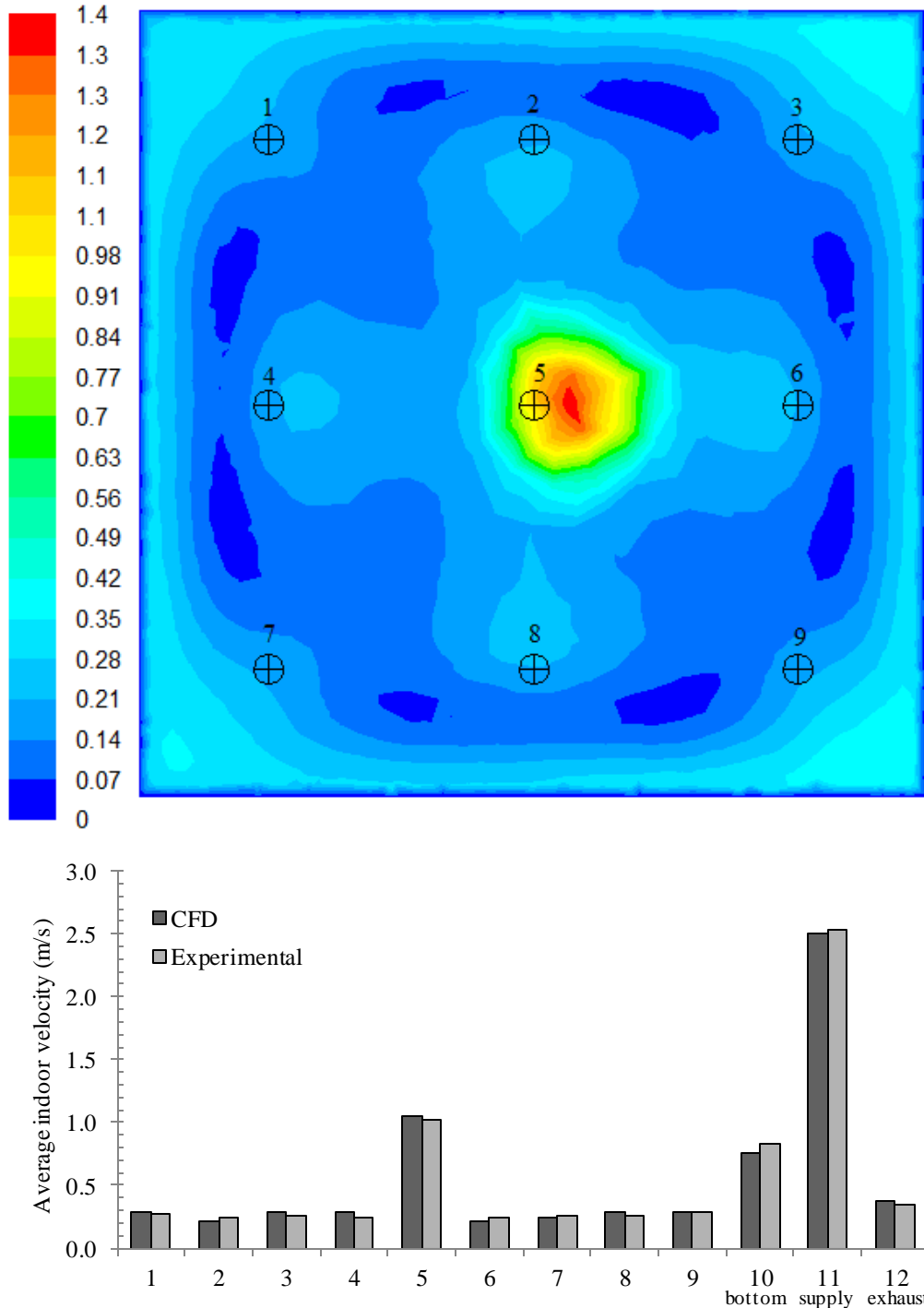


**Figure 7.1** Comparison between CFD and experimental indoor velocity (Four-sided wind tower benchmark model) with external wind speed at 3 m/s.

Figure 7.2 displays the velocity contours inside the wind tower channel. Maximum velocity was achieved at the windward quadrant with a maximum value of 3.1 m/s. The graph compared between the experimental and CFD results for the velocity measurements. Good agreement was observed between both methods of analysis with

the error less than 10% for all points except for point 6 which was located at the exhaust quadrant. Average error across the points was 7.6 %.

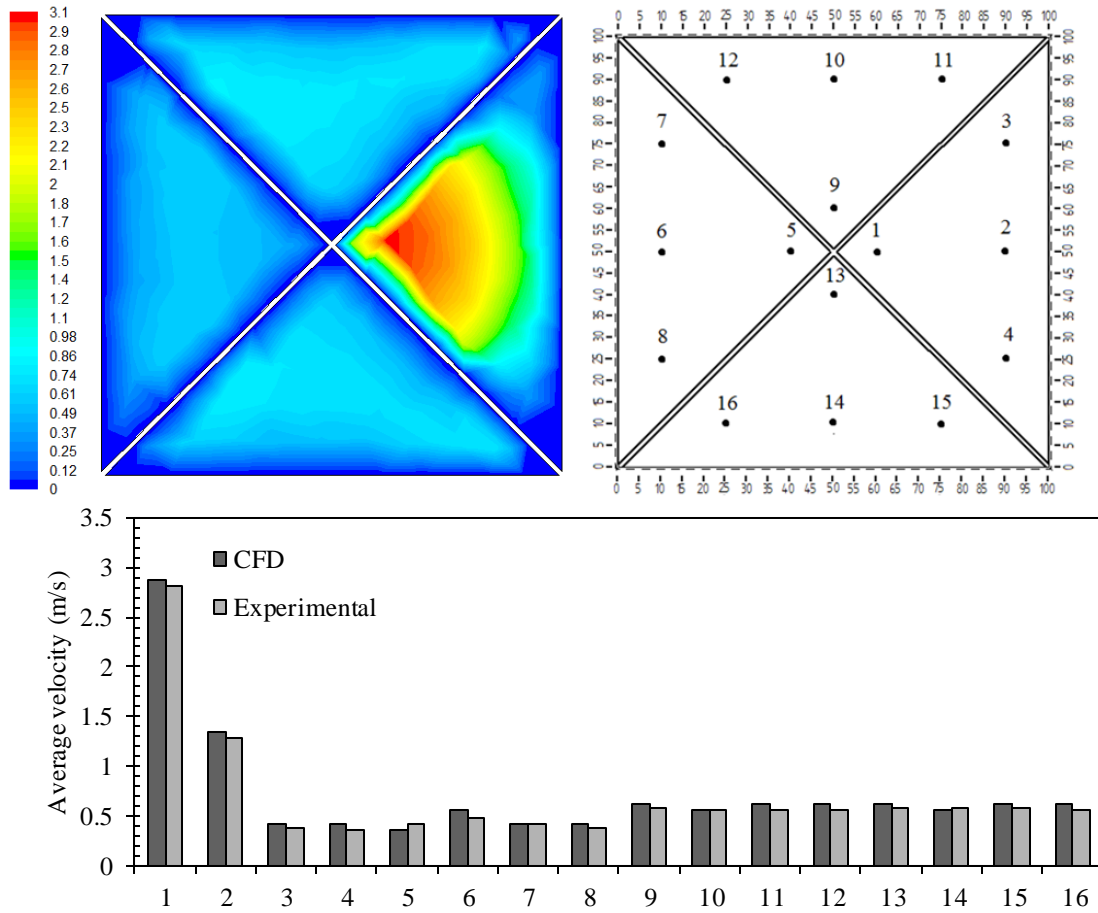


**Figure 7.2** Comparison between CFD and experimental results for the velocity in the supply and exhaust channels with external wind speed at 3 m/s (Four-sided wind tower benchmark model).

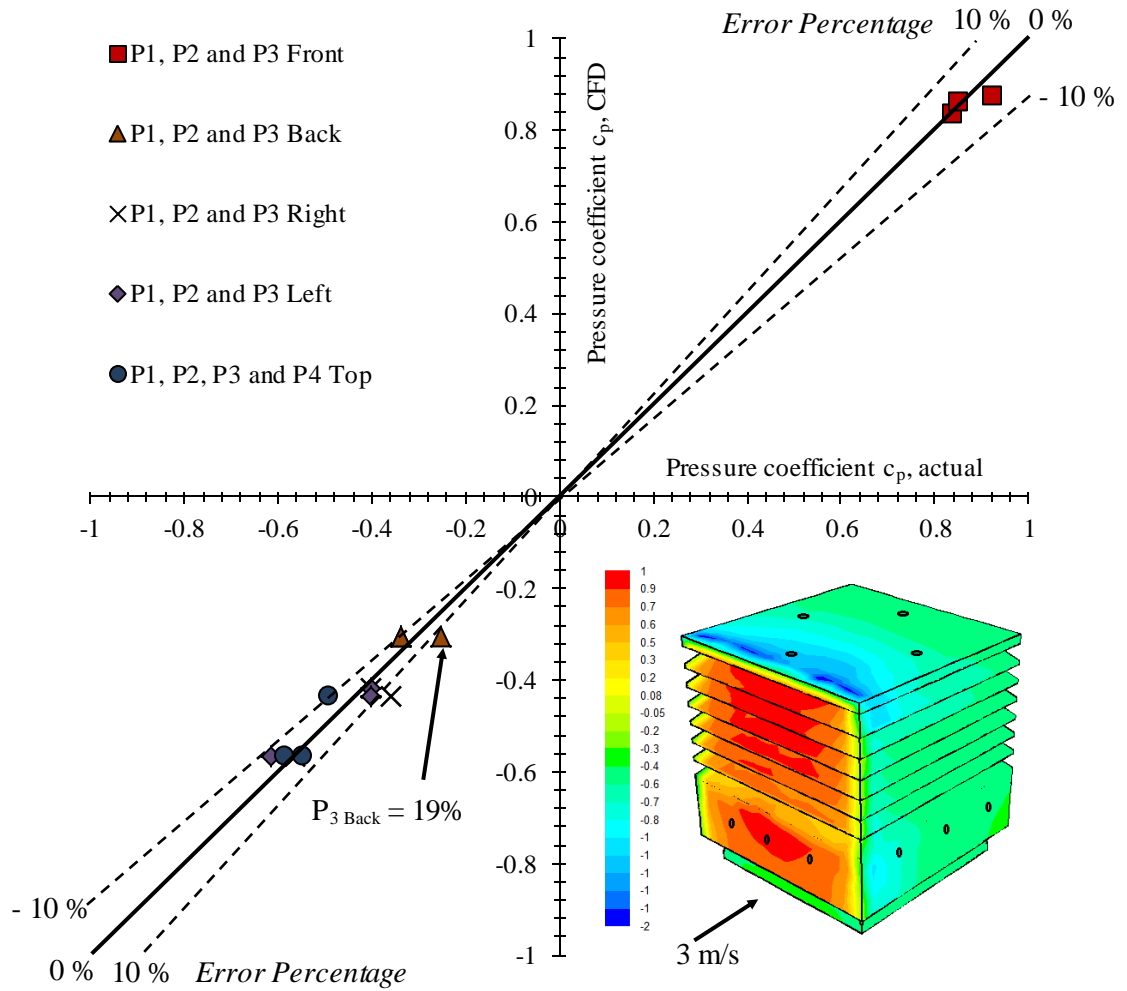
Table 7.1 shows the comparison between the measured and CFD values for the dimensionless velocity X, Y and Z for points A – G around the four-sided wind tower model. The flow speed values were made dimensionless by division by a reference wind speed, which was the measured wind speeds at point A. A good agreement was seen between both methods of analysis with the error less than 10% for all velocity components for all points except for point  $G_x$  (14 %) and  $G_z$  (11 %), which was located at the wake region of the airflow around the wind tower. This was one of the limitations of the k-epsilon turbulence model, it does not perform well for complex flows such as severe pressure gradients and large flow separations. The average error across the points was 8 %.

**Table 7.1** Comparison between measured and CFD results for mean velocity at points A - G (X, Y, Z) (stream wise, vertical and lateral) around the four-sided wind tower model.

Points		$U_X$ actual dimensionless	$U_Y$ actual dimensionless	$U_Z$ actual dimensionless	$U_X$ CFD dimensionless	$U_Y$ CFD dimensionless	$U_Z$ CFD dimensionless
A		<b>1.000</b>	0.063	0.035	<b>1.000</b>	0.065	0.032
B		0.850	0.366	0.384	0.848	0.372	0.394
C		0.689	0.415	-0.025	0.653	0.430	-0.025
D		0.884	0.363	0.380	0.841	0.372	0.386
E		0.918	-	-	0.884	-	-
F		0.468	0.181	-0.004	0.465	0.181	-0.004
G		<b>0.255</b>	0.120	<b>-0.078</b>	<b>0.218</b>	0.116	<b>-0.087</b>

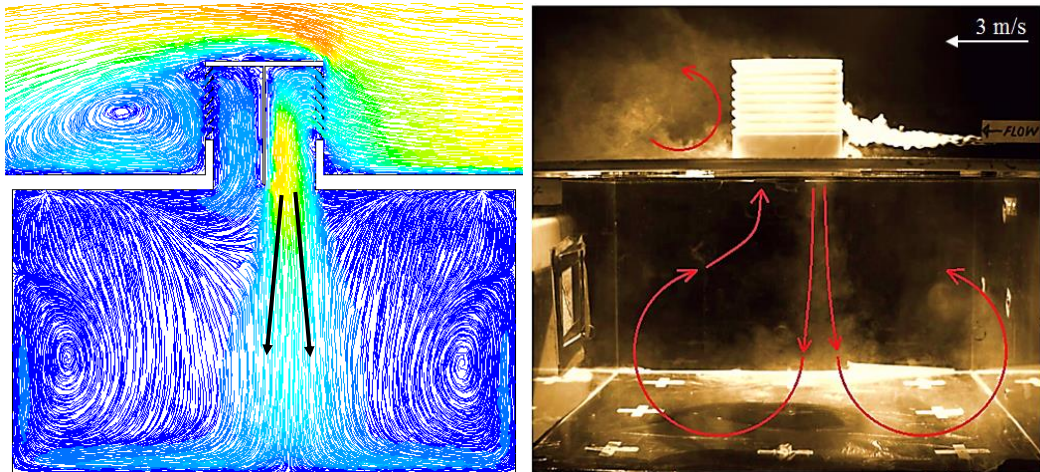
Figure 7.3 shows the measured and CFD values for the pressure coefficients at the front, back, left, right and top surfaces of the four-sided wind tower model. As expected the points located at the front surface experiences the maximum value, and with the moving air stream towards the top, right and left side, the pressure coefficient decreases, indicating the acceleration of the flow. The measured pressure coefficient along the right and left surface of the wind tower were very close, indicating the flow symmetry for the zero incident angle wind. Point P1 – Top, the pressure coefficient drop sharply. This point was at the front edge of the top surface where flow separation occurs. While for the back side of the of the wind tower model, a uniform pressure distribution was observed. This was because of the separation of the air stream from the sides; an almost uniform low pressure wake was formed around the back surface. CFD and experimental results showed good agreement, with the error below 10 % except for point P2 – right and P3 - back. Measurements at the front surface of the wind tower gave the highest accuracy with average error of only 5 % between the points (P1 – P3).

Errors in wind tunnel pressure measurements are typically about 10 - 20 % [Cook, 1990] which suggests that the discrepancy between the CFD and experimental results are due predominantly to errors in the CFD predictions, rather than errors in the measured results.



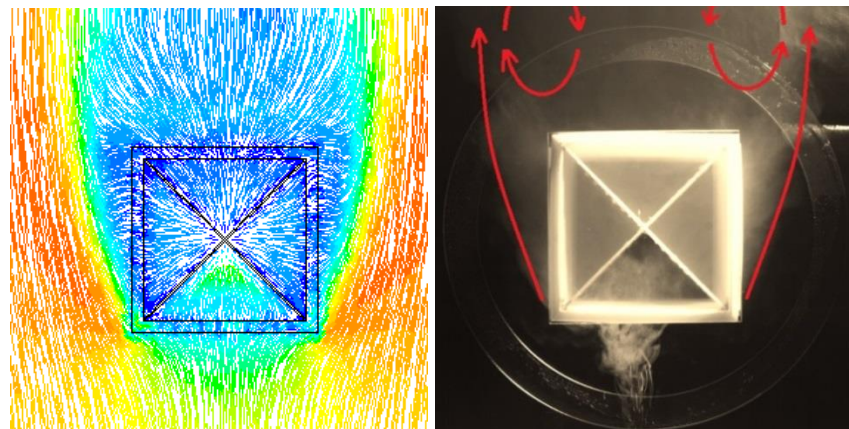
**Figure 7.3** Comparison between CFD and experimental values for surface pressure coefficients around the four-sided wind tower model. Dotted lines represent 10 % error percentage.

Figure 7.4 shows a comparison between CFD and experimental visualised flow pattern inside the test room model with a standard four-sided wind tower. A similar flow pattern was observed; the airflow was directed towards the floor of the test section and spread outwards in all directions. As the airflow hits the bottom surface the air slows down and flows through the side walls, with some of the air escaping through the exhaust quadrant of the wind tower which has a lower air pressure. A region of highly unsteady and recirculating flow was observed immediately at the downstream of the wind tower.



**Figure 7.4** Comparison between the indoor airflow distribution inside the test room with a standard four-sided wind tower model.

Figure 7.5 shows the visualised flow pattern inside the wind tower channels from top view. The flow visualisation method showed that the four quadrants were all working to both draw in the external air and exhaust the stale air out of the test room.



**Figure 7.5** Flow visualisation inside the supply and exhaust quadrant with external wind speed set at 3 m/s.

### 7.2.2 One-sided wind tower

Figure 7.6 displays the velocity contours from top view of the test room model with a standard four-sided wind tower model. Maximum velocity was achieved at the centre of the room with a maximum value of 1.2 m/s. A non-uniform trend was observed inside the room, airflow velocity on the left (Points 1, 4 and 7) was faster compared to the right (Points 3, 6 and 9). This was due to the window on the left extracting the air out of the test room.

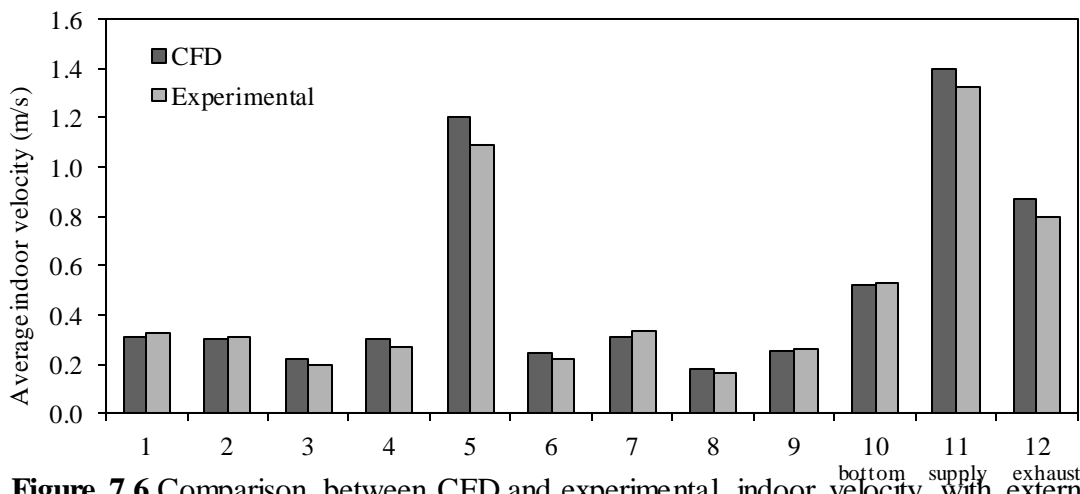
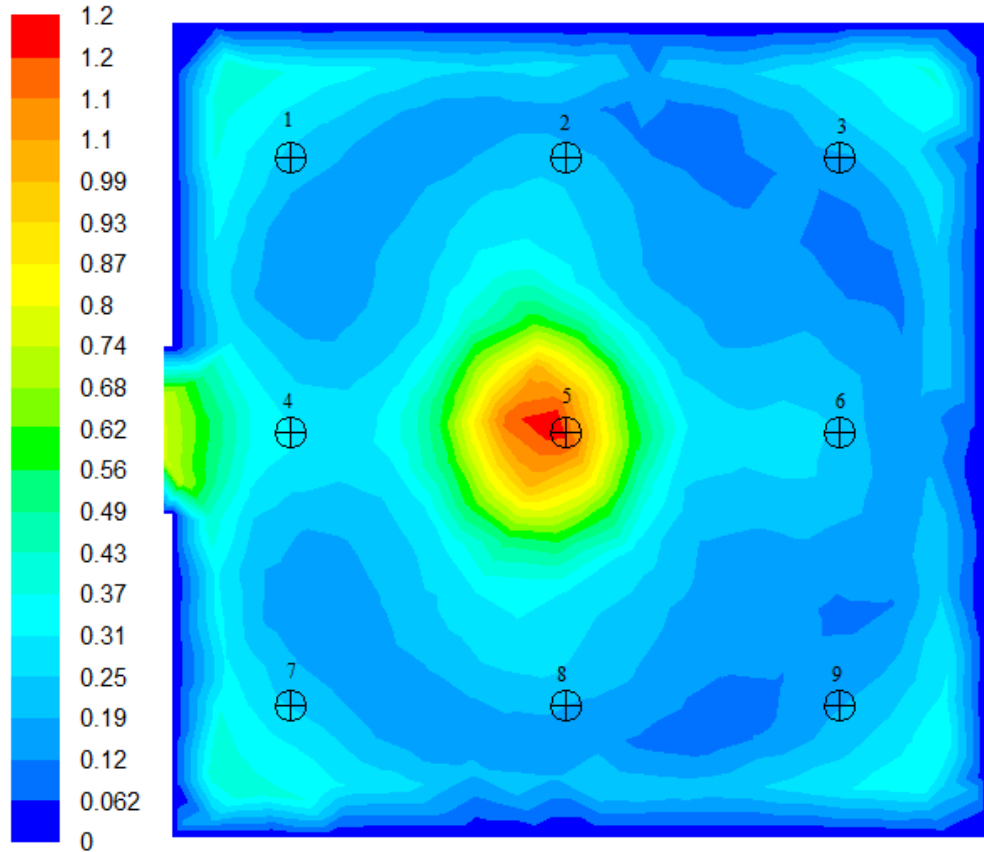


**Figure 7.6** Comparison between CFD and experimental indoor velocity with external wind speed at 3 m/s (One-sided wind tower benchmark model).

The graph shows a comparison between the experimental and CFD results for the velocity measurements. It can be observed that the CFD slightly over or underestimated the airflow speeds at the measurement points. The trend (points 1 -12) shows that the CFD model was capable of predicting the airflow inside the test room. Average error across the points was 6.7 %.

Figure 7.7 depicts the velocity contours inside the wind tower channel with external wind speed at 3 m/s. Maximum velocity was achieved in the left corner of the channel with a maximum value of 2 m/s. The graph compared experimental and CFD results for the velocity measurements. Good agreement was observed between both methods of analysis with the error less than 10% for all points except for point 3 (12.5 % error).

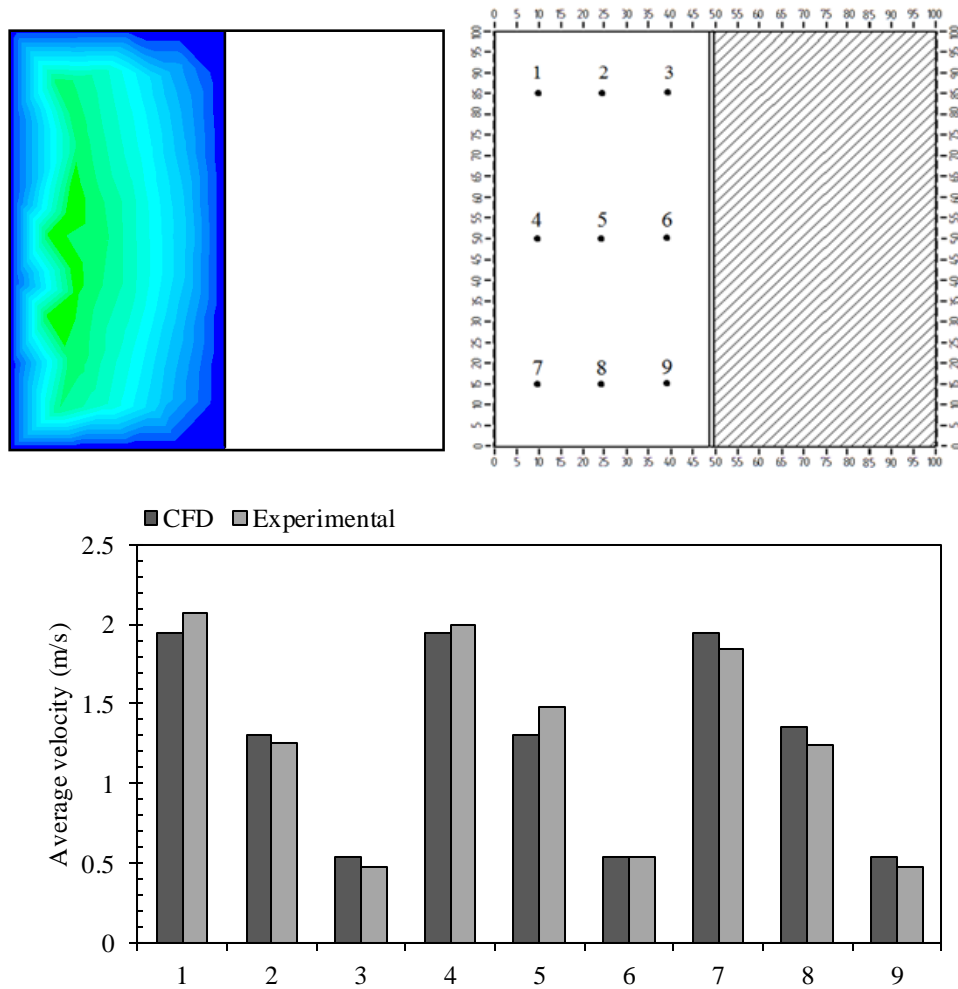


**Figure 7.7** Comparison between CFD and experimental results for the velocity in the supply channel (One-sided wind tower benchmark model).

Table 7.2 shows the comparison between the measured and CFD values for the dimensionless velocity X, Y and Z for points A – G around the four-sided wind tower model. The flow speed values were made dimensionless by division by a reference wind speed, which was the measured wind speeds at point A (mean). A good agreement was seen between both methods of analysis with the error less than 10% for all velocity components for all points except for points G (y and z – velocity components).

**Table 7.2** Comparison between measured and CFD results for mean velocity at points A - G (X, Y, Z) (stream wise, vertical and lateral) around the one-sided wind tower model.

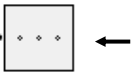
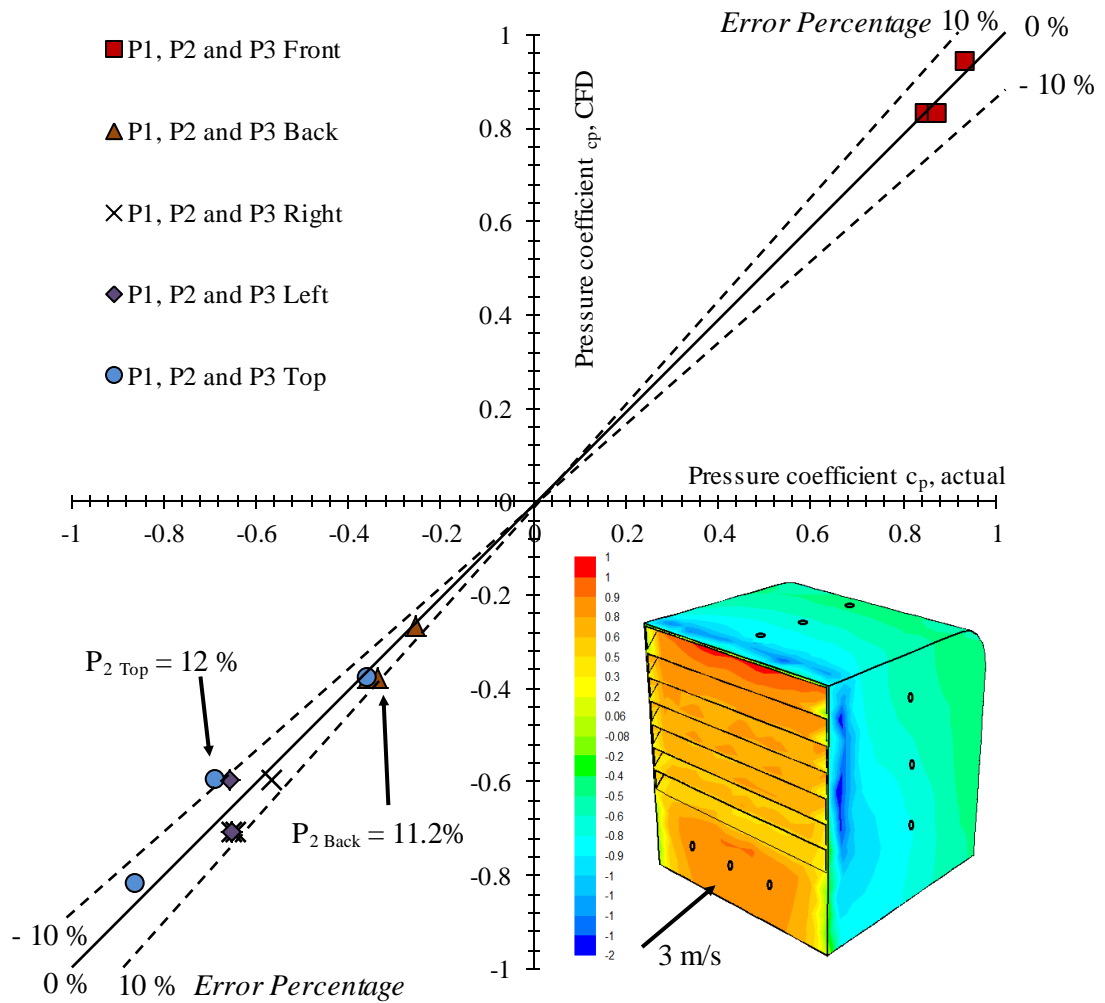
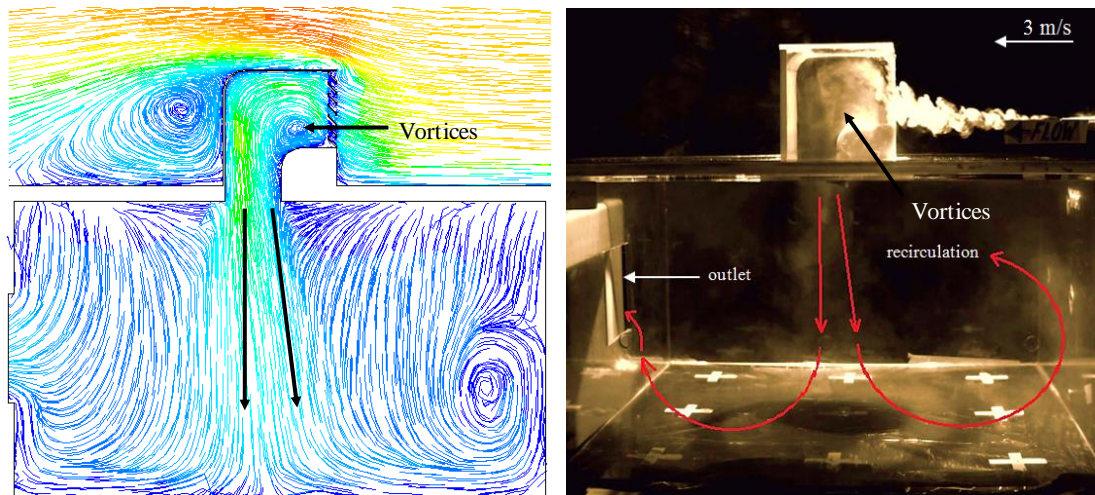
Points		$U_X$ actual dimensionless	$U_Y$ actual dimensionless	$U_Z$ actual dimensionless	$U_X$ CFD dimensionless	$U_Y$ CFD dimensionless	$U_Z$ CFD dimensionless
A		<b>1.00</b>	0.09	0.04	<b>1.00</b>	0.08	0.05
B		0.95	0.48	0.54	0.93	0.51	0.52
C		0.69	0.58	0.01	0.65	0.64	0.01
D		0.88	0.52	-0.55	0.87	0.52	-0.54
E		0.92	-	-	0.88	-	-
F		0.47	0.29	0.03	0.48	0.27	0.04
G		0.22	<b>0.04</b>	<b>-0.07</b>	0.21	<b>0.03</b>	<b>-0.09</b>

Figure 7.8 shows the measured and CFD values for the pressure coefficients at the front, back, left, right and top surfaces of the one-sided wind tower model. CFD and experimental results showed good agreement, with the error below 10 % except for point P2 – top and back. Similarly, measurements at the front surface of the wind tower gave the highest accuracy with average error of only 5 % between the points.



**Figure 7.8** Comparison between CFD and experimental values for surface pressure coefficients around the wind tower model. Dotted lines represent 10 % error percentage.

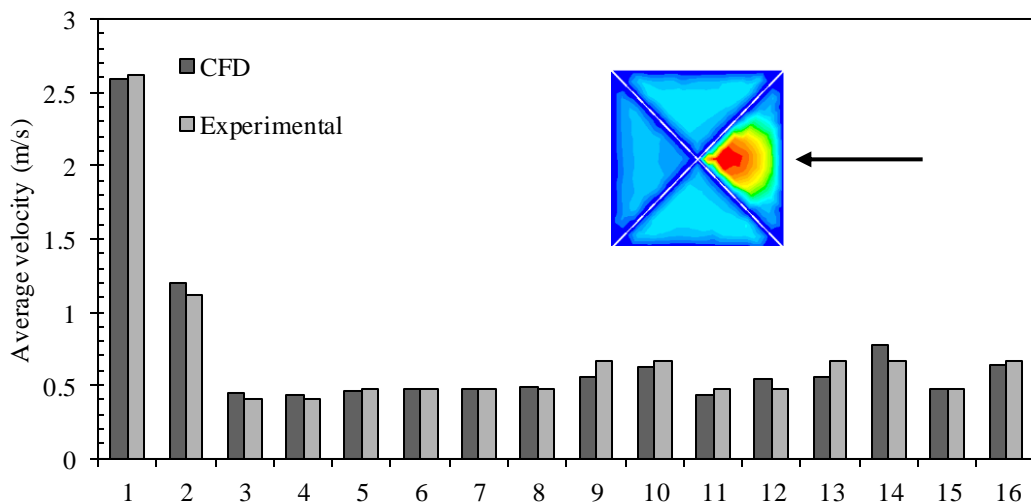
Figure 7.9 shows a comparison between CFD and experimental visualised flow pattern inside the test room model. A similar flow pattern was observed; the airflow was directed towards the floor of the test section and spread outwards in all directions. As the airflow hits the bottom surface the air slows down and flows through the side walls, with some of the air escaping through the exhaust quadrant of the wind tower which has a lower air pressure. A region of highly unsteady and recirculating flow was observed immediately at the downstream of the wind tower.



**Figure 7.9** Comparison between the indoor airflow distribution inside the test room with a one-sided wind tower.

### 7.3 Validation of the wind tower model with heat transfer devices

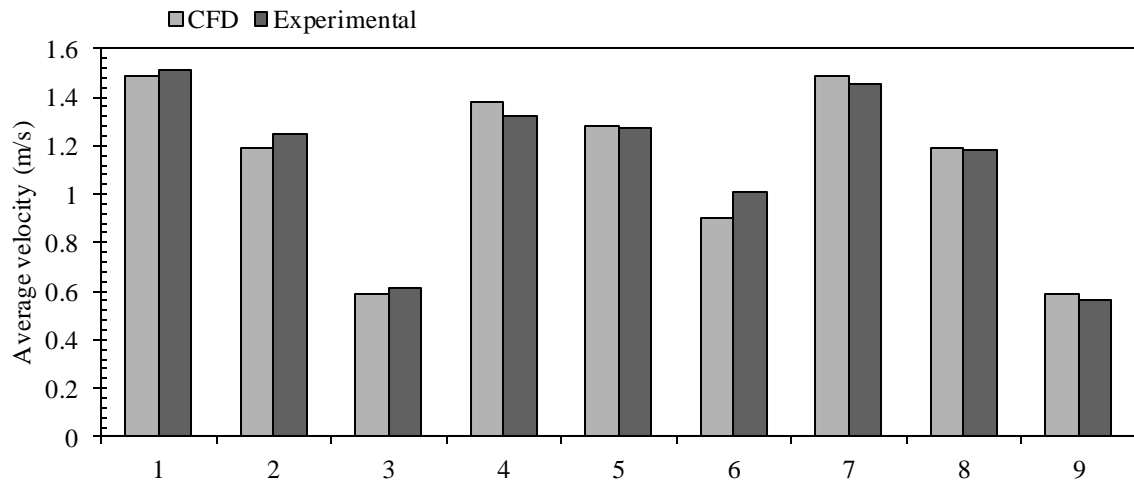
Figure 7.10 shows a comparison between the experimental and CFD results for the velocity measurements inside the wind tower channel with heat transfer devices. The trends for both the CFD and experimental data are in good agreement. The comparison showed a low difference range and the trends to be in good agreement. Average error across the points was 7.5 %.



**Figure 7.10** Comparison between CFD and experimental results for the velocity in the supply and exhaust channels with external wind at 3 m/s (Four-sided wind tower with HTD).

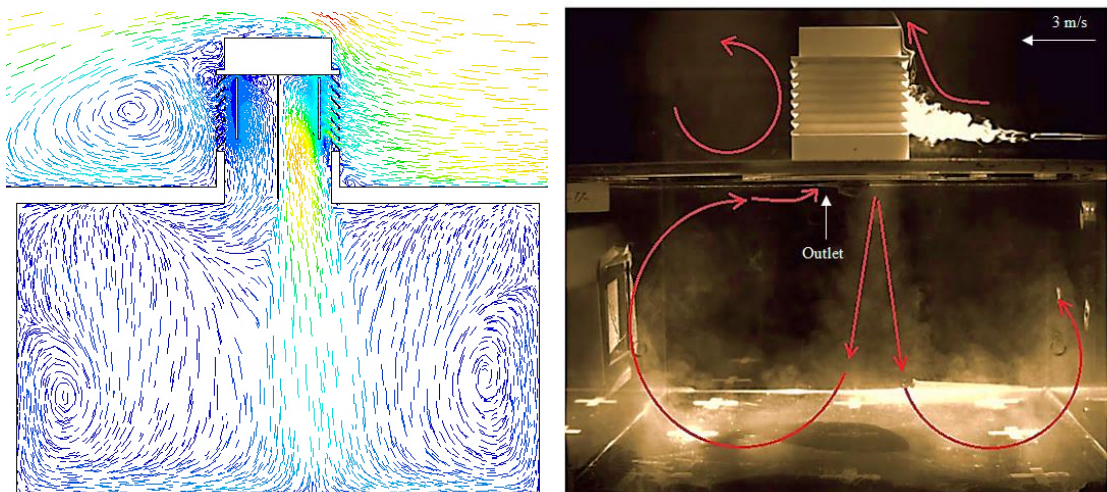
In Figure 7.11, the velocity values obtained from the CFD simulation was compared with the experimental results. It can be seen that CFD simulation have a good agreement

with the experimental results though there are some differences at the points located at the middle of the channel (Point 5) downstream of the heat transfer devices.



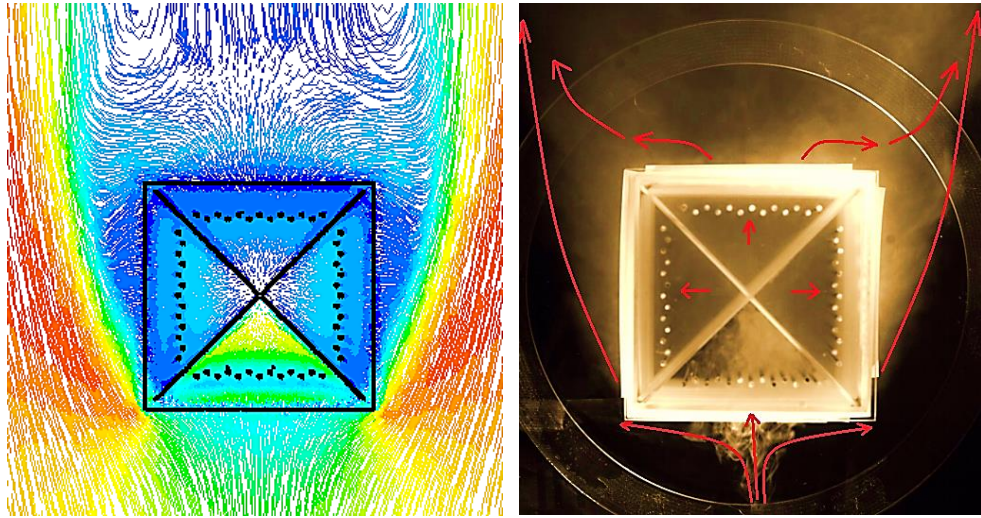
**Figure 7.11** Comparison between CFD and experimental results for the velocity in the supply and exhaust channels with external wind speed at 3 m/s (One-sided wind tower with HTD).

Figure 7.12 shows a comparison between CFD and experimental visualised flow pattern inside the test room model with a four-sided wind with heat transfer devices. The flow pattern in the simulation model is the same as the flow pattern recorded in the experimental test. The method of air-exchange is the same in both cases. Therefore, the simulation flow was considered validated



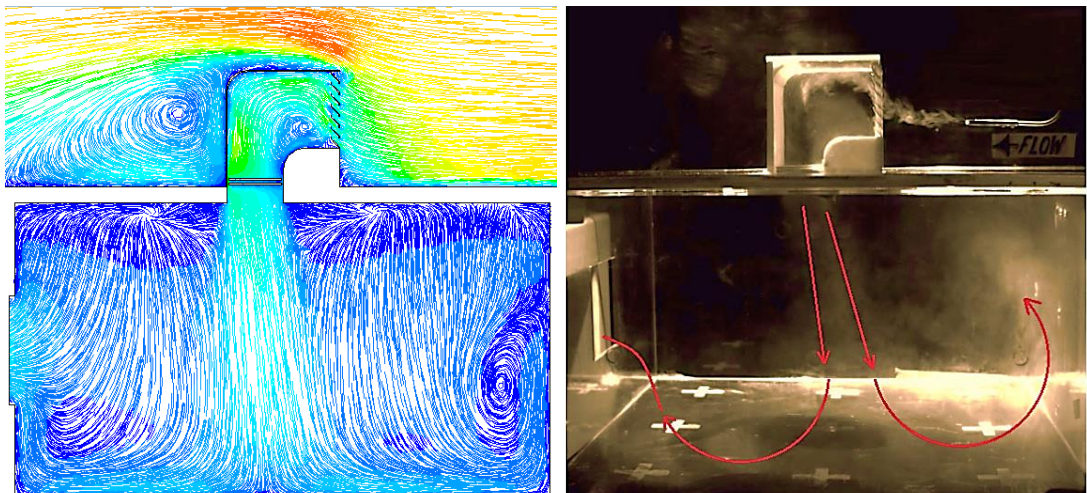
**Figure 7.12** Comparison between the indoor airflow distribution inside the test room (Four-sided wind tower with HTD).

Figure 7.13 illustrates the visualised flow pattern inside the wind tower channels from top view. The flow visualisation method showed that the four quadrants were all working to both draw in the external air and exhaust the stale air out of the test.



**Figure 7.13** Comparison between the airflow distribution inside the wind tower with heat transfer devices .

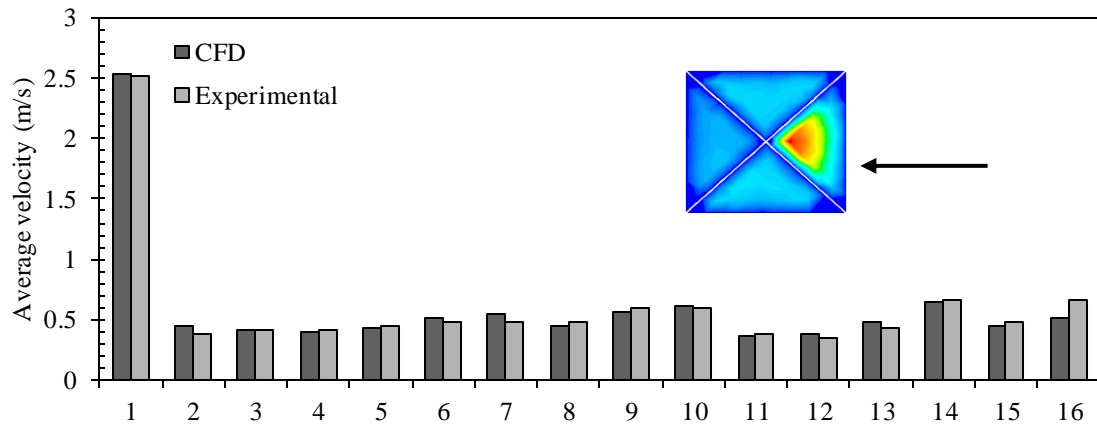
Figure 7.14 shows a comparison between CFD and experimental visualised flow pattern inside the test room model with a one-sided wind with heat transfer devices. The flow pattern in the simulation model is the same as the flow pattern recorded in the experimental test. Therefore, the simulation flow was considered validated.



**Figure 7.14** Comparison between the indoor airflow distribution inside the test room (One-sided wind tower with HTD).

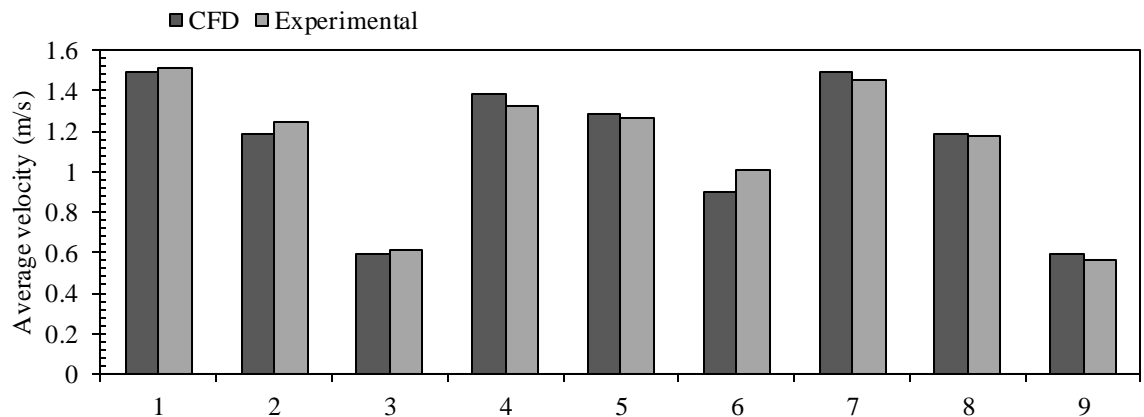
## 7.4 Validation of the wind tower model with heat transfer devices and extended surfaces

Figure 7.15 shows a comparison between the experimental and CFD results for the velocity measurements inside the wind tower channel with heat transfer devices and extended surfaces. The trends for both the CFD and experimental data are in good agreement. The comparison showed a low difference range and the trends to be in good agreement. Average error across the points was 7.7 %.



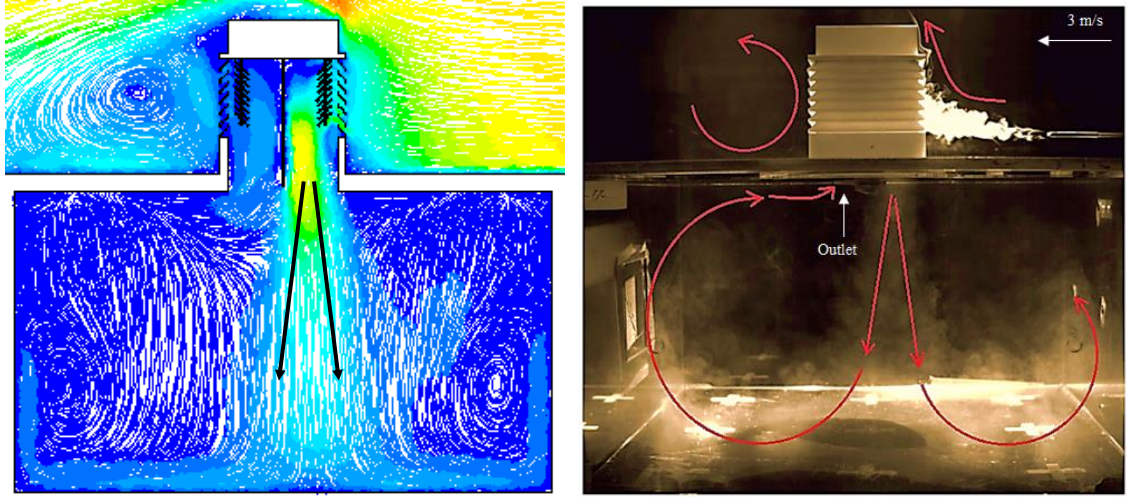
**Figure 7.15** Comparison between CFD and experimental results for the velocity in the supply and exhaust channels with external wind speed at 3 m/s (Four-sided wind tower with HTD and extended surface).

In Figure 7.16, the velocity values obtained from the CFD simulation was compared with the experimental results. It can be seen that CFD simulation has a good agreement with the experimental results. Average error across the points was 9 %.



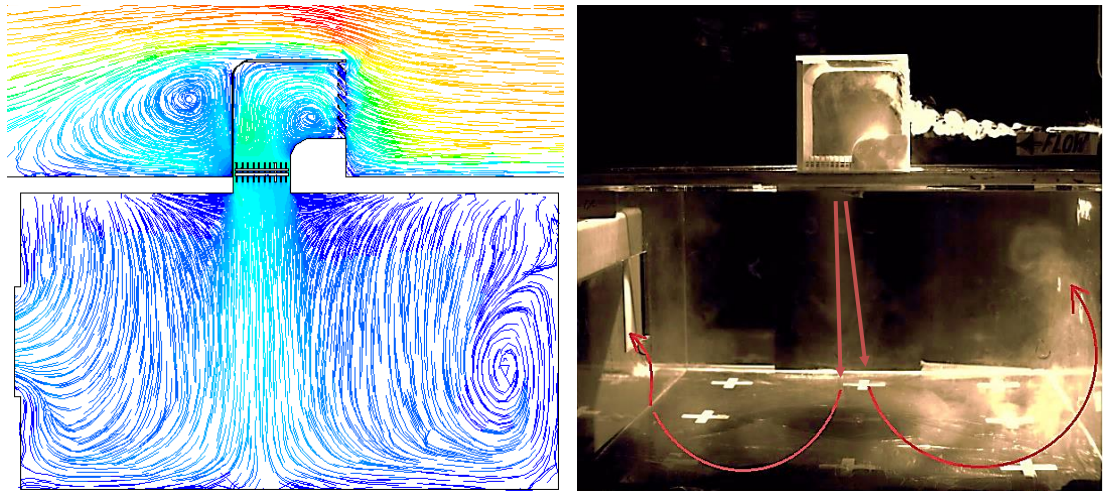
**Figure 7.16** Comparison between CFD and experimental results for the velocity in the supply and exhaust channels with external wind speed at 3 m/s (One-sided wind tower with HTD and extended surfaces).

Figure 7.17 shows a comparison between CFD and experimental visualised flow pattern inside the test room model with a four-sided wind tower with heat transfer devices and extended surfaces.



**Figure 7.17** Comparison between the indoor airflow distribution inside the test room (Four-sided wind with HTD and extended surface).

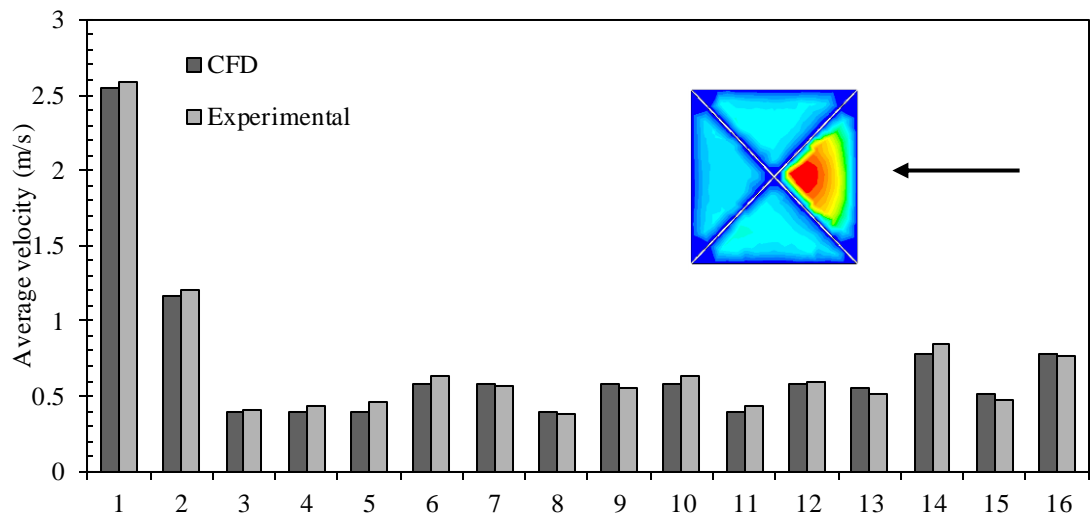
Figure 7.18 displays a comparison between CFD and experimental visualised flow pattern inside the test room model with a one-sided wind with heat transfer devices and extended surfaces.



**Figure 7.18** Comparison between the indoor airflow distribution inside the test room (One-sided wind tower with HTD and extended surfaces).

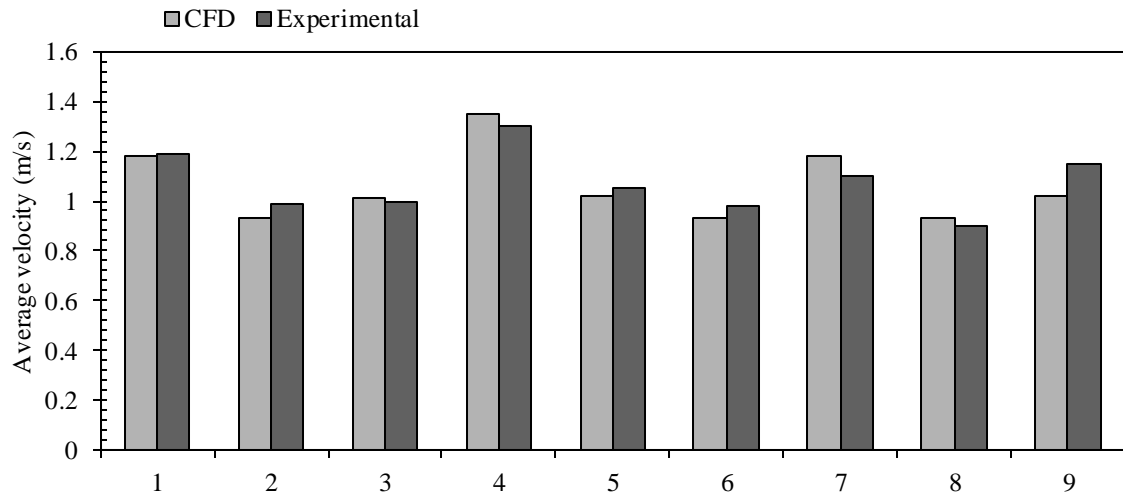
## 7.5 Validation of the wind tower model with heat transfer devices and porous media

Figure 7.19 shows a comparison between the experimental and CFD results for the velocity measurements inside the wind tower channel with heat transfer devices and porous media. The trends for both the CFD and experimental data are in good agreement. The comparison showed a low difference range and the trends to be in good agreement. Average error across the points was 6.4 %.



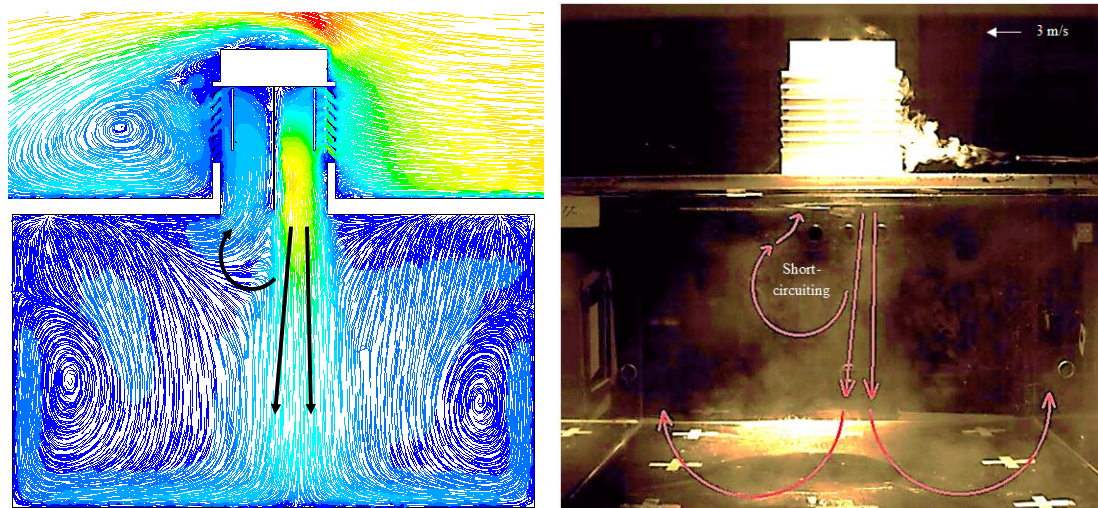
**Figure 7.19** Comparison between CFD and experimental results for the velocity in the supply and exhaust channels with external wind speed at 3 m/s (Four-sided wind tower with HTD and porous media).

In Figure 7.20, the velocity values obtained from the CFD simulation was compared with the experimental results. It can be seen that CFD simulation has a good agreement with the experimental results. Average error across the points was 4.2 %.



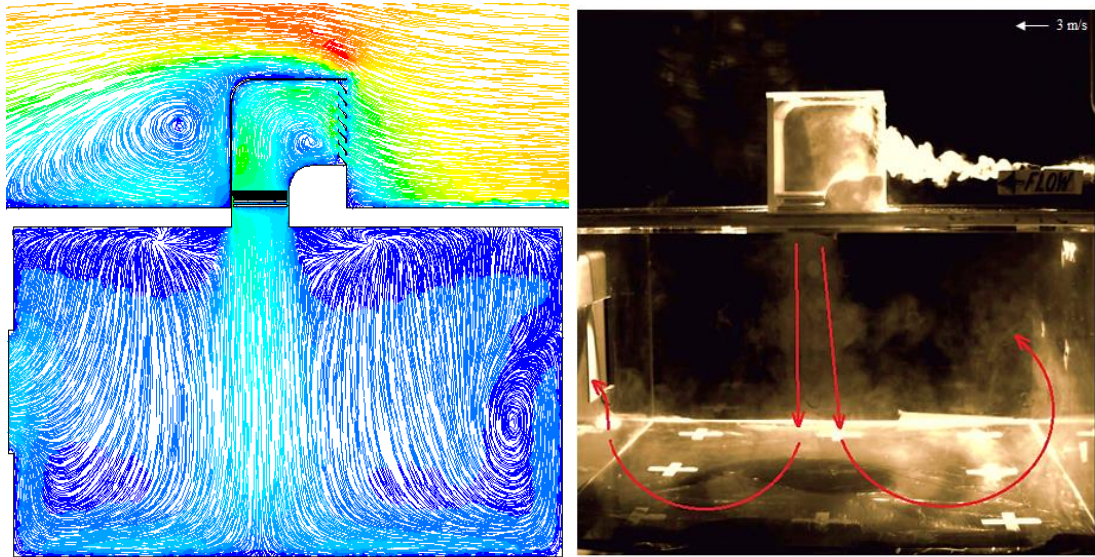
**Figure 7.20** Comparison between CFD and experimental results for the velocity in the supply and exhaust channels with external wind speed at 3 m/s (One-sided wind with HTD and porous media).

Figure 7.21 shows a comparison between CFD and experimental visualised flow pattern inside the test room model with a four-sided wind with heat transfer devices and porous media.



**Figure 7.21** Comparison between the indoor airflow distribution inside the test room (Four-sided wind tower with HTD and porous media).

Figure 7.22 displays a comparison between CFD and experimental visualised flow pattern inside the test room model with a one-sided wind tower with heat transfer devices and porous media.



**Figure 7.22** Comparison between the indoor airflow distribution inside the test room (One-sided wind tower with HTD and porous media).

## 7.6 Quantification of CFD uncertainties

Errors and uncertainties are unavoidable in numerical simulation. It is essential to develop methods to quantify the level of confidence in its results [Xu, 2013]. Physical modelling uncertainty requires comparison of CFD results with experimental or field measurement data. In this study, the error and trend between the CFD prediction and the measured points were used as a major criterion. The errors were found to be within the range of 0 – 20%, using a similar justification as recommended in [Zhang *et al.*, 2007] it can be claimed that the validation of the CFD modelling study was acceptable. Furthermore, the numerical simulation results also followed the same trends as the experimental work. Chen and Serbric [2002] stated "as long as the trends that are predicted are consistent, the less-than-perfect accuracy should be acceptable".

## 7.7 Summary

The numerical simulation data was validated against the experimental results. Comparisons were drawn between the CFD results and experiments and presented in chart form. Good agreement was observed between both methods of analysis. The error was found to be in the range of 0 - 20 %. Agreement between the trends of the two studies was demonstrated. This chapter validated the simulation methods and results in this study.

## Chapter 8

### Conclusions and Future Work

#### 8.1 Conclusions

The research has made a number of significant advances in the understanding of the integration and application of passive cooling within a wind tower for hot and humid climates. These conclusions are made in order that allow direct comparison, against the research objectives of this study defined in Chapter 1 (see Section 1.2). This study has achieved its objectives through systematic numerical and experimental investigations. The objectives met are summarised as follows:

1. The CFD simulation established that the wind tower with the horizontal Heat Transfer Device (HTD) arrangement outperformed the vertical HTD arrangement in terms of temperature reduction. The study showed that the horizontal HTD wind tower was capable of reducing the supply air stream temperature by up to 6.8 K, which was 20 % higher compared to the four-sided wind tower with the vertical HTD arrangement.

Furthermore the results revealed that both systems were capable of providing the recommended supply rates at low wind speeds. The horizontal HTD wind tower device provided 26 – 67 L/s per occupant (total of 15 occupants) at 2 – 5 m/s external wind and the vertical HTD model supplied 16.2 – 45 l/s per occupant at 3 – 5 m/s external wind.

2. The study maximised the cooling performance of the heat transfer device integrated system by varying the the number and spacing of the cylindrical tubes. Two HTD spacing arrangements were compared; 0.05 and 0.1 m horizontal spacing. The simulation confirmed that the model with smaller horizontal spacing outperformed the model with large horizontal spacing in terms of temperature reduction. The wind tower model with 0.1 m HTD horizontal spacing reduced the indoor temperature by 2 – 5.7 K (vertical arrangement) and 2.1 – 6.8 K (horizontal arrangement). While the wind tower model with 0.05 m horizontal HTD spacing reduced the indoor temperature by 4.3 – 12.5 K (vertical arrangement) and 8.6 – 15 K (horizontal arrangement) at 5 – 1 m/s wind speed.

3. The CFD model was coupled with a simulation weather data file (Detailed in Chapter 3) to investigate the performance of the wind tower system under different climatic conditions. The weather data provided the boundary conditions for the wind speed, temperature and relative humidity simulating a very hot and humid environment. Results showed that the maximum temperature reduction was achieved during the month of July when the outside temperature was at 314.5 K and wind speed at 3.8 m/s. However, the reduction in temperature also increased the indoor relative humidity by 90 – 100%. Lowest internal airflow velocity measured inside the test room was during the least windy month of October, with an average speed 3.2 m/s.
4. Extended surfaces and a porous media were integrated to the cooling wind tower system to maximise the contact time between the supplied airflow and the heat transfer devices. The addition of extended surfaces to the heat transfer devices improved the cooling system's thermal performance, increasing the internal temperature drop by 6.7 – 10 K (external wind speed of 5 – 1 m/s). The effect of adding the porous media to the model was demonstrated to be insignificant. Even though the porous media effectively straightened the flow and improved the velocity distribution across the heat transfer devices surfaces, it did not have any positive effect on the cooling performance. This was due to the reduction of flow turbulence which also reduced the heat transfer between the airflow and the cooling device surfaces (Detailed in Chapter 5)
5. The study determined the thermal comfort level inside the test room model employing the heat transfer device integrated wind tower using a coupled CFD model (Detailed in Chapter 3). The model predicted that the proposed cooling system was capable of improving the thermal comfort level over those provided by a standard wind tower during summer conditions. However, due to high humidity levels the improvement was minimal (3 “very hot” to 2.5 “hot”). The study showed that the wind tower with heat transfer device did not provide effective cooling due to extreme external conditions (very high temperature and humidity levels).

6. The investigation compared the ventilation performance of the heat transfer device integrated wind tower measured in the scaled wind tunnel (Chapter 6) with the numerical simulation results (Chapter 5). The comparison between the experimental data and simulation results demonstrated good agreement. The error (difference in results) was found to be in the range of 0 - 20 %. Agreement between the trends of the two studies was also demonstrated (Chapter 7).

## **8.2 Contribution to knowledge**

This work used the simulation and experimental techniques identified throughout the literature review to fill the identified research gap (Chapter 2). The following summarises the contribution this study has made to the knowledge of thermal comfort, natural ventilation, passive cooling and, in particular, wind tower devices for extreme temperature conditions:

1. Extensive numerical simulation data have been provided on the application of modern wind tower systems in extreme temperature conditions.
2. The numerical investigation showed that the cooling load of a standard four-sided and one-sided wind tower can be maximised through integrating a passive heat transfer device. The study investigated vertical and horizontal heat transfer devices (Chapter 5).
3. A coupled simulation model was established to investigate the performance of the wind tower system under different climatic conditions.
4. The investigation showed that the thermal performance of a heat transfer device integrated wind tower system can be maximised using extended surfaces. The effect of adding the porous media to the model was demonstrated to be insignificant (Chapter 5).
5. A coupled simulation method was developed to determine the thermal comfort level in a standard room employing the wind tower systems in terms of air temperature, velocity and relative humidity (Chapter 5).

6. CFD models were validated using wind tunnel and smoke visualisation testing. The level of accuracy using experimental testing to validate the CFD was established in Chapter 7.

### **8.3 Recommendations for further work**

The following areas that require further investigation have been identified:

- Following the successful analysis of the proposed heat transfer device integrated wind tower device, there is broad future scope for the performance optimisation of the system. Further analysis of the heat transfer device configurations such as orientation, shape, sizing, etc. in order to enhance the viability in terms of ventilation and thermal performance of the system is of further interest. Furthermore, the design of the wind tower cool sink which is required for the continuous operation of the system.

The methodology presented in this thesis could be used to investigate the combined changes in order to further optimise the system and also the data can be used as a benchmark. This would significantly reduce the experimental and computational costs.

- This research investigated the ventilation and thermal performance of the heat transfer device integrated wind tower using numerical modelling and wind tunnel testing. Full scale or far-field testing needs to be carried out in order to investigate its performance under real weather conditions.
- The work investigated the thermal comfort level in a standard room employing the wind tower system using the heat-balance approach or the Predicted Mean Vote (PMV) model. An extended study could be carried out to validate the previous work using the adaptive approach. The adaptive approach is based on the findings of surveys of thermal comfort conducted in the field. Full scale field experimental testing is required for this level of investigation.

- The thermal comfort analysis showed that reducing the indoor humidity improved the cooling effectiveness of the proposed wind tower system. An extended study could be carried out to control the humidity levels.
- Further investigation is required to evaluate the effect of the cooling system on the Indoor Air Quality (IAQ) specifically dust levels.

## List of References

- Airpak User Guide [Online] 2001, available from: <http://www.ce.utexas.edu/prof/Novoselac/classes/ARE372/Handouts/AirpakUserGuide.pdf>.
- Ahmed RS. Computational fluid dynamics: Aerodynamics of road vehicles. SAE International, 765-836, 1998.
- Allard F. Natural ventilation in buildings: A design handbook, Routledge 1998
- Arce J, Jiménez MJ, Guzmán JD, Heras MR, Alvarez G and Xamán J. Experimental study for natural ventilation on a solar chimney. *Renewable Energy*, 29, 2928-2934, 2009.
- Asfour O and Gadi M. Effect of Integrating Wind Catchers with Curved Roofs on Natural Ventilation Performance in Buildings. *Architectural Engineering and Design Management*, 2, 289-304, 2006.
- Attia S and Herde A. Designing the Malqaf for Summer Cooling in Low-Rise Housing, an Experimental Study. Conference on Passive and Low Energy Architecture, Canada, 2009.
- Autodesk Simulation, Flow through porous media [Online]. 2011, available from: [http://www.algor.com/news\\_pub/tech\\_reports/2008/cfd\\_analysis](http://www.algor.com/news_pub/tech_reports/2008/cfd_analysis)
- A'zami A. Badgir in traditional Iranian architecture. International Conference for the Built Environment, Greece, 2005.
- Badran A. Performance of cool towers under various climates in Jordan. *Energy and Buildings*, 35, 1031–1035, 2003.
- Bahadori MN. Passive Cooling Systems in Iranian Architecture. *Scientific American*, 1978.
- Bahadori MN. An Improved Design of Wind Towers for Natural Ventilation and Passive Cooling. *Solar Energy*, 35, 119–129, 1985.
- Bahadori MN. Viability of wind towers in achieving summer comfort in the hot arid regions of the Middle East. *Renewable Energy*, 5, 879-892, 1994.
- Bahadori MN, Mazidi M, and Dehghani AR. Experimental investigation of new designs of wind towers. *Renewable Energy*, 33, 2273–2281, 2008.
- Balendra T, Shah D, Tey K and Kong S. Evaluation of flow characteristics in the NUS-HDB Wind Tunnel. *Journal of Wind Engineering and Industrial Aerodynamics*, 90, 675-688, 2002.
- Bansal NK, Mathur R and Bhandari MS. Solar chimney for enhanced stack ventilation. *Building and Environment*, 28, 373-377, 1993.
- Barlow J, Rae W and Pope A. *Low Speed Wind Tunnel Testing*. John Wiley & Sons, 1999.
- Battle McCarthy Consulting Engineers. *Wind Towers: Detail in Building*. London Academy Press, 1999.
- Blazek J. *Computational Fluid Dynamics: Principles and Applications*. Elsevier, 2001.
- Bouchahm Y, Bourbia F and Belhamri A. Performance analysis and improvement of the use of wind tower in hot dry climate. *Renewable Energy*, 36 898-906, 2011.

- Bouchair A. Decline of urban ecosystem of Mzab alley, *Building and Environment*. 39, 719-732, 2004.
- Boustani F. Sustainable Water Utilization in Arid Region of Iran by Qanats. *International Journal of Human and Social Sciences*, 4, 505-508, 2009.
- Building Bulletin 98: Briefing Framework for Secondary School Projects [Online]. 2004, available from: <http://media.education.gov.uk>
- Calautit JK, Hughes BR and Ghani SA. A Numerical Investigation into the Feasibility of Integrating Green Building Technologies into Row Houses in the Middle East. *Architectural Science Review Special Issue*, 1, 1-18, 2012a.
- Calautit JK, Hughes BR and Ghani SA. Numerical Investigation of the Integration of Heat Transfer Device into Wind Tower. The 4<sup>th</sup> International Conference on Applied Energy, Suzhou (ICAE 2012), China, 5-8 July, 2012b.
- Calautit JK, Hughes BR, Chaudhry HN and Ghani SA. Computational analysis of a heat transfer device integrated wind tower system for hot and humid climate. The 7<sup>th</sup> Sustainable Development of Energy, Water and Environment Systems (SDEWES 2012), Ohrid, Macedonia, 2012c.
- Calautit JK, Chaudhry HN, Hughes BR, and Ghani SA. Comparison between evaporative cooling and a heat pipe assisted thermal loop for a commercial wind tower in hot and dry climatic conditions. *Applied Energy*, 101, 740-755, 2013a.
- Calautit JK, Hughes BR and Ghani SA. Numerical Investigation of the Integration of Heat Transfer Devices into Wind Towers. *Chemical Engineering Transactions Special Issue: SDEWES 2012*, 34, 43-48, 2013b.
- Candido C, de Dear RJ, Lamberts R and Bittencourt L. Air movement acceptability limits and thermal comfort in Brazil's hot humid climate zone. *Building and Environment*, 44, 222-229, 2010.
- Catalina T, Virgone J, and Kuznik F. Evaluation of thermal comfort using combined CFD and experimentation study in a test room equipped with a cooling ceiling. *Building and Environment*, 45, 1740-1750, 2010.
- Cebeci T and Cousteix J. *Modelling and Computation of Boundary-layer Flows: Laminar, turbulent and transitional boundary layers in incompressible and compressible flows*. Horizon Publishing, 2005.
- Cermak J. Wind tunnel design for physical modelling of atmospheric boundary layers. *Journal of Engineering Mechanics*, 107, 523-642, 1981.
- Cermak J. Wind-tunnel development and trends in applications to civil engineering. *Journal of Wind Engineering and Industrial Aerodynamics*, 91, 355-370, 2003.
- Chan H, Riffat S. and Zhu J. Review of passive solar heating and cooling technologies. *Renewable and Sustainable Energy Reviews*, 14, 781-789, 2010.
- Cheng V, Ng E and Givoni B. Optimal air temperature and air speed for built environment in Hong Kong from thermal comfort and energy saving perspectives. *World Sustainable Building Conference*, Australia, September, 2007.
- Chong T, Joseph P and Davies P. Design and Characterisation of a Quiet, Low Turbulence Open Jet Blow Down Wind Tunnel in ISVR. ISVR Technical Report NO 322 University of Southampton, 2008.

- Chung T. Computational fluid dynamics. Cambridge University Press, 1, 15-21, 2002.
- Correia Da Silva JJ. Passive downdraught evaporative cooling applied to an auditorium International Conference "Passive and Low Energy Cooling for the Built Environment". Greece, 555-560, 2005.
- Daghigh R, Adam NM, Sopian K and Sahari, BB. Thermal comfort of an air-conditioned office through different window-door opening arrangements. Building Services Engineering Research and Technology, 30, 49, 2009.
- De Dear R and Brager G. Thermal comfort in naturally ventilated buildings: revisions to ASHRAE Standard 55. Energy and Buildings, 34, 549–561, 2002.
- Djongyan N, Tchinda R and Njomo D. Thermal comfort: A review paper. Renewable and Sustainable Energy Reviews, 14, 2626-2640, 2010.
- Duić N, Guzović Z, Kafarov V, Klemeš JJ, Mathiessen B and Yan J. Sustainable development of energy, water and environment systems. Applied Energy, 101, 3-5, 2013.
- Dussin D, Fossati M, Guardone A and Vigevano L. Hybrid grid generation for two-dimensional high-Reynolds flows. Computer & Fluids, 38, 1863-1875, 2009.
- Ealiwa MA, Taki AH, Howarth AT and Seden MR. An investigation into thermal comfort in the summer season of Ghadames, Libya. Building and Environment, 36, 231-237, 2001.
- Edwards B, Sibley M, Hakmi M, Land P. Courtyard Housing: Past, Present and Future. Taylor and Francis, 2005.
- El-Shorbagy A. Design with Nature: Windcatcher as a Paradigm of Natural Ventilation Device in Buildings. International Journal of Civil & Environmental Engineering, 10, 26-31, 2010.
- Elizalde T and Mumovic D. Simulated Pperformance of windcatchers in an urban environment. Conference on Passive and Low Energy Architecture, Dublin, 2008.
- Elmualim A and Awbi GB. Wind Tunnel and CFD Investigation of the Performance of "Wind catcher" Ventilation Systems. International Journal of Ventilation. 1, 53-64, 2002.
- Elmualim A. Dynamic modeling of a wind catcher/tower turret for natural ventilation. Building Services Engineering Research and Technology, 27, 165-182, 2006a.
- Elmualim A. Effect of damper and heat source on wind catcher natural ventilation performance. Energy and Buildings, 38, 939–948, 2006b.
- Esfeh M, Dehghan AA, Manshadi M, Mohagheghian S. Visualized flow structure around and inside of one-sided wind-catchers. Energy and Buildings, 55, 545-552, 2012.
- Etheridge D. Natural Ventilation of Buildings: Theory, Measurement and Design. Wiley-Blackwell, 2011.
- Fanger PO. Thermal comfort: Analysis and application in environmental engineering. Danish Technical Press, 1970.
- FLUENT Incorporated: FLUENT user guide [Online]. 2006, available from: [www1.ansys.com](http://www1.ansys.com)

- Gage SA and Graham JM. Static split duct roof ventilators. *Building Research and Information*, 4, 234-244, 2000.
- Gartmann A, Fister W, Schwanghart W and Müller M. CFD modelling and validation of measured wind field data in portable wind tunnel. *Aeolian Research*, 3, 315-325, 2011.
- Ghaemmaghami PS and Mahmoudi M. Wind tower a natural cooling system in Iranian traditional architecture. International Conference "Passive and Low Energy Cooling for the Built Environment", Greece, 2005.
- Grunecodesign: Thermal Comfort [Online] 2011, available from: [grunecodesign.com](http://grunecodesign.com)
- Griffis G, Helwig T, Waggoner M and Hoit M. Don't Mess with Structural Engineers: Expanding Our Role. Proceedings of the 2009 Structures Congress, Austin, Texas, 2009.
- Hughes BR and Ghani SA. Investigation of a Windvent passive ventilation device against current fresh air supply recommendations. *Energy and Buildings*, 40, 1651-1659, 2008.
- Hughes BR and Ghani SA. A numerical investigation into the effect of Windvent dampers on operating conditions. *Building and Environment*, 44, 237– 248, 2009.
- Hughes BR and Ghani SA. A numerical investigation into the effect of Windvent louvre external angle. *Building and Environment*, 44, 237– 248, 2010a.
- Hughes BR and Ghani SA. A numerical investigation into the feasibility of a passive-assisted natural ventilation stack device. *International Journal of Sustainable Energy*, 30, 193-211, 2010b.
- Hughes BR and Mak C. A Study of wind and buoyancy driven flows through commercial wind towers. *Building and Environment*, 43, 1784-1791, 2011.
- Hughes BR, Chaudhry H. and Ghani SA. A review of sustainable cooling technologies. *Renewable and Sustainable Energy Reviews*, 15, 3112-3120, 2011.
- Hughes BR, Calautit JK, and Ghani SA. The Development of Commercial Wind Towers for Natural Ventilation: A Review. *Applied Energy*, 92, 606-627, 2012.
- Hughes BR, Chaudhry HN, and Calautit JK. Passive energy recovery from natural ventilation air streams. *Applied Energy*, 113, 127-140, 2013.
- Irwin P, Denoon R and Scott D. *Wind Tunnel Testing of High-Rise Buildings*. Routledge, 2013.
- ISO 7730:2005, Ergonomics of the thermal environment - Analytical determination and interpretation of thermal comfort using calculation of the PMV and PPD indices and local thermal comfort criteria [Online]. 2009, available online: [http://www.iso.org/iso/catalogue\\_detail.htm?csnumber=39155](http://www.iso.org/iso/catalogue_detail.htm?csnumber=39155)
- Jones B, Kirby R, Kolokotroni M and Payne T. Air Quality Measured in a Classroom Served by Roof Mounted Natural Ventilation Windcatchers. Conference for the Engineering Doctorate in Environmental Technology, 2008.
- Jones B and Kirby R. Quantifying the performance of a top-down natural ventilation Windcatcher™. *Building and Environment*, 44, 1925-1934, 2009.
- Kalantar V. Numerical simulation of cooling performance of wind tower (Baud-Geer) in hot and arid region. *Renewable Energy*, 34, 246–254, 2009.

- Khan N, Su Y, and Riffat S. A review on wind driven ventilation techniques. *Energy and Buildings*, 40, 1586–1604, 2008.
- Klein G and Green J. The design of corners in fluid channels. *Canadian Journal of Research*, 3, 272-285, 1930.
- Kleiven T. *Natural Ventilation in Buildings: Architectural concepts, consequences and possibilities*. Norwegian University of Science and Technology, 2003.
- Kuchen E and Fisch MN. Spot monitoring: thermal comfort evaluation in 25 office buildings in winter. *Building and Environment*, 44, 839–47, 2009.
- La Fianza G, Fucci F, Brunetti L. Study of a particular stack performance in a building. *International Conference on Renewable Energies and Power Quality*, 2010.
- Lazzarin R and Castellotti F. A new heat pump desiccant dehumidifier for supermarket application. *Energy and Buildings*, 39, 59-65, 2007.
- Lechner. *Heating, Cooling, Lighting: Design Methods for Architects*. John Wiley & Sons, Second Edition, 2001
- Li D, Yang L and Lam J. Zero energy building and sustainable development implications – A review. *Energy*, 54, 1-10, 2013.
- Liu L and Mak CM. The assessment of the performance of a windcatcher system using computational fluid dynamics. *Building and Environment*, 42, 1135-1141, 2007.
- Liu S, Mak CM. and Niu J. Numerical evaluation of louvre configuration and ventilation strategies for the windcatcher system. *Building and Environment*, 46, 1600-1616, 2011.
- Lombard L, Ortiz J, Pout C. A review on buildings energy consumption information. *Energy and Buildings*, 40, 394-398, 2008.
- Marinakos V, Doukas H, Karakosta C, Psarras J. An integrated system for buildings' energy-efficient automation: Application in the tertiary sector. *Applied Energy*, 101, 6-14, 2013.
- Mehta R and Bradshaw P. Technical notes: Design rules for small low speed wind tunnels. *The Aeronautical Journal of the Royal Aeronautical Society*, 1979.
- Mehta U. Some aspects of uncertainty in computational fluid dynamics results. *Journal of Fluids Engineering*, 113, 539–543, 1991.
- Montazeri H. Experimental study on natural ventilation performance of various multi-opening wind catchers. *Building and Environment*, 46, 370-378, 2011.
- Montazeri F and Azizian R. Experimental study on natural ventilation performance of one-sided wind catcher. *Building and Environment*, 43, 2193–2202, 2008.
- Montazeri H, Montazeri F, Azizian R and Mostafavi S. Two-sided wind catcher performance evaluation using experimental, numerical and analytical modelling. *Renewable Energy*, 35, 1424–1435, 2010.
- Montazeri H and Azizian R. Experimental and numerical study on natural ventilation performance of various multi-opening wind catchers. *Building and Environment*, 46, 370-378, 2011.
- Moonen P, Blocken B, Roels S and Carmeliet J. Numerical modelling of the flow conditions in a closed-circuit low-speed wind tunnel. *Journal of Wind Engineering and Industrial Aerodynamics*, 94, 699-723, 2006.

- Moonen P, Blocken B and Carmeliat J. Indicators for the evaluation of wind tunnel test section flow quality and application to a numerical closed-circuit wind tunnel. *Journal of Wind Engineering and Industrial Aerodynamics*, 95, 1289-1314, 2007.
- Morel T. Comprehensive design of axisymmetric wind tunnel contractions. *Journal of Fluids Engineering*, 225-233, 1975.
- Nouanégué HF, Alandji LR and Bilgen E. Numerical study of solar-wind tower systems for ventilation of dwellings. *Renewable Energy*, 33, 434–443, 2008.
- Peeters L, de Dear R, Hensen J, and D’haeseleer W. Thermal comfort in residential buildings: Comfort values and scales for building energy simulation. *Applied Energy*, 86, 772-780, 2009.
- Perez R. Uncertainty analysis of computational fluid dynamics via polynomial chaos. 2008.
- Prianto E, and Depecker R. Optimization of architectural design elements in tropical humid region with thermal comfort approach. *Energy and Buildings*, 35, 273-280, 2003.
- Priyadarsini R, Cheong KW and Wong NH. Enhancement of natural ventilation in high-rise residential buildings using stack system. *Energy and Buildings*, 36, 61–71, 2004.
- Rao VD, Naidu SV, Rao BG and Sharma KV. Heat transfer from a horizontal fin array by natural convection and radiation—A conjugate analysis. *International Journal of Heat and Mass Transfer*, 49, 3379-3391, 2006.
- Roache PJ. Quantification of uncertainty in computational fluid dynamics. *Annual review of fluid mechanics*, 29, 123-160, 1997.
- Roaf S. The Traditional Technology Trap: More lessons from the Windcatchers of Yazd. *Conference on Passive and Low Energy Architecture, PLEA 2008, Dublin*, 2008.
- Saffari H and Hosseinnia SM. Two-phase Euler-Lagrange CFD simulation of evaporative cooling in a Wind Tower. *Energy and Buildings*, 41, 991–1000, 2009.
- Safarzadeh H and Bahadori MN. Passive cooling effects of courtyards. *Building and Environment*, 40, 89-104, 2005.
- Sahin B, Ward-Smith A and Lane D. The pressure drop and flow characteristics of wide-angle screened diffusers of large area ratio. *Journal of Wind Engineering*, 58, 33-50, 1995.
- Sharples S and Bensalem R. Airflow in courtyard and atrium buildings in the urban environment: a wind tunnel study. *Solar Energy*, 70, Pages 237-244, 2001.
- Su Y, Riffat S, Lin Y, and Khan N. Experimental and CFD study of ventilation flow rate of a Monodraught™ windcatcher. *Energy and Buildings*, 40, 1110–1116, 2008.
- Swaminathan MR and Mahalakshmi NV. Numerical modelling of flow through perforated plates applied to electrostatic precipitator. *Journal of Applied Science*, 10, 2426-2432, 2010.
- Taylor P, Fuller RJ and Luther MB. Energy and thermal comfort in a rammed earth office building. *Energy and Buildings*, 40, 793–800, 2008.
- Versteeg H and Malasekera W. *An introduction to computational fluid dynamics: the finite volume method*. Pearson Education Limited, 2007.

- Vlajina M. Design, construction and evaluation of a subsonic wind tunnel. Massachusetts Institute of Technology Department of Aeronautics and Astronautics, 17-20, 1970.
- Wang Z, Zhang L, Zhao J and He Y. Thermal comfort for naturally ventilated residential buildings in Harbin. *Energy and Buildings*, 42, 2406-2415, 2010.
- WBCSD. Energy Efficiency in Buildings: Transforming the Market [Online]. 2011, available from: [www.wbcd.org](http://www.wbcd.org)
- Weather Analytics Station: Actual Meteorological Year (AMY) data file for Doha, Qatar [Online]. 2012, available from: [www.weatheranalytics.com](http://www.weatheranalytics.com)
- Webb R. Towards zero-carbon buildings: Integrated RE systems central to design approach. *Refocus*, 2, 28-31, 2001.
- Wind Catchers: The Cooling System in Traditional Iranian Architecture [Online]. 2011, available from: <http://www.cais-soas.com>
- Xu Y. Wind Effects on Cable-Supported Bridges. John Wiley & Sons, 2013.
- Yao R, Li B and Liu J. A theoretical adaptive model of thermal comfort adaptive predicted mean vote (aPMV). *Building and Environment*, 44, 2089–2096, 2009.
- You D, Mittal R, Wang M and Moin P. Analysis of stability and accuracy of finite-difference schemes on a skewed mesh. *Journal of Computational Physics*, 213, 184-204, 2006.
- Zamora B and Kaiser AS. Numerical study on mixed buoyancy-wind driving induced flow in a solar chimney for building ventilation. *Renewable Energy*, 35, 2080-2088, 2010.
- Zarandi MM. Analysis on Iranian Wind Catcher and Its Effect on Natural Ventilation as a Solution towards Sustainable Architecture (Case Study: Yazd). *Engineering and Technology*, 54, 574-579, 2009.

## **Appendix A**

### **Wind Tunnel Design and Calculations**

#### **A.1 Introduction**

Small scale wind tunnels are fast becoming a significant research apparatus used in aerodynamic investigations to study the effects of air moving past solid objects. The principle components of a wind tunnel are the contraction, the test section and the diffuser section. The contraction section ensures the uniform passage of flow into the test section. Small wind tunnels typically have contraction ratios between 6 and 9 [Mehta and Bradshaw, 1979]. The test section is the chamber in which observations and measurements are made and its shape and size is principally determined by the testing requirements. Simplest test section design's are rectangular or square in cross-section. Diffusers are chambers that expand along their length, allowing fluid pressure to increase with decreasing fluid velocities.

This chapter presents the design parameters and requirements for the subsonic closed-loop wind tunnel components. An analytical pressure loss model to determine the required fan pressure was established in order to determine the pressure curve.

#### **A.2 Test section**

The first step in the design of a tunnel is to determine the size and shape of the test section based on the intended use of the facility. The cross-sectional area of the test section basically determines the overall size of the facility. The overall aerodynamic objective for most wind tunnels is to obtain a flow in the test section that is near as possible to a parallel steady flow with uniform speed throughout the test section. It is almost always desired to obtain the largest size of test section and highest speed. However, high speed and large size will include maximum cost, available space and available time [Barlow *et al.*, 1999]. For an empty test section the traditional view of the ideal flow outside the boundary layer would be the following. The velocity passing through each plane normal to the centreline would be uniformly parallel to the centreline and would have no variation in time; that is, there would be no up-flow or cross-flow and there would be no turbulence.

The rectangular test section had a cross-sectional dimensions of 0.5 m by 0.5 m with an area of 0.25 m<sup>2</sup> which was necessary for the purpose of conducting future experimentation including a greater range of blockage sizes. The hydraulic diameter (DH) of the test section was 0.5 m while the density of air at 60 °C was taken as 1.067 kg/m<sup>3</sup>. At a desirable speed of 10 m/s, the Reynolds Number (Eqn. A.1) was calculated at 264 x 10<sup>3</sup> while the volume-flow rate (Eqn. A.2) inside the test-section was calculated 2.83 m<sup>3</sup>/s.

$$R_e = \frac{u \times D_H}{\nu} \quad \text{Equation A.1}$$

$$Q_{\text{air}} = (A_{\text{test}} - A_{\text{specimen}}) \times u \quad \text{Equation A.2}$$

The volume of the test specimen was 0.034 m<sup>3</sup>, resulting in a blockage factor of 1.35% which was in the recommended range [Barlow *et al.*, 1999]. The pressure loss coefficient (Eqn. A.3) and head loss (Eqn. 4) for the test-section was therefore calculated at 0.91 and 4.64 m.

$$\text{Pressure loss coefficient, } k = 1 - \frac{A_{\text{specimen}}}{A_{\text{test}}} \quad \text{Equation A.3}$$

$$\text{Test-section head loss, } h = k \times \frac{u^2}{2g} \quad \text{Equation A.4}$$

The required power for a specified test section size and dynamic pressure can be varied by altering the geometry of the remaining wind tunnel components. Since the test section area and length for the proposed tunnel were fixed by geometrical constraints, the effect of various diffuser and contraction geometries on the power required were analysed.

### A.3 Contraction section

The contraction section is one of the most important sections of a wind tunnel. The most widely accepted method for an engineering contraction includes a combination of two blended cubic arcs, each having its apex at one end of the contraction. When the dimensions of upstream and downstream contraction sections are fixed, the location of the matched points becomes the only parameter to establish the entire wall shape [Morel, 1975]. Large contraction ratios are advantageous but require higher construction and

running costs besides possible problems of noise and separation near the ends. Therefore contraction ratios between 6 and 9 are generally used for small wind tunnels [Mehta and Bradshaw, 1979].

The designed wind tunnel for this study consisted of a test-section connected to a contraction upstream with a contraction ratio of 4:1 in order to meet the maximum allowable space requirements. The cross-sectional dimensions of the contraction were 1m by 1m with an inlet area of 1 m<sup>2</sup>. For the contraction section, the continuity flow equation was utilised in order to calculate the pressure gradient (Eqn. A.5). The velocity (Eqn. A.6) was calculated 2.28 m/s estimating a pressure differential of 41.6 Pa.

$$\Delta P = \frac{1}{2} \rho u_{in}^2 \left[ \left( \frac{A_{in}}{A_{out}} \right)^2 - 1 \right] \quad \text{Equation A.5}$$

$$\text{Velocity at contraction, } u_{\text{contraction}} = \frac{Q}{A} \quad \text{Equation A.6}$$

Based on the pressure, the head loss (Eqn. A.7) for the diffuser section was calculated at 3.97m. Contraction section head loss,  $h = \frac{P}{\rho g}$  Equation A.7

#### A.4 Diffuser section

Minimum energy loss corresponds to maximum pressure recovery. It is generally desirable to reduce the speed in the shortest possible distance without incurring flow separation [Barlow *et al.*, 1999]. The diffuser of a return wind tunnel normally extends from the downstream end of the test section to the third corner of the tunnel. The conical expansion angle is the total angle formed by the walls of a circular diverging cone given by Equation A.8.

$$\theta_e = \arctan \left( \frac{R_2 - R_1}{L} \right) \quad \text{Equation A.8}$$

where R2 is one-half of the exit hydraulic diameter, R1 is one-half of the entrance hydraulic diameter and L is the length of the diffuser section.

For the present study, the test-section was connected to a diffuser channel downstream with a diffuser area ratio of 3:1 and the conical angle of 8° and 4° which was under the typical guidelines [Barlow *et al.*, 1999]. Diffusers with area ratios of approximately 3

and cone angles exceeding  $3.5^\circ$  have been publicised to experience non-uniform velocity profiles and flow separation, without the addition of control devices or splitting plates [Sahin *et al.*, 1995]. Therefore, 3 horizontal splitting plates with 0.25 m spacing and 3 vertical splitting plates with 0.17 m spacing were installed in the diffuser section [Chen *et al.*, 2009]. The effect of the splitting plate was investigated by initial CFD simulations as show in Figure 3. Without the splitting plate (Figure A.1a), the flow separation occurred at the downstream part of the diffuser. The separation was reduced significantly following the integration of the splitting plate (Figure A.1b). This was evident from the uniformity of the flow field at the diffuser exit (velocity variation was reduced from 30 to 5% following the addition of horizontal and vertical splitting plates).

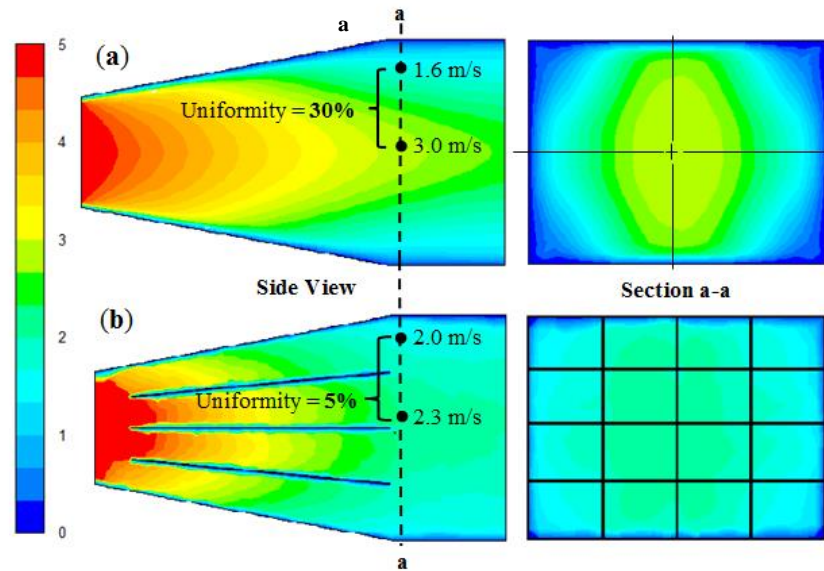


**Figure A.1** Comparison of flow in the wide angle diffuser: (a) without (b) with splitting plates

The velocity (eqn. A.9) in the diffuser and the head loss (eqn. A.10) was calculated at 3.26 m/s and 0.24 m.

$$\text{Velocity at diffuser, } \mathbf{u}_{diffuser} = \frac{Q}{A} \quad \text{Equation A.9}$$

$$\text{Diffuser section head loss, } \mathbf{h} = \mathbf{k} \times \frac{u^2}{2g} \quad \text{Equation A.10}$$

## A.5 Guide vanes

In order to circumvent large losses and to maintain comparatively straight flow throughout the circuit, the corners are equipped with guide vanes. Many wind tunnels

hence use quarterly vanes of circular profile with prolongation at the trailing edge, having a minimum pressure-loss coefficient at a pitch value in between the range of 0.33 and 0.35 [Klein and Green, 1930]. Functional design of the corners is critical since the four combined corners of a conventional closed circuit wind tunnel account for approximately 60% of the total losses within the tunnel [Barlow *et al.*, 1999].

## A.6 Total pressure loss

The power required to maintain steady flow through the wind tunnel is equal to the total losses occurring in the flow through the tunnel. The loss in kinetic energy, which appears as a decrease in total pressure, must be compensated by a pressure rise, in this case provided by the fan. Prior to conducting numerical simulations, the expected pressure loss for each section was determined. The pressure losses for all components of the wind tunnel were calculated in order to comprehend the functionality of the circuit [Vlajina, 1970].

The total pressure loss coefficients and head losses were obtained for upstream and downstream wind tunnel sections alongside the corner vanes which are summarised in Table A.1. The total head loss for the wind tunnel was calculated at 13.35 m providing a total pressure loss of 140.1Pa.

**Table A.1** Summary of sectional pressure head losses

Wind tunnel section	Loss coefficient	Head loss (m)
First corner	0.65	0.35
Upstream horizontal duct	1.00	0.54
Upstream vertical duct	1.00	0.54
Downstream horizontal duct	1.00	0.54
Downstream vertical duct	1.00	0.54
Second corner	0.65	0.35
Contraction	-	3.97
Test-section	0.91	4.64
Diffuser	0.45	0.24
Third corner	0.65	0.35
Fourth corner	0.65	0.35
Annular inlet	-	0.05
Annular outlet	0.09	0.94

## **Appendix B**

### **Wind Tunnel CFD Modelling**

#### **B.1 Introduction**

The commercial ANSYS Fluent numerical code was used for predicting the flow characteristics inside the closed-loop subsonic wind tunnel. The analytical model for estimating the pressure losses were directed as input boundary conditions for the CFD model. Two sets of simulations were conducted: numerical modelling of the wind tunnel with an empty test section and with a test block model located centrally in the test section. As suggested by Moonen *et al.*[2006], a full-scale CFD model of the entire wind tunnel was considered instead of the conventional approach, in which only the flow in the test section was modelled and applying similar inlet boundary conditions as measured in the actual system. The established CFD method accounted for the influence of the specific features of the wind tunnels such as guide vanes and splitting plates. This allowed for the optimisation of the flow not only in the test section but also the flow in other wind tunnel sections.

#### **B.2 Computational domain**

The work combined the advantages of a structured with those of an unstructured grid at the other sections of the domain to minimise the computational expense [Moonen *et al.*, 2006]. Sections of the wind tunnel that were of simple geometry in which one-dimensional flow dominates were meshed with structured prismatic mesh. In the sections of complex geometry with three-dimensional flows such as the diffuser, contraction and in the areas of the guiding vanes, tetrahedral/mixed-mode cells were used. The patch independent mesh algorithm for tetrahedron elements was based on the subsequent spatial subdivision algorithm which ensures refinement of the mesh where essential, but retains larger elements where feasible, therefore allowing faster computing times.

The grid resolution was determined taking into account an acceptable value for the wall Yplus (average value of 222.3), the cell equiangle skewness (average value of 0.38) and the cell equivolume skewness (average value of 0.39) [You *et al.*, 2006]. The complete meshed model comprised of 768,655 nodes and 4,245,896 elements. Modelling the flow conditions in the entire wind tunnel requires more effort than only modelling the flow in

the test section [Moonen *et al.*, 2006]. A very high mesh resolution was applied at the walls of the turning vanes at all four corners where a mixed grid was used in order to increase the accuracy of capturing the flow passing through. Figure B.1 displays the details of the mesh for the corner guide vanes and diffuser splitting plate.

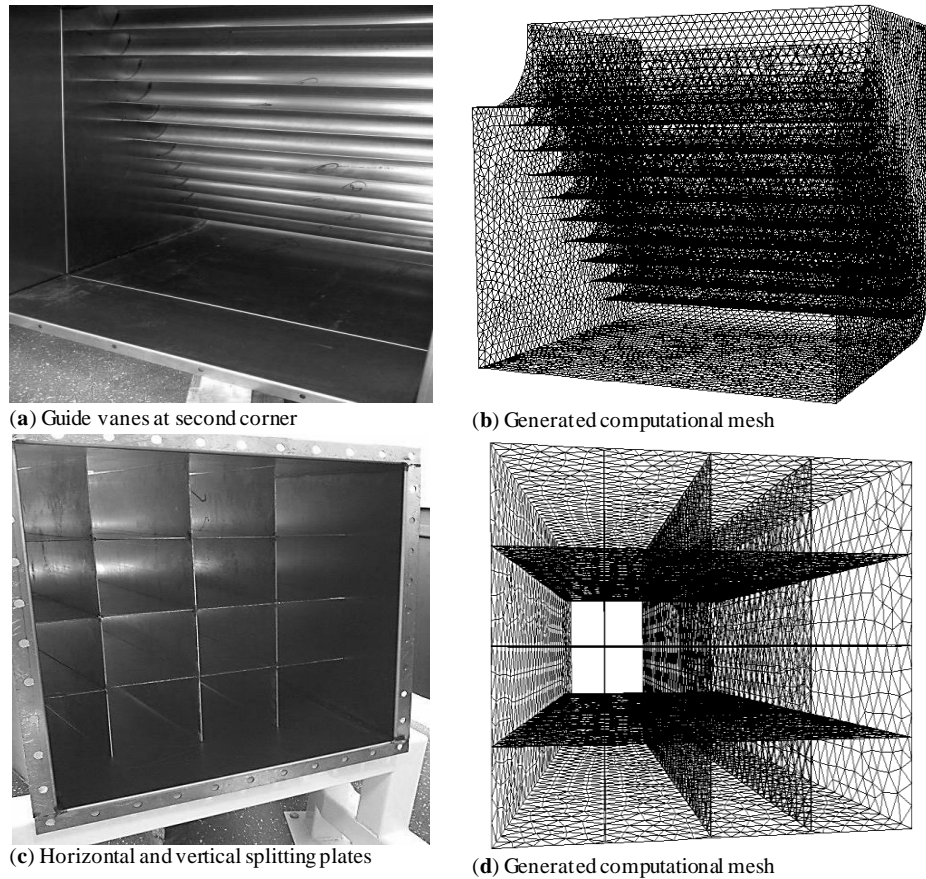


**Figure B.1** Actual photo of: (a) second corner guide vanes (b) diffuser exit. View of the computational mesh at the surface of: (c) the 90 corner guide vanes; (d) the diffuser splitting plates

Table B.1 indicates the type of mesh used and the total number of elements for different sections of the wind tunnel.

**Table B.1** Type and distribution of grid in the wind tunnel.

Wind tunnel section	Grid Type	Number of elements
First corner	Tetrahedral	474,590
Upstream and downstream horizontal duct	Prismatic	351,967
Upstream and downstream vertical duct	Prismatic	297,213
Second corner	Tetrahedral	509,508

Contraction	Tetrahedral	452,131
Test-section (Empty)	Mixed	636,884
Diffuser with splitting plates	Tetrahedral	559,508
Third corner	Tetrahedral	489,508
Fourth corner	Tetrahedral	474,590

Figure B.2 displays the generated mesh for the test section floor with the block type model for the investigation of flow velocity, turbulence intensity and pressure coefficient around scale models.

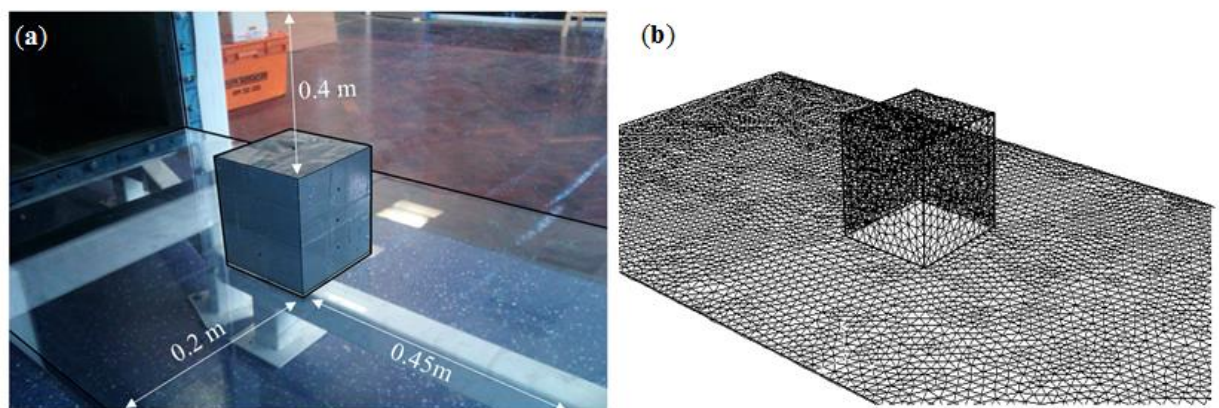


**Figure B.2** (a) block model inside the test section (b) view of the computational mesh of the block model and test section floor

### B.3 Solution methods

The three-dimensional Reynolds-averaged Navier-Stokes (RANS) equations and the continuity equation were solved using the commercial CFD code that employs the control-volume technique and the Semi-Implicit Method for Pressure-Linked Equations (SIMPLEC) velocity-pressure coupling algorithm with the second order upwind discretisation as recommended in literature [Moonen *et al.*, 2006]. Standard k-epsilon model was used primarily for the numerical simulation [Gartmann *et al.*, 2011]. The results obtained using the k-epsilon model was later compared with other turbulence models and experimental data. These included the k- $\epsilon$  Renormalization Group (RNG) turbulence model, the k- $\omega$  Standard and Shear-Stress Transport (SST) model and the Reynolds-Stress Model (RSM) with Linear Pressure-Strain and Stress-Omega models. Table B.2 summarises the CFD model boundary conditions and the applied physical roughness height and constants for the wind tunnel section walls.

**Table B.2** Summary of the CFD model boundary conditions.

Parameter	Set value
Discretisation Scheme	Second-order upwind
Algorithm	SIMPLEC
Time	Steady State
Pressure inlet (Pa)	17.5, 35, 70, 140 Pa
Wall functions	Standard wall function
Gravity	-9.81

## B.4 Grid adaptation

To investigate the solution independency from the grid several meshes were generated. Grid sensitivity analysis was used to validate the programming and computational operation of the computational model. The numerical grid was refined and locally enriched using the hp-method grid adaptation technique [Chung, 2002]. This procedure of evaluation requires the use of different mesh sizes (Meshes ranging from 1,622,108 to 7,149,235 elements) by the use of a posterior error estimates. The grid was evaluated and refined until the posterior estimate error becomes insignificant between the number of nodes and elements, computational iterations and the posterior error indicator [Mehta, 1991]. Figures B.3 display the posterior error percentage for average velocity in the test-section at increasing grid sizes. The maximum error for average velocity was recorded at 4.38%. The discretisation error was found to be the lowest at over 7 million cells for both indicated variables.

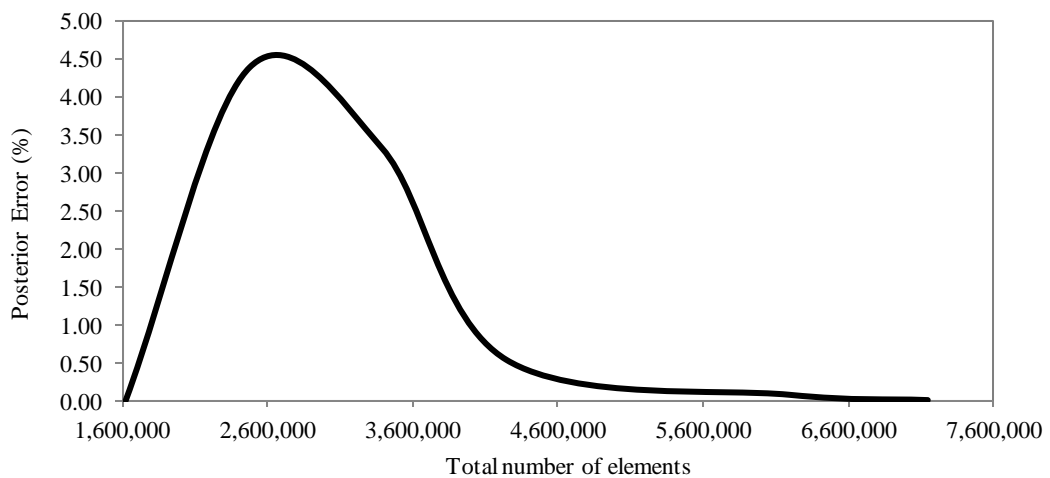


**Figure B.3** Posterior error on the average velocity in the test-section using h-p grid adaptation method

## Appendix C

### Wind Tunnel Experimental Techniques

#### C.1 Introduction

Two sets of experiments were conducted: measurements in the wind tunnel with empty test section and with a block building model located centrally in the test section.

#### C.2 Empty wind tunnel test section

Complete characterisation of wind tunnel test environment is a massive task due to the very extensive range of achievable configurations including scaled model testing. Therefore, initial testing should be conducted with an empty test section [Moonen *et al.*, 2006]. The experiment comprised of measuring air velocities, pressure, and turbulence intensity inside the empty test-section. Wind speed measurements were performed along 9 vertical lines located in the test-section (P01 – P09), at intervals of 0.25m (horizontal) and 0.125 m (vertical) as shown in Figure C.1.

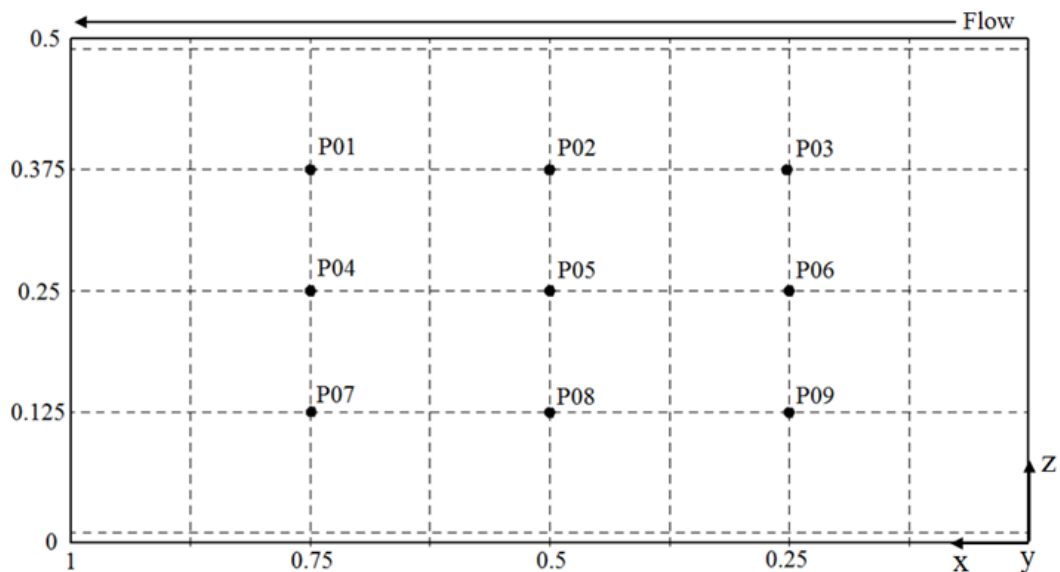


**Figure C.1** Top view of the test section showing the measurement positions (P01 - P09) and coordinates for the case of an empty test section. Dimensions in metres.

The measurements were performed by means of a unidirectional hot wire anemometer, yielding mean air speed and turbulence intensity at the measurement point, and were repeated for different fan setting speeds.

### C.2.1 Flow turbulence measurements

One of the most important qualities which affects measurements in a wind tunnel is the turbulence or unsteady motion superimposed on the mean flow since it indicates the degree to which experiments in different wind tunnels can be compared as well as how measurements performed on a model can be applied to its full-scale version [Chong *et al.*, 2008]. The level of turbulence in a wind tunnel can be expressed as the ratio of the mean velocity fluctuations to free stream velocity. The one-dimensional turbulence intensity can be defined as [Nader *et al.*, 2006]:

$$I = \frac{U'}{U_\infty} \quad \text{Equation C.1}$$

Where  $U'$  is the turbulent velocity fluctuation standard deviation and  $U_\infty$  is the freestream velocity at the same location. The turbulence level in the test section was measured using a hot wire anemometer. It should be noted that measurements were made with a single wires, so that the measured turbulence represents only the longitudinal and vertical velocity fluctuations due to the orientation of the wire.

### C.2.2 Uniformity of the flow field

In a uniform flow field, all streamlines are parallel to the centre plane of the wind tunnel and all velocity vectors have the same magnitude [Moonen *et al.*, 2006]. The mean flow uniformity in the test section was measured using the hot-wire anemometer at points P01 - P09. It is defined as:

$$\mu_i = \frac{U_i - \bar{U}}{\bar{U}} = \frac{U_i}{\bar{U}} - 1 \quad \text{Equation C.2}$$

where  $U_i$  represented the wind speed at the measurement point  $i$  and  $\bar{U}$  represented the average wind speed of all the points.

### C.3 Wind tunnel test section with test block

The second experiment included velocity, pressure and turbulence intensity measurements around a test block model of the length, width and height of 0.11 x 0.11 x 0.11 m located centrally in the test section. The purpose of this test was to evaluate the accuracy of simulating or achieving the flow characteristics for which the wind tunnel was designed. According to the dimension of the model and wind tunnel cross-section, the model produces a maximum blockage of 5%, and no corrections were made to the pressure measurements obtained with this configuration [Esfeh *et al.*, 2012]. Figure C.2 shows the measurement locations around the block model. The values of the velocity and turbulence intensity were obtained from the three components of the vector (X, Y, Z).

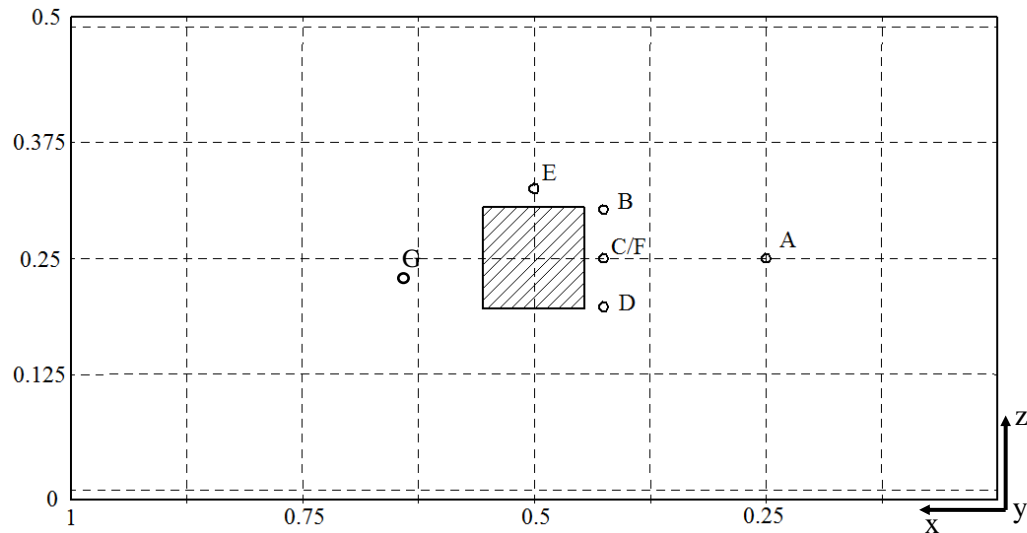


**Figure C.2** Top view of the test section showing the hot-wire anemometer measurement positions and coordinates with the block test model. Dimensions in metres.

#### C.3.1 Pressure coefficients

A geometrical model of a block-type building was employed in the measurements of the surface pressures, see Figure C.3. In this study, the pressure measurements were referred to the upstream dynamic pressure using the reference velocity in the test section in the case of a uniform wind flow. The air pressure coefficient  $C_p$  is calculated using the following equation:

$$C_p = \frac{p - p_s}{\frac{1}{2}\rho V U_{ref}^2} \quad \text{Equation C.3}$$

Where  $p$  is the surface pressure obtained from the pressure tap measurement,  $p_s$  is the static pressure at the upstream and  $\frac{1}{2}\rho U_{ref}^2$  is the dynamic pressure of the uniform wind. The model was furnished with 15 pressure taps located inside the model (See Figure C.3b). The mean velocity and turbulence intensity profiles of the wind flow were measured using the hot-wire anemometer. The reference velocity, static and dynamic pressure were monitored using the pitot and static tubes mounted at the roof height of the block model. Figure C.3c shows the test setup inside the test section.

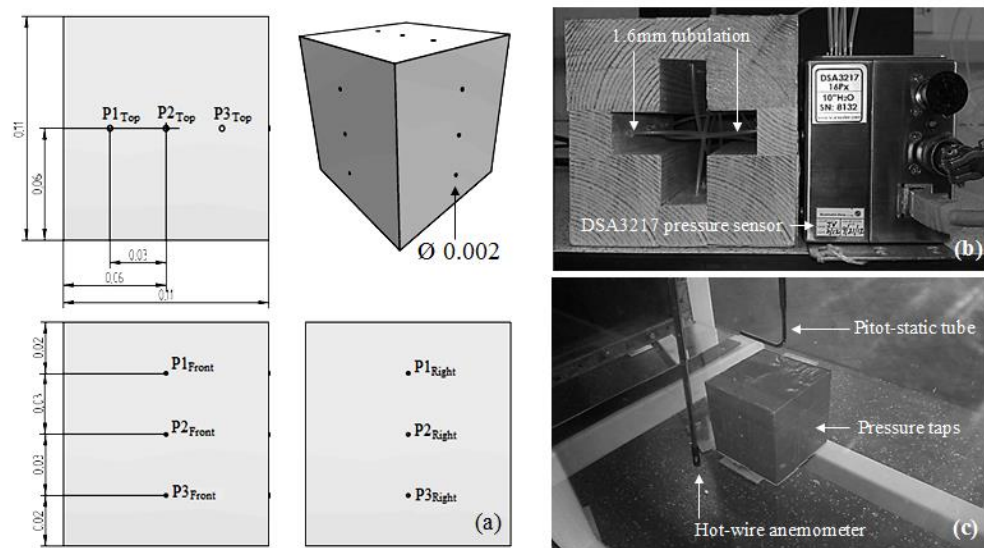


**Figure C.3** (a) Pressure tap locations on the square block model. (b) Internal view of the block model showing the 15 pressure taps connections. (c) Test setup: block model inside the test section. Dimensions in metres.

## **Appendix D**

### **Wind Tunnel CFD and Experimental Results**

#### **D.1 Introduction**

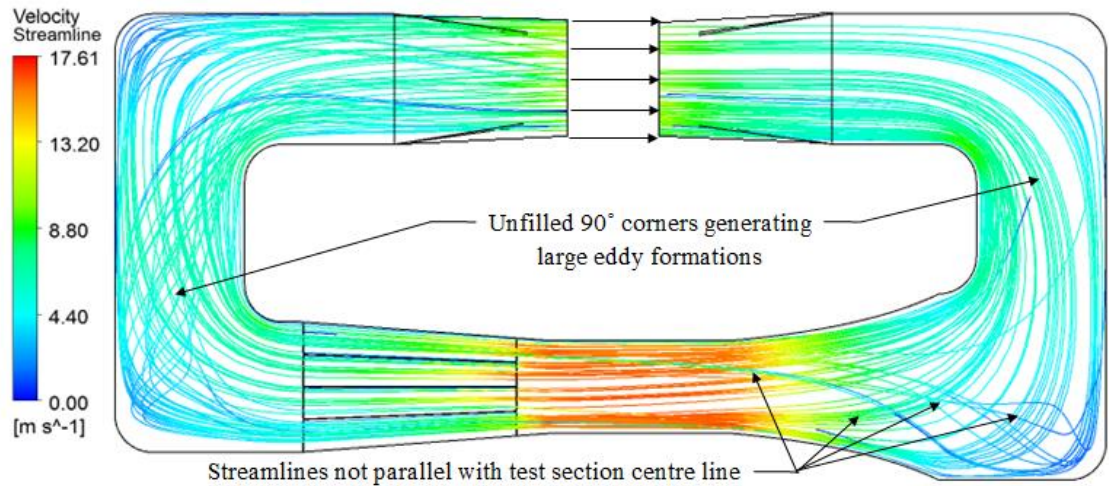
Four different wind tunnel configurations were investigated. The first model was the benchmark configuration in which no guide vanes were present. This configuration was compared to three others: with only guide vanes at the upstream, only guide vanes at the downstream and combined upstream and downstream guide vanes, correspondingly. The study evaluated the influence of the presence of guide vanes on the test section flow quality. The qualities presented were, total velocity and pressure variation, a measure of the streamwise flow uniformity over the measurement area, the flow angularity, a measure of how parallel the flow is and the turbulence intensity.

The second experiment included velocity, pressure and turbulence intensity measurements around a test block model of the length, width and height of 0.11 x 0.11 x 0.11 m located centrally in the test section. The purpose of this test was to evaluate the accuracy of simulating or achieving the flow characteristics for which the wind tunnel was designed.

#### **D.2 Empty wind tunnel test section**

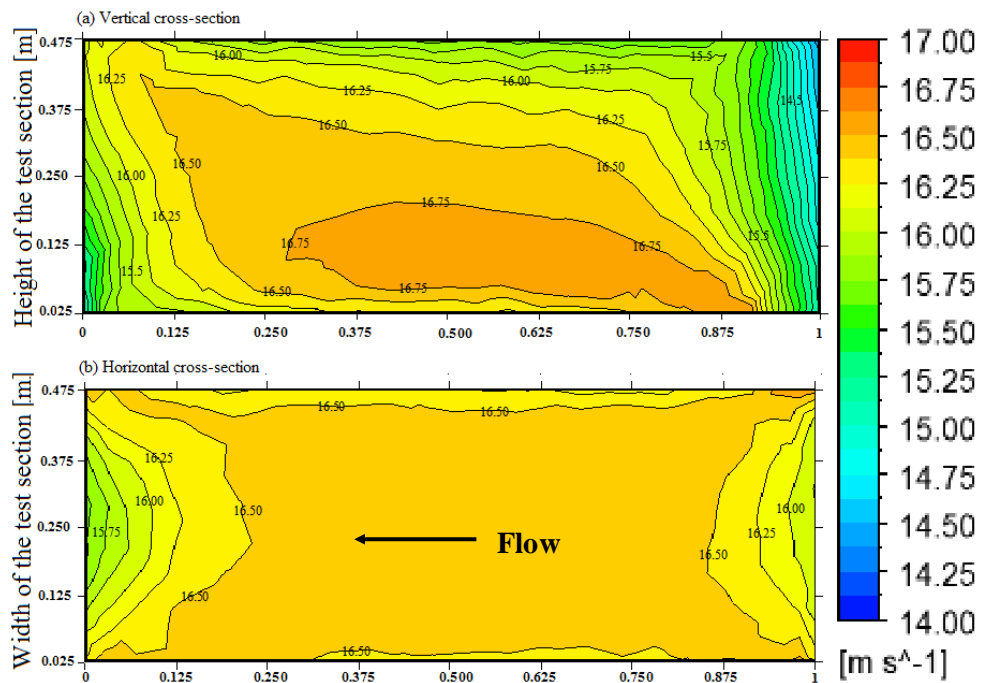
##### **D.2.1 Benchmark case: no guide vanes**

Figure D.1 illustrates the velocity streamlines in the cross-sectional plane for the empty wind tunnel. Formation of velocity rotations can be seen in all corners especially the lower upstream and downstream turns.



**Figure D.1** Velocity streamline for configuration 1: no guide vanes.

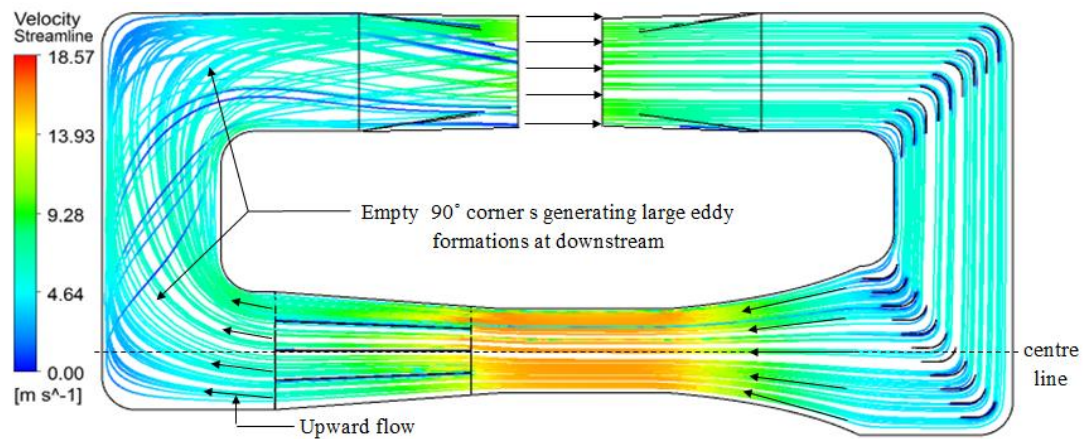
Figure D.2 shows a close up view of the vertical and horizontal wind speed profile in the test section for the benchmark case. The effect of the unsteady flow in the second corners was evident from the velocity contour; airflow at the lower section (0.05 to 0.125 m) was at higher speed than the upper side of the test section. Note that the flow separations occurring near the walls were not included in this analysis hence, the top, bottom and side (0.025 m from wall) of the actual test section were not shown.



**Figure D.2** Contours of velocity magnitude in a (a) vertical plane and (b) horizontal plane at 0.250 m height of the test section for the wind tunnel without guide vanes.

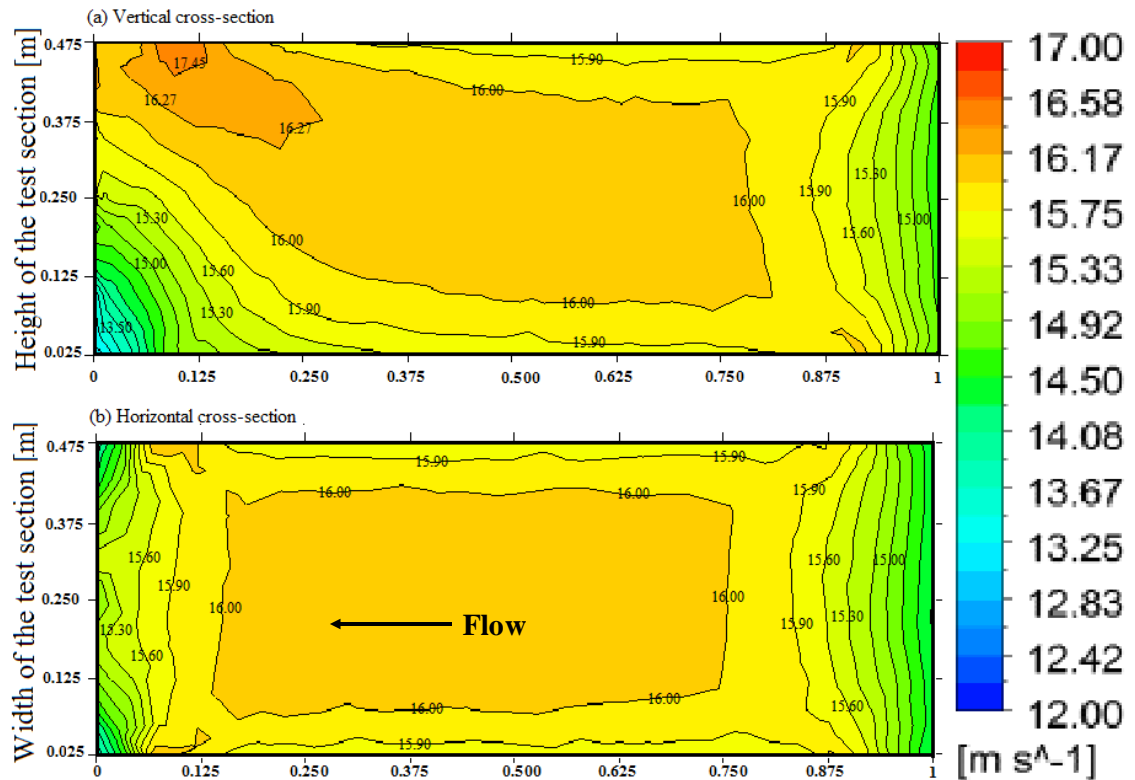
### D.2.2 Configuration 2: Upstream guide vanes

Figure D.3 illustrates the velocity streamlines in the cross-sectional plane for the closed-loop wind tunnel with upstream guide vanes. The formation of velocity rotations at the upstream side were eliminated by adding guide vanes to the upper and lower upstream 90° corners. The effect of the turning vanes was evident as it eliminated the areas of high re-circulations and eddy formations at the two upstream corners. Furthermore, the guide vane 0.1 m trailing edges effectively maintained a comparatively straight flow throughout the upstream circuit and no over or under turn were observed. It can be seen that the lower vanes effectively forcing the flow to be parallel to the test section centre line and improved the uniformity of the flow before the contraction section.



**Figure D.3** Velocity streamline for configuration 2: upstream guide vanes.

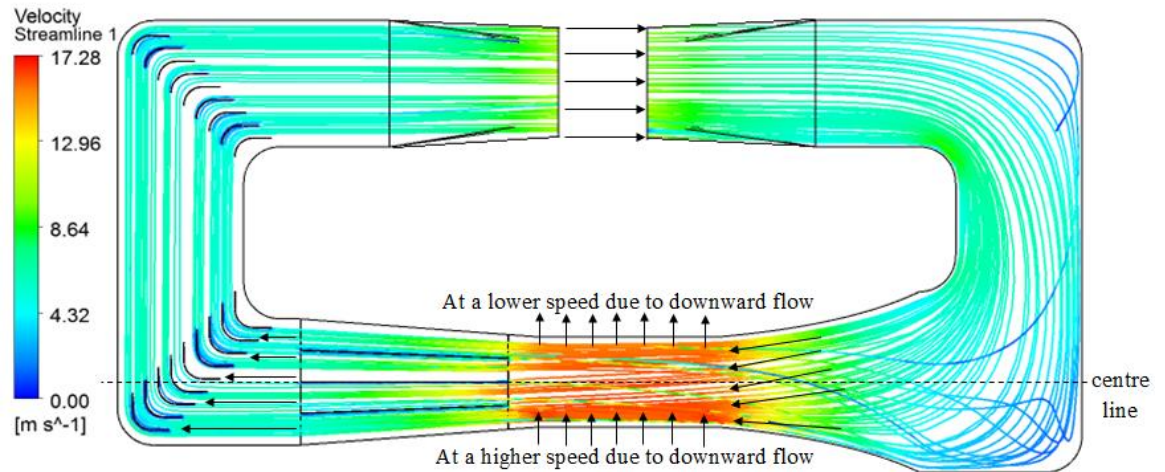
Figure D.4 shows the velocity contour of the vertical and horizontal wind speed profile in the test section for the second configuration: upstream guide vane. The velocity profile at the inlet indicates a laterally uniform profile and parallel to the test section centre line. However, it was seen that the velocity profile was not stable; it changes along the length of the test section. A highly disturbed flow was observed at the downstream due to up-flow present at the upper part of the test section outlet. Large flow separation at the exit of the test section was observed which was caused by the unsteady flows in the downstream corners.



**Figure D.4** Contours of velocity magnitude in a (a) vertical plane and (b) horizontal plane at 0.250 m height of the test section for the wind tunnel with upstream guide vanes.

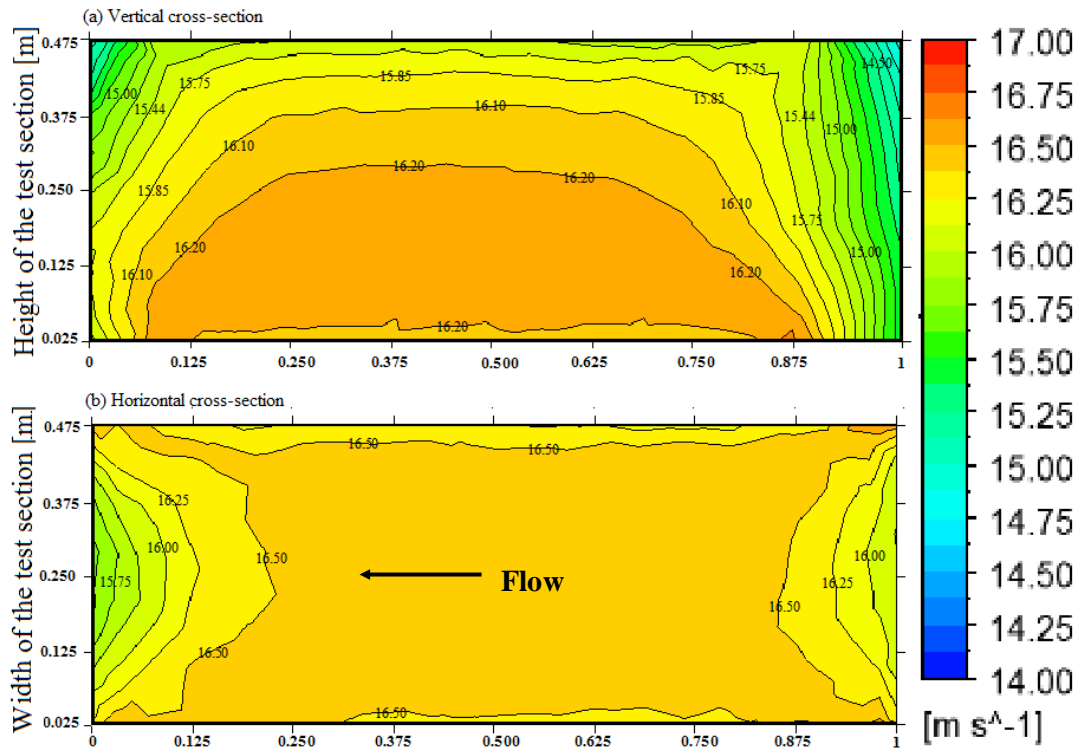
### D.2.3 Configuration 3: Downstream guide vanes

Figure D.5 shows the velocity streamlines in the cross-sectional plane for the wind tunnel with downstream guide vanes. The formation of velocity rotations at the downstream side were eliminated by adding guide vanes to the upper and lower upstream 90° corners. The effect of the turning vanes was evident as it eliminated the areas of high re-circulations and eddy formations at the two downstream corners. Furthermore, the third corner guide vane with 0.1 m leading and trailing edges effectively directed the flow to the upper downstream sections without over and under turn. The fourth corner guide vanes sufficiently reduced the velocity variation of the return flow before the fan section.



**Figure D.5** Velocity streamline for configuration 3: downstream guide vanes.

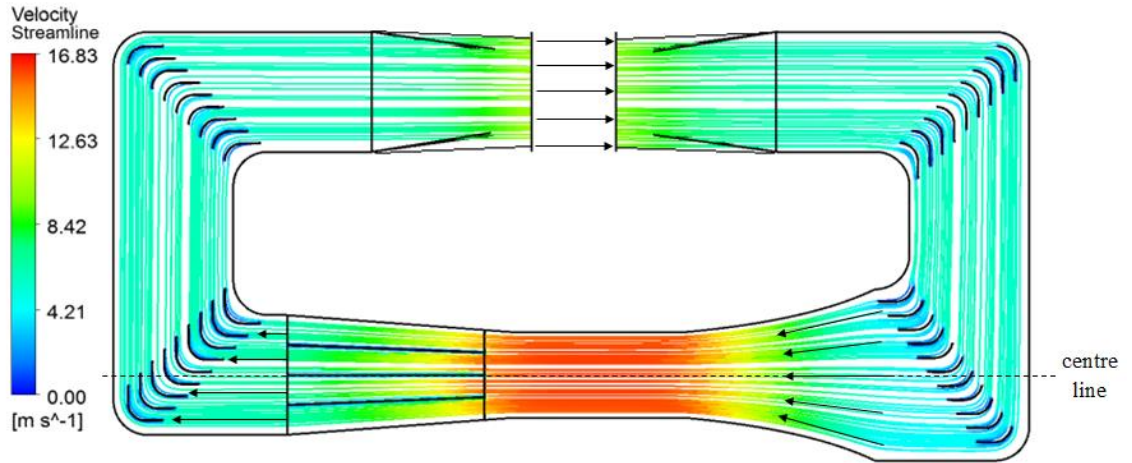
Figure D.6 shows the velocity contour of the vertical and horizontal wind speed profile in the test section for the third configuration: downstream guide vane. From the illustration a non-uniform velocity profile was observed, areas of high velocity were present at the lower areas of the test section while low velocity areas were seen at the upper part of the test section. Down flow and cross-flow into the test section have occurred as a result of the poor flow into the first and second corners. This was very similar to the flow pattern observed from the benchmark model analysis, hence it can be concluded that the guide vanes at the downstream did not have a considerable effect on the flow distribution in the test section. Although, variation in velocity was slightly reduced (10 %) following the addition of the downstream guide vanes.



**Figure D.6** Contours of velocity magnitude in a (a) vertical plane and (b) horizontal plane at 0.250 m height of the test section for the wind tunnel with downstream guide vanes.

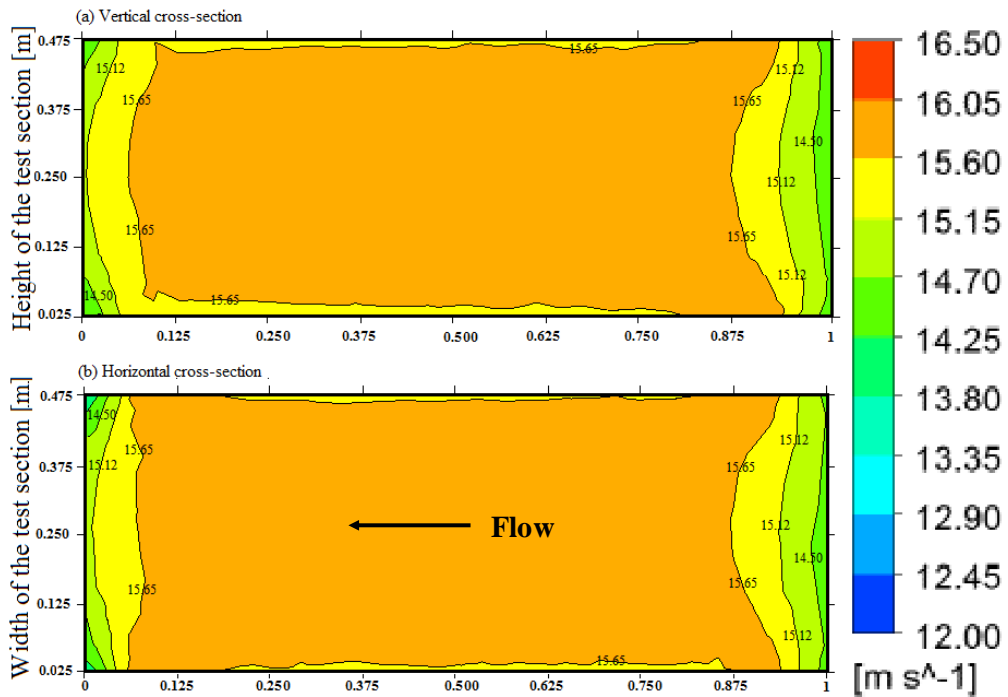
#### D.2.4 Configuration 4: Upstream and Downstream guide vanes

Figure D.7 shows the velocity streamlines of a middle plane in the wind tunnel with upstream and downstream guide vanes. The formation of velocity rotations at the corners which were observed from configurations 1 - 3 were eliminated by adding guide vanes to the upstream and downstream 90° corners. The upstream corner guide vanes with 0.1m trailing edges effectively maintained a comparatively straight flow throughout the upstream circuit and no over or under turn were observed. It can be seen that the lower vanes effectively forcing the flow to be parallel to the test section centre line and improved the uniformity of the flow before the contraction section. Furthermore, the third corner guide vane with 0.1m leading and trailing edges effectively directed the flow to the upper downstream sections without over and under turn. The fourth corner guide vanes sufficiently reduced the velocity variation of the return flow before the fan section.



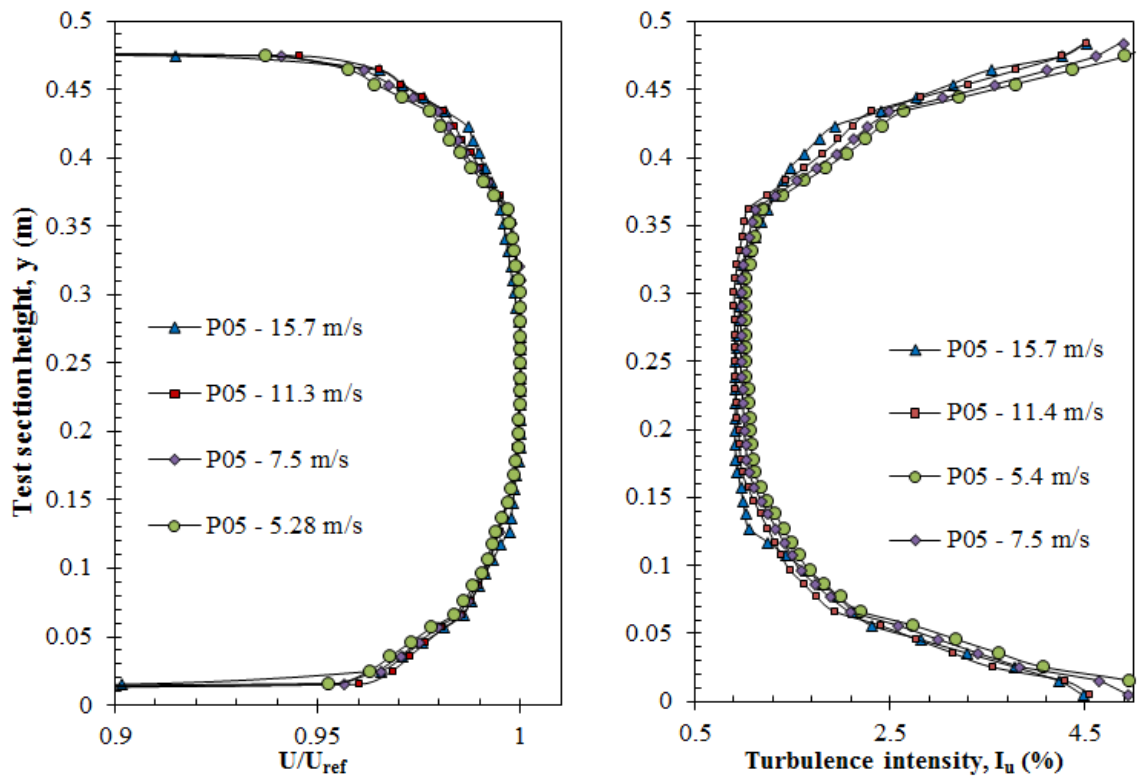
**Figure D.7** Velocity streamline for configuration 4: upstream and downstream guide vanes.

Figure D.8 shows a close up view of the vertical and horizontal wind speed profile in the test section of the fourth configuration. The effect of the addition of the guide vanes in all corners was evident from the velocity contour; symmetric uniform flow was observed throughout the entire test section length.



**Figure D.8** Contours of velocity magnitude in a (a) vertical plane and (b) horizontal plane at 0.250 m height of the test section for the wind tunnel with upstream and downstream guide vanes.

The simulations were carried out with the following inlet pressure: 17.5, 35, 70, and 140. Figure D.9 displays the vertical wind speed and turbulence intensity profile at point P – 05 (middle). Similar trend was observed for the velocity and turbulence profiles at different inlet conditions with the turbulence intensity increasing as the test section speed decreases. Average turbulence intensity across the vertical profile increased by 12% when test section speed was reduced from 15.7 to 7.5 m/s (measured from middle point P05).



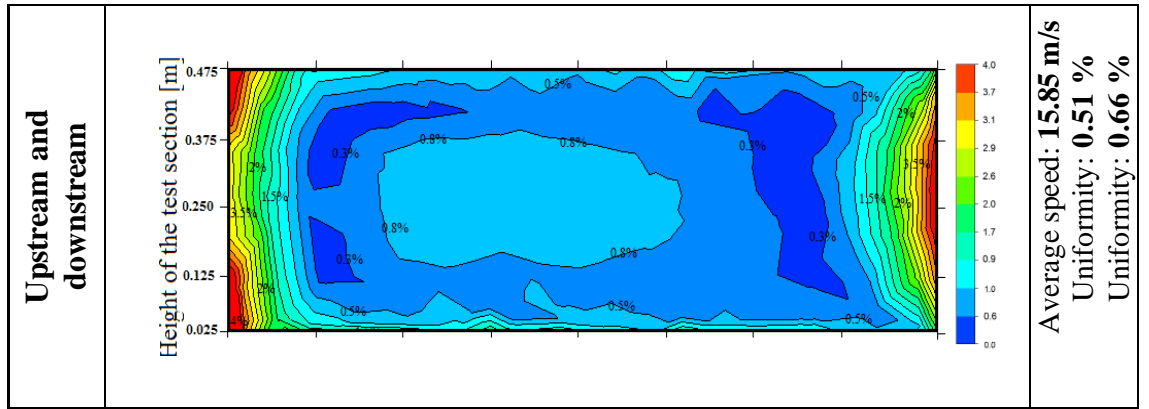
**Figure D.9** Comparison between the dimensionless velocity and turbulence intensity profiles of the flow at the test section for different inlet conditions (Configuration 4).

Table D.1 summarises the flow uniformity results in the test section for the guide vane configurations. Note that the flow separations occurring near the walls were not included in this analysis hence, the top, bottom and side (0.025 m from wall) of the actual test section were not shown. Adding the guide vanes to the wind tunnel upstream corners improved the airflow uniformity by 36% and combining upstream with downstream guide vanes improved the uniformity by 65%. The situation with only downstream guide vane was worse than in the case of only upstream guide vanes, improving the uniformity by only 10%. This clearly indicates that the quality of the flow in the test section was

more affected by the flow condition in the upstream section than the downstream section. Hence, special attention must be given while designing the guide vane at the upstream corners particularly the section in line with the test section.

**Table D.1** Percentage uniformity of flow in test section for the different guide vane configurations.

	Horizontal cross section (Z = 0.25 m)	Data
No guide vanes		Average speed: <b>16.27 m/s</b> Average uniformity: <b>1.44</b>
Upstream guide vanes		Average speed: <b>15.97 m/s</b> Average uniformity: <b>0.92</b>
Downstream guide vanes		Average speed: <b>16.07 m/s</b> Average uniformity: <b>1.28</b>



### D.3 Wind tunnel test section with test block

Figure D.10 shows the comparison between the measured and CFD values for the dimensionless velocity X, Y and Z for points A – G around the block type model. A good agreement was seen between both methods of analysis with the CFD model slightly over (Y - velocity component) and under (X and Z - velocity components) estimating the results. The error was less than 10% for all velocity components for all points except for point C (y – velocity component), which was due to a small misalignment of the positioning or angle of the probe and point G (x and y - velocity component) which was located at the wake region of the airflow around the test block. This was one of the limitations of the k-epsilon turbulence model, not performing well for complex flows such as severe pressure gradients and large flow separations.

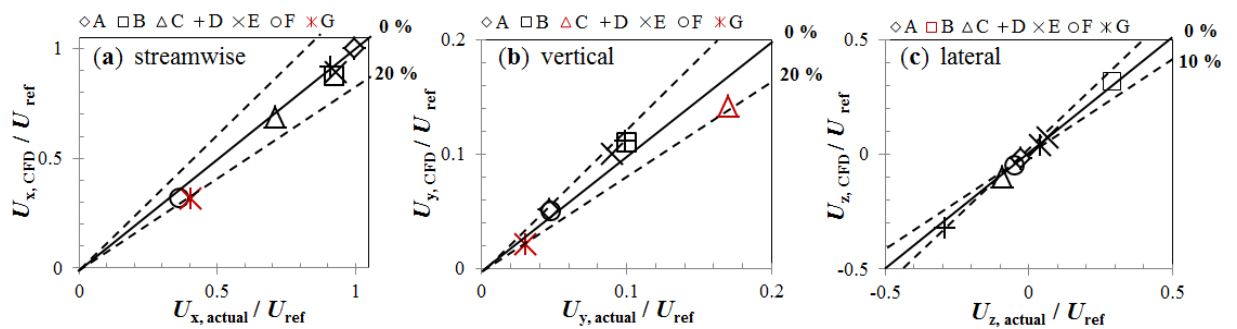


**Figure D.10** Comparison between the measured and CFD values for the dimensionless velocity components X (a), Y (b) and Z (c) for points A – G around the block type model. Data were made dimensionless with respect to the measured value at point A.

Dotted lines indicate  $\pm 10 - 20\%$  error.

Figure D.11 shows the comparison between the measured and CFD values for the turbulence intensity for points A – F around the block type model. As expected highest level of turbulence was observed for point C, E and F (front surface – top and middle point) which corresponds to the reduction of speed at those points. The measured turbulence intensity along the right and left side (Point B and D) of the block were close, indicating the flow symmetry for the zero incident angle wind. The CFD results were consistent with the experimental data; with all the measurement points error below 10% except for point B and G which was slightly above 10%.

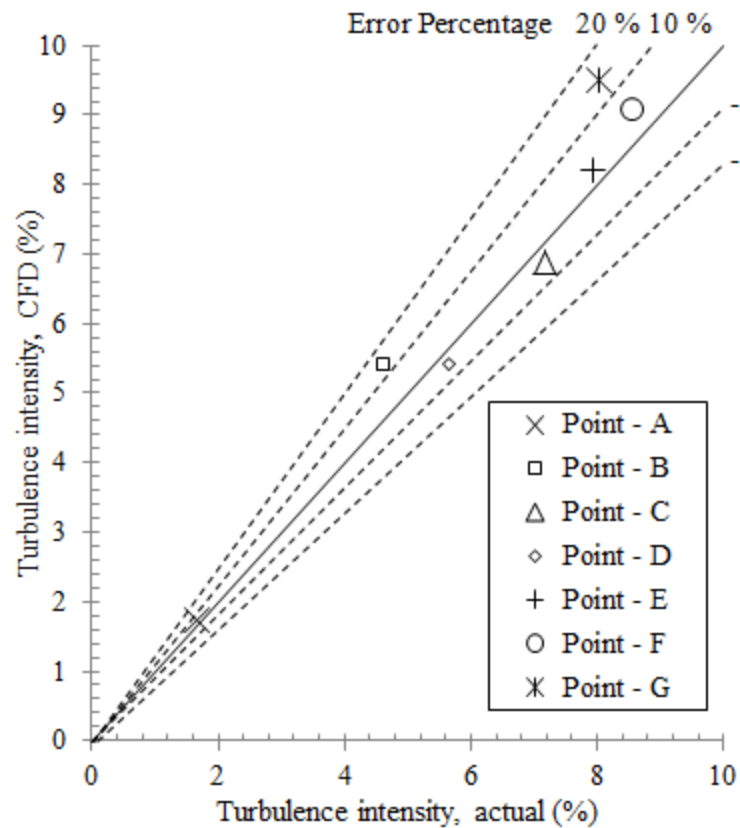


**Figure D.11** Comparison between the measured and CFD values for the turbulence intensity for points A – G around the block model. Dotted lines indicate the error percentage.